PRINT ISSN : 2395-6011
ONLINE ISSN : 2395-602X

Techno Science Academy
The International Open Access Publisher

INTERNATIONAL CONFERENCE ON ADVANCED MATERIALS (ICAM- 2017)

Organised by

Department of Physics
School of Physical Sciences
St. Joseph's College (Autonomous), Tiruchirappalli-620 002
Tamilnadu,India

VOLUME 3, ISSUE 11, NOVEMBER-DECEMBER-2017

INTERNATIONAL JOURNAL OF SCIENTIFIC RESEARCH IN SCIENCE & TECHNOLOGY

Email : editor@ijsrst.com Website : http://ijsrst.com

INTERNATIONAL CONFERENCE ON ADVANCED MATERIALS (ICAM- 2017)

In Association With

International Journal of Scientific Research in Science and Technology

Print ISSN: 2395-6011 Online ISSN : 2395-602X
UGC Approved Journal [Journal No : 64011]

Volume 3, Issue 11, November-December-2017

International Peer Reviewed, Open Access Journal

Organised by

Department of Physics,
School of Physical Sciences, St. Joseph's College (Autonomous)
Tiruchirappalli - 620 002
Tamilnadu, India

Published By

Technoscience Academy
(The International Open Access Publisher)

[www.technoscienceacademy.com]

ABOUT THE INSTITUTION

St. Joseph's College is an affiliated First Grade College of the Bharathidasan University. It was established in 1844 by the Fathers of Society of Jesus. The college celebrated its centenary in 1944, sesquicentenary in 1995 and acquired the Five Star status, awarded by NAAC in 2000. The college was conferred the prestigious status of College with Potential for Excellence (CPE) by UGC in 2004, Reaccredited by NAAC with 'A+' Grade in 2006 and Accredited again by NAAC at 'A' Grade in 2012. Many departments of our college have been sponsored by DST-FIST and DBT-STAR programmes. This is the only college from Tamil Nadu conferred with Special Heritage status by UGC in the year 2015. The college trains young men and women of quality to be leaders in all walks of life so that they serve the people of the Nation in truth, justice and love. Accordingly, this college strives to be an agent of social change, by incorporating the scientific and technological growth in its UG, PG and Research (M.Phil./Ph.D.) curricula. In accordance with the Jesuit vision of higher education, this college aspires to offer holistic education, leading to the total formation of the individual within the human community.

PHYSICS DEPARTMENT

This century-old Department of Physics started B.A Physics (1881), B.Sc (Hons.) Physics (1911), B.Sc Physics (1930), M.Sc Physics (1961), Ph.D. (1971) and M.Phil (1977). Other than its own evolution it had given birth to two departments, Computer Science (1983) and Electronics (1993). The quality of the education imparted in this department can be understood from the message of Sir C.V. Raman, the Indian Nobel Laureate on the occasion of college Centenary Celebration 1944. "The St. Joseph's College, Trichinopoly, has played a great part in the development of higher education in Southern India. Many of its former alumni who have taken the Honours course in Physics from that College have subsequently been research students in my laboratory and achieved conspicuous success. They now hold distinguished positions in various parts of India". It is no wonder that our former President His Excellency Dr. APJ Abdul Kalam is one of our proud alumni. The department is blended with its tradition and growth in science and technology upto date in various dimensions. The department is constantly developing with the continuous support of the management and the funding of UGC, DST-FIST and CSIR. The department faculties are operating minor/major research projects with the funding of UGC, CSIR and DRDO. The department had established National and International collaboration in many fields of research in recent years and organizes symposiums and conferences periodically at National and International level to ignite the students with scientific sprit.

OBJECTIVES OF THE CONFERENCE

Material Science is a multidisciplinary branch of science and technology, investigates the relationship between the structure of materials and their micro/ macroscopic properties. In recent years with significant focus on Nano Science and Nanotechnology, Materials Science becomes a more significant field of science and engineering.

* This conference highlights the fundamentals, synthesis, characterization, analysis and applications of materials.
* To create scientific and research temper among the students and researchers through the interaction with the experts in this field.
* To provide a platform for researchers to share their knowledge and expertise with other researchers of their related fields.
* To get exposure to the latest developments in the field of material science from scientists and experts.

FOCUS AREA OF THE CONFERENCE

This conference focuses on the latest developments on advanced materials such as

Nano Materials, Nonlinear Materials, Composite Materials, Laser Materials, Semiconductors, Conductors, Superconductors, Dielectrics, Luminescence Materials, Organic Materials, Fluorescence Materials and Storage Materials.

CONTENTS

International Journal of
Scientific Research in Science and Technology (IJSRST)
Print ISSN : 2395-6011, Online ISSN : 2395-602X
International Conference on Advanced Materials
Held on 14, 15 December 2017, Organized by Department of Physics,
St. Joseph's College, Trichy, Tamilnadu, India

Synthesis and Optical Studies on Concentration Dependent Dy^{3+} Doped Lithium Fluoroborate Glasses for W-LED Applications

V. Anthony Raj[1, 2] , I. Arul Rayappan[2,*]

[1]Department of Physics, Bishop Heber College, Trichy-620017.

[2]Department of Physics, St. Joseph's College, Trichy-620002.

Corresponding authors: * arulroy@gmail.com

Abstract

A new series of Dy^{3+} doped Lithium fluoroborate glasses with the chemical composition $(40–x)B_2O_3 + 20ZnO + 20NaF + 20Li_2O + xDy_2O_3$ (where x = 0.1, 0.3, 1.0, 2.0 and 3.0 wt%) were prepared following conventional melt quenching technique and characterized using XRD, FTIR, optical absorption and luminescence measurements. The XRD pattern of the prepared glasses confirms the amorphous in nature. The fundamental stretching vibrations of various borates (BO_3, BO_4) were identified through the FTIR analysis. From the UV-Vis-NIR spectra, the oscillator strength and bonding parameter were calculated. The ionic bond nature of the prepared glasses were identify from their negative sign of δ. The luminescence spectra exhibit two visible bands $^4F_{9/2}\rightarrow{}^6H_{15/2}$ (Blue) and $^4F_{9/2}\rightarrow{}^6H_{13/2}$ (Yellow) respectively. The radiative properties such as peak wavelength and effective band width for the $^4F_{9/2}\rightarrow{}^6H_{15/2}$ and $^4F_{9/2}\rightarrow{}^6H_{13/2}$ emission transition were calculated. The decay lifetime of the $^4F_{9/2}$ level has been measured from the decay profiles and compared with the calculated lifetimes. The yellow to blue (Y/B) ratios and color coordinates have been calculated from the luminescence spectra and the utility of the present glasses for white light emitting diodes (W-LEDs) applications.

Keywords: Borate glasses, Melt quenching technique, Bonding parameter, Oscillator strengths, Life time, W-LED.

Introduction

Among the trivalent rare-earth ions, Dy^{3+} ($4f^9$) is quite interesting, because Dy^{3+} doped glasses have been considered as promising luminescent materials and also most suitable to analyze the spectroscopic properties with the change in concentration as well as glass composition. Several researchers reported the luminescence properties of Dy^{3+} ions in different glass matrices [1]. For efficient luminescence from the RE ion, the selection of glass host is an important issue. Among the oxide glasses, borate glasses have been the subject of interest for quite some time due to their high transparency, low melting point, high thermal stability and good rare earth ion solubility [2]. Because borate has been chosen as a host matrix for the present work. There has been a considerable interest in the study of borate based glasses over the past few years due to their interesting structural and optical properties. A striking characteristic feature of the borate glasses is the variations in its structural properties when alkaline or alkali earth cations are introduced [3, 4]. The addition of heavy metal oxides into glasses increases the mechanical strength and radiative transition rate of the RE ions and also reduces the glass transition [5, 6]. The higher phonon energy of the borate glasses can be reduced by adding NaF which enhances the quantum efficiency and the fluoride content reduces the non-radiative decay and in turn enhances the luminescence yield [7].

Dysprosium is the best choice for white light applications because of its two dominant emission bands such as $^4F_{9/2}\rightarrow{}^6H_{15/2}$ and $^4F_{9/2}\rightarrow{}^6H_{13/2}$ energy levels transitions in the visible region [7-10]. The

International Journal of
Scientific Research in Science and Technology (IJSRST)
Print ISSN : 2395-6011, Online ISSN : 2395-602X
International Conference on Advanced Materials
Held on 14, 15 December 2017, Organized by Department of Physics,
St. Joseph's College, Trichy, Tamilnadu, India

$^4F_{9/2} \rightarrow {}^6H_{15/2}$ emission band is due to the magnetic dipole transition and the $^4F_{9/2} \rightarrow {}^6H_{13/2}$ emission band is due to the electric dipole transition and this transition is highly affected by the host matrix and the intensity of the yellow emission band can be modified by the ligand field around the RE-ion site. White light can be stimulated from the Dy^{3+} doped glass materials by adjusting the yellow to blue (Y/B) intensity ratio by varying the glass composition, RE ion concentration and excitation wavelengths [11]. In the CIE 1931 chromaticity diagram, the line related between blue and yellow region usually passes through the white light region and therefore the ability of the white light emission by the Dy^{3+} doped glasses can be confirmed through the CIE color chromaticity coordinates. The better white light can be stimulated from the Dy^{3+} doped glass materials at suitable Y/B intensity ratio by selecting the different ligand field strengths.

The aim of the present work is (i) to prepare Dy^{3+} doped lithium fluoroborate glasses following the melt quenching technique with varying Dy^{3+} ion concentrations; (ii) to identify the different vibrational bands of the borate network in the prepared glasses; (iii) to evaluate the predominant covalent/ionic nature and to determine the direct and indirect band gaps from the absorption spectra; (iv) to calculate the oscillator strengths and Judd-Ofelt parameters (Ω_2, Ω_4, Ω_6) from the absorption energy levels and refractive index of the prepared glasses; (v) to study the luminescence characteristics of the thermally coupled energy level transition $^6F_{11/2} \rightarrow {}^6H_{15/2}$ in the visible region and the $^6H_{11/2} \rightarrow {}^6H_{15/2}$ transition in the NIR region; (vi) to calculate the radiative parameters of the desired transitions; (vii) to determine the stimulated emission cross-section of the $^4F_{9/2} \rightarrow {}^6H_{15/2}$ and $^4F_{9/2} \rightarrow {}^6H_{13/2}$ transitions (viii) to determine the optical gain bandwidth and figure of merit of the $^4I_{13/2} \rightarrow {}^6H_{15/2}$ transition. (ix) The characteristic of the emission color was examined through CIE 1931 chromaticity diagram. And finally (x) Decay curves of the $^4F_{9/2}$ energy level have been measured and the possibility of energy transfer between Dy^{3+}-Dy^{3+} ions in the prepared glasses have also been discussed and reported.

Experimental

The Dy^{3+} doped lithium fluoroborate glasses were prepared with the composition $(40–x)B_2O_3 + 20ZnO + 20NaF + 20Li_2O + xDy_2O_3$ (where x = 0.1, 0.3, 1.0, 2.0 and 3.0 wt%) using conventional melt quenching technique. The Glass Samples are labeled as BZL0.1D, BZL0.3D, BZL1.0D, BZL2.0D and BZL3.0D respectively. All the precursors used for the preparation of glasses are of high purity analytical grade (99.99%) from Sigma Aldrich. About 12g batch of the chemicals were weighted and ground thoroughly in an agate mortar to obtain a homogeneous mixture. The mixture was taken in a porcelain crucible and heated to 950^{0}C in an electrical furnace for 2 hour. The melt was then poured on to a preheated brass plate and kept at 350^{0}C for 7 h in order to remove strains from the annealing process. The glasses were slowly cooled to room temperature (RT). The prepared glasses were well polished on both sides to obtain optical quality glasses for optical measurements.

The XRD patterns were recorded by using JEOL 8030 X-ray diffractrometer employing CuKα radiation. The infrared transmittance spectra of the prepared glasses were recorded using JASCO FTIR 460 plus in the mid-IR region (400–4000 cm^{-1}) with a spectral resolution of ±1.0 cm^{-1} and 16 scans per sample. The absorption spectral measurements were made employing Perkin-Elmer Lambda 950 UV–vis-NIR spectrophotometer in the wavelength range 350–1800 nm. The luminescence spectra were recorded in the wavelength range 500–600 nm with JobinYVon Fluorolog-3 spectrofluorometer using xenon lamp (450 W) as an excitation source. Luminescence spectra in the wavelength region 1400–1700 nm were recorded using EG&G Princeton Applied Research model 5210 with a spectral resolution of ±0.5 nm. The decay measurements were made employing the FLS 920 Edinpurgh spectrometer. All the measurements were carried out as room

International Journal of
Scientific Research in Science and Technology (IJSRST)
Print ISSN : 2395-6011, Online ISSN : 2395-602X
International Conference on Advanced Materials
Held on 14, 15 December 2017, Organized by Department of Physics,
St. Joseph's College, Trichy, Tamilnadu, India

temperature (RT) only. The physical properties of prepared glasses were calculated using the relevant expressions reported in literature [12] and the results are presented in Table 1.

Results and discussion

XRD Analysis

The X-ray diffraction (XRD) pattern has been recorded in the range 10°≤θ≤ 80°.The XRD pattern of the BZL1.0D glass shown in figure1. The XRD Pattern does not exhibit and detectable sharp characteristics peak, but the broad diffused scattering occurs at the lower angles, which is the characteristic long range structural disorder confirms the amorphous nature and non-crystalline structure of the prepared glass. Remaining the glass samples also exhibit similar in nature, so they are not shown for the glasses in figure1.

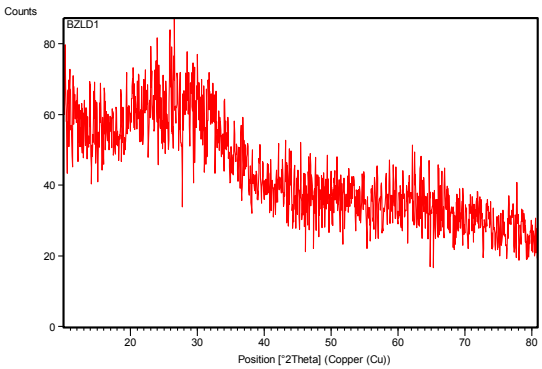

Figure 1. XRD pattern of Dy^{3+} doped lithium fluoroborate BZL1D glass

Table 1. Physical properties of the Dy^{3+} doped lithium fluoroborate glasses

Physical Properties	BZL0.1D	BZL0.3D	BZL1.0D	BZL2.0D	BZL3.0D
Density, ρ (g/cm³)	3.064	3.233	4.620	3.537	3.626
Refractive index, n_d (589.3 nm)	1.582	1.585	1.589	1.592	1.597
Dy^{3+} ion concentration, N_E (10^{20} ions/cm³)	0.662	2.104	9.647	14.01	20.50
Polaron radius, r_p (Å)	9966	677.3	407.7	360.0	317.1
Inter ionic distance, r_i (Å)	2472	1681	1012	893.5	787.0
Field strength, F (10^{14} cm^{-2})	0.491	1.061	2.928	3.757	4.842
Molar refractivity, R_m (cm³)	13.35	12.65	9.256	11.63	11.40
Dielectric constant, (ε)	2.502	2.512	2.524	2.534	2.550
Reflection losses, R (%)	5.080	5.121	5.175	5.216	5.284
Molar volume, V_m (cm³/mol)	0.109	0.349	1.601	2.327	3.405
Electronic polarizability, α_e (10^{-22} cm³)	12.04	3.803	0.834	0.576	0.396

FTIR spectral studies

Figure 2 shows the FTIR spectra of the prepared glasses recorded between 400-4000 cm^{-1}. The FTIR spectra of Dy^{3+} doped lithium fluoroborate glasses and band positions corresponding to their band assignments of all the glasses matrices are given in table 2. The FTIR spectra are the powerful tool to analyze the structure of B-O network and also influenced by the addition of dopant ions. The broad absorption band around 3440-3446 cm^{-1}is observed in all the glasses are attributed to the fundamental O-H stretching vibrations which reveals the presence of strong hydroxyl groups. The observed bands around 2620–2920 cm–1 are mainly due to the occurrence of Hydrogen bonding.

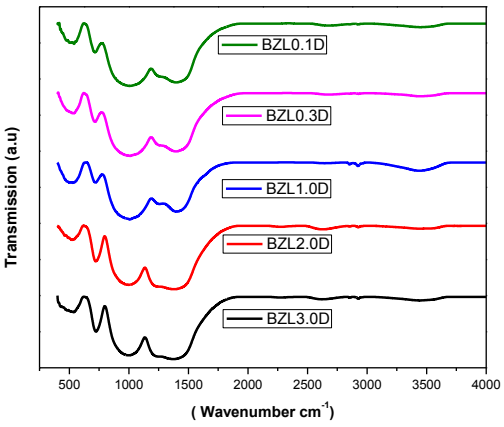

Figure 2. FTIR spectra of Dy^{3+} doped lithium fluoroborate glasses

The absorption bands centred at around 1370 cm^{-1}-1391 cm^{-1} are attributed to B-O vibrations bond in isolated pyroborate group, trigonal boron groups and B–O bond asymmetric vibrations from pyro- and ortho-borate groups respectively. The absorption band is 991-1004 cm^{-1}, are attributed to presence of Stretching of BO_4 groups and the absence of the absorption band around 806 cm^{-1} indicates that, there is no boroxyl ring formation in the prepared glasses. The peak at 715-720 cm^{-1} is due to the bending vibrations of bridging oxygen in B-O-B from pentaborate groups. The asymmetric bending vibration of [BO_3] pyramidal units are

International Journal of
Scientific Research in Science and Technology (IJSRST)
Print ISSN : 2395-6011, Online ISSN : 2395-602X
International Conference on Advanced Materials
Held on 14, 15 December 2017, Organized by Department of Physics,
St. Joseph's College, Trichy, Tamilnadu, India

observed around 522-535 cm^{-1}. The Zn-O stretching vibrations was confirmed from the band around 450-466 cm^{-1}.

Absorption spectra

The UV–Vis-NIR absorption spectra of the Dy^{3+} doped lithium fluoroborate glasses recorded in the wavelength region between 350 nm and 2000 nm is shown in figure 3. The absorption band positions of the prepared glasses are presented in Table 3. The absorption spectra for all the prepared glasses are alike with small variations in intensities of the observed transitions and closely resemble the spectra reported for Dy^{3+} doped glasses [13]. The absorption spectra of the title glasses exhibit nine distinct in-homogeneously broadened absorption bands were observed. These absorption bands are due to the transitions from the $^6H_{15/2}$ ground state to the several excited states such as $^6H_{11/2}$, $^6F_{11/2}$, $^6F_{9/2}$, $^6F_{7/2}$, $^6F_{5/2}$, $^6F_{3/2}$, $^6F(3)_{9/2}$, $^4I(3)_{15/2}$ and $^4H(4)_{11/2}$ corresponding to the wavelengths at 1665, 1260, 1080, 890, 799, 748, 523, 447 and 421 nm respectively.

Table 2. FTIR spectra of Dy^{3+} Doped lithium fluoroborate glasses

S. No.	BZL0.1D	BZL0.3D	BZL1.0D	BZL2.0D	BZL3.0D	Assignments
1	3440	3446	3431	3440	3440	Fundamental stretching of OH group
2.	2672	2670	2920	2637	2628	Hydrogen bonding
4.	1392	1398	1398	1378	1370	B-O Stretching vibration in BO_3 units of meta, pyroborate and orthoborate groups.
5.	1004	1003	1002	997	991	Stretching of BO_4 groups
6.	717	715	717	720	716	Bending vibrations of bridging oxygen in B-O-B from pentaborate groups
7	523	535	525	529	522	Stretching vibrations of [BO_3] pyramidal units
8	450	466	463	457	465	Zn-O stretching vibration

The spin allowed ($\Delta S=0$) transitions $^6H_{15/2} \rightarrow {}^6F_{11/2}$ possess higher absorption intensity than the other transitions and the same is observed in the lower energy region. Nephelauxetic ratios (β) were calculated from the absorption spectra using the relation $\beta = \nu_c/\nu_a$, where β is the ratio between the wavenumber (in cm^{-1}) of a particular transition of the RE ion under investigation and the wavenumber (in cm^{-1}) for the corresponding transition of an aquo-ion. Bonding parameter (δ) have been calculated from the average values of β (referred as $\bar{\beta}$) using the following expression, $\delta = (1- \bar{\beta})/\bar{\beta}$. The nature of the bonding will be covalent or ionic depending upon the positive or negative sign of δ and the values are found to be -1.6487, -1.5779, -1.4897, -1.1083 and -1.1267 corresponding to the prepared BZL0.1D, BZL0.3D, BZL1.0D, BZL2.0D and BZL3.0D glasses respectively.

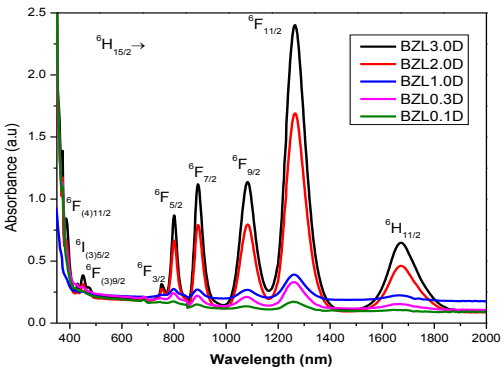

Figure 3. Absorption spectra of Dy^{3+} doped lithium fluoroborate glasses

It is observed from these results that, the bonding between Dy^{3+} ion and ligands is of ionic in nature and the ionic nature gradually decreases with the increase in Dy^{3+} ion concentration.

Oscillator strengths and Judd-Ofelt parameters

The intensity of the absorption bands can be characterized through the oscillator strength values of the f-f electronic transitions in the RE ions. The experimental oscillator strengths (f_{exp}) of the absorption bands are calculated from the relative areas under the absorption bands of the individual transition in the absorption spectra of the RE ions

International Journal of
Scientific Research in Science and Technology (IJSRST)
Print ISSN : 2395-6011, Online ISSN : 2395-602X
International Conference on Advanced Materials
Held on 14, 15 December 2017, Organized by Department of Physics,
St. Joseph's College, Trichy, Tamilnadu, India

doped materials. The experimental (f_{exp}), calculated (f_{cal}) oscillator strengths and rms deviation for the observed band positions of the Dy^{3+} doped lithium fluoroborate glasses are presented in table 4. Judd-Ofelt intensity parameters Ω_2, Ω_4, and Ω_6, are obtained from the experimental spectral intensities and the doubly reduced matrix elements using JO theory [14]. The JO parameters have been calculated and the same are presented in table 5. The JO analysis for the Dy^{3+} ions is in good agreement with f_{exp} and f_{cal} for the intense transitions and moderate agreement in the case of weak transitions.

The JO intensity parameters of all the prepared glasses follow the trends $\Omega_2 > \Omega_4 > \Omega_6$ and is similar to the reported glasses [15-20]. The Ω_2 values are found to be higher than the Ω_4 and Ω_6 intensity parameter. The higher magnitude of Ω_2 in the present glasses suggests that degrees of covalancy of Dy-O bond and higher asymmetry around the Dy^{3+} ions. The spectroscopic quality factor (Ω_4 / Ω_6) is an important parameter used to describe the optical quality of the prepared glasses and is calculated from the Ω_4/Ω_6 ratio values of the prepared glasses and the results are presented in table 5. It is observed from these results that among the prepared glasses, BZL0.3D glass is 1.7460 appears to be a better optical glasses. The larger spectroscopic quality factor predicts higher stimulated emission cross section among the prepared glasses.

Table 3. Observed band positions (cm^{-1}) and bonding parameters (β and δ) Dy^{3+} doped lithium fluoroborate glasses\

Transition	ENERGY					Aqua Ion (v_a) (3)
	BZL0.1D	BZL0.3D	BZL1.0D	BZL2.0D	BZL3.0D	
$^6H_{11/2}$	5998	6006	6006	5981	5988	5850
$^6F_{11/2}$	7936	7924	7918	7905	7911	7700
$^6F_{9/2}$	9285	9242	9225	9234	9233	9100
$^6F_{7/2}$	11261	11211	11186	11211	11211	11000
$^6F_{5/2}$	12531	12516	12500	12500	12500	12400
$^6F_{3/2}$	13459	13333	13333	13333	13298	13250
$^6F(3)_{9/2}$	21186	21277	21231	21142	21141	21100
$^4I(3)_{15/2}$	22371	22371	22321	22222	22222	22100
$^4H(4)_{11/2}$	23585	23810	23866	23310	23364	23400
β	1.0167	1.0160	1.0151	1.0112	1.0113	-
δ	-1.6487	-1.5779	-1.4897	-1.1083	-1.1267	

Table 4.The experimental (f_{exp}) and calculated (f_{cal}) oscillator strengths (10^{-6}), number of transitions (N) and rms deviation (δ) of the Dy^{3+} doped lithium fluoroborate glasses

Transition from $^6H_{15/2}$	BZL0.1D		BZL0.3D		BZL1.0D		BZL2.0D		BZL3.0D	
	f_{exp}	f_{cal}	f_{exp}	f_{cal}	f_{exp}	f_{cal}	f_{exp}	f_{cal}	f_{exp}	f_{cal}
$^6H_{11/2}$	0.010	0.025	0.345	0.519	0.791	0.956	0.962	0.933	1.002	0.976
$^6F_{11/2}$	0.190	0.188	3.508	3.484	5.136	5.115	4.947	4.950	4.763	4.766
$^6F_{9/2}$	0.040	0.049	1.230	1.270	1.835	1.890	2.090	2.036	1.861	1.812
$^6F_{7/2}$	0.700	0.035	0.941	0.852	1.279	1.804	1.336	1.591	1.353	1.593
$^6F_{5/2}$	0.010	0.014	0.926	0.344	0.535	1.076	1.028	0.711	1.058	0.758
$^6F_{3/2}$	0.010	0.003	0.090	0.064	0.100	0.202	0.220	0.1342	0.279	0.142
$^6F(3)_{9/2}$	0.030	0.003	0.230	0.064	0.100	0.258	0.066	0.1205	0.117	0.121
$^4I(3)_{15/2}$	0.030	0.008	0.260	0.171	0.278	0.153	0.332	0.0141	0.318	0.337
$^4H(4)_{11/2}$	0.040	0.002	0.182	0.051	0.078	0.230	0.041	0.0244	0.178	0.046
N	9		9		9		9		9	
rms	0.022		0.223		0.218		0.141		0.144	

Luminescence Spectra

The Luminescence behavior of the Dy^{3+} doped Alkali lithium fluoroborate glasses have been studied through the excitation and emission spectral measurements. The excitation spectrum of the title glasses recorded by monitoring an emission at 574 nm is shown in figure 4. It exhibits six bands owing to the electronic transitions at 346nm ($^6P_{7/2}$), 358nm ($^4P_{3/2}$), 382nm ($^4I_{13/2}$) 420nm ($^4G_{11/2}$), 447nm ($^4I_{15/2}$) and 470nm ($^4F_{9/2}$) the transitions respectively [21, 22]. These excitation wavelength are in good agreement with the wavelength of the commercially available UV LEDs having emission range from 350 to 420 nm and blue LEDs having emission ranges from 450-470nm. The intensity of the excitation band observed at 382nm to the $^6H_{15/2} \rightarrow {}^4I_{13/2}$ transition is found to be higher when compared to other transitions, these transitions $^4I_{13/2}$ is more intense which is used to record emission spectra with excitation wavelength of 382nm. The luminescence spectra of Dy^{3+} doped Alkali lithium fluoroborate glasses were recorded by excitation 382nm are shown in figure 5. The luminescence spectra of the prepared glasses exhibit two intense emission bands in the blue (478 nm) and yellow (574 nm) region of the visible spectrum corresponding to the $^4F_{9/2} \rightarrow {}^6H_{15/2}$ and $^4F_{9/2} \rightarrow {}^6H_{13/2}$ transitions respectively. The white light can be generated in Dy^{3+} doped glass materials by UV excitation with the suitable combination of these blue and yellow emission bands.

International Journal of
Scientific Research in Science and Technology (IJSRST)
Print ISSN : 2395-6011, Online ISSN : 2395-602X
International Conference on Advanced Materials
Held on 14, 15 December 2017, Organized by Department of Physics,
St. Joseph's College, Trichy, Tamilnadu, India

The intensity of electric dipole transition $^4F_{9/2} \rightarrow {}^6H_{13/2}$ is found to be higher than the magnetic dipole transition $^4F_{9/2} \rightarrow {}^6H_{15/2}$. The dominant electric dipole transition is a hypersensitive in nature strongly depends upon only by the host matrix strength around the rare earth ion. The bands of the emission peaks are similar in all the glass matrices except the variations in the intensity of the emission transition.

The radiative properties such as radiative transition probability (A) effective band width ($\Delta\lambda_{eff}$) stimulated emission cross-section $\left(\sigma_p^E\right)$ and branching ratios (β_R) for the $^4F_{9/2} \rightarrow {}^6H_{15/2}$ and $^4F_{9/2} \rightarrow {}^6H_{13/2}$ levels for the prepared glasses have been calculated and presented in table 6. The variations in calculated and experimental branching ration values are probably due to the involvement of non-radiative processes. In the present work, branching ratio (β_R), and stimulated emission cross-section $\left(\sigma_p^E\right)$ for the $^4F_{9/2} \rightarrow {}^6H_{13/2}$ lasing transition is found to be higher compared to other transitions. The higher stimulated emission cross-section value indicates the suitability of the prepared BZL1.0D glass for low threshold and high gain laser applications. The gain bandwidth and the optical gain are the two important parameters which should be considering by laser designer to fabricate new efficient visible lasers.

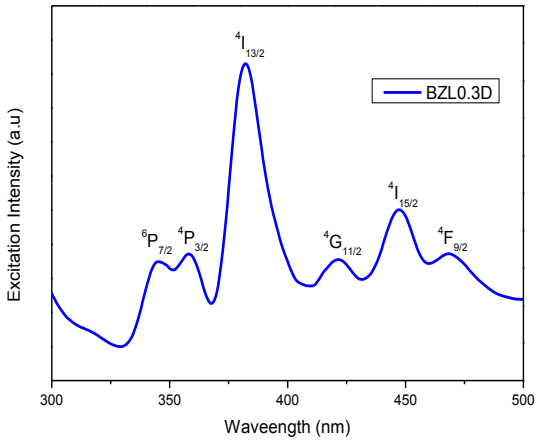

Figure 4. Excitation spectra of Dy^{3+} doped lithium fluoroborate glasses

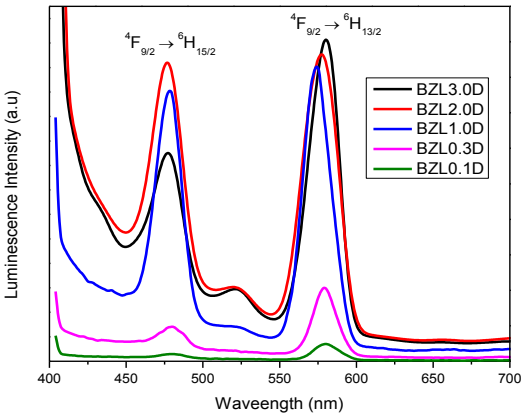

Figure 5. Luminescence spectra of Dy^{3+} doped lithium fluoroborate glasses

Table 5. Judd-Ofelt intensity parameters (Ω_λ, 10^{-20} cm^2) for the Dy^{3+} doped lithium fluoroborate glasses and other reported Dy^{3+} doped glasses

Glass code	Ω_2	Ω_4	Ω_6	Ω_4/Ω_6	Trend	Ref.
BZL0.1D	0.21	0.05	0.03	1.518	$\Omega_2>\Omega_4>\Omega_6$	[Present]
BZL0.3D	3.39	1.44	0.82	1.746	$\Omega_2>\Omega_4>\Omega_6$	[Present]
BZL1.0D	5.12	1.99	1.28	1.559	$\Omega_2>\Omega_4>\Omega_6$	[Present]
BZL2.0D	4.88	1.82	1.69	1.073	$\Omega_2>\Omega_4>\Omega_6$	[Present]
BZL3.0D	5.08	1.80	1.24	1.453	$\Omega_2>\Omega_4>\Omega_6$	[Present]
Lithium borate	3.24	0.92	0.82	1.122	$\Omega_2>\Omega_4>\Omega_6$	15
L4BA	9.85	4.35	2.47	1.761	$\Omega_2>\Omega_4>\Omega_6$	16
Dy:LiLTB	8.75	2.62	2.07	1.266	$\Omega_2>\Omega_4>\Omega_6$	17
L2BTAFDy	9.36	2.87	2.82	1.018	$\Omega_2>\Omega_4>\Omega_6$	18
1.0LBTPD	10.30	3.53	2.79	1.265	$\Omega_2>\Omega_4>\Omega_6$	19
BTLN2D	6.00	1.86	1.25	1.490	$\Omega_2>\Omega_4>\Omega_6$	20

Table 6. Emission band position (λ_p, nm), effective band width ($\Delta\lambda_{eff}$, nm), radiative transition probability (A, s^{-1}), stimulated emission cross-section ($\sigma_p^E \times 10^{-22}$ cm^2), calculated and experimental radiative branching ratios (β_R), for the Dy^{3+} doped lithium fluoroborate glasses

Glass code	Transitions	λ_p	$\Delta\lambda$eff	A	σ_p^E	β_R (cal)	β_R (exp)
BZL0.1D	$^6H_{15/2}$	480	1.3370	3.14	0.6417	0.1447	0.0295
	$^6H_{13/2}$	579	4.2361	18.37	2.5840	0.8735	0.1727
BZL0.3D	$^6H_{15/2}$	480	4.1039	78.72	5.3783	0.2120	0.1361
	$^6H_{13/2}$	579	3.6647	340.15	55.0989	0.7879	0.5882
BZL1.0D	$^6H_{15/2}$	478	6.2528	119.83	5.2578	0.3916	0.1436
	$^6H_{13/2}$	577	5.1518	516.20	57.7114	0.6083	0.6184
BZL2.0D	$^6H_{15/2}$	476	5.7884	150.10	6.9697	0.3564	0.1705
	$^6H_{13/2}$	577	6.0657	531.48	50.8483	0.6435	0.6036
BZL3.0D	$^6H_{15/2}$	477	6.2286	116.64	5.0441	0.2751	0.1407
	$^6H_{13/2}$	580	5.4634	514.14	55.4080	0.7249	0.6203

International Journal of
Scientific Research in Science and Technology (IJSRST)
Print ISSN : 2395-6011, Online ISSN : 2395-602X
International Conference on Advanced Materials
Held on 14, 15 December 2017, Organized by Department of Physics,
St. Joseph's College, Trichy, Tamilnadu, India

Energy level diagram

The figure 6 shows the partial energy level diagram of the Dy^{3+} doped lithium fluoroborate glasses along with the probable radiative and non-radiative emission transitions are presented. While exciting the Dy^{3+} doped lithium fluoroborate glasses at 384 nm the $^4I_{13/2}$ excited state is more popular. Meanwhile it non-radiatively decays from the $^4I_{13/2}$ to $^4F_{9/2}$ lower excited state. The visible emission lines arises from the $^4F_{9/2}$ excited state due to the large energy gap between the $^4F_{9/2}$ energy level to the next lower level $^6F_{3/2}$. From the excited state $^4F_{9/2}$ two characteristic emission transitions $^4F_{9/2} \rightarrow {}^6H_{15/2}$ (blue) and $^4F_{9/2} \rightarrow {}^6H_{13/2}$ (yellow) are observed. In addition to these, at higher concentrations cross-relaxation between adjacent Dy^{3+} ions occur, leading to the observed concentration quenching in the luminescence of the prepared glasses. The Luminescence quenching occurs by the resonant energy transfer (RET) from the $^4F_{9/2}$ excited state to the nearby Dy^{3+} ions in the ground state. Generally cross-relaxation occurs only when the energy of the emission transitions perfectly match with the absorption transition. In energy cross-relaxation channels two Dy^{3+} ions, one ion in ground state and another one in the excited state interchange their energies and reach some intermediate states and then relax non-radiatively. The resonant cross relaxation channels of the Dy^{3+} doped lithium fluoroborate glasses are ($^4F_{9/2} \rightarrow {}^6F_{7/2}$, $^6H_{15/2} \rightarrow {}^6F_{9/2}+{}^6F_{7/2}$), ($^4F_{9/2} \rightarrow {}^6F_{3/2}$, $^6H_{15/2} \rightarrow {}^6F_{11/2}+{}^6F_{9/2}$) and these relaxations quenching visible emissions $^4F_{9/2} \rightarrow {}^6H_{15/2}$ and $^4F_{9/2} \rightarrow {}^6H_{13/2}$. The Dy^{3+} ions after reaching the $^6F_{3/2}$ and $^6F_{7/2}$ intermediate states de-excite to the $^6H_{15/2}$ ground state non-radiatively [9, 11, 23].

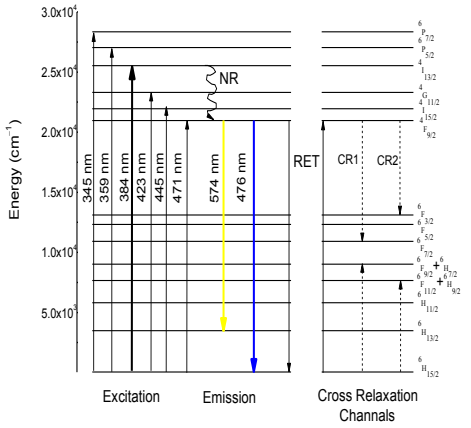

Figure 6. Energy level diagram of the Dy^{3+} doped lithium fluoroborate glasses

Decay analysis

The decay profile corresponding to the $^4F_{9/2}$ excited level of the Dy^{3+} doped lithium fluoroborate glasses were measured by monitoring luminescence at 574nm under 382nm excitation as shown in fig 7. The decay curves exhibit single exponential behavior for the lower concentration glasses up to 0.3 mol % and turn into the non-exponential nature for higher concentration ($\geq$1.0 mol % Dy^{3+}). The non-exponential nature of the luminescence decays increases with increasing concentration of the Dy^{3+} ions indicating that the enhancement of energy transfer processes between the Dy^{3+} ions with increasing concentration in these matrices. The experimental life time of the prepared glasses have been obtained by using non-exponential fitting methods and can be expressed as

$$I = y_0 + A_1 \exp\left(-\frac{t}{\tau_1}\right) + A_2 \exp\left(-\frac{t}{\tau_2}\right)$$

where A_1 and A_2 are constants, τ_1 and τ_2 are the luminescence life times for the two channels responsible for the decay and the experimental lifetime (τ_{exp}) has been calculated by using the relation,

$$\tau_{exp} = \frac{(A_1\tau_1^2 + A_1\tau_2^2)}{A_1\tau_1 + A_2\tau_2}$$

The rate of energy transfer by cross relaxation can be represented as

$$W_{NR} = \frac{\frac{1}{\tau_{exp}} - 1}{\tau_{cal}}$$

The quantum efficiency (η) can be defined as the ratio of number of photons emitted to the number of photons absorbed. For rare earth ions, it is the ratio between the experimental and the radiative lifetimes of the excited state can be expressed as

$$\eta = \frac{\tau_{exp}}{\tau_{cal}} \times 100$$

Table 7 represented the experimental and calculated life times (λ_{exp} and λ_{cal}) non radiative relaxation rates (W_{NR}) and quantum efficiencies (η) for $^4F_{9/2}$ state of Dy^{3+} doped lithium fluoroborate glasses. From the data, it observed that the experimental life times are lower than the calculated life times in all glass matrices. This is mainly due to the presence of non-radiative channels. Among the prepared glasses, BZL0.3D glass exhibit higher quantum efficiency corresponding to the $^4F_{9/2}$ energy level as 68% and is suggested as a potential material for

International Journal of
Scientific Research in Science and Technology (IJSRST)
Print ISSN : 2395-6011, Online ISSN : 2395-602X
International Conference on Advanced Materials
Held on 14, 15 December 2017, Organized by Department of Physics,
St. Joseph's College, Trichy, Tamilnadu, India

laser applications.

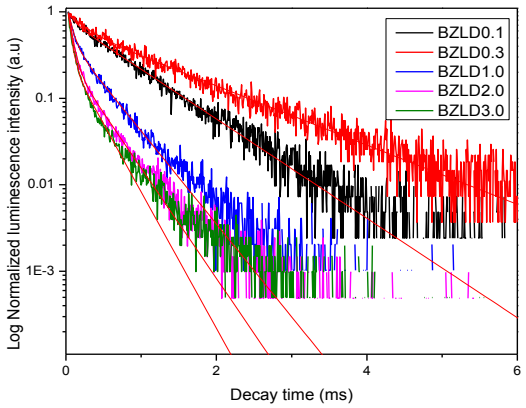

Figure 7. Decay profile corresponding to the $^4F_{9/2}$ energy level of the Dy^{3+} doped lithium fluoroborate glasses

Table 7. The calculated (λ_{cal}) experimental (λ_{exp}) lifetime, quantum efficiency η (%) energy transfer parameter (Q), critical transfer distance (R_0) Energy Transfer rate (C_{DA}) and the non-radiative transition (W_{NR}) of the Dy^{3+} doped lithium fluoroborate glasses

Glass code	λ_{cal}	λ_{exp}	η (%)	W_{NR}
BZL0.1D	9400	730	7.7659	0.001263
BZL0.3D	1729	1180	68.2475	0.000269
BZL1.0D	1198	330	27.5459	0.002196
BZL2.0D	1135	222	19.5594	0.003623
BZL3.0D	1206	179	14.8424	0.004757

White Light Emission

The assessment and quantification of color is referred as colorimetry and the CIE system is the commonly used method to describe the composition of any color. The color of the luminescent source can be described through the color matching function values and they are dimensionless quantities. The degree of stimulation required to match the color of spectral power density p(λ) is expressed as,

$$X = \int \bar{x}(\lambda)p(\lambda)d\lambda$$

$$Y = \int \bar{y}(\lambda)p(\lambda)d\lambda$$

$$Z = \int \bar{z}(\lambda)p(\lambda)d\lambda$$

where X, Y, Z are the tristimulus values which gives the power for each of three primary colors to match with the color of p(λ) and from the tristimulus values the color chromaticity coordinates x and y can be determined from the following expression,

$$x = \frac{x}{X+Y+Z}$$

$$y = \frac{y}{X+Y+Z}$$

The (x, y) coordinates are used to represent the color and locus of all the monochromatic color coordinates which produces the perimeter of the CIE1931 chromaticity diagram. All the multi chromatic wavelengths are expected to lie within the area of chromaticity diagram. The luminescent intensity of the emission spectral measurements has been characterized using the CIE1931 chromaticity diagram.

The x, y color chromaticity coordinates of the Dy^{3+} doped lithium fluoroborate glasses have been determined and presented in table 8 along with the x, y color chromaticity coordinates of the reported Dy^{3+} doped systems. The chromaticity coordinates are found to be (0.33, 0.31), (0.32, 0.30), (0.30, 0.31), (0.28, 0.28), and (0.29, 0.28) corresponding to the BZL0.1D, BZL0.3D, BZL1.0D, BZL2.0D and BZL3.0D glasses respectively. Figure 8 represents the location of chromaticity coordinates of Dy^{3+} doped title glasses on CIE1931 chromaticity diagram. The chromaticity coordinates of the title glasses appear in the near white light region of the CIE1931 chromaticity diagram. Though they are in the white light region they emit yellowish white light but there is a tendency to move towards the exact white light region due to the decreasing Y/B ratio values.

The correlated color temperature (CCT) has been calculated using the color coordinates employing the McCamy's approximate formula.

$$CCT = -449n^3 + 352n^2 - 6823n + 5520.33$$

where $n = (x - x_e)/(y - y_e)$ is the inverse slope line $x_e = 0.332$, $y_e = 0.186$ is the epicentre. The CCT values of the prepared glasses are prepared glasses are presented in Table 9 and compared with the reported Dy^{3+} doped system [19, 20, 24].

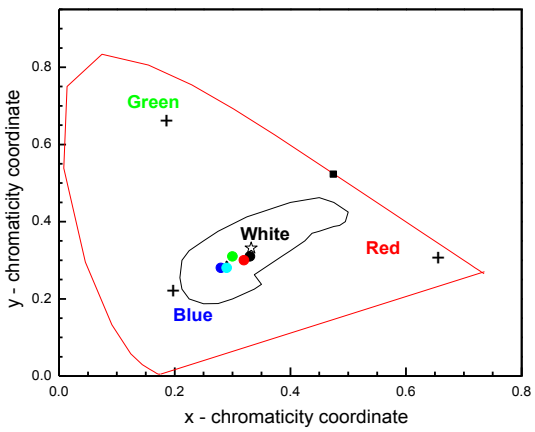

International Journal of
Scientific Research in Science and Technology (IJSRST)
Print ISSN : 2395-6011, Online ISSN : 2395-602X
International Conference on Advanced Materials
Held on 14, 15 December 2017, Organized by Department of Physics,
St. Joseph's College, Trichy, Tamilnadu, India

Figure 8. CIE Color Chromaticity diagram of the Dy^{3+} doped lithium fluoroborate glasses

Table 8. Yellow to blue (Y/B) intensity ratio, chromaticity color coordinates (x, y) and correlated color temperature (CCT, K) of the Dy^{3+} doped lithium fluoroborate glasses with the reported Dy^{3+} doped glasses

Glass Code	Y/B ratio	X	Y	CCT	Ref
BZL0.1D	1.2134	0.33	0.31	5531	[Present work]
BZL0.3D	1.207	0.32	0.30	5596	[Present work]
BZL1.0D	1.1987	0.30	0.31	5727	[Present work]
BZL2.0D	1.212	0.28	0.28	6081	[Present work]
BZL3.0D	1.216	0.29	0.28	5935	[Present work]
LFBMDy10	1.047	0.44	0.42	3080	6
LBO:xDy^3	0.949	0.344	0.37	-	11
1.0LBTPD	-	0.26	0.31	-	19
BTLN2D	1.889	0.39	0.45	4034	20
Lithium fluoroborate	0.600	0.29	0.34	7416	24

Conclusion

The Dy^{3+} doped lithium fluoroborate glasses were prepared and their structural and optical properties were studied through XRD, absorption and luminescence spectral measurements. The XRD pattern confirms the amorphous nature of the prepared glasses. Negative δ values indicate the ionic nature of the Dy^{3+}– O bond in the prepared glasses. The peak wavelength and effective bandwidth were calculated for $^4F_{9/2} \rightarrow {}^6H_{15/2}$ and $^6H_{13/2}$ transitions through the luminescence spectra and the results were reported. The x, y coordinates of the prepared glasses are located in the white light region of the CIE diagram and thus suggests their suitability for white light applications.

References

[1] P.Babu, C.KJayasankar, Journal of optical materials 15(2000) 65-79.

[2] J.S. Kumar, A.M. Bahu, N.K. Giri, S.B. Rai, L.R. Moorthy Journal of Luminescence 130 (2010) 1916-1923.

[3] R.T Karunakaran, K. Marimuthu, S.SurendraBabu, S.Arumugam, Journal of Luminesence 130(2010) 1067-1072.

[4] I. Arul Rayappan, K. Marimuthu, Journal of Non-Crystalline Solids 367 (2013) 43-50.

[5] M.V. Sasikumar, D.Rajesh, A.Balakrishna, Y.C.Ratnakaram Journal of Molecular Structure 1041 (2013) 100-105.

[6] A. Balakrishna, D. Rajesh, Y.C. Ratnakaram Journal of Luminescence 132 (2012) 2984-2991.

[7] R.Vijayakumar, K Marimuthu Journal of Molecular Structure 1092 (2015) 166-175.

[8] Kummara Venkata Krishnaiah, Kagola Upendra Kumar et al. Mater. Express, Vol. 3, No. 1, 2013.

[9] P.P. Pawar, S.R. Munishwar, R.S. Gedam Journal of Alloys and Compounds 660 (2016) 347e355.

[10] D.D. Ramteke, R.S. Gedam Spectroscopy letters 48 (2015) 417-421.

[11] Xin-Yuan Sun, Shuai Wu, Xi Liu, Pan Gao, Shi-Ming Huang Journal of Non-Crystalline Solids 368 (2013) 51-54.

[12] K. Annapoorani, Ch. Basavapoornima, N. Suriya Murthy, K. Marimuthu Journal of Non-Crystalline Solids 447 (2016) 273-282.

[13] R.T. Karunakaran, k.Marimuthu, S.SurendraBabu, Physica B 404 (2009) 3995-4000.

[14] G.S. Ofelt Journal of Chem. Phys.37 (1962) 511.

[15] A Renuka Devi, C.K. Jayasankar, Non-Crystalline Solids 197 (1997) 111.

[16] O. Ravi C. Madhukar Reddy, B. Sudhakar Reddy, B. Deva Prasad Raju Optics Communications, (2014) 312:263.

[17] S.A. Saleem, B.C.Jamalaiah, M. Jayasimhadri et al. Journal of Quantitative Spectroscopy & Radiative Transfer 112 (2011) 78-84.

[18] B.C. Jamalaiah, L. RamaMoorthy, Hyojinseo, Journal of Non Crystalline Solids 358 (2012) 204-209.

[19] S. Selvi, G Venkataiah, S. Arun Kumar, G. Muralidharan, K. Marimuthu Physics B 454 (2014) 72-81.

[20] V. Uma, K. Maheshvaran, K. Marimuthu, G.Muralidharan. Journal of Luminesence 176 (2016) 15-24.

[21] L Vijayalakshmi, V. Naresh B.H. Rudramadevi, S. BuddhuduInternationa Journal of Engineering and Science Vol.4, Issue 9 (2014) 19-25.

[22] R.T. Karunakaran, K. Marimuthu, S. Surendra Babu, S. Arumugam Physics B 404(2009) 3995-4000.

[23] S.A. Azizan, S Hashim, N.A. Razak, M.H.A. Mhareb Journal of Molecular Structure 176 (2014) 20-25.

[24] Sd.Z.A. Ahamed, C.M. Reddy, B.D.P. Raju, Opt. Mater. 35 (2013) 1385-1394.

International Journal of
Scientific Research in Science and Technology (IJSRST)
Print ISSN : 2395-6011, Online ISSN : 2395-602X
International Conference on Advanced Materials
Held on 14, 15 December 2017, Organized by Department of Physics,
St. Joseph's College, Trichy, Tamilnadu, India

Structural and Optical Studies on Dy^{3+} Doped Alkali Zinc Fluoroborate Glasses for White Light Stimulation

P. Arun Jeganatha Joseph[1], I. Arul Rayappan[1*]
[1]Department of Physics, St. Joseph's College, Tiruchirappalli – 620002
*Corresponding author: arulroy@gmail.com

Abstract

The trivalent Dy^{3+} ions doped Alkali zinc fluoroborate glasses with the chemical composition (40-x)B_2O_3+20ZnO+20Na_2O+20NaF+xDy_2O_3 (x = 0.1, 0.3 and 1.0 wt%) were prepared by melt quenching technique. Spectroscopic properties of the prepared glasses were characterized through XRD, FTIR, UV-VIS-NIR absorption spectra and Photoluminescence spectra. The bonding parameters (β and δ) and the oscillator strength were calculated from the absorption spectrum. The negative values of bonding parameters reveal the ionic nature of the prepared glasses. The luminescence spectra exhibit two visible $^4F_{9/2}\rightarrow{}^6H_{15/2}$ (Blue) and $^4F_{9/2}\rightarrow{}^6H_{13/2}$ (Yellow) transitions. The Judd-Ofelt intensity parameters (Ω_2, Ω_4, Ω_6) were determined from the absorption spectra to investigate the nature of metal-ligand bond and symmetry around the Dy^{3+} ion site.The radiative properties bandwidth ($\Delta\lambda_{eff}$, nm), transition probability (A), branching ratios (β_R) and stimulated emission cross-section ($\sigma_P^E \times 10^{-22}$ cm^2) for the $^4F_{9/2}\rightarrow{}^6H_{15/2}$ and $^4F_{9/2}\rightarrow{}^6H_{13/2}$ transitions were calculated. The CIE chromaticity co-ordinates were calculated for all glass samples. The emission colors were found to lie in white light region for prepared glasses and thus can be used for bright white LED's.

Keywords: Glasses, Hypersensitive transitions, Bonding parameter, Emission, White light emission

1. Introduction

Spectroscopic studies of rare earth (RE) ions doped materials draw much attention due to their potential applications in the field of photonics [1,2]. Rare earth (RE)-doped glasses have attracted great attention because of their capability to control the properties like refractive index, density, structure and optical absorption. Among the oxide glasses borate (B_2O_3) is a good glass former, good transparency, good RE ion solubility and thermal stability [3]. Boron is normally established in the glasses in the form of triborate and tetraborate units. The Dy^{3+} ion is an attractive laser ion with optical transitions in the visible as well as infrared region due to its intricate energy level structure. Dy^{3+} ion exhibits strong luminescence in the Blue and yellow spectral region suitable for stimulation of white light where the emission intensities strongly depend upon the concentration of Dy^{3+} ions, glass matrix and excitation energies. The present work reports the structural and optical studies on Dy^{3+} doped alkali zinc fluoroborate glasses for white LED applications.

2. Experimental technique

The Dy^{3+} doped alkali zinc fluoroborate glasses were prepared by conventional melt quenching technique followed by the literature [1,2]. The X-ray diffraction of prepared glasses were recorded using XPERT-PRO X-ray Diffractometer with CuK_α radiation. The FTIR spectra were recorded using Perkin-Elmer in the range of 400 to 4000 cm^{-1} for prepared glass samples. The UV-VIS-NIR spectra were measured at room temperature using JASCO V-750 spectrometer for all glasses. The luminescence

International Journal of
Scientific Research in Science and Technology (IJSRST)
Print ISSN : 2395-6011, Online ISSN : 2395-602X
International Conference on Advanced Materials
Held on 14, 15 December 2017, Organized by Department of Physics,
St. Joseph's College, Trichy, Tamilnadu, India

studies were carried out using Perkin Elmer LS45 Fluorescence spectrometer.

3. Results and discussion

3.1. Structural analysis

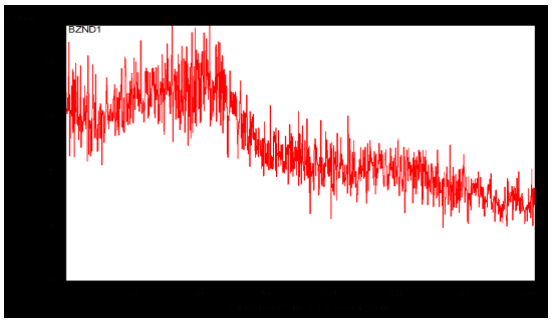

Figure 1. XRD pattern of Dy^{3+}:BZND1.0 alkali zinc fluoroborate glass

The XRD pattern of the Dy^{3+}:BZND1.0 glass as shown in Figure 1. It exhibits broad pattern diffuse at lower scattering angle structural disorder which is confirmed the amorphous nature of the prepared glasses [4].The fundamental stretching units of various functional groups have been identified through FTIR spectra and is shown in Figure 2. The peak appeared at 3437 cm^{-1} is owing to O-H stretching vibrations. The formation of Hydrogen bonding is confirmed at 2924 and 2857 cm^{-1}. The broad band at 1377 cm^{-1} reveals B-O stretching vibrations of BO_3 unit. The band position at around 1007 cm^{-1} is stretching of BO_4 group. The narrow peak at 724 cm^{-1} is because of B-O-B bending vibrations. The Zn-O metal oxide bond formation is ensured by the peak appeared at 485 cm^{-1} [1-3].

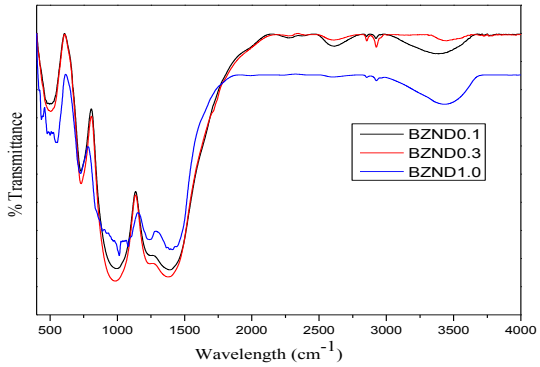

Figure 2. Infrared spectra of Dy^{3+}: alkali zinc fluoroborate glass

3.2. Absorption spectra

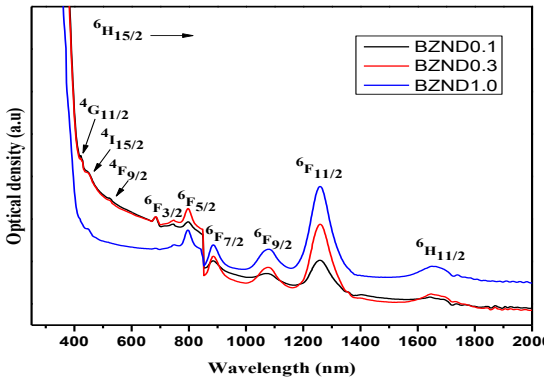

Figure 3. Absorption spectra of Dy^{3+}: alkali zinc fluoro borate glasses

The absorption spectra of Dy^{3+} doped alkali zinc fluoroborate glasses are recorded in the region 200–2000 nm and are shown in Figure 3 which are similar to the other reported Dy^{3+}-doped glasses [2,5]. The optical absorption spectra exhibit several in-homogeneously broadened bands due to f–f transitions from the ground state $^6H_{15/2}$ to various excited state. Among the all transitions $^6H_{15/2} \rightarrow {}^6F_{11/2}$ is the hypersensitive transition which obey the selection rules $|\Delta S| = 0$, $|\Delta L| \leq 2$ and $|\Delta J| \leq 2$ possess higher intensity and also Dy^{3+} ions is sensitive in local environment. From the observed band positions (in cm^{-1}), nephelauxetic ratio (β) and bonding parameter (δ) of the Dy^{3+} doped fluoroborate glasses are calculated and listed in table 1 along with aqua-ion [2]. The bonding parameters were identified as covalent / ionic depending on the positive or negative sign of δ. It is observed from the table 1 that, the negative values indicates the ionic nature.

International Journal of
Scientific Research in Science and Technology (IJSRST)
Print ISSN : 2395-6011, Online ISSN : 2395-602X
International Conference on Advanced Materials
Held on 14, 15 December 2017, Organized by Department of Physics,
St. Joseph's College, Trichy, Tamilnadu, India

Table 1. Observed band positions (in cm^{-1}), $\bar{\beta}$ and δ of the prepared Dy^{3+} doped BZNDx glasses

$^6H_{15/2}$	BZND0.1	BZND0.3	BZND1.0	[2]
$^4G_{11/2}$	23697	23697	23810	23400
$^4I_{15/2}$	22222	22124	22222	22100
$^4F_{9/2}$	21231	21186	21097	21100
$^6F_{3/2}$	13477	13369	13405	13250
$^6F_{5/2}$	12531	12531	12563	12400
$^6F_{7/2}$	11312	11287	11287	11000
$^6F_{9/2}$	9328	9294	9276	9100
$^6F_{11/2}$	7949	7937	7949	7700
$^6H_{11/2}$	6024	6039	6031	5850
$\bar{\beta}$	1.0125	1.0164	1.0204	-
δ	−1.8299	−1.6150	−1.9999	-

Table 2. Experimental and calculated oscillator strengths ($\times 10^{-6}$) of the Dy^{3+} doped alkali Zinc fluoroborate glasses

$^6H_{15/2}$ →	BZND0.1		BZND0.3		BZND1.0	
	f_{exp}	f_{cal}	f_{exp}	f_{cal}	f_{exp}	f_{cal}
$^4G_{11/2}$	0.575	0.058	0.433	0.030	0.314	0.029
$^4I_{15/2}$	0.506	0.209	0.563	0.183	0.369	0.142
$^4F_{9/2}$	0.543	0.080	0.201	0.071	0.188	0.050
$^6F_{3/2}$	0.589	0.085	0.341	0.0823	0.268	0.056
$^6F_{5/2}$	0.996	0.449	0.457	0.4367	0.436	0.297
$^6F_{7/2}$	1.270	1.080	0.945	0.9374	0.741	0.668
$^6F_{9/2}$	1.467	1.539	1.096	1.1045	0.833	0.859
$^6F_{11/2}$	3.872	3.841	2.391	2.3888	2.581	2.571
$^6H_{11/2}$	0.386	0.631	0.506	0.5354	0.348	0.428
N	9		9		9	
n_d	1.567		1.569		1.567	
Ω_2	3.701		2.382		2.747	
Ω_4	1.647		1.393		0.785	
Ω_6	1.087		1.055		0.715	
σ	0.369		0.209		0.160	

The experimental (f_{exp}) and calculated (f_{cal}) oscillator strengths of the absorption bands of individual transition are calculated from the absorption spectra of the relative areas under the absorption spectra and presented in table 2 [2]. The Judd–Ofelt [6,7] intensity parameters (Ω_λ) (λ = 2, 4, 6) are determined from the experimental oscillator strength values (f_{exp} values) by using least square fit procedure. The obtained J-O intensity parameters are as follows for all the prepared glasses. However, the Ω_2 values are found to be higher than the Ω_4 and Ω_6 intensity parameter values in the prepared glasses. Thus lower of Ω_4 and Ω_6 values suggests that the structural network will be more open and becoming high rigid due to the formation of NBO which reflects the deformation of BO_4 unit to BO_{3+1} or BO_3 structural units and vice versa. The trend $\Omega_2 > \Omega_4 > \Omega_6$ has been observed for all the prepared glasses in the experiment.

3.3. Emission and Excitation spectra

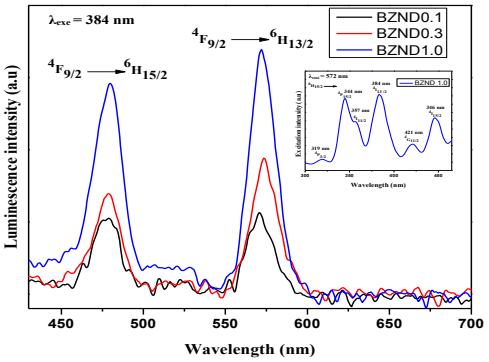

Figure 4. Luminescence spectra of Dy^{3+}:Zinc fluoro borate glasses [inset shows the excitation spectrum of BZND1.0 glass]

Inset Figure 4 shows excitation spectrum of BZND0.1 glass. The excitation spectra contains of six bands owing to the electronic transitions at 319, 344, 357, 384, 421 and 446nm corresponding to $^4P_{3/2}$, $^6P_{7/2}$, $^4I_{11/2}$ $^4I_{13/2}$, $^4G_{11/2}$ and $^4I_{15/2}$ transitions respectively. Among these transitions, the intensity of the excitation band observed at 384 nm corresponding to the $^6H_{15/2} \rightarrow {}^4I_{13/2}$ transition is found to be higher when compared to other transitions and the same is used as an excitation wavelength to record the emission spectra of the prepared glasses. The luminescence spectra of Dy^{3+}doped alkali zinc fluoroborate glasses were recorded in the region 400–700nm and is shown in Figure 4. Luminescence spectra exhibit two emission bands at 480nm and 572nm corresponding to $^4F_{9/2} \rightarrow {}^6H_{15/2}$ (Blue) and $^4F_{9/2} \rightarrow {}^6H_{13/2}$ (Yellow) transitions respectively. From the emission spectra, the intensity of peaks increases

International Journal of
Scientific Research in Science and Technology (IJSRST)
Print ISSN : 2395-6011, Online ISSN : 2395-602X
International Conference on Advanced Materials
Held on 14, 15 December 2017, Organized by Department of Physics,
St. Joseph's College, Trichy, Tamilnadu, India

with increase of Dy^{3+} ion concentration. The yellow emission (electric dipole) transition possesses higher intensity than the blue emission (magnetic dipole) transitions for all prepared glasses. The hypersensitive in nature and its intensity of electric dipole transition is strongly influenced by the ligand field around the Dy^{3+} ion site [10]. Appropriate combination of the dominant emission transitions corresponding to the blue ($^4F_{9/2}\rightarrow{}^6H_{15/2}$) and yellow ($^4F_{9/2}\rightarrow{}^6H_{13/2}$) bands exhibit white light emission [6]. The $^4F_{9/2}\rightarrow{}^6H_{13/2}$ emission transition possess higher intensity compared to the other transitions thus indicates the higher asymmetry possessed by the Dy^{3+} ions with its surrounding ligands. The radiative properties such as peak wavelength (λ_p, nm), the effective bandwidth ($\Delta\lambda_{eff}$, nm), transition probability (A), experimental branching ratios (β_R) and stimulated emission cross-section ($\sigma_P^E \times 10^{-22}$ cm^2) for the $^4F_{9/2}\rightarrow{}^6H_{15/2}$ and $^4F_{9/2}\rightarrow{}^6H_{13/2}$ transitions were calculated from luminescence spectra and presented in table 3. It is observed from table 3 that, the branching ratio of the $^4F_{9/2}\rightarrow{}^6H_{13/2}$ emission transition is found to be higher than the other emission transitions and follows the trend as $^4F_{9/2}\rightarrow{}^6H_{13/2} > {}^4F_{9/2}\rightarrow{}^6H_{15/2} > {}^4F_{9/2}\rightarrow{}^6H_{11/2}$ uniformly for all the prepared glasses. Among the prepared glasses BZND0.1 (21.602) higher stimulated emission cross-section values. The higher stimulated emission cross-section is suggested for low-threshold, high gain applications and are utilized to obtain continuous wave laser action.

Table 3. Bandwidth ($\Delta\lambda_{eff}$, nm), transition probability (A), branching ratios (β_R) and stimulated emission cross-section ($\sigma_P^E \times 10^{-22}$ cm^2) for the $^4F_{9/2}\rightarrow{}^6H_{15/2}$ and $^4F_{9/2}\rightarrow{}^6H_{13/2}$ transitions of the Dy^{3+}doped alkali zinc fluoroborate glasses

Parameters		BZND0.1	BZND0.3	BZND1.0
$^4F_{9/2}\rightarrow{}^6H_{15/2}$	λ_p	479	479	480
	$\Delta\lambda_{eff}$	12.348	14.489	14.105
	A	97.11	92.28	61.05
	σ_P^E	2.237	1.802	1.233
	β_R(cal)	0.152	0.180	0.571
	β_R(exp)	0.503	0.506	0.474
$^4F_{9/2}\rightarrow{}^6H_{13/2}$	λ_p	571	573	572
	$\Delta\lambda_{eff}$	9.967	8.315	10.113
	A	374.80	276.79	263.29
	σ_P^E	21.602	19.476	14.965
	β_R(cal)	0.589	0.541	0.132
	β_R(exp)	0.497	0.494	0.526

3.5. White Light Stimulation

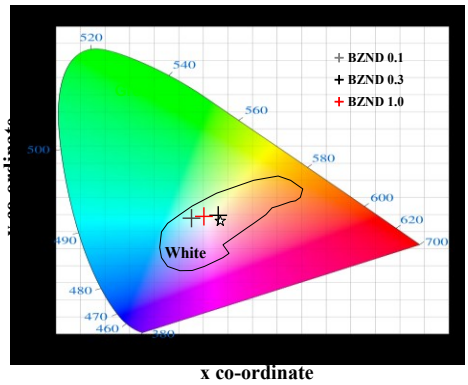

Figure 5. CIE chromaticity co-ordinates of Dy^{3+}: alkali zinc fluoro borate glasses

The CIE chromaticity co-ordinates were calculated for all glass samples and present in Table 4. The emission colors were found to lie in white light region for prepared glasses as shown Figure 5 and thus can be used for bright white LED's [12-14]. Among the prepared glasses, it is observed that BZND 0.3 glass (0.32795, 0.34813) is closer to the standard (0.33, 0.33) equal energy white light illuminate.

Table 4. The Y/B ratio (yellow to blue) and chromaticity co-ordinates (x, y) values for the Dy^{3+}doped alkali zinc fluoroborate glasses.

International Journal of
Scientific Research in Science and Technology (IJSRST)
Print ISSN : 2395-6011, Online ISSN : 2395-602X
International Conference on Advanced Materials
Held on 14, 15 December 2017, Organized by Department of Physics,
St. Joseph's College, Trichy, Tamilnadu, India

Glasses	Y/B ratio	chromaticity co-ordinates		Ref
		x	y	
BZND0.1	1.192	0.2737	0.3398	Present work
BZND0.3	1.198	0.3279	0.3481	
BZND1.0	1.191	0.2989	0.3451	
0.5DPTFB	0.590	0.311	0.302	[9]
LSBP0.1Dy	1.871	0.380	0.397	[10]
TZPPN	0.88	0.38	0.43	[11]

4. Conclusion

Dy^{3+} doped alkali zinc fluoroborate glasses were prepared by melt quenching technique and their structural and spectroscopic behavior were discussed and reported. The XRD pattern confirms the amorphous nature of the prepared glasses. The FTIR studies exhibit the B-O stretching vibrations of BO_3 units. The bonding parameter studies reveal the ionic nature of the metal-ligand bond in the title glasses and the ionicity decreases with the increase in Dy^{3+} ions. The obtained J-O intensity parameters are as follows $\Omega_2>\Omega_4>\Omega_6$ for all the prepared glasses. However, the Ω_2 values are found to be higher than the Ω_4 and Ω_6 intensity parameter values in the prepared glasses. Through the luminescence spectra, the peak wavelength, effective bandwidth, experimental branching ratios (β_R) and stimulated emission cross-section ($\sigma_P^E \times 10^{-22}$ cm^2) calculated for $^4F_{9/2}\rightarrow{}^6H_{15/2}$ and $^6H_{13/2}$ transitions and the results were reported. The prepared glasses exhibit emission in visible region. These results demonstrate that the present glass system is one of the promising material for visible laser and white light stimulation applications.

References

[1] M. Vijayakumar, K. Marimuthu, J. Alloys Compds. 629 (2015) 230–241.

[2] R.T. Karunakaran, K. Marimuthu, S. Surendra Babu, S. Arumugam, Physica B, 404 (2009) 3995–4000.

[3] J.N. Ayuni, M.K. Halimah, Z.A. Talib, H.A.A. Sidek, W.M. Daud, A.W. Zaidan, A.M. Khamiru, Mat. Sci. Engg. 17 (2011) 012027.

[4] M. Jayasimhadri, Kiwan Jang, Ho Sueb Lee, Baojiu Chen, Soung-Soo Yi, Jung-Hyun Jeong, J. Appl. Phys. 106 (2009) 013105.

[5] I. Arul Rayappan, K. Maheshvaran, S. Surendra Babu, K. Marimuthu, Phys. Status Solidi A, 209 (2012) 570–578.

[6] B.R. Judd, Phys. Rev. 127 (1962) 750.

[7] G.S. Ofelt, J. Chem. Phys. 37 (1962) 511

[8] L. Vijayalakshmi, V. Naresh, B.H. Rudramadevi, S. Buddhudu, Inter. J. Engg. Sci. 4 (2014) 19–25.

[9] S.Arunkumar, G.Venkataiah, K.Marimuthu1, Molecular and Biomolecular Spectroscopy (2014), doi: http://dx.doi.org/10.1016/j.saa.2014.10.067.

[10] R. Vijayakumar, G. Venkataiah, K. Marimuthu Journal of Alloys and Compounds (2015), doi: 10.1016/j.jallcom.2015.08.219.

[11] Journal of Quantitative Spectroscopy & Radiative Transfer 134(2014)55–63 Kamel Damak, El Sayed Yousef, Christian Rüssel, Ramzi Maâlej.

[12] K. Swapna, Sk. Mahamuda, A. Srinivasa Rao, M. Jayasimhadri, T. Sasikala, L. Rama Moorthy, Journal of Luminescence 139 (2013) 119–124.

[13] P. Babu, C.K. Jayasankar Optical Materials 15 (2000) 65.

[14] C.R. Kesavulu, C.K. Jayasankar Materials Chemistry and Physics 130 (2011) 1078– 1085.

International Journal of
Scientific Research in Science and Technology (IJSRST)
Print ISSN : 2395-6011, Online ISSN : 2395-602X
International Conference on Advanced Materials
Held on 14, 15 December 2017, Organized by Department of Physics,
St. Joseph's College, Trichy, Tamilnadu, India

Spectroscopic, Hyperpolarizability and Optical Properties of N-benzyl-2-methyl-4-nitro aniline (BNA) Single Crystal

S.Attralarasan[1], J.Madhavan[1], P.Christuraj[2] and, M.Dinesh Raja[2]*
[1]Department of Physics, Loyola College, Chennai – 600 034, India
[2]Department of Physics, St. Joseph's College (Autonomous), Tiruchirappalli – 620 002, India
*Corresponding Author Email: mdineshraja6@gmail.com

Abstract
N-benzyl-2-methyl-4-nitro aniline (BNA) has been investigated with the help of B3LYP density functional theory with 6-31 G (d, p) basis set. Fourier transform infrared Spectrum identifies the various functional groups. The theoretical frequencies showed very good agreement with experimental values. Optical characterization was done by UV-Vis techniques. HOMO and LUMO energies were calculated which reveal the transfer of charge within the molecule. SHG and DFT calculations predicted first order hyperpolarizability of BNA as 0.225355 x 10^{-30}esu, which suggests that the title compound is an attractive material for non-linear optical applications.

Keywords: BNA, B3LYP6-31 G (d, p), HOMO and LUMO, SHG, DFT, hyperpolarizability

1. Introduction
Nonlinear optics, referring to spatially and temporally simultaneous mixing process of multiphotons in materials, has attracted a lot of interest in several applications, such as optical frequency or phase modulation, or spectroscopic techniques for probing photo-chemical reactions [1–4]. So far, a lot of inorganic and organic nonlinear optical materials have been developed with large nonlinear optical susceptibility [3]. Among them, 2-methyl-4-nitroaniline (MNA) has been known as a prominent organic nonlinear optical material. Recently, we developed the N-benzyl MNA (BNA) with a sufficiently large second harmonic activity and applicability of practical use [5]. BNA is a derivative of MNA, where an amino group is substituted into a benzyl group. Condensation of primary amines with aldehydes or ketones yields Schiff bases containing imine (CaN) function group [6]. Some of these compounds are donor–acceptor benzene derivatives, which can conform conjugated p-electron systems easily, and they are known to exhibit extremely large second order optical non-linearities, such as 4-nitro-40-methyl benzylidene aniline (NMBA) [7], 4-nitro-40-methoxy benzylidene aniline (NMOBA) [8], N-2-[30-(methoxysalicylideneimino) benzyl]-300-methoxysalicylideneimine [9]. Organic crystals in terms of non-linear optical property possess advantages when compared to their inorganic counterparts, and they have larger structural diversity [10], so the preparation of this kind of materials has gained increasing importance. With the advance of quantum chemistry method and high performance computers, the structures of some organic compounds can be theoretically predicted in high accuracy. Density functional theory (DFT) method has recently been successfully applied to investigate the structures and predict properties of some compounds [11,12]. The present work deals with the growth and detailed spectral investigation of BNA.

International Journal of
Scientific Research in Science and Technology (IJSRST)
Print ISSN : 2395-6011, Online ISSN : 2395-602X
International Conference on Advanced Materials
Held on 14, 15 December 2017, Organized by Department of Physics,
St. Joseph's College, Trichy, Tamilnadu, India

2. Synthesis of BNA

The primary amine (aniline) and substituted amine (2-methyl-4-nitro aniline) were used to prepare N-benzyl-2-methyl-4-nitro aniline. The sample was synthesized from aqueous methanol. Using methanol, the BNA ingredients were highly purified by several recrystallization processes to exclude impurities. The photograph of the crystal is shown in Figure 1

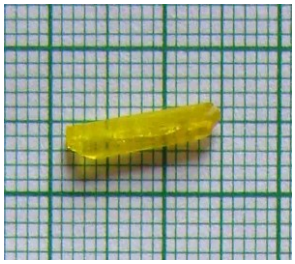

Figure 1. Photograph of as grown BNA crystal

3. FT-IR Analysis

FT-IR spectrum of the grown crystal was recorded in the range 500 cm^{-1} to 4000 cm^{-1}, using KBr pellet technique on BRUKKER IFS FT-IR Spectrometer. For comparison, the experimental FT-IR and theoretically simulated spectra were presented in Figure 2 and 3.

The analysis of the vibrational spectra is based on the observed and computed wave numbers. The theoretical and experimental wave numbers are in fair agreement and the assignments of wave numbers for different functional groups are discussed below. The heteroaromatic structure shows the presence of C–H stretching vibration in the region 3100–3000 cm^{-1} [13,14]. This is the characteristic region for the ready identification of C–H stretching vibration. In this region, the bands are not affected appreciably by the nature of the substitutions. The expected C–H stretching vibrations appeared at 3212 cm^{-1} in FT-IR spectrum. Theoretically computed C–H vibrations by B3LYP/6-31G(d,p) method at 3230 cm^{-1} show good agreement with recorded spectrum.

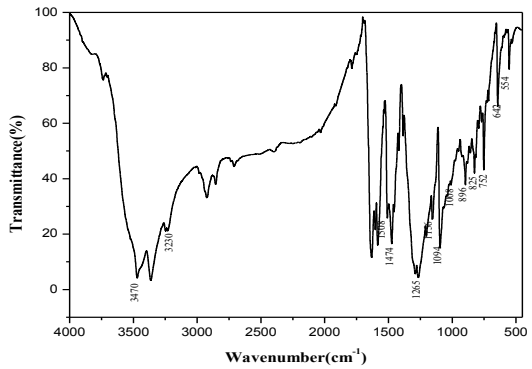

Figure 2. Experimentally obtained FT-IR spectrum of BNA

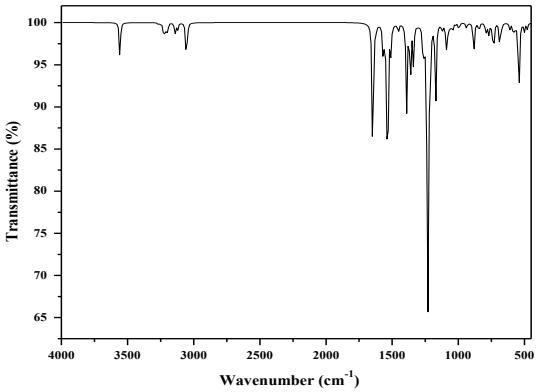

Figure 3. Theoretically simulated FT-IR spectrum of BNA

There are six equivalent C–C bands in benzene and one band in outside of the ring and consequently there will be seven C–C stretching vibrations. In general, the bands around 1650–1300 cm^{-1}[15,16] in benzene derivatives are assigned to skeletal stretching C–C bands. The title compound posses C-C stretching occurs at 1508 cm^{-1}in experimental and its well matched with theoretical value. And the 1534, 1538, 1549 cm^{-1} shows the C-C stretching modes of vibrations.

International Journal of
Scientific Research in Science and Technology (IJSRST)
Print ISSN : 2395-6011, Online ISSN : 2395-602X
International Conference on Advanced Materials
Held on 14, 15 December 2017, Organized by Department of Physics,
St. Joseph's College, Trichy, Tamilnadu, India

The title molecule under investigation possess five NH_2 group and six internal modes of vibrations for NH_2group as, the symmetric (sy st) and asymmetric stretchings (asy st), the symmetric planar deformation or scissoring (β_s), the antisymmetric planar deformation or rocking (β_{as}), the symmetric non-planar deformation or wagging (ω) and the anti-symmetric non-planar deformation or torsion (τ). The NH_2 group has five N–H stretching vibrations, one being asymmetric (asy st) stretching modes. The NH_2 asymmetric stretching vibrations give rise to a strong band in the region 3390±60$cm^{-1}$and the Assignment shows The NH_2 asymmetric occurs in IR spectrum at 3470 and theoretically at 3450 cm^{-1} this shows that both value are matched with the literature value.

4. Optical absorption spectrum

The UV-Vis spectral analysis of the crystal is recorded between 200 and 1200 nm using a Varian Cary 5E UV-VIS-NIR spectrometer. The absorption spectrum obtained is shown in Figure 4 When absorbance is monitored from longer to shorter wavelength, the absorbance is less and almost insignificant between 500 and 1200 nm, which may be important for the materials possessing NLO properties. At the wavelength just above 500 nm, there is a sudden increase in absorbance in the crystal due to the electronic excitation, since the crystal has a delocalized electronic cloud it shows less absorbance between 500 and 1200 nm. Hence, it may be well suited for second harmonic generation devices. The band gap was also studied and the value of the band for BNA is 4.03 eV. Its shows in the Figure 5.

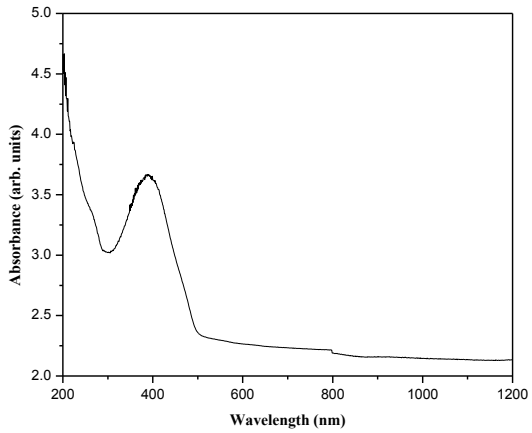

Figure 4. Optical absorption spectrum of BNA crystal

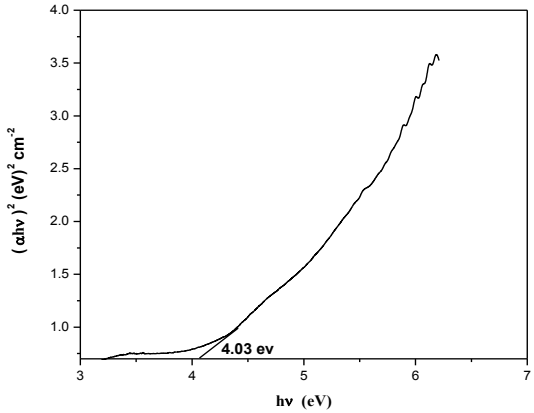

Figure 5. Optical band gap of BNA crystal

5. HOMO-LUMO Analysis

Both the highest occupied molecular orbital (HOMO) and the lowest unoccupied molecular orbital (LUMO) are the main orbital take part in chemical stability. The HOMO represents the ability to donate an electron, LUMO as an electron acceptor represents the ability to obtain an electron. The HOMO and LUMO energy calculated by B3LYP/6-31G (d, p) method as shown below:

HOMO energy (B3LYP) = -0.21711a.u

LUMO energy (B3LYP) = -0.07806a.u

HOMO–LUMO energy gap (B3LYP) = -0.13905a.u

The HOMO is located over the phenyl ring and the carboxylic acid group attached to the phenyl ring.

International Journal of
Scientific Research in Science and Technology (IJSRST)
Print ISSN : 2395-6011, Online ISSN : 2395-602X
International Conference on Advanced Materials
Held on 14, 15 December 2017, Organized by Department of Physics,
St. Joseph's College, Trichy, Tamilnadu, India

The HOMO→LUMO transition implies an electron density transfer to the carboxylic acid group from the phenyl ring. Moreover, these orbital significantly overlap in their position for BNA (Figure 6). The HOMO and LUMO energy gap explains the eventual charge transfer interactions taking place within the molecule.

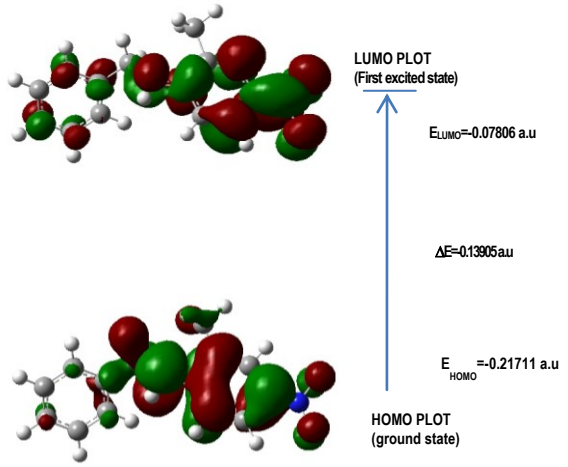

Figure 6. HOMO – LUMO plot of BNA molecule

6. Hyperpolarizability studies

Interests in organic optoelectronic materials and devices have motivated experimental and theoretical studies of molecular structures with enhanced hyperpolarizabilities. [17] Molecules with electronic asymmetry, or "push-pull" donor-bridge-acceptor electronic framework, have been demonstrated to have large first hyperpolarizabilities (β) [18]. The first static hyperpolarizability (β_0) the electric dipole moment μ of the BNA are calculated by finite field method using B3LYP/6-31G (d,p) level basis sets. The calculated first hyperpolarizability of BNA is0.225355 x 10^{-30}esu. The calculated first hyperpolarizability components are and Dipole moments were given in Table 1 and 2.

Table1. Hyperpolarizability of BNA in esu

β_{xxx}	-28.1633958
β_{xxy}	12.3885477
β_{xyy}	5.5313826
β_{yyy}	27.4244763
β_{xxz}	133.0376559
β_{xyz}	-16.9692876
β_{yyz}	47.6005725
β_{xzz}	16.3511383
β_{yzz}	-162.4658587
β_{zzz}	-2873.2795683
β_{tot}	0.225355 x 10^{-30}

Table 2. Dipole Moments of BNA in debye

μ_X	-7.8978
μ_Y	1.1999
μ_Z	1.0547
μ_{tot}	8.0578

7. Conclusion

Good optical quality bulk single crystal of BNA has been grown successfully by slow evaporation growth technique. (DFT) computations of BNA molecule calculated by DFT (B3LYP) level with 6-31G (d,p) basis set gives the optimized structure. The optical properties of the grown crystal were evaluated from the absorption spectrum. Theoretical and experimental IR spectroscopic analyses were carried out and the presence of functional groups in BNA molecule was qualitatively analyzed. HOMO-LUMO analysis reveals the molecular energy gap. SHG and DFT calculations predicted first order hyperpolarizability of BNA as 0.225355 x 10^{-30}esu, which suggests that the title compound is an attractive material for non-linear optical applications.

International Journal of
Scientific Research in Science and Technology (IJSRST)
Print ISSN : 2395-6011, Online ISSN : 2395-602X
International Conference on Advanced Materials
Held on 14, 15 December 2017, Organized by Department of Physics,
St. Joseph's College, Trichy, Tamilnadu, India

References

[1] Shen, Y.R. The Principles of Nonlinear Optics, Wiley, New York, 1984.

[2] Yariv, A. Quantum Electronics, third ed., Wiley, New York, 1988.

[3] Dmitriev, V.G., Gurzadyan, G.G. and Nikogosyan, D.N., Handbook of Nonlinear Optical Crystals, second ed., Springer, Berlin, 1995.

[4] Mukamel, S., Principle of Nonliear Optical Spectroscopy, Oxford University Press, New York, 1995.

[5] Hashimoto, H., Okada, Y., Fujimura, H., Morioka, O., Sugihara, M., Okamoto, N. and Matsushima, R., Jpn. J. Appl. Phys. 36 (1997) 6754.

[6] Rao, R.V., Rao, C.P., Wegelius, E.K. and Rissanen, K., J. Chem. Crystallogr. 33 (2003) 139.

[7] Srinivasan, K., Sankaranarayanan, K., Thangavelu, S. and Ramasamy, P., J. Cryst. Growth 212 (2000) 246.

[8] Azariah, A.N., Hameed, A.S.H., Thenappan, T., Noel, M. and Ravi, G., Mater. Chem. Phys. 88 (2004) 90.

[9] Dey, D.K., Dey, S.P., Elmali, A., and Elerman, Y., J. Mol. Struct. 562 (2001)177.

[10] Jiang, M.H. and Fang, Q., Adv. Mater. 11 (1999) 1147.

[11] Clarkson, J., Smith, W.E., and Batchelder, D.N., J. Mol. Struct. 648 (2003) 203.

[12] Ivan, B. and George, K.F., J. Am. Soc. Chem. 86 (1964) 1671.

[13] Arivazhagan, M., Krishnakumar, V., John Xavier, R. Ilango, G. and Balachandran, V., Spectrochimica Acta Part A: Molecular and Biomolecular Spectroscopy Volume 72, Issue 5, June 2009, Pages 941-946.

[14] Varsányi, G. and Holly T. Faragó, S., Spectrochimica Acta Volume 19, Issue 3, March 1963, Pages 675-681.

[15] Sajan Jose, D., Abraham I. Hubert Joe, P., Jayakumar V.S., Aubard, J. and Faurskov Nielsen, O., Journal of Molecular Structure Volume 889, Issues 1–3, 29 October 2008, Pages 129-143.

[16] Bellamy L.J., and Pace, R.J., Spectrochimica Acta Part A: Molecular Spectroscopy Volume 28, Issue 10, October 1972, Pages 1869-1876.

[17] Zyss, J., and Chemla, D.S. Nonlinear Optical Properties of Organic Molecules and Crystals 1987, Pages 23–191.

[18] Satyam Priyadarshy, Michael J. herien and David N. Beratan, J. Am. Chem. Soc., 1996, 118(6), 1504–1510.

International Journal of
Scientific Research in Science and Technology (IJSRST)
Print ISSN : 2395-6011, Online ISSN : 2395-602X
International Conference on Advanced Materials
Held on 14, 15 December 2017, Organized by Department of Physics,
St. Joseph's College, Trichy, Tamilnadu, India

Growth and Characterization of Glutamine Potassium Carbonate – New Semi Organic Crystal

K.Suganya[1], V. S. Kumar[2] R. S. Sundararajan[1]

[1]Department of Physics, Government Arts College (Autonomous), Kumbakonam, Tamilnadu, India

[2]Department of Physics, Swami Dayananda College of Arts and Science, Manjakkudi, Tiruvarur Dt., Tamilnadu, India

Corresponding Author: rssphy66@gmail.com

Abstract

A new semi organic crystal of Glutamine potassium carbonate (GPC) crystal has been grown by slow evaporation method by using water as solvent. The particle size of the GPC crystal was calculated by powder X-Ray diffraction method. Using UV-VIS-NIR spectral analysis, it was found that the crystal has good transparency in the expected region and the lower cut off wavelength is observed. The vibrational modes are assigned by recording the FT-IR spectrum. The Vickers hardness test has also been taken for experimental crystals. The NLO behavior of GPC crystal was tested by Kurtz-Perry powder technique.

Keywords: GPC - Glutamine potassium carbonate crystal, UV-Vis-NIR-Ultraviolet –visible - Near infrared, FT-IR-Fourier transform of Infrared, NLO-Non linear optic.

Introduction

Semi organic crystals play a vital role in the applications of optoelectronic communications, optoelectronic devices and in lasers also. In recent years organic nonlinear optical crystals have attracted much attention for their large non linear coefficient, high laser damage threshold. However, most of organic NLO materials have poor mechanical and thermal properties, resulting in the damage of crystal during processing. To avoid this drawback, a new type of NLO material has been grown from organic-inorganic complexes. These semi organic materials have high optical nonlinearity of a purely organic compound combined with the mechanical and thermal properties of inorganic materials. [1-3].

Experimental procedure

Synthesis and growth

Single crystals of Glutamine potassium carbonate were grown at room temperature by slow evaporation of an aqueous solution containing Glutamine and potassium carbonate in the ratio 1:1 as per the reaction. Crystals have come to the shape in 90 days and shown in the Figure1.

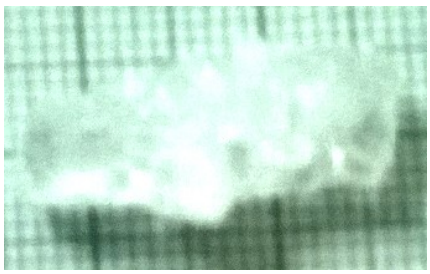

Figure 1. Photograph of GPC crystals

Characterization

Powder XRD analysis was done by using X-ray diffractometer with λ=1.5406X10^{-10}m radiation to identify the size of the particle. By varying the position and height FWHM and d-spacing are determined. UV-Vis-NIR spectral analysis of GPC

International Journal of
Scientific Research in Science and Technology (IJSRST)
Print ISSN : 2395-6011, Online ISSN : 2395-602X
International Conference on Advanced Materials
Held on 14, 15 December 2017, Organized by Department of Physics,
St. Joseph's College, Trichy, Tamilnadu, India

crystal was recorded in the range 200-1100 nm and the percentage of transmittance was also recorded. The FT-IR spectrum has also been taken in order to find the vibrational modes. The Vickers hardness test was also done to measure the physical strength of the crystal. SHG test was done to find out the NLO property of the crystal.

Results and discussion

Powder X ray diffraction

The particle size of Glutamine mixed potassium carbonate crystal was done by using XRD. The size of the particle was estimated using the formula of Scherer by monochromatic radiation.

$$D = 0.9 \lambda/\beta \cos\theta$$

where, D stands for the size of the particle.

$\lambda = 1.5406 \times 10^{-10}$ m

$\theta = 30.0606$ (observed diffracting angle)

$D = 3.9042 \times 10^{-8}$ m

By varying 2θ, the (d-spacing) inter-planar spacings are noted.

FTIR spectral analysis

FT-IR spectrum was recorded by FT-IR spectrophotometer in the range 400- 4000cm^{-1}. By changing the wave numbers, the different assignments obtained are given in the following table.

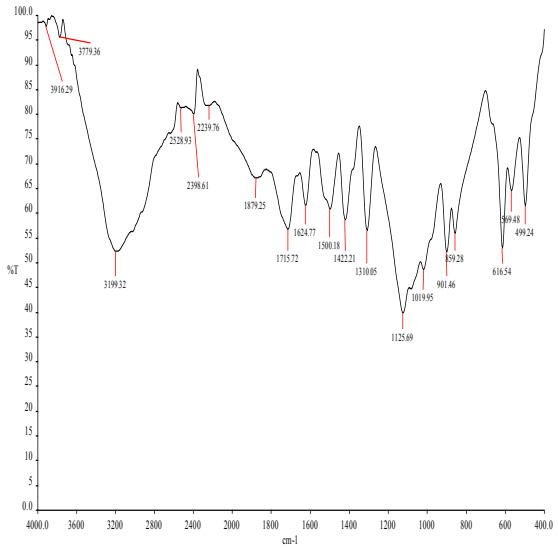

Figure 2. FTIR spectrum of GPC crystal

From the FT-IR spectrum, (of the experimental crystal) assignments of vibrational modes are made and are tabulated. [4-5]

Wavenumber	Assignment
3199	N-H Symmetric Stretching
2528	S-H stretching
2239	N=C=O antisymmetric stretching
1879	C=C ring
1715	C=O stretching
1624	C=O stretching & NH2 deformation
1500	N-H Symmetric
1422	In plane OH bending
1310	COO^- symmetric stretching
1125	C-O stretching
1019	C-O stretching
901	CH_2 out of plane wagging
859	NH_2 wagging
569	COO^- Rocking
499	C-N-C bending

International Journal of
Scientific Research in Science and Technology (IJSRST)
Print ISSN : 2395-6011, Online ISSN : 2395-602X
International Conference on Advanced Materials
Held on 14, 15 December 2017, Organized by Department of Physics,
St. Joseph's College, Trichy, Tamilnadu, India

UV-VIS spectrum analysis

From the spectrum, it is found that, the GPC is transparent in the region from 200nm-1100nm. It has good transmittance and the lower cut off wavelength is observed at 208.03nm. The large range of transmittance in the visible region enables the GPC to be good for optoelectronic applications. [6]

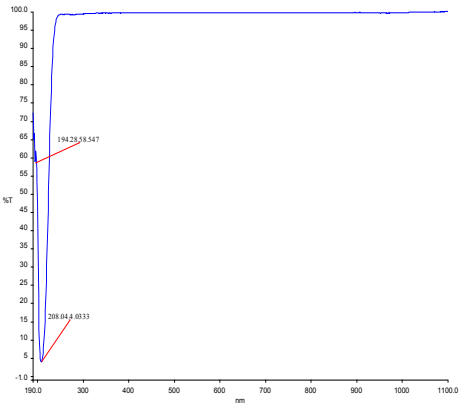

Figure 3. Transmission spectrum of GPC

Mechanical studies

The micro hardness of a substance is a key property to interpret the mechanical strength of the material which is basically related to the crystal structure and about the atomic package. This test affords useful details about the mechanical properties like elastic constants, yield strength etc., of materials. [7] The variation of H_v with the applied load for the crystals are shown in fig.4. In this crystal, hardness increases, if we increase the load Thus, this crystal has good physical strength.

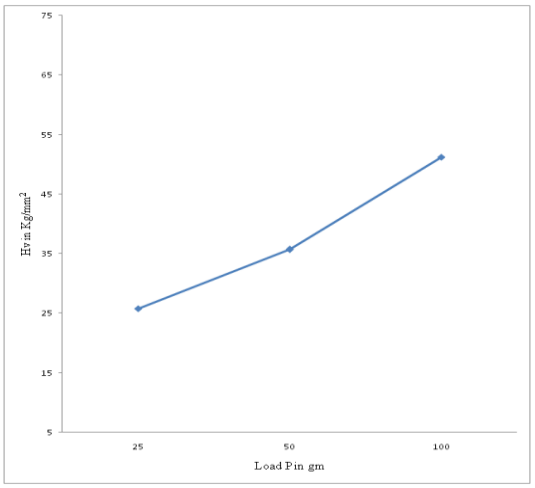

Figure 4. Load versus H_v

Second Harmonic Generation studies

Dynamic research has been engaged to find the NLO property of the crystal. The NLO conversion efficiency was tested using Kurtz and Perry setup [8]. A Q-switched Nd:YAG laser beam of wavelength 1064 nm was used. The output energy of the sample is 0.910 times of the KDP reference energy. Hence, the GPC compound crystal has nonlinearity nature.

Conclusion

Single crystals of GPC have been grown by slow evaporation method. The particle size is estimated using XRD. From UV-Vis-NIR spectral analysis, the crystal may be recommended for optoelectronic applications. In FT-IR spectrum analysis, the vibrational modes are identified. The physical strength of the crystal has been measured in the Vicker's hardness test. The GPC compound crystal has nonlinearity nature and it has been found out by Kurtz Perry method.

Acknowledgements

The authors are thankful for the authorities of St. Joseph's College, Tiruchy, NIT, Tiruchy for

providing instrumental facilities for characterization.

References

[1] G. Ramesh Kumar, S. Gokul Raj, R. Mohan, R. Jeyavel, Cryst. Growth Des. 6 (2006) 1308–1310.

[2] P.N. Prasad, D.J. Williams, Introduction to Nonlinear Effects in Molecules and Polymers, Wiley, New York, 1991.

[3] J.J. Rodrigues, L. Misoguti, F.D. Nunes, C.R. Mendonca, S.C. Zilo, Opt.Mater. 22 (2003) 235–240.

[4] John Coates., Interpretation of IR Spectra, A practical approach.

[5] Joseph B. Lambert et al, Introduction to organic spectroscopy, Mc Millan pub., N.Y. (1987), 174-177.

[6] N. Vijayan, R. Ramesh Babu, R. Gopalakrishnan, P. Ramasamy, W.T.A. Harrison, J. Cryst. Growth 262 (2004) 490–498.

[7] Mott, B.W. (1956) Micro-Indentation Hardness Testing. Butterworths, London, 206.

[8] Kurtz, S.K. and Perry, T.T. (1968) A Powder Technique for the Evaluation of Nonlinear Optical Materials. Journal of Applied Physics, **39**, 3798-3813.

International Journal of
Scientific Research in Science and Technology (IJSRST)
Print ISSN : 2395-6011, Online ISSN : 2395-602X
International Conference on Advanced Materials
Held on 14, 15 December 2017, Organized by Department of Physics,
St. Joseph's College, Trichy, Tamilnadu, India

Structural Analysis of Pure and Potash Alum Doped KDP Crystals Grown by Gel Medium

M.P. Rameela[1], T.H. Freeda[2] & T. Asaithambi[3]
[1]Dept. of Physics Sarah Tucker College for Women, Tirunelveli
[2]Dept. of Physics S.T. Hindu College Nagercoil
[3]P.G and Research Department of Physics, Alagappa Govt. Arts College, Karaikudi
Corresponding Author : rameelajustin@gmail.com

Abstract

Optically good quality pure and metal doped KDP crystals have been grown by gel method at room temperature and their characterization have been studied. Gel method is a much uncomplicated method and can be utilized to synthesize crystals which are having low solubility. Potassium dihydrogen orthophosphate KH_2PO_4 (KDP) continues to be an interesting material both academically and industrially. KDP is a representative of hydrogen bonded materials which possess very good electro–optic and nonlinear optical properties in addition to interesting electrical properties. Due to this interesting properties, we made an attempt to grow pure and Potash Alum doped KDP crystals in various concentrations (0.002, 0.004, 0.006, 0.008 and 0.010) using gel method. The grown crystals were collected after 20 days. We get crystals with good quality and shaped. The electrical conductivity increases with increase of temperature crystals. The Structural properties were found out by using FTIR and XRD studies. Results were discussed in detail.

Keywords: Gel growth, KDP, FTIR, XRD

1. Introduction

Gel growth in aqueous solution is now a wide spread technique for production of high quality crystals in a large range of solubilities and temperatures [1-3]. In gel growth, crystals are mostly formed at ambient temperature and hence are free from strain often present in crystals prepared from the melt or from the vapour [4]. In this method, two soluble reactants are diffused into a gel where they react to form an insoluble product. This is achieved by incorporating one of the reactants with the gel before setting in a test tube and adding the reactant in solution above the gel as supernatant. In this method, large scale movements like convection currents are almost completely suppressed, which otherwise could be harmful to the quality of crystal. The presence of gel does not considerably affect the rate of diffusion of crystallizing species [5] and the related crystal growth kinetics. The principle role of gel appears to be the suppression of turbulence and nucleation, [6] due to which crystallization occurs by diffusion of reactants to a small number of nucleation centre.

Potassium dihydrogen orthophosphate (KDP) KH_2PO_4 continues to be an interesting material both academically and industrially. KDP is a representative of hydrogen bonded materials which possess very good electro-optic and nonlinear optical properties in addition to interesting electrical properties. The demand for high quality large single crystals of KDP increase due to the application as frequency conversion crystal in inertial confinement fusion [7-8]. The piezo electric property of KDP crystal makes it useful for the construction of crystal filters and frequency stabilizers in electronic circuit's.

International Journal of
Scientific Research in Science and Technology (IJSRST)
Print ISSN : 2395-6011, Online ISSN : 2395-602X
International Conference on Advanced Materials
Held on 14, 15 December 2017, Organized by Department of Physics,
St. Joseph's College, Trichy, Tamilnadu, India

The excellent properties of KDP include transparency in a wide region of optical spectrum, resistance to damage by laser radiation and relatively high non-linear efficiency, in combination with reproducible growth to large size. Therefore, it is commonly used in several applications such as laser fusion, electro-optical modulation and frequency conversion. Many studies on the growth and properties of KDP crystals in the presence of impurities have been reported [9-10]. Potassium dihydrogen phosphate (KDP) crystal draws persistent attention of scientists due to its excellent quality and possibility of growing large-size crystals [11-12]. Microscopically, crystal growth includes crystal morphology, crystal defects, and growth rate, which are all related to the constituent growth units and their chemical bonding process [13-14]. KDP, ADP and DKDP are the only nonlinear crystal currently used for these applications due to their exclusive properties. The grown crystals were characterized using dielectric constant, electrical properties, optical transmittance, for pure and Potash alum doped KDP crystals.

2. Materials and Methods

Pure and Potash alum doped KDP single crystals are grown in sodium meta silicate gel medium using analar grade KDP and Potash alum with in concentrations of 0.002, 0.004, 0.006, 0.008 and 0.010 of dopant and sodium meta silicate (1.08g/cm^3). During the process pH was maintained at 5-6 at room temperature. Ethyl alcohol of equal volume is added over the set gel without damaging the cell surface. When the alcohol diffuses into the set gel, it reduces the solubility. This induces nucleation and the nuclei are grown into the single crystals. The crystal growth was carried out at room temperature. The growth period was about 20 days for pure and Potash alum doped KDP crystals.

Results and Discussions

FT-IR studies on pure and Potash alum doped KDP crystals

The observed FT-IR spectra of pure and **Potash alum** doped KDP crystals are shown in figure.

From FT-IR spectra, the broad band which appears in the range 3261 to 2922 cm^{-1} is due to free O-H stretching of KDP [15]. It is seen that these are very weak bonds. The peak at 2922 cm^{-1} is due to P-O-H asymmetric stretching. The strong intensity band at 2433 cm^{-1} is due to one of the P-O-H bending of KDP. A sharp band in the spectral wavelengths of 1384 cm^{-1} is due to asymmetric bending modes. The sharp and strong intense bands appearing at 1147 cm^{-1} is due to P=O symmetric stretching. The spectrum shows an additional peak at 906 cm^{-1}. This is attributed to P-O-H stretching of KDP. Another sharp band at 537 cm^{-1} was due to bending mode of $Al(H_2O)_6$. A detailed assignment of the frequencies observed in FTIR spectrum is given table.

Figure 1

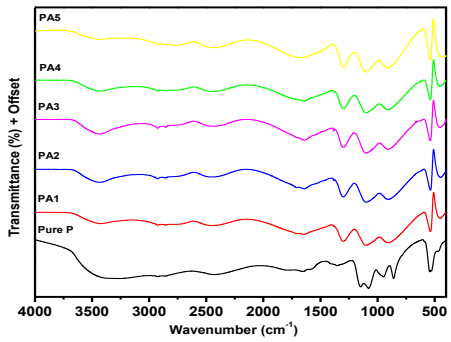

Figure 1. shows the FTIR pattern of (a) Pure KDP and (b) PA1 (c) PA2 (d) PA3 (e) PA4 (f) PA5 are doped Potash alum in different concentration

Pure KDP	PA1	PA2	PA3	PA4	PA5	Assignments
3261vw	3422vw	3432vw	3433vw	3431vw	3422vw	Free–O-H stretching
2922s	2925s	2926s	2925s	2925s	2923s	P-O-H Symmetric

International Journal of
Scientific Research in Science and Technology (IJSRST)
Print ISSN : 2395-6011, Online ISSN : 2395-602X
International Conference on Advanced Materials
Held on 14, 15 December 2017, Organized by Department of Physics,
St. Joseph's College, Trichy, Tamilnadu, India

						stretching
------	1384	1384	1384	1384	1384	Asymmetric Bendingmode
1147vs	1100vs	1100vs	1101vs	1100vs	1102vs	P=O stretching of KDP
948vs	906vs	906vs	906vs	909s	912s	P-O stretching
543sh	536sh	537sh	538sh	537sh	537sh	Bending mode of $Al(H_2O)_6$

vs – very strong; s – strong; vw – very weak; sh – sharp

Powder XRD Studies

The powder X-ray Diffractometer analysis (XPERT-PRO) has been carried out for the rapid identification and quantification of grown crystal at 2 theta position of 10° to 80°. At maximum intensity the various structure parameters like the crystalline size, micro strain and dislocation density has been calculated by Debye-Scherer's formula and tabulated below [16-17].

$$D = 0.9\,\lambda/\beta\cos\theta$$

where λ is wavelength of the X-ray radiation, β is full width at half maximum (FWHM) of diffraction peak (in rad), and θ is scattering angle.

Further, the dislocation density (δ) and micro strain (ε) was estimated by the relation

$$\delta = 1/D^2 \quad \text{and} \quad \varepsilon = \beta\cos\theta/4$$

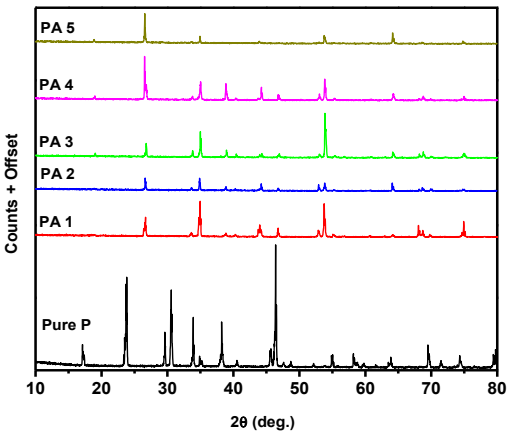

Figure 2. shows the Powder XRD pattern of (a) Pure KDP and (b) PA1 (c) PA2 (d) PA3 (e) PA4 (f) PA5 are doped Potash alum in different concentration.

X-Ray Diffraction data (crystalline size, micro strain and dislocation) for KDP doped with PA1-0.002, PA2-0.004, PA3-0.006, PA4-0.008, PA5-0.01 concentration of Potash alum

Sample	d spacing	2θ	FWHM - β	Crystalline Size nm	Dislocation 10^{14} $1/m^2$	Microstrain 10^{-4}
Pure KDP	3.738	23.784	0.0047	31.487	10.085	11.497
KDP+ PA1	3.728	23.866	0.0011	126.830	0.6217	2.690
KDP+ PA2	3.733	23.833	0.0014	97.720	1.0472	3.424
KDP+ PA3	3.711	23.974	0.0018	87.086	1.4143	4.401
KDP+ PA4	3.746	23.749	0.0012	123.321	0.6575	2.935
KDP+ PA5	3.742	23.774	0.0008	184.997	0.2921	1.957

Conclusion

Pure KDP crystals and metal doped KDP crystals were grown by gel method. In gel growth, due to the three dimensional structures, the crystals were free from microbes. KDP crystal is a queen of all crystals because of its high transparency and best NLO property. Addition of Potash alum with KDP gives some changes in its basic character. Here the characteristic properties of pure KDP and Potash alum with KDP crystal has been investigated through FTIR, XRD analysis The lower the value of dielectric constant more is the enhancement of SHG signals. The electrical conductivity of the pure KDP and Potash alum doped KDP crystals were found to be increase with increase of temperature and frequencies. The FT-IR spectral studies confirm the presence of all the functional groups and also the presence of Potash alum in the grown crystals. The presence of additional peaks in the XRD spectrum of doped KDP crystals shows the presence of additional phases due to doping.

International Journal of
Scientific Research in Science and Technology (IJSRST)
Print ISSN : 2395-6011, Online ISSN : 2395-602X
International Conference on Advanced Materials
Held on 14, 15 December 2017, Organized by Department of Physics,
St. Joseph's College, Trichy, Tamilnadu, India

References

[1] Lefaucheux, F, Roberts, M C & Manghi, E, (1982) "A Comparison Between Gel Grown and Solution Grown Crystals — Case of ADP and KDP" J. Crystal Growth, Vol.56, No.1, pp 141-150.

[2] Brouwer, G, Rosmalen, G M V & Bennama, P, (1974) "The Growth of Single Crystals of Rb_2PtCl_6 and Similar Alkali Precious Metal Chlorides and of $BaSO_4$ in an Ion-exchanged Sodium-free Silica Gel", J. Crystal Growth, Vol. 23, No. 3, pp 228-232.

[3] Garcia Ruiz, J M & Amoros, J L, (1981) "Morphological Aspects of Some Symmetrical Crystal Aggregates Grown by Silica Gel technique", J. Crystal Growth, Vol.55, No.2, pp 379-383.

[4] Boulin, D & Ellis, W C, (1970) "Gel-growth of Silver Acetate Crystals", J. Crystal Growth, Vol.6, No.3, pp 290-292.

[5] Gits, S, F, Cheux, Le Au & Robert, M C, (1978) "Effect of Stirring on Crystalline Quality of Solution Grown Crystals — Case of Potash Alum", J. Crystal Growth, Vol.44, No.3, pp 345-355.

[6] Armington, A F & O'Connor, J J, (1968) "Gel Growth of Cuprous Halide Crystals", J. Crystal Growth, Vol.3, No.4, pp 367-371.

[7] Ramet X. Sun, X, Xu, Z. Gao, Y. Fu, S. Wahg, H. Zong, Y. Li, J. Cryst. Growth 217 (2000) 404.

[8] N. Zaitseva, L. Carman, I. Smolsky, J. Cryst. Growth 241 (2002) 363.

[9] Bo Wang. Chang – Shui Fang. Sheng – Iai Wang, Xun Sun, Quing-tian Gu, Yi-ping Li, Xin-guang Xu, Jianqin Zhang, Bing Liu, with potassium carbonate as additives. J. Cryst. Growth 2008; 310: 5341-5346.

[10] N.Pattanaboonmee, P.Ramasamy, P.Manyumprocedia Engineering, 32 (2012), 1019-1025.

[11] Dongli Xu, Dongfeng Xue. J. Cryst. Growth 310 (2008) 1385.

[12] Dogli Xu, Dongfeng Xue, J. Alloys Compd. 449 (2008) 353.

[13] Dongli Xu, Dongfeng Xue. J. Cryst. Growth 310 (2008) 1385.

[14] S.Balamurugan, P.Ramasamy, Spectrochimica Acta part A 71 (2009) 1979-1983.

[15] P. Santhana Raghavan, P. Ramasamy, Recent Trends in Cryst Growth, Pinsa 68(2002)235

[16] Jingran Su, Youting Song, Daofan Zhang and Xinan Chang, Powder diffraction, 24, (2009) pp. 234.

[17] James R. Connolly, "Introduction to X-Ray Powder Diffraction", Spring EPS400-002 (2007).

International Journal of
Scientific Research in Science and Technology (IJSRST)
Print ISSN : 2395-6011, Online ISSN : 2395-602X
International Conference on Advanced Materials
Held on 14, 15 December 2017, Organized by Department of Physics,
St. Joseph's College, Trichy, Tamilnadu, India

Optical, Structural and Mechanical Properties of a Zinc Magnesium Sulphate Crystal

V.S. Kumar[1], R.S. Sundararajan[2]

[1]Department of Physics, Swami Dayananda College of Arts and Science, Manjakkudi, Tiruvarur, Tamilnadu, India

[2]Department of Physics, Government Arts College (Autonomous), Kumbakonam, Tamilnadu, India

Corresponding Author : shanmugavsk.2010@gmail.com

Abstract

Single crystals of zinc magnesium sulphate were grown from a non aqueous solution by slow evaporation method at room temperature. Good quality transparent crystals were harvested by slow evaporation technique within 25 days. The crystals were subjected to single X ray diffraction and its structure was determined. UV-Vis spectrum confirms that the material has wide optical transparency. FTIR analysis confirms the vibrational modes of the crystal and the presence of functional groups. The Vicker's hardness property shows its mechanical strength. The surface morphology is studied by SEM technique..

Keywords: MZE–zinc magnesium sulphate crystal, XRD-X-ray diffraction, SEM–scanning electron microscope, FTIR–fourier transform infrared, UV-Vis – ultraviolet-visible.

Introduction

Crystal growth is a highly interdisciplinary area of research. Crystals grown now-a-days find places ranging from microelectronics, optoelectronics, medical instruments, communication systems, defence sources etc., High efficient photovoltaic cells and detectors, fabrication of LEDs, traffic purpose illumination devices widely depend on the crystal growth techniques. Magnesium sulphate crystals have wide application in the field of medicine and in agriculture. To the best of our knowledge this composite crystal zinc sulphate with magnesium sulphate has excellent optical property with good mechanical strength [1-3].

Experimental procedure

Synthesis and growth

High purity salts (99.9%) were used for the crystal growth. Single crystals of Magnesium sulphate mixed Zinc sulphate(MZE) were grown at room temperature by solution growth using slow evaporation method, of an organic solution (ethanol) containing zinc sulphate and magnesium sulphate in equal stoichiometric ratio. The temperature of water in the bath was controlled digitally by using microprocessor. Variation in temperature of the bath can be tuned to an accuracy of ±0.1°C. Transparent good quality crystals of the MZE crystals were harvested in span of 25 days. The photograph of the crystal is shown in Figure 1.

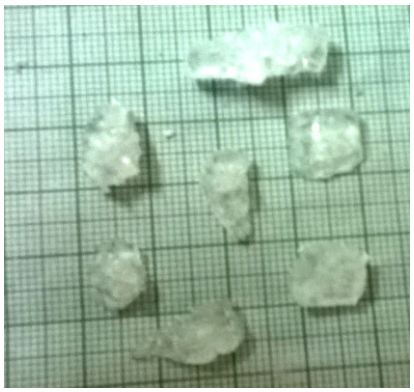

Figure 1. Photograph of MZE crystals

International Journal of
Scientific Research in Science and Technology (IJSRST)
Print ISSN : 2395-6011, Online ISSN : 2395-602X
International Conference on Advanced Materials
Held on 14, 15 December 2017, Organized by Department of Physics,
St. Joseph's College, Trichy, Tamilnadu, India

Characterization

The single crystal X-ray diffraction studies of the grown MZE crystals were carried out using ENRAF NONIUS CAD 4 diffractometer. The UV-Visible spectrum was recorded in the range 190nm-1100nm using Perkin Elmer lambda 35 model. FTIR spectrum analysis was recorded in the range of 4000-400 cm^{-1} using Perkin Elmer spectrum RX I. The hardness property of the crystal was carried out by Vicker's microhardness method and the structural morphology of this material are reported by SEM technique.

Results and discussion

Single crystal X ray diffraction

The structure of the grown MZE crystal was studied by single crystal X ray diffraction method. The crystallographic data obtained from the analysis revealed that the crystal possesses monoclinic structure. The unit cell dimensions were a=10.053 A˚, b= 7.210 A˚, c= 24.378 A˚, α= 90˚, β= 98.21˚, γ= 90˚ and cell volume was 1748.7 $A^{\circ 3}$.

FTIR spectral analysis

The FTIR spectrum was recorded for the sample of the crystals using the KBr pellet technique in the region 4000-400 cm^{-1}. The various functional groups present in the material are identified and confirmed in this study. The FTIR spectrum is shown in Figure 2.

The broad band between 3588 cm^{-1} and 3200 cm^{-1} represents the presence of OH stretching vibrations. The OH inoximes stretching is observed at 3318 cm^{-1} whereas OH stretching is observed at 3246 cm^{-1}. Peaks from 3500-3200 cm^{-1} represent the presence of medium hydrogen bonded OH group. Peaks between 1145-1170 cm^{-1} represent the presence of SO_2 symmetric stretching. Peak at 1081 cm^{-1} represents C-O stretching. Peaks 983 cm^{-1}, 868 cm^{-1}, represents very strong CH out of plane deformation, whereas peak at 762 cm^{-1} intimates the strong CH out of plane deformation. The position of S=O depends on the electronegativity of the attached group and tends to raise the frequency since they tend to stabilize the form S=O and increase stretching vibrations [4-6].

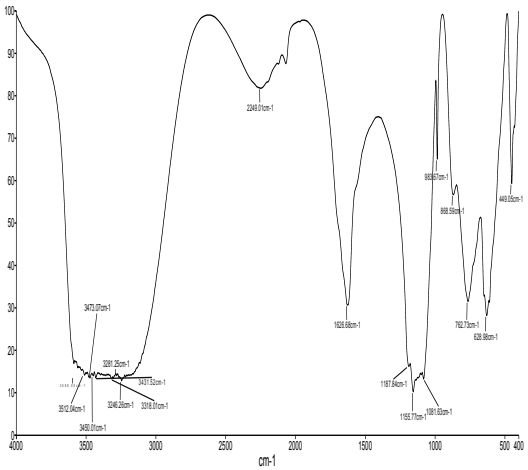

Figure 2. FTIR spectrum of MZE crystal

UV-VIS spectrum analysis

The optical absorption spectra of MZE crystal were recorded in the region 190-1100nm at a scanning speed of 480 nm/min. Figure 3(a&b) shows the absorbance spectra and transmission spectra which hold good in the entire visible region. The lower cutoff wavelength of this crystal was found to be 198.3 nm. The optical behavior of this MZE material is suitable for opto-electronic applications.

International Journal of
Scientific Research in Science and Technology (IJSRST)
Print ISSN : 2395-6011, Online ISSN : 2395-602X
International Conference on Advanced Materials
Held on 14, 15 December 2017, Organized by Department of Physics,
St. Joseph's College, Trichy, Tamilnadu, India

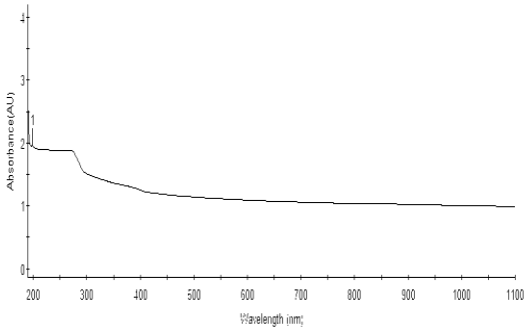

Figure 3(a). Absorption spectrum of MZE

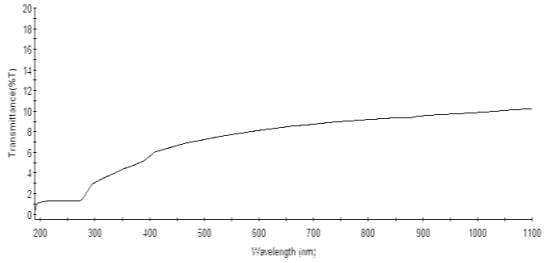

Figure 3(b). Transmission spectrum of MZE

Mechanical studies

The micro hardness of a substance is a key property to interpret the mechanical strength of the material which is basically related to the crystal structure and about the atomic package. It also reveals the electronic factors operating to make the stable structure. It is the resistance offered by the crystal for the movement of dislocations and for localized plastic deformation. This test affords useful details about the mechanical properties like elastic constants, yield strength etc., of materials. The variation of H_v with the applied load for the crystals are shown in Figure 4(a). The hardness number was found to increase with increase in applied load, which confirms the hardness.

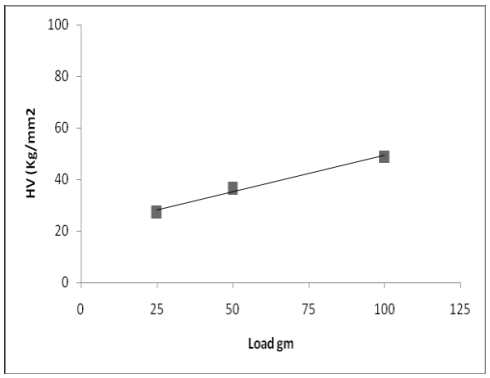

Figure 4(a). Load versus H_v

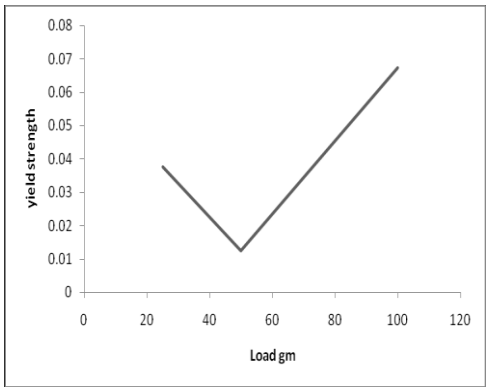

Figure 4(b). Load versus yield strength

The calculated values of yield strength σ_v for grown crystals are shown in Figure 4(b). For load 50gm, it decreases and then suddenly for 100gm it reaches a higher value. The elastic stiffness constant C_{11} has been calculated for the crystals using Wooster's empirical relation $C_{11} = H_v^{7/4}$. The calculated stiffness constant for different loads are shown in Figure 4(c). A plot of log p versus log d provides a straight line, the slope of which gives the work hardening coefficient n.

International Journal of
Scientific Research in Science and Technology (IJSRST)
Print ISSN : 2395-6011, Online ISSN : 2395-602X
International Conference on Advanced Materials
Held on 14, 15 December 2017, Organized by Department of Physics,
St. Joseph's College, Trichy, Tamilnadu, India

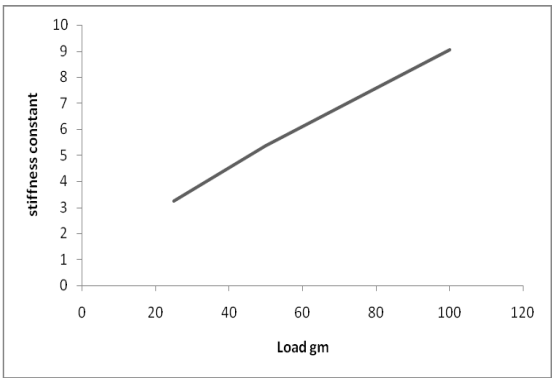

Figure 4(c). Load versus stiffness constant

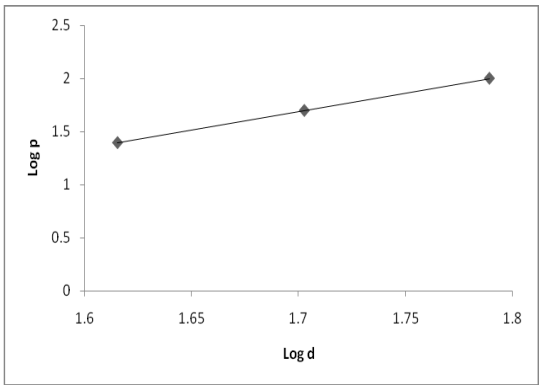

Figure 4(d). Log d versus Log p

In the present study, work hardening coefficient n is found to be higher than 2 for the sample, indicating that the lattices are soft. MZE crystal has higher microhardness H_v with respect to loads. Figure 4(d) shows that MZE crystal has a linear variation in strength.

SEM analysis

The grown MZE crystal was subjugated by SEM analysis. The quality of the grown crystal can be inferred to some extent by observing the surface morphology of the crystal. The recorded SEM picture Figure 5 (a, b & c) confirmed the formation of smooth surface. But in Figure 5b at higher magnification it is observed that some macro steps with pits and inclusion appeared due to high growth rates. In Figure 5c, plate like crystals show the thick and coarse granular type of growth [7].

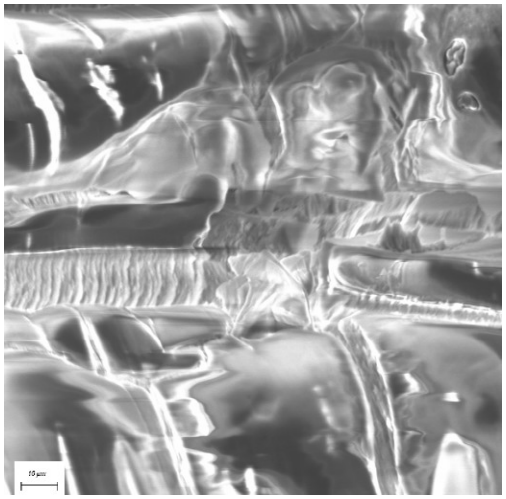

(a)

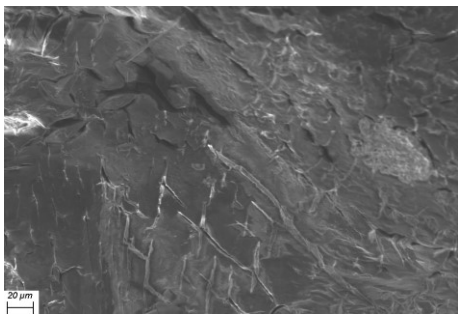

(b)

(c)

Figure 5. SEM pictures of MZE crystals

Conclusion

Single crystals of zinc and magnesium sulphate crystal was grown from an organic solution by slow evaporation method at room temperature. Good quality transparent crystals were harvested by slow evaporation technique within 25 days. The crystals

were subjected to single X ray diffraction method. The lattice parameters and structure were found. UV-Vis spectrum confirms that the material has wide optical transparency. FTIR analysis confirms the vibrational modes of the crystal and the expected presence of functional groups were identified. The Vicker's hardness property shows its good mechanical strength. The surface morphology is studied by SEM technique. The crystal has good optical, mechanical and morphological reports and may be considered for optoelectronic applications.

Acknowledgements

The authors are thankful for the authorities of IITM, Chennai, St. Joseph's College, Tiruchy, M.K. Univeristy, Madurai, B.S. Abdul Rahuman University, CECRI, Karaikudi for providing instrumental facilities for characterization.

References

[1] Brice, J. C., Crystal Growth Process. John Wiley and Sons, New York, 1986.

[2] Buckley, H.E., Crystal Growth. John Wiley and Sons, New York, 1951.

[3] Pasupathi. G., Philominathan. P., Material letters, 62 (2008) 4386-4388.

[4] John Coates., Interpretation of IR Spectra, A practical approach.

[5] Pavia, D.L., Lampman, G.M., Kriz, G.S., 1979, Introduction to spectroscopy: A guide for students of organic chemistry.

[6] Joseph B. Lambert et al., Introduction to Organic Spectroscopy., Mac million Pub.N.Y.1987.

[7] Mikiyasu Inoue, Izumi Hirasawa., Journal of Crystal Growth., 380 (2013) 169-175.

International Journal of
Scientific Research in Science and Technology (IJSRST)
Print ISSN : 2395-6011, Online ISSN : 2395-602X
International Conference on Advanced Materials
Held on 14, 15 December 2017, Organized by Department of Physics,
St. Joseph's College, Trichy, Tamilnadu, India

Growth and Characterization of A Novel Organic Stilbazolium Family Single Crystal: 4-(4-Methoxystyryl)-1-Methylpyridinium 4-Chlorobenzenesulfonate

Priya Antony[1], A. Antony Raj[1] , S. John Sundaram[1], S. Mary Margaret[1], S. Dominique[2], N. Lawrence[2], P. Sagayaraj[1*]

[1]Department of Physics, St. Joseph's College (Autonomous), Trichy-620 002, India

[2]Department of Physics, Loyola College (Autonomous), Chennai-600 034, India

*Corresponding author Email: psagayaraj@hotmail.com

Abstract

A new organic stilbazolium family single crystal of 4-(4-methoxystyryl)-1-methylpyridinium 4-chlorobenzene sulfonate (MBSC) has been successfully grown from methanol solution by adopting slow solvent evaporation technique. Single crystal X-ray diffraction analysis revealed that the crystal belongs to triclinic system with space group P1. The chemical composition of the title compound was identified by CHN elemental analysis. The characteristic functional groups of the grown crystal were identified by FT-IR spectroscopy. The crystal was found to be transparent in the region between 490 and 700 nm as indicated by the UV-Vis spectral studies. Photoluminescence spectrum of MBSC crystal shows a strong blue emission peak at 485 nm and a green emission at 521 nm.

Keywords: Organic compound; X-ray diffraction; Optical properties; Stilbazolium

1. Introduction

In recent scientific trend, organic nonlinear optical (NLO) materials attracted increasing attention due to remarkable growth of optoelectronic and photonic technologies because of their potential applications in optical communications, high-speed information processing, optical data storage devices, optical bi-stability etc [1]. Organic crystals with extended π-conjugated systems with hydrogen bonding greatly enhance the mobility of the electron density, which leads to high optical nonlinearity and molecular hyperpolarizability. In this context, many research efforts have been made to design and synthesize of new π-conjugated crystal structure for second and third harmonic generation applications [2].

In this article, we have synthesized a novel stilbazolium derivative crystal 4-(4-methoxy styryl)-1-methylpyridinium 4-chlorobenzenesulfonate (MBSC). Single crystals of MBSC were grown by slow evaporation method at room temperature and subjected to structural, spectral, optical and photoluminescence studies.

2. Experimental

2.1. Synthesis and crystal growth

4-(4-Methoxystyryl)-1-methylpyridinium iodide (MBSI) cation was synthesized by the condensation of 1,4-dimethyl pyridinium iodide (2.35 g, 10 mmol), methanol (50 ml) and 4-methoxy benzaldehyde (1.63 g, 10 mmol) in the presence of piperidine (0.2 ml).The mixture was taken in a round-bottom flask of a Dean-Stark apparatus and refluxed at 60 °C for 8 h and then cooled to room temperature. The product was filtered and recrystallized from methanol at least three times.

During the next stage, the metathesization reaction was carried out by the following procedure. MBSI

International Journal of
Scientific Research in Science and Technology (IJSRST)
Print ISSN : 2395-6011, Online ISSN : 2395-602X
International Conference on Advanced Materials
Held on 14, 15 December 2017, Organized by Department of Physics,
St. Joseph's College, Trichy, Tamilnadu, India

(0.706 g, 2 mmol) was dissolved in 60 ml of distilled water and simultaneously sodium p-chlorobenzene sulfonate (0.429 g, 2 mmol) was dissolved in 30 ml of distilled water by heating at 70 °C.These two hot solutions were mixed and further heated for 30 min. Yellow colour precipitate was obtained as a result of exchange reaction between anion and cation. Crystal growth was performed by employing slow solvent evaporation technique. Saturated solution of MBSC in methanol was prepared and sealed with a perforated cap, which was kept for crystallization at room temperature. After a period of 10-15 days of evaporation, MBSC crystals were obtained. Photograph of MBSC crystal is shown in Figure1.

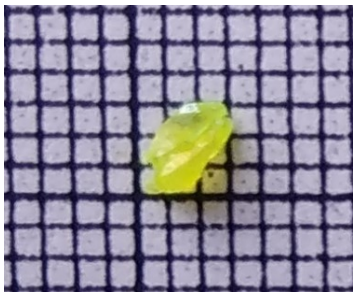

Figure 1. Photograph of MBSC crystal

3. Result and discussions

3.1. Single crystal X-ray diffraction

Single crystal X-ray diffraction analysis was performed by using Bruker Kappa APEX II diffractometer with MoKα radiation of wavelength 0.7170 Å. The calculated lattice parameters show that the MBSC crystal belongs to triclinic system with space group P1. The unit cell parameters are found to be a = 6.72 Å, b = 7.90 Å, c = 9.56 Å, α = 78.68°, β = 81.72°, γ = 84.66° and volume = 492 Å^3.

3.2. CHN analysis

The elemental composition of the MBSC crystal was analyzed using PerkinElmer series-II 2400 CHNS/O elemental analyzer. The percentage of calculated values (Figure2) of $C_{21}H_{20}ClNO_4S$ are C = 60.35%, H = 4.82%, N = 3.35% and the values experimentally found are C =60.14%, H = 4.98% and N = 3.49%. Thus, there is a close agreement between the calculated and experimental values of CHN.

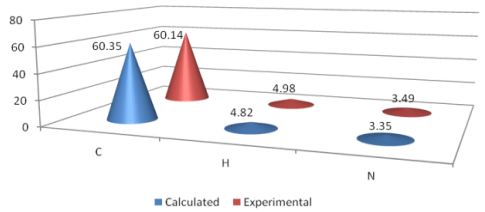

Figure 2. CHN data of MBSC crystal

3.3. FT-IR analysis

In order to identify the functional groups and detect the vibrational modes of molecules, the sample was characterized by Fourier transform infrared (FT-IR) spectroscopy. The measurement was done with KBr pellet technique in the wavelength range of 400–4000 cm^{-1}. The FT-IR spectrum of the MBSC crystal is shown in Figure 3. The peak observed at 3435 cm^{-1} is due to the stretching of hydroxyl group. The aromatic C–H group is confirmed by the presence of peak at 3066 cm^{-1} [3]. The peak corresponds to C=C stretch of the olefinic double bond is seen at 1589 cm^{-1}. The aromatic ring skeletal in-plane stretching vibration can be confirmed by the presence of the peaks at 1518 and 1467 cm^{-1}. Asymmetric and symmetric stretching mode vibrations of sulfonate group give peak around 1344 and 1117 cm^{-1}, respectively [4]. The peaks at 1032 and 838 cm^{-1} are assigned to the phenolic C–O stretch and olefinic C–H bond vibrations. Cis orientation of the substitute at the olefinic double bond produces peak at 637 cm^{-1}. The characteristic frequencies observed between 500 and 700 cm^{-1} are due to the out-of-plane ring bending modes and frequencies between 1100 and 1200 cm^{-1} are assigned to the in-plane ring deformation modes

International Journal of
Scientific Research in Science and Technology (IJSRST)
Print ISSN : 2395-6011, Online ISSN : 2395-602X
International Conference on Advanced Materials
Held on 14, 15 December 2017, Organized by Department of Physics,
St. Joseph's College, Trichy, Tamilnadu, India

are observed [5]. Thus, the presence of various functional groups in the structure has been confirmed. The wavenumbers correspond to different modes of vibration are given in Table 1.

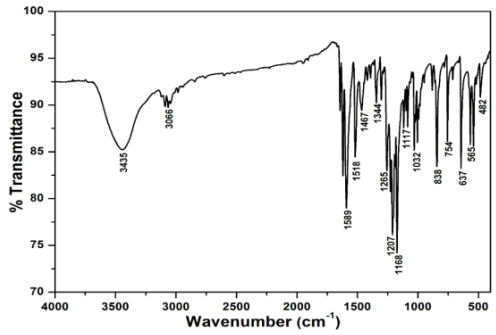

Figure 3. FT-IR spectrum of MBSC crystal

Table 1. FT-IR wavenumber assignments for MBSC

Wavenumber (cm^{-1})	Assignment
3435	O–H stretch
3066	Aromatic C–H stretch
1589	C=C stretch of the olefinic double bond
1518, 1467	Aromatic ring vibrations
1344, 1117	Asymmetric and symmetric stretching vibrations of $–SO_2$
1265	Phenolic C–O stretch
1032	Olefinic C–H bond
838	C–H bending vibration of 1,4 disubstituted aromatic rings
637	Cis orientation of the substitute at the olefinic double bond

3.4. UV-Vis absorption study

UV-Vis absorption spectrum was recorded in the wavelength range of 200-700 nm in solution form using methanol as solvent. The UV-Vis spectrum (Figure4) shows two distinct absorption peaks; the minor peak observed at 220 nm corresponds to the n-π^* transition and the major peak with maximum absorption at around 380 nm represents the π-π^* transition [6].The material shows a wide transparency in the region between 450 and 700 nm. The lower absorption of light in the visible and good transparency window over a near IR wavelength range are highly desired parameters for NLO applications [7].

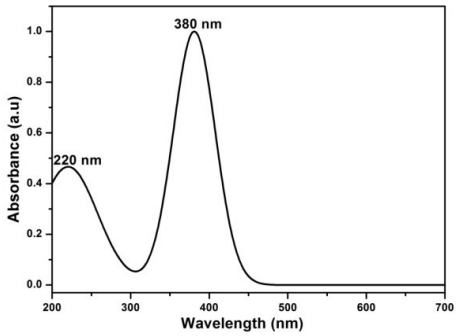

Figure 4. UV-Vis absorption spectrum of MBSC crystal

3.5. Photoluminescence study

Photoluminescence (PL) study for MBSC crystal was performed at room temperature. The sample was excited at the wavelength of 380 nm chosen from UV-Vis spectral studies, and the emission spectrum was recorded in the wavelength range of 450-650 nm (Figure5). The spectrum consists of two peaks in the visible region. The highly intense emission peak at 485 nm corresponds to blue emission and the other one at 521 nm refers to green emission, which may due to the anionic and cationic group present in MBSC crystal matrix [8]. The PL spectrum reveals that organic molecules with strong donor-π-acceptor system exhibit high photoluminescence properties. Especially, organic stilbazolium salts are potentially

International Journal of
Scientific Research in Science and Technology (IJSRST)
Print ISSN : 2395-6011, Online ISSN : 2395-602X
International Conference on Advanced Materials
Held on 14, 15 December 2017, Organized by Department of Physics,
St. Joseph's College, Trichy, Tamilnadu, India

used as fluorescence probe monitor in the active area of biomedical research [9,10].

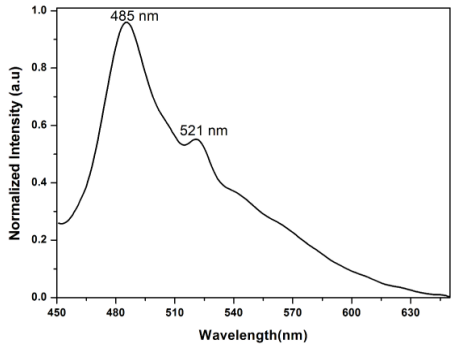

Figure 4. PL spectrum of MBSC crystal

4. Conclusion

A novel stilbazolium derivative crystal, 4-(4-methoxystyryl)-1-methylpyridinium 4-chlorobenzenesulfonate (MBSC) was successfully synthesized by condensation followed by metathesization reaction mechanism. Single crystal of MBSC was grown by slow solvent evaporation technique and the crystal structure was confirmed by single crystal XRD analysis. The functional groups identification and the structure of compound were confirmed by FT-IR spectral analysis. The percentage of carbon, hydrogen, and nitrogen in the synthesized sample was identified by CHN elemental analysis. From the absorption spectrum, the nature of transition was identified. Photoluminescence result suggests that the MBSC crystal could be used as a blue or green emission material by employing appropriate filters depending on the applications.

Acknowledgement

The authors greatly acknowledge DST-SERB (SR/S2/LOP-29/2013) India for funding this research work.

References

[1] K. Nivetha, W. Madhuri, S. Kalainathan, "Synthesis, growth, crystal structure and characterization of new stilbazolium derivative single crystal: (E)-4-(3-ethoxy-2-hydroxystyryl)-1-methyl pyridinium, Synthesis, growth, crystal structure and characterization of new stilbazolium iodide (3ETSI)", J Mater Sci: Mater Electron, 28 (2017) 8937-8949.

[2] C. Zhan, Y. Li, D. Li, D. Wang, Y. Nie, "Multi-photon absorption and optical limiting from six stilbazolium derivatives: donor influences", Opt. Mater., 28 (2006) 289-293.

[3] A. Antony Raj, S. John Sundaram, R. Gunaseelan,
P. Sagayaraj, "Bulk size crystal growth, spectroscopic, dielectric and surface studies of 4-N,N-dimethylamino- 4-N'-methylstilbazolium m-nitrobenzenesulfonate (DSMNS): A potential THz crystal of stilbazolium family", Spectrochim Acta A: Mol Biomol Spectroscopy, 149 (2015) 957-64.

[4] A. Antony Raj, R. Gunaseelan, P. Sagayaraj, "Investigation on third order nonlinear optical, electrical and surface properties of organic stilbazolium crystal of 4-N,N-dimethylamino-N'-methylstilbazolium p-methoxybenzene sulfonate", Opt. Mater, 38 (2014) 102-107.

[5] R. Jerald Vijay, N. Melikechi, Tina Thomas, R. Gunaseelan, M. Antony Arockiaraj, P. Sagayaraj, "Growth, structural, optical and thermal properties of potential THz material: N, N-dimethylamino-N'-methylstilbazolium 4-styrenesulphonate", J. Crystal Growth, 338 (2012) 170-176.

[6] R. Gunaseelan, P. Sagayaraj, "Bulk size crystal growth and physicochemical properties of ionic organic NLO crystal of DSMOS: A potential THz emitter", Materials Chemistry and Physics, 136 (2012) 379-385.

[7] M.K. Kumar, S. Sudhahar, P. Pandi, G. Bhagavannarayana, R.M. Kumar, "Studies of the structural and third-order nonlinear optical properties of solution grown 4-hydroxy-3-methoxy-4′-N′-methylstilbazolium tosylate monohydrate crystals", Opt. Mater., 36 (2014) 988-995.

[8] K. Senthil, S. Kalainathan, A. Rubankumar, "Effect of additives on the large size growth of 4-N, N-dimethylamino-4-N-methyl stilbazolium naphthalene-2-sulfonate (DSNS) single crystal: An efficient stilbazolium derivative NLO crystal with potential terahertz wave properties", Cryst Eng Comm, 16 (2014) 9847-9856.

[9] A. Bajorek, I. Wrzesniewska, M. Pietrzak, "Stilbazolium salts as fluorescence probes for monitoring local viscosity and pH of solutions", Chemik, 65 (2011) 255-260.

[10] J.N. Wilson, A.S. Brown, W.M. Babinchak, C.D. Ridge, J.D. Walls, "Fluorescent stilbazolium dyes as probes of the norepinephrine transporter: structural insights into substrate binding", Org. Biomol. Chem, 10 (2012) 8710.

International Journal of
Scientific Research in Science and Technology (IJSRST)
Print ISSN : 2395-6011, Online ISSN : 2395-602X
International Conference on Advanced Materials
Held on 14, 15 December 2017, Organized by Department of Physics,
St. Joseph's College, Trichy, Tamilnadu, India

A Comparative Study on Morphological and Optical Properties of Pure and Oleic Acid Added Organic Nanocrystal of DAST Embedded in PVA Matrix for NLO Applications

S. Dominique[1], Priya Antony[2], S. John Sundaram[2], R. Mahesh[2], Jerald V Ramaclus[1], N. Lawrence[1], P. Sagayaraj[2]*

[1]Department of Physics, St. Joseph's College (Autonomous), Trichy-620 002, India

[2]Department of Physics, Loyola College (Autonomous), Chennai-600 034, India

*Corresponding author Email: psagayaraj@hotmail.com

Abstract

Organic nanocrystals exhibit enhanced nonlinear optical (NLO) properties over the bulk crystals of those organic molecules. In this article, an attempt has been made to prepare organic nanocrystal of DAST via two different approaches. In the first case, the synthesis of nanocrystal was explored via a cost effective and low temperature solvothermal method. In the second case, the DAST nanocrystal/PVA and oleic acid assisted DAST nanocrystal/PVA composite films were prepared in order to combine the enhanced nonlinear optical properties of the organic nanocrystalline material with flexible polymers. The structure and morphology of as-prepared DAST nanocrystal embedded in PVA matrixwere analyzed using powder XRD and scanning electron microscope (SEM). Fourier transform infrared (FT-IR) analysis confirms the presence of various functional groups. The optical property of the DAST/PVA composites was characterized by UV-Vis absorption spectrum. The addition of oleic acid significantly alters the crystal growth process of DAST nanocrystal, resulting in the generation and stabilization of regular nanosized DAST nanorods.

Keywords: Organic nanocrystals, functional groups, optical absorption, morphology, composite

1. Introduction

Terahertz (THz) technology has attracted much attention in the recent years due to its potential applications such as nonlinear optics, topographic imaging, label-free genetic analysis, cellular level imaging and chemical and biological sensing [1]. The most pressing component technology to be developed remains in the area of THz sources and many applications yet to be realized lie in wait [2]. Among the various classes of materials investigated worldwide, ionic organic crystals like 4-N, N-dimethylamino-4-N-methyl-stilbazolium tosylate (DAST) have been a recent source of interest as THz emitters due to its high nonlinearities in combination with a low dielectric constant [3]. The growth of high quality bulk DAST crystal is still a limitation and this hinders to exploit its high figure of merit. The use of organic materials for optical applications is generally limited by their insufficient chemical stability and mechanical resistance. In order to avoid these basic drawbacks and to take advantages of the optical properties of organic materials at the nanometer scale, Sanz and co-workers have developed hybrid (organic-inorganic) material by preparing organic nanocrystals in sol-gel glasses [4]. It has been proposed that organic nanocrystals could exhibit enhanced nonlinear optical (NLO) properties over the bulk crystals of those organic nonlinear molecules [5]. In this connection, DAST nanocrystals, which combine the unusual properties of nanocrystals have been prepared by dispersing them in a non-polar liquid using reprecipitation method [6]. However, only submicrometre DAST microcrystals have been achieved. Zheng et al. [7] have prepared DAST nanocrystals with enhanced NLO properties at nanometre scale due to influence of carbosiloxane dendrimer, employing the re-precipitation method. Stable and size controlled DAST nanocrystals were prepared and the size is reduced significantly below

International Journal of
Scientific Research in Science and Technology (IJSRST)
Print ISSN : 2395-6011, Online ISSN : 2395-602X
International Conference on Advanced Materials
Held on 14, 15 December 2017, Organized by Department of Physics,
St. Joseph's College, Trichy, Tamilnadu, India

100 nm. Macchi et al. [8] have prepared DAST nanocrystals in a poly methyl methacrylate (PMMA) film by electric poling. However, it was found that the nanocrystal is not of high quality because of the instability caused by the PMMA polymer under the electronic beam. Hence, significant challenges are involved in the preparation of DAST nanoparticle to incorporate them into a matrix while preserving the size distribution. Poly vinyl alcohol (PVA) is one of the most frequently used host molecules and it forms a cross-linked structure that could hold cavities within [9].In the present work, an attempt has been made to prepare organic nanoparticles of DAST by two different approaches. In the first case, the synthesis of DAST nanoparticles was explored via a cost effective and low temperature solvothermal method. In the second case, the DAST nanocrystal/PVA composite films were prepared in order to combine the enhanced nonlinear optical properties of the organic nanocrystalline material with flexible reprocessability of polymers. The morphologies of the nanocrystals embedded in PVA matrix were analyzed by scanning electron microscope (SEM) and the structural characterization was carried out using powder XRD and Fourier transform infrared (FT-IR) analyses. The optical properties were characterized by UV-Vis absorption spectroscopy.

2. Experimental

2.1. Synthesis of DAST nanorods

DAST (0.088 g) was dissolved in 10 ml of methanol. To this solution, 1 ml of oleic acid was added and stirred for 1 h. After stirring, 100 ml of decalin was added to the above solution.The mixture was transferred into an autoclave and kept inside a furnace at 100°C for 2 h. After 2 h, the autoclave was taken out and allowed to cool to room temperature. The resultant precipitate was filtered and dried at 100 °C for 1 h.

2.2. Preparation of DAST nanocrystals in PVA matrix

An aqueous PVA (10 wt%) solution was prepared and stirred for 24 h. Simultaneously, an equal volume of saturated DAST-methanol solution was prepared at room temperature. Later, the DAST-methanol solution was added to the PVA gel and stirred for 1 hand then casted into a Petri dish. After drying at room temperature for 2 days, the film was kept in a furnace at 100 °C for 2 h in order to remove the water molecules. Later, the film was peeled off from the dish. The colour of the film appeared red, which is the typical colour of DAST (Fig. 1).

2.3. Preparation of oleic acid assisted DAST nanorods in PVA matrix

In another synthesis procedure, oleic acid assisted DAST nanorods were prepared. The same procedure was followed as in case of DAST in PVA but in addition to that an equal mole percent of oleic acid with respect to DAST was also mixed in the DAST-methanol solution. This solution is stirred for 30 min and then added to the PVA hydro-gel.

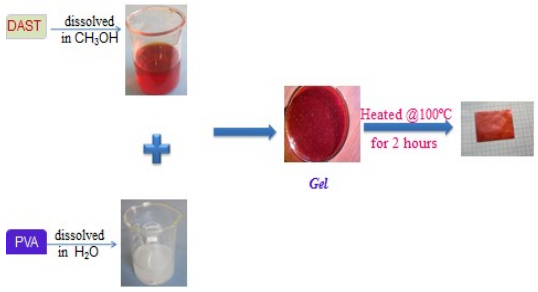

Figure 1. Synthesis scheme for preparation of DAST nanocrystals in PVA matrix

3. Result and discussions

3.1. Powder XRD analysis

Powder X-ray diffraction analysis was performed on the organic nanocrystals of DAST, at room temperature. The powder XRD pattern of DAST nanoparticles is shown in Figure 2. The (0 2 0) and (2 2 $\bar{2}$) planes are observed to be more intense than the (0 2 2) and (0 0 $\bar{4}$) which are the usually observed intense peaks for DAST crystals. At the same time, the peaks corresponding to the SHG inactive hydrated DAST crystal is not seen in the resulting pattern [5]. Further, the appearance of (0 2 0)

International Journal of
Scientific Research in Science and Technology (IJSRST)
Print ISSN : 2395-6011, Online ISSN : 2395-602X
International Conference on Advanced Materials
Held on 14, 15 December 2017, Organized by Department of Physics,
St. Joseph's College, Trichy, Tamilnadu, India

and (2 2 $\bar{2}$) planes as dominant ones indicate the formation of good quality DAST nanorods. It is found that DAST crystallized into monoclinic system. The lattice parameters are; a = 10.219 Å, b = 11.328 Å, c = 17.859 Å, and β = 90.08° and V = 2067.45 Å^3. The XRD data for DAST nanocrystals obtained in this work is matching with those data for bulk crystals of DAST reported by Marder et al. [10].

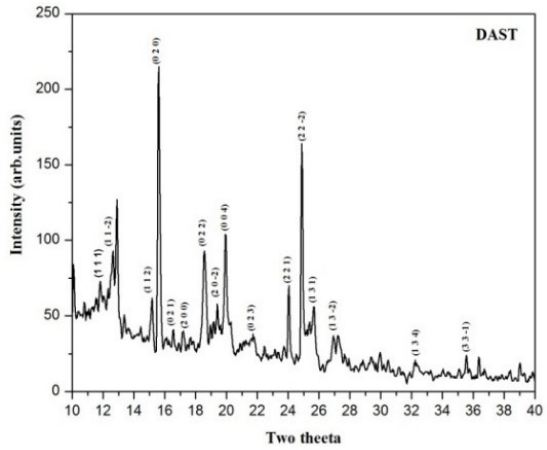

Figure 2. Powder XRD pattern of DAST nanorods

3.2. SEM analysis

SEM micrographs reveal different morphological behavior of DAST nanorods, nanocomposites of DAST/PVA and oleic acid assisted DAST/PVA (Fig. 3a-c). The size and shape of the nanocrystals embedded in PVA film was examined. The shape observed are rectangular plate-like crystals with size ranging from 200to 500nm. In an earlier report, the mean size distribution of DAST nanocrystals was found around 400 × 400 ×70 nm^3 and thus it is evident that the size of the DAST nanocrystals formed in the present work is better controlled than the previously repoterd work[6].It reveals the nanorod formation in the case of oleic acid assisted DAST/PVA matrix. In general, oleic acid assisted nanoparticles preparation helps to form onedimensional (1D) nanostructures. In the present case, the SEM picture reveals the domination of DAST nanorods along with few plate-like nano aggregates. The effect of oleic acid on the growth and morphology of the DAST nanorods is evident in the SEM micrograph (Figure 3c). It is clear that very distinct DAST nanorods with relatively high aspect ratio are obtained. The presence of DAST nanorods of diameter 300 nm – 1 μm and length 5-10 μm are evident. The images further reveal that the level of agglomeration is low for the DAST nanorods.

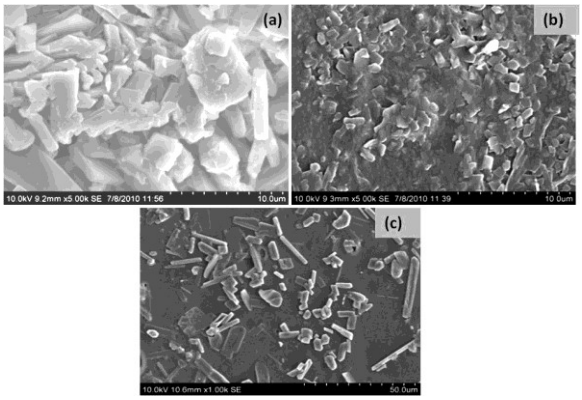

Figure 3. SEM micrograph of (a) DAST nanorods (b) DAST nanocrystals embedded in PVA matrix (c) oleic acid assisted DAST nanorods in PVA matrix

3.3. Optical absorption studies

UV-Vis absorption spectrum was recorded in the range 200 nm to 900 nm using SHIMADZU 2450 spectrophotometer. Figrue 4 shows the absorption spectra of DAST nanocrystal, DAST/PVA, oleic assistedDAST/PVA and DAST dissolved in methanol. The absorption for DAST in methanol is at 475 nm and for DAST nanorods, it is at 520 nm. When we compare the absorption spectrum of DAST nanocrystals with the DAST bulk crystal, the corresponding $\lambda_{(max)}$ is observed at 545 nm for bulk crystals. Thus there is a blue shift of 25 nm for the nanosample synthesized. The blue shift indicates the nanostructure nature of the developed sample. This result clearly indicates that the synthesized DAST nanorods are in between the molecular and bulk form. The absorption spectrum of the DAST nanocrystals embedded in PVA film is quite similar to that of bulk crystalline DAST. The narrow red shifted absorption band at 580 nm (475 nm is the cut off wavelength of DAST in molecular form) is the fingerprint of the J-type organization of the

International Journal of
Scientific Research in Science and Technology (IJSRST)
Print ISSN : 2395-6011, Online ISSN : 2395-602X
International Conference on Advanced Materials
Held on 14, 15 December 2017, Organized by Department of Physics,
St. Joseph's College, Trichy, Tamilnadu, India

chromophore (4-N,N-dimethylamino-4-N-methylstilbazolium) within the crystalline structure of DAST [8]. The UV absorption spectrum of DAST nanorods prepared via oleic acid assisted synthesis reveals a strong absorption at 475 nm which is similar to that of DAST in molecular form. This result indicates that the addition of oleic acid significantly alters the crystal growth process of DAST nanocrystal, resulting in the generation and stabilization of regular nanosized DAST nanorods.

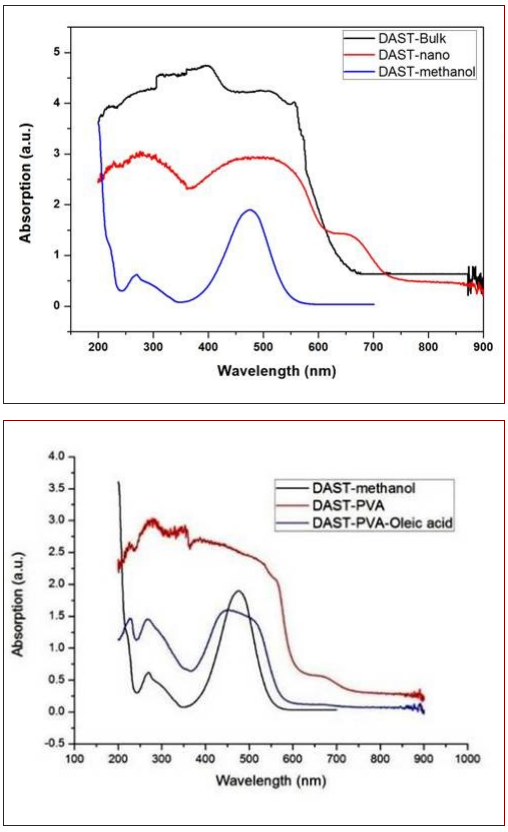

Figure 4. UV-Vis absorption spectra of DAST nanocrystal, DAST/PVA, oleic acid assisted DAST/PVA and DAST in methanol

3.5. FT-IR analysis

FT-IR spectrumof DAST/PVA and oleic acid assisted DAST/PVAwas recorded in the wavelength range 400 to 4000 cm^{-1}. For comparison, the spectrum of PVA is also provided in order to identify the functional groups and their corresponding vibrational characteristics (Fig. 5).The typical signatures in PVA which are due to O–H stretching (3435 cm^{-1}), C–H stretching (2912-2945 cm^{-1}), C–H bending (1638 cm^{-1}) and C–O (1050-1150 cm^{-1}) are observed in the FT-IR spectrum (Figure 5a). The presence of DAST nanocrystals/nanorods in PVA is confirmed by the identification of strong infrared active modes in DAST. The sharp peaks at 2924 cm^{-1} and 2919 cm^{-1} are due to the C–H stretching; the intensity of this peak is increased in DAST nanocrystals as well as in the sample with DAST nanorods. The peaks at 1585 cm^{-1} and 1581 cm^{-1} are typical C–C=C–C in-plane stretching frequency which are carbon backbone between the aromatic rings of the stilbazoliumchromophore, these peaks are also observed in both the cases. The peaks at 1179 cm^{-1}, 1163 cm^{-1} and 1179 cm^{-1}, 1165 cm^{-1} are assigned to the in-plane aromatic ring deformations, which are typical for para substituted benzenes [11]. The peaks at 564 cm^{-1} and 567 cm^{-1} are attributed to the vibrations of aromatic rings. In case of oleic acid assisted DAST nanorods in PVA, the peaks of DAST are more distinct and prominent when compared to DAST nanocrystals in PVA matrix.

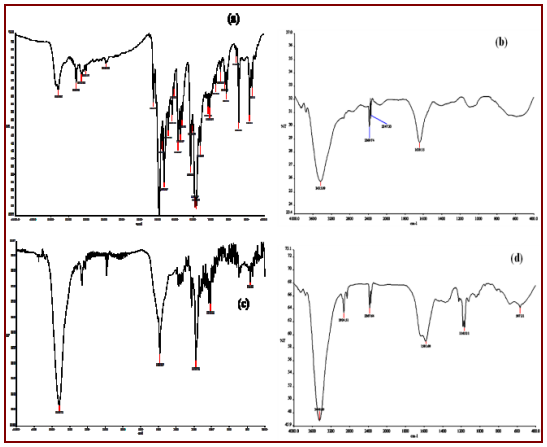

Figure 5. FT-IR spectra of (a) pure DAST (b) PVA (c) DAST nanocrystals embedded in PVA (d) oleic acid assisted DAST nanorods embedded in PVA

4. Conclusion

Organic nanocrystals of DAST, DAST nanocrystals embedded in PVA matrix and oleic acid assisted DAST/PVA matrix were successfully synthesized via cost effective and simple solvothermal method under

mild conditions. The structure of the nanoparticle was confirmed by powder XRD method. The surface features, morphology were investigated by SEM analysis. SEM analysis of nanocomposites of DAST/PVA, oleic acid assisted DSSS/PVA showed the formation of different morphologies.The UV-Vis absorption study on DAST nanoparticles confirms the blue shift of 25 nm when compared to the bulk DAST crystals.The stretching vibrations of the various functional groups were identified by FT-IR spectral studies. The flexible free-standing DAST/PVA film could be employed as potential material for THz applications.

Acknowledgement

The authors greatly acknowledge DST-SERB (SR/S2/LOP-29/2013) India for funding this research work.

References

[1] Ferguson B, Zhang X.C, "Materials for terahertz science and technology", Nature Materials, 1 (2002) 26-33.

[2] Siegel P.H, "Terahertz technology", IEEE Transactions on Microwave Theory and Techniques, 3 (2002) 910-928.

[3] Jazbinsek M, Mutter L, Gunter P, "Photonic applications with the organic nonlinear optical crystal DAST", IEEE Journal on Selected Topics in Quantum Electronics, 5(2008)1298-1311.

[4] Sanz N, Baldeck P.L,Ibanez A, "Organic nanocrystals embedded in sol-gel glasses for optical applications", Synthetic Metals, 115(2000) 229-234.

[5] Oikawa H, Fujita S, Kasai H, Okada S, Tripathy S.K., Nakanishi H, "Electric field-induced orientation of organic microcrystals with large dipole moment in dispersion liquid", Colloids and Surfaces A: Physicochemical and Engineering Aspects, 169 (2000) 251-258.

[6] Kaneko Y, Fukuda T, Onodera T, Kasai H, Okada S, Oikawa H, Nakanishi H, Matsuda H, "Anisotropic orientation control of nonpolar organic nanocrystal dispersion by external fields", Jpn. J. Appl. Phys., 42 (2003) L1343.

[7] Zheng M.L, Chen W.Q, Fujita K, Duan X.M, Kawata S, "Dendrimer adjusted nanocrystals of DAST: organic crystal with enhanced nonlinear optical properties", Nanoscale, 2(2010)913-916.

[8] Macchi R, Cariati E, Marinotto D, Roberto D, Tordin E, Ugo R, Bozio R, Cozzuol M, Pedron D, Mattei G, "Stable SHG from in situ grown oriented nanocrystals of [(E)-N,N-dimethylamino-N-methylstilbazolium] [p-toluenesulfonate] in a PMMA film", Journal of Materials Chemistry, 20 (2010) 1885-1890.

[9] Kim JM, Chae SK, Lee YB, Lee JS, Lee GS, Kim TY, Ahn DJ, "Ploydiacetylene supramolecules embedded in PVA film for strip-type chemosensors", Chemistry Letters, 35 (2006) 560-561.

[10] Marder SR, Perry JW, Schaefer WP, "Synthesis of organic salts with large second order optical nonlinearities", Science, 245(1989)626-628.

[11] Bosshard C, Spreiter R, Degiorgi l, Gunter P, "Infrared and Raman spectroscopy of the organic crystal DAST: polarization dependence and contribution of molecular vibrations to the linear electro-optic effect", Phys. Rev. B, 66 (2002) 205107-1-9.

International Journal of
Scientific Research in Science and Technology (IJSRST)
Print ISSN : 2395-6011, Online ISSN : 2395-602X
International Conference on Advanced Materials
Held on 14, 15 December 2017, Organized by Department of Physics,
St. Joseph's College, Trichy, Tamilnadu, India

Growth and Characterization of L-Glycine Sodium Nitrate Single Crystal for Electro-optic Applications

S. Arockia Avila, A. Leo Rajesh*
Department of Physics, St. Joseph's College, Tiruchirappalli - 620 002, India
Corresponding Author: aleorajesh@gmail.com

Abstract

Single crystals of semiorganic nonlinear optical material of L-Glycine Sodium Nitrate (LGSN) have been successfully grown by slow evaporation solution growth technique. Cell parameters of the grown crystal were identified using single crystal X-ray diffraction analysis and it was found that the material crystallizes in monoclinic system with space group Cc. The presence of functional groups and the spectral properties were assessed by FTIR analysis. Optical transparency of the grown crystals was investigated by UV-Vis-NIR spectrum. The scanning electron microscope analysis was carried out to determine the surface morphology of the grown crystal. Second harmonic generation efficiency of the grown crystal have been measured by Kurtz and Perry technique and it was found to be 2.5 times greater than that of KDP. The obtained results show that L-Glycine Sodium Nitrate crystals are potential materials for NLO device fabrication.

Keywords: Solution growth, UV-Vis-NIR, SEM, SHG test.

1. Introduction

In recent years, non-linear optical (NLO) crystals with high conversion efficiencies are needed for optical second harmonic generation (SHG) because of their applications in opto-electronics, photonics, high speed information processing, telecommunications and optical information storage devices [1]. Amino acid family crystals are promising materials for these applications and it depends on the properties such as transparency, birefringence, refractive index, dielectric constant and thermal, photochemical and chemical stability [2]. Amino acids are considered to be interesting organic materials for NLO devices as they contain donor carboxylic (COOH) group and the proton acceptor amino acid (NH_2) group known as zwitterions which create hydrogen bonds. Considerable efforts have been made on amino acid mixed complex crystals in order to make them suitable for device fabrications [3–6]. Glycine has no centre of chirality and is optically inactive. Glycine family crystals have been subjected to extensive research by several researchers for their efficient non-linear optical properties [7-10]. Since the glycine molecule can exist in zwitterionic form, it is capable of forming compounds with anionic, cationic and neutral chemical compounds. Thus a large variety of glycine coordinated compounds can be formed. However, only those complexes of glycine, which crystallizes in non-centrosymmetric structure, are expected to exhibit nonlinear optical second harmonic generation [11].

Most of the organic NLO crystals usually have poor mechanical and thermal properties whereas the inorganic NLO materials have excellent mechanical and thermal properties, but possess relatively modest optical nonlinearity. Therefore semi organic crystals are those which combine the positive aspects of organic and inorganic materials resulting in desired nonlinear optical properties [12]. The properties of large nonlinearity, high resistance,

International Journal of
Scientific Research in Science and Technology (IJSRST)
Print ISSN : 2395-6011, Online ISSN : 2395-602X
International Conference on Advanced Materials
Held on 14, 15 December 2017, Organized by Department of Physics,
St. Joseph's College, Trichy, Tamilnadu, India

low angular sensitivity, good mechanical hardness and further significance are centred on semi organic crystals. Hence, investigations were done to develop various semi-organic crystals which are more suitable for device fabrication [13,14]. A series of semi-organic compound such as L-Alanine potassium chloride [15], L-Alanine sodium nitrate [16], L-Histidine tetrafluroborate [17] have been reported earlier. The present manuscript reports on the crystal growth of L-Glycine sodium nitrate crystals from aqueous solution followed by the characterizations like single crystal X-ray diffraction, Fourier transform infrared spectroscopy, optical absorption, scanning electron microscopy, second harmonic generation efficiency and the results are discussed.

2. Experimental

2.1. Materials and method

Analytical reagent grade (AR) samples of glycine and sodium nitrate were used as a precursor materials. Double deionized water (Merck) was used as a solvent. Slow evaporation solution growth technique was adopted for the growth of single crystals. Equimolar ratio of L-glycine and sodium nitrate were taken and stirred well for 4 hours separately and mixed. The solution was then filtered and kept in a vibration free ambiance. Transparent seed crystals were obtained by spontaneous nucleation. Among them, defect free seed crystal was suspended in the mother solution. Single crystals of dimension 9×8×2 mm^3 have been grown within the period of 30 days. The photograph of the as grown glycine sodium nitrate crystal is shown in Figure 1.

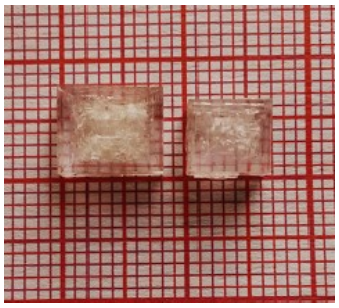

Figure 1. As grown LGSN single crystal

2.2. Characterization techniques

The grown crystals were subjected to various characterization analyses to test their suitability for optical device applications. Single crystal X-ray diffraction analysis was carried out using Four-circle Enraf Nonius CAD4/MACH3 single crystal diffractometer to determine the lattice parameters and space group. The presence of functional groups in the grown crystal was identified using Fourier Transform Infrared spectral analysis using a PERKIN ELMER SPECTROMETER by KBr pellet technique within the range of 400-4000 cm^{-1}.

In order to examine the optical properties of the grown crystal in the UV-Vis-NIR regions of electromagnetic spectrum, the linear optical study was carried out using PERKIN ELMER LAMBDA 35 UV-Visible spectrophotometer within the range of 200-1000 nm. SEM analysis was carried out by using CARL ZEISS SIGMA VP scanning electron microscope to analyse the crystal surface morphology. Second Harmonic Generation efficiency test for the grown samples was performed by Kurtz and Perry powder technique using a Q - switched high energy Nd:YAG Laser (QUANTA RAY Model LAB-170-10) Model HG-4B- High efficiency with repetition rate at 10 Hz.

International Journal of
Scientific Research in Science and Technology (IJSRST)
Print ISSN : 2395-6011, Online ISSN : 2395-602X
International Conference on Advanced Materials
Held on 14, 15 December 2017, Organized by Department of Physics,
St. Joseph's College, Trichy, Tamilnadu, India

3. Results and discussion

3.1. Single crystal XRD analysis

The L-Glycine sodium nitrate crystal was subjected to single crystal X-ray diffraction analysis to determine the lattice parameters and space group. The title compound crystallizes into monoclinic system with space group Cc [18]. From the XRD data, the calculated lattice parameter values are found to be a = 14.32Å, b = 5.25Å, c= 9.11Å, and are tabulated in Table 1.

Table 1. Single crystal XRD analysis data of L-GSN

L-Glycine SN	Crystal data
Crystal System	Monoclinic
Space group	Cc
Unit Cell dimensions	a = 14.32 Å b = 5.25 Å c = 9.11 Å

3.2. Fourier Transform Infrared spectral analysis

Fourier transform infrared spectral studies were carried out for the samples to identify the functional groups. The presence of functional groups in the compound L-Glycine sodium nitrate was identified and was shown in Figure 2. The vibration peak at 3441 cm^{-1} represents $(NH_3)^+$ asymmetric stretching vibration. The absorption peak at 2098 cm^{-1} shows asymmetrical NH_3 bending vibration.

The absorption band at 1614 cm^{-1} represents C=O stretching vibration. The sharp peak at 1392 cm^{-1} is due to NO_3^- asymmetric stretching vibration. The peak at 938 cm^{-1} is due to CH_2 rocking vibration. The C-C stretching vibration is attributed to 837 cm^{-1}. The absorption band at 665 cm^{-1} shows NO_3^- in plane bending vibration. The vibration peak at 503 cm^{-1} represents COO- rocking vibration [19]. The observed bands along with their vibration assignment are presented in Table 2.

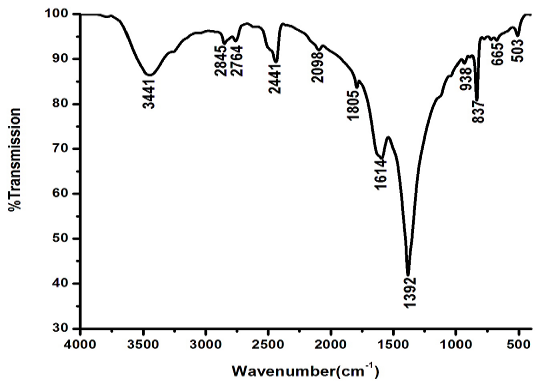

Figure 2. FTIR Spectrum of L-Glycine SN

Table 2. Tentative assignments of L-Glycine SN

Wavenumber (cm^{-1})	Assignment
3441	$(NH_3)^+$ asymmetric
2098	Asymmetric NH_3 bending
1614	C=O stretching
1392	NO_3^- asymmetric stretching
938	CH_2 rocking
837	C-C stretching
665	NO_3^- in plane bending
503	COO- rocking

3.3. UV-Visible NIR Spectral analysis

Optical transparency in the entire visible region with a good percentage of transmission is the key properties of an NLO material. The transmission spectrum of L-Glycine sodium nitrate is shown in Figure 3. From the figure it was observed that the material has high transmittance in the entire visible region of about 70% and the lower cut off wavelength was observed at 200 nm. This is one of the most desirable properties of the NLO material for device fabrication.

International Journal of
Scientific Research in Science and Technology (IJSRST)
Print ISSN : 2395-6011, Online ISSN : 2395-602X
International Conference on Advanced Materials
Held on 14, 15 December 2017, Organized by Department of Physics,
St. Joseph's College, Trichy, Tamilnadu, India

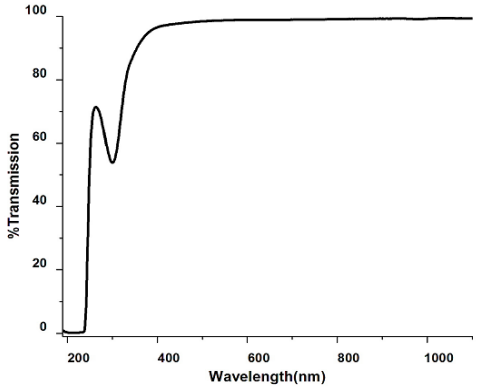

Figure 3. UV-Visible-NIR transmission spectrum of L-Glycine SN

3.4. Morphological study

Scanning electron microscopy (SEM) analysis has been carried out for the grown crystal to study the nature, surface morphology and the presence of imperfections in the grown crystals. The transparent regions of the crystals are cut into few mm for examining the surface morphology. From the SEM micrograph it can be observed that the grown crystal has cracks and few inclusions which may be due to the impact of growth conditions and was shown in Figure 4.

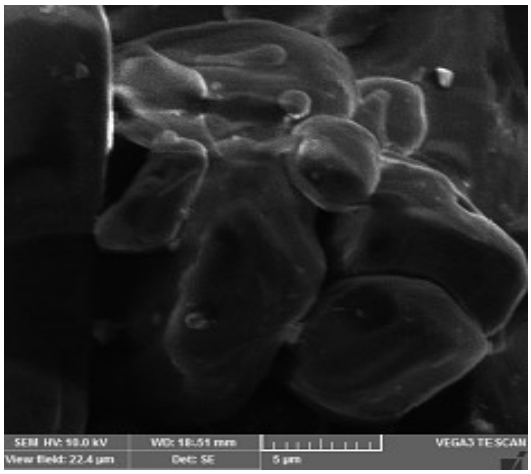

Figure 4. SEM image of LGSN

3.5. Second Harmonic Generation

Second Harmonic Generation efficiency of L-glycine sodium nitrate crystal was determined by Kurtz and Perry technique. Finely powdered samples are packed tightly in a micro capillary tube. The SHG efficiency of the LGSN crystal is measured with compared to the efficiency of the KDP crystals. A Q-switched Nd:YAG laser emitting fundamental wavelength of 1064 nm is allowed to strike on the powdered sample. The experiment is carried out at room temperature [20]. The SHG efficiency of L-glycine SN crystal was observed to be 2.5 times greater than that of KDP and it confirms the suitability of LGSN crystals in NLO applications.

4. Conclusion

A Semi-organic NLO material LGSN has been grown by slow evaporation solution growth technique. The harvested crystals of size 9×8×2 mm^3 were obtained after a period of 30 days. Unit cell parameters were by single crystal X-ray diffraction analysis, which confirmed that the grown crystal belongs to monoclinic system with space group Cc. The various functional groups and their vibrational interactions of the grown crystal were confirmed by Fourier transform infrared analysis. The optical study shows that the lower cutoff wavelength is below 200 nm and possess good transparency in the entire visible region. SEM study reveals the crystal morphology of the grown crystal. The estimated SHG efficiency of L-glycine SN was found to be 2.5 times greater than that of KDP. Thus L-GSN crystal can be exploited as a potential material for photonics, electro-optic and SHG device applications.

References

[1] Karunanithi, U., Arulmozhi, S. and Madhavan, J., "Structural, Optical and Dielectric Studies on Pure and Doped L-Alaninium Maleate Single Crystals", J. Appl. Phys. 1, 19 (2012).

[2] Arun, K.J. and Jayalekshmi, J.," Growth and Characterisation of Nonlinear Optical Single Crystals of L-Alaninium Oxalate ", J. Miner. Mater. Character. Eng. 8, 635 (2009).

[3] Lydia Caroline, M., Prakash, M., Geetha, D., Vasudevan, S., "Growth, structural, vibrational, optical, laser and dielectric aspects of L-alanine alaninium nitrate single crystal", Spectrochim. Acta Part A 79, 1936 (2011).

[4] Rajan Babu, D., Jayaraman, D., Mohan Kumar, R., Ravi, G. and Jayavel, R., "Growth aspects of semi-organic nonlinear optical L-arginine tetrafluroborate single crystals", J. Cryst. Growth 250, 157 (2003).

[5] Bhagavannarayana, G., Riscob, B., Shakir, M., "Growth and Characterization of L-Leucine L-Leucinium picrate single crystal: A new nonlinear optical material", Mater. Chem. Phys. 126, 20 (2011).

[6] Natarajan, S., Chitra, G.P., Martin, S.A., Dhas, B., Athimoolam, S., "Growth, structural, thermal and optical studies on L-glutamic acid hydroboromide - A new semiorganic NLO material", Cryst. Res. Technol. 43, 713 (2008).

[7] Ambujam, K., Rajarajan, K., Selvakumar, S., Madhavan, J., Mohammed, G. and Sagayaraj, P., "Growth and characterization of gel grown single crystals of bis-glycine hydrogen chloride (BGHC)", Opt. Mater., 29, 657 (2007).

[8] Selvaraju, K., Valluvan, R. and Kumararaman, S., "New nonlinear optical material: Glycine Hydrofluoride", Mater. Lett., 60, 2848 (2006).

[9] Shanmugavadivu, Ra., Ravi, G. and Azariah, A.N., "Crystal growth, thermal and optical studies of nonlinear optical material: Glycine potassium sulphate", J. Phys. Chem. Solids, 67, 440 (2006).

[10] Ambujam, K., Rajarajan, K., Selvakumar, S., Potheher, I.V., Joseph, G.P. and Sagayaraj, P., "Growth and Characterization of a novel NLO crystal bis-glycine hydrogen chloride (BGHC)", J. Cryst. Growth, 286, 440 (2006).

[11] Balasubramanian, D., Murugakoothan, P., Jayavel, R., "Synthesis, growth and characterization of organic nonlinear optical bis-glycine maleate (BGM) single crystals", J. Cryst., Growth 312, 1855 (2010).

[12] Natarajan, S., Shanmugam, G., Martin, S.A., Dhas, B., "Growth and characterization of a new semi organic NLO material: L-tyrosine hydrochloride", Cryst. Res. Technol. 5, 561 (2008).

[13] Selvakumar, S., Leo Rajesh, A., "Synthesis and characterization of semi-organic nonlinear optical material: Sodium para-nitrophenolate", Opt. Int. J. Light Electron Opt. 127, 6982 (2016).

[14] Selvakumar, S., Leo Rajesh, A., "Crystal growth and DFT insight on sodium para-nitrophenol dihydrate single crystal for NLO applications", J. Mol. Struct. 1125, 1 (2016).

[15] Arockia Avila, S., Selvakumar, S., Francis, M., Leo Rajesh, A., "Synthesis, growth and characterization of L-alanine Potassium Chloride single crystal: a phase-matchable semi-organic material for second and third order NLO applications", J. Mater. Sci. Mater. Electron. DOI 10.1007/s10854-016-5628-5.

[16] Arockia Avila, S., Leo Rajesh, A., "Growth and characterization of L-alanine sodium nitrate single crystal for second and third order NLO

applications", International journal for research in science engineering and technology. 3, 14 (2016).

[17] Arockia Avila, S., Leo Rajesh, A., "Synthesis, growth and characterization of NLO single crystal: L-Histidine tetrafluroborate", J. Chem. Pharm. Sci. 9, 129 (2016).

[18] Narayan Bhat, M., Dharmaprakash, S.M., "New nonlinear optical material: glycine sodium nitrate", J. Cryst. Growth, 235, 511 (2002).

[19] Suresh, S., Ramanand, A., Jayaraman, D., Navis Priya, S.M., Anand, K., "Growth and characterization of glycine sodium nitrate (GSN) single crystal", International Journal of the physical sciences, 6, 3875 (2011).

[20] Suresh, S., Ramanand, A., Mani, P., Kaliya urthyanand, "Growth, structural, optical, mechanical and dielectric properties of glycine sodium nitrate (GSN) single crystal", Journal of optoelectronics and Biomedical Materials, 1, 129 (2010).

International Journal of
Scientific Research in Science and Technology (IJSRST)
Print ISSN : 2395-6011, Online ISSN : 2395-602X
International Conference on Advanced Materials
Held on 14, 15 December 2017, Organized by Department of Physics,
St. Joseph's College, Trichy, Tamilnadu, India

Spectroscopic, Mechanical and Optical Studies of L-Valine Picrate (LVP) Single Crystal

P. Christuraj[1]* A. Varalakshmi[1] and M. Dinesh Raja[1]
[1]Department of Physics, St. Joseph's College (Autonomous), Tiruchirappalli – 620 002, India
*Email: christy18_sjc@yahoo.co.in.com

Abstract: L-Valine Picrate (LVP) single crystal was grown for the aqueous solution. The grown crystal was characterized by single crystal XRD studies to confirm the crystal structure. Functional groups present in the sample were analyzed using FT-IR spectrum. The UV- Visible spectrum of LVP was recorded in the wavelength region from 200 nm to 1100 nm and the evaluated band gap is 2.33 eV. The mechanical properties of the grown crystals have been studied using Vickers micro hardness tester. This crystal can be a suitable material for the optoelectronic devices like LED and Laser diodes.

Keywords: LVP, monoclinic, space group $P2_1$, UV-Visible spectrum, Band gap

1. Introduction

Nowadays NLO materials are having potential applications in the area of telecommunication and optical storage devices [1].Amino acid crystals are potential candidates for optical second harmonic generation because all amino acids except glycine contain chiral carbon atom and crystallize in non-centrosymmetric space groups. The nonlinear susceptibility of an organic material would be larger when it has donor - acceptor conjugate or molecular system. Organic π-conjugated systems are interesting because they exhibit large molecular quadratic hyperpolarizabilities, scope for altering the properties by changing electron donor and electron acceptor moieties at their two ends [2]. Picric acid, as an electron acceptor, forms charge transfer molecular complexes with number of electron donor compounds through electrostatic or hydrogen bonding interactions. There are numerous studies which analyze the formation of picric compounds with amino acids like L-valine, L-glycine, L-asparagine and L-proline [3-5]. The aim of the present communication is to study the growth, physical and chemical properties of L-Valine Picrate crystals that may find wide applications inoptoelectronic devices.

2. Growth of L-valine picrate (LVP) crystals

LVP was synthesized by the reaction between the equimolar picric acid and the aminoacid, L-valine. The reactants were thoroughly dissolved in double distilled water and stirred well using a temperature controlled magnetic stirrer at 45°C to yield a homogeneous mixture of solution. Then the solution was allowed to evaporate at room temperature, which yielded yellow crystalline salt of LVP after 20 days. The process of recrystallization was carried out to purify the synthesized salt. The photograph of the harvested crystals are shown in figure 1.

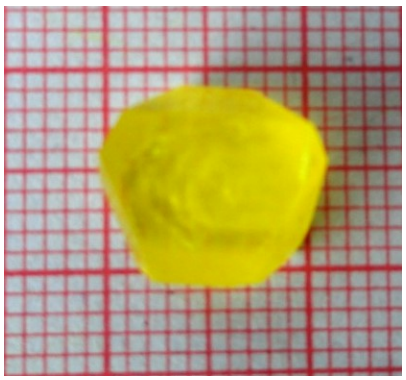

Figure 1. Photograph of LVP single crystal

International Journal of
Scientific Research in Science and Technology (IJSRST)
Print ISSN : 2395-6011, Online ISSN : 2395-602X
International Conference on Advanced Materials
Held on 14, 15 December 2017, Organized by Department of Physics,
St. Joseph's College, Trichy, Tamilnadu, India

3. Single Crystal XRD Analysis

The grown crystals were subjected to single crystal X-ray diffraction studies using an ENRAF NONIUS CAD4 automatic X-ray diffractometer with MoKα (λ=0.7170 Å) to determine the cell parameters. The crystal exhibits a monoclinic system with space group $P2_1$ with cell parameters

a= 9.974 Å
b=6.263 Å
c=12.635 Å
β=110.37 Å

Calculated volume of the unit cell =789.272 $Å^3$.

4. FT-IR analysis of LVP

Functional groups present in the sample were analyzed using FT-IR spectrum. The Fourier transform infrared spectral analysis of LVP was carried out between 400cm^{-1} and 4000 cm^{-1} by recording the FT-IR spectrum using Perkin Elmer spectrophotometer by KBr pellet technique and is shown in Figure 2. From Table 1, assignments, the formation of all the functional groups could be confirmed.

1630	NH_3^+ asymmetric deformation
1536	NH_3^+ symmetric deformation
1338	(NO_2) symmetric stretching
1285	phenolic C–O stretching
1059	C–C stretching
900	$[NH_3]^+$ rocking; C–C stretching
701	CH_3 rocking
541	NO_2 rocking

5. UV-Visible Spectral Analysis of LVP

The UV-Visible spectrum for LVP was recorded in the wavelength region from 200 nm to 1100 nm with the resolution of 1nm using Perkin Elmer Lambda 35 spectrophotometer and is shown in Figure 3. The material is found to be transparent to all radiations in the wavelength range 200–1100 nm.

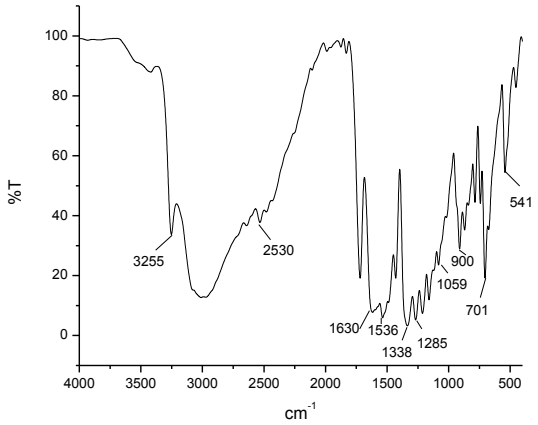

Figure 2. FTIR spectra of LVP single crystal

The absence of absorption in the visible region clearly indicates that LVP crystals can be used as window material in optical instruments. The higher percentage of transmission in the visible region clearly depicts the intrinsic property of the compound and the crystal is free from any defects. The lower cut off wavelength is 512 nm. Excellent optical transmittance with the lower cut-off wavelength at 512 nm makes it as a potential material for device fabrication.

6. Optical Band Gap of LVP

Optical materials are becoming increasingly important in communications where an entire network of optical fibers, LEDs, laser and detectors has already been installed for transmission of voice and data. Optical disk recordings with semiconductor laser playback are replacing the conventional piezoelectric pickups. Solar cells are now common components in toys, calculators and other consumer electronics. The dependence of optical absorption coefficient with the photon energy helps to study the band structure and the type of transition of electrons.

International Journal of
Scientific Research in Science and Technology (IJSRST)
Print ISSN : 2395-6011, Online ISSN : 2395-602X
International Conference on Advanced Materials
Held on 14, 15 December 2017, Organized by Department of Physics,
St. Joseph's College, Trichy, Tamilnadu, India

The absorption coefficient (α) were determined using Beer's law

$$\alpha = \frac{2.3036 \log\left(\frac{1}{T}\right)}{d}$$

where, t-thickness of the sample cell, T-transmittance.

A graph is plotted between the Photon energy (E) in eV and $(\alpha h\nu)^{1/2}$ and the linear region of the curve were extrapolated to find the x-intercept which gives the Band gap of the compound. From the band gap value, the optical property of the crystal can be justified. The band gap curve is shown in Figure 4 and the band gap evaluated is 2.33 eV. As a consequence of wide band gap, this crystal can be a suitable material for the optoelectronic devices like LED and Laser diodes.

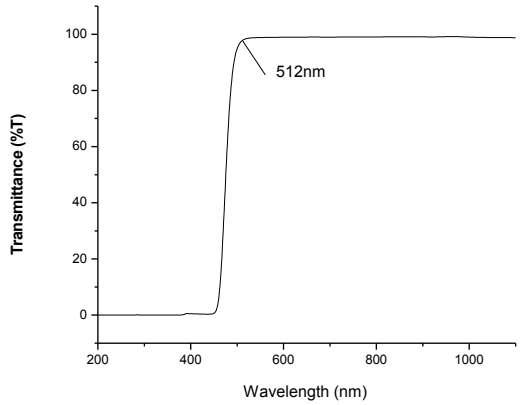

Figure 3. UV spectra of LVP crystals

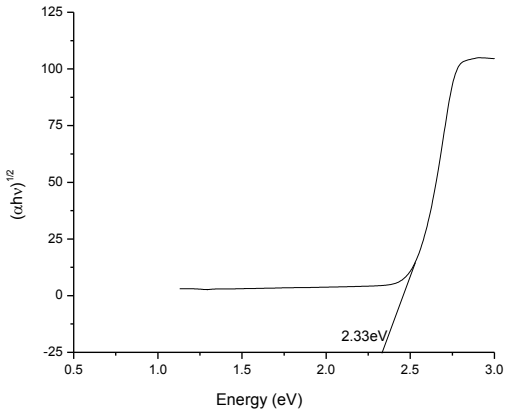

Figure 4. Bandgap curve for LVP crystals

7. Vicker's Micro Hardness Analysis of LVP

Micro hardness is primarily used to study the mechanical strength of a material. Selected smooth surfaces of the LVP crystals were subjected to static indentation test at room temperature with a constant indentation time of 15 s.

Indentations were made with a Leitz microhardness tester on the surfaces by varying the load from 25 g to 100 g. Vicker's micro hardness number have been calculated using

$$H_v = 1.8544\ P/d^2\ kg/mm^2$$

where P is the applied load and d is the mean diagonal length of the indenter impression. Vickers micro hardness plot as a function of the applied load is shown in Figure 5.

It is evident from the plot that the micro hardness value of LVP increases with increasing load, which confirms the high mechanical strength of the crystal.

The value of the work hardening coefficient n was estimated from the plot of log P versus log d (Figure 6). A linear graph was observed with the slope of 4.09 which also confirms the mechanical strength of the crystal. According to Onitsch and Hanneman 'n' should be between 1 and 1.6 for hard materials and above 1.6 for softer ones. Hence LVP belongs to soft category.

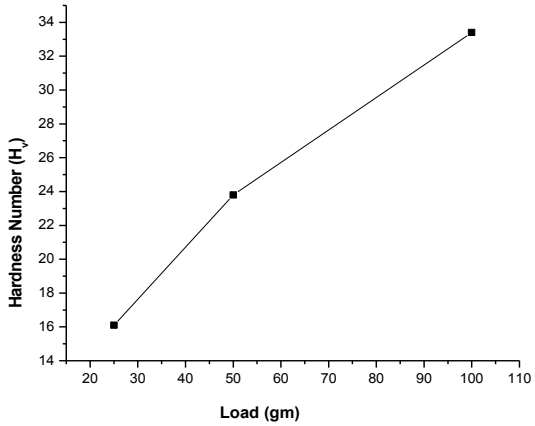

Figure 5. Hardness curve for LVP crystal

International Journal of
Scientific Research in Science and Technology (IJSRST)
Print ISSN : 2395-6011, Online ISSN : 2395-602X
International Conference on Advanced Materials
Held on 14, 15 December 2017, Organized by Department of Physics,
St. Joseph's College, Trichy, Tamilnadu, India

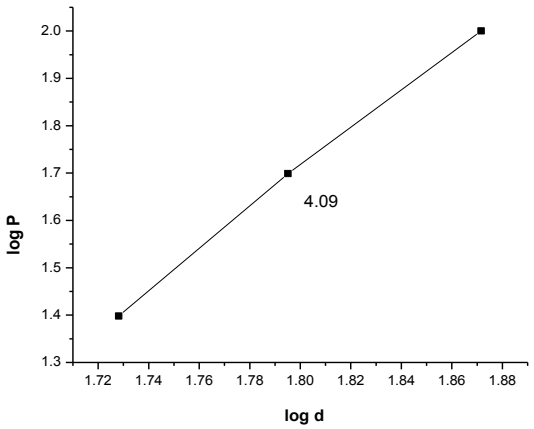

Figure 6. Work hardening Coefficient curve for LVP crystal

8. Conclusion

L-Valine Picrate (LVP) single crystal was grown for the aqueous solution. The grown crystal was characterized by single crystal XRD studies to confirm the crystal structure. The crystal exhibits a monoclinic system with space group $P2_1$. Functional groups present in the sample were analyzed using FT-IR spectrum. The UV- Visible spectrum of LVP was recorded in the wavelength region from 200 nm to 1100 nm and the evaluated band gap is 2.33 eV. The mechanical properties of the grown crystals have been studied using Vickers micro hardness tester. According to Onitsch and Hanneman 'n' should be between 1 and 1.6 for hard materials and above 1.6 for softer ones. Hence LVP belongs to soft category. This crystal can be a suitable material for the optoelectronic devices like LED and Laser diodes.

References

[1] Renuka, N., Vijayan, N., Rathi, B., Ramesh Babu, R. Nagarajan, K., Haranath, D. and Bhagavannarayana, G., Synthesis, growth and optical properties of semi organic non linear optical single crystal: l-arginine acetate, Optik 123 (2012)189–192.

[2] Chemla, D.S. and Zyss, J., (Eds.), Academic Press, New York, 1987.

[3] Zyss, J., Molecular Nonlinear Optics, Academic Press, New York, 1993.

[4] Koopmans, B., Janner, A.M., Jonkman, H.T., Sawatzky, G.A., and Van der Woude, F., Rev. Lett. 71 (1993) 3569–3572.

[5] Shuai, Z. and Bredas, J.L., Adv. Mater. 6 (1994) 486–488.

International Journal of
Scientific Research in Science and Technology (IJSRST)
Print ISSN : 2395-6011, Online ISSN : 2395-602X
International Conference on Advanced Materials
Held on 14, 15 December 2017, Organized by Department of Physics,
St. Joseph's College, Trichy, Tamilnadu, India

Synthesis, Growth and Characterization of Trifluoroacetyl Glycine (TFAG) Single Crystal

P. Christuraj* N. Sellam, M. Dinesh Raja
Department of Physics, St. Joseph's College (Autonomous), Tiruchirappalli – 620 002, India
*Email: christy18_sjc@yahoo.co.in

Abstract: Trifluoroacetyl Glycine (TFAG) Single crystal have been grown by slow evaporation solution growth technique. The presence of functional groups is identified by Fourier transform infrared (FTIR) analyses. UV–vis-NIR spectroscopy shows that minimum absorption in the entire visible region. The optical band gap (E_g) value of the grown crystal is obtained from the Tauc's plot also transparency, band gap, extinction coefficient and the refractive index were calculated. The mechanical properties have been studied by vicker's microhardness test.

Keywords: TFAG, FTIR, UV–vis-NIR, Band gap (E_g), Tauc's plot

1. Introduction

Glycine is a sweet tasting, non-essential amino acid that was first isolated in 1820 from gelatin and is also found in good quantity in silk fibroin. Also glycine is 'crystal friendly' since it easily crystallizes along with the added inorganic constituents like acids or salts [1–6]. Glycine is the simplest amino acid. Unlike other amino acids, it has no asymmetric carbon atom and is optically inactive. It has three polymeric crystalline forms α, β and γ. Glycine and its methylated analogues form complexes with mineral acids exhibiting interesting physical properties like ferroelastic, ferroelectric or antiferroelectric behaviour often associated with transitions to commensurate or incommensurate phases. According to the structural analysis of ferroelectric triglycine sulphate [7] there are two kinds of glycine groups, glycinium ions and zwitter ions. Such configurations of glycine ions interconnected by short O–H…O hydrogen bonds are regarded as particularly important for the ferroelectric behaviour of this crystal. In the ferroelectric and paraelectric structure of (glycine) $2HNO_3$, one of the glycine molecules has the zwitterionic configuration and the other is monoprotonated [8,9]. In the present study, we have grown single crystals of Trifluoroacetyl Glycine (TFAG) Single crystal and characterized by carrying out X-ray diffraction (XRD), FTIR, UV–Vis-NIR spectroscopic and microhardness measurements.

2. Synthesis of TFAG crystals

For preparing the title compound of Trifluoro acetic acid (CF_3COOH) and Glycine (NH_2CH_2COOH), water is taken as a solvent. Trifluoro acetic acid and Glycine were mixed 1:1 ratio in 50 ml doubly distilled water and stirred well to form homogeneous solution. The solution was maintained at constant temperature of 333K over a period of 30 hours till the solvent get evaporated and a white coloured salt was extracted. The purity of the synthesized yield was increased by successive recrystallization process. The saturated solution of the synthesized salt was prepared by dissolving it in 20 ml of doubly distilled water and stirred well for about 6 hours with a temperature controlled magnetic stirrer to give a homogeneous mixture of solution. The solution was filtered with high quality

International Journal of
Scientific Research in Science and Technology (IJSRST)
Print ISSN : 2395-6011, Online ISSN : 2395-602X
International Conference on Advanced Materials
Held on 14, 15 December 2017, Organized by Department of Physics,
St. Joseph's College, Trichy, Tamilnadu, India

filter paper and kept undisturbed. Colorless crystals of dimensions 40 x11 x 8 mm^3 were harvested after 25 days and shown in Fig.1. The good quality crystals were selected for further studies.

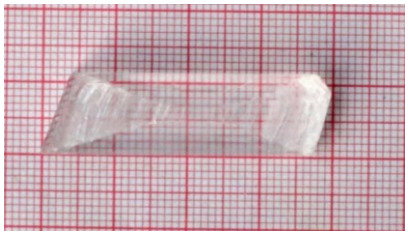

Figure 1. Photograph of TFAG crystal

3. X-Ray Analysis

The grown crystals have been subjected to single crystal X-ray diffraction studies using an ENRAF NONIUS CAD4 automatic X-ray Diffractometer. The crystallographic details are given in Table.1.

Molecular Formula	$C_4H_4F_3NO_3$
Crystal system	Orthorhombic
a (A°)	10.651
b (A°)	8.891
c (A°)	21.452
α (°)	90
β (°)	90
γ (°)	90
V(A^{o3})	2031.462

4. FT-IR Analysis of TFAC

The FTIR spectrum of grown crystal was revealed at room temperature in the range of 400–4000 cm^{-1} and shown in Fig 2. Grown crystals were crushed and few mg of the powder was used for making pellets with KBr. The pellets were then exposed to IR radiation. The FTIR spectrum was taken using Perkin Elmer FTIR spectrometer. The tentative frequency assignments were made by comparing it with standard values of frequency. The following table reveals the absorption peaks corresponds to TFAG crystal.

The asymmetric stretching mode of NH_3^+ present at 3091 cm^{-1}. The C=O stretch of carbonyl groups displays its characteristic peak at 1758 cm^{-1}. The CH_2 bending mode of glycine is located at 1447 cm^{-1}. The NH_3^+ displays its characteristic bending modes at 1534 and 1659 cm^{-1}. The intense sharp peaks position between 1000 and 1200 cm^{-1} are assigned to stretching modes of carboxyl group. The peaks due do NH_3^+ oscillation are seen at 601 and 513 cm^{-1}. The peaks at 2655, 1173 and 1123 cm^{-1} and the medium are assigned to F-C stretching vibrations.

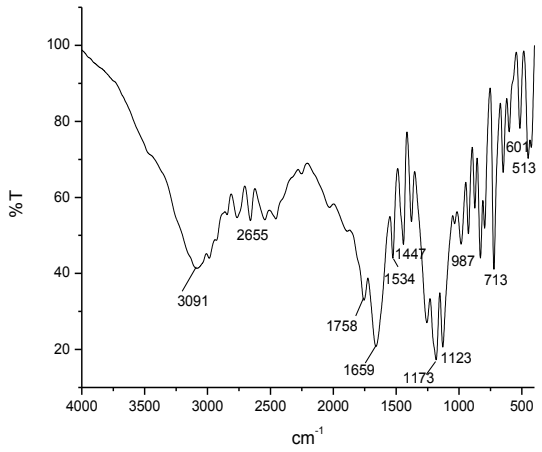

Figure 2. FTIR spectra of TFAG single crystal

International Journal of
Scientific Research in Science and Technology (IJSRST)
Print ISSN : 2395-6011, Online ISSN : 2395-602X
International Conference on Advanced Materials
Held on 14, 15 December 2017, Organized by Department of Physics,
St. Joseph's College, Trichy, Tamilnadu, India

5. UV-Visible Spectral Analysis of TFAG

In a crystalline material, the region of transparency to electromagnetic radiation defines the intrinsic loss mechanism and also theoretical transmittance achievable within the region. The transmission range of Trifluoroacetyl Glycine crystal was determined by recording an optical transmission spectra in the wavelength region 200 – 1200 nm. A graph of transmission Vs wavelength ignoring the loss due to absorption is shown in Fig.3. For TFAG the lower cutoff is at 273nm and it has the large transmission in the entire visible region. Hence it may be a suitable material for up to electronic applications.

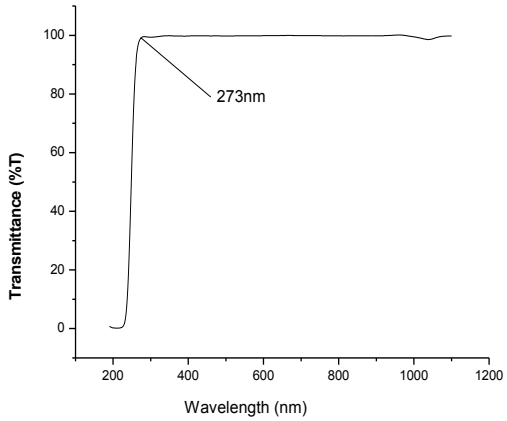

Figure 3. UV-Visible spectra of TFAG crystal

6. Optical Band Gap

The dependence of optical absorption coefficient with the photon energy helps to study the band structure and the type of transition of electrons. The absorption coefficient (α) were determined using Beer's law

$$\alpha = \frac{1}{d}\log(\frac{1}{T})$$

where T is the transmittance and d is the thickness of the cell. As the indirect band gap, the crystal under study has an absorption coefficient (α) obeying the following relation for high photon energies,

$$\alpha = \frac{A(h\nu - E_g)^2}{h\nu}$$

where E_g is optical bandgap of the crystal and A is a constant. The plot of variation of Photon energy (E) in eV and $(\alpha h\nu)^{1/2}$ is shown in Fig.4. The linear region of the curve was extrapolated to find the x-intercept which gives the Band gap of the compound.

The band gap is found to be 4.77eV. As a consequence of wide band gap, this crystal can be a suitable material for the optoelectronic devices like LED and Laser diodes.

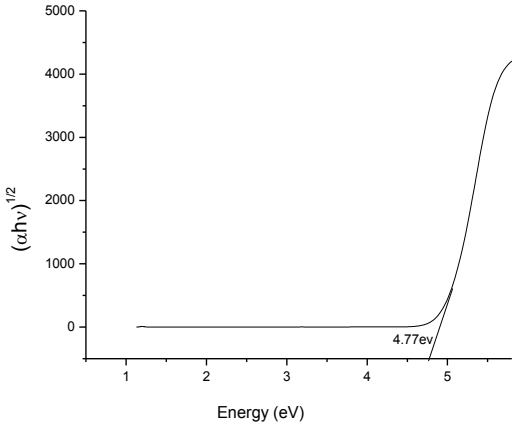

Figure 4. Bandgap curve of TFAG crystal

7. Optical Constants

The optical properties of a crystal can be evolved mainly from its optical transparency, band gap, extinction coefficient and the refractive index. The optical properties of the crystals are governed by the interaction between the crystal and the electric and magnetic fields of the electromagnetic wave. Extinction coefficient is the fraction of light lost due to scattering and absorption per unit distance in a participating medium. In electromagnetic terms, the extinction coefficient can be explained as the decay or damping of the amplitude of the incident electric and magnetic fields. The extinction coefficient can be calculated from the following relation,

International Journal of
Scientific Research in Science and Technology (IJSRST)
Print ISSN : 2395-6011, Online ISSN : 2395-602X
International Conference on Advanced Materials
Held on 14, 15 December 2017, Organized by Department of Physics,
St. Joseph's College, Trichy, Tamilnadu, India

$$K = \frac{\lambda \alpha}{4\pi}$$

The reflectance gives the ratio of the energy of reflected to incident light from a crystal. The reflectance in terms of the absorption coefficient can be calculated using

$$R = \frac{1 \pm \sqrt{(1 - \exp(-\alpha t) + \exp(\alpha t)}}{1 + \exp(-\alpha t)}$$

The refractive index can be determined from the reflectance (R) data using the relation

$$n = \frac{-(R+1) \pm \sqrt{-3R^2 + 10R - 3}}{2(R-1)}$$

A profile on the above calculated optical constants as a function of wavelength is graphically illustrated in fig.5. From the graph it is clear that the extinction coefficient (k), reflectance(R) and refractive index (n) vary with wavelength and hence depend on the photon energy. The internal efficiency also depends on the photon energy. Hence by tailoring the photon energy, one can achieve the desired material for the device fabrication.

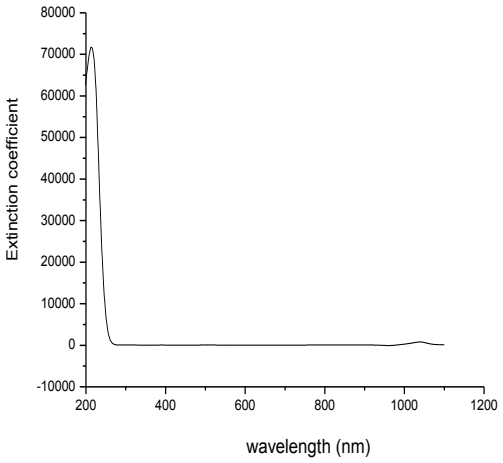

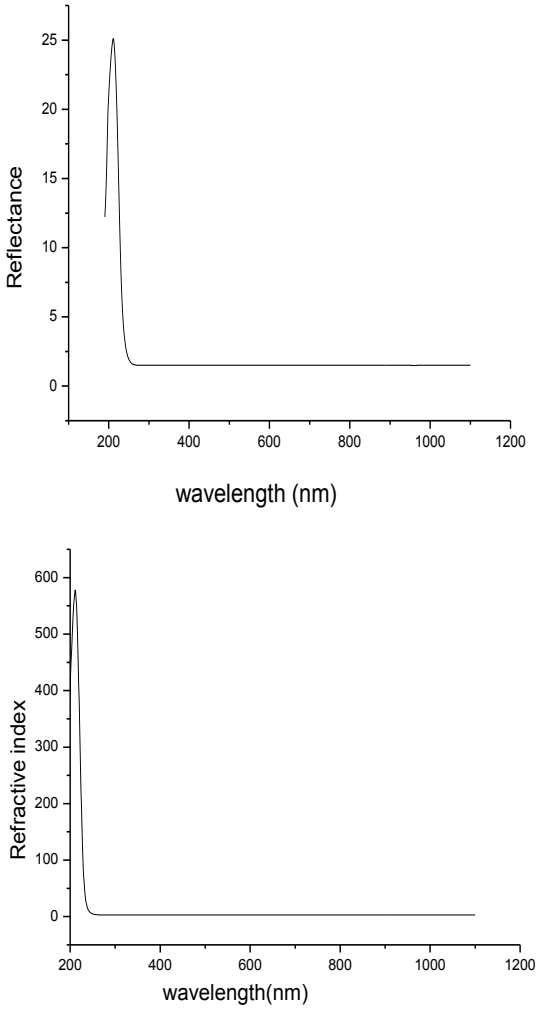

Figure 5. Profile of the variation of optical Constants of TFAG crystal

8. Mechanical Analysis of TFAG

The mechanical strength of a material is primarily studied from its micro hardness. The micro hardness studied have been carried out on the grown crystals using Leitz Weitzler tester fitted with Vickers diamond pyramidal indenter. Vickers micro hardness as a function of the applied load is shown in Fig. 6. From the graph it is observed that the hardness number increases with increase of load. The value of the work hardening coefficient n (Fig. 7) is found to be 3.996. According to Onitsch and Hanneman, 'n' should be between 1 and 1.6 for

International Journal of
Scientific Research in Science and Technology (IJSRST)
Print ISSN : 2395-6011, Online ISSN : 2395-602X
International Conference on Advanced Materials
Held on 14, 15 December 2017, Organized by Department of Physics,
St. Joseph's College, Trichy, Tamilnadu, India

hard materials and above 1.6 for softer ones. Hence TFAG single crystal belongs to soft material category.

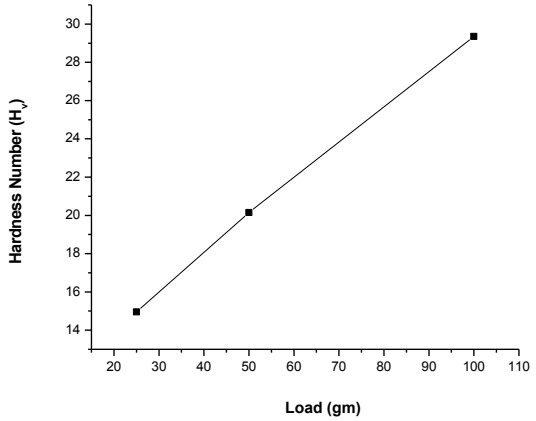

Figure 6. Hardness variation of TFAG crystal

The toughness of the material is the resistance to fracture. The fracture toughness K_c of the material is dependent on the micro structural features and is generally insensitive to the chemical species in the surrounding environment.

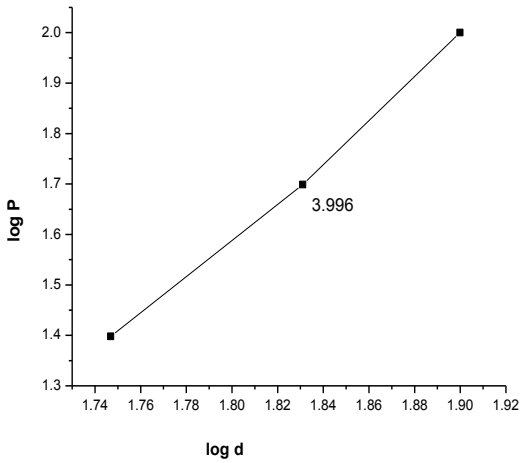

Figure 7. Work hardening coefficient curve of TFAG crystal

9. Conclusion

Trifluoroacetyl Glycine (TFAG) Single crystal have been grown by slow evaporation solution growth technique. The presence of functional groups is identified by Fourier transform infrared (FTIR) analyses. UV–vis-NIR spectroscopy shows that minimum absorption in the entire visible region. The optical band gap (E_g) value of the grown crystal is obtained from the Tauc's plot also transparency, band gap, extinction coefficient and the refractive index were calculated. The mechanical properties have been studied by vicker's microhardness test.

References

[1] Ambujam, K., Selvakumar, S., Prem Anand, D., Mohammed, G. and Sagayaraj, P., Crystal growth, optical, mechanical and electrical properties of organic NLO material _-glycine, Cryst. Res. Technol. 41 (2006) 671–677.

[2] Ambujam, K., P. and Sagayaraj, P. Growth and characterization of a novel NLO crystal Bis glycine hydrogen chloride, J. Cryst. Growth 286 (2006) 440–444.

[3] Uma devi, T., Lawrence, N. Ramesh Babu, R., Ramamurthi, K., and Bhagvan-narayanan, G., Structural, electrical and optical characterization studies on glycinepicrate single crystal: a third order nonlinear optical material, J. Min. Mater.Charact. Eng. 8 (2009) 755–763.

[4] Fleck, M., Ghazaryan, V.V., and Petrosyan, A.M. Glycine hydrogen fluoride: remarkable hydrogen bonding in the dimeric glycine glycinium cation, J. Mol. Struct.984 (2010) 83–88.

[5] Sekar, C. and Parimaladevi, R., Effect of silver nitrate ($AgNO_3$) on the growth, opti-cal, spectral, thermal and mechanical properties of β-glycine single crystal, J. Optoelect. Biomed. Mater. 1 (2009) 215–225.

[6] Sampath Krishnan, S., Balamurugan, N. Kumutha, R., Vidhyalakshmi, Y., and Muthu,

R., Growth and characterisation of new non linear optical bis-glycinehydro bromide (BGHB) single crystal, J. Min. Mater. Charact. Eng. 11 (2012) 597–607.

[7] Hoshino, S., Okaya, Y., and Pepinsky, R., Phys. Rev. 115 (1959) 323.

[8] Sato, S., J. Phys. Soc. Japan 25 (1968) 185.

[9] Baran, J., Barnes, A.J., and Ratajczak, H., Spectrochim. Acta 51A (1995) 197.

International Journal of
Scientific Research in Science and Technology (IJSRST)
Print ISSN : 2395-6011, Online ISSN : 2395-602X
International Conference on Advanced Materials
Held on 14, 15 December 2017, Organized by Department of Physics,
St. Joseph's College, Trichy, Tamilnadu, India

Synthesis Structural and Optical Studies on Composition Dependent Dy^{3+} doped Fluoroborate Glasses

J. Jemma vinothini[1], K. Maheshvaran[2], I. Arul Rayappan[1*]
[1]Department of Physics, St. Joseph's College, Trichy ,Tamil Nadu, India
[2]Department of Physics, Kongu Engineering College, Erode, Tamil Nadu, India
*Corresponding author: arulroy@gmail.com

Abstract

The Dy^{3+} ions doped fluoroborate glasses with composition $39B_2O_3$ + 20ZnO + 20NaF + $20XCO_3$ + $1Dy_2O_3$ in mol% (where X = Li_2, Mg) have been prepared by melt quenching technique and characterized through XRD, FTIR, absorption and luminescence spectral analysis. The XRD measurement was made to examine the amorphous nature of the prepared glasses. The stretching and bending vibrations of various functional groups have been investigated through FTIR spectra. The bonding parameters (β and δ) were calculated from the absorption spectra to understand the nature of bonding of chemical environment in the prepared glasses. The Judd-Oflet (JO) intensity parameters (Ω_λ (λ=2,4,6)) were determined from the measured oscillator strength of various absorption bands in order to study the symmetry around the RE ion site and used to compute the radiative properties such as emission band position(λ_P) effective bandwidth ($\Delta\lambda_{eff}$), transition probability (A), stimulated emission cross-section ($\sigma^E{}_P$) and branching ratios (β_R). The emission spectra exhibit two emission bands $^4F_{9/2}\rightarrow{}^6H_{15/2}$ and $^6H_{13/2}$ corresponding to nblue and yellow emission under 374 nm excitation. The emission intensities were calculated and compared with the reported literature.

Keywords: Bonding parameters, Ligand field effect, Judd-Oflet parameter, Emission, Radiative properties.

1. Introduction

The development of the new luminescent materials with appropriate composition doped with RE^{3+} ions is of interest for understanding the electronic excitation and relaxation phenomena RE ions in the chosen glass matrices [1-5]. The choice of choosing host matrix is an important key to improve the spectroscopic behavior of RE ions for various applications such as optical storage solid state lighting, updown conversion display devices etc., [6-8]. Among various glass host matrices borate based glasses are widely preferred due to its high transparency, low melting point, high rare earth ion solubility and good infrared transmission [9,10]. Fluroborate glasses are highly preferred because of its high ionic conductivity, short-range order around network forming boron, high chemical durability and lower phonon energy (≤600cm^{-1}) which reduces the non-radiative rates thus increasing the luminescence quantum efficiency [11]. Moreover these fluroborate glasses are favorable hosts to energy transfer and excited state absorption processes, which give rise to frequency up/down conversion mechanisms [12-15]. Among the RE ions, Dy^{3+} ion plays a major role in the production of white light emitting luminescent materials because it can be easily excited by the commercially available UV or blue LEDs due to its several excitation bands in the

International Journal of
Scientific Research in Science and Technology (IJSRST)
Print ISSN : 2395-6011, Online ISSN : 2395-602X
International Conference on Advanced Materials
Held on 14, 15 December 2017, Organized by Department of Physics,
St. Joseph's College, Trichy, Tamilnadu, India

range 320–480 nm [5]. Arul Rayappan et al [6] studied Dy^{3+} concentration effect on structural, thermal and optical behavior of B_2O_3–PbO–PbF_2 glasses and reported the occurrence of luminescence quenching caused by the energy transfer among the Dy^{3+} ions through various cross-relaxation channels. The present work reports the structural and optical behavior of Dy^{3+}doped fluroborate glasses for photonic applications and compared with reported Dy^{3+} doped glasses.

2. Experimental procedure

Dy^{3+} doped BZXD glasses were prepared by conventional melt quenching technique by [5,6]. H_3BO_3, ZnO, NaF, Li_2CO_3, $MgCO_3$, Dy_2O_3 were taken as precursors. About 8g batch of relevant compositions were mixed and grinded in an agate mortar then it's heated up to 950 °C for 45mins with periodic stirring. The melt was allowed to sudden quenching onto a preheated brass plate and then annealed at 350° C for 7 hrs to remove the thermal strains. X-Ray Diffraction pattern was recorded using JEOL 8030 X-ray diffractometer. FTIR spectra have been recorded using Perkin –Elmer paragon 500 FTIR spectrometer. The absorption spectra were recorded using CARY 500 spectrophotometer. Luminescence spectra of the prepared glass samples were measured using LS45 Spectrophotometer. The other physical properties of the Dy^{3+}: BZXD glasses were calculated using the expression given in the literature and are given in table 1.

Table 1. Physical properties of Dy^{3+}:BZLD glasses

Physical Properties	BZLD	BZMD
Density ρ (g/cm^3)	3.3246	3.6076
Refractive index n_d (nm)	1.589	1.602
REconcentration N (10^{20} ions/cm^3)	5.9501	6.2620
Polaron radius r_p(A˚)	479.05	4.7096
Inter ionic distance r_i(A˚)	118.89	11.688
Field strength F (10^{14} cm^{-2})	2.1222	2.1958
Polarizability (α_e)10^{-22} cm^3	1.3528	1.3084
Molar refractivity R_m (cm^3)	8.1853	7.9166
Dielectric constant (ε)	2.5249	2.5664
Reflection losses R (%)	5.1756	5.3527

3. Result and discussion

3.1. XRD and FTIR spectra

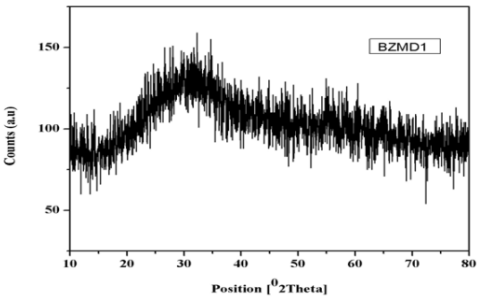

Figure 1. XRD pattern of Dy^{3+}:BZMD glass

Fig. 1 shows the x-Ray diffraction pattern of BZMD glass and it exhibit a broad diffuse scattering at lower angles, suggesting structural disorder which confirms the amorphous nature of the prepared glass. Fig. 2 shows the FTIR spectra of the glasses and their corresponding band position along with the assignment are presented in table 2. The peaks observed around 2800 and 2900 cm^{-1} are characteristic of hydrogen bonds in the glass systems. The peaks around 1409cm^{-1} are assigned to

International Journal of
Scientific Research in Science and Technology (IJSRST)
Print ISSN : 2395-6011, Online ISSN : 2395-602X
International Conference on Advanced Materials
Held on 14, 15 December 2017, Organized by Department of Physics,
St. Joseph's College, Trichy, Tamilnadu, India

B-O vibrations and the bands around this value for the different glass systems are found to be broader [7]. The broad peak around 1023 cm^{-1} is due to B-O vibrations associated with BO_4 units and B-O-B linkages exhibit a band around 721 cm^{-1} [8].

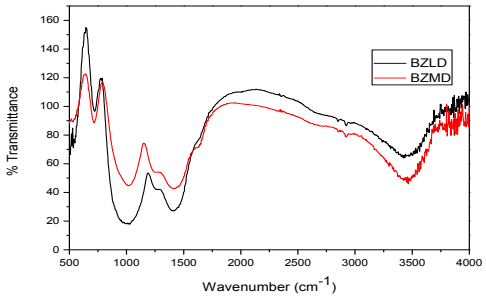

Figure 2. FTIR spectra of Dy^3:BZxD glasses

Table 2: Band assignments (cm^{-1}) of Dy3:BZxD glasses

BZLD	BZMD	[7]	[8]	Assignments
3445	3447	3430	3449	O-H stretching
2920	2907	2924	2922	Hydrogen bonding
2848	2353	1630	2845	Hydrogen bonding
1409	1414	1421	1348	B-O⁻ vibrations
1023	1022	1084	1011	B-O vibrations
721	790	710	695	Pyroborate Group

3.2. Absorption spectra

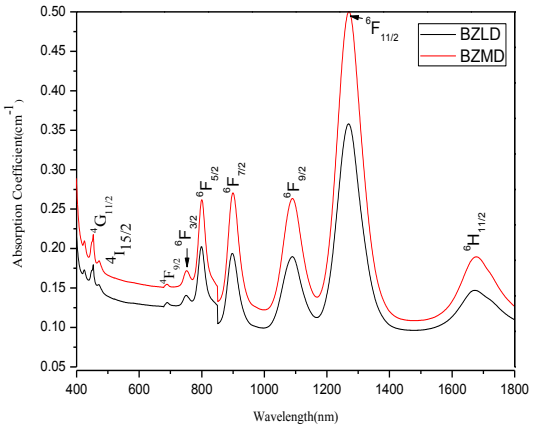

Figure 3. Absorption spectra of Dy^{3+}: BZXD glasses

Figure 3 shows the UV-Vis-NIR absorption spectra of Dy^{3+} doped BZXD glasses and the observed band positions are presented in Table 3. The absorption spectra exhibit 9 absorption bands which originates from $^6H_{15/2}$ ground state to various excited $^6H_{11/2}$, $^6F_{9/2}$, $^6F_{7/2}$, $^6F_{5/2}$, $^6F_{3/2}$, $^4F_{9/2}$, $^4I_{15/2}$, $^4G_{11/2}$, $^6P_{5/2}$ states of the Dy^{3+} ions. The intensity of the $^6H_{11/2}$ absorption transitions is higher than other transition due to its hypersensitive nature. It is observed from the figure 3 that, the band position and intensities of the absorption transitions undergoes small variation due to the Nephlauxetic effect. Thus influence of ligand environment on the RE energy levels can be measured by Nephelauxetic intensity ratio and bonding parameter of the prepared samples using the expression given on the literature [5,7,8] The bonding will be covalent or ionic depending upon the positive and negative sign of δ and the measured β and δ values are presented in table 3. The negative values of δ values indicates the ionic nature of the prepared glasses.

International Journal of
Scientific Research in Science and Technology (IJSRST)
Print ISSN : 2395-6011, Online ISSN : 2395-602X
International Conference on Advanced Materials
Held on 14, 15 December 2017, Organized by Department of Physics,
St. Joseph's College, Trichy, Tamilnadu, India

Table 3. Observed band positions (cm^{-1}), β and δ of Dy^{3+} doped fluoroborate glasses

Transition $^6H_{15/2}\rightarrow$	Energy		Reported values [7,9]		Aqua [8]
	BZLD	BZMD			
$^6H_{11/2}$	5977	5949	5968	5974	5850
$^6F_{11/2}$	7874	7874	7867	7794	7700
$^6F_{9/2}$	9174	9158	9187	9166	9100
$^6F_{7/2}$	11148	11099	11102	11161	11000
$^6F_{5/2}$	12516	12484	12498	12531	12400
$^6F_{3/2}$	14440	13333	13337	13332	13250
$^4F_{9/2}$	21231	21231	21070	21132	21100
$^4I_{15/2}$	22075	22075	22051	22075	22100
$^4G_{11/2}$	23585	23529	------	23830	23400
β	1.010	1.007	-	-	-
δ	-1.040	-0.793	-	-	-

3.3. Oscillator strength and Judd-Oflet analysis

The spectral intensity of the absorption bands of RE ions are analysed based on the calculated and experimental oscillator strength (f_{exp}) values and are measured using the expressions reported in literature [13] and are presented in table 4. The observed experimental oscillator strength are found to be similar with the f_{exp} of other reported papers [10], [7] and [8]. Generally, JO parameters provide information about the nature of the bond between RE ions and surrounding ligand as well as the symmetry of the environment around the RE ions. The spectral intensity of $^6F_{11/2}$ hypersensitive transition is found to be more than other transitions.

Table 4. Experimental and calculated oscillator strength ($\times 10^{-6}$) of Dy^{3+} doped BZLD and BZMD glass

$^6H_{15/2}\rightarrow$	BZLD		BZMD		1.0LBTPD [7]		Dy:LiLTB [11]	
	f_{exp}	f_{cal}	f_{exp}	f_{cal}	f_{exp}	f_{cal}	f_{exp}	f_{cal}
$^6H_{11/2}$	0.95	0.79	1.52	1.58	1.64	1.93	0.90	1.26
$^6F_{11/2}$	5.11	5.13	6.86	6.85	11.7	11.6	7.93	7.88
$^6F_{9/2}$	1.89	1.83	2.61	2.61	4.05	4.19	2.43	2.55
$^6F_{7/2}$	1.80	1.27	2.50	2.56	3.64	3.11	2.26	1.90
$^6F_{5/2}$	1.07	0.53	1.67	1.29	1.56	1.36	1.67	0.83
$^6F_{3/2}$	0.20	0.10	0.21	0.24	0.35	0.25	0.23	0.16
$^4F_{9/2}$	0.25	0.10	0.30	0.20	0.25	0.23	-	-
$^4I_{15/2}$	0.15	0.27	0.63	0.55	0.78	0.64	-	-
$^4G_{11/2}$	0.23	0.07	0.27	0.04	-	-	-	-
N	9		9		8		6	
σ_{rms}	±0.21		±0.15		±0.24		±0.41	

The JO intensity parameters of the present Dy^{3+} doped glasses were calculated using leat square fitting method followed by the literature [12,15] and are presented in table 5 along with the reported Dy^{3+} doped glasses. The values of Ω_2 is very sensitive to the local environment of the RE ions and often gives information about the symmetry of the coordination structure, polarizability of ligands and the nature of the RE–O bonding in the ligand field [31]. The Ω_4 parameters is related to the bulk properties and Ω_6 is inversely related to the rigidity of the medium and also affected by the vibronic transitions of the RE ions. It is observed from table 5 that, the JO parameters follow the trend as $\Omega_2>\Omega_4>\Omega_6$ for BZLD and $\Omega_2>\Omega_6>\Omega_4$ for BZMD glasses. The JO intensity parameters of the title glasses are found to be similar and comparable to the reported literature [6,8,11,14].

International Journal of
Scientific Research in Science and Technology (IJSRST)
Print ISSN : 2395-6011, Online ISSN : 2395-602X
International Conference on Advanced Materials
Held on 14, 15 December 2017, Organized by Department of Physics,
St. Joseph's College, Trichy, Tamilnadu, India

Table 5. JO intensity parameters of Dy^{3+}:BZXD glasses

Glass code	JO Parameters Ω_λ ($\times10^{-20}cm^2$)				Ref
	Ω_2	Ω_4	Ω_6	Trends	
BZLD	5.12	1.98	1.27	$\Omega_2>\Omega_4>\Omega_6$	Present
BZMD	7.71	1.21	3.06	$\Omega_2>\Omega_6>\Omega_4$	Present
L6BD	12.8	3.47	3.43	$\Omega_2>\Omega_4>\Omega_6$	[8]
1DPTFB	7.38	1.65	2.30	$\Omega_2>\Omega_6>\Omega_4$	[11]
LBZLB	14.4	5.23	5.71	$\Omega_2>\Omega_6>\Omega_4$	[14]

3.4. Luminescence Spectra: Radiative properties

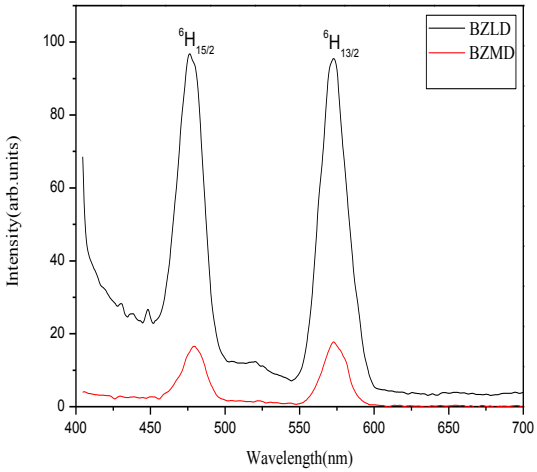

Figure 4. Emission spectra of Dy^{3+}:BZLD &BZMD glasses

The luminescence spectra of the Dy^{3+}: BZXD glasses were recorded at 374 nm excitation and the same is presented in Fig. 4. The luminescence spectra exhibit two emission peaks at 474 and 575nm corresponding to $^4F_{9/2}\rightarrow{}^6H_{15/2}$ (blue) and $^6H_{13/2}$ (yellow), transitions respectively. The $^4F_{9/2}\rightarrow{}^6H_{13/2}$ transition is hypersensitive electric dipole transition ($\Delta J=\pm2$) which has been strongly influenced by the coordination environment. The $^4F_{9/2}\rightarrow{}^6H_{15/2}$ transition is a magnetic dipole transition ($\Delta J=0, \pm1$ but $0\leftrightarrow0$ forbidden) and less sensitive to the coordination environment. In Appropriate combination of the dominant emission transitions corresponding to the blue ($^4F_{9/2}\rightarrow{}^6H_{15/2}$) and yellow ($^4F_{9/2}\rightarrow{}^6H_{13/2}$) bands exhibit white light emission [36]. The $^4F_{9/2}\rightarrow{}^6H_{13/2}$ emission transition possess higher intensity compared to the other transitions thus indicates the higher asymmetry possessed by the Dy^{3+} ions with its surrounding ligands.

The JO intensity parameters (Ω_2 ,Ω_4 ,Ω_6) and refractive index were used to obtain the radiative parameters like effective bandwidth ($\Delta\lambda_{eff}$, nm), transition probability (A s^{-1}), calculated and experimental branching ratios (β_R) and stimulated emission cross-section ($\sigma_p\times10^{-22}$ cm^2) for the emission transitions $^4F_{9/2}\rightarrow{}^6H_{15/2}$ and $^4F_{9/2}\rightarrow{}^6H_{13/2}$ of Dy^{3+}doped fluoroborate glasses. The radiative properties of Dy^{3+}:BZXD glasses along with the reported literatures are presented in table 6. The branching ratio (β_R) is a significant parameter for the fabrication of laser devices, because it characterizes the possibility of attaining stimulated emission from any particular transition of the studied glasses. The experimental branching ratio values (β_{exp}) are calculated using the relative intensities of the individual peaks to that of the total intensity of the emission peaks and are found to be comparable to the calculated (β_{cal}) values obtained within the frame work of JO theory. It is observed from table 6 that, the branching ratio of the $^4F_{9/2}\rightarrow{}^6H_{13/2}$ emission transition is found to be higher than the other emission transitions. The stimulated emission cross-section is an important parameter for the design of low threshold and high gain lasers. The effective line width ($\Delta\lambda_{eff}$) of the $^4F_{9/2}\rightarrow{}^6H_{13/2}$ emission transition indicates the sharpness of the transition compared to other transitions and is found to be very low compared to the reported Dy^{3+} doped glasses [16]. Thus the higher σ_p and small $\Delta\lambda_{eff}$ values suggest that the $^4F_{9/2}\rightarrow{}^6H_{13/2}$ transition is most potential for laser

International Journal of
Scientific Research in Science and Technology (IJSRST)
Print ISSN : 2395-6011, Online ISSN : 2395-602X
International Conference on Advanced Materials
Held on 14, 15 December 2017, Organized by Department of Physics,
St. Joseph's College, Trichy, Tamilnadu, India

action. Among the observed transitions, the σ_p^E value is found to be higher for the $^4F_{9/2} \rightarrow {}^6H_{13/2}$ transition. The higher σ_p^E cross-section of BZMD glass is suggested for low-threshold, high gain applications and are utilized to obtain continuous wave laser action [17].

Table 6. The values of λ_P(nm), $\Delta\lambda_{eff}$ (nm), A (s^{-1}), β_R and σ_p^E($\times 10^{-22}$ cm^2) of Dy^{3+}doped BZXD glasses

Parameters		BZLD	BZMD	[8]	[13]
$^4F_{9/2} \rightarrow {}^6H_{15/2}$	λ_P	474	478.5	479	472
	$\Delta\lambda_{eff}$	8.7473	0.5618	7	9.7506
	A	119.83	250.97	267.47	75.11
	β_R(cal)	0.1436	0.1857	0.201	0.0911
	β_R(exp)	0.3916	0.5618	0.306	0.2805
	σ_p^E	3.6340	6.5930	13.107	2.44
$^4F_{9/2} \rightarrow {}^6H_{13/2}$	λ_P	575	572.5	574	571
	$\Delta\lambda_{eff}$	6.2598	0.4382	15	6.65
	A	516.20	848.03	917.29	726.19
	β_R(cal)	0.6184	0.6275	0.688	0.6685
	β_R(exp)	0.6083	0.4381	0.656	0.6616
	σ_p^E	47.373	81.786	37.076	69.5

4. Conclusion

The Dy^{3+}: BZXD(X= Li_2, Mg) fluroborate glasses have been synthesized and their structural and optical behavior were studied. The amorphous nature of glasses were confirmed through XRD. The FTIR spectra of both BZLD and BZMD reveal the presence of various stretching units of borate networks along with the O-H stretching and bending vibrations. From the optical absorption spectra it is clear that Dy^{3+}ions exhibit a strong ionic nature. The oscillator strength and JO intensity parameters (Ω_λ, λ=2, 4,6) have been calculated and it follows the trend $\Omega_2 > \Omega_4 > \Omega_6$ for BZLD and $\Omega_2 > \Omega_6 > \Omega_4$ for BZMD glasses. The radiative properties such as effective bandwidth, transition probability, calculated and experimental branching ratios and stimulated emission cross-Section for various transitions of Dy^{3+} ions were calculated and compared with the literatures. The higher values of σ_p^E and β_R of the BZMD glass implies its suitability for the fabrication of highly monochromatic yellow laser applications [36].

References

[1] V.Uma, K. Maheshvaran,K. Marimuthu, G.Muralidharan. doi: 10.1016/j.jlumin.2016.03.016.

[2] C.K Jayasankar, V.Venkatramu, S.SurendraBabu, P.Babu, Journal of Alloys and Compounds 374(2004) 22-26.

[3] Proceedings of SPIE Vol. 4282 (2001) © 2001 SPIE · 0277-786X/01/$15.00.

[4] S.S.Babu, P.Babu, C.K.Jayasankar, Th.Tröster, W. Sievers, G.Wortmann, Opt. Mater. 31 (2009) 624-631.

[5] B. Shanmugavelu, V.V. Ravi Kanth Kumar, Journal of Luminescence 146 (2014)358–363.

[6] I. Arul Rayappan, K. Maheshvaran K. Marimuthu, S.S. Babu, Phys. Status Solidi A, 209 (2012) 570–578.

[7] S. Selvi, G.Venkatiah, S.Arunkumar, G.Muralidharan, K.Marimuthu, PhysicaB 454 (2014) 72-81.

[8] P.Babu, C.K Jayasankar, Journal of Optical Materials 15(2000) 65-79.

[9] R.T Karunakaran, K. Marimuthu, S.SurendraBabu, S.Arumugam, J. Lumin.130(2010) 1067-1072.

[10] I. Arul Rayappan, K.Marimuthu, S.S.Babu, M.Sivaraman, J. Lumin. 130 (2010) 2407–2412

[11] S.Arunkumar, G.Venkatiah. K.Marimuthu, Spectrochem. Part A, 136 (2015) 1684-1697.

[12] K. Maheshvaran, K. Marimuthu, Journal of Alloys and Compounds 509 (2011) 7427–7433.

[13] M.Vijayakumar, K.Maheshwaran, Dinesh K.Patel, S.Arunkumar, K.Marimuthu, Optical Materials 37 (2014) 695-705.

[14] Sd.Z Ali Ahamed,C.Madhuker Reddy, B.D.P Raju, Opt.Mater.35(2013) 1385-1394.

[15] N.Wantana, O.Chamlek, N.Chanthima, C.K.Jayasankar, H.J.Kim, M.Djamal, J. Kaewkhao K Eng. Materials, 675-676 (2016) 389-392.

[16] M. Vijayakumar, S. Arunkumar, K. Annapoorani and K. Marimuthu AIP Conference Proceedings 1591, 775 (2014).

International Journal of
Scientific Research in Science and Technology (IJSRST)
Print ISSN : 2395-6011, Online ISSN : 2395-602X
International Conference on Advanced Materials
Held on 14, 15 December 2017, Organized by Department of Physics,
St. Joseph's College, Trichy, Tamilnadu, India

Composition dependent Synthesis, Structural and Optical Properties of Dy^{3+} Doped Fluoroborate Glasses

A. Josuva D'Silva[1], K. Mahesvaran[2] & I. Arul Rayappan[3]
[1]Department of Physics, St. Joseph's College, Tiruchirappalli-02, Tamilnadu, India
[2]Department of Physics, Kongu Engineering College, Erode-52, Tamilnadu, India
*Corresponding author: arulroy@gmail.com

Abstract

The spectroscopic properties of Dy^{3+} ions doped fluoroborate glasses with the composition $39B_2O_3$ + 20ZnO + 20NaF + $20M_2O$ + $1Dy_2O_3$ (where M=Na, K and Ca) have been prepared by melt quenching technique and investigated through XRD,FTIR, absorption and luminescence. The x-Ray diffraction pattern reveals the amorphous nature of the prepared glasses. FTIR results showed the presence of various stretching and bending vibrational modes of the functional groups. From the absorption spectra, the bonding nature of the Dy^{3+} ions with the ligand field environment is found to be ionic. The variation in hypersensitive transitions with the change in Na, K and Ca content have been studied and discussed. JO intensity parameter have been calculated from absorption spectral intensities and are used to calculate ratiative properties such as the effective bandwidth ($\Delta\lambda_{eff}$, nm), transition probability (A), calculated and experimental branching ratios (β_R) and stimulated emission cross-section (σ_P^E) for the $^4F_{9/2} \rightarrow {}^6H_{15/2}$ and $^4F_{9/2} \rightarrow {}^6H_{13/2}$ transitions of the Dy^{3+} ions in prepared fluoroborate glasses.

Keywords: FTIR, Oscillator strength, JO parameters, Radiative properties, White light emission

1. Introduction

Recent years, the trivalent rare earth (RE) ions doped fluoroborate glasses have been received much attention in development of new optoelectronic devices due to their high ionic conductivity short range order around the boron network [1-3]. The borate based glasses provide interesting structural and optical properties. The borate glass structure is not a random distribution of BO_3 triangles and BO_4 tetrahedrals, but all these units form a clear and stable borate groups like diborates, triborates and tetraborates that forms a three dimensional random glass network [4]. These structural changes usually occur due to the chosen chemical composition, involvement of various types of modifiers and conditions applied during glass preparation [5-7]. Generally fluoroborate glasses possess the advantages of both oxides and fluorides such as intermediate phonon energy with higher mechanical strength and chemical durability which helps to improve the luminescence intensity and quantum efficiency. Among the RE^{3+} ions, Dy^{3+} ions are promising for application in solid state visible lasers [8,9], up converters and optical amplifiers [9], commercial display devices [10]. Further the appropriate combination of yellow to blue emission of Dy^{3+} ion could generate white light emission [11]. Shanmugavelu and Kumar [12] investigated the luminescence behavior of Dy^{3+} ions in bismuth zinc borate glasses for white light generation and laser applications. Xiong et al. [13] explored the high-efficiency fluorescence radiation of Dy^{3+} ions in alkaline earth borate glasses for laser application. the spectroscopic properties of Dy^{3+} ions in borate [14], oxyfluoride [15], fluorophosphate [16], zinc–lead–

International Journal of
Scientific Research in Science and Technology (IJSRST)
Print ISSN : 2395-6011, Online ISSN : 2395-602X
International Conference on Advanced Materials
Held on 14, 15 December 2017, Organized by Department of Physics,
St. Joseph's College, Trichy, Tamilnadu, India

phosphate [17], Ge–Ga–As–S–CsBr [18], chalcohalides [19] and Li_2O–LiF–B_2O_3–CdO [20] glasses have been investigated and the energy transfer between Dy^{3+}–Dy^{3+} ions through various cross-relaxation were discussed. The present work reports the composition dependent spectroscopic investigations of Dy^{3+} ions doped fluoroborate glasses for white light emission. The aim of the present paper is to (i) examine the structure of the prepared glass through XRD; (ii) identify the structural groups from FTIR; (iii) calculate the bonding parameter form absorption spectra ; (iv) find the oscillator strengths for each absorption transitions (v) evaluate and compare the JO parameters with the other reported Dy^{3+} doped glasses, and (vi) derive the radiative properties and compare the results with reported literature.

2. Experimental

The appropriate amount of high quality analytical grate (99.9) chemicals such as B_2O_3, NaF, Na_2Co_3, K_2Co_3, Ca_2Co_3Zno and Dy_2O_3 from sigma Aldrich for the prepared Dy^{3+} doped fluoroborate glasses by melt quenching technique. The glass code and the composition are given below.

BZKD1:39B_2O_3+20ZnO+20NaF+20K_2O+1Dy_2O_3

BZCD1:39B_2O_3+20ZnO+20NaF+20Ca_2O+1Dy_2O_3

BZND1:39B_2O_3+20ZnO+20NaF+20Na_2O+1Dy_2O_3

The relevant chemicals were mixed and grained in an agate mature as a 12 g batch. The batch in the crucible was melted in an electronic furnace at 950°C. The melt was quenched by pouring in it on a preheated brass plate and then annealing at 350°C for removing the strains and improve the mechanical strength. The glasses were slowly cooled at room temperature and polished for the optical measurements. The optical absorption spectra were measured in the spectral region 200–2000 nm by JASCO V-670 UV–Vis–NIR spectrophotometer. The luminescence spectra were recorded in the LS 45 Perkin-Elmer paragon spectrometer. The density of the glass samples were measured by Archimedes principle with xylene as an immersion liquid. The refractive indices of the prepared glasses were measured using Abbe refractometer at sodium wavelength using 1-bromonaphthaline as a contact liquid. The physical properties of the prepared glasses were calculated and presented in Table 1.

Table 1: Physical properties Density ρ (g/cm³), Refractive index n_d (589.3 nm), Rare earth ion concentration N(×10^{20} ions/cm³), Polaron radius r_p(A˚), Interionic distance r_i (A˚), Field strength F (10^{14} cm^{-2}), Electronic polarizability(α_e) 10^{-22} cm^3, Molar refractivity R_m (cm³), Dielectric constant (ε) and Reflection losses R (%)of the prepared Dy^{3+}: BZKD, BZND and BZCD1glasses

Properties	BZKD	BZND	BZCD
ρ	2.9882	2.9896	3.1838
n_d	1.5	1.5	1.575
N	0.7455	0.8111	0.8778
r_p	5.2519	5.1161	4.9829
r_i	1.3050	1.2697	1.2366
F	1.7591	1.8608	1.9615
α_e	1.5645	1.4381	1.4928
R_m	7.8900	7.2522	9.0345
ε	2.25	2.25	2.4806
R	4	4	4.9863

3. Results and discussion

3.1. XRD and FTIR spectra

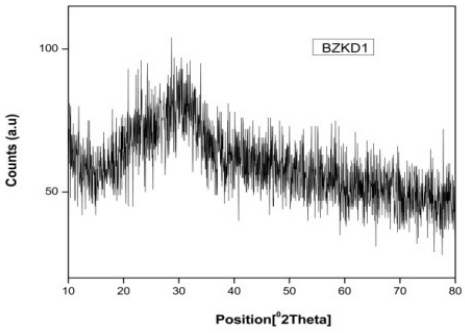

Figure 1. XRD pattern of the Dy^{3+}: BZKD 1 glass.

International Journal of
Scientific Research in Science and Technology (IJSRST)
Print ISSN : 2395-6011, Online ISSN : 2395-602X
International Conference on Advanced Materials
Held on 14, 15 December 2017, Organized by Department of Physics,
St. Joseph's College, Trichy, Tamilnadu, India

Figure 1 shows the XRD spectrum of the BZKD glass and exhibits the broad scattering at lower angles the long range structural disorder. The absence of the sharp peaks in the XRD confirms the amorphous nature of the prepared glass.

FTIR spectra have been recorded in the region 400-4000 and is shown in figure 2. The band position and their assignments are presented in table 2. The band around 3437 cm^{-1} can be attributed to the fundamental stretching of hydroxyl groups. The band at 2926 cm^{-1} is assigned to the hydrogen bond [3]. The band around 1446 cm^{-1} is attributed to the asymmetric mode of B-O stretching vibrations in BO_3 units in boroxol rings. The band at 1227 cm^{-1} is arises due to the B-O stretching vibration of BO_3 units in boroxol rings. The peaks around 1019 cm^{-1} is attributed to the stretching of BO_4 group and the broad bands around 717 cm^{-1} are due to the bending of B-O-B linkages in the borate network. Zn–O stretching vibrations exhibit a band around 466 cm^{-1}.

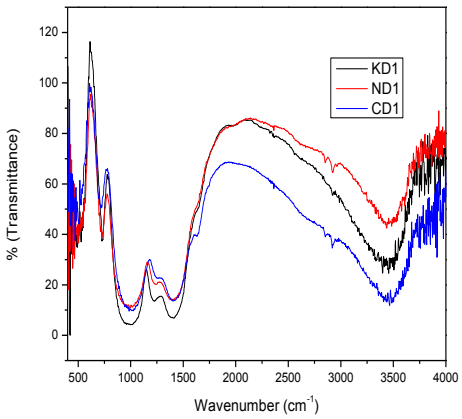

Figure 2. Infrared spectra of Dy^{3+}: BZKD1, BZND1 and BZCD1 glasses

Table 2. Band positions (in cm^{-1}) of FTIR spectra of the Dy^{3+}doped Fluoroborate glasses

BZKD1	BZND1	BZCD1	Assignments
3439	3434	3437	stretching of OH groups
2920	2923	2922	hydrogen bonding
2836	2827	2831	hydrogen bonding
1412	1455	1437	B-O vibrations
1227	1226	1226	Tetrahedral BO4 units
1019	1016	1017	stretching of BO4 units
717	712	715	bending of B-O-B linkages
466	466	462	Zn-O stretching vibration

3.2. Optical analysis

3.2.1. Absorption and Bonding parameters

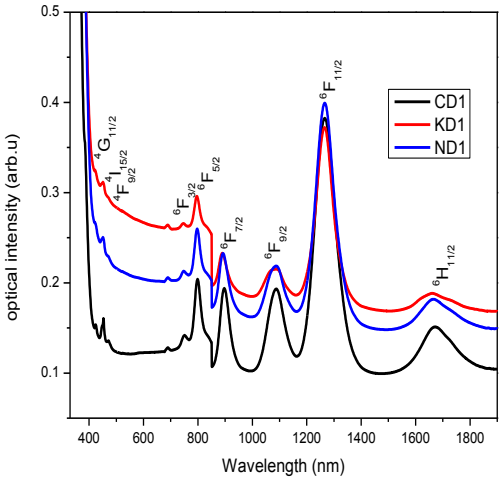

Figure 3. Absorption spectra of Dy^{3+}: BZKD1, BZND1 and BZCD1 glasses

The absorption spectra of the prepared glasses are shown in figure 3 and recorded in the wave length region 400-1800 nm. The absorption spectra exhibits nine absorption bands counterseal at around 1661, 1265, 1089, 889, 796, 746, 471, 451, and 417 nm. Corresponding to that various excited state such as $^6H_{11/2}$, $^6F_{11/2}$, $^6F_{9/2}$, $^6F_{7/2}$, $^6F_{5/2}$, $^6F_{3/2}$, $^4F_{9/2}$, $^4I_{15/2}$ and $^4G_{11/2}$ the absorption band position for the prepared glassesoccurs almost the wave length slight variation in the intensity peaks can be observed for the various compositions. The transition from the ground $^6H_{15/2}$ state to ^6H to ^6F terms are spin allowed

International Journal of
Scientific Research in Science and Technology (IJSRST)
Print ISSN : 2395-6011, Online ISSN : 2395-602X
International Conference on Advanced Materials
Held on 14, 15 December 2017, Organized by Department of Physics,
St. Joseph's College, Trichy, Tamilnadu, India

(Δs=0). Moreover, the transition with in the 6H term are also allowed by the orbital angular momentum selection rule, ΔL=0 and hence, this transitions lying in the NR region are intense [3]. The position and spectral intensities of certain transitions of rare earth ions are found to be sensitive to the environment of the rare earth ion. They follow the selection rules ΔJ≤2, ΔL≤2 and ΔS=0 and such transitions are known as hypersensitive transitions. For Dy^{3+} ion the transition $^6H_{15/2}\rightarrow{}^6F_{11/2}$ is identified to be a hypersensitive transition and is found to be more intense than the other transitions. The bonding parameter (δ) is calculated by using nephelauxetic ratio and is written as δ =(1-β̄)/ (β̄)×100, where β̄ = $\Sigma_n\beta/N$, β is the nephelauxetic ratio [4]. Depending upon the environmental field, δ may be positive or negative indicating the covalent or ionic nature [21]. The negative values of bonding parameters indicate ionic nature of the prepared glasses.

Table 3. Absorption band positions (in cm^{-1}), β and δ values of the Dy^{3+}doped fluoro borate glasses

Transition $^6H_{15/2}\rightarrow$	BZKD1	BZND1	BZCD1	Aquo ion [13]
$^4G_{11/2}$	23981	23753	23585	23400
$^4I_{15/2}$	22173	22173	22075	22100
$^4F_{9/2}$	21231	21142	21231	21100
$^6F_{3/2}$	13405	13369	13333	13250
$^6F_{5/2}$	12563	12547	12516	12400
$^6F_{7/2}$	11249	11211	11148	11000
$^6F_{9/2}$	9183	9200	9191	9100
$^6F_{11/2}$	7905	7899	7899	7700
$^6H_{11/2}$	6020	6006	5984	5850
β̄	1.01633	1.01377	1.01111	
δ	-1.6070	-1.3590	-1.0989	

3.2.2. Oscillator Strength and J-O Intensity Parameter

The intensities of an absorption bands are expressed in terms of their oscillator strengths using the expression as $f_{exp}= 4.318\times10^{-9}\int\varepsilon(v)dv$. The experimental oscillator strength (f_{exp}) of the absorption bands is calculated from the relative areas under the absorption bands of the individual transition in the absorption spectra of the RE ions doped materials. The experimental and calculated oscillator strength ($\times10^{-6}$) of the Dy^{3+}doped fluoroborate glasses are presented in table 4, with rms (σ) deviation values. The JO analysis for the Dy^{3+}ions is in good agreement with (f_{exp}) and (f_{cal}) for some of the energy levels and there is an amount of moderate deviation in case of weak transition. Judd–Ofelt (J–O) model gives the theoretical estimation of the intensities of intra configurational f–f transitions of RE^{3+} ions as following the procedure in the liteture [3]. The J-O theory has been applied to evaluate the intensity parameters $\Omega_\lambda(\lambda = 2, 4, 6)$ from the measured spectral intensities of absorption bands.

Table 4. Experimental and Calculated oscillator strengths ($\times10^{-6}$) of the Dy^{3+}doped fluoroborate glasses

$^6H_{15/2}\rightarrow$	BZKD		BZND		BZCD	
	f_{exp}	f_{cal}	f_{exp}	f_{cal}	f_{exp}	f_{cal}
$^4G_{11/2}$	0.058	0.022	0.054	0.032	0.026	0.013
$^4I_{15/2}$	0.108	0.141	0.198	0.213	0.094	0.074
$^4F_{9/2}$	0.024	0.465	0.023	0.078	0.040	0.027
$^6F_{3/2}$	0.092	0.053	0.105	0.092	0.041	0.031
$^6F_{5/2}$	0.400	0.283	0.716	0.487	0.220	0.162
$^6F_{7/2}$	0.644	0.611	0.973	1.026	0.350	0.348
$^6F_{9/2}$	0.717	0.721	1.189	1.183	0.419	0.426
$^6F_{11/2}$	2.582	2.576	2.999	2.995	1.187	1.185
$^6H_{11/2}$	0.381	0.423	0.588	0.621	0.202	0.219
N	9		9		9	
Rms	0.048		0.082		0.023	

The JO parameters play an important role in studying the coordination environment around the trivalent rare-earth ions and moreover on the covalency between the rare-earth and oxygen ions in any host glass. The intensity parameter Ω_2 has been identified as associated with the asymmetry and the covalency of the lanthanide sites. Ω_4 and Ω_6 are related to the bulk property and rigidity of the samples respectively. However, the Ω_2 values are found to be higher than the Ω_4 and Ω_6 intensity

International Journal of
Scientific Research in Science and Technology (IJSRST)
Print ISSN : 2395-6011, Online ISSN : 2395-602X
International Conference on Advanced Materials
Held on 14, 15 December 2017, Organized by Department of Physics,
St. Joseph's College, Trichy, Tamilnadu, India

parameter values in the prepared glasses. All the prepared glasses follow the trend as $\Omega_2>\Omega_6>\Omega_4$ presented in table 5 and compared with the similar studies. The Ω_2 ($\times10^{-20}$ cm^2) values are found to be 3.3138, 3.3375 and 1.276 for the prepared glasses BZKD1, BZND1 and BZCD1 respectively.

Table 5. JO intensity parameters ($\Omega_\lambda\times10^{-20}$ cm^2), spectroscopic quality factor (Ω_4/Ω_6) of the Dy^{3+}doped fluoroborate glasses

Glasses	Ω_2	Ω_4	Ω_6	Ref
BZKD1	3.138	0.6008	0.7234	Present
BZND1	3.337	0.9129	1.2382	
BZCD1	1.276	0.3430	0.3892	
PSB glass d2	2.27	0.94	1.31	22
Lead borate	4.90	0.94	2.07	23
BZBDy05	4.72	0.58	1.99	12
BZBDy2	4.29	1.05	1.72	12
ZBLA(1)	3.22	1.35	2.38	24
1DPTFB	7.381	1.654	2.306	25

3.3. Luminescence studies and Radiative Properties

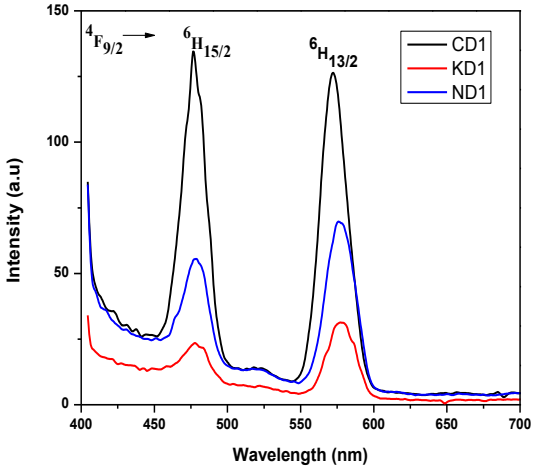

Figure 4. Emission spectra of Dy^{3+}: BZKD1, BZND1 and BZCD1 glasses

The luminescence spectra of the Dy^{3+}: fluoroborate glasses were recorded with 384 nm excitation and is shown in Figure 4. The luminescence spectra exhibit two emission band peaks at 476 nm and 571 nm corresponding to $^4F_{9/2}\rightarrow{}^6H_{15/2}$ (blue) and $^6H_{13/2}$ (yellow) transitions respectively as shown in Figure 4. Among the transitions, $^4F_{9/2}\rightarrow{}^6H_{13/2}$ electric dipole transition is found to have a higher intensity than the $^4F_{9/2}\rightarrow{}^6H_{15/2}$ magnetic dipole transition. The luminescence intensity of the $^4F_{9/2}\rightarrow{}^6H_{13/2}$ transition is hypersensitive because it is more sensitive to the environment around the Dy^{3+} ion site when compared to the $^4F_{9/2}\rightarrow{}^6H_{15/2}$ transition. The radiative properties such as the transition probability (A), branching ratios (β_R) and stimulated emission cross-section ($\sigma_P^E\times10^{-22}$ cm^2) for the emission transition $^4F_{9/2}\rightarrow{}^6H_{15/2}$ and $^4F_{9/2}\rightarrow{}^6H_{13/2}$ of the Dy^{3+} ions have been calculated using the expression given in the literature [1,13]. The calculated radiative properties of the prepared glasses are presented in table 6. The branching ratios (β_R) and stimulated emission cross-section ($\sigma_P^E\times10^{-22}$ cm^2) values are important parameters for the potential laser applications. The higher magnitude of the stimulated emission cross-section ($\sigma^E{}_P$) is an indication for efficient laser emission. Among the prepared glasses, BZND1 glass possesses higher ($\sigma^E{}_P$) value (35.1475×10^{-22}cm^2) correspond to the $^4F_{9/2}\rightarrow{}^6H_{13/2}$ (electric dipole) emission transition and higher than the reported glasses such as M.V. Vijayakumar et al. [26] and CH. Basavapoornima et al. [27] respectively.

The optical gain bandwidth and optical gain these are the important laser parameters for the development of new optical devices and the optical gain band width [$\sigma_P^E\times\Delta\lambda_{eff}$] and optical gain [$\sigma_P^E\times\tau_R$] values of the prepared glasses have been calculated and presented in table 6. It is observed from the tabulated results that among the prepared glasses, BZND glass is found to be more suitable for developing visible lasers and fiber optic amplifiers since it exhibit higher magnitude of A, β_R, σ_P^E and

International Journal of
Scientific Research in Science and Technology (IJSRST)
Print ISSN : 2395-6011, Online ISSN : 2395-602X
International Conference on Advanced Materials
Held on 14, 15 December 2017, Organized by Department of Physics,
St. Joseph's College, Trichy, Tamilnadu, India

$\sigma_P^E \times \Delta\lambda_{eff}$ stimulated emission cross section and branching ratio values.

Table 6. The effective bandwidth ($\Delta\lambda_{eff}$, nm), transition probability (A), calculated and experimental branching ratios (β_R) and stimulated emission cross-section ($\sigma_P^E \times 10^{-22}$ cm^2) for the $^4F_{9/2} \rightarrow {}^6H_{15/2}$ and $^4F_{9/2} \rightarrow {}^6H_{13/2}$ transitions of the Dy^{3+}doped fluoroborate glasses

Transition	Parameters	BZKD	BZND	BZCD
$^4F_{9/2} \rightarrow {}^6H_{15/2}$	λ_p	478	478	476
	$\Delta\lambda_{eff}$	4.6434	5.6981	4.4546
	A	51.23	86.53	32.37
	σ_P^E	3.3968	4.6754	1.9955
	β_R(cal)	0.2848	0.3227	0.4742
	β_R(exp)	0.118	0.1671	0.1217
	$\sigma_P^E \times \Delta\lambda_{eff}$	1.5772	2.6641	0.8893
$^4F_{9/2} \rightarrow {}^6H_{13/2}$	λ_p	577	576	572
	$\Delta\lambda_{eff}$	4.9550	5.5320	3.6886
	A	157.57	299.51	126.89
	σ_P^E	33.977	35.147	19.699
	β_R(cal)	0.7151	0.6772	0.5257
	β_R(exp)	0.5968	0.5785	0.4770
	$\sigma_P^E \times \Delta\lambda_{eff}$	16.836	19.443	7.2662

4. Conclusion

Composition dependent structural and optical properties of Dy^{3+} doped fluoroborate glasses have been studied for photonic applications. Structural analysis has been carried out using XRD and FTIR specta. The ionic nature of the Dy^{3+} metal ligand bonding was explored from the absorption spectral measurement. The higher Ω_2 values indicate the higher asymmetry around Dy3+ ion site. Two emission band peaks corresponding to $^4F_{9/2} \rightarrow {}^6H_{15/2}$ and $^6H_{13/2}$ transitions were observed from emission spectra. Among the prepared glasses, BZND1 glass possess higher (σ^{E_P}) value correspond to the $^4F_{9/2} \rightarrow {}^6H_{13/2}$ (electric dipole) emission transition which is an indication for efficient laser emission.

References

[1] Sd. Zulfiqar Ali Ahamed , C. Madhukar Reddy, B. Deva Prasad Raju, Optical materials 35 (2013) 1385-1394.

[2] S. Babu, V. Reddy Prasad, D. Rajesh, Y.C. Ratnakaram, Journal of Molecular Structure 1080 (2015) 53–161.

[3] S. Arunkumar, G. Venkataiah, K. Marimuthu, Spectrochimica Acta Part A: Molecular and Biomolecular Spectroscopy 136 (2015) 1684–1697.

[4] S.Selvi, G.Venkataiah, S.Arunkumar, G.Muralidharan, K. Marimuthu Physica B 454 (2014) 72-81.

[5] V.K. Rai, S.B. Rai, Opt. Commun. 257 (2006) 112.

[6] Y. Dwivedi, S.B. Rai, Opt. Mater. 31 (2009) 1472.

[7] K. Linganna, Ch.S. Rao, C.K. Jayasankar, J. Quant. Spectrosc. Radiat. Transfer 118 (2013) 40–48.

[8] V.B. Sreedhar, D. Ramachari, C.K. Jayasankar, Phys. B 408 (2013) 158–163.

[9] Anal Tarafder, AtiarRahamanMolla, Basudeb Karmakar, J.M. Fdez-Navarro, Opt. Mater. 35 (2013) 1549–1556.

[10] L. Jyothi, G. Upender, R. Kuladeep, D. Narayana Rao, Mater. Res. Bull. 50 (2014) 424–431.

[11] N. Vijaya, K. Upendra Kumar, C.K. Jayasankar, Spectrochim. Acta A 113 (2013) 145–153.

[12] B. Shanmugavelu, V.V.R.K. Kumar, J. Lumin. 146 (2014) 358–363.

[13] H.H. Xiong, L.F. Shen, E.Y.B. Pun, H. Lin, J. Lumin. 153 (2014) 227–232.

[14] SK. Mahamuda, K. Swapna, P. Packiyaraj, A.S. Rao, G.V. Prakash, J. Lumin. 153 (2014) 382–392.

[15] K.V. Krishnaiah, K.U. Kumar, C.K. Jayasankar, Mater. Express 3 (1) (2013) 61– 70.

[16] V.B. Sreedhar, D. Ramachari, C.K. Jayasankar, Physica B 408 (2013) 158–163.

[17] V. Naresh, S. Buddhudu, J. Lumin. 147 (2014) 63–71.

[18] Y.B. Shin, C.K. Yang, J. Heo, J. Non-Crystall. Solids 298 (2002) 153–159.

[19] H. Guo, L. Liu, Y. Wang, C. Hou, W. Li, M. Lu, K. Zou, B. Peng, Opt. Express 17 (2009) 15350–15358.

[20] R.J. Amjad, M.R. Sahar, S.K. Ghoshal, M.R. Dousti, R. Arifin, Opt. Mater. 35 (2013) 1103–1108.

[21] R.T.Karunakaran, K.Marimuthu, S.SurendraBabu, S.Arumugam, Journal of Luminescence 130 (2010) 1067-1072.

[22] Kamel Damak, El Sayed Yousef, Christian Rüssel, Ramzi Maâlej, J. Quant. Spect. Radiat. Trans. 134 (2014) 55–63.

[23] D.V.R. Murthy, B.C. Jamalaiah, A. Mohan Babu, T. Sasikala, L. Rama Moorthy, J. Opt. Mater. 32 (2010) 1112–1116.

[24] J. Hormadaly, R. Reisfield, J. Non-Cryst. Solids 30 (1979) 337–348.

[25] J.L. Adam, A.D. Docq, J. Lucas, J. Solid State Chem. 75 (1988) 403–412.

[26] M.V. VijayaKumar, B.C. Jamalaiah, K. Rama Gopal, R.R. Reddy, J. Lumin. 132 (2012) 86–90.

[27] Ch. Basavapoornima, C.K. Jayasankar, P. Chandrachoodan, Physica B 404 (2009) 235–242.

International Journal of
Scientific Research in Science and Technology (IJSRST)
Print ISSN : 2395-6011, Online ISSN : 2395-602X
International Conference on Advanced Materials
Held on 14, 15 December 2017, Organized by Department of Physics,
St. Joseph's College, Trichy, Tamilnadu, India

Lattice Dynamical Investigation on the Diffusion of Hydrogen Isotopes in Mg_2Ni

[a]Lakshmi Balasubramanian, [b]Prakash Iruthayanathan, [c]Antony Muthaiyan and [b]Lawrence Nallathambi

[a]Department of Physics, Vivekanandha College of Arts & Sciences for Women, Namakkal- Tamilnadu - 637 205, India.

[b]Department of Physics, St. Joseph's College (Autonomous), Tiruchirappalli, 620 002, India

[c]Department of Physics, Arul Anandar College, Karumathur, Madurai, 625514, India

Corresponding Author: nlawdines@yahoo.co.in

Abstract

Metals and alloys play a vital role in the storage of hydrogen and its isotopes. To store hydrogen is to store energy. The storage capacity of a metal/ alloy is determined mainly by the diffusion parameters namely the pre-exponential factor of diffusion constant and the activation energy. Not much work is done regarding diffusion parameters of hydrogen isotopes in Mg_2Ni except the ab-initio calculation and green's function approach. Hence in this theoretical investigation, the diffusion parameters of hydrogen isotopes in Mg_2Ni are computed using a reaction coordinate approach incorporating a scattering matrix formalism and green function technique. Our results are compared with the existing theoretical results.

Keywords: Mg_2Ni, eigen values, eigen vectors, mean square displacement, diffusion parameters, hydrogen isotopes, green function techniques, scattering matrix formalism and reaction coordinates.

1. Introduction

Hydrogen energy is a kind of high efficient and clean secondary energy. Hydrogen storage plays a vital role in both hydrogen production and hydrogen applications. The important properties of the hydrogen storage materials in automotive applications are (i) light weight, (ii) cost and availability, (iii) high volumetric and gravimetric density of hydrogen, (iv) fast kinetics, (v) ease of activation, (vi) low temperature of dissociation or decomposition, (vii) appropriate thermodynamic properties, (viii) long-term cycling stability, and (ix) high degree of reversibility [1-3].

Recently, many researchers have focused their attention towards exploring Mg and Mg based alloys for hydrogen storage. The Mg-based metallic hydrides have low specific weight, low cost and high hydrogen capacity for e.g. 7.6 wt.% for MgH_2, 3.6 wt.% for Mg_2NiH_4 [4]. In order to use metal hydrides as energy carriers in mobile vehicles, the total mass of the storage system needs to be reduced. The metallic Mg has hexagonal crystal structure. After absorption of hydrogen Mg_2NiH_4 has become cubic antiflurite structure [5]. By calculation, the bond length of Mg_2NiH_4 is d_{Ni-H}= 1.548 Å while the experimental value is 1.55 Å [6]. The electronic bond structure of this compound with regular tetrahedral arrangement produces a semiconductor with an indirect gap of 1.17 eV. It is conformed that hydrogen is covalently bonded with nickel forming a complex $[NiH_4]^{4-}$ which in turn bonds ionically to the Mg^{2+} ions in Mg_2NiH_4 by the calculated charge distribution [7]. Not much work is done regarding diffusion parameters except the ab initio calculation and green's function approach [2,5]. In this paper the estimated results of diffusion parameters of hydrogen isotopes $_1H^1$, $_1H^2$ and $_1H^3$ in Mg_2Ni using reaction coordinate incorporating

International Journal of
Scientific Research in Science and Technology (IJSRST)
Print ISSN : 2395-6011, Online ISSN : 2395-602X
International Conference on Advanced Materials
Held on 14, 15 December 2017, Organized by Department of Physics,
St. Joseph's College, Trichy, Tamilnadu, India

green's function technique and scattering formalism are reported.

2. Method of calculation

In this lattice dynamical investigation, the first step is to compute the phonon frequencies and eigen vectors of the host material Mg_2Ni. The phonon frequencies and eigen vectors of Mg_2Ni are estimated using Born-von Karman formalism considering interactions up to three neighbors.

The force constant values in the dynamical matrix are estimated using the Morse potential with parameters [8,9] and are listed in Table 1.

The dynamical matrix thus obtained is a (9 × 9) Hermitian matrix. It has been converted into a real symmetric matrix of the order (18 × 18). Diagonalization of this matrix yields the phonon frequencies and polarization vectors.

Table 1. Force constant values in 10^4 dynes/cm

Parameter	A_{11}	B_{11}	A_{12}	B_{12}	C_{12}	A_{13}
Value	0.9123	0.022	-0.0291	-0.0291	0.0654	-0.0667
Parameter	B_{13}	A_{21}	B_{21}	A_{22}	B_{22}	C_{22}
Value	0.014	0.5682	0.5682	-0.0619	-0.0249	0.0044
Parameter	D_{22}	A_{23}	B_{23}	C_{23}	D_{23}	A_{31}
value	0.0044	-0.0045	-0.0045	-0.0019	0.00065	0.9123
Parameter	B_{31}	A_{32}	B_{32}	C_{32}	A_{33}	B_{33}
value	0.022	-0.291	0.0291	0.0654	-0.0171	-0.0171
Parameter	A_{51}	B_{51}	C_{51}	A_{52}	B_{52}	A_{53}
value	0.8827	0.8827	0.0485	-0.1388	0.016	-0.0016
Parameter	B_{53}	C_{53}	A_{61}	B_{61}	A_{62}	B_{62}
value	-0.0016	0.00026	0.5682	0.5682	-0.0619	-0.0249
Parameter	C_{62}	D_{62}	A_{63}	B_{63}	C_{63}	D_{63}
value	0.0044	0.0044	-0.0045	-0.0045	-0.0019	0.00065

Using the phonon frequencies and eigen vectors, the Green's function values are calculated by using the equation [10],

$$G_{\alpha\beta}\begin{pmatrix} l & l' \\ k & k' \end{pmatrix};\omega^2 = \frac{1}{N\sqrt{m_k m_{k'}}} \sum_{qj} \frac{e_\alpha(k|\vec{q}j)\, e_\beta^*(\kappa|\vec{q}j)}{\omega_{\max}^2} \exp\left[i\vec{q}.(\kappa(l) - \vec{\kappa}(l'))\right] \quad \ldots (1)$$

where ω_{max} is the maximum frequency among all normal modes of the host crystal. Using eigen values and eigen vectors, the green's function values have been evaluated which in turn are used to calculate the diffusion parameters.

The defect modes are obtained by solving the secular equation

$$\Delta(\omega^2) = |I - g(\delta l + a\gamma a^T)| = 0 \quad \ldots (2)$$

where I is the Unit matrix, g is the Green's function matrix, δl in the change in dynamical matrix, a is the matrix of interaction of hydrogen with neighbours and γ is the interstitial green's function matrix.

The displacement of the four neighboring metal atoms surrounding the interstitial hydrogen is obtained using the equation,

$$u_1 = \left\{ I + g(\delta l + a\gamma a^T)\left[I - g(\delta l + a\gamma a^T)\right]^{-1} \right\} u_\alpha \ldots (3)$$

with u_α as

$$u_\alpha\begin{pmatrix} l \\ k \end{pmatrix};\vec{q}j = \left\{\frac{1}{2Nm_k\omega_{qj}}\right\} e_\alpha(\kappa,\vec{q}j) \exp\left[i\vec{q}.r\begin{pmatrix} l \\ k \end{pmatrix}\right] \quad \ldots (4)$$

where ω_{qj} are the frequencies of normal modes and $e_\alpha(k,\vec{q}j)$ are the eigen vectors.

The displacement of hydrogen isotope is computed using the equation

$$\xi = -\gamma a^T u_1 \quad \ldots (5)$$

In the jumping process of hydrogen isotope, the jump is initiated as a result of fluctuation in the energy and momentum of the hydrogen isotope assisted by the phonons created by lattice vibrations.

The reaction coordinate is estimated using the equation

International Journal of
Scientific Research in Science and Technology (IJSRST)
Print ISSN : 2395-6011, Online ISSN : 2395-602X
International Conference on Advanced Materials
Held on 14, 15 December 2017, Organized by Department of Physics,
St. Joseph's College, Trichy, Tamilnadu, India

$$\chi = \left(\xi_d - \frac{1}{m} \sum_j \bar{u}_j \right) . \xi \qquad \ldots (6)$$

where ξ_d and u_j are displacements of diffusing atom and host atoms respectively.

Using the reaction coordinates the jump frequency is computed using the equation

$$\Gamma = \left[\frac{\Sigma_{q,j} \omega^2(q,j) |\chi(q,j)|^2}{\Sigma_{q,j} |\chi(q,j)|^2} \right] \times \exp\left[-\frac{\chi_c^2}{\Sigma_{q,j} |\chi(q,j)|^2} \right] \qquad \ldots (7)$$

From this equation, Γ_0 is identified as

$$\Gamma_0 = \left[\frac{\Sigma_{q,j} \omega^2(q,j) |\chi(q,j)|^2}{\Sigma_{q,j} |\chi(q,j)|^2} \right]^{\frac{1}{2}}$$

the activation energy E_a is calculated using the golden rule.

$$\Gamma = \Gamma_0 \exp\left(-\frac{E_a}{k_B T} \right) \qquad \ldots (8)$$

The pre exponential factor of diffusion D_0 is calculated by

$$D_0 = \frac{\Gamma_0 l^2}{6} m^2 s^{-1}$$

3. Results and Discussion

a) Phonon frequencies and eigen vectors

The phonon frequencies and eigen vectors have been calculated for a set of 122 wave vector points obtained by uniformly dividing the Brillouin zone [11,12].

b) Mean Square Displacement

The displacement of nearby host atoms changes due to the presence of interstitial hydrogen. The mean square displacement values for different temperatures are estimated and are compared with defect free material as shown in fig. 1. MSD values is increases with temperature as expected. More over the MSD of atoms surrounding H defect, D defect and T defect is decreased effectively. This is because of the creation of resonance modes. During the resonance nodes of vibration, the vibrational amplitude of hydrogen isotopes are expected to be huge with the expense of that of the neighboring atoms.

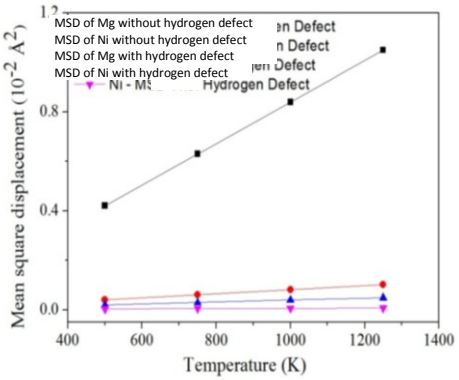

Figure 1(a). Mean square displacement of atoms surrounding the H-defect

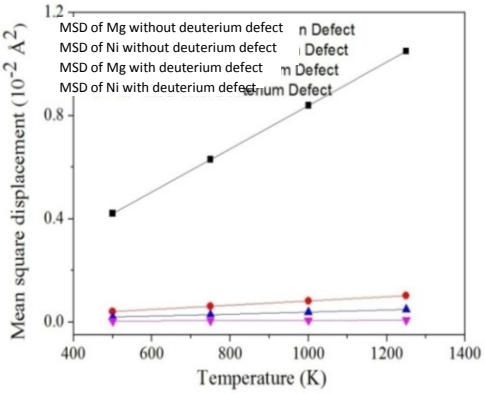

Figure 1(b). Mean square displacement of atoms surrounding the D-defect

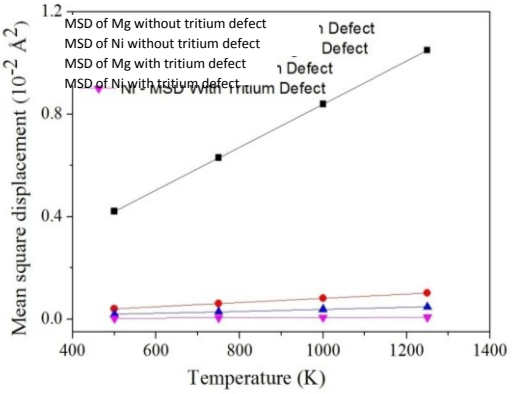

Figure 1(c). Mean square displacement of atoms surrounding the T-defect

International Journal of
Scientific Research in Science and Technology (IJSRST)
Print ISSN : 2395-6011, Online ISSN : 2395-602X
International Conference on Advanced Materials
Held on 14, 15 December 2017, Organized by Department of Physics,
St. Joseph's College, Trichy, Tamilnadu, India

c) Jump frequency values

Using green's function values and the reshape in dynamical matrix due to the presence of hydrogen and their isotopes (H, D and T) the jump frequency values were estimated using reaction coordinate technique at different temperatures and these values are given in table 2.

Table 2. Jump frequency values at different temperature

Isotopes	Temperature (K)	Jump frequency Γ sec^{-1}
hydrogen	500	2.80E+07
	750	2.35E+09
	1000	2.16E+10
	1250	8.17E+10
deuterium	500	1.57E+07
	750	1.59E+09
	1000	1.60E+10
	1250	6.43E+10
tritium	500	8.72E+06
	750	1.09E+09
	1000	1.22E+10
	1250	5.21E+10

d) Diffusion parameters

The lnΓ versus reciprocal of temperature curve is as shown in fig. 2, which was found to be a straight line. From the intercept and slope, the Γ_0 and activation energy values are determined. The D_0 value was calculated using the Eqn.

$$D_0 = \frac{\Gamma_0 l^2}{6} \qquad \ldots (9)$$

which is found be $D_0 = 2.84615 \times 10^{-8}$ m^2 sec^{-1} for hydrogen. E_a calculated from the slope is found to be 0.564 eV. Our calculated results are compared with that computed employing Quasielastic neutron scattering and NMR studies [13] in table 3. Our result is found to be comparable with the experimental results. The activation energy increases with isotopic mass. This is a welcome trend. Moreover the activation energy for hydrogen diffusion is found to be 0.564 eV, which is low. Hence hydrogen can easily diffuse and occupy the interstitical positions. Moreover the stored hydrogen can easily be retrieved for end use.

Table 3. Diffusion parameters of H in Mg_2Ni

Diffusing Atom	Pre-exponential factor D_0 (10^{-8} m^2 sec^{-1})	Activation energy E_a (meV)	Reference
H	2.84615	564	This study
D	2.84428	594	
T	2.84895	615	
H	1.084	563.8	[13]

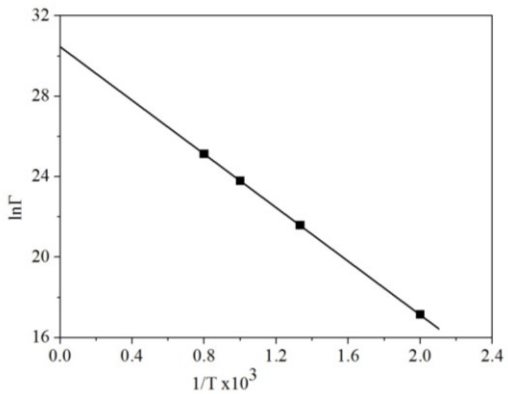

Figure 2(a). Logarithm of Jump frequency vs. 1/T for Hydrogen in Mg_2Ni

International Journal of
Scientific Research in Science and Technology (IJSRST)
Print ISSN : 2395-6011, Online ISSN : 2395-602X
International Conference on Advanced Materials
Held on 14, 15 December 2017, Organized by Department of Physics,
St. Joseph's College, Trichy, Tamilnadu, India

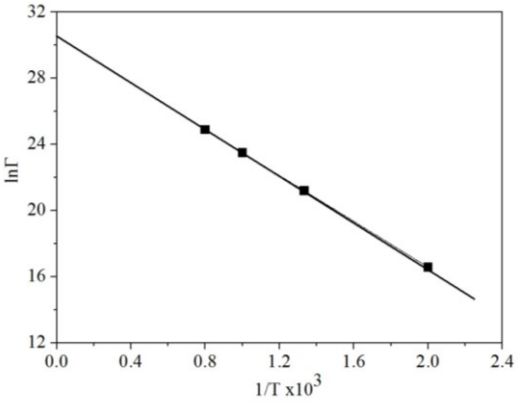

Figure 2(b). Logarithm of Jump frequency vs. 1/T for Deuterium in Mg_2Ni

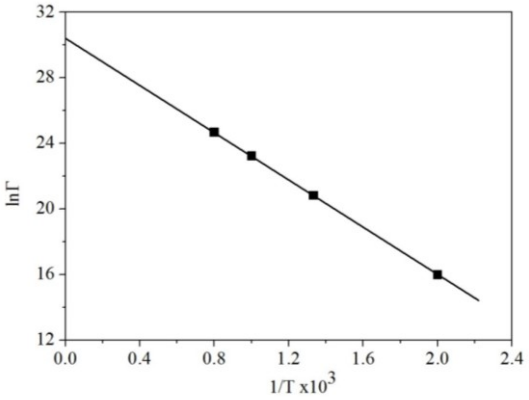

Figure 2(c). Logarithm of Jump frequency vs. 1/T for Tritium in Mg_2Ni

A comparative study is made as shown in table 4.

Table 4. Comparative study

Temperature (K)	D_H	D_D	D_T	Ratio D_D / D_H	Ratio D_T / D_H
500	5.81187 E-14	3.1981E-14	2.01346 E-14	0.550271	0.346439
750	4.58E-12	3.07552 E-12	2.26042 E-12	0.67	0.49
1000	4.06711 E-11	3.016E-11	2.39504 E-11	0.741559	0.58888
1250	1.50758 E-10	1.1867E-10	0.98716 E-10	0.787153	0.654798

From the last two columns it is concluded, D_D/D_H and D_T/D_H values are found to be less than one as expected. This result is in support of usage of this alloy for the application towards hydrogen isotope separation.

4. Conclusion

The eigen values and eigen functions of the cubic Laves phased compound Mg_2Ni are estimated by Born-von Karman formalism. The localized vibrational modes have been used to worked out with hydrogen atoms as an interstitial defect in this system. A green's function technique and the scattering matrix formalism are used to calculated the MSD values of Hydrogen isotopes (H, D and T) and its neighbors at 500, 750, 1000 and 1250 K temperatures. A reaction coordinate technique has been used to compute the diffusion parameters of Hydrogen isotopes (H, D and T) in Mg_2Ni. These values are found to be in good agreement with the existing experimental result.

5. References

[1] Haussermann, U., Blomqvist, H. and Noréus, D., "Bonding and Stability of the Hydrogen Storage Material Mg_2NiH_4". Inorganic Chemistry, 41, 2002, 3684-3692. http://dx.doi.org/10.1021/ic0201046.

[2] Van Setten, M.J., De Wijs, G.A. and Brocks, G., "Ab Initio Study of the Effects of Transition Metal Doping of Mg_2NiH_4". Physical Review B, 76, 2007, Article ID: 075125. http://dx.doi.org/10.1103/PhysRevB.76.075125

[3] Jezierski, A., Jurczyk, M. and Szajek, A., "Electronic Structure of $Mg_2Ni_{1-x}Cu_x$". Actaphysicapolonica A, 115, 2009, 223-225.

[4] Zhang Yanghuan, Yang Tai, Shang Hongwei, Zhang Guofang, CAI Ying, Zhao Dongliang, Gaseous and

Electrochemical Hydrogen Storage Kinetics of As-quenched Nanocrystalline and Amorphous, Mg_2Ni-type Alloys, 604, Vol.28, No.3, ZHANG Yanghuan et al. Gaseous and Electrochemical Hydrogen Storage.

[5] Antony, M., Lawrence, N. and Rayappan, J.B., J. Comput. Theor. Nanosci. 12, 2015, 413-417.

[6] Garcia, G.N., Abriata, J.P. and Sofo, J.O., Phys. Rev. B 59, 1999, 746.

[7] Wang, S.P., Guo, J.G. and Jiang, Y., J. Comput. Theor. Nanosci. 10, 2013, 250.

[8] Rui Yu, Pengcheng Zhai, Guodong Li and Lisheng Liu, J. Elect. Materials 41, 2012, 1465.

[9] Girifalcom, L.A. and Weizer, V.G., Phys. Rev. 114, 1959, 687.

[10] Maradudin, A.A., E.W. Montroll, C.H. Weiss and I.P. Ipatova, "Theory of Lattice Dynamics in the Harmonic Approximation", Academic Press, New York, 1971, 708.

[11] Balaguru, R.J.B., Lawrence, N. and Raj, S.A.C., Int. J. Mod. Phys. B 16, 2002, 4111.

[12] Disalvo, F.J., Moncton, D.E. and Waszczak, J.V., Phys. Rev. B 14, 1976, 4321.

[13] Cermak, J. and Kral, L., Acta Materialia 56, 2008, 2677.

International Journal of
Scientific Research in Science and Technology (IJSRST)
Print ISSN : 2395-6011, Online ISSN : 2395-602X
International Conference on Advanced Materials
Held on 14, 15 December 2017, Organized by Department of Physics,
St. Joseph's College, Trichy, Tamilnadu, India

Thermodynamic Properties of Phenetole with 2-Chlorophenol and 3-Chlorophenol at Different Temperatures

S. Arulappan[1], R. Raj Muhamed[1*], R. Rajesh[2]

[1] Department of Physics, Jamal Mohamed College, Tiruchirappalli-620 020, India

[2] PG and Research Department of Physics, Sri Vijay Vidyalaya College of Arts and Science, Dharmapuri-636 807, India

Corresponding Author: ponnu_68@yahoo.co.in

Abstract

Acoustical and excess thermo acoustical properties of 2-Chlorophenol (2-ChP), 3-Chlorophenol (3-ChP) with Phenetole in Tetrahydrofuran (THF) mixtures are investigated by measuring ultrasonic velocity (u), density (ρ) and viscosity (η) in different concentration range at atmospheric pressure at different temperatures. The trend in the acoustical parameters and magnitude of excess thermo acoustical parameters has been used to identify the existence of intra and intermolecular interaction through charge transfer complex formation. The formation of 1:1 complex was also confirmed by UV–Visible spectroscopic method at 303.15 K in these systems. It may be pointed out that the formation constants of the charge transfer complexes determined by Benesi–Hildebrand spectroscopic method and Kannappan equation in ultrasonic method. Thermodynamic parameters such as ΔG, ΔH and ΔS for these equilibria are determined.

Keywords: Excess parameters, phenols, Phenetole, THF, ultrasonic technique, thermo acoustic parameters.

1. Introduction

Study of hydrogen bonded systems is essential and helpful as hydrogen bond plays a vital role in chemical, physical and biological process. Organic compounds containing electronegative group can interact with compounds containing active hydrogen through hydrogen bond. This type of hydrogen bond takes part in role in the stability of biologically important molecules. The Phenotole are self-associated through intermolecular hydrogen bonds. They are both π - as well as n-electron donors and they allow specific interactions with other electron deficient molecules [**1,2**]. The present investigation is Phenotole on the detection of specific interaction between 2-ChP, 3-ChP with Phenetole in THF medium through the acoustic method. The complexes formed between Phenetole and phenols have been attributed to the hydrogen bonding between oxygen and active hydrogen.

2. Experimental

The density, ρ of the pure liquids and their ternary systems were found by using a 10 ml specific gravity bottle. The ultrasonic velocities in pure liquids and their ternary liquid mixtures were measured using a single crystal variable path ultrasonic interferometer operating at 2 MHz frequency supplied by Mittal Enterprises, Model F81, with an accuracy of ± 0.2 ms^{-1}. Viscosity measurements were made with an Ostwald's viscometer in which the flow time for solutions was measured through a digital stop clock of accuracy ± 0.01s.

International Journal of
Scientific Research in Science and Technology (IJSRST)
Print ISSN : 2395-6011, Online ISSN : 2395-602X
International Conference on Advanced Materials
Held on 14, 15 December 2017, Organized by Department of Physics,
St. Joseph's College, Trichy, Tamilnadu, India

Table 1. Ultrasonic velocity, MCE and excess internal pressure for the two ternary systems of Phenetole with 2 – ChP, 3 – ChP in THF at different temperatures

C Mol dm^{-3}	Phenetole + 2–chlorophenol + THF			Phenetole + 3 chlorophenol + THF		
	303 K	308 K	313 K	303 K	308 K	313 K
U / m s^{-1}						
0.01	1244.0	1222.1	1200.4	1251.2	1230.5	1207.5
0.02	1244.9	1222.4	1201.1	1251.8	1230.9	1207.9
0.03	1245.3	1222.8	1201.6	1252.4	1231.7	1208.6
0.04	1246.2	1223.5	1202.1	1253.3	1232.0	1209.3
0.05	1246.8	1223.9	1202.8	1254.2	1232.9	1210.0
0.06	1247.0	1224.7	1203.7	1255.0	1233.3	1210.8
0.07	1247.5	1225.6	1204.3	1255.8	1234.0	1211.4
0.08	1248.5	1227.9	1205.2	1256.0	1234.7	1212.1
0.09	1249.5	1228.0	1205.9	1256.7	1235.3	1213.0
0.10	1250.9	1229.1	1206.8	1257.9	1236.5	1214.3
MCE / k J						
0.01	32.201	32.370	32.296	31.978	32.164	31.893
0.02	32.191	32.358	32.330	32.017	32.212	31.983
0.03	32.191	32.411	32.453	32.050	32.244	32.045
0.04	32.192	32.446	32.487	32.102	32.312	32.086
0.05	32.167	32.469	32.462	32.158	32.367	32.147
0.06	32.174	32.470	32.540	32.196	32.448	32.222
0.07	32.263	32.468	32.614	32.247	32.503	32.276
0.08	32.291	32.458	32.663	32.297	32.554	32.280
0.09	32.283	32.490	32.700	32.344	32.577	32.353
0.10	32.286	32.529	32.777	32.400	32.661	32.426
π_i^E / x 10^2 atm						
0.01	-3.147	-2.952	-2.786	-5.485	-4.884	-4.902
0.02	-3.394	-3.200	-2.960	-5.864	-5.193	-5.152
0.03	-3.619	-3.356	-3.033	-6.232	-5.512	-5.422
0.04	-3.828	-3.540	-3.198	-6.564	-5.782	-5.703
0.05	-4.073	-3.714	-3.427	-6.884	-6.064	-5.958
0.06	-4.272	-3.921	-3.543	-7.220	-6.305	-6.188
0.07	-4.374	-4.122	-3.645	-7.530	-6.567	-6.433
0.08	-4.539	-4.322	-3.789	-7.838	-6.823	-6.728
0.09	-4.699	-4.476	-3.917	-8.132	-7.112	-6.939
0.10	-4.871	-4.604	-3.990	-8.402	-7.319	-7.136

3. Result and discussion

3.1. Acoustical parameters

Ultrasonic velocity, MCE and excess internal pressure for the two ternary systems of Phenetole are arranged in Table 1. The ultrasonic velocity versus concentration is similar in the two ternary systems suggesting the presence of a similar type of interaction in two systems. The increase in velocity may be attributed to strong solute–solute interactions. The strong polar nature of the chlorophenols may disrupt the dipolar association in pure phenetole leading to the possibility of unlike molecular attraction. The steep increase in the ultrasonic velocity may be an indication of stronger molecular interactions such as dipole–dipole or charge transfer complex formation [3]. MCE also increases non-linearly with concentration in two systems. The valley in the two systems indicates the rupture of hydrogen bonds due to interaction between cholorophenol and solvent molecules (dipole–induced dipole) and above this concentration the interactions between chlorophenol and molecules of Phenetole dominate. The magnitude of molar cohesive energy substantiates the possibility of hydrogen bonded interaction [4]. The strength of interaction increases with concentration as evident from the table of MCE against concentration.

3.2. Excess thermo acoustic parameters

Plots showing variation of excess velocity (u^E) with concentration at different temperatures is depicted in, Figs. 1a–b. The thermodynamic excess properties of organic liquid mixtures depend on the chemical structure, size and shape of their constituent molecules. The negative deviations in ultrasonic velocity explain the non-ideal nature of these two ternary liquid mixtures and greater deviations suggest stronger intermolecular interactions between the component molecules [5]. It was reported that strong intermolecular interactions such as hydrogen bonding and charge transfer complexes lead to negative deviation in ultrasonic velocity. The negative deviation in internal pressure is an indication of stronger adhesion between the components in the mixture [6].

Table 2. The values of stability constants K and correlation coefficient for various donors 'D' at different temperatures and thermodynamic parameters obtained by ultrasonic method at 303.15 K

D	Solvent: THF			Acceptor: Phenetole			Correlation coefficient
	K (mol^{-1})			ΔG ($kJmol^{-1}$)	ΔH ($kJmol^{-1}$)	ΔS (JK^{-1} mol^{-1})	
	303.15K	308.15K	313.15K				
2-ChP	18.01	15.70	13.64	-7.282	-29.830	-74.415	0.987
3-ChP	20.55	17.15	15.07	-7.615	-32.466	-82.017	0.999

International Journal of
Scientific Research in Science and Technology (IJSRST)
Print ISSN : 2395-6011, Online ISSN : 2395-602X
International Conference on Advanced Materials
Held on 14, 15 December 2017, Organized by Department of Physics,
St. Joseph's College, Trichy, Tamilnadu, India

Table 3. Thermodynamic parameters of stability constant K (by Benesi-Hildebrand equation), free energy of formation ΔG, wave length of maximum absorption of charge transfer complex λ_{max}, absoptivity and correlation coefficient obtained by UV spectrometric technique for different proton donors at 303.15K

Solvent: THF			Proton acceptor: Phenetole	
Proton donor	k (mol^{-1})	ΔG (kJ mol^{-1})	λ_{max} (nm)	ε (dm^2 mol^{-1})
2-Chlorophenol	38.20	-9.18	232	2171
3-Chlorophenol	76.91	-10.94	241	1033

3.3. Thermodynamic parameters

The values of equilibrium constant for the charge transfer of Phenetole with chlorophenols in THF solutions were calculated at 303, 308 and 313 K by employing Kannappan equation **[7–9]** from the measured values of ultrasonic velocity. Formation constants of the two charge transfer species stabilized through hydrogen bond at three different temperatures are given in Table 2. The thermodynamic parameters obtained by UV-spectrometric technique are arranged in Table 3. The decreasing trend of K with increase in temperature reveals that the charge transfer interaction between the chlorophenols and Phenetole is exothermic. Fairly good correlation is obtained between ln K values and 1/T in accordance with van't Hoff equation (Fig. 2a-b). The enthalpy changes for protonation equilibrium are obtained from the slopes of the plots of ln K vs. 1/T. The computed values of free energy of formation (ΔG), enthalpy changes (ΔH) and entropy changes (ΔS) are summarized in Table 2. The negative values of free energy of formation suggest that the charge transfer species are stabilized through hydrogen bond.

4. Conclusion

The present investigation deals with determination of thermodynamic properties of charge transfer complexes formed between an Phenetole and 2ChP, 3ChP in THF medium by ultrasonic method. The formation constant values computed by ultrasonic method .The trend in the acoustical properties and negative values of entropy of formation clearly establish the formation of donor–acceptor complex between these two component molecules in a non-polar medium. The stability is in the order 3ChP-Phenetole > 2ChP-Phenetole. The negative values of free energy of formation of these two complexes indicate that these complexes are thermodynamically stable.

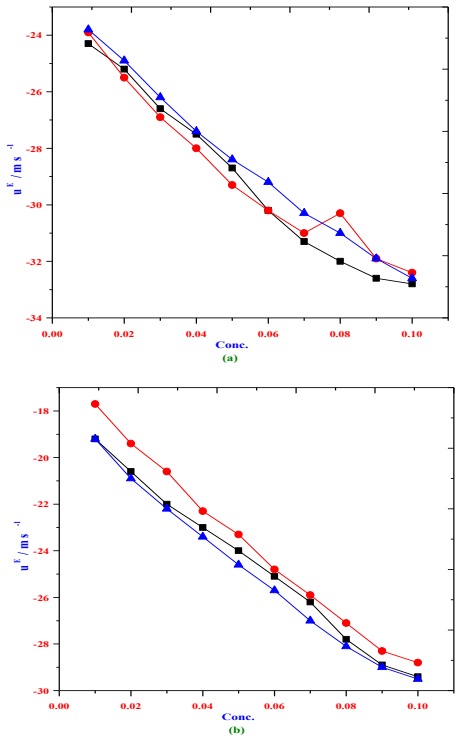

Figure 1. Plot of Excess velocity versus concentration a) 2-ChP b) 3-ChP with Phenetole in THF system at different temperatures T = (■) 303 K, (●) 308 K and (▲) 313 K

International Journal of
Scientific Research in Science and Technology (IJSRST)
Print ISSN : 2395-6011, Online ISSN : 2395-602X
International Conference on Advanced Materials
Held on 14, 15 December 2017, Organized by Department of Physics,
St. Joseph's College, Trichy, Tamilnadu, India

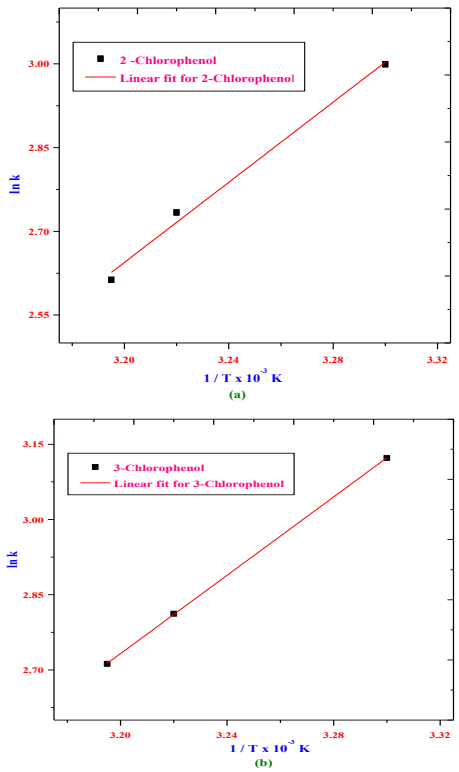

Figure 2. Plot of reciprocal of temperature versus logarithm of stability constant for a) 2-ChP b) 3-ChP with Phenetole in THF solution

5. References

[1] B.S. Santhi, D. Krishnamurthy, V. Kannappan, R. Kumar. J. Molecular Liquids, 188, 2013, 120-125.

[2] R. Kumar, P. Ashokan, S.J. Askar Ali. J. Molecular Liquids, 179, 2013, 124-129.

[3] V.K. Syal, S. Chauhan, Uma Kumari. Indian J. Pure Appl. Phys. 43, 2005, 844-848.

[4] G. Mahendran, L. Palaniappan. Indian J. Pure Appl. Phys. 49, 2011, 803-808.

[5] A. Ali, A.K. Nain, V.K. Sharma, S. Ahmad. Phys. Chem. Liq. 42, 2004, 375-383.

[6] A.K. Nain, D. Chand, P. Chandra, J.D. Pandey. Phys. Chem. Liq. 47, 2009, 195-209.

[7] V. Kannappan, N. Indragandhi. Phys. Chem. Liq. 46, 2008, 510-515.

[8] V. Kannappan, R. Jaya Shanthi, S. Xavier Jesuraja. Phys. Chem. Liq. 41, 2003, 133-138.

International Journal of
Scientific Research in Science and Technology (IJSRST)
Print ISSN : 2395-6011, Online ISSN : 2395-602X
International Conference on Advanced Materials
Held on 14, 15 December 2017, Organized by Department of Physics,
St. Joseph's College, Trichy, Tamilnadu, India

X-Ray Diffraction Analyses of Titanium Dioxide Nanoparticles

M. Iniya Pratheepa[1], M. Lawrence[1*]

[1]Department of Physics, St. Joseph's College, Trichy-620 002, Tamilnadu, India

E-mail: jefflara1968@yahoo.co.in, Contact Number: +91- 9842459119, Trichy- 620 002, Tamilnadu, India

Abstract

Titanium dioxide (TiO_2) nanopowder was synthesized by cost effective hydrothermal method. The sample was subjected to X-ray diffraction analysis (XRD) and the average crystallite size was estimated from Debye Scherrer's formula and was found to be 30nm. XRD pattern measures the micro strain, bond length, volume, and dislocation density. The instrumental broadening analysis reveals the size and micro strain by Williamson-Hall Plot method. The result revealed that the morphology index is interrelated with particle size and specific surface area.

Keywords: XRD, Particle Size, Morphology Index, Specific Surface Area

Introduction

TiO_2 is a most popular material with a large scale production. Several articles are reporting that anatase, brookite, and rutile are the most common phases. Each and every crystalline structure attributes particular physical properties, band gap, surface morphology and so on [1,2]. With the most noteworthy refractive index, rutile phase is used in artworks, paintings and inks [3].The Catalysis and photo catalysis applications were effective in anatase nanoparticles [4–6]. It is additionally considered as the best contender for photovoltaic and electro chromic devices [7]. Brookite has not been used in the commercial product, but rather a dye sensitized solar cell as of recently reported with empowering out comes [8]. An essential effect on the surface properties of particle size was investigated and reported by a number of researchers [9-11]. It is for the most part used as a photo-catalyst material on account of its lesser monetary value and chemical stability. It owns many applications in several industries like aerospace, medicine, paint, and cosmetics.

The present work is a report on synthesis of TiO_2 nanoparticles by cost effective co precipitation method. The synthesized material was investigated by X-Ray diffraction (XRD) analysis. Particle size, Microstrain, Dislocation density, Morphology index and specific surface area were estimated from the powder x-ray diffraction data.

Experimental

Synthesis of TiO_2 nanoparticles

TiO_2 nanoparticles have been synthesized by hydrothermal method using 10 ml of titanium tetra isopropoxide (TTIP) in a mixture of 50 ml ethanol and 50 ml double distilled water. All procedures of synthesis of TiO_2 nanoparticles were proclaimed in this literature [12]. The final gel was dried at 80°C for 4 hour. Finally, a white powder was conflagrated at 500°C and the activities of TiO_2 samples were investigated.

The synthesized TiO_2 nanoparticles were subjected to powder X-Ray diffraction analysis using JEOL JDX Powder X-Ray diffractometer equipped with Cu-K^{α} radiation of wavelength (λ)=1.5406 Å and the data were taken within the rangeof10° to 70° with the step scan of 0.04.

International Journal of
Scientific Research in Science and Technology (IJSRST)
Print ISSN : 2395-6011, Online ISSN : 2395-602X
International Conference on Advanced Materials
Held on 14, 15 December 2017, Organized by Department of Physics,
St. Joseph's College, Trichy, Tamilnadu, India

Results and Discussion

The XRD pattern Figure 1 affirms the presence of TiO_2 nanoparticles. The prominent peaks were compared with JCPDS data (PDF No: 21-1272) and the peaks obtained in the pattern coincides well with the literature. The intensity of the peak is high and the width of (101) plane at 2θ=25.313° becomes narrow [13]. The sharpness of the peak uncovers that the samples possess a good crystalline nature. The strong diffraction peak around 25.313° and 48.089° indicates TiO_2 is in anatase phase [14]. The spacious diffraction peak is not found in the pattern.

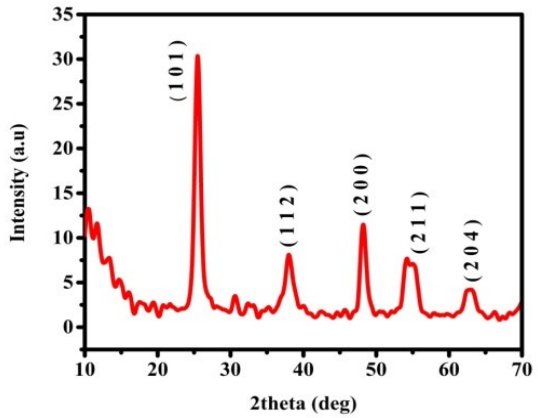

Figure 1. XRD Pattern of TiO_2 Nanoparticles

Particle Size

Average crystallite size of TiO_2 was estimated from the Scherrer's equation as follows [20]

$$D = \frac{K\lambda}{\beta \cos\theta}$$

where, D is the crystallite size, K is the Scherer constant (0.89), λ is the X-ray wavelength (1.54 nm), β the peak width of half maximum, and θ is the Bragg diffraction angle. From the XRD result, grain sizes were calculated by X-Ray line broadening method using Scherrer equation and the plots were drawn with 1/β on X-axis and cosθ along the Y-axis as shown in Figure 2. By fitting the data, crystalline size (D) was extracted from the slope.

Instrumental Broadening

At a point when the particle size is under 100 nm, appreciable broadening will occur in x-ray diffraction pattern because of particle size and strain. The average particles size is evaluated by the observed peak broadening. The total broadening of the diffraction peak is because of the material and instrument. The sample broadening is calculated by

$$FW(S)\times\cos = \frac{K\lambda}{\text{si}\,ze} + 4\times strain \times \sin\theta$$

The total broadening βt equation is described by

$$\beta t^2 \approx \left(\frac{0.9\lambda}{D\cos\theta}\right)^2 + \left(4\varepsilon\tan\theta\right)^2 + \beta_0^2$$

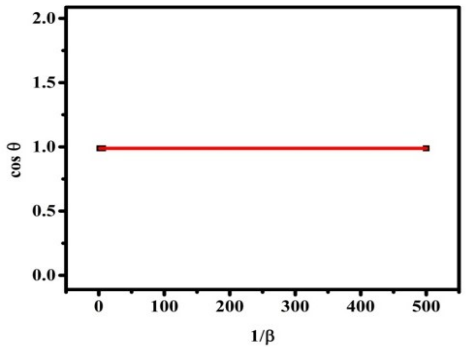

Figure 2. Scherrer Equation Plot of TiO_2 Nanoparticles

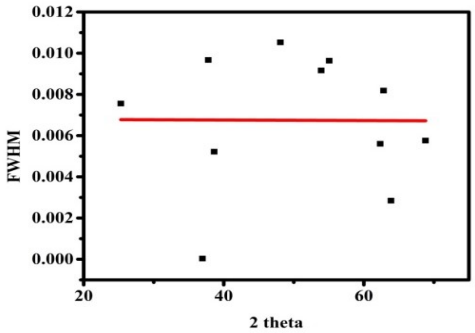

Figure 3. Typical Instrumental Broadening of TiO_2 nanoparticles

where D is average particle size, ∈ is strain and β_0 is instrumental broadening. The size and strain were experimentally observed. The broadening of several peaks was estimated using least squares method and presented in Figure 3. When, particle size becomes smaller, due to size effect, the peaks become broad

International Journal of
Scientific Research in Science and Technology (IJSRST)
Print ISSN : 2395-6011, Online ISSN : 2395-602X
International Conference on Advanced Materials
Held on 14, 15 December 2017, Organized by Department of Physics,
St. Joseph's College, Trichy, Tamilnadu, India

and widths larger. The broadening of peak may likewise happen because of micro strains of the crystal structure emerging from defects like dislocation and twinning [16].

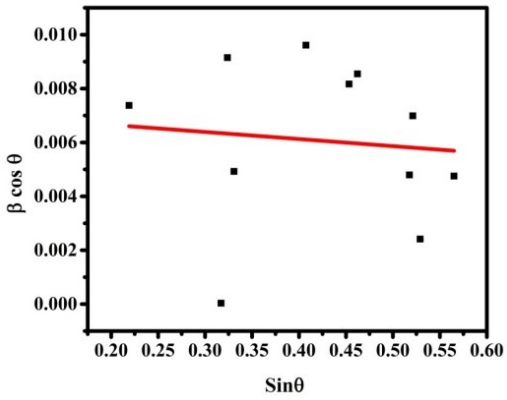

Figure 4. Williamson Hall Plot - TiO_2 Nanoparticles

Williamson and Hall proposed a method for deconvoluting size and strain broadening by looking at the peak width as a function of 2θ which is called as W-H method. The graph plotted is known as W-H plot and it is shown in Figure 4. It is plotted with sin θ on the x-axis and β cos θ on the y-axis (in radians). A linear fit gives the y-intercept and slope of which the particle size and strain are estimated respectively.

XRD - Specific Surface Area

Specific surface area (SSA) is a material property. It is an inferred scientific value that can be utilized to determine the type and properties of a material. It has a specific significance if there should arise an occurrence of adsorption, heterogeneous catalysis and responses on surfaces.

$$SSA = \frac{SA_{part}}{V_{part} \times D_{ensity}}$$

where SSA is the SA per mass, SSA & S are the specific surface area, V_{part} is particle volume and SA_{part} is Surface Area of particle and density of TiO_2 (4.23 g.cm^{-3}).

$$S = \frac{6 \times 10^3}{D_p \times \rho}$$

where S is the specific surface area, D_p is the size of the particles, and ρ is the density of particle [17,18].

Dislocation Density

The dislocation density is the length of dislocation lines per unit volume of the crystal [19]. A dislocation is a crystallographic deformity, or irregularity, within a crystal structure. The presence of dislocation will change the properties of materials. Scientifically, it is a kind of topological imperfection. It increases with plastic deformation; an instrument for the making of dislocations must be initiated in the material. Dislocation has three mechanisms which is homogeneous nucleation, grain boundary initiation, and interface, the lattice and the surface.

It is well known that above a certain grain size limit (~30 nm).The material strength will increase with decreasing grain size [20,21]. The X-ray diffraction analysis has been used to evaluate the intrinsic stress and dislocation density [22,23]. The dislocation density (δ) in the sample has been determined using expressions.

$$\delta = \frac{1}{D^2}$$

where, δ-dislocation density, β-diffraction broadening - measured at half of its maximum intensity (radian), θ-diffraction angle (degree), α- lattice constant (nm) and D-particle size (nm).

International Journal of
Scientific Research in Science and Technology (IJSRST)
Print ISSN : 2395-6011, Online ISSN : 2395-602X
International Conference on Advanced Materials
Held on 14, 15 December 2017, Organized by Department of Physics,
St. Joseph's College, Trichy, Tamilnadu, India

Table 1. Cell Parameters estimated from X-ray diffraction

D size nm	Dislocation density δ	Morphology index x	surface area $(nm)^2$	SSA $m^2 g^{-1}$	SA to Vol Ratio
1.96E-08	2.593E+15	2.3094	1.211E-15	1.239E+15	5.237E+15
4.37E-06	5.226E+15	1.2500	6.012E-11	4.253E+19	1.795E+20
1.58E-08	3.991E+15	1.8050	7.836E-16	5.223E+14	2.302E+15
2.94E-08	1.157E+15	3.3444	2.712E-15	1.824E+15	7.775E+15
1.51E-08	4.405E+15	1.6583	7.142E-16	3.978E+14	1.657E+15
1.77E-08	3.182E+15	1.9047	9.815E-16	4.871E+14	2.063E+15
1.7E-08	3.481E+15	1.8115	9.228E-16	4.317E+14	1.849E+15
3.02E-08	1.096E+15	3.1152	2.577E-15	1.244E+15	5.245E+15
2.07E-08	2.328E+15	2.1326	1.924E-15	5.797E+14	2.452E+15
1.26E-08	2.779E+14	6.1369	1.986E-14	4.749E+15	2.023E+16
3.05E-08	1.077E+15	3.0303	2.605E-15	1.153E+15	4.889E+15

It is observed from the tabulated details and from Figure 5 dislocation density of the material is indirectly proportional to particle size. It implies that the prepared TiO_2 nanoparticles have more strength and hardness than their bulk (TiO_2) counterpart.

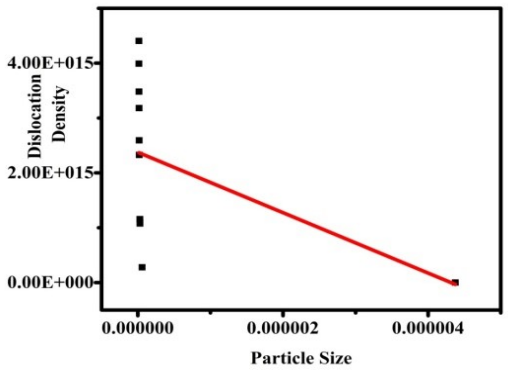

Figure 5. Particle Size Vs Dislocation Density of TiO_2 Nanoparticles

Morphology Index (MI)

The TiO_2 nanopowder is broadly utilized in many industries. Such uses are derived from its unique structural, physical and chemical properties, which are reflected by its surface properties, particle size, and morphology. The specific surface area of TiO_2 nanopowder depends on the interrelationships of particle size and morphology. MI is ascertained from FWHM of XRD, to investigate this relationship based on the literature reported [24].

MI is obtained using equation,

$$MI = \frac{FWHM_h}{FWHM_h + FWHM_p}$$

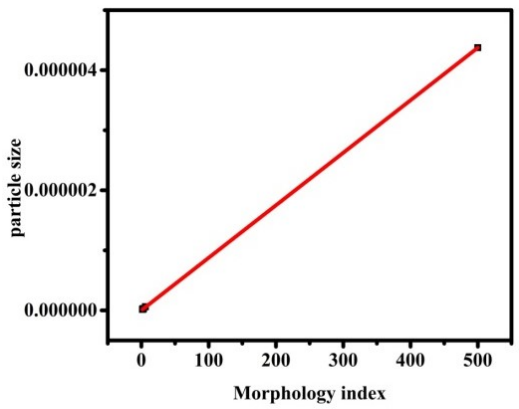

Figure 6. MI Vs Particle Size of TiO_2 Nanoparticles

International Journal of
Scientific Research in Science and Technology (IJSRST)
Print ISSN : 2395-6011, Online ISSN : 2395-602X
International Conference on Advanced Materials
Held on 14, 15 December 2017, Organized by Department of Physics,
St. Joseph's College, Trichy, Tamilnadu, India

where, MI is morphology index, $FWHM_h$ highest FWHM value obtained from peaks and $FWHM_p$ is particular peak's FWHM for which MI is to be calculated. MI range of experimental TiO_2 nanopowder is from 1.8 to 6.1 and the details are presented in Table1.

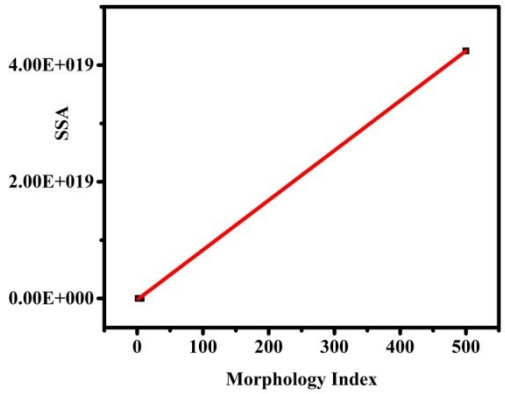

Figure 7. MI Vs Specific Surface Area of TiO_2 Nanoparticles

It is correlated with the particle size (range from 15 to 45 nm) and specific surface area (range from 11.3 to 57.9 m^2g^{-1}). It is observed that MI is directly proportional to particle size and inversely proportional to the specific surface area with a small deviation. The results are shown in Figure 6 & 7. Linear fit in the figures demonstrates the deviations and relationships between them. The observed results of MI affirm the uniformity and fineness of the synthesized nanoparticles.

Conclusion

TiO_2 nanoparticles were synthesized employing a flexible, non-toxic and bio-safe approach, at room temperature. This method is a single source, catalyst free, simple, conservative and environmentally benign which will make it suitable for various applications. XRD investigations have affirmed that the synthesized particles are tetragonal anatase phase TiO_2 and their nano size. The different characters like Instrumental broadening, specific surface area, dislocation density and morphology index were investigated by using XRD analysis.

Acknowledgement

The authors are thankful to the University of Madras, Chennai for providing us the XRD instrumentation facilities to analyze the sample.

References

[1] M. Koelsch, S. Cassaignon, J.F. Guillemoles, J.P Jolivet, Comparison of optical and electrochemical properties of anatase and brookite TiO_2 synthesized by the sol–gel method Thin Solid Film 403–404 (2002) 312-319.

[2] H. Tang, K. Prasad, R. Sanjines, P.E. Schmid, and F.L & y Electrical and optical properties of TiO_2 anatase thin films J. Appl. Phys. 75 (1994) 2042.

[3] J.H. Braun, A. Baidins, R.E. Marganski, TiO_2 pigment technology – review Prog. Org. Coat. 20 (1992) 105.

[4] P.A. Mandelbaum, A.E. Reggazzoni, M.A. Blesa, Bilmes, S. A., The influence of applied bias potential on the photooxidation of methanol and salicylate on titanium dioxide films J. Phys. Chem. B 103 (1999) 5505.

[5] J. Augustynski, J. Hinden, C. Stalder Novel Semiconducting Electrodes for the Photosensitized Electrolysis of Water, J. Electrochem. Soc.124 (1977) 1063.

[6] P.S.M. Dunlop, J.A. Byrne, N. Manga, B.R. Eggins., The photocatalytic removal of bacterial pollutants from drinking water J. Photochem. Photobiol. 148 (2002) 355.

[7] T. Ohzuku, T. Hirai, Nonaqueous An electrochromic displayed based on lithium/titanium dioxide cell. Electrochim. Acta 27 (1982) 1263.

[8] K. J. Jiang, T. Kitamura, H. Yin, S. Ito and S. Yanagida, Dye-sensitized solar cells using brookite nanoparticle TiO_2 films as electrodes Chem. Lett., 2002, 31(9), 872–873.

[9] S.C. Tsai, Y.W. Chung, Effects of particle size on photoassisted water-gas shift reaction over Pt-TiO_2 J. Catal. 86 (1984) 231.

[10] R. Krol, A. Goossens, J. Schoonman, Mott-Schottky Analysis of Nanometer-Scale Thin-Film Anatase TiO_2 J. Electrochem. Soc. 144 (1997) 1723.

[11] C.J. Barbe´, F. Arendse, P. Comte, M. Jirousek, F. Lenzmann., Nanocrystalline Titanium Oxide Electrodes for Photovoltaic Applications J. Am. Ceram. Soc.80 (1997) 3157.

[12] I. Cservenyak, G.H. Kelsall, W.Wang, Reduction of Ti-IV species in aqueous sulfuric and ... 1. titanium speciation Electrochem. Acta 23 (1997) 563.

[13] Antic Z, Krsmanovic RM, Nikolic MG, Cincovic MM, Mitric M, Polizzi S, Dramicanin MD. Multisite luminescence of rare earth doped TiO_2 anatase nanoparticles. Mat. Chem. Phys. 135 (2012) 1064-1069.

[14] Thamaphat K, Limsuwan P, Ngotawornchai B. Phase Characterization of TiO_2 Powder by XRD and TEM. Kasetsart. J. (Nat. Sci.) 42 (2008) 357-361.

[15] S. Ito, P. Chen, P. Comte, M. Khaja, K. Nazeeruddin, P. Liska, P. Péchy and M.Grätzel, "Fabrication of Screen-Printing Pastes From TiO_2 Powders for Dye-Sensitized Solar Cells," Progress in Photovoltaics: Research and Applications, Inter Science. 56(2007) 465-472.

[16] Ghosh SC, Thanachayanont C, Dutta J. Studies on Zinc sulphide nanoparticles for Field Emission Devices. The 1st ECTI Annual Conference (ECTI-CON 2004) Pattaya, Thailand 3-14 (2004) 145-148.

[17] Jiji A, Joseph N, Donald RB, Daniel M, Amit S, You Qiang. Size-Dependent Specific Surface Area of Nanoporous Film Assembled by Core-Shell Iron Nanocluster. J. Nanomater. 54961 (2006) 1-4.

[18] L, Ki-Won J, Jin-OokBg, Dae JY. Chemical Synthesis and Characterization of Highly Oil Dispersed MgO Nanoparticles. J.Ind. Eng. Chem. 12(6) (2006) 882-887.

[19] Nehru LC, Swaminathan V, Sanjeeviraja C. Photoluminescence Studies on Nanocrystalline Tin Oxide Powder for Optoelectronic Devices American. J. Mat. Sci. 2(2) (2012) 6-10.

[20] Gubicza J, Chinh NQ, Lábár JL, Z. Heged Delayed microstructural recovery in silver processed by equal-channel angular pressing. J Mater Sci.43 (2008) 5672–5676.

[21] Majeed Khan MA, Kumar S, Ahamed M, Alrokayan SA, Alsalhi MS. Structural and thermal studies of silver nanoparticles and electrical transport study of their thin films. Nanoscale.Res.Lett.6 (2011) 434).

[22] Subbaiah YPV, Prathap P, Reddy KTR. Structural, electrical and optical properties of ZnS films deposited by close-spaced evaporation. Appl. Surf. Sci. 253(5) (2006) 2409-2415.

[23] Velumani S, Mathew X, Sebastian PJ, Narayandass Sa K, Mangalaraj D. Structural and optical properties of hot wall deposited CdSe thin films. Solar Energy Material & Solar Cells. 76(3) (2003) 347-358.

[24] Theivasanthi T, Alagar M, An Insight Analysis of Nano sized powder of Jackfruit Seed. Nano Biomed Eng. 3 (2011)163–168.

International Journal of
Scientific Research in Science and Technology (IJSRST)
Print ISSN : 2395-6011, Online ISSN : 2395-602X
International Conference on Advanced Materials
Held on 14, 15 December 2017, Organized by Department of Physics,
St. Joseph's College, Trichy, Tamilnadu, India

Ultrasonic and Viscometric Studies of Molecular Interaction in Binary Liquid Mixtures of Propylene Glycol and Dimethyl Sulphoxide at Various Temperatures

A. Mary Girija[1], M. M. Armstrong Arasu[2] and D. Devi[3]

[1]Assistant Professor, Department of Physics, Cauvery College for Women Tiruchirappalli, Tamil Nadu, India

[2]Assistant Professor, Department of Physics, St. Joseph's College (Autonomous), Tiruchirappalli, Tamil Nadu, India

[3]Assistant Professor, Department of Physics, Cauvery College for Women, Tiruchirappalli, Tamil Nadu, India

Corresponding author E-mail address: armstrongarasu@gmail.com

Abstract

Ultrasonic studies are extensively used in the confirmation analysis of organic molecules. The binary liquid mixtures play a major role in understanding the nature and strength of molecular interaction. The thermo physical properties such as density (ρ), viscosity (η), and velocity (U) of binary liquid mixtures of Propylene glycol with Dimethyl sulphoxide were determined experimentally over the entire composition range at 303.15K, 308.15K, and 313.15K. From the experimental data the thermo acoustic parameters such as adiabatic compressibility (β_a), intermolecular free length(L_f), acoustic impedance(Z),free volume(V_f),relaxation time(τ), Gibb's free energy(ΔG), internal pressure (π_i), molar sound velocity (R), interaction parameter (χ), were calculated, which are more useful to predict and confirm the molecular interaction present in the binary liquid mixtures.

Keywords: Propylene Glycol, Ultrasonic velocity, intermolecular free length, adiabatic compressibility, interaction parameter, molar sound velocity, internal pressure.

Introduction

The essential frame work of manufacturing material is composed of the scientific and practical interpolation at play among the structure, structural properties and performance of all classes of materials that are potentially useful to the society (1). Even after manufacturing the materials, it is important that one has to analyze its physical and chemical properties. One such property can be investigated by exposing the liquid and solid materials to ultrasonic sound vibrations. Liquid-Liquid mixtures and solutions have found wide application in medical, pharmaceutical, chemical, solvent and related industries. Ultrasonic study of liquids and liquid mixtures has gained much importance in recent years in understanding the nature of molecular interactions in pure liquids and liquid mixtures .Ultrasonic velocity measurements are widely used to study the physical and chemical behavior of liquid mixtures (2-4).

Propylene glycol, also calledpropane-1,2-diol, is a synthetic organic compound with the chemical formula $C_3H_8O_2$. It is a viscous colourless liquid which is nearly odorless but possesses a faintly sweet taste. Chemically it is classed as a diol and is miscible with a broad range of solvents, including water, acetone, and chloroform. It is produced on a large scale and is primarily used in the production of polymers, but also seeks use in food processing, and as a process fluid in low temperature heat exchange applications. Dimethyl sulfoxide (DMSO) is an organosulfur compound with the formula

International Journal of
Scientific Research in Science and Technology (IJSRST)
Print ISSN : 2395-6011, Online ISSN : 2395-602X
International Conference on Advanced Materials
Held on 14, 15 December 2017, Organized by Department of Physics,
St. Joseph's College, Trichy, Tamilnadu, India

$(CH_3)_2SO$. This colorless liquid is an important polar aprotic solvent that dissolves both polar and nonpolar compounds and is miscible in a wide range of organic solvents as well as water. It has a relatively high melting point.

In the investigation, we presented the values of ultrasonic velocity, density and viscosity and evaluated their related thermo acoustical parameters for the binary system of Prpoylene Glycol + Dimethyl Sulphoxide at 303.15K, 308.15K & 313.15K. The results are explained and discussed in terms of molecular interactions present in the binary mixtures.

Experimental

The binary mixtures were prepared by mass, by mixing the calculated volumes of liquid components in airtight glass bottles. In all the measurements, INSREF thermostat with a constant digital temperature display accurate to ±0.01K was used. For all the mixtures and pure solvent triplicate measurements were performed and the average of all values were considered in the calculation. The mass measurements (±0.0001g) were made using an electronic balance. The accuracy of density measurements was 0.0001g.cm^3. A set of 11 compositions were prepared for binary mixtures respectively and also their physical properties were measured. Viscosity is measured by calibrated Ostwald's Viscometer. The speed of sound was determined using a constant frequency (2MHz) ultrasonic interferometer with an accuracy of ± 0.1 m.s^{-1}.

Theory

The adiabatic compressibility β_a was obtained from sound velocity and density measurements as

$$\beta_a = 1/(u^2\rho) \quad (1)$$

The intermolecular free length was calculated using the formula given by Jacobson et al.

$$L_f = K_J \sqrt{\beta_a} \quad (2)$$

where KJ is Jacobson's constant. K_J is the temperature dependent parameter which varies directly with the square root of the absolute temperature i.e.,

$$K_J \alpha \sqrt{T} \quad (3)$$

The acoustic impedance is given as

$$Z = \rho u, \quad (4)$$

where u is the ultrasonic velocity and ρ the density.

On the basis of the dimensional analysis using the free volume concept, Suryanarayana suggested the expression for the internal pressure as

$$\pi_i = bR_gT\,[K_a\eta/u]^{1/2}\rho^{2/3}/M_{eff}^{7/6} \quad (5)$$

where b is the space packing factor (equal to 2 in the present case), R_g, is the gas constant and T is the temperature in degree Kelvin.

From the Eyring's rate process theory, the Gibb's free energy of activation for the relaxation process ΔG was obtained as

$$\Delta G = KT \ln(KT\tau / h) \quad (6)$$

where k is the Boltzmann's constant, h is the Planck's constant and T is the Absolute temperature.

Molar sound velocity (R) and interaction parameter (χ) have been calculated from the following relations.

$$R = (M/\rho)\, U^{1/3} \quad (7)$$

$$\chi = (U/U_{ideal})^2 - 1 \quad (8)$$

The ideal mixing velocity U_{ideal} is given by

$$U_{ideal} = X_1U_1 + X_2U2$$

International Journal of
Scientific Research in Science and Technology (IJSRST)
Print ISSN : 2395-6011, Online ISSN : 2395-602X
International Conference on Advanced Materials
Held on 14, 15 December 2017, Organized by Department of Physics,
St. Joseph's College, Trichy, Tamilnadu, India

Results and Discussion

Table 1. Density(ρ), viscosity (η), ultrasonic velocity(U) for the binary mixtures of propylene Glycol and Dimethyl Sulphoxide at temperatures 303.15K, 308.15K,&313.15K

S. No	X(i) PG	Y(i) DMSO	ρ x 10^{-3} kgm^{-3}			η x 10^{-3} Nsm^{-2}			Ums^{-1}		
			303.15K	308.15K	313.15K	303.15K	308.15K	313.15K	303.15K	308.15K	313.15K
1	0.0000	1.0000	1.1633	1.0881	1.0842	1.3688	1.3608	1.3038	1455.94	1443.97	1438.74
2	0.1000	0.9000	1.1524	1.0767	1.0748	1.6840	1.6346	1.5546	1469.20	1457.17	1451.17
3	0.2000	0.8000	1.1415	1.0758	1.0663	2.0390	1.8803	1.8567	1483.82	1471.17	1464.12
4	0.3000	0.7000	1.1336	1.0720	1.0649	2.5450	2.3385	2.2361	1497.68	1485.65	1477.58
5	0.4000	0.6000	1.1169	1.0701	1.0635	3.1067	2.7159	2.5193	1511.64	1499.31	1490.34
6	0.5000	0.5000	1.0892	1.0664	1.0550	4.1015	3.5442	3.2195	1525.08	1513.8	1503.84
7	0.6000	0.4000	1.0803	1.0579	1.0521	5.3470	4.3711	4.0710	1539.20	1527.62	1516.68
8	0.7000	0.3000	1.0764	1.0512	1.0446	7.4590	5.5922	5.2068	1553.94	1541.37	1529.32
9	0.8000	0.2000	1.0724	1.0465	1.0389	10.5485	7.2825	6.4956	1567.51	1555.82	1542.84
10	0.9000	0.1000	1.0635	1.0409	1.0333	13.9035	9.8541	8.0321	1581.20	1569.57	1555.52
11	1.0000	0.0000	1.0428	1.0342	1.0223	16.9960	13.6214	10.5058	1595.25	1583.65	1568.26

Table 2. Adiabatic compressibility(β_a), intermolecular free length (L_f), acoustic impedance(Z) for the binary mixtures of propylene Glycol and Dimethyl Sulphoxide at temperatures 303.15K, 308.15K & 313.15K

S. No.	X(i) PG	Y(i) DMSO	β_a x 10^{-10} m^2n^{-1}			L_f x 10^{-10} m			$ZKgm^{-2}$ s^{-1}		
			303.15K	308.15K	313.15K	303.15K	308.15K	313.15K	303.15K	308.15K	313.15K
1	0.0000	1.0000	4.0552	4.4077	4.4558	1.2608	1.3145	1.3216	1.6936	1.5711	1.5598
2	0.1000	0.9000	4.0200	4.3740	4.4181	1.2554	1.3095	1.3160	1.6931	1.5689	1.5597
3	0.2000	0.8000	3.9788	4.2948	4.374	1.2489	1.2975	1.3096	1.6937	1.5826	1.5611
4	0.3000	0.7000	3.9328	4.2264	4.3012	1.2417	1.2872	1.2985	1.6977	1.5926	1.5734
5	0.4000	0.6000	3.9182	4.1571	4.2334	1.2393	1.2766	1.2882	1.6883	1.6044	1.5849
6	0.5000	0.5000	3.9473	4.0920	4.1912	1.2440	1.2665	1.2818	1.6611	1.6143	1.5865
7	0.6000	0.4000	3.9072	4.0506	4.1319	1.2376	1.2601	1.2727	1.6627	1.6160	1.5956
8	0.7000	0.3000	3.8473	4.0040	4.0931	1.2281	1.2529	1.2667	1.6726	1.6202	1.5975
9	0.8000	0.2000	3.7950	3.9476	4.0437	1.2197	1.2440	1.2590	1.6809	1.6281	1.6028
10	0.9000	0.1000	3.7608	3.8996	3.9996	1.2142	1.2364	1.2522	1.6816	1.6378	1.6073
11	1.0000	0.0000	3.7682	3.8554	3.9772	1.2154	1.2294	1.2487	1.6635	1.6337	1.6082

International Journal of
Scientific Research in Science and Technology (IJSRST)
Print ISSN : 2395-6011, Online ISSN : 2395-602X
International Conference on Advanced Materials
Held on 14, 15 December 2017, Organized by Department of Physics,
St. Joseph's College, Trichy, Tamilnadu, India

Table 3. Internal pressure(π_i), molar sound velocity (R), relaxation time (τ) for the binary mixtures of Propylene Glycol and Dimethyl Sulphoxide at temperatures 303.15K, 308.15K& 313.15K

S. No.	X(i) PG	Y(i) DMSO	π_i x 10^{6Pa}			R			$\tau \times 10^{-10}$(s)		
			303.15K	308.15K	313.15K	303.15K	308.15K	313.15K	303.15K	308.15K	313.15K
1	0.0000	1.0000	0.7020	0.6833	0.6793	0.7395	0.7884	0.7903	0.7401	0.7997	0.7745
2	0.1000	0.9000	0.7726	0.7426	0.7366	0.7487	0.7992	0.7995	0.9026	0.9533	0.9157
3	0.2000	0.8000	0.8432	0.7946	0.7996	0.7584	0.8024	0.8083	1.081	1.0767	1.0830
4	0.3000	0.7000	0.9362	0.8825	0.8755	0.7660	0.8079	0.8118	1.3345	1.3178	1.2823
5	0.4000	0.6000	1.0226	0.9485	0.9273	0.7799	0.8118	0.8152	1.6230	1.5053	1.4220
6	0.5000	0.5000	1.1540	1.0791	1.0412	0.8021	0.8172	0.8242	2.1586	1.9337	1.7991
7	0.6000	0.4000	1.3084	1.1903	1.1673	0.8112	0.8263	0.8289	2.7855	2.3607	2.2428
8	0.7000	0.3000	1.5391	1.3388	1.3125	0.8167	0.8340	0.8371	3.8262	2.9855	2.8416
9	0.8000	0.2000	1.8235	1.5209	1.4587	0.8221	0.8404	0.8442	5.3376	3.8332	3.5022
10	0.9000	0.1000	2.0793	1.7606	1.6147	0.8314	0.8474	0.8511	6.9719	5.1237	4.2834
11	1.0000	0.0000	2.2661	2.0583	1.8318	0.8504	0.8554	0.8626	8.5393	7.0022	5.5712

Table 4. Free volume (V_f), Gibb's free energy (ΔG), interaction parameter (χ) for the binary mixtures of Propylene Glycol and Dimethyl Sulphoxide at temperatures 303.15K, 308.15K & 313.15K

S. No	X(i) PG	Y(i) DMSO	V_f x 10^{-3} m^3			(-ΔG) x10^{-21}KJ/mole			χ		
			303.15K	308.15K	313.15K	303.15K	308.15K	313.15K	303.15K	308.15K	313.15K
1	0.0000	1.0000	8.5559	8.6252	9.0410	3.8519	3.9095	3.9740	0.0166	0.0254	0.0531
2	0.1000	0.9000	6.3309	6.5389	7.0066	3.8394	3.8982	3.9631	0.0155	0.0239	0.0502
3	0.2000	0.8000	4.8039	5.3555	5.4187	3.8280	3.8904	3.9521	0.0162	0.0236	0.0481
4	0.3000	0.7000	3.4796	3.9030	4.1402	3.8147	3.8775	3.9411	0.0159	0.0239	0.0467
5	0.4000	0.6000	2.6058	3.1491	3.4932	3.8024	3.8689	3.9344	0.0157	0.0231	0.0445
6	0.5000	0.5000	1.7339	2.1346	2.4412	3.7844	3.8529	3.9191	0.0149	0.0235	0.0432
7	0.6000	0.4000	1.1763	1.5736	1.7320	3.7683	3.8401	3.9047	0.0150	0.0229	0.0411
8	0.7000	0.3000	0.7213	1.0978	1.2076	3.7483	3.8250	3.8893	0.0158	0.0223	0.0388
9	0.8000	0.2000	0.4328	0.7461	0.8747	3.7273	3.8090	3.8756	0.0152	0.0226	0.0377
10	0.9000	0.1000	0.2886	0.4784	0.6414	3.7104	3.7903	3.8625	0.0147	0.0220	0.0355
11	1.0000	0.0000	0.2155	0.2971	0.4323	3.6976	3.7703	3.8454	0.0147	0.0218	0.0334

International Journal of
Scientific Research in Science and Technology (IJSRST)
Print ISSN : 2395-6011, Online ISSN : 2395-602X
International Conference on Advanced Materials
Held on 14, 15 December 2017, Organized by Department of Physics,
St. Joseph's College, Trichy, Tamilnadu, India

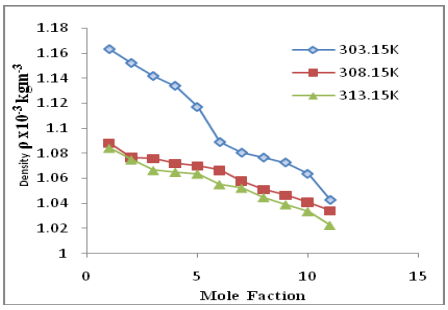

Figure 1. Variation of Density with Mole Fraction

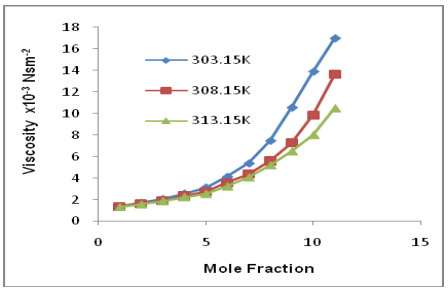

Figure 2. Variation of Viscosity with Mole Fraction

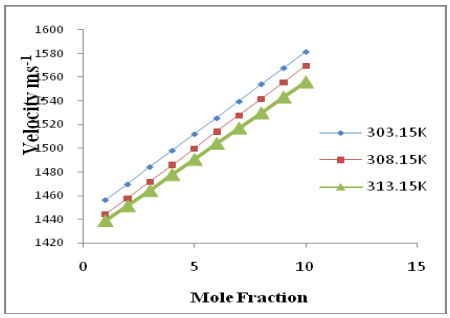

Figure 3. Variation of Velocity with Mole Fraction

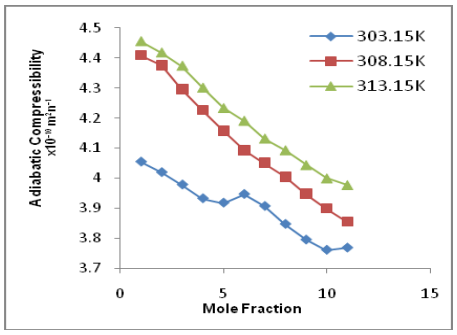

Figure 4. Variation of adiabatic Compressibility with Mole Fraction

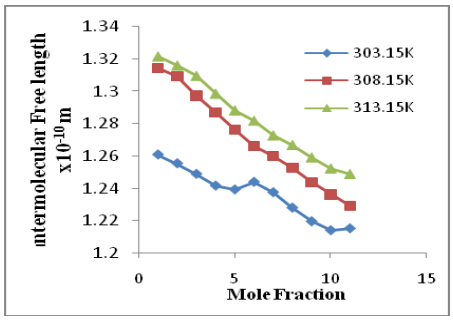

Figure 5. Variation of Intermolecular free length with Mole Fraction

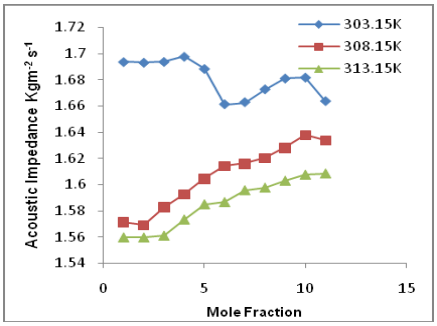

Figure 6. Variation of Acoustic impedance with Mole Fraction

International Journal of
Scientific Research in Science and Technology (IJSRST)
Print ISSN : 2395-6011, Online ISSN : 2395-602X
International Conference on Advanced Materials
Held on 14, 15 December 2017, Organized by Department of Physics,
St. Joseph's College, Trichy, Tamilnadu, India

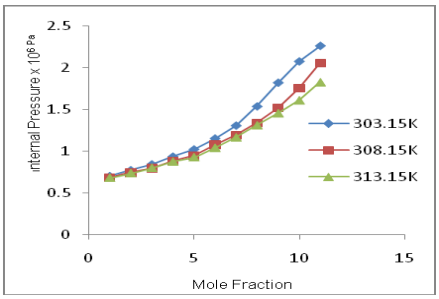

Figure 7. Variation of Internal pressure with MoleFraction

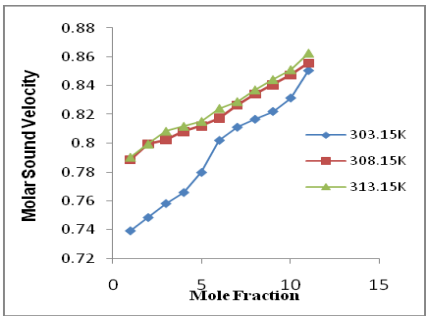

Figure 8. Variation of Molar sound velocity with Mole Fraction

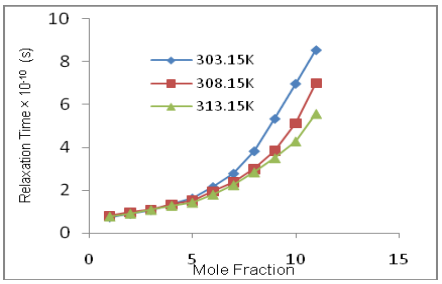

Figure 9. Variation of Relaxation Timewith Mole Fraction

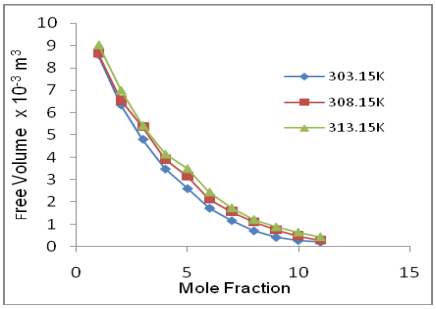

Figure 10. Variation of Free volumewith Mole Fraction

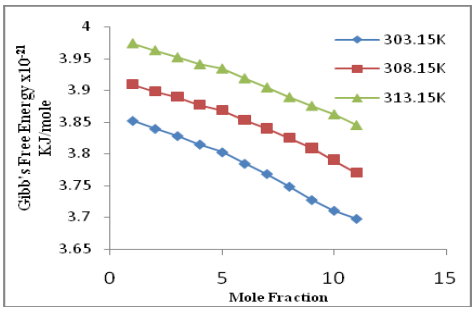

Figure 11. Variation of Gibb's Free Energywith Mole Fraction

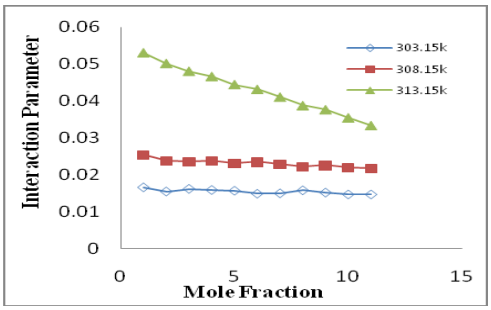

Figure 12. Variation of Interaction parameterwith Mole Fraction

Density, viscosity and ultrasonic velocity of binary mixtures of PG with DMSO are determined experimentally at temperatures 303.15K, 308.15K and 313.15K over the entire mole fraction range and the values are given in Table 1. The values for derived thermo acoustic parameters are computed and are reported in Table 2, 3 and 4 for all the liquid mixtures at the experimental temperatures.

The variation of deviations in density, viscosity and velocity ; thermo acoustic properties like adiabatic compressibility (β_a), intermolecular free length (L_f), acoustic impedance (Z), free volume (V_f), relaxation time (τ), Gibb's free energy (ΔG), internal pressure (π_i), molar sound velocity (R), interaction parameter(χ) as a function of mole fraction at different temperatures are shown in Figure 1-12.

It is observed that density is found to decrease with increase in concentration and decrease with increase in temperature. The decrease in density with mole fraction is due to the shrinkage in volume which in turn is due to presence of solvent molecules. The viscosity is an important parameter in understanding

International Journal of
Scientific Research in Science and Technology (IJSRST)
Print ISSN : 2395-6011, Online ISSN : 2395-602X
International Conference on Advanced Materials
Held on 14, 15 December 2017, Organized by Department of Physics,
St. Joseph's College, Trichy, Tamilnadu, India

the structure as well as molecular interaction occurring in the solutions. Viscosity of solution increases with increase in mole fraction suggest that the extent of complexion increase and more association between solute and solvent molecules. As the temperature increases the cohesion and frictional forces have been diminished due to thermal motion of molecules and relative velocity increases and hence viscosity is found to decrease with increase in temperature. Ultrasonic velocity increase with increase in mole fraction, this behavior shows a moderate strong electrolytic nature in which the solute tend to attract the solvent molecules. Molecular interaction is thus responsible for the observed increase in velocity in these mixtures.

From Table 2, the decrease in adiabatic compressibility (β_a) with increase in mole fraction of Propylene glycol indicates closed packing and increased ionic repulsion. At higher temperature 313.15K, rise in thermal energy causes increase in kinetic energy and volume expansion of the system which results in a increase in adiabatic compressibility. The ultrasonic velocity increases with decrease in intermolecular free length in binary liquid mixture. Therefore, intermolecular free length (L_f) is one of the predominating factor for deciding the nature of variation in ultrasonic parameters in the liquid mixture. In the present study the decrease in intermolecular free length causes increase in ultrasonic velocity, decrease in adiabatic compressibility. Acoustic impedance (Z) is the opposition offered by the medium for the propagation of sound energy. The acoustic impedance decreases with increasing mole fraction of Propylene glycol with DMSO, indicates that significant interaction between the component molecules.

In the study of liquid mixtures, the variation of internal pressure may give some suitable information regarding the nature and strength of forces existing between molecules. It is found that internal pressure (π_i) increases with increase in mole fraction shows that the extent of complex formation. However, the degree of complex formation decreases with increase in temperature.

The molar sound velocity(R) indicates the cube root of sound velocity through one molar volume of solutions called as Rao's constant. The increasing trend of molar sound velocity indicates the availability of more number of components in a given region thus leads to a tight packing of the medium and thereby increase the concentration. Relaxation time (τ) depends on viscosity and adiabatic compressibility of Propylene glycol+ DMSO mixture. From this the time increases with increases in concentration of Propylene glycol +DMSO.

From Table 4, it is observed that free volume (V_f) of liquid mixtures is found to decrease with increase in concentration and increase with increase in temperature. The decrease in free volume may be due to strong association between binary mixtures. The Gibb's free energy (ΔG), decreases with increase in concentration indicating the need for longer time for the co-operative process or the rearrangement of molecules in the mixtures. The Gibb's free energy of activation flow in the mixtures can be obtained on the basis of Eyring rate process theory. These values confirm the availability of intermolecular interactions. The values of interaction parameter (χ) are positive for all the temperatures. This indicates the existence of strong interactions in the binary mixtures.

Conclusion

Ultrasonic studies have been carried out in the solutions of Propylene glycol with DMSO at different temperatures. The study of solution properties of liquid mixtures consisting of organic as well as organosulfur compound finds applications in industrial and technological process. On the basis of experimental values of density, viscosity, ultrasonic velocity and related thermo acoustic parameters for the binary mixtures are calculated. It is concluded that there exists molecular association and molecular interaction between components in the binary mixtures of Propylene Glycol and Dimethyl sulphoxide. The temperature variation indicates that the strength of intermolecular interaction decreases with increase in temperature.

References

[1] G. Sridevi 2016, Journal of Chemical, Biological and Physical Sciences, Vol.6, No.2 486-497.

[2] Vijay Alexander, Sasikumar and Meenakshi, 2015 International Journal of Research in Engineering and Technology, Vol.4, 412-418.

[3] P. Vasantha Rani, L. Bala and R. Ezhil Pavai, 2009 Global Journal of Molecular Sciences, 4(1), 48-49.

[4] S. Thiru Murugan and D. Priya, 2013 Indian Journal of Pure and Applied Physics, Vol. 51, pp. 413-420.

[5] Harish Kumar and Deepika, 2012 International Journal of Research in Physical Chemistry, 2(3), 20-29.

[6] S. Ajitha, A. Hemamalini and V.N. Meena Devi, 2013 Research Journal of Pharmaceutical, Biological and Chemical Sciences, Vol. 4, pp 218-222.

[7] A.A. Mistry, V.D. Bhandakkar and O.P. Chimankar, 2013 Advanced in Applied Science Research, 4(2) 54-59.

[8] Rose Venis and Rosario Raj Kumar, 2011 Journal of Chemical Pharmacy Research, 3(2) 878-885.

[9] Mishra Sujatha and Paikary Rita, 2013 Research Journal of Physical Science, Vol. 1(4), 15-21.

[10] A.N. Kannapan, S. Thirumaran and R. Palani, 2009 Journal of Physical Science, Vol. 2(20) 97-108.

[11] V.D. Bhandakkar, 2014 International Journal of Advanced Research in Physical Science, Vol. 1(5) pp 1-5.

[12] S. Thirumaran and J. Earnest Jayakumar, 2009 Indian Journal of Pure and Applied Physics, Vol. 47 pp 265-272.

[13] R. Palani and K. Meenakshi, 2007 Indian journal of Chemistry, Vol. 46A pp 252-257.

[14] M. Pushpalatha, C.H. Srinivasu and K. Narendar, 2013, International journal of Research in Pharmacy and Chemistry, 3(1) 129-131.

[15] P. Kumar, S. Kumar, S. Singh and R.S. Gangwar, 2011 Oriental Journal of Chemistry, 27(2) 639-644.

[16] S. Nagaraj, M.C.S Subha C. Nagamani and K. Chowdoji Rao, 2016 World Journal of Pharmacy and Pharmaceutical Sciences, 5(1) 1423-1441.

International Journal of
Scientific Research in Science and Technology (IJSRST)
Print ISSN : 2395-6011, Online ISSN : 2395-602X
International Conference on Advanced Materials
Held on 14, 15 December 2017, Organized by Department of Physics,
St. Joseph's College, Trichy, Tamilnadu, India

Investigation of Molecular Interactions in Binary Mixtures of Anisole with Methyl Isobutyl Ketone at Different Temperatures

D.Devi[1], M. M. Armstrong Arasu[2], A.Mary Girija[3]

[1]Assistant Professor, Department of Physics, Cauvery College for Women, Trichy-18, Tamilnadu, India

[2]Assistant Professor, Department of Physics, St. Joseph's College (Autonomous) Trichy-02, Tamilnadu, India

[3]Assistant Professor, Department of Physics, Cauvery College for Women, Trichy-18, Tamilnadu, India

Corresponding author E-mail address: armstrongarasu@gmail.com

Abstract

The ultrasonic velocity(U), density (ρ) and viscosity (η) of pure solvents and binary mixtures of Anisole and Methyl Isobutyl Ketone have been investigated at three different temperatures 303.15K, 308.15K and 313.15K and correlated with concentration. The observed data have been used to evaluate some of the thermo acoustical parameters such as adiabatic compressibility (β_a), intermolecular free length (L_f), internal pressure (π_i), acoustic impedance (Z), available volume (V_a), relaxation time (τ), molar volume (V_m) and Gibb's free energy (ΔG), Lennard Jones potential repulsive term exponent(n) to elucidate the molecular association in the mixture. The variation of these parameters with concentration of solute indicates the nature of interaction present in the binary mixture.

Keywords: Anisole, Ultrasonic velocity, adiabatic compressibility, acoustic impedance, molecular association.

Introduction

The study of molecular interactions in liquid mixture provides valuable information regarding internal structure, molecular association, Internal pressure and complex formation. The propagation of ultrasonic waves in liquid is a tool by researcher to probe into the properties of liquids [1-3]. The measurement of ultrasonic velocity in liquid mixtures have greater importance in predicting the physico-chemical properties of liquid mixtures.

In the present study, the density, ultrasonic velocity and viscosity were measured for the binary system of Anisole and Methyl isobutyl Ketone at various temperatures. Anisole is an organic compound with the formula C_7H_8O. It is a colourless liquid and its derivatives are found in natural and artificial fragrances insoluble in water. It is used as a precursor to perfumes and pharmaceuticals. The second component is Methyl isobutyl Ketone, it is a colourless liquid with the formula $C_6H_{12}O$. It is a ketone, used as a solvent for gums, varnishes and nitrocellulose. These liquids have been chosen on the basis of their industrial applications. These applications stimulated the need for extensive information on the thermodynamic and acoustic properties of these mixtures.

From the experimental data, an attempt has been made to study some thermo acoustical properties such as adiabatic compressibility (β_a), intermolecular free length (L_f), internal pressure (π_i), acoustic impedance (Z), relaxation time (τ), molar volume (V_m), available volume (V_a) and Gibb's free energy (ΔG), Lennard Jones potential repulsive term exponent (n). These parameters have been used to understand different kinds of association in pure components, as well as, in the binary mixture.

International Journal of
Scientific Research in Science and Technology (IJSRST)
Print ISSN : 2395-6011, Online ISSN : 2395-602X
International Conference on Advanced Materials
Held on 14, 15 December 2017, Organized by Department of Physics,
St. Joseph's College, Trichy, Tamilnadu, India

Results are used to explain the nature of molecular interactions between mixing Compounds.

2. Experimental Section

The mixtures of various concentrations in mole fraction were prepared by taking analytical reagent grade chemicals with minimum assay of 99.9% and obtained from E. Merck Ltd (India). All the component liquids were purified by the standard methods. The density, viscosity, and ultrasonic velocity were measured as a function of concentration of the binary liquid mixture at 303.15K, 308.15K & 313.15K. Ultrasonic velocity measurements were made using an ultrasonic interferometer with the accuracy of ±0.1m·s–1. An electronically operated digital constant temperature bath operating with an accuracy of ±0.1°C has been used to circulate water through the outer jacket of the double-walled measuring cell containing the experimental liquid. The densities of the mixture were measured using a 10-ml specific gravity bottle by relative measurement method with an accuracy of ±0.01 kg·m–3. An Oswald viscometer (10 ml) with an accuracy of ±0.001 Ns·m–2 was used for the viscosity measurement. The flow time was determined using a digital racer stopwatch with an accuracy of ±0.1s.

Theory

The various thermo acoustical parameters were determined using the following equations [5-11]

Adiabatic Compressibility (β_a):

$$\beta_a = 1/ (U^{2*}\rho) \quad (1)$$

Intermolecular Free Length (L_f):

$$L_f = K_J (\beta_a)1/2 \quad (2)$$

where K_J is the temperature dependent Jacobson's constant but independent of the nature of liquid.

Free Volume (V_f)

$$V_f = [(M_{eff}\, U) / (K\, \eta)]^{3/2} \quad (3)$$

where, M_{eff} (Effective mass) = $\Sigma\, m_i x_i$, in which mi and xi are the molecular weight and the mole fraction of the individual constituents respectively.

K is the temperature independent constant, which is equal to 4.28 *10^9 for all liquids and η be the viscosity.

Internal Pressure (π_i)

$$\pi_i=(bRT)[(K^*\eta)/(U)]^{½*}[(\rho^{2/3})/(M_{eff}^{7/6})] \quad (4)$$

where, b is the cubic packing which is assumed to be 2 for all liquids and solutions, K is the temperature independent constant ,T is the absolute temperature, R is universal gas constant.

Relaxation Time (τ)

Relaxation time (τ) is the time taken for the excitation energy to appear as translational energy and it depends on temperature and on impurities. The dispersion of ultrasonic velocity in binary mixture reveals information about the characteristic time of the relaxation process that causes dispersion.

$$\tau = (4/3)\, \beta_a{}^*\, \eta \quad (5)$$

Acoustic Impedance (Z)

$$Z = U^*\rho \quad (6)$$

Gibb's Free Energy (ΔG)

The relaxation time for a given transition is related to the activation energy. The variation of relaxation time (τ) with temperature (T) can be expressed in the form of Eyring self-process theory.

$$\Delta G = (K_B T)\log [(K_B T\tau)/h] \quad (8)$$

where K_B is the Boltzmann's constant (1.3806 × 10^{23} Jk^{-1}), h is the plank's constant 6.63*10^{-34} JS), T be the absolute temperature and τ be the relaxation time.

Available volume (V_a)

International Journal of
Scientific Research in Science and Technology (IJSRST)
Print ISSN : 2395-6011, Online ISSN : 2395-602X
International Conference on Advanced Materials
Held on 14, 15 December 2017, Organized by Department of Physics,
St. Joseph's College, Trichy, Tamilnadu, India

$V_a = (M_{eff}/\rho)(1-(U/U\infty))$ (10)

Molar Volume (V_m)

Lennard Jones Potential Repulsive Term Exponent (n)

$V_m = M_{eff}/\rho$ (12)

$n = (6V_m/V_A)-13$ (11)

Results and Discussion

Table 1. Measured Values of Density (ρ), Viscosity (η) and velocity (U) of binary mixture of Anisole with Methyl Isobutyl Ketone at 303.15K, 308.15K & 313.15K

S. No.	X(i) ANI	Y(i) MIK	ρ x 10^{-3} kgm^{-3}			η x 10^{-3} Nsm^{-2}			U ms^{-1}		
			303.15K	308.15K	313.15K	303.15K	308.15K	313.15K	303.15K	308.15K	313.15K
1	0	1	0.8405	0.7864	0.7850	0.6103	0.5853	0.5695	1177.5	1162.0	1149.3
2	0.1	0.9	0.8689	0.8171	0.8071	0.6459	0.6231	0.6093	1195.8	1180.8	1162.5
3	0.2	0.8	0.8861	0.8353	0.8321	0.6645	0.6523	0.6417	1215.8	1199.8	1189.5
4	0.3	0.7	0.9023	0.8554	0.8523	0.6830	0.6764	0.6634	1233.1	1218.2	1207.1
5	0.4	0.6	0.9306	0.8746	0.8744	0.7175	0.6919	0.6852	1251.3	1236.1	1224.3
6	0.5	0.5	0.9528	0.8967	0.8917	0.7380	0.7106	0.7012	1267.5	1252.5	1237.8
7	0.6	0.4	0.9690	0.9159	0.9099	0.7680	0.7554	0.7252	1288.5	1271.0	1257.8
8	0.7	0.3	0.9913	0.9350	0.9282	0.7904	0.7784	0.7459	1304.3	1287.3	1274.0
9	0.8	0.2	1.0105	0.9523	0.9484	0.8370	0.8168	0.7671	1323.9	1306.9	1291.6
10	0.9	0.1	1.0267	0.9696	0.9618	0.8685	0.8401	0.7924	1339.6	1327.6	1313.5
11	1	0	1.0439	0.9868	0.9791	0.9065	0.8776	0.8599	1357.5	1345.5	1331.1

Table 2. Values of Adiabatic compressibility (β_a), Intermolecular free length (L_f), Acoustic impedance (Z) at 303.15K, 308.15K & 313.15K

S. No.	X(i) ANI	Y(i) MIK	β_a x 10^{-10} m^2n^{-1}			L_F x 10^{-10} m			Z Kgm^{-2} s^{-1}		
			303.15K	308.15K	313.15K	303.15K	308.15K	313.15K	303.15K	308.15K	313.15K
1	0	1	8.5810	9.4168	9.6434	0.8495	0.9322	0.9547	989.68	913.8	902.2
2	0.1	0.9	8.0473	8.7763	9.1753	0.7966	0.8688	0.9083	1039.1	964.8	937.6
3	0.2	0.8	7.6340	8.3157	8.5001	0.7557	0.8232	0.8415	1077.3	1002.2	989.4
4	0.3	0.7	7.2887	7.8800	8.0535	0.7215	0.7801	0.7972	1112.6	1041.8	1028.2
5	0.4	0.6	6.863	7.4839	7.6331	0.6794	0.7409	0.7556	1164.4	1081.0	1070.1
6	0.5	0.5	6.5328	7.1139	7.3188	0.6467	0.7042	0.7245	1207.6	1122.7	1103.8
7	0.6	0.4	6.2159	6.7581	6.9458	0.6153	0.6690	0.6876	1248.5	1164.1	1144.7
8	0.7	0.3	5.9294	6.4536	6.6372	0.5870	0.6389	0.6570	1292.9	1203.6	1182.3
9	0.8	0.2	5.6458	6.1477	6.3200	0.5589	0.6086	0.6256	1337.8	1244.5	1225.0
10	0.9	0.1	5.4271	5.8511	6.0259	0.5372	0.5792	0.5965	1375.4	1287.2	1263.1
11	1	0	5.1979	5.5972	5.7641	0.5146	0.5541	0.5706	1417.1	1327.7	1303.6

Table 3. Values of Relaxation time(τ),Internal pressure (□i), Gibbs Free energy(ΔG) at 303.15K,308.15K&313.15K

S. No.	X(i) ANI	Y(i) MIK	τ× 10^{-10} (s)			π_i x10^{6} Pa			(-ΔG)x10^{-21} KJ/mole		
			303.15K	308.15K	313.15K	303.15K	308.15K	313.15K	303.15K	308.15K	313.15K
1	0	1	6.9826	7.3489	7.3226	0.7812	0.6755	0.6729	3.8575	3.9168	3.9795
2	0.1	0.9	6.9304	7.2913	7.4540	0.8229	0.7227	0.7120	3.8580	3.9173	3.9784
3	0.2	0.8	6.7638	7.2325	7.2726	0.8196	0.7364	0.7372	3.8595	3.9178	3.9800
4	0.3	0.7	6.6376	7.1067	7.1236	0.8154	0.7469	0.7458	3.8607	3.9189	3.9813

International Journal of
Scientific Research in Science and Technology (IJSRST)
Print ISSN : 2395-6011, Online ISSN : 2395-602X
International Conference on Advanced Materials
Held on 14, 15 December 2017, Organized by Department of Physics,
St. Joseph's College, Trichy, Tamilnadu, India

5	0.4	0.6	6.5656	6.9042	6.9736	0.8505	0.7455	0.7573	3.8614	3.9208	3.9827
6	0.5	0.5	6.4283	6.7402	6.8426	0.8579	0.7529	0.7551	3.8627	3.9223	3.984
7	0.6	0.4	6.3651	6.8067	6.7162	0.8611	0.7797	0.7586	3.8633	3.9217	3.9852
8	0.7	0.3	6.2488	6.6979	6.6009	0.8689	0.7840	0.7603	3.8645	3.9227	3.9863
9	0.8	0.2	6.3007	6.6952	6.4641	0.8937	0.7975	0.7639	3.8640	3.9228	3.9877
10	0.9	0.1	6.2846	6.5540	6.3666	0.8979	0.7945	0.7574	3.8641	3.9241	3.9887
11	1	0	6.2826	6.5495	6.6088	0.9078	0.8054	0.7980	3.8642	3.9242	3.9862

Table 4. Values of Available volume (V_a), Molar volume(V_m), Lennard Jone Potential repulsive exponent (n) at 303.15K, 308.15K & 313.15K

S. No.	X(i) ANI	Y(i) MIK	V_a m^3/mol			V_m x 10^{-5} m^3/mol			N		
			303.15K	308.15K	313.15K	303.15K	308.15K	313.15K	303.15K	308.15K	313.15K
1	0	1	3.1467	3.4862	3.5937	1.1916	1.2736	1.2759	9.721	8.920	8.302
2	0.1	0.9	2.9346	3.2365	3.4238	1.1619	1.2355	1.2508	10.755	9.905	8.920
3	0.2	0.8	2.7571	3.0466	3.1408	1.1483	1.2181	1.2228	11.990	10.99	10.360
4	0.3	0.7	2.6063	2.8623	2.9554	1.1365	1.1989	1.2032	13.165	12.131	11.428
5	0.4	0.6	2.4204	2.6881	2.7774	1.1105	1.1817	1.1819	14.530	13.375	12.533
6	0.5	0.5	2.2715	2.5258	2.6436	1.0930	1.1614	1.1679	15.872	14.590	13.508
7	0.6	0.4	2.1085	2.3557	2.4662	1.0830	1.1458	1.1534	17.818	16.183	15.060
8	0.7	0.3	1.9712	2.2100	2.3208	1.0667	1.1309	1.1392	19.469	17.704	16.452
9	0.8	0.2	1.8191	2.0492	2.1650	1.0543	1.1188	1.1234	21.775	19.75	18.133
10	0.9	0.1	1.7012	1.8844	1.9981	1.0455	1.1070	1.1160	23.873	22.248	20.512
11	1	0	1.5698	1.7428	1.8560	1.0359	1.0958	1.1044	26.594	24.726	22.703

International Journal of
Scientific Research in Science and Technology (IJSRST)
Print ISSN : 2395-6011, Online ISSN : 2395-602X
International Conference on Advanced Materials
Held on 14, 15 December 2017, Organized by Department of Physics,
St. Joseph's College, Trichy, Tamilnadu, India

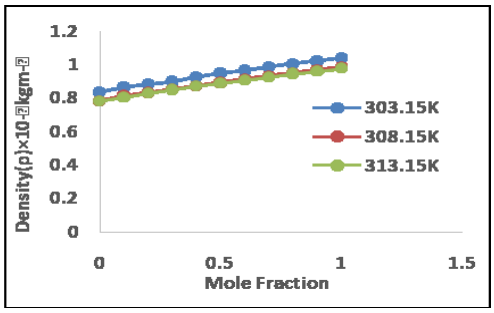

Figure 1. Mole fraction Vs Density

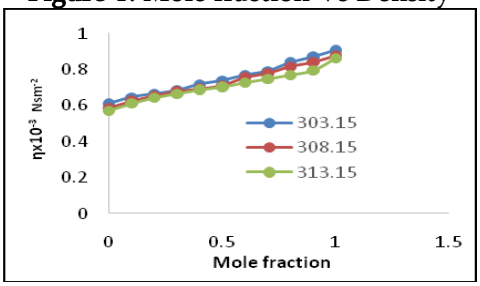

Figure 2. Mole fraction Vs Viscosity

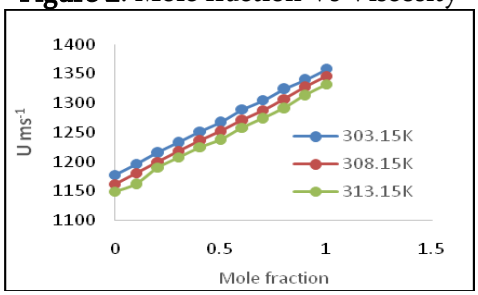

Figure 3. Mole fraction Vs Velocity

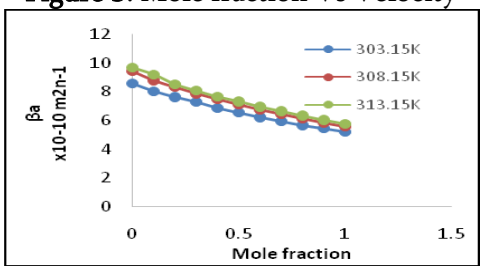

Figure 4. Molefraction Vs Adiabatic compressibility

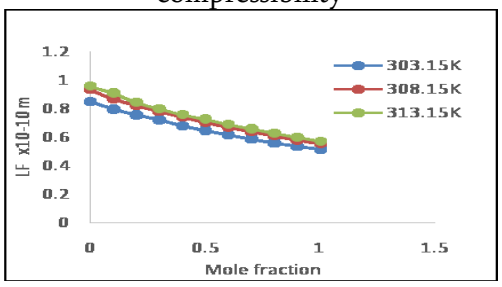

Figure 5. Mole fraction Vs Intermolecular free length

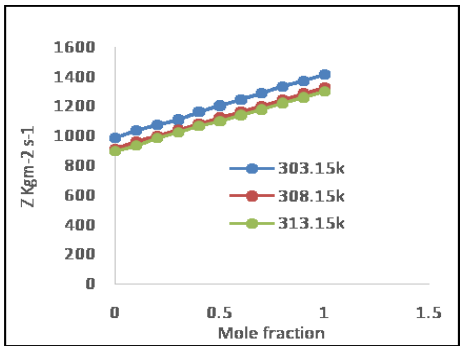

Figure 6. Molefraction Vs Acoustic impedance

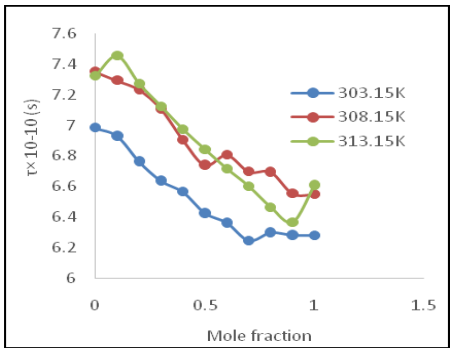

Figure 7. Mole fraction Vs Relaxation time

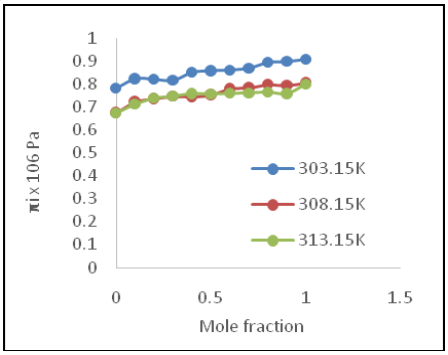

Figure 8. Molefraction Vs Internal Pressure

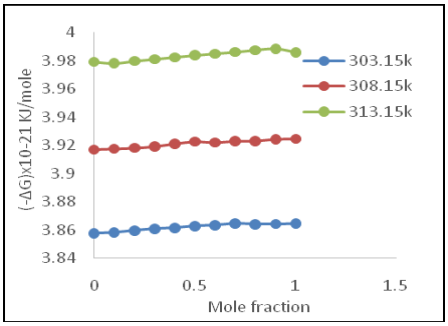

Figure 9. Molefraction Vs Gibb's Free energy

International Journal of
Scientific Research in Science and Technology (IJSRST)
Print ISSN : 2395-6011, Online ISSN : 2395-602X
International Conference on Advanced Materials
Held on 14, 15 December 2017, Organized by Department of Physics,
St. Joseph's College, Trichy, Tamilnadu, India

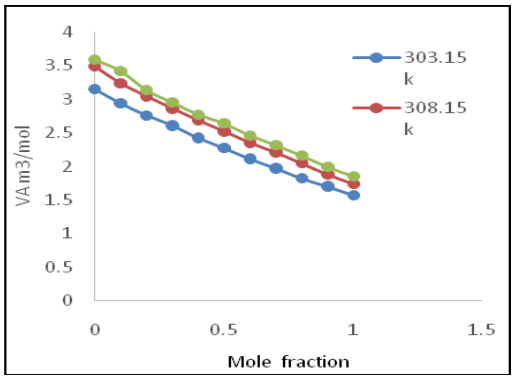

Figure 10. Mole fraction Vs Available volume

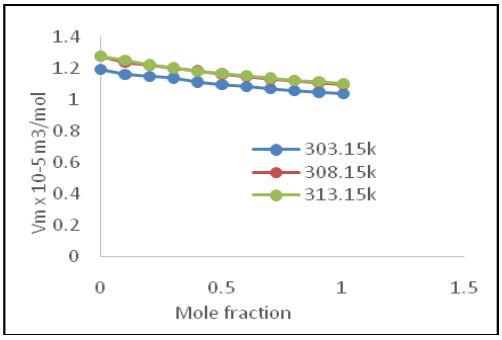

Figure 11. Molefraction Vs Molar volume

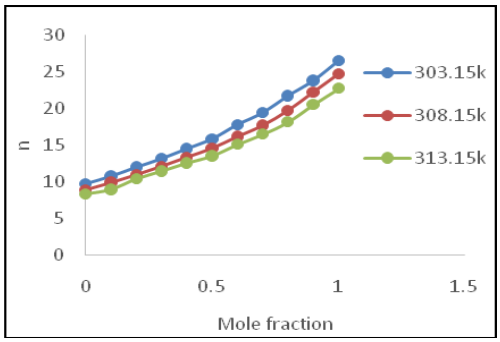

Figure 12. Mole fraction Vs LJP Repulsive term

Results and Discussion

The experimental values of density, velocity and viscosity at three different temperatures for the binary mixture were used to calculate the acoustical and thermos dynamical parameters and the relevant data are presented in Tables 1 to 4. The variation of these parameters are displayed graphically in Figures 1-12.

Density is a parameter giving information about solvent-solvent interactions. From the Table 1and Figure1 it is observed that in all the three temperatures the density and velocity increases with increasing mole fraction and decreases with higher temperatures. The increase in density indicates the presence of solvent-solvent interactions in the binary mixture which may bring a bonding between them [11]. Figure3 Shows that ultrasonic velocity increases with mole fraction and decreases with temperature. The structural changes occurring in the mixture with the increase in mole fraction leads to increase in velocity which may result in the increase in intermolecular forces. From Table1 and Figure 2, it is found that the viscosity of all liquid mixtures were found to be increased with increasing concentration of Anisole. Due to the increase of Anisole molecules in solution, the medium became denser. Further, the increase in the number of particles in solution is responsible for increasing the cohesive force between the liquid layers. Thereby, the co-efficient of viscosity increases in all systems.

The variation of adiabatic compressibility (β_a), Intermolecular free length (L_f) and acoustic impedance (Z) with the increase in mole fraction are presented in Table 2. Based on the model for sound propagation proposed by Eyring and Kincaid [11], ultrasonic velocity should increase, if the intermolecular free length decreases and vice versa. A reduction in adiabatic compressibility is an indication that component molecules are held close to each

International Journal of
Scientific Research in Science and Technology (IJSRST)
Print ISSN : 2395-6011, Online ISSN : 2395-602X
International Conference on Advanced Materials
Held on 14, 15 December 2017, Organized by Department of Physics,
St. Joseph's College, Trichy, Tamilnadu, India

other. The intermolecular free length (L_f) is the distance covered by a sound wave between the surface of the neighbouring molecules and it depends upon the intermolecular attractive and repulsive forces. The decrease in the value of adiabatic compressibility (β_a) and Intermolecular free length (Lf) with concentration further strengthens the strong molecular association between the unlike molecules through hydrogen bonding.

The increase in the value of L_f with temperature implies that the mean distance between the molecules increases thereby decreasing the potential energy of interaction between them, leading to the decrease in the values of velocity and density. Molecular association increases the acoustic impedance (Z). It is the opposition exerted by the medium to displacement of the mediums particles by sound energy. A continuous decrease in (β_a), L_f and increase of Z with concentration are the clear evidence for the existence of strong interactions like dipole-dipole and dipole induced dipole interaction.

The relaxation time decreases with increase in concentration, is due to the structural relaxation process and in such a situation, it is suggested that the molecule get rearranged due to co-operative process. The Gibb's free energy increase with increasing temperature may be due to the dissociation of intermediate compound between binary liquids. It is observed that free energy increase favours the dissociation of products from reaction.

Internal pressure in a liquid system is a measure of intermolecular cohesive forces [16]. From the Table 3, it is observed that as the mole fraction of Anisole increases, free volume decreases whereas internal pressure increases. This suggests the close packing of the molecule inside the shield, which may be brought about by the increasing magnitude of interactions. [17,18].

It can be observed that the molar volume V_m decreases with increase in concentration of Anisole. This is because of the fact, that molecular weight is directly proportional to the molar volume. Moreover, molar volume increase with rise in temperature in our study, which probably from the fact that thermal energy facilitates an increase in the molecular separation in the liquid mixtures and thus leads to an increase in molar volume.

Table 4 and Figure 11 shows that the available volume V_a decreases with the increase in molefraction of Anisole. Available volume is a direct measure of compactness and strength of bonding between the molecules of the liquid mixture. [14]. The decrease in V_a is due to the net packing of molecules inside the shell which may be formed by complexation between unlike molecules through hydrogen bonding in the binary mixture.

Lennard-Jones potential $\varphi(r)$ is given by the relation [17].

$$\varphi(r) = -Ar^{-6} + Dr^{-n}$$

where r and n are intermolecular distance and Lennard-Jones potential repulsive term exponent respectively. A and D are constants. The first term arises from

attractive forces while the second term arises from repulsive forces. Larger the value of n smaller is the second term. Thus large value of n indicates the dominance of attractive forces over repulsive forces. The values of n increase with the increase in mole fraction of Anisole as shown in Table 4 and Figure 12 for a fixed frequency. The increase in n indicates the increasing dominance of attractive force over repulsive forces in the binary liquid mixture. Further, the values of n decrease with the increase in temperature for a particular concentration which indicates the increase in repulsive forces due to reduction in molecular interaction in the binary mixture [18].

Conclusion

The ultrasonic method was found to be a powerful tool in characterizing the physico-chemical behavior of liquid mixtures. It is concluded from the experimental and calculated parameters that the density, viscosity, velocity increases with increase in mole fraction of Anisole. This is due to the dipole induced dipole interaction between the binary mixture. The temperature variation indicates that the strength of intermolecular interaction decreases with rise in temperature.

References

[1] K. Dash and R. Paikaray, "Acoustical study in binary liquid mixture containing dimethyl acetamide using ultrasonic and viscosity probes", Der Chem. Sinica, vol. 5, no. 1, (2014), pp. 81-88.

[2] R. Palani, S. Saravanan and R. Kumar, "Ultrasonic studies on some ternary organic liquid mixtures at 303, 308 and 313K", RASAYAN J. Chem., vol. 2, no. 3, (2009), pp. 622-629.

[3] R. Paikaray and N. Mohanty, "Evaluation of Thermodynamical Acoustic Parameters of Binary mixture of DBP with Toluene at 308K and at Different Frequencies", Research Journal of Chemical Sciences, vol. 3, no. 5, (2013), pp. 71-82.

[4] AA Mistry; VD Bhandakkar; O.P. Chimankar, J. of Chem. & Pharm. Res., 2012, 4(1), 170-174.

[5] Paul Divakar; k Samatha, International Journal of Advanced Science and Technology, 2016, 55-70.

[6] Mishra Sujatha and Paikary Rita, 2013 Research Journal of Physical Science, Vol 1(4) 15-21.

[7] A.N.Kannapan, S.Thirumaran and R.Palani, 2009 Journal of Physical Science, Vol 2(20) 97-108.

[8] V.D.Bhandakkar, 2014 International Journal of Advanced Research in Physical Science, Vol. 1(5) pp 1-5.

[9] S.Thirumaran and J.Earnest Jayakumar, 2009 Indian Journal of Pure and Applied Physics, Vol. 47, pp 265-272.

[10] R.Palani and K.Meenakshi, 2007 Indian journal of Chemistry, Vol. 46A pp 252-257.

[11] M.Pushpalatha, C.H. Srinivasu and K.Narendar, 2013 International journal

of Research in Pharmacy and Chemistry, 3(1) 129-131.

[12] P.Kumar,S.Kumar,S.Singh and R.S.Gangwar, 2011 Oriental Journal of Chemistry, 27(2) 639-644.

[13] S.Nagaraj, M.C.S Subha C. Nagamani and K. Chowdoji Rao, 2016 World Journal of Pharmacy and Pharmaceutical Sciences, 5(1) 1423-1441.

[14] M.K. Praharaj, P.R. Mishra, S. Mishra and A. Satapathy, "Ultrasonic study of ternary liquid mixture containing substituted benzene", Arch. of. Phys. Res., vol. 3. No.3, (2012), pp. 192-200.

[15] S. Thirumaran and M. Rajeswari, "Acoustical studies on binary liquid mixtures of some aromatic hydrocarbons with dimethylsulphooxide (DMSO) at 303.15K", Arch. of. Phys. Res., vol. 2, no. 2, (2011), pp. 149-156.

[16] K. Rajagopal and S. Chenthilnath, "Excess thermodynamic studies of binary mixtures of 2-methyl 2-propanol with ketones", Indian J. Pure and Appl. Phys., vol. 48, (2010), pp. 326-333.

[17] K. Gupta, K. Kumar and B. K. Karn, "Studies of binary liquid mixtures of o-cresol with ethylmethyl ketone, acetone acetophenone and ethylacetate", J. Ind. Coun. Chem., vol. 26, (2009) pp. 77-81.

[18] K. Dash and R. Paikaray, "Ultrasonic Study on Ternary Mixture of Dimethyl Acetamide (DMAC) in Diethyl ether and Acetone", Res. J. of Phys. Sc., vol. 1, no. 3, (2013), pp. 12-20.

[19] K. Dash and R. Paikaray, "Study of molecular interaction in binary liquid mixture of dimethyl acetamide and acetone using ultrasonic probe", Adv. in Appl. Sc. Res., vol. 4, no. 3, (2013), pp. 130-139.

[20] K. Dash and R. Paikaray, "Acoustical study on ternary mixture of dimethyl acetamide (DMAC) in diethyl ether and isobutyl methyl ketone at different frequencies", Phys. and Chem. of Liquids, vol. 51, no. 6, (2013), pp. 749-763.

Books

1. Riddick, J.A., Bunger, W.B., Sanako, T.K., 1986, Physical properties and methods of purification, John Willy & Sons, New York.
2. Hirschfelder, J.O, Curtio and Byron bird. R., 1950, Molecular theory of gases and Liquids, John Willy & Sons, New York.

International Journal of
Scientific Research in Science and Technology (IJSRST)
Print ISSN : 2395-6011, Online ISSN : 2395-602X
International Conference on Advanced Materials
Held on 14, 15 December 2017, Organized by Department of Physics,
St. Joseph's College, Trichy, Tamilnadu, India

Effect of Preparative Parameters on Structural, Optical and Electrical Properties of Mn_2O_3 Nano Particles Prepared Via Microwave Assisted Technique

L. Jayaselvan[1*], C. Gnana Sambandam[1], C. Ravidhas[2], A. Moses Ezhil Raj[3]

[1]Physics Research Centre, S.T. Hindu College, Nagercoil, Tamilnadu, India

[2]Postgraduate and Research Department of Physics, Bishop Heber College (Autonomous), Tiruchirapalli, Tamilnadu, India

[3] Department of Physics & Research Centre, Scott Christian College (Autonomous) Nagercoil, Tamilnadu, India

*Corresponding authore-mail:jjphy1982@gmail.com

Abstract

In the present investigation Mn_2O_3 nanoparticles were prepared by microwave assisted co-precipitation method using $MnCl_2$ and NaOH precursors. Obtained nanoparticles were characterized using X-ray powder diffraction (XRD) for the confirmation of Mn_2O_3 formation with cubic structure. Nelson – Riley and William – Hall plots were constructed to estimate the lattice parameter, crystalline size and microstrain precisely. Variations in Structural parameters with preparative conditions was discussed and analyzed. Metal-oxide phase formation was confirmed from the bands in the specified finger print region of FTIR spectra of metal oxides. Scanning electron microscopy (SEM) micrographs revealed the reducing agent dependent morphology of particles, size and its distribution. Optical absorption measurements were used to obtain the band gap by nothing the absorption edge in the lower wavelength region and its dependence to preparative parameters was identified. Electrical conductivity and its variations with temperatures were used to evaluate the activation energy and temperature co-efficient of resistance.

Keywords: Microwave synthesis, Mn_2O_3, XRD, FTIR, optical and electrical

1. Introduction

Metal oxide nanostructures are an important class of nanomaterials with unique properties and useful functionalities that are attractive for a variety of applications ranging from electronics to biomedicine and energy conversion [1,2]. Among the transition metal oxides, manganese exhibits many oxidation states and thereforeforms different oxides (MnO, Mn_2O_3, Mn_3O_4, Mn_5O_8 and MnO_2). Manganese oxide materials are of considerable importance due to their wide-spread applications in catalysis, ion-exchange, and rechargeable batteries. Among the oxide of manganese, Mn_2O_3 has vital application in various fields.

Until now, numerous processes have been developed for the synthesis of inorganic nanostructures, in that, chemical routes have proved to be more effective and versatile [3]. A wide variety of morphological forms of manganese sesquioxide (Mn_2O_3), ranging from one- to three-dimensional structures such as rods, wires, cubes, octahedra, and hollow spheres have been synthesized through various methods [4–8]. However, the morphology controlled synthesis of manganese sesquioxide nanostructures, particularly those with novel and attractive morphologies is difficult and it remains a great challenge. Manganese sesquioxide nanoparticles with various morphologies and different

International Journal of
Scientific Research in Science and Technology (IJSRST)
Print ISSN : 2395-6011, Online ISSN : 2395-602X
International Conference on Advanced Materials
Held on 14, 15 December 2017, Organized by Department of Physics,
St. Joseph's College, Trichy, Tamilnadu, India

crystallographic structures are obtained by various researchers. Recently α-Mn_2O_3 nanoparticles was prepared through sol-gel method using manganese acetate tetrahydrate and oxalic acid as a precursor and ethanol as a solvent. [9,10] Manganese sesquioxide exhibiting different morphologies were prefund by giving nanostructure using heat treatment of manganese alkoxide precursor, which was synthesized from the reaction of manganese acetate with ethylene glycol [11]. Various manganese sesquioxide hollow nanostructures were prepared by oxidation of manganese carbonate using potassium permanganate as oxidizer. Tsang et al. [12] investigated the reduction of potassium permanganate by the use of potassium borohydride in aqueous solutions to obtain binary and ternary manganese oxides. Synthesis of various manganese oxides via thermal decomposition of manganese oxalate obtained using manganese acetate as precursor and ethyl trimethyl ammonium bromide (CTAB) as surfactant have been reported [13]. Hydrothermal cleavage-decomposition mechanism which was used to synthesize a single-crystal α-Mn_2O_3 nanorod at 160^{0}C for 16 h using potassium permanganate and ethyl trimethyl ammonium bromide as reducing reagent, was also been reported [14].

In the present study α-Mn_2O_3 nanoparticles have been prepared by sol-gel method using $MnCl_2$ and sodium hydroxide. Amount of reducing agent was changed to vary the morphology of the prepared α- Mn_2O_3 nanoparticles and its consequences over the structural, optical and electrical properties are reported in this manuscript.

2. Experimental

Mn_2O_3 nano powder were prepared from the aqueous solution of $MnCl_2$ at a concentration of 1M and the concentration of the reducing agent was varied (0.25, 0.5, 0.75 and 1.0M). In a typical synthesis process, 19.78 grams of $MnCl_2$ was added to 100 ml of distilled water in a round bottom flask and then the required amount of NaOH pellets were slowly added in to the above solution. Resulted solution was kept under constant stirring for an hour to from a brown color solution. The solution thus obtained was heated in a domestic microwave oven (540 W, 92^0 C) for 20 minutes. After microwave processing, the mixture was cooled to room temperature and the resulted brown precipitate was separated by centrifugation followed by repeated washing with distilled water and absolute ethanol to remove the impurities and residual materials. After washing, the nano particles were dried at 60^0 C for 2 hrs for removing hydrated species. Finally, the prepared materials were heated at 500^0 C for three hours. The same procedure is repeated for the all the Mn_2O_3 nano particles prepared using NaOH solution of various concentrations. In order to differentiate the obtained products, the samples were named MnO-1, MnO-2, MnO-3, and MnO-4 respectively for the sample prepared using NaOH solutions of various concentrations, 0.25,0.50,0.75 and 1M respectively.

Prepared samples were characterized using various instruments. XRD patterns were recorded in Bruker AXS D8 Advanced diffractometer with Cu Kα radiation (λ=1.5406Å) and the voltage and current was maintained at 40 KV and 30 mA, respectively. FT-IR spectra were recorded in the range of 400-4000 cm^{-1} on a Thermo Nicolet, Avatar 370 using KBR pellet technique. Morphology of Mn_2O_3 nano particles were visualized by recording micrographs in JEOL Model JSM - 6390LV instrumentation. Optical absorption spectra were recorded in the wavelength range (200-2500nm) in a spectrophotometer (Varian, carry 5000). For measuring dcelectrical conductivity, powder samples were pelletized and then the measurements were carried out in the temperature range 35-90^{0}C in a two probe set-up.

International Journal of
Scientific Research in Science and Technology (IJSRST)
Print ISSN : 2395-6011, Online ISSN : 2395-602X
International Conference on Advanced Materials
Held on 14, 15 December 2017, Organized by Department of Physics,
St. Joseph's College, Trichy, Tamilnadu, India

3. Result and Discussion

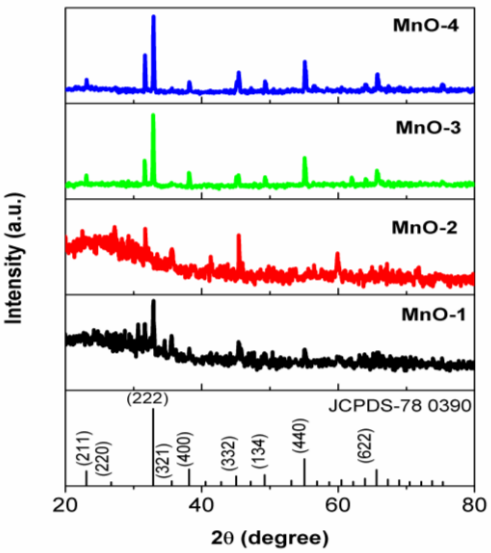

Figure 1.X-ray diffraction pattern of α-Mn_2O_3 samples prepared using NaOH solutions of different concentration (0.25, 0.50, 0.75 and 1.0M)

The phase and purity of the prepared Mn_2O_3 nano particles were verified by X-ray diffraction measurements (Figure1). XRD analysis confirmed that the obtained nanoparticles are in α-Mn_2O_3 polymorph with cubic structure [space group: Ia-3 (206)]. No impurity peaks are found in the XRD pattern. The obtained peak positions are comparable to the standard JCPDS value (JCPDS No. 78- 0390), and are in perfect match with the standard peaks. The lattice parameter of the prepared samples was estimated from the known (hkl) values and d-spacing. Estimated average crystallite sizesare below 100nm. The unit cell volume, density and micro strain are also estimated. Nelson – Riley function $f(\theta) = 1/2\left[\frac{\cos 2\theta}{\sin\theta} + \frac{\cos 2\theta}{\theta}\right]$ has been plotted against the lattice parameter to estimate exact value of unit cell edges.

Figure2 shows the constructed Nelson-Riely plot of the Mn_2O_3 nano particles. Obtained straight lines are extrapolated and the intercept point gives the true value of the lattice parameter. Estimated structural parameter values from the XRD and N-R plot are listed in Table 1.

Williamson-Hall plot has been constructed to evaluate the crystallite size and microstrain of the prepared Mn_2O_3 nanoparticles (Fig.3). From the intercept and the slope of the extrapolated line, the crystalline size and microstrains are estimated. Since W-H plot includes both line broadening caused due to instrumental error, crystallite size and strain, obtained values of crystallite size and microstrain are error free. Calculated crystallite size and microstrain are listed in Table 1.

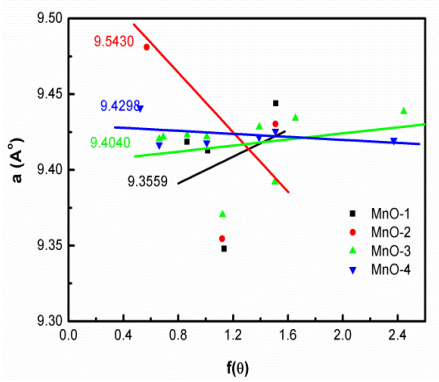

Figure 2. Nelson-Riley plots of α-Mn_2O_3 samples

As observed from Table 1, all the stractural parameters are varying with respect to the amount of reducing agent added at the time of preparing the samples. For the lower NaOH concentration, the lattice constant is 9.4057Å, which deviates more from the standard value (9.43 Å). However, on adding more NaOH (1M), the lattice constant of the sample is approaching to the standard value. Related unit cell volume and density variations also revealed the same kind of variations with respect to the concentrations of NaOH. Crystallite size gradually increases with used NaOH and the microstrain in the lattice of the sample prepared using 0.75 M NaOH solution is less.

International Journal of
Scientific Research in Science and Technology (IJSRST)
Print ISSN : 2395-6011, Online ISSN : 2395-602X
International Conference on Advanced Materials
Held on 14, 15 December 2017, Organized by Department of Physics,
St. Joseph's College, Trichy, Tamilnadu, India

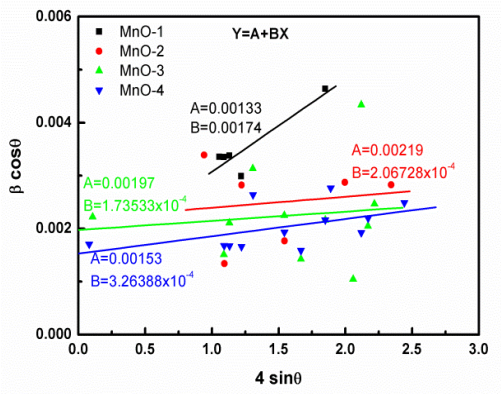

Figure 3. Williamson - Hall plots of α- Mn_2O_3 samples

Table 1. Structural parameters of α-Mn_2O_3 samples

Sample Details	Lattice Parameter (Å)			Volume (Å)^3		Density (g/cm^3)		Crystalline Size (nm)		Strain x 10^{-3}	
	Exp.	N-R Plot	Std.	Exp.	Std.	Exp.	Std.	XRD	W-H plot	Cal.	W-H plot
MnO-1	9.4057	9.3589	9.3589	832.16	838.56	5.0374	5.0374	39.5	108.8	0.8839	1.74
MnO-2	9.4455	9.5430	9.5430	842.81	838.56	4.9737	4.9737	63.5	66.13	0.6269	0.2067
MnO-3	9.4298	9.4040	9.4040	835.04	838.56	5.0200	5.0200	66.9	73.51	0.5645	0.1735
MnO-4	9.4040	9.5295	9.5295	836.80	838.56	5.0090	5.0090	73.7	94.65	0.5085	0.3263

Figure 4 shows the Fourier Transform IR spectra of the prepared α-Mn_2O_3 samples

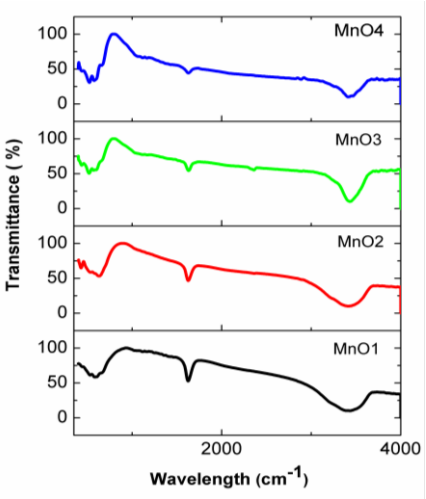

Figure 4. FTIR spectra of α-Mn_2O_3 samples prepared using NaOH solutions of different concentrations

The appearance of two strong bands at ~690, and ~ 570 cm^{-1} in MnO-1 and MnO-2 samples are the clear evidence for the presence of the crystalline Mn_2O_3. However these two bands appear as single broad band. On deconvolution, the band centered at 690 cm^{-1} is ascribed to the longitudinal-optical (LO) mode and the one at 570 cm^{-1} is due to the transverse-optical (TO) mode of α-Mn_2O_3. On increasing the concentration of the reducing agent (MnO-3 and MnO-4) three separate bands are distinctly visible at ~ 410, ~ 508 and ~ 598 cm^{-1}. The peak positioned at 410 cm^{-1} is assigned to the bending vibrations of Mn–O–Mn bonding. The 510 cm^{-1} peak is assigned to the symmetric stretching vibration mode in Mn–O-Mn bond. Peak at 598 cm^{-1} is due to the asymmetric Mn–O–Mn stretching vibrations. Moreover, it is observed that all of the associated peaks are red-shifted with decreasing particle size, which might be due to the different local stresses. With decreasing grain size of Mn_2O_3 nanocrystals, many defects and morphological changes are expected at the surface and interface of Mn_2O_3 nanocrystals, cause lattice distortion and lowering the lattice space symmetry. On comparing the band positions with the standard Mn_2O_3 bulk material [15], remarkable

International Journal of
Scientific Research in Science and Technology (IJSRST)
Print ISSN : 2395-6011, Online ISSN : 2395-602X
International Conference on Advanced Materials
Held on 14, 15 December 2017, Organized by Department of Physics,
St. Joseph's College, Trichy, Tamilnadu, India

differences are observed and these changes are attributed to the microstructural evolution, which results surface disorder due to morphological changes in the Nanomaterials on changing the preparative conditions. Since the surface of nanoparticles is very reactive, exposure to humid moisture environment, water molecules are co-ordinated at the surface. Hence, the band appearing at ~3410 cm^{-1} reveals the presence of OH stretching vibration in H_2O. The presence of the absorption band centered at ~ 1625 cm^{-1} may be due to the bending vibration of OH in H_2O [16]. Thus FTIR study also confirms the formation of α- Mn_2O_3 as that of the results of XRD.

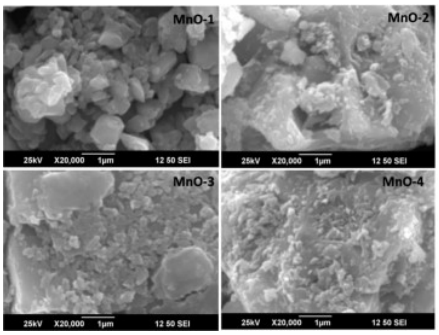

Figure 5. SEM micrographs of Mn_2O_3 Samples

Scanning electron microscope facilitates an understanding of the microstructure of the surface of the nano particles. Figure5 shows the recorded SEM images of α-Mn_2O_3 samples for the magnification of × 20000. It is obvious that the size and morphology of powers mainly depend on the preparation conditions [17]. A detailed examination of SEM micrograph from a selected region of Mn_2O_3 samples, observed clusters are non spherical but some particles are rectangular and irregularly shaped. Randomly 10 clusters are chosen from the image for the calculation of size of the agglomerated particles. The average value of the agglomerated particle size is found to be 0.9366 μm (~936nm). The size distribution and shape of the particles are not uniform. On increasing the concentration of the reducing agent, the cluster size reduces, but the size of the cluster is in μm range. Since the resolution of SEM is very limited, size estimation of single particle is not possible. There seems a mismatch in average size of the grains determined through Scherrers calculation using the XRD data and SEM analysis. XRD usually provides the crystallite size of the particles, where as SEM provides the size of the surface clusters alone.

The optical absorption spectra of the prepared α-Mn_2O_3 samples are shown in Fig 6.

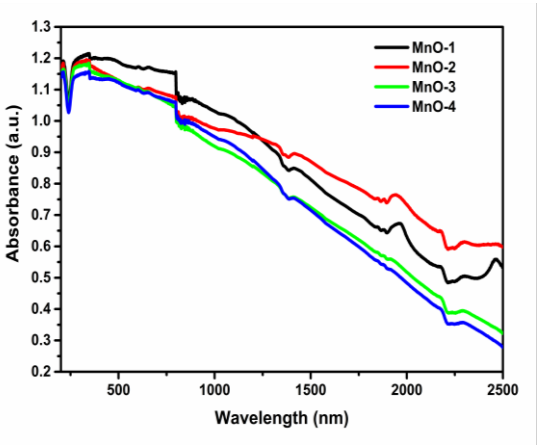

Figure 6. Optical absorption spectra of α-Mn_2O_3 samples prepared using NaOH solutions of different concentrations

It can be seen that, the strong absorptions of sample appears in the band range from 430 to 250 nm. Hence, the optical band gap for the absorption peak can be obtained by extrapolating the linear portion of the $(\alpha h\nu)^2$ – hν curve. The optical band gap values of the samples prepared for different preparative conditions are respectively, 5.490, 5.483, 5.332 and 5.37eV. Blue shift shows low dimension of α-Mn_2O_3 nanoparticles and due to their property variations.

Figure 7 shows the reflectance spectra of the prepared Mn_2O_3 nano particles using different concentrations of reducing agent.

International Journal of
Scientific Research in Science and Technology (IJSRST)
Print ISSN : 2395-6011, Online ISSN : 2395-602X
International Conference on Advanced Materials
Held on 14, 15 December 2017, Organized by Department of Physics,
St. Joseph's College, Trichy, Tamilnadu, India

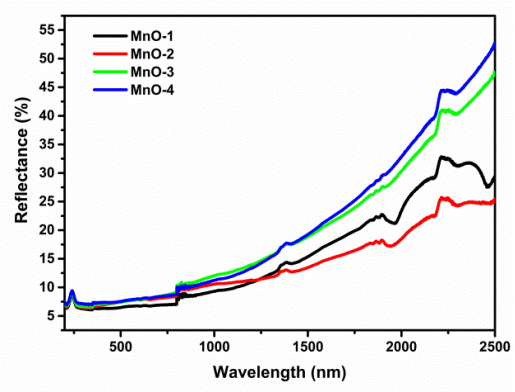

Figure 7. Optical reflectance spectra of α-Mn_2O_3 samples prepared using NaOH solutions of different concentrations

Reflectivity variations clearly show the inverse trend of the absorption curve. Since reflectivity is more in the IR region, it can be used as reflective coatings to eliminate IR radiations.

The electrical conductivity of the samples are measured by preparing pellets of known dimension. For that, initially the Mn_2O_3 powders were mixed with polyvinyl alcohol which was used as a binder and then pressed in to pellets of known dimension. Pellets were then heated at 150ºC for 1 hour to remove the binder. Using the two probe set-up, electrical measurements were carried out in the temperature range RT to 100 ºC. Figure8 shows the electrical resistivity variations with respect to temperature in all the α-Mn_2O_3 samples.

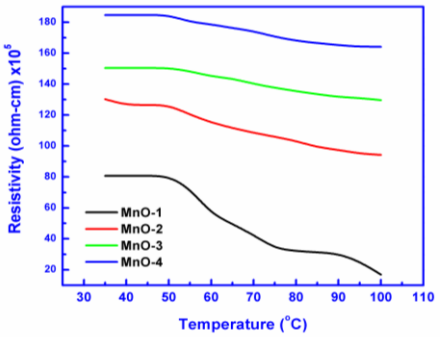

Figure 8. Resistivity variation with temperature in α-Mn_2O_3 samples prepared using NaOH solutions of different concentrations

In all the samples the resistivity values decreases with temperature, which shows the semiconducting behavior of the α-Mn_2O_3 samples. As observed, MnO-1 samples is having lower resistivity of about 80×10^5 Ω cm at RT and it decrease to 10×10^5Ωcm on increasing the temperature to 100ºC. For the other three samples MnO-2, MnO-3, MnO-4, the same trend prevails, however the room temperature resistivity gradually rises as the concentration of reducing agent is increased. In these samples, gradual improvement in crystallinity is observed, so the resistivity of the prepared powder sample increases.

The conductivity variations in the prepared samples are useful in finding the activation energy, temperature co-efficient of resistance etc. Fig 9 shows the conductivity variation with temperature

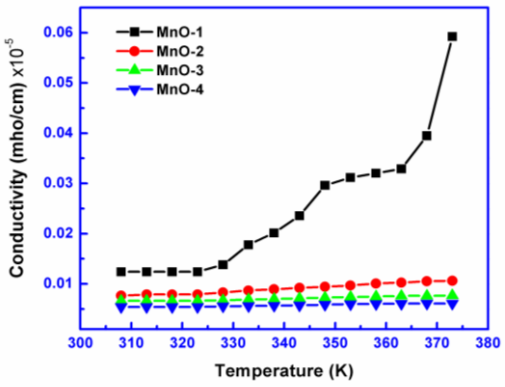

Figure 9. Conductivity variations with temperature in α-Mn_2O_3 samples

The conductivity variation is prominent inMnO-1 samples. However, the conductivity variation in the other samples MnO-2, MnO-3 and MnO-4 are very small. Since the MnO-1 sample is almost amorphous, there may be more defect sites that make them to conduct heavily. The other samples MnO-2, MnO-3, and MnO-4 exhibit less conductivity variations with temperature.

Activation energy is the minimum amount of energy that is required to activate atoms or molecules to a condition in which they can undergo physical

International Journal of
Scientific Research in Science and Technology (IJSRST)
Print ISSN : 2395-6011, Online ISSN : 2395-602X
International Conference on Advanced Materials
Held on 14, 15 December 2017, Organized by Department of Physics,
St. Joseph's College, Trichy, Tamilnadu, India

charge transport. On measuring the variation of (σ) with temperature, Activation energy "E_a"can be determined from the slope of the straight line obtained by plotting 1000\T against ln(σ) as shown in Figure 10.

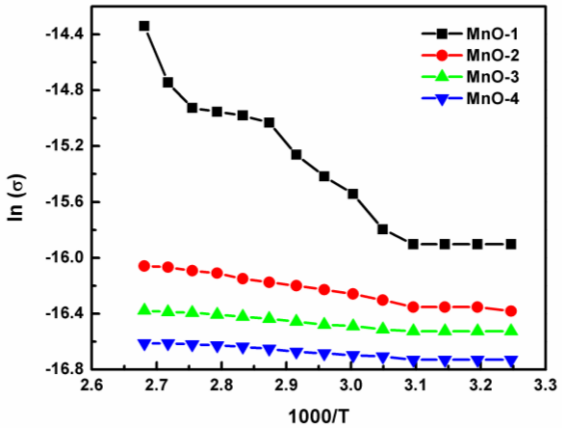

Figure 10. Arrhenius plots to estimate activation energy of α-Mn_2O_3 samples

Slope of the Arrhenius plot directly gives the activation energy of the Mn_2O_3 samples. Temperature co-efficient of resistance (TCR) can be measured from the noted conductivity values at two specific temperatures. Obtained activation energy and the TCR values are listed in Table 2.

Table 2. Electrical data of Mn_2O_3 samples

Samples details	E_a(eV)	TCR (K^{-1})
MnO-1	0.6207	-0.0176
MnO-2	0.1168	-0.0056
MnO-3	0.0640	-0.0022
MnO-4	0.0960	-0.0021

The activation energy gradually decreases on increasing the proportion of the reducing agent during preparations. The negative value of TCR indicates the presence of semiconducting behavior in Mn_2O_3 nanoparticles [18].

4. Conclusion

α-Mn_2O_3 nanoparticles have been successfully synthesized using the simple microwave assisted sol-gel method by varying the concentration of the reducing agent NaOH. Property variations were systematically interpreted for the samples prepared for different conditions. XRD analysis confirmed the α-Mn_2O_3 polymorph with a cubic structure. The Nelson-Riley and Williamson - Hall plots were constructed to estimate the lattice constant, crystallite plot and microstrain precisely FTIR spectral investigations confirmed the metal-oxide phase formation in the prepared manganese oxide nanoparticles. The surface morphology and agglomerated clusters and their size variations with preparative conditions were investigated using SEM. The optical absorption studies revealed the presence of fundamental absorption edge in the lower wavelength side. The optical band gap of the samples and their variations (5.39-5.49 eV) are explained based on the preparative conditions. The electrical resistivity values and their variations with temperature was explained with the aid of the obtained activation energy and TCR values.

References

[1] Cavicchi, R.E., Silsbe, R.H., "Coulomb Suppression of Tunneling Rate from Small Metal. Particles", Physical review letters, 52, April 1984, pp. 1453-1456.

[2] Ball, p., Garwin, L., "Science at the atomic scale", Nature, 355, 1992, 761–766.

[3] Rao, C.N.R., Vivekchand, S.R.C., Biswas, K., Govindaraj, A., "Synthesis of inorganic nanomaterials", Dalton Transactions, July 2007, pp. 3728–3749.

[4] Chen, Y., Zhang, Y., Qi-Zhi Yao, Gen-Tao Zhou, Fu, S., Fan, H., "Formation of α-Mn2O3 nanorods via a hydrothermal-assisted cleavage-

decomposition mechanism", Journal of Solid State chemistry, 180, April 2007, pp. 1218-1223L.

[5] Wang, Z., Ebina, Y., Takada, K., Sasaki, T., "Ultrathin hollow nanoshells of manganese oxide" Chemical Communication., 8, 2004, pp. 1074–1075.

[6] Zhang, Z.L., Du, G.H, Ren, T.Z., Su, B.L., "A simple method to synthesise single-crystalline manganese oxide nanowires", Chemical Physics Letters, 378, September 2003, pp. 349-353.

[7] Lei, S.J., Tang, K.B., Fang, Z., Liu, Q.C., Zheng, H.G., "Preparation of α-Mn_2O_3 and MnO from thermal decomposition of $MnCO_3$ and control of morphology", Materials Letters, 60, January 2006, pp. 53–56.

[8] Li, W.N., Zhang, L.C., Sithambaram, S., Yuan, J.K., Shen, X.F., Aindow, M., Suib, S.L., "Shape Evolution of Single-crystalline Mn_2O_3 Using a Solvothermal Approach", The Journal of Physical Chemistry C, 111, September 2007, pp.14694–14697.

[9] Subhash T., Bhagwati P., Jitendra K., "Formation and magnetic behaviour of manganese oxide nanoparticles", Materials Science and Engineering: B, 167, March 2010, pp. 153-160

[10] L. Liu, Z. Yang, H. Liang, H. Yang, Y. Yang, "Facile synthesis of $MnCO_3$ hollow dumbbells and their conversion to manganese oxide", Materials Letters, 64, October 2010, pp. 891–893.

[11] Cao, J., Zhu, Y., Bao, K., Shi, L., Liu, S., Qian, V., "Microscale Mn_2O_3 Hollow Structures: Sphere, Cube, Ellipsoid, Dumbbell, and Their Phenol Adsorption Properties", The Journal of Physical Chemistry C., 113, September 2009, pp. 17755–17760.

[12] Tsang, C., Kim, J., Manthiram, A., "Synthesis of Manganese Oxides by Reduction of $KMnO_4$ with KBH4in Aqueous Solutions", Journal of Solid State Chemistry, 137, April 1998, pp. 28–32.

[13] Ahmad, T., Ramanujachary, K.V., Lofland, S.E., Ganguli, A.K., "Nanorods of manganese oxalate: a single source precursor to different manganese oxide nanoparticles (MnO, Mn_2O_3, Mn_3O_4)", Journal of Materials Chemistry, 14, December 2004, pp. 3406–3410.

[14] Masoud Salavati-Niasari, Fatemeh Mohandes, Fatemeh Davar, Kamal Saberyan, "Fabrication of chain-like Mn_2O_3 nanostructures via thermal decomposition of manganese phthalate coordination polymers", Applied Surface Science., 256, December 2009, pp. 1476–1480.

[15] Sadtler Research Laboratories, INC, Inorganics IR Grating Spectra, Philadelphia, PA 19104, USA, 3–5 (1972) Y1173K.

[16] Chen, Z.W., Lai, J.K.L., Shek, C.H., "Influence of grain size on the vibrational properties in Mn_2O_3 nanocrystals", J. Non-Crystalline Solids, 352 September 2006, pp. 3285–3289.

[17] Siti Aida Ibrahim, Srimala Sreekantan, Proceedings of ICXRI 2010, International Conference on X-Rays & Related Techniques in Research & Industry June 9 – 10, 2010, Aseania Resort Langkawi, Malaysia.

[18] http://physics.mipt.ru/S 111/t

International Journal of
Scientific Research in Science and Technology (IJSRST)
Print ISSN : 2395-6011, Online ISSN : 2395-602X
International Conference on Advanced Materials
Held on 14, 15 December 2017, Organized by Department of Physics,
St. Joseph's College, Trichy, Tamilnadu, India

Bulk Synthesis and Characterization of Multiwalled Carbon Nanotubes by CVD method

S. A. Thaneswari , A. J. Clement Lourduraj
PG and Research Department of physics, St. Joseph's College (Autonomous), Trichy-620002, Tamilnadu, India
*Corresponding author's Email: ajeevaclement@gmail.com

Abstract

Multiwalled Carbon nanotubes (MWCNTs) were effectively synthesized by Chemical vapor deposition (CVD) using metallic catalyst Fe-MgO with growth temperature 700 °C and pyrolysis time at 30 min. The synthesized MWCNTs were characterized by X-ray diffraction (XRD) pattern confirmed the crystalline structure like hexagonal structure (002) plane. SEM morphology of MWCNTs are having in the diameter range of 50-80 nm and length is up to few μm. From the TEM images shown that the MWCNTs with evidence of clear graphitic walls around 15 layers were clearly visualized in 5nm scale. Fe-MgO as good catalytic growth for MWCNTs and also well supported to enhance the bulk production. In future, pure carbon nanotubes and MWCNTs composite materials have been apply for energy storage applications.

Keywords: Multiwalled carbon nanotubes, catalyst, chemical vapor deposition, energy.

1. Introduction

In 1985 chemists invented a new allotrope of carbon like fullerene related structures [1]. Nowadays, Carbon nanotubes CNTs are attracts significantly interest of the scientific community because of their outstanding functions in all areas. The properties CNTs have been attracted for the large variety of interesting and important applications has been suggested supercapacitors, batteries, fuel cells, solar cells, polymer nanocomposites, sensors and biological applications. Carbon nanotubes were exposed by Sumio Iijima in 1991 by electric arc discharge method [2]. The succeeding discoveries of Carbon nanotubes are a tubular structure and their unique properties, an optical, electronic, thermal, mechanical and chemical characteristics a fine distribution nano size, highly surface area, low resistivity, and high thermal stability research into all aspects of CNTs [3&4]. CNTs are widely classified into single walled carbon nanotubes (SWNTs) and multi walled carbon nanotubes (MWNTs) and double walled carbon nanotubes (DWNTs)[5]. Generally, SWCNTs are MWCNTs synthesis different methods, but most widely used common technique carbon arc discharge, Laser ablation techniques [6]. There is a huge demand for quality CNTs both as research materials and large scale industrial applications with optimizing methods to produce more consistent and higher yields. The CNTs were grown by these methods are some difficulties, with unwanted other impurities, which can make them difficult to purify, size control for convenient applications. Currently, the widely follow the chemical vapour decomposition (CVD) method is a controllable process for the selective synthesis of CNTs either individually or in bulk [7]. CVD method has been believed as the most suitable bulk synthesis method in terms of quality of both SWCNTs and MWCNTs [8,9]. Chemical vapor deposition techniques employing the on supported bimetallic metal catalysts have been demonstrated as viable large scale production methods. CNTs are

International Journal of
Scientific Research in Science and Technology (IJSRST)
Print ISSN : 2395-6011, Online ISSN : 2395-602X
International Conference on Advanced Materials
Held on 14, 15 December 2017, Organized by Department of Physics,
St. Joseph's College, Trichy, Tamilnadu, India

synthesis from the carbon containing gaseous decomposition of hydrocarbon sources acetylene (C_2H_2) and ethylene (C_2H_4) as it decomposes at elevated temperature and passes over a transition metal catalyst (typically Fe, Co and Ni). A high yield of nanotubes can be achieved by this method [10 &11]. In the present work, thermal chemical vapour deposition (T-CVD) in the preparation of high yield and multiwalled Carbon nanotubes (MWCNTs) through the decomposition of acetylene over an MgO supported Fe catalyst at pyrolysis temperatures carried out from 700 °C.

2. Experimental

The Fe-MgO catalyst was prepared by impregnating method. Fe $(NO_3)_3.9H_2O$ (Sigma-Aldrich) were dissolved in millipore water with constant stirring. After ultrasonicating of MgO powder in an iron nitrate aqueous solution well mixed, the resulting gel was dried at 100 °C and then grained into a mortar in fine powder. The resulting material wascalcinationsin a furnace at temperature 500 °C for 3 hours [12]. After the impregnation/ incorporation method Catalyst powder materials was grained into fine powder using mortar.

Preparation of CNTs was synthesized using tubular furnace shown schematic diagram of thermal CVD setup fig.1. The catalyst 50 mg was spread over the quartz boat (length-10 cm). CNTs production in tubular furnace with catalyst (Fe-MgO) was placed in the centre of the furnace.

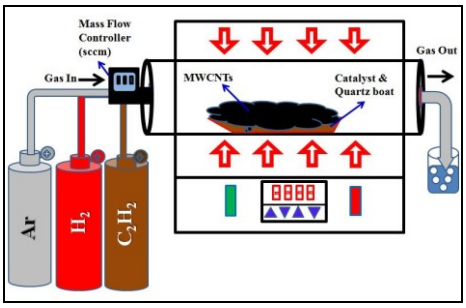

Figure 1. shows the schematic diagram of the experimental setup of CVD method

CNTs growth supported flowing gases sources the argon (Ar) 99.99% gas (gas flow rate 60 sccm) for CNTs growth in inert atmosphere and hydrogen (H_2) 99.99% gas (gas flow rate 60 sccm) was used for the reduction of catalyst. Then the nanotubes growth was started with the introducting acetylene (C_2H_2) (99.9%) gas flow rate 40 sccm with a flow mixed with Ar (Gas) at 700 °C at 30 min CNTs growth. The flow rate of the gases was controlled by a mass flow controller (MFC) in (standard cubic centimeter per minute). After completion the (CNT) Carbon Nanotubes growth reaction the quartz tube was cool to room temperature under Argon (Ar) atmosphere at 60 sccm. The final product was obtained block fine powder from the quartz tube further goes to purification process.

The above obtained CNTs were some impurities and catalytic particles. Hence, the CNTs powder was purified by using acid and heat treatment. These CNTs were stirred with Hydrochloric acid (HCl) (about 35% pure). The CNTs solution was washed continuously and centrifuged. Finally, the filtered material was dried at annealing the 300 °C for in 4 hrs in muffle furnace to remove the impurities amorphous carbon and catalyst. Finally the pure CNT fine powder was materials characterized studies.

2.1. Characterization

Purified MWCNTs crystallographic structures and planes was determined by a powder X-ray diffraction (XRD) system by X'PERT-PRO model with Cu Kα radiation (λ = 0.15406 nm). The Surface morphology structure was analyzed by Scanning electron microscope (SEM) VGA-3 TESCON (30 Kv) instrument and Transmission Electron Microscopy (TEM) model (JEOL 3010) operated at 300 Kv.

International Journal of
Scientific Research in Science and Technology (IJSRST)
Print ISSN : 2395-6011, Online ISSN : 2395-602X
International Conference on Advanced Materials
Held on 14, 15 December 2017, Organized by Department of Physics,
St. Joseph's College, Trichy, Tamilnadu, India

3. Result and Discussion

3.1. X-Ray Diffraction (XRD)

The X-ray diffraction pattern of purified (MWCNTs) is shown in the Fig. 2. The pattern shows the broad diffracted peaks appears at 2θ=26° was assigned correspond to (002) plane. The diffraction peak corresponds to (002) plane and d-spacing value 3.39 Å. From XRD pattern shows for MWCNTs the results reveals that the carbon nanotubes with hexagonal structure with carbon phase and diffraction patterns typically well graphitized.

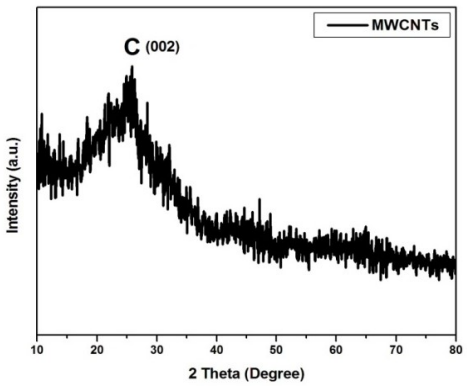

Figure 2. XRD pattern of the MWCNTs

3.2. SEM and TEM

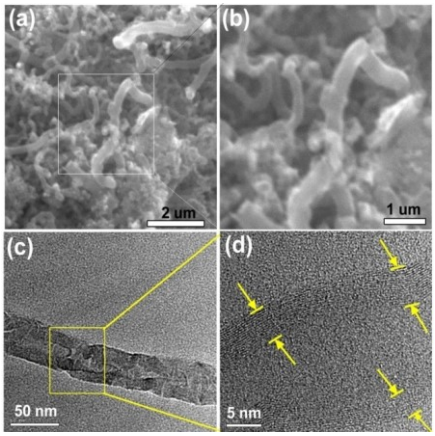

Figure 3 (a) (b). SEM morphological images of MWCNTs and (c) TEM images of MWCNTs. (d) TEM images of MWCNTs in multi walls pattern (scale bar = 5 nm).

The Scanning electron microscope for purified MWCNTs micro scale images are shown in Fig 3 (a) and 3(b). In Fig (a) SEM micrograph are entangled clear morphological view for few CNTs. Fig. 3 (a) shown an magnified view of fig. 3(b) the bended MWCNTs are having in the diameter range of 50-80 nm and length is up to few μm in different magnification. SEM images are clearly indicates the formation of CNTs on the surface of the (Fe) Feric loaded MgO catalyst.

The Transmission Electron Microscopy (TEM) nanoscale images are shown in fig. 3(c) and (d) for purified the MWCNTs. Fig 3(c) shows the individual MWCNTs focused in TEM analysis was confirms that walled that the purifications acid treatments and does not affected the nanotubes structure. Fig 3(d) shows the highest resolution for TEM images can reveal fine details of nanotube structure, including the number of carbon (graphene) layers in their walls, and multi walled carbon nanotubes and fine graphene layers with around 15 graphene walls were clearly visualized (yellow colored aero mark) indicated by TEM image in 5nm scale. The diameter of the Multi walled carbon nano layers nanotubes was found to be few nm and it shows multi layers formed over the MWCNTs during decomposition of acetylene carbon source over the Fe -MgO by Thermal Chemical Vapour Deposition method.

In order to conclude that the SEM and TEM strongly reveals that the MWCNTs obtained over Fe-MgO at 700°C were pure and thermally stable due to the constructions of well graphitized walls due to (Fe) catalyst supported. Which is clearly indicates the MWCNTs were uniformly distributed without any contamination with nano tubular morphologies. The SEM and TEM good morphology and high yield for used Fe-MgO catalyst. Furthermore, Fe catalyst support is enhanced CNTs growth. So the better high

yield preparation defects free CNTs from catalytic-Thermal CVD.

4. Conclusion

Multiwalled Carbon nanotubes (MWCNTs) have successfully synthesized by thermal chemical vapour deposition (TCVD) and catalytic decomposition of acetylene over the Fe metallic nanoparticles catalyst loaded in porous support MgO at 700°C. The XRD result confirms the carbon peak at broad diffracted patterns as graphitized in hexagonal structure. From XRD there are no peaks related to Fe metals used for catalyst due to the purified MWCNTS. The SEM and TEM images showed the morphology of MWCNTs were confirmed the purity of multiwaled CNTs structures and graphitic mutilayers reveals that few nanometer scales. In Future, industrial scale possible production of large scale for energy storage increased the specific capacitance value to develop the symmetric supercapacitor, CNTs to use to electrical energy storage device applications.

Acknowledgments

The authors wish to thank the PG and Research Department of Physics, St. Joseph's College, Trichy, for providing lab facilities and instrumentation center facilities to carry out characterization.

References

[1] H.W. Kroto, J.R. Heath, S.C. O'Brien, R.F. Curl, R.E. Smalley, C60: Buckminster, fullerene., Nature 318 November 1985, pp. 162–163.

[2] S. Iijima. Helical Microtubules of Graphitic Carbon. Nature, 354, August 1991, pp.56.

[3] Carbon Nanotubes, T. W. Ebbesen, Ann. Rev. Mater. Physics Today, 381, June 1996, pp.678.

[4] C.M. Niu, E.K. Sichel, R. Hoch, D. Moy, H. Tennent, Applied Physics Letters, 70, January 1997, 1480.

[5] M.S. Dresselhaus et al., The Science of Fullerenes and Carbon Nanotubes: Their Properties and Applications, Academic Press (1996) ISBN 0-12221-820-5.

[6] T.W. Ebbesen ed., Carbon Nanotubes-Preparation and Properties, CRC Press (1996) ISBN 0-84939-602-6.

[7] M.S. Dresselhaus et al eds., Carbon Nanotubes: Synthesis, Structure, Properties and Applications, Springer-Verlag (2000) ISBN 3-54041-086-4.

[8] B.H. Guan, I. Ramli, N. Yahya, L.K. Pah., Purification of Carbon nanotubes synthesized by catalytic decomposition of methane using bimetallic Fe-Co catalysts supported on MgO, IOP Conferance Series: Materials Science and Engineering. 17, February 2011, 012025.

[9] Seo, J.W., Hernadi, K., Miko, C. and Forro, L., Behaviour of transition metals catalysts over laser-treated vanadium support surfaces in the decomposition of acetylene, Applied Catalysis A: General, Vol. 260, March 2004, pp. 87-91.

[10] V. Thirumal, A. Pandurangan, R. Jayavel, S.R. Krishnamoorthi, R. Ilangovan, Synthesis of nitrogen doped coiled double walled carbon nanotubes by chemical vapor deposition method for supercapacitor applications, Current Applied Physics, 16,August 2016, pp-816-825.

[11] B. Zheng, Y. Li, and J. Liu, "CVD synthesis and purification of single-walled carbon nanotubes on aerogel-supported catalyst," Applied Physics A, vol. 74, March 2002, pp. 345–348.

[12] M. Kumar, Y. Ando., Chemical Vapor Deposition of Carbon Nanotubes: A Review on

Growth Mechanism and Mass Production, Journal of Nanoscience and Nanotechnology, 10, June 2010, pp. 3739–3758,

[13] O. Guellati, S. Detriche, M. Guerioune, Gasflow and temperature synthesis dependence on the CNTs structure and yield, International Journal of J. Nanoelectronics and Materials, 3, November 2010, pp. 123-131.

[14] Guoqing Ning, Fei Wei, Qian Wen, Guohua Luo, Yao Wang and Yong Jin. Improvement of Fe/MgO Catalysts by Calcination for the Growth of Single and Double Walled Carbon Nanotubes. J. Phys. Chem. B, 110, December 2006, pp.1201-1205.

International Journal of
Scientific Research in Science and Technology (IJSRST)
Print ISSN : 2395-6011, Online ISSN : 2395-602X
International Conference on Advanced Materials
Held on 14, 15 December 2017, Organized by Department of Physics,
St. Joseph's College, Trichy, Tamilnadu, India

Photoluminescence Studies of $(Nd_{0.93}Sm_{0.07})_2O_3$ Nanoparticles

Morris Marieli Antoinette, S. Israel
P.G and Research Department of Physics, The American College, Madurai-625 002, India.
Corresponding Author: [2]israel.samuel@gmail.com

Abstract

$(Nd_{0.93}Sm_{0.07})_2O_3$ nanocrystalline powders were prepared using modified Pechini method. Powder X-ray diffraction was used to study the structural characterization of the synthesized sample and the results confirmed that Sm^{3+} doped Nd_2O_3 nanoparticles having a nanocrystalline structure with a hexagonal phase and $P\bar{3}m1$ space group were formed with lattice parameters a=b=3.8348Å, c=6.0031Å. These parameters were refined using CELREF software and the cell parameters were refined to give minimum R factor. The surface morphology and the size of the particles were examined using SEM and TEM. The surface micrographs showed small amount of agglomeration. TEM results also confirmed that the synthesized particles are in nanosize. The EDX spectroscopy confirmed the purity of the synthesized sample. The optical properties of the sample were studied using U-V data analysis and photoluminescence studies. The results of the optical studies proved that these materials can be highly efficient in solid state lightings.

Keywords: Modified Pechini method, Photoluminescence

1. Introduction

In recent years, nanotechnology has attracted major scientific interest because nanomaterials show distinctive or improved properties due to its nanoscale dimensions. [1] Synthesis of new materials in the nanoscale often shows unique optical, magnetic, electronic and structural properties, which are different from their respective bulk. [2-5] Rare earth elements possess unique properties and wide uses owing to their special electronic configurations. Due to the special electronic, optic, magnetic, catalytic and chemical properties, arising from the confinement of their 4f electrons, rare earth oxides with one dimensional structure such as La_2O_3, Sm_2O_3, Gd_2O_3 and Nd_2O_3 have been widely used in many functional devices. [6,7] The change in the electrical and optical characteristics of nanoparticles is caused by quantum effects due to their high surface to volume ratio, which increases the band gap. [8,9] The rare earth oxides have been synthesized by various methods including microwave-assisted, solvothermal, sol gel, hydrothermal, solution combustion, co-precipitation etc. [10-15]

Nd_2O_3 have attracted many researchers due to its extensive range of applications. It is a semiconductor with wide band gap. [16] Among rare-earth ions, the Nd^{3+} ion is one of the most efficient rare-earth ion for solid state lasers in various materials. Neodymium ions could also be good candidates for upconversion fluorescence and lasers. [17, 18] It is also used in ceramic capacitors, colour TV tubes, coloring glass, and catalyst for automotive industry. [19]

In this paper, we have synthesized Sm^{3+} doped Nd_2O_3 nanoparticles using the modified Pechini method. This method allows a molecular mixing of constituents, leading to an excellent chemical homogeneity, an increase in the reaction rate and a decrease of the temperature of crystallization. [20]

2. Experimental

2.1. Synthesis of Sm^{3+} doped Nd_2O_3 nanoparticles

Sm^{3+} doped Nd_2O_3 nanoparticles were prepared using the modified Pechini method. At first, 2 gms of Nd_2O_3 were dissolved in concentrate nitric acid under stirring to generate $Nd(NO_3)_3$. This was mixed with $Sm(NO_3)_3.6H_2O$ and dissolved in distilled water. Then EDTA was added to this solution with a molar ratio [EDTA]/[Metal] = 1, where [Metal] is the concentration of Neodymium and Samarium in the solution. In this way, a solution of metal-EDTA

International Journal of
Scientific Research in Science and Technology (IJSRST)
Print ISSN : 2395-6011, Online ISSN : 2395-602X
International Conference on Advanced Materials
Held on 14, 15 December 2017, Organized by Department of Physics,
St. Joseph's College, Trichy, Tamilnadu, India

complexes was obtained. Then ethylene glycol [EG] was added with a molar ratio [EDTA]/[EG] = 2, while stirring and heating the solution until a gel was formed. Two reactions are involved in this process: the formation of a complex between an organic acid, EDTA, with the precursor metals, and an esterification reaction with ethylene glycol (EG). The aim of the polymeric organic net produced by esterification is to reduce any segregation of the cations. It was then heated at 200 K to obtain the precursor powders. Finally, the precursor powders were calcined at 750 K for 3 hours to obtain Sm^{3+} doped Nd_2O_3 nanopowders. [16, 20-23]

2.2. Instruments used

The powder X-ray diffraction studies have been carried out by using Bruker AXS D 8 Advance X-ray diffractometer equipped with monochromatic CuK_α radiation in the 2θ range of 10-120° (λ=1.5406Å). The morphologies and composition of the prepared samples were inspected on a scanning electron microscope (SEM,VEGA 3 TESCAN, USA) equipped with an energy- dispersive X-ray spectrum (EDS, Bruker Nano, German). The transmission electron microscope (TEM, JEOL JEM-2100) studies were performed (accelerating voltage upto 200kV). The UV-VIS absorption of the sample was recorded on Varian Cary 5000 UV-VIS Spectrophotometer. Room temperature photoluminescence measurements were performed on Jobin Yvon FloroMax-3 spectroflourometer as the excitation source at 230 nm.

3. Results and Discussion

Figure 1 shows the powder X-ray diffraction pattern of the synthesized Sm^{3+} doped Nd_2O_3. Using the software Powder X the diffractogram is imported. The data is smoothened using the adaptive smooth technique. After separating the background and subtracting from the total profile, Cu-$K\alpha_2$ profile has been stripped out of the recorded profile. Sample peaks have been identified and indexing was done. On comparing these peaks with JCPDS data, it was confirmed that these belong to hexagonal system with lattice parameters a=b=3.8348Å, c=6.0031Å. These parameters were refined using CELREF software and the cell parameters were refined to give minimum R factor (R (%) =0.031). The crystallite size was calculated using the Scherrer equation,

$$\tau = \frac{0.9\lambda}{\beta \cos\theta}$$

where τ is the average grain size of the crystallites, λ is the incident wave length, β is the line broadening at half the maximum intensity (FWHM), θ is the diffraction angle.[24] The crystallite size was found to be 27 nm.

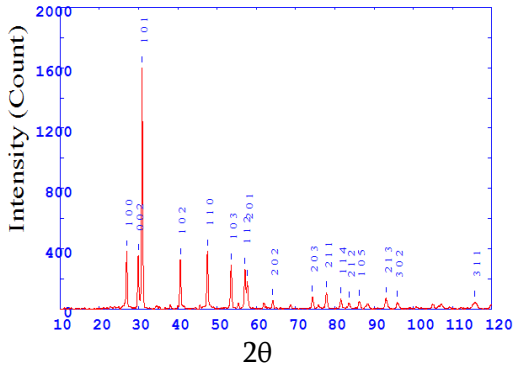

Figure 1. Indexed XRD of $(Nd_{0.93}\ Sm_{0.07})_2O_3$ nanoparticles

The morphologies of the grown nanostructures were examined using a scanning electron microscope (SEM). The morphologies of the nanostructures are demonstrated by SEM images as shown in Figure 2.

The surface morphology observed in SEM micrograph of Sm^{3+} doped Nd_2O_3 showed small amount of agglomeration which may be due to the strong interactions among the nanoparticles owing to their high surface energy during calcination. These appeared to be sponge-like structures. To get better informations, it further needs to be characterized by Transmission electron microscopy (TEM) to obtain exact morphology and size of the particles.

International Journal of
Scientific Research in Science and Technology (IJSRST)
Print ISSN : 2395-6011, Online ISSN : 2395-602X
International Conference on Advanced Materials
Held on 14, 15 December 2017, Organized by Department of Physics,
St. Joseph's College, Trichy, Tamilnadu, India

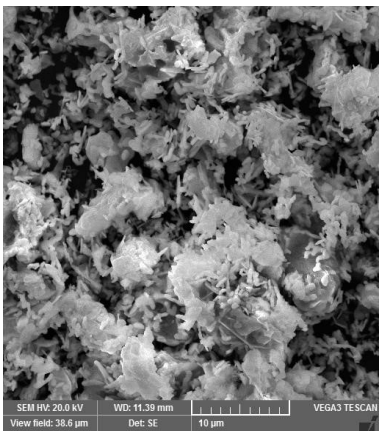

Figure 2. SEM image of $(Nd_{0.93}\ Sm_{0.07})_2O_3$ nanoparticles

The EDX spectroscopy was performed to know the percentage of the elements present in the samples and to examine the purity of the sample. The obtained percentage of the elements is shown in Table 1. The EDX spectrum observed is shown in Figure 3. It was observed that the spectrum consisted of neodymium, samarium and oxygen and there was no presence of other elements from the organic compounds which were initially used in the synthesis.

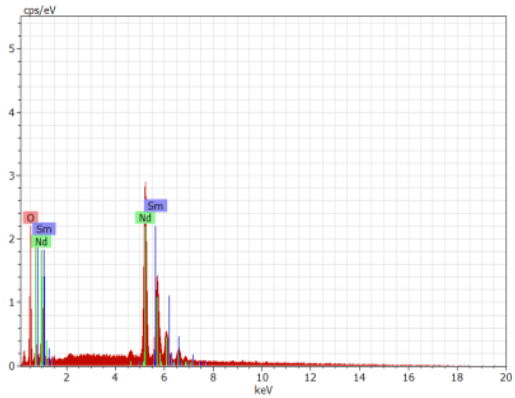

Figure 3. EDX spectra for $(Nd_{0.93}\ Sm_{0.07})_2O_3$ nanoparticles

Table 1. Percentage of elements present in the sample

Element	Wgt.%	At.%
Nd	78.53	36.22
Sm	6.86	3.03
O	14.61	60.75

TEM results confirmed that the particles are in nanosize. The TEM image obtained are shown in the Figure 4. The morphology obtained in TEM analysis was similar to SEM analysis. The particle size obtained from TEM was found to be around 35 nm, approximately equal to that of Scherrer's equation.

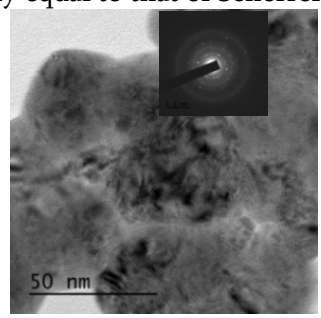

Figure 4. TEM image of $(Nd_{0.93}\ Sm_{0.07})_2O_3$ Nanoparticles

Figure 5 represents UV-VIS absorption spectrum of Sm^{3+} doped Nd_2O_3 nanoparticles. It is found that the absorption peak of nanomaterials, unlike that of bulk (~264 nm) occurs at 239 nm clearly indicating a widening of band gap. The calculated band gap value of Nd_2O_3 nanoparticles was 5.2 eV which are higher than the value of bulk Nd_2O_3, 4.7 eV. This can be attributed to the quantum confinement effect of the nanoparticles. [25]

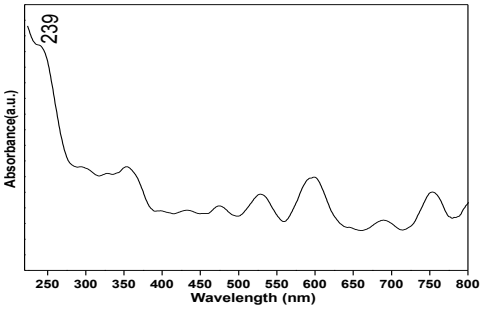

Figure 5. Absorption spectrum of $(Nd_{0.93}\ Sm_{0.07})_2O_3$ nanoparticles

International Journal of
Scientific Research in Science and Technology (IJSRST)
Print ISSN : 2395-6011, Online ISSN : 2395-602X
International Conference on Advanced Materials
Held on 14, 15 December 2017, Organized by Department of Physics,
St. Joseph's College, Trichy, Tamilnadu, India

The photoluminescence spectrum of the synthesized Sm^{3+} doped Nd_2O_3 excited under 230 nm wavelength is shown in Figure 6. The PL spectra shows a broad series of emission bands at ~ 320 - 367 nm (UV) which can be attributed to the singly ionized oxygen vacancies in Nd_2O_3. [19] It is reported that the broad UV emission can also arise due to radiative recombination of photo-generated hole with an electron occupying the oxygen vacancy. [26] The peaks at 381 and 390 nm are mainly due to the presence of surface defects that exists in the lattice. The peak at 460 nm is formed due to the second order diffraction from the source.

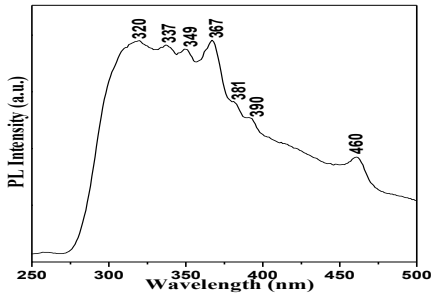

Figure 6. PL spectra of $(Nd_{0.93}\ Sm_{0.07})_2O_3$ nanoparticles

4. Conclusion

$(Nd_{0.93}Sm_{0.07})_2O_3$ nanoparticles were synthesized using modified Pechini method and were calcined at 750^{0}C. $(Nd_{0.93}\ Sm_{0.07})_2O_3$ nanoparticles were found to be highly crystalline and hexagonal in structure. Scherrer formula was used to calculate the size of the particles and the average crystallite size of the synthesized sample was 27 nm. SEM was used for surface morphology studies. SEM micrograph of the prepared samples showed small amount of agglomeration. The percentage of composition of the elements present in the sample was found from the EDAX analysis. TEM results also confirmed that the particles are in nanosize. The surface morphology obtained in TEM analysis was similar to SEM analysis. The optical band gap of Nd_2O_3 was calculated as Sm^{3+} doped 5.2 eV which are higher than the required value of bulk Nd_2O_3, 4.7 eV. This can be attributed to the quantum confinement effect of the nanoparticles. Upon 230 nm excitation, Sm^{3+} doped Nd_2O_3 nanoparticles showed a series of emission bands in the range 319 - 367 nm (UV) which reveals that the synthesized material is a promising candidate in applications for solid state lightings.

Acknowledgements

The characterization facilities provided by STIC, CUSAT, Cochin and GRI-SEM are gratefully acknowledged.

References

[1] Mortazavi-Derazkola, S., Zinatloo-Ajabshir, S., and Salavati-Niasari, M., "Preparation and characterization of Nd_2O_3 nanostructures via a new facile solvent-less route", J Mater Sci: Mater Electron, 26, 2015, pp. 5658-5667.

[2] Neto, M.C., Silva, G.H., Carmo, A.P., Pinheiro, A.S., Dantas, N.O., Bell, M.J.V., and Anjos, V., "Optical properties of oxide glasses with semiconductor nanoparticles co-doped with rare earth ions", Chem. Phy. Lett., 588, 2013, pp. 188-192.

[3] Tsuchiya, T., Watanabe, A. , Nakajima, T., and Kumagai, T., "Preparation of Y_2O_3:Eu thin films by excimer-laser-assisted metal organic deposition", Appl. Phys. A, 101, 2010, pp. 681-684.

[4] Jun, H., Qi, P., Xia, L. and Jie, L.C., "Luminescence properties of YAG: Nd^{3+} nano-sized ceramic powders via co-microemulsion and microwave heating", Bull. Mater. Sci., 36, 2013, pp. 1191–1194.

[5] Wang, G., Peng, Q., and Li, Y., "Lanthanide-doped nanocrystals: Synthesis, optical-magnetic properties and applications", Acc. Chem. Res., 44, 2011, pp. 322–332.

[6] Zhang, N., Yi, R., Zhou, L., Gao, G., Shi, R., Qui, G., and Liu, X., "Lanthanide hydroxide nanorods and their thermal decomposition to lanthanide oxide nanorods", Mater. Chem. Phys., 114, 2009, pp. 160-167.

[7] Panda, A.B., Glaspell G., and El-Shall, M. S., "Microwave synthesis and optical properties of uniform nanorods and nanoplates of rare earth oxides", J. Phys. Chem. C, 111, 2007, pp.1861-1864.

[8] Umesh, B., Eraiah, B., Nagabhushana, H., Sharma, S.C., Sunitha, D.V., Nagabhushana, B.M., Shivakumara, C., Rao, J.L., and Chakradhar, R.P.S., "Thermoluminescence and EPR studies of nanocrystalline Nd_2O_3:Ni^{2+} phosphor", Spectrochim. Acta, Part A 93, 2012, pp. 228-234.

[9] Liu, T., Zhang, Y., Shao, H. and Li, X., "Synthesis and Characteristics of Sm_2O_3 and Nd_2O_3 Nanoparticles", Langmuir, 19, 2003, pp. 7569-7572.

[10] Zawadzki, M., "Microwave-assisted synthesis and characterization of ultrafine neodymium oxide particles", J. Alloys Compd., 451, 2008, pp. 297–300.

[11] Zawadzki, M., and Kepinski, L., "Synthesis and characterization of neodymium oxide nanoparticles", J. Alloys and Compd., 380, 2004, pp. 255–259.

[12] Liu, L., Jiang, H., Chen, Y., Zhang, X., Zhang, Z. and Wang, Y., "Power dependence of upconversion luminescence of Er^{3+} doped Yttria nanocrystals and their bulk counterpart.", J. Lumin., 143, 2013, pp. 423–431.

[13] Kepinski, L., Zawadzki, M. and Mista, W., "Hydrothermal synthesis of precursors of neodymium oxide nanoparticles", Solid State Sciences, 6, 2004, pp. 1327-1336.

[14] Jayasimhadri, M., Ratnam, B.V., Jang, K., Lee, H. S., Yi, S-S., and Jeong, J-H, "Conversion of green emission into white light in Gd_2O_3 nanophosphors", Thin Solid Films, 518, 2010, pp. 6210–6213.

[15] Chandrasekhar, M., Nagabhushana, H., Sudheerkumar, K.H., Dhananjaya, N., Sharma, S.C., Kavyashree, D., Shivakumara, C., and Nagabhushana, B.M., "Comparison of structural and luminescence properties of Dy_2O_3 nanopowders synthesized by co-precipitation and green combustion routes.", Mater. Res. Bull., 55, 2014, pp. 237–245.

[16] Mendez, M., Carvajal, J.J., Cesteros, Y., Aguilo, M., Diaz, F., Giguere, A., Drouin, D., Martinez-Ferrero, E., Salagre, P., Formentin, P., Pallares, J. and Marsal, L.F., "Sol–gel Pechini synthesis and optical spectroscopy of nanocrystalline La_2O_3 doped with Eu^{3+} ", Opt. Mater., 32, 2010, pp. 1686-1692.

[17] Que, W., Kam, C. H., Zhou, Y., Lam, Y.L., and Chan, Y.C., "Yellow-to-violet upconversion in neodymium oxide nanocrystal / titania / ormosil composite sol–gel thin films derived at low temperature", J. Appl. Phys., 90, 2001, pp. 4865-4867.

[18] Lupei, V., Lupei, A. and Ikesue, A., "Transparent Nd and (Nd, Yb)-doped Sc_2O_3 ceramics as potential laser materials", Appl. Phy. Lett., 86, 2005, pp. 111118.

[19] Jian-Hua, R., Tong-Gang, Z., Jian-Hua, L., Juan, K., Jia-Xin, H., and Lin, G., "Synthesis and photoluminescence properties of Nd_2O_3 nanoparticles modified by sodium bis(2- ethylhexyl) sulfosuccinate", Chinese Phy. B, 17, 2008, pp. 4669-4672.

[20] Galceran, M., Pujol, M.C., Aguilo, M., and Diaz, F., "Sol-gel modified Pechini method for obtaining nanocrystalline $KRE(WO_4)_2$ (RE=Gd and Yb)", J. Sol–Gel Sci. Technol., 42, 2007, pp. 79-88.

[21] William, E.B., Pujol, M.C., Cascales, C., Carvajal, J.J., Mateos, X., Aguilo, M. and Diaz, F., "Synthesis and structural characterization of Tm:Lu_2O_3 nanocrystals. An approach towards new laser Ceramics", Opt. Mater., 33, 2011, pp. 722-727.

[22] Galceran, M., Pujol, M.C., Carvajal, J.J., Mateos, X., Zaldo, C., Aguilo, M., and Diaz, F., "Structural characterization and ytterbium spectroscopy in Sc_2O_3 nanocrystals.", J. Lumin., 130, 2010, pp. 1437-1443.

[23] Galceran, M., Pujol, M.C., Aguilo, M., and Diaz, F., "Synthesis and characterization of nanocrystalline Yb:Lu_2O_3 by modified Pechini method", Mater. Sci. Eng. B, 146, 2008, pp. 7-15.

[24] Kulkarni, S.K., "Analysis Techniques" in Nanotechnology: Principles and Practices, Springer, New Delhi, 2015, pp.169.

[25] Umesh, B., Eraiah, B., Nagabhushana, H., Sharma, S.C., Nagabhushana, B.M., Shivakumara, C., Rao, J.L., and Chakradhar, R.P.S., "Structural, EPR, optical and Raman studies of $Nd_2O_3:Cu^{2+}$ Nanophosphors", Spectrochim. Acta, Part A, 94, 2012, pp. 365– 371.

[26] Umesh, B., Eraiah, B., Nagabhushana, H., Nagabhushana, B.M., Nagaraja, G., Shivakumara, C., and Chakradhar, R.P.S., "Synthesis and characterization of spherical and rod like nanocrystalline Nd_2O_3 phosphors", J. Alloys and Compd., 509, 2011, pp.1146–1151.

International Journal of
Scientific Research in Science and Technology (IJSRST)
Print ISSN : 2395-6011, Online ISSN : 2395-602X
International Conference on Advanced Materials
Held on 14, 15 December 2017, Organized by Department of Physics,
St. Joseph's College, Trichy, Tamilnadu, India

Synthesis and characterization of MnO_2 Nanoparticles using Co-precipitation Technique

F. Celin Hemalatha, Dr. A.J. Clement Lourduraj
Department of Physics, St. Joseph's College (Autonomous), Trichy, Tamilnadu, India
*Corresponding author id: ajeevaclement@gmail.com

Abstract

Manganese dioxide nanoparticles were synthesized using co-precipitation method for 0.1 mol and 0.2mol concentration, which is the simple way to prepare the aqueous solution. The dried samples were characterized using various techniques such as XRD, SEM, FTIR and UV-Visible spectroscopy. The average particle size of manganese oxide nanoparticles was calculated from the XRD study. The Morphology and size of the synthesized MnO_2 particles are studied by scanning electron microscopy (SEM). The band gap energy for MnO_2 is found using UV-Visible spectroscopy. The FT-IR spectra of MnO_2 shows the peaks corresponding to stretching and bending vibration. There are large number of potential applications of MnO_2 metal nanoparticles such as in the field of electrode materials in different rechargeable batteries, biosensors, coatings, nanofibres, nanowires and bioscience applications.

Keywords: MnO_2 nanoparcticles, Co-Precipitation technique (CPT), XRD, FTIR, UV-Vis, SEM.

Introduction

Nanotechnology is science, engineering, and technology conducted at the nanoscale, which is about 1 to 100 nanometres. It's hard to imagine just how small nanotechnology is. One nanometer is a billionth of a meter, or 10^{-9} of a meter. There are 25,400,000 nanometers in an inch. A sheet of newspaper is about 100,000 nanometers thick. Nano is derived from the Greek word meaning "dwarf". Nanoscience and nanotechnology are the study and application of extremely small things and can be used across all the other science fields, such as chemistry, biology, physics, materials science, and engineering.

1.1. Dimensional Classification

1.1.1. Zero Dimensional

These nanoparticles have nano-dimension in all three directions Metallic nanoparticles including gold and silver nanoparticles and semiconductors such as quantum dots are the perfect examples of this type. Most of these nanoparticles are spherical in size. The dimension of the particle will be between 1-50nm range.

1.1.2. One Dimensional

In these nanostructures, one dimension of Nano structure will be outside the range. These include nano wires nano rods and nanotubes. These material are long (several micro meter in length) but with diameter of only some nanometer. Examples: Nanowires and nanotubes of metals, oxides, nano rods, nano filaments, quantum wires.

1.1.3. Two Dimensional

In these nanomaterials, two dimensions are outside the nanometer range. These include different kind of Nano film such as coating and thin film-multilayer, Nano sheets or Nano walls. The area of the thin film can be large but the thickness is always

International Journal of
Scientific Research in Science and Technology (IJSRST)
Print ISSN : 2395-6011, Online ISSN : 2395-602X
International Conference on Advanced Materials
Held on 14, 15 December 2017, Organized by Department of Physics,
St. Joseph's College, Trichy, Tamilnadu, India

in Nano scale range. Examples: Discs, Platelets, Ultrathin films, Super lattices, Quantum wells.

1.1.4. Three Dimensional

All dimensions are outside the nanometer range. This include bulk materials composed of individual blocks which are in nanometer range. (1-100nm)
Example: Fullerenes, Semiconductor Quantum dots, Quasi-crystal.

Co-precipitation (CPT) is the carrying down by a precipitate of substances normally soluble under the conditions employed. Analogously, in medicine, co-precipitation is specifically the precipitation of an unbound "antigen along with an antigen-antibody complex". The present work reports synthesis of MnO_2 nano particles and its characterization by Scanning Electron Microscopy (SEM), UV-Visible spectroscopy (UV), Fourier transform infrared spectroscopy (FTIR), X-Ray Diffraction (XRD) Technique.

2. Experimental Method

All chemical used in the experiment were of AR grade. The synthesis of manganese dioxide was performed using co-precipitation method by using two different salts should be of equal mol concentration mixed together with constant stirring at 40˚C. While stirring NaOH solution was added till the pH of the solution reaches 12. The stirring process was continued for one hour at constant temperature 40˚C. The precipitate was separated using the centrifuge (4000rpm). The sample was collected and heated for 24 hours in hot air oven at 100˚C.

2.1. Characterization technique

The properties of formed MnO_2 nanoparticles were determined by X-ray diffraction (XRD) (2 Theta: 0.001; Minimum step size Omega:0.001). UV-Visible spectroscopy in the wavelength range 200-1000cm^{-1}, Fourier transorm Infra-Red Spectroscopy (FTIR) in the wavelength range 400-4000 cm^{-1}.

3. Results and Discussion

3.1 X-Ray Diffraction

Figure 1 shows that X-ray diffraction study of manganese dioxide metal nanoparticles synthesized by co-precipitation method. From the XRD pattern it is clear that manganese dioxide metal nanoparticle synthesized were purely crystalline in nature. The average particle size of manganese dioxide nanoparticle was calculated from the Debye-Scherrer equation for the preferential peaks at 2θ for all the peaks present in fig (a) 0.1 mol concentration and is found to be 52.6 nm and for Figure(b) 0.2 mol concentration is found to be 32nm.

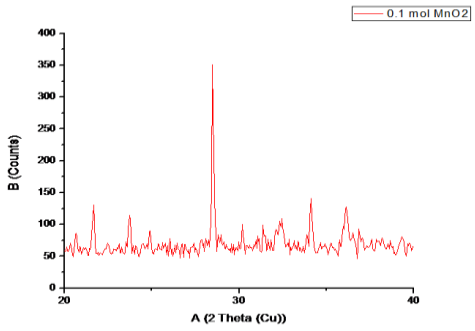

(a)

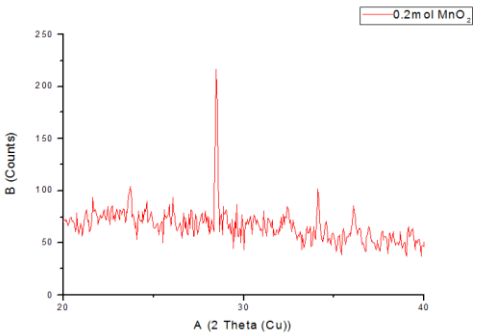

(b)

Figure 1. X-ray diffraction pattern of manganese dioxide metal nanoparticles synthesized by co-precipitation method

International Journal of
Scientific Research in Science and Technology (IJSRST)
Print ISSN : 2395-6011, Online ISSN : 2395-602X
International Conference on Advanced Materials
Held on 14, 15 December 2017, Organized by Department of Physics,
St. Joseph's College, Trichy, Tamilnadu, India

3.2. FT-IR Analysis

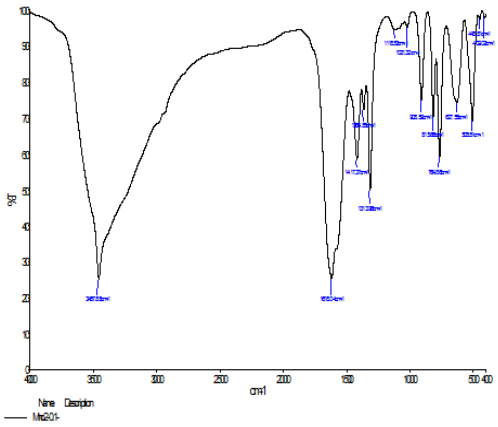

(a)

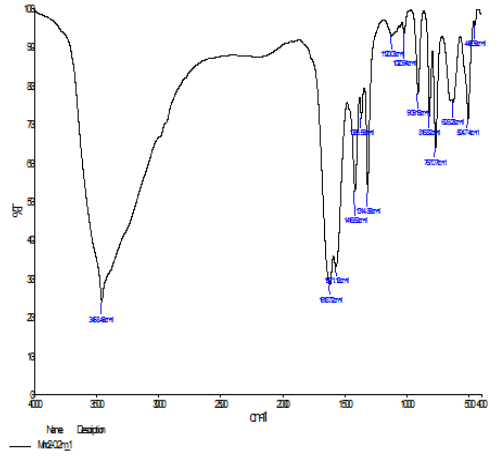

(b)

Figure 2. FT-IR spectra of manganese dioxide metal nanoparticles synthesized by co-precipitation method

Figure 2 shows that FT-IR spectra of MnO_2. The bands at 515 and 480cm^{-1} correspond to the Mn-O bond. The absorption peak for fig (a) 0.1 mol concentration at 1313.96cm^{-1} corresponds to O-C Bending. For1118.53cm^{-1} and 1021.32cm^{-1} corresponds to C-N stretching. The peaks at 908.59, 815.66 and 764.85cm^{-1} corresponds to O-H bending and 627.55cm^{-1} correspond to C-H Bending.

The absorption peaks for fib (b) 0.2 mol concentration at 901.19 cm^{-1} corresponding to =C-H and $=CH_2$ Bending and 816.8, 767.07cm^{-1} and 626.9 cm^{-1} corresponds to CH Bending.

3.3. UV-Visible Spectroscopy

Figure 3 shows that the UV-Visible spectra of manganese dioxide nanoparticles. The band gap for Figure(a) 0.1 mole concentration is found to be 5.17eV. The band gap for Figure(b) 0.2 mol concentration is found to be 5.22eV.

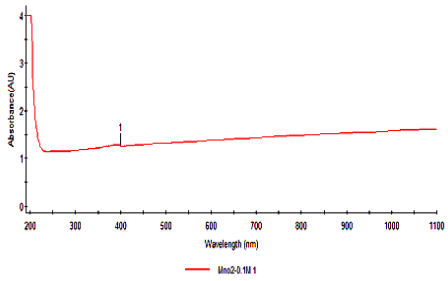

(a)

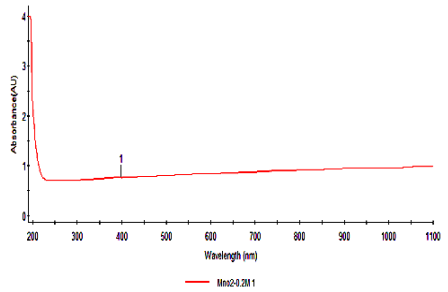

(b)

Figure 3. Uv-spectra

4. Scanning Electron Microscope (SEM)

The morphology and size of the synthesized MnO_2 particles are studied by SEM. The figures represents the SEM pictures of prepared MnO_2 nanoparticles at different magnification. These pictures confirm the formation of MnO_2 nanoparticles. SEM morphology of MnO_2 nano crystalline particles found to have an irregular spherical shape.

International Journal of
Scientific Research in Science and Technology (IJSRST)
Print ISSN : 2395-6011, Online ISSN : 2395-602X
International Conference on Advanced Materials
Held on 14, 15 December 2017, Organized by Department of Physics,
St. Joseph's College, Trichy, Tamilnadu, India

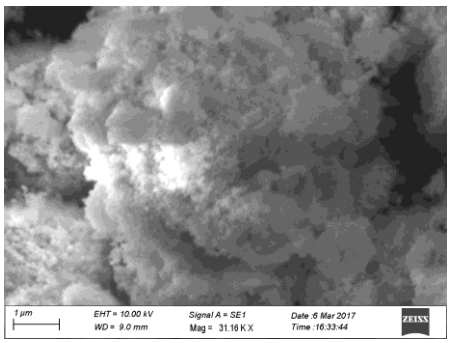

(a)

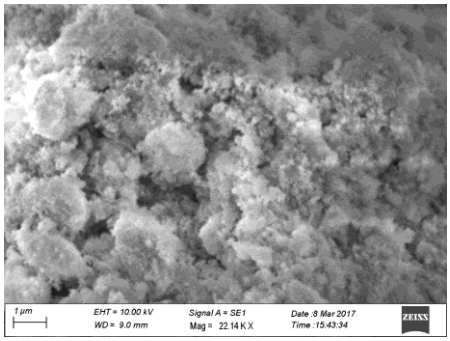

(b)

4. Conclusion

MnO_2 nanoparticles of simple cubic structure were synthesized by co-precipitation method. The FT-IR spectral analysis reveals the characteristic peaks of Mn-O stretching. The UV-Visible absorption shows sharp absorption at 240.3nm due to metal nanoparticles. XRD spectra predicts the average size for 0.1 mol of MnO_2 and is found to be 52.6nm and for 0.2 mol of MnO_2 found to be 32nm. SEM image reveals the particles is found to have an irregular spherical shape. There are large number of potential applications of MnO_2 metal nanoparticles such as in the field of electrode materials in different rechargeable batteries, biosensors, coating, nanofibres and bioscience applications.

References

[1] Hydrothermal synthesis and pseudocapacitancce properties of MnO_2 nanopstructures V. Subramanian, Hongwei Zhu, Robert Vajtai: October, 12, 2005.

[2] Catalytic characteristics of MnO_2 nanostructures for the reduction process Ramchandra S. Kalubarme, chan-jin park published 6 sep 2011.

[3] Preparation of MnO_2 nano particles and application in the Synthesis of 2-2 arylmethylene bis(3-hydroxy-5, 5-dimethyl-2-cyclohexene-1-one)

[4] Preparation of MnO_2 nanoparticles for the adsorption of environmentally hazardous malachite green dye B.M Pradeep Kumara and B.M. Nagabhushanac.

[5] Synthesis and characterization of MnO_2 nanoparticles loaded chitosan and its application in $Pb2^+$ adsorption chung Le Ngoc1, phuc Dinh van2, Tuan Nguyen Ngoc3.

International Journal of
Scientific Research in Science and Technology (IJSRST)
Print ISSN : 2395-6011, Online ISSN : 2395-602X
International Conference on Advanced Materials
Held on 14, 15 December 2017, Organized by Department of Physics,
St. Joseph's College, Trichy, Tamilnadu, India

One-pot Synthesis of MPA Capped CdTe Quantum Dots for Non-Enzymatic Hydrogen Peroxide Biosensor Application

G. Sindhu[1,2], M. Manikandan[1], S. Dhanuskodi[2,*] and M.M. Armstrong Arasu[2]
[1]School of Physics, Bharathidasan University, Tiruchirappalli-620024, India
[2]Department of Physics, St. Joseph's College (Autonomous), Tiruchirappalli-620002, India.
*Corresponding Author Email id: dhaus2k3@gmail.com

Abstract

Mercaptopropionic Acid (MPA) capped CdTe QDs with crystallite size is 0.8 nm were successfully synthesized in aqueous medium by reflux method. The HRSEM demonstrates the spherical shape with varying sizes in the nanometer scales. From the electrochemical studies, the prepared QDs improve the electron transfer between electrode and H_2O_2. The sensor exhibits a linear range from 0.67-8.04 µM with a sensitivity of 0.2833 mA $mM^{-1}cm^{-2}$ with a linear coefficient of 0.9877. The sensor shows detection limit of 6.7 µM with a rapid amperometric response time of 5s and possesses a good reproducibility. It shows the selectivity toward H_2O_2 and interference free phenomenon for other electro active species like oxalic acid and ascorbic acid. MPA capped CdTe QDs sensor was used in rat and human serum samples and cell labeling.

Keywords: CdTe Quantum Dots, Hydrogen peroxide, Sensitivity, Selectivity, Limit of Detection.

1. Introduction

Hydrogen peroxide (H_2O_2) is simplest and colorless peroxide and plays an important role in biological systems. It is widely applicable in biological, industrial, pharmaceutical and environmental [1-3]. H_2O_2 is not only a byproduct of almost all oxidases in mitochondria and separate out freely through membranes and reaches various cellular components [4]. Many analytical tools such as volumetric, photometry, chemiluminescence, chromatography, flurometric and electrochemical have been employed for the detection of H_2O_2. Electrochemical method has attracted considerable interest due to high sensitivity, low cost, lower limit detection, less response time, efficiency, linear range and selectivity [5-7]. In last decades the electrochemical biosensor modified with several metal nanomaterial's and QDs have been studied. The modified TGA capped CdTe QDs based on electrode shows high selective detection of dopamine in the presence of ascorbic acid and uric acid has been proposed by Roushani et al.[8]. Carbon paste electrode modified with CdTe QDs was fabricated and used to study the electro oxidation of dopamine and uric acid in some real samples [9].

II-VI semiconductor nanocrystals also known as quantum dots (QDs) has received extensive attention due to their size dependent optical properties, efficient emission and potential applications in biosensor, nonlinear optics, electronics, light emitting diode, photovoltaic devices, bio imaging and cell labeling [10-12]. In this work, Glassy carbon electrode (GCE) modified with MPA capped CdTe QDs for determination of H_2O_2 in the presence of excess amount of interfaces like oxalic acid (OA) and ascorbic acid (AA).

International Journal of
Scientific Research in Science and Technology (IJSRST)
Print ISSN : 2395-6011, Online ISSN : 2395-602X
International Conference on Advanced Materials
Held on 14, 15 December 2017, Organized by Department of Physics,
St. Joseph's College, Trichy, Tamilnadu, India

2. Experimental

2.1. Synthesis of CdTe QDs

Mercaptopropionic Acid (MPA) capped CdTe QDs is synthesis by following method. In a typical synthesis, 0.2279 g of cadmium chloride was diluted in 150 ml of double distilled water in a two-necked flask, followed by the addition of 0.2763 g of MPA and 1M of sodium hydroxide to a final pH value of 11. After that, the solution was stirred under Nitrogen gas (N_2) for 20 min. In addition to that, 0.4842 g of trisodium citrate, 0.0319 g of sodium telluride, 0.0284 g of sodium borohydride were added and refluxed under nitrogen flow (N_2) at 100°C. Subsequently the reaction mixture was heated to reflux for 3 h under N_2. Finally the resulting QD solution was mixed with propanol at the rate of 1:1 and centrifugalized at 10,000 rpm for 10 min and kept at room temperature. The sample is codes as MCQ.

2.2. Material Characterization

XRD pattern was recorded (PANalytical X-pert pro) with CuKα (1.5406 Å) in the range of 20 to 80º and FTIR spectrometer (JASCO FTIR 460 plus spectrometer) was recorded in the range of 400-3500 cm^{-1}. HRSEM image (FEI Quanta FEG 200) was taken. Optical properties like absorption and emission were studies using UV-Visible (Shimadzu 1800) and fluroscence (Floromax) spectrophotometers. Cyclic voltammetry (CV) and amperometric analyses were performed using (BioLogic SP-150) electrochemical workstation.

2.3. Preparation of the Electrode

In the three electrode system, glassy carbon electrode as a working electrode, Ag/AgCl as a reference electrode and Pt wire as a counter electrode were used and 0.1 M of phosphate buffer solution (PBS) were used as a electrolyte. For preparing MPA capped CdTe QDs (MCQ) modified GCE electrode, 1mg of MCQ powder was first dispersed in 50 µl of chitosan solution and then in 0.5 ml of ethanol and sonicated for 30 min. 5 µl of the dispersed solution was dropped on GCE electrode, dried at atmospheric air and then modified electrode was used for H_2O_2 sensing.

3. Results and Discussion

3.1. Structural and Morphological

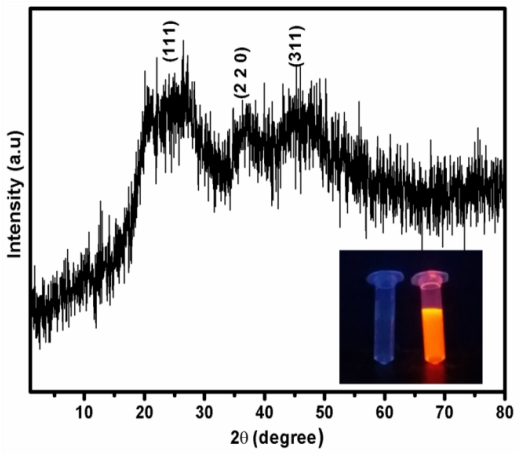

Figure 1. XRD pattern of MPA capped CdTe QDs

Figure 1 shows the XRD pattern of MPA capped CdTe QDs. The diffraction peaks centered at 23º, 39º and 46º are indexed to the (1 1 1), (2 2 0) and (3 1 1) plane respectively, for MPA of cubic CdTe lattice (JCPDS card: 65-0880) [13]. The average crystallite sizes calculated from Scherrer formula was 0.8 nm for MPA capped CdTe QDs. Figure 2. Shows the HRSEM image of MPA capped CdTe QDs with spherical shape. From the histogram, the average particle size is about 50 nm with a range dispersion of 30-90 nm for MPA capped CdTe QDs.

International Journal of
Scientific Research in Science and Technology (IJSRST)
Print ISSN : 2395-6011, Online ISSN : 2395-602X
International Conference on Advanced Materials
Held on 14, 15 December 2017, Organized by Department of Physics,
St. Joseph's College, Trichy, Tamilnadu, India

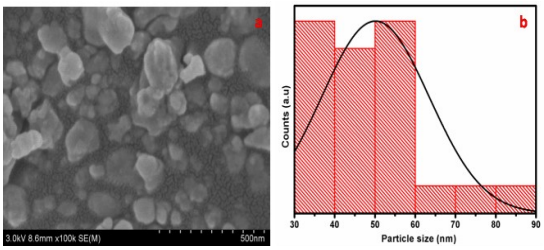

Figure 2. HRSEM image of MPA capped CdTe QDs

To identify the functional groups, FTIR spectra were taken and shown in figure 3. The infrared absorption band observed at 3445 cm^{-1} is due to the overlapping of O-H and N-H stretching. The bands at 2360 and 1586 cm^{-1} denote the existence of C-N asymmetric stretching and carbonyl group respectively. The presence of asymmetric C-H bending and C-S stretching vibrations indicated by the bands at 1384 and 676 cm^{-1} respectively [14,15].

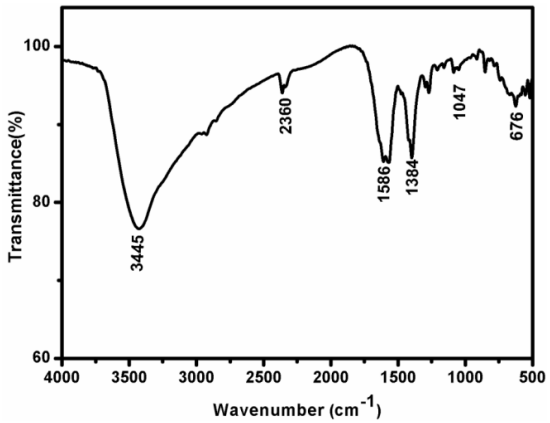

Figure 3. FTIR spectrum of MPA capped CdTe QDs

3.2. Optical Properties

Figure 4 shows the absorption and fluorescence spectra of MPA capped CdTe QDs. An absorption maximum centered at 356 nm is observed for MPA capped CdTe QDs respectively. The line width of the fluorescence spectrum is relatively narrow, and the maximum emission wavelength is 570 nm indicates the consequence of quantum confinement for an excitation wavelength of 350 nm.

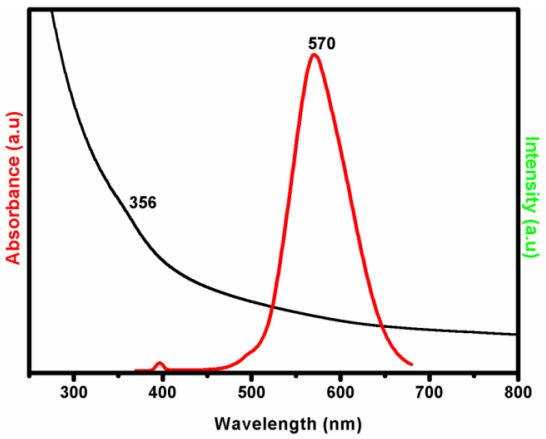

Figure 4. UV-visible spectrum of MPA capped CdTe QDs

3.3. Electrochemical Studies

3.3.1. Cyclic Voltammetry

The electrochemical characteristics of MCQ QDs were analyzed through CV using chitosan as a binder in PBS. Figure 5(a) shows the voltammograms recorded on GCE, MCQ/GCE, and MPCQ/GCE/Chitosan at a sweep rate of 40 mV/s between -1.0 to 1.0 V range. GCE bare electrode shows oxidation peak at -0.70 V and in the presence of MCQ, it shows -0.58 V and -0.57 V for MCQ/GCE/chitosan. Figure 5(b) illustrates the CV for MCQ/GCE/chitosan in deoxygnated PBS at scan rate from 20 to 100 mV/s in the potential range between -1.0 to 1.0 V. It is found that as the scan rate increases the oxidation peak current get decreased from -0.574 V to -0.570 V [16]. Figure 5(c) shows the voltammograms recorded on MCQ/GCE/chitosan in the absence and presence of H_2O_2 with different concentrations. In the absence of H_2O_2, an oxidation peak is found at -0.57 V, while adding H_2O_2 in an electrochemical cell, a decrease is found at -0.63 V. On increasing the H_2O_2 concentration, the redox peak current gets decresed [2].

International Journal of
Scientific Research in Science and Technology (IJSRST)
Print ISSN : 2395-6011, Online ISSN : 2395-602X
International Conference on Advanced Materials
Held on 14, 15 December 2017, Organized by Department of Physics,
St. Joseph's College, Trichy, Tamilnadu, India

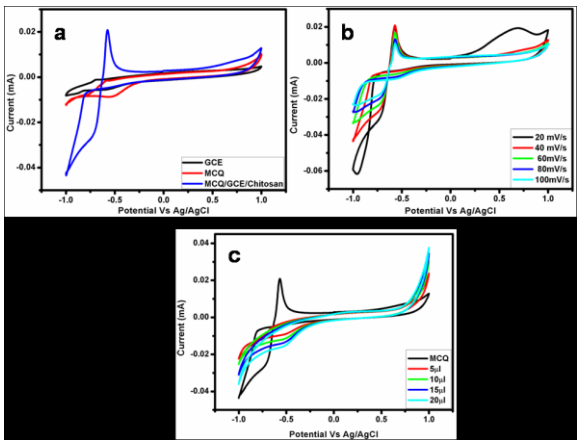

Figure 5(a). CV for bar GCE, GCE/MCQ, GCE/MCQ/chitosan (b) CV of different GCE/MCQ/chitosan at different scan rate (c) CV for GCE/MCQ/chitosan with different concentration of H_2O_2 for MPA capped CdTe QDs

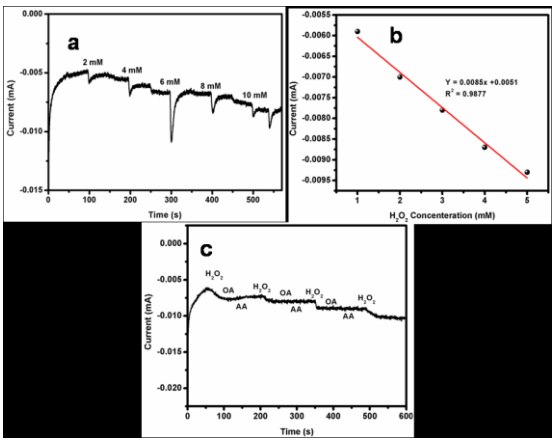

Figure 6 (a). Amperometric analysis for different concentration of H_2O_2 (b) linear relation between current and H_2O_2 concentration (c) Amperometric analysis with the addition of H_2O_2, OA and AA for MPA capped CdTe QDs

3.3.2. Amperometric Biosensors

Amperometric response to H_2O_2 is shown in Figure 6(a). While maintaining PBS in a stirring condition, different concenteration of H_2O_2 are added at regular intervals. The amperometric analysis was studied on the chemically modified electrode by applying constant potential of -0.4 V. The amperometric responses were linearly increased in the concenteration range of 0.67-8.04 µM with the correlation coefficient 0.9877. With the addition of H_2O_2 into the electrolyte solution and the catalytic current increases and reaches its steady state within 5 s and a plot between H_2O_2 and current exhibits good linearity figure 6(b). The MCQ sensitivity and detection limit of sensor were calculated to be 0.2833 mA $mM^{-1}cm^{-2}$ and 6.7 µM respectively. The Limit of Detection of the sensor was calculated by using the formula is $3s_b/S$ where, s_b is the standard deviation of blank signal and S is the sensitivity [17].

The selectivity of the sensor to the determination of H_2O_2 has been investigated in the presence of likely interfering agents. Figure 6(c) showed the amperometric response of the electrode towards 0.67 µM of H_2O_2, OA, AA. The electrode quickly responded to H_2O_2 however, it was insensitive the other species. On the contrary, a rapid and large decrease in current response is observed with the subsequent addition of H_2O_2, suggesting a excellent selectivity of MCQ for H_2O_2 sensor.

4. Conclusion

MPA capped CdTe QDs were prepared by reflux method. XRD confirms the zinc blende cubic structure of CdTe QDs and the average crystallite sizes is 0.8 nm for MPA capped CdTe QDs. HRSEM image show the spherical particles and from the histogram, the average particle sizes is 50 nm for MPA capped CdTe QDs. MCQ electrode exhibits an excellent non-enzymatic electrocatalytic activity towards H_2O_2 in CV experiments. The fabricated sensor exhibits a linear range from 0.67-8.04 µM with a sensitivity of 0.2833 mA $mM^{-1}cm^{-2}$ with a

linear coefficient of 0.9877. The sensor shows detection limit of 6.7 μM for the determination of H_2O_2. The MCQ sensor holds great potential for the fabrication of electrochemical sensing applications.

5. References

[1] S. Kogularasu, M. Govindasamy, S. M. Chen, M. Akilarasan, V. Mani, "3D graphene oxide-cobalt oxide polyhedrons for highly sensitive non-enzymatic electrochemical determination of hydrogen peroxide", Sensors and Actuators B: Chemical, Volume 253, December 2017, Pages 773-783.

[2] C. Revathi, G. Mohan Rao, R.T. Rajendra Kumar, "Synthesis and electrocatalytic properties of manganese dioxide for non-enzymatic hydrogen peroxide sensing", Materials Science in Semiconductor Processing, Volume 31, March 2015, Pages 709-714.

[3] K.J. Babu, A. Zahoor, K.S. Nahm, R. Ramachandran, M.A. Jothi Rajan, G. Kumar, "The influences of shape and structure of MnO_2 nanomaterials over the non-enzymatic sensing ability of hydrogen peroxide", Journal of Nanoparticle Research, Volume 16, February 2014, 2250.

[4] M. Manikandan, S. Dhanuskodi, N. Maheswari, G. Muralidharan, C. Revathi, R.T. Rajendra Kumar, G. Mohan Rao, "High performance supercapacitor and non-enzymatic hydrogen peroxide sensor based on tellurium nanoparticles", Sensing and Bio-Sensing Research, Volume 13, April 2017, Pages 40-48.

[5] M.R. Guascito, D. Chirizzi, C. Malitesta, T. Siciliano, A. Tepore, "Te oxide nanowires as advanced materials for amperometric nonenzymatic hydrogen peroxide sensing", Talanta. 2013 Oct 15; 115: 863-9.

[6] W. Jia, M. Guo, Z. Zheng, T. Yu, E.G. Rodriguez, Y. Wang, Y. Lei, "Electrocatalytic oxidation and reduction of H_2O_2 on vertically aligned Co_3O_4 nanowalls electrode: Toward H_2O_2 detection", Journal of Electroanalytical Chemistry, Volume 625, Issue 1, 1 January 2009, Pages 27-32.

[7] X. Li, X. Liu, W. Wang, L. Li, X. Lu, "High loading Pt nanoparticles on functionalization of carbon nanotubes for fabricating nonenzyme hydrogen peroxide sensor", Biosens Bioelectron, 15 September 2014, Volume 59, 221-6.

[8] M. Roushani, M. Shamsipur, H.R. Rajabi, "Highly selective detection of dopamine in the presence of ascorbic acid and uric acid using thiolglycolic acid capped CdTe quantum dots modified electrode", Journal of Electoanalytical Chemical, Volume 712, January 2014, Pages 19-24.

[9] H. Beitollahi, M. Hamzavi, M. T. Mahani, M. Shanesaz, H. K. Maleh, "A Novel Strategy for Simultaneous determination of Dopamine and Uric Acid using a Carbon Paste Electrode Modified with CdTe quantum dots", Electroanalysis, Volume 27, February 2015, Pages 524 – 533.

[10] T. Zhang, X. Sun, B. Liu, "Synthesis of positively charged CdTe quantum dots and detection for uric acid", Spectrochimca Acta, Part A: Molecular and Biomolecular Spectroscopy, Volume 79, September 2011, Pages 1566-1572.

[11] M. Asha Jhonsi, R. Reganathan, "Investigations on the photoinduced interaction of water soluble thiolglycolic acid (TGA) capped CdTe quantum dots with certain porphyrins", Journal of

Colloid and Interface Science, Volume 344, 15 April 2010, Pages 596 – 602.

[12] R.M. Rezaei, H. Razmi, H.A. Zadeh, "D-penicillamine capped CdTe Quantum Dots as a novel fluorometric sensor of copper(II), Lumiescence, Volume 28, July/August 2013, Pages 503-509.

[13] J. Duan, L. Song, J. Zhan, "One-pot synthesis of highly luminescent CdTe quantum dots by microwave irradiation reduction and their Hg^{2+}-sensitive properties", Nano Research, Volume 2, January 2009, Pages 61-68.

[14] T. Pazhanivel, D. Nataraj, V. P. Devarajan, V. Mageshwari, K. Senthil, D. Soundarajan, "Improved sensing performance from methionine capped CdTe and CdTe/ZnS quantum dots for the detection of trace amounts of explosive chemicals in liquid media", Analytical Methods, Volume 5, 2013, Pages 910-916.

[15] H. Kumar, R. Srivastava, P. K. Dutta, "Highly luminescent chitosan-L-cysteine functionalized CdTe quantum dots film: Synthesis and characterization", Carbohydrate. Polymers, Volume 97, September 2013, Pages 327-334.

[16] S. Palanisamy, S. Cheemalapati, S.M. Chen, "Highly sensitive and selective hydrogen peroxide biosensor based on hemoglobin immobilized at multiwalled carbon nanotubes-zinc oxide composite electrode", Analytical Biochemistry, Volume 429, October 2012, Pages 108-115.

[17] M. Govindasamy, V. Mani, S.M. Chen, R. Karthik, K. Manibalan, R. Umamaheswari, "MoS_2 Flowers Grown on Graphene/Carbon Nanotubes: a Versatile Substrate for Electrochemical Determination of Hydrogen Peroxide, International Journal of Electrochemical Science, Volume 11, April 2016, Pages: 2954-2961.

International Journal of
Scientific Research in Science and Technology (IJSRST)
Print ISSN : 2395-6011, Online ISSN : 2395-602X
International Conference on Advanced Materials
Held on 14, 15 December 2017, Organized by Department of Physics,
St. Joseph's College, Trichy, Tamilnadu, India

Microwave Synthesis Titanium Doped Zinc Oxide for Solar Cell Application

Vignesh P[1], Kanikairaj B[1]

[1]Department of Physics, St. Joseph's College (Autonomous), Tiruchirappalli-620 002, India

Corresponding Author: bmkgaa@gmail.com

Abstract

In this study the Titanium doped Zinc oxide nanoparticles were successfully synthesized by exposing microwave for 3min with 800W power. 1 mole of Ti concentration were doped into ZnO. Detailed crystal and local atomic structure of synthesized samples were characterized via X-ray diffraction. Obtained Ti doped ZnO nanoparticles degraded with increasing Ti content. The grain size of the Ti doped ZnO is also determined. These studies clearly suggest that microwave synthesis make fast and homogeneous reactions, to synthesis highly crystalline nano sized Ti doped ZnO nanoparticles. Solar cell is one of the best applications in future.

Keywords: Titanium doped Zinc Oxide, Nano particles, Microwave synthesis, Solar Cell applications.

1. Introduction

ZnO is a semiconductor with a wide and direct band gap (Eg: 3.2–3.4 eV at 300 K), excellent chemical and thermal stability, and specific electrical and optoelectronic property of having a large exaction binding energy (60 meV)[1]. It has recently gained much interest because of its potential use in many applications, ranging from transparent conductive contacts, solar cells, laser diodes, ultraviolet lasers, thin film transistors, optoelectronic and piezoelectric applications to surface acoustic wave devices.

However, un-doped ZnO usually contains various intrinsic defects such as Zn vacancies, interstitial Zn, O vacancies, interstitial O, and antisite O. These intrinsic defects form either acceptor level or donor level in the band gap that would greatly affect the luminescent properties of ZnO. In order to improve this deficiency, many researchers have investigated how the electrical and optical properties of ZnO films are manipulated by doping with metallic elements. Ti-doped ZnO films, in comparison with the ZnO films doped with Group III elements, have more than one charge valence state. This means Ti-doping can create more free electrons and enhance N-type conductivity. The electrical and optical properties of Ti doped ZnO films have also been extensively investigated. The Reported statement is that the resistivity of Ti-doped ZnO films decreases with the increasing of the Ti-doping amount. Ti-doped ZnO films have a wide optical energy band gap (3.29–3.86 eV) and relatively low resistivity. Conclude that Ti incorporated within the ZnO thin films increased optical transmittance and electrical resistivity such as UV-light emitting diodes or laser diodes. However, detailed studies on the optical properties of ZnO films have not yet been performed. In this paper, undoped and Ti-doped ZnO thin films were prepared on glass substrates via radio frequency reactive magnetron sputtering technique. The crystal structures, optical transmission in Ti-doped ZnO films were systematically investigated via X-ray diffraction, and ultraviolet visible spectrophotometer.

International Journal of
Scientific Research in Science and Technology (IJSRST)
Print ISSN : 2395-6011, Online ISSN : 2395-602X
International Conference on Advanced Materials
Held on 14, 15 December 2017, Organized by Department of Physics,
St. Joseph's College, Trichy, Tamilnadu, India

2. Experimental Procedure

To prepared the undoped zinc oxide (ZnO) nanoparticles by adding 1 mole zinc nitrate hexahydrate ($Zn(Ni_3)_2$). $6H_2O$ and 2g of NaOH into 100ml distilled water. For Ti(ZnO) nanoparticles, Titanium tetra isopropoxide ($C_{12}H_{28}O_4Ti$) was added into 75ml of ethanol solution to serve as the Titanium source[4]. The atom content of Titanium will be added in the concentration of 1% into 25ml of distilled water. The solution is treated in microwave oven for 3 minutes at 800W. The treated solution is filtered with the help of filter papers. After this method the filtered salt is dried in hot air oven for 4Hours. The dried salt is collected and then grinded. The Titanium doped Zinc oxide is prepared.

3. Calculation

1mole of zinc nitrate hexa hydrate

= (molecular weight / 1000) × solvent.
= (297.49 / 1000) × 100
=29.749 g

1% Titanium tetra isopropoxide calculation is

Titanium tetra isopropoxide	=10ml
Distilled Water	= 50ml
Ethanol	= 75ml

4. Result and Discussion

4.1. FTIR Analysis

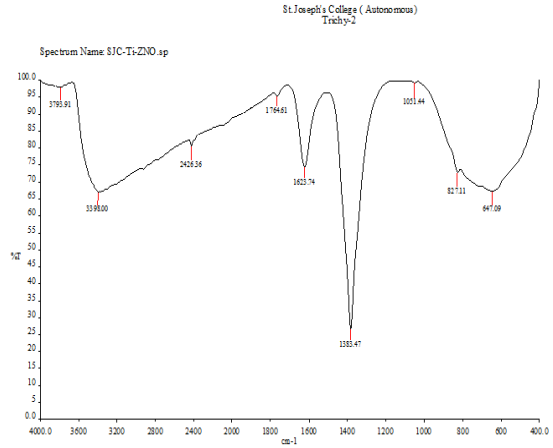

Figure 4.1. FTIR spectrum of Ti doped ZnO

To analyze qualitatively the presence of the functional in titanium doped Zinc Oxide was recorded using spectrum FTIR spectrometer in the range 400-4000 cm^{-1}.

The obtained FTIR value:
3793.91- monomeric-alcohols
3398.0 - hydrogen – bonded - alcohols, phenols
2426.36- nitrites
1764.61- aldehydes, ketones, carboxylic acids, esters
1623.74- nitro compounds
1383.47- amines
1051.44 - amines
827.11 - phenyl ring substitution overtones
647.09 - Ti=Zn=O

4.2. UV–Visible Spectrum

4.2.1. Determination of Band Gap

The UV-Vis absorption spectra of Titanium doped Zinc oxide is shown in figure. The sharp characteristic peak at 356nm indicates the presence of TZO nanostructure. The band gap of the zinc oxide nanoparticle changed with titanium doping. This changes lead to the reduction in band gap of the nanoparticle.

International Journal of
Scientific Research in Science and Technology (IJSRST)
Print ISSN : 2395-6011, Online ISSN : 2395-602X
International Conference on Advanced Materials
Held on 14, 15 December 2017, Organized by Department of Physics,
St. Joseph's College, Trichy, Tamilnadu, India

4.2.2. Optical Band Gap Energy

In order to determine the value and type of energy gap as well as the dominant absorption processes in such material, the relation $E_g = h\gamma = hc/\lambda$ eV is used.

The band gap values are determined from the equation: $E_g = 1240/\lambda$ eV .where, E_g is the band gap energy, λ is the maximum wavelength E_g = 3.48eV. Band gap of Titanium doped Zinc Oxide is found to be 3.48eV.

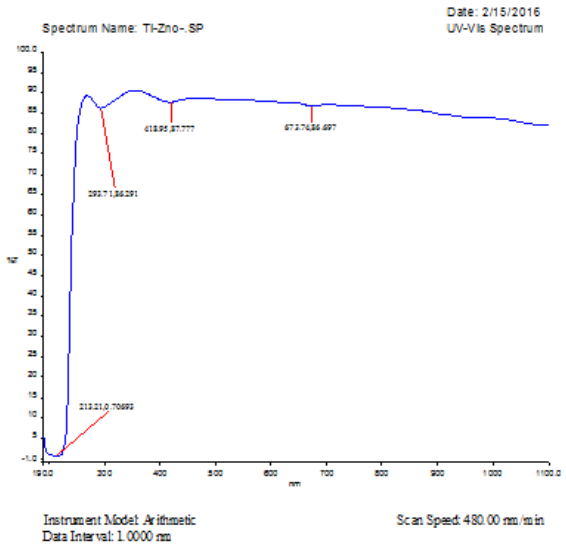

Figure 4.2. Emission Spectrum of UV-Visible Spectrum

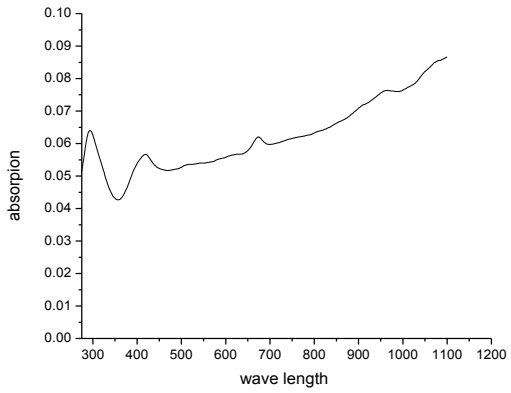

Figure 4.3. Absorption spectrum of UV-Visible Spectrum

4.3. XRD Analysis

Titanium doped zinc oxide nanoparticles were subjected to powder X-ray diffraction analysis using diffractometer system XPERT-PRO with mono chromatic nickel filtered Titanium doped zinc oxide radiation of wavelength 1.54060Å. The spectrum is plotted between the intensity of light and angle 2θ in the range of as shown in figure. The result is agreed with the literature (JCPDS card No: 82-1438). The lattice constants A and C for Titanium doped Zinc Oxide nanoparticles were found to be 5.992 and 8.426 respectively.

The obtained XRD values (PCPDF Card No: 82-1438)

are λ = 1.54060 Å

A = 5.992

C = 8.426

Crystal structure: Tetragonal

Grain size of the material

Grain size (D) = $(0.9\lambda / \beta \cos\theta)$

Where,

D is the grain size of the sample

B is full width half maximum (FWHM)

θ is the diffraction angle

λ is the wavelength of copper K_α line (1.54 Å)

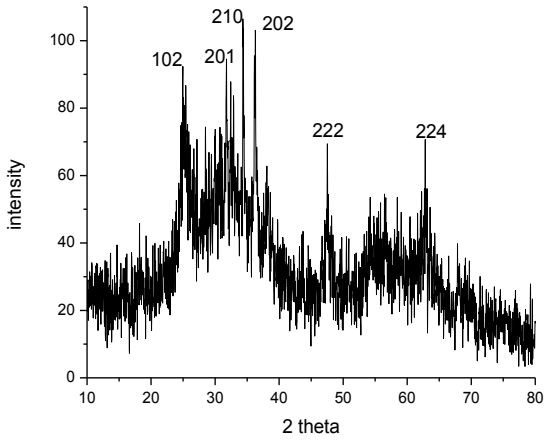

Figure 4.4. XRD of Ti doped ZnO nanoparticles.

International Journal of
Scientific Research in Science and Technology (IJSRST)
Print ISSN : 2395-6011, Online ISSN : 2395-602X
International Conference on Advanced Materials
Held on 14, 15 December 2017, Organized by Department of Physics,
St. Joseph's College, Trichy, Tamilnadu, India

Table 1. Grain Size of Ti doped ZnO Nanoparticles

POSITION 2θ (degree)	GRAIN SIZE D (nm)	h k l
25.171	11.45	1 0 2
31.811	24.25	2 1 0
34.380	19.69	2 1 0
34.230	17.02	2 0 2
47.659	24.07	2 2 2
62.766	45.46	2 2 4

5. Conclusion

Titanium doped zinc oxide nanoparticle were prepared by microwave method technique utilizing titanium tetra isopropoxide and zinc nitrate hexa hydrate. Also the effect of dopant concentration, optical and structural properties of the nanoparticle has been studied.

The optical measurements show that transmittance improves with doping of titanium (concentration of 1%). The optical band gap value of the titanium doped zinc oxide nanoparticle is calculated from the transmission data shows a value of 3.48eV which is nearly matches with the standard value of 3.4-3.7eV. Also evident from X-ray diffraction analysis, TZO in nanoparticle prepared in 3min at 800watts power in 1% of titanium concentration are tetragonal crystalline in nature.

The transparency of Titanium doped zinc oxide nanoparticle in the visible region is around 85%. Since the TZO nanoparticles are highly transparent, it can be widely used in solar cell application. There is a lot of scope for future work in these materials.

6. References

[1] Surya Prakashghosh, "Synthesis and Characterization of zinc oxide nanoparticles by sol-gel process", National Institute of Technology, Rourkela-769008, Orissa, India, May-2012.

[2] Robinaashraf, Sairariaz, Muhammad khaleeq-ur-rehman and Shahzadnaseem, "Synthesis and Characterization of ZnO Nanoparticles", The 2013 World Congress on Advances in Nano, Biomechanics, Robotics and Energy Research, Seoul Korea, August 25- 28, 2013.

[3] Surabhisivakumar, Putcha Venkateswarlu, Vanka Rangarao and Gollapalli Nageswararao, Synthesis, Characterization and Optical properties of Zinc Oxide Nanoparticles, Kumar et al. international nano letters 2013.

[4] Muneer M. Ba-Abbad, Abdul Amir H. Kadhum, Abu Bakar Mohamad, Mohd S. Takriff, Kamaruzzaman Sopian, "Synthesis and Catalytic Activity of TiO_2 Nanoparticles for Photochemical Oxidation of Concentrated Chlorophenols under Direct Solar Radiation", International Journal of Electrochemical Science, 1 June 2012.

[5] Ladislav Kavan, Brian O'Regan, Andreas Kay and Michael Grgtzel, "Preparation of TiO, (anatase) films on electrodes by anodic oxidative hydrolysis of TiCl", Electroanal. Gem., 346 (1993) 291-307.

[6] Masahiko Hiratani, Masaru Kadoshima, Tatsumi Hirano, Yasuhiro Shimamoto, Yuichi Matsui, ToshihideNabatame, Kazuyoshi Torii, Shinichiro Kimura, "Ultra-thin titanium oxide film with a rutile-type structure", Applied Surface Science 207 (2003) 13–19.

[7] A. Bendavid, P.J. Martin, A. Jamting, H. Takikawa, "Structural and optical properties of titanium oxide thin films deposited by filtered arc

deposition", Thin Solid Films 355-356 (1999) 6-11.

[8] Gabriella Di Carlo, Giuseppe Calogero, Marco Brucale, Daniela Caschera, Tilde de Caro, Gaetano Di Marco, Gabriel M. Ingo, "Insights into meso-structured photoanodes based on titanium oxide thin film with high dye adsorption ability", Journal of Alloys and Compounds 609 (2014) 116–124.

[9] Ya-Qi Hou, Da-Ming Zhuang, Gong Zhang, Ming Zhao, Min-Sheng Wu, "Influence of annealing temperature on the properties of titanium oxide thin film", Applied Surface Science 218 (2003) 97–105.

[10] M. Fusi, V. Russo, C.S. Casari, A. Li Bassi, C.E. Bottani, "Titanium oxide nanostructured films by reactive pulsed laser deposition", Applied Surface Science 255 (2009) 5334–5337.

International Journal of
Scientific Research in Science and Technology (IJSRST)
Print ISSN : 2395-6011, Online ISSN : 2395-602X
International Conference on Advanced Materials
Held on 14, 15 December 2017, Organized by Department of Physics,
St. Joseph's College, Trichy, Tamilnadu, India

Synthesis and Characterization of Cerium doped $CaMnO_3$ Nanoparticles

S. Berbeth Mary, A. Leo Rajesh*

Department of Physics, St. Joseph's College (Autonomous), Tiruchirappalli-620 002, Tamil Nadu, India

*corresponding author: E-mail address: aleorajesh@gmail.com;

Tel.:+91-944412207

Abstract

Nanostructured cerium doped calcium manganite $Ca_{1-x}Ce_xMnO_3$ (x=0.0, 0.1, 0.2, 0.3, 0.4, 0.5) samples were synthesized successfully using the citric acid complexing coupled with hydrothermal method followed by annealing at 900°C. Powder X-ray diffraction (XRD) analysis showed that the single phases of orthorhombic pervoskite structure of $CaMnO_3$ and the cell volume increased from undoped to cerium doped $CaMnO_3$ structure due to the ionic radius of added R^{3+} cations. The crystallinity decreased with increased concentration of Ce^{3+} doping and the average crystallite size was about 10-20 nm. Sphere like nanoparticles observed by the scanning electron microscopy. FTIR analysis showed a strong peak around 600 cm^{-1} revealed the formation of pervoskite oxides and the obtained band gap was 3.56 eV.

Keywords: calcium manganite, hydrothermal, single phase, pervoskite oxide

1. Introduction

The development of environmental friendly and cost effective power sources overcomes the problems of energy crises and global warming. Thermoelectric power generation is a promising method by converting waste heat directly into electricity without any greenhouse gas emission. The conversion efficiency is measured by the dimensionless figure of merit

$$ZT = \left(\frac{S^2\sigma}{k}\right)T$$

where S, σ, K, T are seebeck coefficient, electrical conductivity, thermal conductivity and absolute temperature respectively. Good thermoelectric materials should have large seebeck coefficient, high electrical conductivity and low thermal conductivity where large electrical conductivity minimize joule heating while low thermal conductivity maintains temperature gradient between the hot and cold sides in thermoelectric device. The intermetallic materials such as Bi_2Te_3 and $CoSb_3$ have high ZT at low temperatures. However, they are toxic, rare and degrade at high temperatures under air [1]. Besides, thermoelectric materials are required to be stable at higher temperatures. Oxides are one of the best candidate materials for this requirement but most oxides with high stability at high temperature in air are unsuitable for thermoelectric applications due to high electrical resistivity. These limitations were overcomed by the discovery of Na_xCoO_2 with a high seebeck coefficient (100mV/K at 300 K) and a low electrical resistivity (0.2 m Ω at 300K) by Terasaki et al in 1997 [2].

The interesting physical properties such as electrical, electrochemical, magnetic, superconducting and thermoelectrical make them great candidates in various energy storage applications like supercapacitor, solid oxide fuel cells and thermoelectric devices [3-5]. Several pervoskite type oxides are well known as highly conductive ceramics whereas $CaMnO_3$ based oxides are the major n-type thermoelectric oxide which produces granular fine particles with high chemical and thermal stability. The undoped

International Journal of
Scientific Research in Science and Technology (IJSRST)
Print ISSN : 2395-6011, Online ISSN : 2395-602X
International Conference on Advanced Materials
Held on 14, 15 December 2017, Organized by Department of Physics,
St. Joseph's College, Trichy, Tamilnadu, India

$CaMnO_3$ has poor TE property due to the high electrical resistivity whereas calcium substitution with various rear earth elements can enhance the carrier mobility which progress the electrical conductivity [6]. The thermoelectric performance of pervoskite type oxides can be enhanced by doping, band engineering and nanostructuring [7]. Reduction of thermal conductivity can be accomplished by nanotailoring with controlled grain size. $Ca_{1-x}Re_xMnO_3$ can be successfully synthesized by various bottom up methods such as chemical combustion, sol-gel, coprecipitation, hydrothermal method and so on [8-11]. Here citric acid complexing coupled with hydrothermal method has been employed to obtain high purity, homogenous, environmental friendly and fine particles with controlled grain size [12 -14].

$CaMnO_3$ based thermoelectric materials has high seebeck coefficient but the dimensionless figure of merit is low because of low electrical conductivity. N- type doping at A-site (Ca), B-site (Mn) and dual doping at both sites has been done to improve the TE property, while A- site rare earth elements doping shows the enhancement in ZT values [15-18]. In rare earth doped manganite, dopant occupies either A-site or B-site depending on its radius. Doping cerium in $CaMnO_3$, Ce occupies the A-site and raises the Thermoelectric (TE) performance by strongly reducing the resistivity [19]. In this paper, the effects of Ce substitution on nanostructured n-type thermoelectric oxide $Ca_{1-x}Ce_xMnO_3$ (CCMO) samples are systematically studied.

2. Materials and Methods

$Ca_{1-x}Ce_xMnO_3$ (x=0.0, 0.1, 0.2, 0.3, 0.4, 0.5) powders were prepared using the strategy of citric acid complexing coupled with hydrothermal method. Stoichiometric amounts of nitrates such as cerium, calcium, manganese and equal amount of citric acid (metal/citric acid molar ratio = 1/1) were dissolved in deionized water to obtain homogeneity in the metal ions. A certain amount of ammonia solution was added drop wise to the above mixed solution. Part of ammonia added to neutralize the unreacted citric acid. When the pH value of the solution reached around 9.2 a sol was obtained. This sol was transferred to a 150 ml stainless steel autoclave was placed it in hot air oven at 200 °C for 20 hr. once the assigned time was over the oven was switched off and allowed to cool down to room temperature. The obtained products were in turn filtered, washed with deionized water and ethanol, filtered again, and dried around 120 °C overnight. The dried powders were well ground and annealed in air at 900 °C for 4 hr.

Crystal structure and phase identification were determined by Powder X-ray diffraction (XRD) and data were collected using a XRD diffractometer (D8 Advanced) with CuKα radiation (λ =0.15406 nm). The surface morphology was observed with scanning electron microscopy (SEM). Fourier transform infrared (FTIR) spectra of the powder samples were recorded from 4000 to 400 cm^{-1} using a Fourier transform infrared spectrometer (Perkin Elmer) equipped with a KBr beam splitter. The optical properties of the nanoparticles were characterized by UV-Vis spectroscopy Lambda 35 UV-Vis spectrometer.

3. Results and Discussion

The yellowish colour of the manganese nitrate solution is turned into bluish when pH value of the solution reached to 9.2. After centrifugation and drying, the powder is darkish due to the presence of different manganese valance states [20]. Figure 1

International Journal of
Scientific Research in Science and Technology (IJSRST)
Print ISSN : 2395-6011, Online ISSN : 2395-602X
International Conference on Advanced Materials
Held on 14, 15 December 2017, Organized by Department of Physics,
St. Joseph's College, Trichy, Tamilnadu, India

represents the XRD patterns of annealed undoped and doped $CaMnO_3$ powders. They clearly demonstrate the single phase of orthorhombic pervoskite structure of $CaMnO_3$ which is matching with JCPDS Card no 76-1133 with space group Pnma, indicating that annealing under oxygen atmosphere leads to the formation of $CaMnO_3$ structure [21]. The strong doublet of the main pervoskite peak in the 2θ region, 33° of the CCMO nanostructure exhibited a tendency to unify with increasing the doping concentration [22, 23]. Fig 1(d) shows that there is shift in peaks due to the release of large volume of gases while annealing.

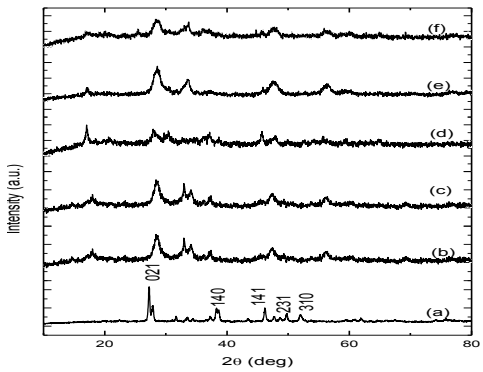

Figure 1. XRD Pattern of $Ca_{1-x}Ce_xMnO_3$ (x = 0.0, 0.1, 0.2, 0.3, 0.4, 0.5) samples

The average grain size of the synthesized samples are calculated from the major diffraction peaks using the Scherrer formula $D = K\lambda/\beta\cos\theta$, where K is constant (K = 0.94), λ is the wavelength (1.5406 Å). θ is the Bragg angle; β is full width half maximum that is, broadening due to the crystallite dimensions [24]. The average grain size of the prepared samples is in the range of 10-20 nm. Partial substitution of Ce^{3+} (Ln^{3+}) for Ca^{2+} decreases the average grain size with increasing the cerium concentration [25-27].

Figure 2 shows SEM images of undoped and cerium doped $CaMnO_3$ samples. It can be seen that all the samples shows a porous nature. This porous morphology is attributed to the release of a large volume of gases during the synthetic process due to the addition of citric acid as chelating agent and post heating treatment. The majority of the particles are nearly round shaped and the others are elongated. The average size of spherical particles deduced from SEM lies in the range of few nanometers. Microstructures of cerium doped samples are downgraded, which is associated with the most decrease of electrical conductivity. The decrease of electrical conductivity leads to a decrease of κ_e, which is due to the partial substitution of Ce^{3+} for Ca^{2+}, the decrease of κ_{total} can be mainly attributed to the reduction of lattice contribution arising from incorporation of heavier Ce^{3+} ions in the structure as compared to Ca^{2+} ions [28] ($\kappa_{total} = \kappa_{ph} + \kappa_e$, where κ_e and κ_e are the thermal conductivity due to lattice and electronic contribution) which leads to the enhancement in thermo power S.

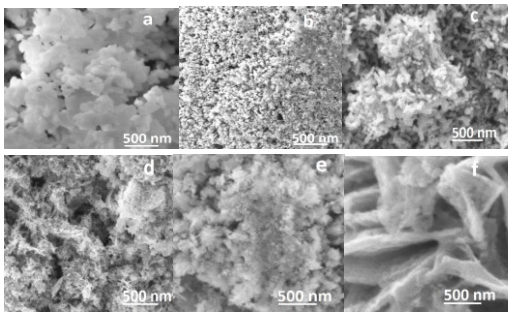

Figure 2. SEM Micrograph of $Ca_{1-x}Ce_xMnO_3$ (x = 0.0, 0.1, 0.2, 0.3, 0.4, 0.5) samples

The FTIR study is carried out to correlate the relative change in the high frequency stretching mode and mid frequency bending mode with the bond lengths and consequently to the unit cell volume [29, 30]. Figure 3 shows the FTIR spectra of CCMO nanoparticles. The typical peak of CCMO nanoparticle is observed around 500-600 cm^{-1}. The symmetric stretching occurs about 800 cm^{-1} indicates the vibration of NO_3^{-1} ions. The strong

International Journal of
Scientific Research in Science and Technology (IJSRST)
Print ISSN : 2395-6011, Online ISSN : 2395-602X
International Conference on Advanced Materials
Held on 14, 15 December 2017, Organized by Department of Physics,
St. Joseph's College, Trichy, Tamilnadu, India

asymmetric stretching mode of vibration of C=O is observed around 1300-1500 cm^{-1}. The band at 3500 cm^{-1} corresponds to O-H mode of vibration [31,32].

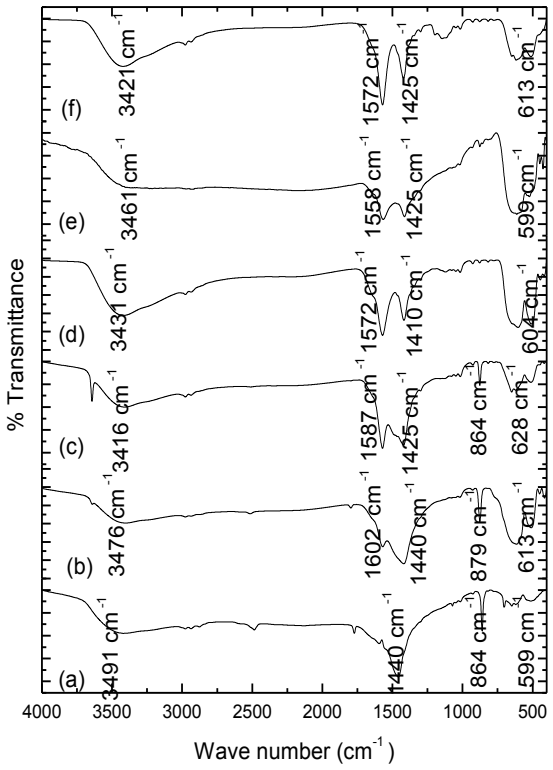

Figure 3. FTIR Spectra of $Ca_{1-x}Ce_xMnO_3$ (x = 0.0, 0.1, 0.2, 0.3, 0.4, 0.5) samples

Figure 4(a) shows UV-Visible spectra of $Ca_{1-x}Ce_xMnO_3$ nanoparticles. The absorption peaks are around 300 cm^{-1}. When the concentration of cerium increases peak value also increases. The band gap E_g can be calculated from the equation

$$(\alpha h\upsilon)^n = B(h\nu - E_g)$$

where α is absorption coefficient, $h\nu$ is the photon energy, B is constant, and n can be either 1/2 or 2 for indirect and direct transitions respectively [33]. The $(\alpha h\nu)^2$ versus $h\nu$ curve is shown in figure 4(b) and it is found to be 3.56 eV which is good agreement with the optimum value. These results show that this material it is suitable for thermoelectric application.

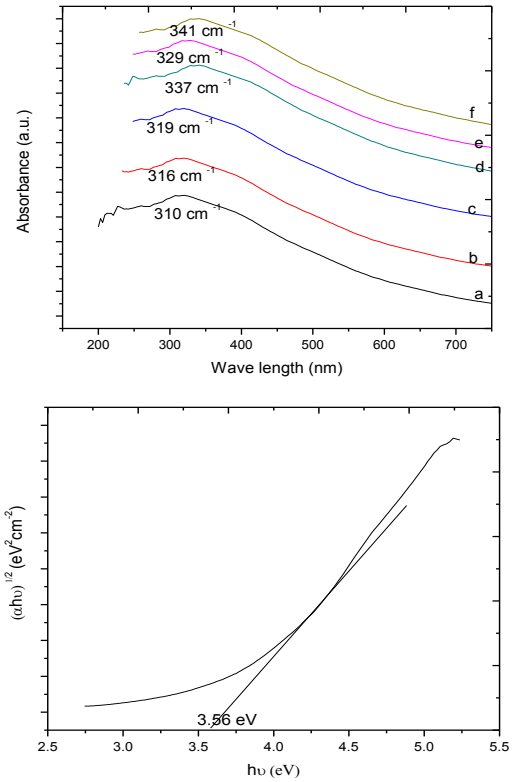

Figure 4(a). UV- Visible Spectra of $Ca_{1-x}Ce_xMnO_3$ (b) Band gap determination

4. Conclusion

This work exhibited that Cerium is a suitable alternative material for Ca in $Ca_{1-x}Ce_xMnO_3$,, here the concentration was ($x \leq 0.5$) in which there is no chance in the crystal structure and the improved thermoelectric properties were obtained using citric acid complexing coupled with hydrothermal method. Crystalline and single phase structure of the nanoparticle was observed for all the samples. The observed porous nanoparticles lead to the connectivity in microstructure due to chelating reagent. The peaks at 600 cm^{-1} concluded the presence of Cerium doped $CaMnO_3$ nanoparticle and the band gap energy was calculated t o be 3.56 eV. The crystalline nature, porosity and low band

International Journal of
Scientific Research in Science and Technology (IJSRST)
Print ISSN : 2395-6011, Online ISSN : 2395-602X
International Conference on Advanced Materials
Held on 14, 15 December 2017, Organized by Department of Physics,
St. Joseph's College, Trichy, Tamilnadu, India

gap nature of these samples confirms that it is suitable for thermoelectric application. Sphere shaped surface morphology was observed for majority of the samples. The chelating agent played major role obtains the reduced particle size and good porous nature of the material.

References

[1] G. Chen, M. S. Dresselhaus, D. Dresselhaus, J.P. Fleurial, T. Caillat, Int. Mater. Rev., 48, 45 (2003).

[2] J. Pei, G. Chen, N. Zhou, D.Q. Lu, F.Q Xiao, Physica B., 406, 571 (2011)

[3] M.A. Pena, J.L.G. Flerro, Chem. Rev., 101, 7 (2001)

[4] E. Konysheva, J.T.S. Irvine, J. Mater. Chem., 18, 5147 (2008).

[5] F. Azough, C. Leach, R. Freer, J. Eur. Ceram. Soc., 26, 10 (2006).

[6] J. Dho, W.S. Kim, E.O. Chi, N.H. Hur, S.H. Park, H.-C. Ri, Solid State Commun., 125, 143 (2003)

[7] Michitaka Ohtaki, Hisako Koga, Tsutomu Tokunaga, Koichi Eguchi, Hiromichi Arai, J. Solid State Chem., 120, 105 (1995)

[8] R.V. Mangalaraja, J. Mouzon, P. Hedström, I. Kero, K.V.S. Ramam, C.P. Camurri, M. Odén, J. Mater. Process. Technol., 208 415 (2008)

[9] N.P. Bansal, J. Mater. Sci. 27, 2922 (1992)

[10] C.S. Sanmathi, Y. Takahashi, D. Sawaki, Y. Klein, R. Retoux, I. Terasaki, J.G. Noudem, Mater. Res. Bull., 45, 558 (2010)

[11] Jianrong Niu, Jiguang Deng, Wei Liu, Lei Zhang, Guozhi Wang, Hongxing Dai, Hong He, Xuehong Zi, Catal. Today., 126, 420 (2007)

[12] Yoshimura M, Yoo S. E, Hayashi M, Ishizawa N, J. Appl. Phys., 28, 2007 (1989)

[13] Sridhar Komarneni , Young Dong Noh , Joo Young Kim , Seok Han Kim , Hiroaki Katsuki, Naturforsch., 65b, 1033 (2010)

[14] A. Pathak , P. Pramanik, Pinsa., 67, 47 (2001)

[15] T. Okuda, Y. Fujii, J. Appl. Phys., 108, 103702 (2010)

[16] D. Sousa, M.R. Nunes, C. Silveira, I. Matos, A.B. Lopes, M.E. Jorge, Mater. Chem. Phys., 109, 311 (2008)

[17] G. Xu, R. Funahashi, Q. Pu, B. Liu, R. Tao, G. Wang, Z. Ding, Solid State Ionics., 171, 147 (2004).

[18] Y.H. Zhu, C.L. Wang, W.B. Su, J.C. Li, J. Liu, Y.L. Du, L.M. Mei, Ceram. Int., 40, 15531 (2014)

[19] Mohamed Mouyane, Brahim Itaalit, Jérôme Bernard, David Houivet, Jacques G. Noudem, Powder Technology., 264 ,71 (2014)

[20] Ma R, Takada K, Fukuda K, Iyi N, Bando Y, Sasaki T, Angew, Chem. Int. Ed., 47, 86 (2008)

[21] Mohamed Mouyane, Brahim Itaalit, Jerome Bernad, David Houuivet, Jacques G Noudem, Powder Tech., 264, 71 (2014)

[22] Millini R, Gagliardi MF, Piro G, J. Mater. Sci., 29, 4065 (1994)

[23] Gaudon M, Laberty-Robert C, Ansart F, Stevens P, Rousset A, Solid State Sci., 4, 125 (2002)

[24] S. Enzo, G. Fagherazzi, A. Benedetti, S. Polizzi, J. Appl. Cryst., 21, 536 (1988)

[25] N.V. Nong, Chia Jyi Liu, M. Othaki, J. Alloys. Compds., 509, 977 (2011)

[26] W. Koshibae, K. Tsutsui, S. Maekawa, Phys. Rev. B., 62, 6869 (2000)

[27] R. Asahi, J. Sugiyama, T. Tani, Phys. Rev. B., 66, 155103 (2002)

[28] R. K. Gupta, C.M. Whang, Solid State Ionics., 178, 1617 (2007)

[29] M. Daturi, G. Busca, R. J. Willey, Chem. Mater., 7, 2115 (1995)

[30] Rizwan Wahab, Young-Soon Kim, Hyung-Shik Shin, Mater.Trans., 50, 2092 (2009)

[31] G. De Marzi, Z. V. Popovic, A. Cantarero, Z. Dohcevic-Mitrovic N.Paunovic, J. Bok, F. Sapina, Phys. Rev. B., 68, 064302 (2003)

[32] K. Rekha, M. Nirmala, Manjula G.Nair, A. Anukaliani, Physica B, Cond Matr., 405, 3180 (2010)

[33] K. Omri, J. El Ghoul, O. M. Lemine, M. Bououdina, B. Zhang, L. El Mir, Superlattices and Microstructures., 60, 139 (2013)

International Journal of
Scientific Research in Science and Technology (IJSRST)
Print ISSN : 2395-6011, Online ISSN : 2395-602X
International Conference on Advanced Materials
Held on 14, 15 December 2017, Organized by Department of Physics,
St. Joseph's College, Trichy, Tamilnadu, India

Luminescence Studies on Eu^{3+} Doped Telluro-Borate Glasses for Laser and LED Applications

P. Adlin Helen[1], M. Vijayakumar[2], S. Arunkumar[1], K. Marimuthu[1,*]

[1]Department of Physics, Gandhigram Rural Institute-Deemed University, Gandhigram-624 302, India

[2]Department of Physics, International Research Centre, Kalasalingam University,
Krishnankoil- 626 126, India

*Corresponding author: mari_ram2000@yahoo.com

Abstract

A new series of Eu^{3+} ions doped telluroborate glasses have been prepared with the chemical composition $(55-x)B_2O_3 + 25TeO_2 + 10K_2O + 10Bi_2O_3 + xEu_2O_3$ (where x=0, 0.25, 0.5, 0.75, 1 and 2 in wt%) following the melt quenching technique. The Luminescence spectra for all the titled glasses exhibit five emission bands corresponding to the $^5D_0 \rightarrow {}^7F_J$ (J=0, 1, 2, 3, 4) transitions located at 577 nm, 592 nm, 613 nm, 652 nm and 702 nm. The Judd-Ofelt intensity parameters have been used to calculate the radiative properties such as transition probability (A), branching ratio (β_R), stimulated emission cross-section (σ_P) and radiative lifetime (τ_R) for the various emission transitions of the Eu^{3+} ions. Luminescence quenching has been observed beyond 1 wt% Eu^{3+} ions concentration and is due to the interaction takes place between the Eu^{3+} ions at higher concentration. The decay curves possess single exponential behavior uniformly for all the titled glasses and the experimental lifetime values were obtained following the curve fitting method.

Keywords: Telluroborate glasses, luminescence, Judd-Ofelt parameters, stimulated emission cross-section

1. Introduction

Rare earth (RE) ions doped glasses play a most significant role in the field of photonics including the design and fabrication of new optical devices such as color display devices, solid state lasers, sensors, telecommunication and semiconductors induced LEDs etc., [1,2]. RE ions doped glasses draw a great deal of attraction among the researchers due to their key features such as inhomogeneous distinct visible emission, better thermal stability, less expensive and simple manufacturing process. Among the oxide glasses, telluroborate glasses are known to be the best host matrices because of their good optical quality, higher transparency, low melting temperature, high refractive index and high dielectric constant. Among the several RE^{3+} ions, Eu^{3+} ions acquire much attention because of their narrow band emission (almost monochromatic) around 613 nm (Red emission) due to the $^5D_0 \rightarrow {}^7F_2$ transition and higher quantum yield. The present work reports Luminescence behavior of the Eu^{3+} doped B_2O_3–TeO_2–K_2O–Bi_2O_3–glasses. The motivation of the present study is to (i) synthesis Eu^{3+} doped telluroborate glasses following melt quenching (ii) evaluate the Judd-Ofelt (JO) parameters (Ω_λ, λ=2, 4, 6) (iii) estimate the radiative properties of the Eu^{3+} ions and finally (iv) to determine the experimental lifetime of the $^5D_0$ metastable state of the Eu^{3+} ions.

2. Experimental

Eu^{3+} doped telluroborate glasses were prepared following the conventional melt quenching technique with high purity (99.99%) chemicals from

International Journal of
Scientific Research in Science and Technology (IJSRST)
Print ISSN : 2395-6011, Online ISSN : 2395-602X
International Conference on Advanced Materials
Held on 14, 15 December 2017, Organized by Department of Physics,
St. Joseph's College, Trichy, Tamilnadu, India

Sigma-Aldrich as starting materials. The 15gm batch of the chemical composition (55–x) B_2O_3 + 25TeO_2 + 10K_2O + 10Bi_2O_3 + xEu_2O_3 (where x = 0, 0.25, 0.5, 0.75, 1 and 2 in wt% named as BTPxE) were weighed and thoroughly mixed in an agate mortar to obtain homogeneous mixture. The chemical mixtures were taken into a porcelain crucible and kept in an electrical furnace at 1080 °C for 2 hrs. The melt was then poured onto a preheated brass plate and pressed by another brass plate to obtain uniform thickness. The prepared glasses were annealed for 8 hrs at 350 °C to remove the thermal strain and to improve the mechanical strength. Luminescence spectra of the prepared glasses were recorded at room temperature (RT) using Perkin Elmer LS55 spectrophotometer with a spectral resolution of ±1.0 nm and the lifetime measurements were carried out employing Sciencetech modular spectrometer using xenon flash lamp an excitation source.

3. Excitation and Emission Spectra

The inset of figure 1 shows the excitation spectrum of the BTP1E glass and the sharp intense peaks around 200–600 nm are mainly attributed to the f–f transitions of Eu^{3+} ions. The observed excitation bands are assigned to the various electronic transitions of Eu^{3+} ions such as $^7F_0 \rightarrow {}^5D_4$ (363 nm), $^7F_0 \rightarrow {}^5G_2$ (376 nm), $^7F_1 \rightarrow {}^5L_7$ (381 nm), $^7F_0 \rightarrow {}^5L_6$ (395 nm), $^7F_0 \rightarrow {}^5D_3$ (415 nm), $^7F_0 \rightarrow {}^5D_2$ (465 nm), $^7F_0 \rightarrow {}^5D_1$ (526 nm), $^7F_1 \rightarrow {}^5D_1$ (533 nm) and $^7F_0 \rightarrow {}^5D_0$ (578 nm) transitions. It is observed from the excitation spectrum that, the $^7F_0 \rightarrow {}^5D_2$ band possesses strong excitation at 465 nm and is used as a source of excitation wavelength for the emission spectral measurements of the present glasses.

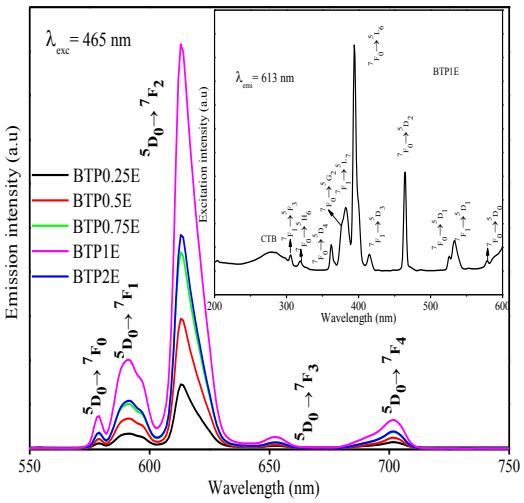

Figure 1. Luminescence spectra of the BTPxE glasses [Inset shows the excitation spectrum of the BTP1E glass]

The emission spectra of the prepared BTPxE glasses have been recorded as a function of Eu^{3+} ions concentration exciting at 465 nm and the same is shown in figure 1. The emission spectra exhibit five emission bands at around 577, 592, 613, 652 and 702 nm in the visible region corresponding to the $^5D_0 \rightarrow {}^7F_J$ (J = 0, 1, 2, 3 and 4) transitions and the $^5D_0 \rightarrow {}^7F_5$ emission transition found to occur in the near infrared region could not be observed because of the experimental limitations [3]. Among the emission bands, $^5D_0 \rightarrow {}^7F_2$ (613 nm) electric dipole allowed transition exhibit strong red emission and its intensity is hypersensitive to the environment around the Eu^{3+} ions. Whereas the $^5D_0 \rightarrow {}^7F_1$ transition is a magnetic dipole allowed and its intensity is independent of the environment around the Eu^{3+} ions [2]. It can be used for the estimation of transition probabilities of various excited levels. The luminescence intensity ratio (R) is defined as the ratio between the integrated intensity of $^5D_0 \rightarrow {}^7F_2$ and $^5D_0 \rightarrow {}^7F_1$ transitions and it is used to determine the nature of the chemical environment around the Eu^{3+} ions thus provides information pertaining to the

International Journal of
Scientific Research in Science and Technology (IJSRST)
Print ISSN : 2395-6011, Online ISSN : 2395-602X
International Conference on Advanced Materials
Held on 14, 15 December 2017, Organized by Department of Physics,
St. Joseph's College, Trichy, Tamilnadu, India

strength of covalent/ionic bonding. Higher R values indicate the higher asymmetry around the Eu^{3+} ion site in the present glasses. It is observed from table 1 that the increase in R value upto 1 wt% of Eu^{3+} ions concentration thus indicate that asymmetry around the Eu^{3+} ions increases due to the formation of bonds between different network formers like B–O–Eu–O–Te [3]. The characteristic emission of the prepared glasses are made through CIE 1931 chromaticity coordinates and the (x,y) coordinates of the title glasses are presented in table 2. The inset of figure 2 shows the CIE 1931 chromaticity diagram and it is observed that the all the coordinates are found to lie in the reddish orange region.

Table 1. Luminescence intensity ratio (R), Judd-Ofelt parameters ($\Omega_\lambda \times 10^{-20} cm^2$) of the Eu^{3+} telluroborate glasses

Glass code	R	JO Parameters			Trends of Ω_λ
		Ω_2	Ω_4	Ω_6	
BTP0.25E	3.54	5.58	0.73	0	$\Omega_2 > \Omega_4 > \Omega_6$
BTP0.5E	3.63	5.69	0.77	0	$\Omega_2 > \Omega_4 > \Omega_6$
BTP0.75E	3.73	5.74	0.82	0	$\Omega_2 > \Omega_4 > \Omega_6$
BTP1E	3.91	5.95	0.89	0	$\Omega_2 > \Omega_4 > \Omega_6$
BTP2E	3.89	5.80	0.76	0	$\Omega_2 > \Omega_4 > \Omega_6$

4. Judd-Ofelt Analysis and Radiative Parameters

In case of Eu^{3+} ions, determination of Judd-Ofelt (JO) parameters following the least square fit procedure is not applicable due to the zero magnitude of matrix elements $\|U^\lambda\|^2$. The Judd-Ofelt intensity parameters (Ω_2, Ω_4, Ω_6) provide valuable information such as Ω_2 is related to the short-range effects such as polarizability of the ligand ions, Ω_4 and Ω_6 parameters are related to the long-range effects such as viscosity and rigidity of the glass [4]. The JO theory of trivalent europium ion possesses serious difficulties, because of the availability of few absorption transitions in the absorption spectra originate from the $^7F_0$ and $^7F_1$ states to the various excited states such as $^5D_1$, $^5D_2$ and $^5L_6$. Hence emission spectra of the Eu^{3+} ions are used to determine the JO parameters of the Eu^{3+} ions. Peng and Izumitani [3] used the electric dipole transitions $^5D_0 \rightarrow {}^7F_2$, $^7F_4$ and $^7F_6$ of the Eu^{3+} ions to determine the JO parameters. The luminescent intensity of the magnetic dipole allowed transition ($^5D_0 \rightarrow {}^7F_1$) is independent of the crystal field around the Eu^{3+} ions.

This property of the $^5D_0 \rightarrow {}^7F_1$ transitions is used to estimate the transition probability of the various electric dipole transitions such as $^5D_0 \rightarrow {}^7F_J$ (2,4,6) and are used to determine the JO parameters (Ω_λ, λ=2, 4, 6). The $^5D_0 \rightarrow {}^7F_5$ and $^5D_0 \rightarrow {}^7F_6$ emission transitions could not be observed due to the experimental limitations and the Ω_6 parameter is negligible in the determination of radiative lifetime of Eu^{3+} ions. The Judd-Ofelt parameters of the title glasses have been calculated and the results are presented in table 1. The trends of the JO parameters are found to be in the order $\Omega_2 > \Omega_4 > \Omega_6$ uniformly for all the prepared glasses. The higher Ω_2 value is often an indication of higher covalence and higher asymmetry around the Eu^{3+} ions site and is further confirmed through the luminescence intensity ratios of the prepared glasses.

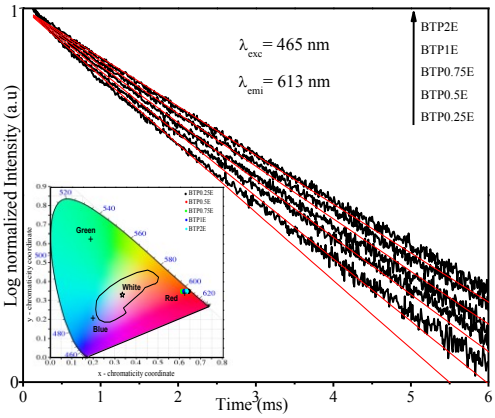

Figure 2. Decay curve of the $^5d_0$ excited state of the eu^{3+} doped teullroborate glasses

International Journal of
Scientific Research in Science and Technology (IJSRST)
Print ISSN : 2395-6011, Online ISSN : 2395-602X
International Conference on Advanced Materials
Held on 14, 15 December 2017, Organized by Department of Physics,
St. Joseph's College, Trichy, Tamilnadu, India

Table 2. Emission band position (λ_p, nm), effective bandwidth ($\Delta\lambda_{eff}$, nm), radiative transition probability (A, s^{-1}), stimulated emission cross-section ($\sigma_p \times 10^{-22}$ cm^2), experimental, calculated branching ratio (β_R) and CIE 1931 coordinates of the BTPxE glasses

Transition	Parametes	BTP 0.25E	BTP 0.5E	BTP 0.75E	BTP 1E	BTP 2E
$^5D_0 \rightarrow {}^7F_0$	λ_p	578	578	579	578	578
	$\Delta\lambda_{eff}$	2.51	2.41	2.62	2.42	2.32
	A	0.00	0.00	0.00	0.00	0.00
	σ_P	0.00	0.00	0.00	0.00	0.00
	β_R(Exp)	0.022	0.023	0.024	0.026	0.024
	β_R(Cal)	0.00	0.00	0.00	0.00	0.00
$^5D_0 \rightarrow {}^7F_1$	λ_p	592	590	591	591	591
	$\Delta\lambda_{eff}$	6.27	6.48	6.08	6.38	6.17
	A	60.2	59.6	59.4	58.3	55.5
	σ_P	5.96	5.73	6.12	5.79	5.87
	β_R(Exp)	0.18	0.19	0.17	0.18	0.18
	β_R(Cal)	0.20	0.20	0.193	0.203	0.195
$^5D_0 \rightarrow {}^7F_2$	λ_p	613	613	613	613	613
	$\Delta\lambda_{eff}$	5.20	5.00	5.18	5.25	5.12
	A	223.4	208.7	231.7	244.5	214.3
	σ_P	30.9	30.1	32.4	33.1	31.6
	β_R(Exp)	0.707	0.692	0.708	0.713	0.712
	β_R(Cal)	0.749	0.734	0.754	0.758	0.755
CIE	x	0.64	0.64	0.61	0.62	0.63
	y	0.35	0.35	0.35	0.35	0.35

The JO parameters have been used to calculate the radiative properties such as radiative transition probability (A), stimulated emission cross-section (σ_p), radiative lifetime (τ) and branching ratios (β) for the $^5D_0 \rightarrow {}^7F_J$ (J=0,1,2,3,4) transitions and the results are presented in table 2. The radiative transition probability (A) and the stimulated emission cross-section value of the $^5D_0 \rightarrow {}^7F_2$ transition are found to be higher for all the prepared BTPxE glasses compared to the other transitions and the values are presented in table 2. The experimental branching ratio values of the $^5D_0 \rightarrow {}^7F_2$ transition are found to be 0.675, 0.707, 0.692, 0.708, 0.713 and 0.712 for the BTP0.1E, BTP0.25E, BTP0.5E, BTP0.75E, BTP1E and BTP2E glasses respectively and is quite comparable to the branching ratio values estimated using JO theory.

5. Decay Curve Analysis

Luminescence decay profile of the prepared Eu^{3+} doped telluroborate glasses have been recorded by monitoring an excitation at 465 nm and emission at 613 nm corresponding to the $^5D_0 \rightarrow {}^7F_2$ transition and the same is shown in figure 2. It is clearly observed from the figure that, the decay curve exhibits single exponential behavior for all the prepared glasses and the experimental lifetime values were evolved by fitting with a single-experimental function $I_t = I_0\, e^{-t/\tau}$, where I_t and I_0 is the emission intensity at time 't' and at t=0 respectively, τ is the lifetime of the excited state energy level.

The calculated (τ_{cal}) and experimental (τ_{exp}) lifetime values for the $^5D_0$ level are found to be3.332, 3.355, 3.517, 3.260, 3.468, 3.527 ms and 1.192, 1.316, 1.517, 1.526, 1.878, 1.7694 ms corresponding to the BTP0.1E, BTP0.25E, BTP0.5E, BTP0.75E, BTP1E and BTP2E glasses respectively.

6. References

[1] Non L. Yao, G. Chen, H. Zhong and C. Wen, J. -Cryst. Solids **444**, 2016, pp. 38–42.

[2] C. Zhu, D. Wu, Y. Zhang, M. Zhang and Y. Yue, J. Alloys and Compds **632**, 2015, pp. 291–295.

[3] B. Peng and T. Izumitani, Rev. Laser Eng. **22**, 1994, 16–27.

[4] G. Kaur, M. Kumar, A. Arora, O.P. Pandey and K. Singh, J. Non-Cryst. Solids **357**, 2011, pp. 858–864.

[5] S.N. Rasool, L.R. Moorthy and C.K. Jayasankar, Mater. Express **3**, 2013, pp. 231–240.

International Journal of
Scientific Research in Science and Technology (IJSRST)
Print ISSN : 2395-6011, Online ISSN : 2395-602X
International Conference on Advanced Materials
Held on 14, 15 December 2017, Organized by Department of Physics,
St. Joseph's College, Trichy, Tamilnadu, India

Spectroscopic Properties of Eu^{3+} Ions Doped Boro-phosphate Glasses for Optoelectronic Applications

P. Jayanthi, R. Nagaraj, K. Marimuthu*
Department of Physics, Gandhigram Rural Institute–Deemed University, Gandhigram – 624 302, India
*Corresponding author: mari_ram2000@yahoo.com

Abstract
A new series of Eu^{3+} ions doped boro-phosphate glasses with the chemical composition $(60–x)B_2O_3 + 10P_2O_5 + 20Li_2O + 10ZnO + xEu_2O_3$ (where, x = 0.25, 0.5, 1 and 2 in wt %) have been prepared by conventional melt quenching technique and labeled as 0.25EuBP, 0.5EuBP, 1EuBP and 2EuBP glasses respectively. From the absorption spectra, bonding parameters have been calculated to examine the nature of the bond between the Eu^{3+} ions and its surrounding ligands. The Judd-Oflet (JO) intensity parameters were calculated from the emission spectra to explore the symmetry of the ligand environment around the Eu^{3+} ion site. Radiative properties were obtained from the emission spectra to ensure the suitability of studied glasses for solid state laser applications. The decay curves exhibit single exponential behavior for all the title glasses irrespective of the change in Eu^{3+} ion concentration and the observed results were discussed in detail and reported.

Keywords: Glasses, Absorption, Luminescence, JO Parameters, Decay Analysis.

1. Introduction

For the past few decades considerable work on rare earth (RE) doped materials have been carried out for the design and development of efficient optoelectronic devices such as solid state lasers, LED's and color display devices. Of all the RE ions, Eu^{3+} ion possess lots of importance because of its narrow band emission around 612 nm due to its $^5D_0 \rightarrow {}^7F_2$ transition for red laser applications. The f–f transition of Eu^{3+} ions provide information about the local structure around the RE ions in different host matrices and hence they can be used as a probe to analyze the ligand structure around the RE^{3+} ions site [1]. In order to avail the advantages of both borate and phosphate glass formers like high refractive index, high RE ion solubility, low melting temperature, high transparency and high thermal stability it is combined together as boro-phosphate glasses to attain good optical quality glasses.

Spectroscopic properties of Eu^{3+} ions doped boro-phosphate glasses have been studied as a function of Eu^{3+} ion concentration and the results were discussed and reported

2. Experimental

Eu^{3+} doped title glasses have been prepared by conventional melt quenching technique following the procedure reported in literature [2]. The absorption spectral measurements were made employing Perkin Elmer Lambda 35 UV-Vis-NIR spectrophotometer. Luminescence spectra of the prepared glasses were recorded using Perkin Elmer LS55 spectrophotometer. Sciencetech modular spectrometer was employed for lifetime measurements using xenon flash lamp as an excitation source.

3. Optical absorption spectra

The absorption spectra of the Eu^{3+} doped boro-phosphate glasses were recorded in the wavelength region 375–2300 nm and as a representative case absorption spectrum of the 1EuBP glass is shown in figure 1. The spectrum exhibit ten absorption bands at 394, 401, 414, 465, 524, 533, 578, 587,

International Journal of
Scientific Research in Science and Technology (IJSRST)
Print ISSN : 2395-6011, Online ISSN : 2395-602X
International Conference on Advanced Materials
Held on 14, 15 December 2017, Organized by Department of Physics,
St. Joseph's College, Trichy, Tamilnadu, India

2097 and 2205 nm analogous to the $^7F_0 \rightarrow ^5L_6$, $^7F_1 \rightarrow ^5L_6$, $^7F_1 \rightarrow ^5D_3$, $^7F_0 \rightarrow ^5D_2$, $^7F_0 \rightarrow ^5D_1$, $^7F_1 \rightarrow ^5D_1$, $^7F_0 \rightarrow ^5D_0$, $^7F_1 \rightarrow ^5D_0$, $^7F_0 \rightarrow ^7F_6$ and $^7F_1 \rightarrow ^7F_6$ transitions respectively. Among them, $^7F_0 \rightarrow ^5L_6$ transition is found to be higher in intensity.

The bonding parameter (δ) values can be estimated using the relation δ = ((1−)/)×100, where $\bar{\beta}$ is the average value of the Nephelauxetic ratios (β). The calculated δ values of the studied glasses are found to be 0.0052, 0.0050, 0.0046 and 0.0040 corresponding to the 0.25EuBP, 0.5EuBP, 1EuBP and 2EuBP glasses respectively. The positive δ values indicate the covalent nature of the Eu–O bond. The decreasing B_2O_3 content reduces the polarization of oxygen ions upon Eu^{3+} ions which in turn leads to have a fall in the covalency of the Eu–O bonds.

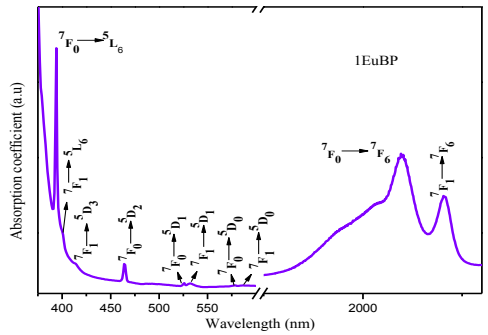

Figure 1. Absorption spectrum of the 1EuBP glass

4. Phonon sideband and luminescence spectral analysis

Figure 2 shows the excitation spectrum of the 1EuBP glass recorded in the wavelength region 350–550 nm by monitoring the emission at 612 nm. The spectrum exhibit six excitation bands at around 363, 380, 395, 412, 463 and 532 nm corresponding to the $^7F_0 \rightarrow ^5D_4$, $^7F_1 \rightarrow ^5L_7$, $^7F_0 \rightarrow ^5L_6$, $^7F_1 \rightarrow ^5D_3$, $^7F_0 \rightarrow ^5D_2$ and $^7F_1 \rightarrow ^5D_1$ transitions respectively. The $^7F_0 \rightarrow ^5L_6$ transition observed at 405 nm is found to be higher in intensity compared to all other transitions and is used as an excitation wavelength to record the emission spectra.

Table 1. The JO parameters ($\times 10^{-20}$ cm^2), (x,y) color coordinates, peak position of PET and PSB (in cm^{-1}), Phonon energy (cm^{-1}) and g of the xEuBP glasses

Parameters	0.25Eu BP	0.5Eu BP	1Eu BP	2Eu BP
Ω_2	3.82	3.76	3.54	2.74
Ω_4	0.692	0.759	0.620	0.629
Ω_6	0	0	0	0
X	0.603	0.624	0.629	0.644
Y	0.345	0.346	0.348	0.35
PET	21515	21518	21523	21531
PSB	22617	22621	22624	22618
Phonon energy	1172	1166	1160	1153
G	0.0032	0.0029	0.0025	0.0021

The occurrence of phonon sideband in the excitation spectra of the Eu^{3+} ions corresponds to the phonon assisted absorption transition. The phonon sideband (PSB) coupled with the excitation spectrum of the 1EuBP glass and the PSB of all the studied glasses are shown in the insert of figure 2. The electron-phonon coupling constant have been obtained using the expression,

$$(\int I_{PSB}\, d\lambda)/(\int I_{PET}\, d\lambda)$$

where, is the intensity of the phonon sideband and is the intensity of pure electronic transition respectively. Further, phonon energy involved in the non-radiative decay process which leads to luminescence quenching can also be obtained by finding the difference between the energy of the

International Journal of
Scientific Research in Science and Technology (IJSRST)
Print ISSN : 2395-6011, Online ISSN : 2395-602X
International Conference on Advanced Materials
Held on 14, 15 December 2017, Organized by Department of Physics,
St. Joseph's College, Trichy, Tamilnadu, India

pure electronic transition and that of the phonon side band. Table 1 shows the calculated g values and the phonon energies of the title glasses. It is observed from table 1 that the phonon energy of the xEuBP glasses are found to be in the range 1153–1172 cm^{-1} and the same may be due to the vibrations of different borate groups. The lower g values indicate the less covalency of the Eu–O bonds in the studied glasses which is already confirmed through the bonding parameter values.

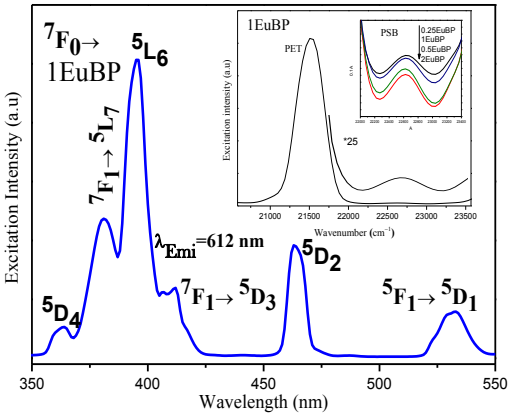

Figure 2. Excitation spectrum of the 1EuBP glass [Inset shows the phonon side bands of the xEuBP glasses]

The luminescence spectra recorded in the wavelength region 550–720 nm is shown in figure 3. The spectra exhibit emission bands at around 574, 595, 612, 653 and 702 nm corresponding to the $^5D_0 \rightarrow ^7F_0$, $^5D_0 \rightarrow ^7F_1$, $^5D_0 \rightarrow ^7F_2$, $^5D_0 \rightarrow ^7F_3$ and $^5D_0 \rightarrow ^7F_4$ transitions respectively. The intensity of the emission bands are found to increase upto 1wt% Eu^{3+} ion concentration and after that luminescence quenching is observed due to the energy transfer process takes place between the Eu^{3+} ions through cross-relaxation mechanism [2]. The CIE chromaticity coordinates have been determined to estimate the emission color of the prepared glasses. The calculated chromaticity coordinates (x,y) of the studied glasses are presented in table 1 and the (x,y) values are found to lie in the red region of the CIE 1931 diagram and the same is shown in the inset of figure 3.

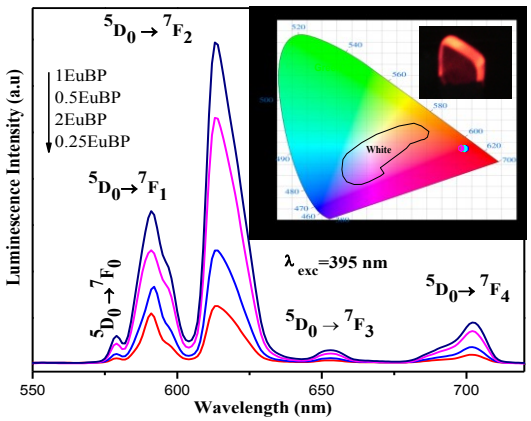

Figure 3. Luminescence spectra of the xEuBP glasses [Inset shows the CIE 1931 diagram of the xEuBP glasses]

1. Judd-ofelt analysis and decay curves

The JO parameters give valuable information about the metal-ligand bonding nature and the symmetry of the ligand field around the RE ion site. The JO parameters of the studied glasses were calculated from the emission spectra following the procedure reported in literature [3,4] and they mainly depend upon the emission intensities of the $^5D_0 \rightarrow ^7F_{2,4,6}$ transitions. Table 1 shows the calculated JO parameters of the title glasses and the Ω_2 values are found to decrease with the increase in Eu^{3+} content which indicates that Eu^{3+} ions are located in the lower asymmetrical ligand environment and the Eu–O bond possess less covalency. The Ω_6 values of all the prepared were taken as zero because the $^5D_0 \rightarrow ^7F_6$ transition usually occurs in the near infrared region which could not be observed due to experimental limitations.

Using the JO parameters, radiative properties such as radiative transition probability (A_R), stimulated emission cross-section (σ_P^E), branching ratios (β_R) and radiative lifetime of the $^5D_0 \rightarrow ^7F_J$

International Journal of
Scientific Research in Science and Technology (IJSRST)
Print ISSN : 2395-6011, Online ISSN : 2395-602X
International Conference on Advanced Materials
Held on 14, 15 December 2017, Organized by Department of Physics,
St. Joseph's College, Trichy, Tamilnadu, India

(J=1,2,4) transitions were obtained from the emission spectra and the same is shown in table 2. The stimulated emission cross-section and the branching ratio values should be on higher side to avail good lasing action [5]. Among the studied glasses, 1EuBP glass possess higher A_R, β_R and σ_P^E values pertaining to the $^5D_0 \rightarrow {}^7F_2$ transition and the same can be suggested as an active medium for red laser applications. The decay profile of the $^5D_0 \rightarrow {}^7F_2$ transition have been recorded by fixing the excitation at 395 nm and emission at 612 nm and the same is shown in figure 4. The decay curves exhibit single exponential behavior for all the studied glasses and the obtained τ_{exp} values are presented in table 2 along with the quantum efficiency values (η).

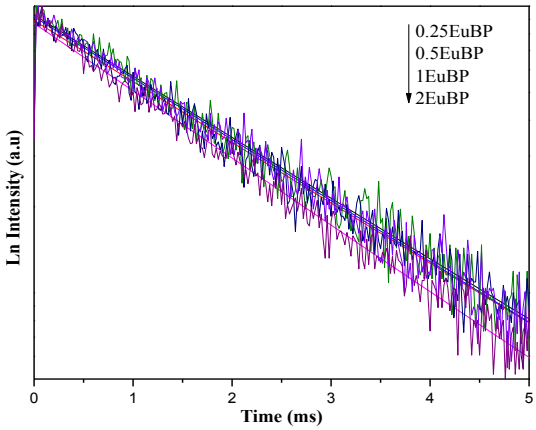

Figure 4. Decay curves of the xEuBP glasses

It is observed that the τ_{exp} values are found to be lower than the τ_{cal} values and is due to the non-radiative relaxation caused by the interaction of Eu^{3+} ions with the vibrations of the host matrix.

Table 2. The A (s^{-1}), β and (10^{-22} cm^2), τ_{cal}, τ_{exp} and η values of the xEuBP glasses

Transitions	Factors	0.25Eu BP	0.5Eu BP	1Eu BP	2Eu BP
$^5D_0 \rightarrow {}^7F_1$	A	61.8	61.6	61.4	61.1
	σ_P^E	3.63	5.01	5.88	4.07
	β_R	0.313	0.303	0.253	0.263
$^5D_0 \rightarrow {}^7F_2$	A	114.4	109.6	148.8	149.0
	σ_P^E	7.83	9.14	12.24	10.05
	β_R	0.597	0.609	0.683	0.658
$^5D_0 \rightarrow {}^7F_4$	A	13.16	13.3	10.2	13.1
	σ_P^E	1.96	2.47	1.65	2.14
	β_R	0.068	0.067	0.044	0.057
τ_{cal} (ms)		3.774	3.610	3.247	3.450
τ_{exp} (ms)		1.857	1.844	1.832	1.817
η (%)		49	51	56	53

5. Conclusion

Eu^{3+} doped boro-phosphate glasses have been synthesized following the melt quenching technique. The decreasing δ and Ω_2 values indicate the fact that colvalency of the metal-ligand bond decreases with the increase in Eu^{3+} ion concentration in the title glasses. It is observed from all these studies that among the prepared glasses, 1EuBP glass exhibit higher A_R, β_R, σ_P^E and η values pertaining to the $^5D_0 \rightarrow {}^7F_2$ transition and the same is suggested as

a suitable candidate for red light emitting sources and for the fabrication of solid state lasers.

6. References

[1] R. Reisfeld and C.K. Jorgensen, Lasers and Excited States of Rare Earths, Springer, Berlin, 1977.

[2] K. Maheshvaran and K. Marimuthu, J. Lumin. **132,** 2012, pp. 2259–2267.

[3] B.R. Judd, Phys. Rev. **127**, 1962, pp. 750–761.

[4] G.S. Ofelt, J. Chem. Phys. **37**, 1962, pp. 511–520.

[5] Joanna Pisarska, Opt. Mater. **31**, 2009, pp. 1784–1786.

International Journal of
Scientific Research in Science and Technology (IJSRST)
Print ISSN : 2395-6011, Online ISSN : 2395-602X
International Conference on Advanced Materials
Held on 14, 15 December 2017, Organized by Department of Physics,
St. Joseph's College, Trichy, Tamilnadu, India

Optical Properties of Dy^{3+} Doped Zinc Boro-Phosphate Glasses for Photonic Applications

P. Karthikeyan, P. Suthanthirakumar, K. Marimuthu*
Department of Physics, Gandhigram Rural Institute–Deemed University, Gandhigram – 624 302, India
*Corresponding author: mari_ram2000@yahoo.com

Abstract

Zinc boro-phosphate glasses doped with Dy^{3+} ions (DZBP) have been synthesized following the melt quenching technique and their spectroscopic properties were studied through absorption and emission spectra. The bonding parameters (δ and β) and Judd-Ofelt (JO) intensity parameters were calculated from the absorption spectra. The luminescence properties of the present Dy^{3+} doped glasses have been analyzed through radiative properties. The luminescence spectra of the Dy^{3+} doped zinc boro-phosphate glasses exhibit two intense emission bands corresponding to the $^4F_{9/2}\rightarrow{}^6H_{15/2}$ and $^4F_{9/2}\rightarrow{}^6H_{13/2}$ transitions. The Y/B intensity ratio values have been calculated from the emission spectra of the prepared glasses and the combination of dominant blue and yellow emissions generate white light emission. The results obtained from the CIE chromaticity diagram suggest that the present Dy^{3+} doped glasses are suitable for white light applications.

Keywords: Absorption Spectra, Bonding Parameter, JO intensity parameter, luminescence, radiative properties.

1. Introduction

Nowadays, many researchers focus on rare earth (RE) ions doped optical materials for solid state lighting (SSL) applications such as white LEDs, color displays and cellular phone illumination etc., [1,2]. Among the several rare earth ions, Dy^{3+} ions play a vital role in the design and development of white LED's because of the dominant two emission bands in the visible region corresponding to the $^4F_{9/2}\rightarrow{}^6H_{15/2}$ (blue), $^4F_{9/2}\rightarrow{}^6H_{13/2}$ (yellow) transitions [3]. The Y/B intensity ratio depends upon structural changes in the environment around the Dy^{3+} ions and the white light emission has been obtained by adjusting the Y/B ratio by optimizing the RE ions concentration, chemical composition, pumping wavelength and heat treatment. B. Shanmugavelu et al. [4] and K. Swapna et al. [5] have also studied the variation of Y/B ratio for the white light applications. In the present work, Emission properties of Dy^{3+} doped zinc boro-phosphate glasses have been analyzed for the fabrication of white light emitting devices and the results are discussed and reported.

2. Experimental

The Dy^{3+} doped Zinc boro-phosphate glasses with the chemical composition $(59–x)P_2O_5+ xB_2O_3 + 10SrO + 10BaF_2 + 20ZnO + 1Dy_2O_3$ (where x = 10, 20, 30 and 40 in wt %) have been prepared by conventional melt quenching technique [6] and labeled as 10DZBP, 20DZBP, 30DZBP and 40DZBP based on the borate content. The absorption spectra were recorded between 400 and 2000 nm using Perkin-Elmer-Lambda 950 UV/Vis/NIR spectrophotometer with a resolution of ±0.1 nm. Luminescence spectra of the glasses were measured employing Perkin Elmer LS55 spectrophotometer in the wavelength range 450–700 nm with a spectral resolution of ±1.0 nm. All these measurements were carried out at room temperature (RT) only.

International Journal of
Scientific Research in Science and Technology (IJSRST)
Print ISSN : 2395-6011, Online ISSN : 2395-602X
International Conference on Advanced Materials
Held on 14, 15 December 2017, Organized by Department of Physics,
St. Joseph's College, Trichy, Tamilnadu, India

3. Absorption Spectra and Bonding Parameter

The optical absorption spectra of the prepared Dy^{3+} doped Zinc boro-phosphate glasses recorded in the visible and near infrared regions are shown in figure 1. The absorption spectra exhibit eight inhomogeneous bands at around 1680, 1273, 1092, 900, 800, 750, 471 and 451 nm due to the absorption transitions from the $^6H_{15/2}$ ground state to the various excited states such as $^6H_{11/2}$, $^6F_{11/2}+^6H_{9/2}$, $^6F_{9/2}$, $^6F_{7/2}$, $^6F_{3/2}$, $^6F_{5/2}$, $^6F_{7/2}+^6H_{5/2}$ and $^4I_{15/2}$. From the absorption spectra, it is observed that the $^6H_{15/2} \rightarrow {}^6F_{11/2}+{}^6H_{9/2}$ transition is sensitive to the ligand environment around the RE ion site which obey the selection rules $|\Delta S| = 0, |\Delta L| \leq 2$ and $|\Delta J| \leq 2$ and is known as hypersensitive transition.

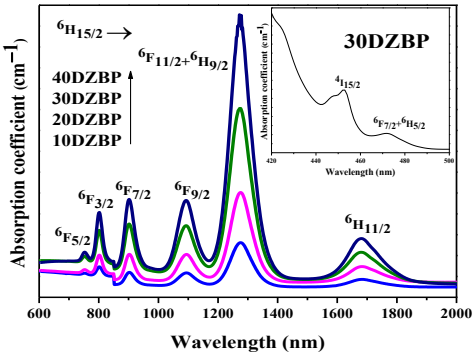

Figure 1. NIR absorption spectra of the Dy^{3+} doped zinc boro-phosphate glasses [Inset shows the absorption spectrum of the 30DZBP glass in the visible region]

From the optical absorption spectra, Nephelauxetic ratios and bonding parameter values have been calculated using the expressions reported in the literature [6] to study the nature of the Dy^{3+}-ligand bond in the prepared glasses and the values are presented in table 1. The positive sign of the δ values indicate the fact that the Dy–O bond is of covalent in nature and the covalency increases due to the increase in the B_2O_3 content in the studied glasses.

4. Judd-Ofelt Intensity Parameters

The JO intensity parameters (Ω_2, Ω_4 and Ω_6) provide information about the local structure of the ligand environment and nature of the metal-ligand bonds in RE doped glasses and the values are shown in table 1. It is observed from the table that the magnitude of the JO intensity parameters follow the trend as $\Omega_2 > \Omega_6 > \Omega_4$ uniformly for all the studied glasses and the Ω_2 values were found to increase with the increase in borate content in the prepared glasses compared to the reported literature [7,8] thus indicates the increasing asymmetry in the prepared glasses. Spectroscopic quality factor is ($\chi = \Omega_4/\Omega_6$) used to predict the stimulated emission in any active medium and is found to be higher for 30DZBP glass compared to other prepared glasses thus suggests its suitability for the photonic applications.

Table 1. Judd-Ofelt ($\times 10^{-20}$cm^2) parameters and bonding parameters ($\bar{\beta}$ and δ) of the Dy^{3+} doped zinc boro-phosphate glasses

Glass code	JO Parameters			Ω_4/Ω_6	$\bar{\beta}$	δ
	Ω_2	Ω_4	Ω_6			
10 DZBP	5.24	1.72	2.60	0.66	0.989	0.993
20 DZBP	7.13	1.20	1.54	0.77	0.990	1.006
30 DZBP	8.47	1.71	1.95	0.87	0.990	1.019
40 DZBP	8.51	1.73	3.75	0.46	0.991	1.023
LKZBSB[7]	5.36	1.46	1.95	0.74	-	-
BaO–TeO_2[8]	3.20	1.35	2.47	0.54	-	-

5. Luminescence spectral analysis

Figure 2 shows the luminescence spectra of the prepared Dy^{3+} doped zinc boro-phosphate glasses monitoring an excitation wavelength at 387 nm.

International Journal of
Scientific Research in Science and Technology (IJSRST)
Print ISSN : 2395-6011, Online ISSN : 2395-602X
International Conference on Advanced Materials
Held on 14, 15 December 2017, Organized by Department of Physics,
St. Joseph's College, Trichy, Tamilnadu, India

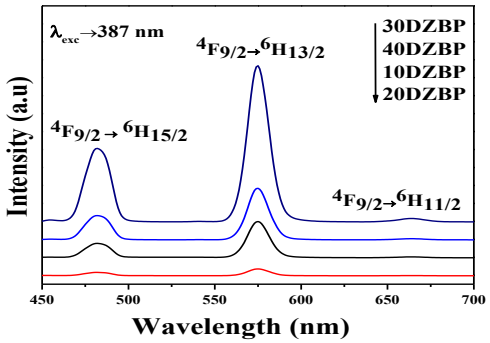

Figure 2. Emission spectra of the Dy^{3+} doped zinc boro-phosphate glasses

The luminescence spectra exhibit three emission bands centered at 482, 575 and 664 nm attributed to the $^4F_{9/2}\rightarrow{}^6H_{15/2}$ (blue), $^4F_{9/2}\rightarrow{}^6H_{13/2}$ (yellow) and $^4F_{9/2}\rightarrow{}^6H_{11/2}$ (red) transitions respectively. Among these transitions, $^4F_{9/2}\rightarrow{}^6H_{13/2}$ possess higher intensity compared to the other transitions and the ratio between integral intensities of $^4F_{9/2}\rightarrow{}^6H_{13/2}$ (yellow) and $^4F_{9/2}\rightarrow{}^6H_{15/2}$ (blue) transitions helps one to determine the local symmetry around the Dy^{3+} ion site. These values are found to increase with the increase in borate content in the prepared glasses indicating the increasing asymmetry in the prepared glasses. The luminescence intensity increases with the increase in borate content and found to quench beyond 30 wt% of B_2O_3 content in the prepared glasses.

6. Radiative properties

The radiative properties of the Dy^{3+} doped zinc boro-phosphate glasses have been calculated from the emission spectra using JO theory and the results are shown in table 2.

Table 2. Emission band position (λ_p, nm stimulated emission cross-section ($\sigma_P^E \times 10^{-22}$ cm^2), experimental and calculated branching ratios (β_R) values and Y/B intensity ratio values and (x, y) co-ordinates of the Dy^{3+} doped zinc boro-phosphate glasses

Transition parameters		10DZ BP	20DZ BP	30DZ BP	40DZ BP
$^4F_{9/2}\rightarrow{}^6H_{15/2}$	λ_p	482	482	482	481
	σ_P^E	1.2999	2.6911	3.4920	3.4284
	β_R(Exp)	0.2295	0.2977	0.2287	0.2910
	β_R(Cal)	0.4537	0.4474	0.4689	0.4318
$^4F_{9/2}\rightarrow{}^6H_{13/2}$	λ_p	574	574	584	574
	σ_P^E	46.5589	27.8518	63.3970	59.1955
	β_R(Exp)	0.7638	0.7088	0.7700	0.7399
	β_R(Cal)	0.6408	0.6583	0.6934	0.6864
$^4F_{9/2}\rightarrow{}^6H_{11/2}$	λ_p	663	664	674	663
	σ_P^E	7.1590	6.7055	9.8339	8.1244
	β_R(Exp)	0.0908	0.0774	0.0703	0.0797
	β_R(Cal)	0.0862	0.0919	0.0931	0.0918
x		0.372	0.371	0.381	0.375
y		0.379	0.368	0.379	0.373
Y/B intensity ratio		1.529	1.607	1.608	1.767

The branching ratio values of the $^4F_{9/2}\rightarrow{}^6H_{13/2}$ emission transition is found to be higher compared to the other emission transitions and follow the trend as $^4F_{9/2}\rightarrow{}^6H_{13/2} > {}^4F_{9/2}\rightarrow{}^6H_{15/2} > {}^4F_{9/2}\rightarrow{}^6H_{11/2}$ uniformly for all the prepared glasses. Among all the observed transitions, the σ_P^E value is found to be higher for the $^4F_{9/2}\rightarrow{}^6H_{13/2}$ transition pertaining to the prepared 30DZBP glass and further it possess higher σ_P^E value compared to the reported glasses PTBDy10 (2.86×10^{-21}cm^2) [9], Dy^{3+}: NMAP (25.65×10^{-22}cm^2) [10] thus suggests its suitability for yellow laser applications.

7. White Light Stimulation

Figure 3 shows the CIE diagram plotted for the prepared Dy^{3+} doped zinc boro-phosphate glasses using the expressions reported in the literature [6]. The x, y coordinate values are presented in table 2

International Journal of
Scientific Research in Science and Technology (IJSRST)
Print ISSN : 2395-6011, Online ISSN : 2395-602X
International Conference on Advanced Materials
Held on 14, 15 December 2017, Organized by Department of Physics,
St. Joseph's College, Trichy, Tamilnadu, India

and are found to be closer to the standard equal energy point thus confirms the suitability of the present glasses for white light applications. In general, cool white light sources (high CCT values) are mostly used in schools, houses, hospitals etc.,

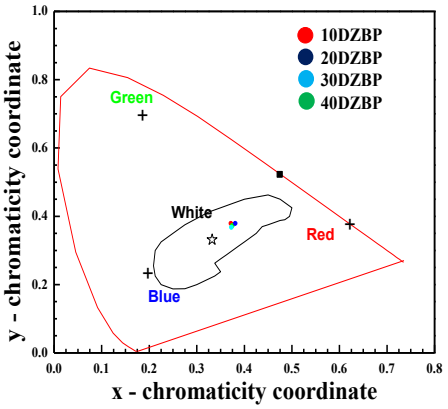

Figure 3. The CIE 1931 color chromaticity diagram of the Dy^{3+} doped zinc boro-phosphate glasses

The warmer white light sources (low CCT values) are used in offices, restaurants, hotels etc., The calculated CCT values for the prepared glasses are found to be 3641K, 4131K, 6234K and 3510K corresponds to the 10DZBP, 20DZBP, 30DZBP and 40DZBP glasses respectively. Among them, 30DZBP glass possesses higher CCT value suggesting its suitability for cool white light applications.

8. Conclusion

The covalency nature of the Dy–O bond increases with the increase in borate content in the prepared glasses. The Ω_2 and Y/B ratio values increases with the increase in borate content thus indicates the increasing asymmetry in the prepared glasses. Higher stimulated emission cross-section and branching ratio values of the $^4F_{9/2} \rightarrow {}^6H_{13/2}$ transition corresponding to the 30DZBP glass confirms its suitability for yellow laser applications. The CIE color chromaticity coordinates (x, y) and higher CCT values suggests that the 30DZBP glass is a better choice for cool white light applications.

International Journal of
Scientific Research in Science and Technology (IJSRST)
Print ISSN : 2395-6011, Online ISSN : 2395-602X
International Conference on Advanced Materials
Held on 14, 15 December 2017, Organized by Department of Physics,
St. Joseph's College, Trichy, Tamilnadu, India

9. References

[1] L. Mishra, A. Sharma, A. K. Vishwakarma, K. Jha, M. Jayasimhadri, B.V. Ratnam, K. Jang, A.S. Rao, R.K. Sinha, J. Lumin **169,** 2016, pp. 121–127.

[2] L. Vijayalakshmi, K.N. Kumar, R.P. Vijayalakshmi, Opt. Mater **57,** 125–133 (2016).

[3] B. Klimesz, W.R. Romanowski, R. Lisiecki, Opt. Mater **42,** 2015, pp. 538–543.

[4] B. Shanmugavelu, V.V. Ravi Kanth Kumar, J. Lumin **146,** 2014, pp. 358 – 363.

[5] K. Swapna, Sk. Mahamuda, A. Srinivasa Rao, M. Jayasimhadri, T. Sasikala, L. Rama Moorthy, J. Lumin **139,** 2013, pp. 119–124.

[6] P. Karthikeyan, P. Suthanthirakumar, R. Vijayakumar, K. Marimuthu, J. Mol. Struct **1083,** 2015, pp. 268–277.

[7] R. Vijayakumar, G. Venkataiah, K. Marimuthu, J. Alloys Compd **652,** 2015, pp. 234 – 243.

[8] N. Vijaya, K.U. Kumar, C.K. Jayasankar, Spectrochim. Acta, Part A **113,** 2013, pp. 145-153.

[9] M.V.V. Kumar, B.C. Jamalaiah, K.R. Gopal, R.R. Reddy, J. Lumin **132,** 2012, pp. 86–90.

[10] F. Wang, B. Chen, E.Y.B. Pun, H. Lin, J. Non-Cryst. Solids **391,** 2014, pp. 17–22.

International Journal of
Scientific Research in Science and Technology (IJSRST)
Print ISSN : 2395-6011, Online ISSN : 2395-602X
International Conference on Advanced Materials
Held on 14, 15 December 2017, Organized by Department of Physics,
St. Joseph's College, Trichy, Tamilnadu, India

Spectroscopic Investigations on Er^{3+} doped Lead Borotellurite Glasses for Amplifier Applications

M. Mariyappan, P. Karthikeyan, K. Marimuthu*
Department of Physics, Gandhigram Rural Institute–Deemed University, Gandhigram – 624 302, India
*Corresponding author: mari_ram2000@yahoo.com

Abstract

Er^{3+} ions doped lead borotellurite glasses were prepared by melt quenching technique and their structural and spectroscopic behaviors were studied through recording FTIR, UV–Vis–NIR absorption and photoluminescence measurements. Through the absorption spectra the bonding parameters (δ) and Judd–Ofelt intensity parameters Ω_λ (λ = 2, 4 and 6) has been evaluated. From the JO intensity parameters the radiative properties such as transition probability (A), stimulated emission cross section (σ_e), radiative life time (τ_{cal}) and branching ratios (β_R) of the prepared glasses were determined and their results were discussed and reported. The obtained higher values of A, σ_e, FWHM and ΔG for the LTB0.5E glass suggest its feasibility for the development of laser and optical amplifier devices.

Keywords: Amplifier, Bonding Parameter, JO intensity parameter, Gain Bandwidth, Stimulated emission cross section

1. Introduction

Rare earth (RE) ions are visible to near-infrared ultra narrow band emitters with long luminescence lifetimes and thus have wide applications in many fields such as solid laser, display and optical amplification [1]. Er^{3+} doped glasses are especially attractive for numerous applications mainly due to the 1550 nm emission and in fact, Er^{3+}-doped fiber amplifiers (EDFA) are well known and used in telecommunication systems, temperature sensors, solar cells, light wave circuits [1,2]. Owing to the low phonon energy, excellent material exhibiting low melting points, higher chemical stability, high refractive index and suitable lattice size for doping rare earth ions borotellurite based glass system has been selected as the host matrix [1–3]. In this present work, the concentration effect on spectroscopic behaviors of Er^{3+} ions doped lead borotellurite glasses have been investigated and reported.

2. Experimental

Er^{3+} ions doped lead borotellurite glasses were prepared by melt quenching technique with the chemical composition of $(45\text{-}x)B_2O_3$+$30TeO_2$+ $15PbO$+$10Na_2O$+xEr_2O_3 (where x = 0.1, 0.25, 0.5, 1 and 2 wt%) following the procedure reported in literature [3]. The prepared Er^{3+} ions doped lead borotellurite glasses are labeled as LTB0.1E, LTB0.25E, LTB0.5E, LTB1E and LTB2E with respect to the erbium ion concentration in the host matrix. The FTIR spectrum has been recorded using Perkin–Elmer Paragon–500 spectrophotometer in the wave number region 400–4000 cm^{-1} following KBr pellet method. The optical absorption spectra were recorded in the wavelength range 350–2000 nm using CARY 500 UV–Vis–NIR spectrophotometer. The NIR emission spectra were carried out using JOBIN YVON fluorolog–3 spectrofluorometer with a PMT by exciting at 980 nm laser diode with a resolution of ±1.0 nm. All these measurements were carried out at room temperature (RT) only.

International Journal of
Scientific Research in Science and Technology (IJSRST)
Print ISSN : 2395-6011, Online ISSN : 2395-602X
International Conference on Advanced Materials
Held on 14, 15 December 2017, Organized by Department of Physics,
St. Joseph's College, Trichy, Tamilnadu, India

3. FTIR analysis

The FTIR spectra of LTB0.5E glass displayed in figure 1 as a representative case which is used to identify the existing functional groups present in the borotellurite glasses. The presence of principle IR vibration bond around 703 cm^{-1} is attributed B–O–B bond bending vibrations in [BO_3] units and Te–O bond stretching vibrations in TeO_3 and TeO_6 units [4]. The absence of O–B–O boroxol ring formation in the prepared glass around the region 806 cm^{-1} confirms that the glass system consists of randomnly connected BO_3 and BO_4 groups. The broad band around 1004 cm^{-1} is due to B–O stretching vibrations of BO_4 units in tri-, tetra- and penta borate groups. The peaks observed around 1370 cm^{-1} indicates the presence of B–O stretching in [BO_3] units [3,4]. The small hump observed around 1632 cm^{-1} is due to the asymmetric stretching relaxation of the B–O bond of trigonal BO_3 units [3,4]. The presence of small peak around 3422 cm^{-1} indicates the OH bond vibrations in the titled glass [4].

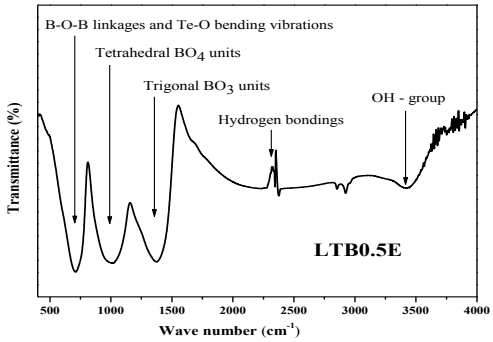

Figure 1. FTIR spectrum of the Er^{3+} doped LTB0.5E glass

Thus the presence of bending and stretching vibrations of borate and tellurite are confirmed in the prepared glasses.

4. Absorption spectral analysis

Figure 2 shows the UV–Vis absorption spectrum of the 0.5 wt% Er^{3+} doped lead borotellurite glass recorded in the wavelength region 400–850 nm. The sharp and narrow peaks of the titled glasses which arise due to the electrostatic and spin orbit interactions of the 4f–4f energy level. The spectrum consist of 6 absorption bands, which attributed to the transition from ground level $^4I_{15/2}$ to the various excited states $^4I_{9/2}$, $^4F_{9/2}$, $^4S_{3/2}$, $^2H_{11/2}$, $^4F_{7/2}$, and $^4F_{3/2}$ at around 797, 651, 544, 521, 487 and 450 nm respectively.

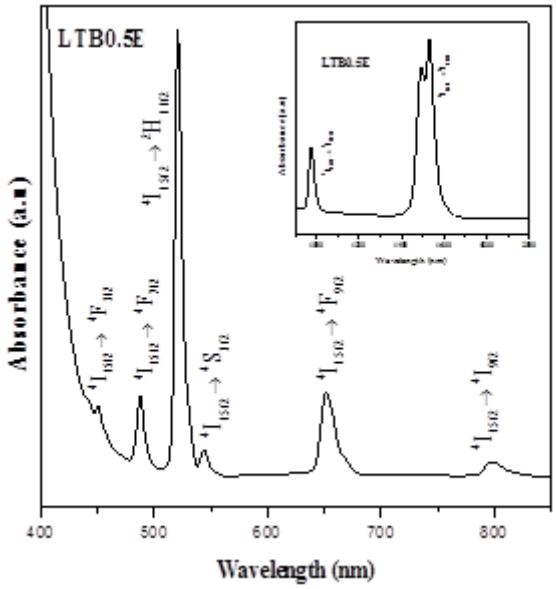

Figure 2. Absorption spectrum of the Er^{3+} doped LTB0.5E glass. [Inset shows the NIR Absorption spectrum of the LTB0.5E glass]

The inset of figure 2 shows the NIR absorption spectra of the same glass recorded in the wavelength region 900–2000 nm which exhibits two intense bands due to the transition from $^4I_{15/2}$ $\rightarrow$$^4I_{11/2}$ and $^4F_{13/2}$ at around 977 and 1527 nm. The hypersensitive nature of the rare earth ion to the host matrix ,which holds it, must satisfies the

International Journal of
Scientific Research in Science and Technology (IJSRST)
Print ISSN : 2395-6011, Online ISSN : 2395-602X
International Conference on Advanced Materials
Held on 14, 15 December 2017, Organized by Department of Physics,
St. Joseph's College, Trichy, Tamilnadu, India

forbidden selection rule $|\Delta L| \leq 2$, $|\Delta J| \leq 2$ and $\Delta S = 0$. According to it, $^4I_{15/2} \rightarrow {}^2H_{11/2}$ is hypersensitive in nature. The predominant covalent/ionic nature can be determined by Nephelauxetic ratios (β) and bonding parameter (δ) values which are calculated using the reported expressions [4,5]. The obtained bonding parameter values are tabulated in table 1 and the negative δ values indicate the ionic nature of the Er^{3+} metal-ligand bond. It founds to be ionic and on higher concentration a gradual increase is observed owing to the ionic nature in the glass, which means interaction between electron is reduced in lower concentration and increased in higher concentration due to increase in erbium content.

5. Judd-Ofelt Intensity Parameters

From the spectral intensities of the absorption spectra, the JO intensity parameters were determined by least squares fitting method [4,5] and are presented in Table 1 along with the spectroscopic quality factor. Judd-Ofelt theory is the most useful theory in estimating the probability of forced electric dipole transitions of rare earth ions in various environments. Generally, Ω_2 intensity parameter describes asymmetric of coordinate structure, bodings nature and polarizability of ligand ion or molecule, Ω_4 and Ω_6 refers to the viscosity of the glass matrix and dielectric of the media.

Table 1. Judd-Ofelt ($\times 10^{-20}$cm^2) parameters and bonding parameters (δ) of Er^{3+} doped LTBxE glasses

Glass codes	Ω_2	Ω_4	Ω_6	Ω_4/Ω_6	δ
LTB0.1E	4.61	1.36	1.11	1.23	–0.113
LTB0.25E	4.69	1.43	1.19	1.20	–0.125
LTB0.5E	4.77	1.60	1.25	1.28	–0.138
LTB1E	4.86	1.74	1.37	1.27	–0.162
LTB2E	5.27	1.81	1.44	1.26	–0.227

In the present study, the trends of the JO parameters are found to be in the order $\Omega_2 > \Omega_4 > \Omega_6$ for all the prepared glasses. The higher Ω_2 values suggest the higher rigidity and higher covalency around the Er^{3+} ion site. The ratio between Ω_4 and Ω_6 is known as spectroscopic quality factor and the magnitude of the same is important predictor to claim a good laser material. The higher Ω_4/Ω_6 value of the prepared LTB0.5E glass can be suggesting the suitability for the development of lasers and photonic devices.

6. NIR Luminescence spectral analysis

NIR emission spectra of the Er^{3+} ions in the title glasses monitoring at an excitation wavelength at 980 nm displayed in the figure 3. The emission band at around 1554 nm corresponding to $^4I_{13/2} \rightarrow {}^4I_{15/2}$ transition which is most important one has received much attention as it is useful for optical communication, IR laser applications and eye-safe laser for range finding applications. It is observed from the figure that, the luminescence intensity of the $^4I_{13/2} \rightarrow {}^4I_{15/2}$ transition is found to increase with the increase in Er^{3+} ion concentration upto 0.5wt% of Er^{3+} ion content and after that quenching occurs. Decreases of luminescence intensity at higher concentration of Er^{3+} ions is mainly due to the higher prospect of Er^{3+}–Er^{3+} interactions where the inter ionic distance decreases thus in turn causes the close packing of large number of Er^{3+} ions energy levels and it shortens the lifetime of the $^4I_{13/2}$ excited level.

International Journal of
Scientific Research in Science and Technology (IJSRST)
Print ISSN : 2395-6011, Online ISSN : 2395-602X
International Conference on Advanced Materials
Held on 14, 15 December 2017, Organized by Department of Physics,
St. Joseph's College, Trichy, Tamilnadu, India

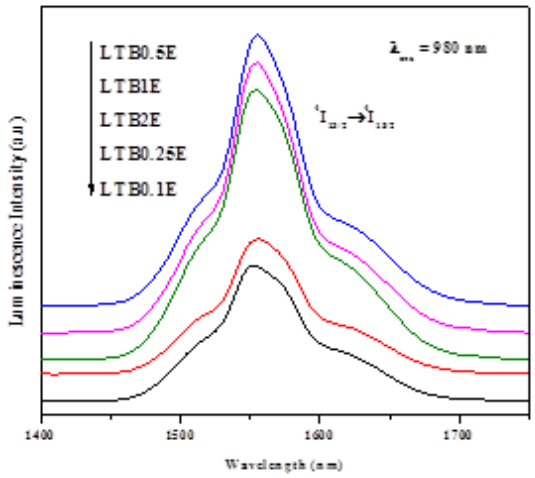

Figure 3. NIR Emission spectra of the Er^{3+} doped lead borotellurite glasses

The Decreases of luminescence intensity at higher concentration of Er^{3+} ions is mainly due to the higher prospect of Er^{3+}–Er^{3+} interactions where the inter ionic distance decreases thus in turn causes the close packing of large number of Er^{3+} ions energy levels and it shortens the lifetime of the $^4I_{13/2}$ excited level.

7. Radiative properties

The radiative properties helpful in determining the best optical device such as transition probability (A), gain band width, emission cross-section(σ_e) and branching ratio (β_R) for this NIR transition were calculated using formulae available in the literature [4]. The most predominant parameter the full width at half maximum (FWHM) of the $^4I_{13/2} \rightarrow {}^4I_{15/2}$ transition is very important in telecommunication since it allows to cover two of the optical communication bands, the C and L bands and another important parameter is the Gain band width (ΔG) which is the product of effective band width ($\Delta\lambda_{eff}$) and stimulated emission cross-section (σ_e). The FWHM values for the prepared glasses are found to 61, 63, 77, 73and 70 nm corresponding to the as LTB0.1E, LTB0.25E, LTB0.5E, LTB1E and LTB2E glasses respectively. Among all the prepared glasses, the A, σ_e, FWHM and ΔG for the LTB0.5E glass is found to be higher and same is compared with the reported glasses [4,5,7] and displayed in the table 2.

Table 2. Radiative properties (λ_p (nm), $\Delta\lambda_{eff}$ (nm), A (s^{-1}), τ_R (ms), σ_e ($\times10^{-22}$ cm^2), β_R and ΔG ($\times10^{-28}$)) for the $^4I_{13/2}$ level under 980 nm excitation of the LTB0.5E glass with the other reported Er^{3+} doped glasses

$^4I_{13/2} \rightarrow {}^4I_{15/2}$ Transition	Parameters	LTB 0.5E	LZB 0.5E[4]	A05 [5]	PKAZF Er10[7]
	λ_p	1554	1532	1531	1529
	$\Delta\lambda_{eff}$	62	66	73	-
	A	190	184	137	230
	τ_R	4.27	4.40	7.31	4.36
	σ_e	86	93	54	32
	β_R (cal)	1	1	1	1
	β_R (exp)	1	1	1	1
	ΔG	527.7	613.8	466.3	260.8

It is observed from the table that, the radiative properties A, σ_e, FWHM and ΔG of LTB0.5E glass comparable to the reported glasses, it can be suggested as the potential candidate for the development of laser and optical amplifier devices.

8. Conclusion

In the present work, the presence of B–O stretching vibrations of $[BO_3]^-$ units and in BO_4 units and the stretching vibrations of Te–O–Te linkages in TeO_4 units were confirmed through FTIR spectra. The bonding parameter of all the

International Journal of
Scientific Research in Science and Technology (IJSRST)
Print ISSN : 2395-6011, Online ISSN : 2395-602X
International Conference on Advanced Materials
Held on 14, 15 December 2017, Organized by Department of Physics,
St. Joseph's College, Trichy, Tamilnadu, India

glasses was calculated and the increasing negative values indicate the increasing ionic nature in the LTBxE glasses. The trend follows the usual manner of erbium as $\Omega_2 > \Omega_4 > \Omega_6$. The spectroscopic factor (Ω_4/Ω_6) was found to be 1.28 for LTB0.5E glass which suggest for photonic applications. The broad luminescence with high intensity was observed in LTB0.5E glass and the other optical device determining properties such as A, σ_e, FWHM and ΔG for the same glass is found to be higher thus, suggest its feasibility for the development of laser and optical amplifier devices.

9. References

[1] J.F. Gomes, A.M.O. Lima, M. Sandrini, A.N. Medina, A. Steimacher, F. Pedrochi, M.J. Barboza, "Optical and spectroscopic study of erbium doped calcium borotellurite glasses", Optical Materials, 66, 2017, pp. 211-219.

[2] M.N. Azlan, M.K. Halimah, H.A.A. Sidek, "Linear and nonlinear optical properties of erbium doped zinc borotellurite glass system", Journal of Luminescence, 181, 2017, pp. 400 – 406.

[3] K. Annapoorani, K. Maheshvaran, S. Arunkumar, N. Suriya Murthy, K. Marimuthu, "Structural and luminescence behavior of Er^{3+} ions doped Barium tellurofluoroborate glasses", Spectrochimica Acta Part A: Molecular and Biomolecular Spectroscopy, 135, 2015, pp. 1090– 1098.

[4] K. Selvaraju, K. Marimuthu, "Structural and spectroscopic studies on concentration dependent Er^{3+} doped boro-tellurite glasses", Journal of Luminescence, 132, 2012, pp. 1171–1178.

[5] A. Maaoui, M. Haouari, Z. Zaaboub, I. Fraj, F. Saidi, H. Ben Ouada, "Concentration effects on the optical spectroscopic properties of Er^{3+}-doped TeO_2-Nb_2O_5-ZnO vitreous system", Journal of Alloys and Compounds, 663, 2013, pp. 395–406.

[6] P. Karthikeyan, P. Suthanthirakumar, R. Vijayakumar, K. Marimuthu, "Structural and luminescence behaviour of Er^{3+} doped telluro-fluoroborate glasses", Journal of Molecular Structure, 1083, 2015, pp. 268 –277.

[7] V.B. Sreedhar, N. Vijaya, D. Ramachari, C.K. Jayasankar, "Luminescence studies on Er^{3+} -doped zincfluorophosphate glasses for 1.53 μm laser applications", Journal of Molecular Structure, 1130, 2017, pp. 1001 –1008.

International Journal of
Scientific Research in Science and Technology (IJSRST)
Print ISSN : 2395-6011, Online ISSN : 2395-602X
International Conference on Advanced Materials
Held on 14, 15 December 2017, Organized by Department of Physics,
St. Joseph's College, Trichy, Tamilnadu, India

Structural and Luminescence Studies of Sm^{3+} Doped Telluro-Fluoroborate Glasses for Photonic Applications

P. Suthanthirakumar, M. Mariyappan, K. Marimuthu*
Department of Physics, Gandhigram Rural Institute–Deemed University, Gandhigram – 624 302, India
*Corresponding author: mari_ram2000@yahoo.com

Abstract

A new series of Sm^{3+} ions doped telluro-fluoroborate (xSTFB) glasses have been prepared following melt quenching technique and the structural and luminescence behaviors were studied by recording X-ray diffraction, FTIR, absorption and photoluminescence spectral measurements. The amorphous nature of the glasses was confirmed through XRD pattern and the different vibrational bonds of borate and tellurite networks were identified through FTIR spectra. The bonding parameters (β, δ) and Judd-Ofelt intensity parameters (Ω_λ) have been calculated from the absorption spectra in order to explore the bonding nature of the ligand environment around Sm^{3+} ions. The luminescence spectra exhibit four emission bands in the visible region due to the $^4G_{5/2} \rightarrow {}^6H_{5/2}$, $^6H_{7/2}$, $^6H_{9/2}$ and $^6H_{11/2}$ transitions and the same are characterized through CIE 1931 chromaticity diagram. The radiative parameters such as transition probability (A), stimulated emission cross-section (σ_e), branching ratios (β_R) and radiative lifetime (τ_R) have been determined to elucidate the suitability of the studied glasses for the fabrication of various photonic devices.

Keywords: Telluro-fluoroborate, Bonding parameter, JO intensity parameter, Luminescence, stimulated emission cross-section, Laser

1. Introduction

In the recent years, glasses doped with trivalent rare earth (RE^{3+}) ions receive lot of interest due to their potential applications in the design and development of photonic devices such as solid state lasers, display monitors, solar cells, sensors and light emitting diodes (LEDs) [1,2]. Among the variety of glass hosts, telluro-fluoroborate glasses are proven to be the better host due to their excellent physical and chemical properties such as high RE ion solubility, low melting point, high thermal stability, low phonon energy, super hardness and higher refractive index [3]. Among the RE ions, Sm^{3+} is one of the most attractive ion for investigating luminescent properties because of its applications in various fields such as visible solid state lasers, high density optical memory storage, under sea communications and color displays etc.,[4]. The motivation of the present investigation is to prepare a new series of Sm^{3+} doped telluro-fluoroborate glasses and to explore their structural and luminescence properties through XRD, FTIR, optical absorption and luminescence measurements for the possible photonic applications.

2. Experimental

Sm^{3+} ions doped telluro-fluoroborate glasses with the chemical composition $(40–x)B_2O_3 + 25TeO_2 + 20ZnF_2 + 15CaF_2 + xSm_2O_3$ (where x= 0.1, 0.25, 0.5, 1 and 1.5 in wt% hereafter named as 0.1STFB, 0.25STFB, 0.5STFB, 1STFB and 1.5STFB respectively) have been synthesized by conventional melt quenching technique following the procedure reported in literature [3]. The X-ray diffraction measurements were carried out using JEOL 8030 X-ray diffractometer employing CuKα radiation. The FTIR spectra have been recorded using Perkin-Elmer paragon-500 FTIR spectrophotometer following the KBr Pellet technique. The absorption spectra of the prepared glasses have been recorded using Perkin Elmer Lambda-950 UV-Vis-NIR spectrophotometer in the wavelength range 350–1700 nm. Jobin Yvon Fluorolog-3 Spectrofluorimeter was used to record the luminescence spectra with a spectral resolution of ±0.5 nm in the wavelength range 550–750 nm.

International Journal of
Scientific Research in Science and Technology (IJSRST)
Print ISSN : 2395-6011, Online ISSN : 2395-602X
International Conference on Advanced Materials
Held on 14, 15 December 2017, Organized by Department of Physics,
St. Joseph's College, Trichy, Tamilnadu, India

3. X-ray diffraction and FTIR spectral analysis

The inset of figure 1 shows the XRD pattern of Sm^{3+} ions doped 1STFB glass recorded in the range of $5^{o} \leq \theta \geq 80^{o}$. The spectrum does not show any characteristic sharp diffraction crystalline peaks, but shows broad diffused scattering at lower angles which illustrate the amorphous nature of the prepared glasses. The FTIR spectroscopy is one of the efficient analytical tools to identify the functional groups and to characterize the bonding information in the glass samples. The FTIR spectra of the prepared glasses were recorded in the range between 400 to 4000 cm^{-1} and the FTIR spectrum of 1STFB glass is shown in figure 1 as a representative case. The broad IR transmission band at around 3422 cm^{-1} is due to the stretching vibrations of O–H groups. The observed bands at 2927 and 2857 cm^{-1} are the characteristic of the hydrogen bond present in the glasses. The asymmetric stretching vibrations of B–O bonds in BO_3 units have been identified through the band at 1275 cm^{-1}. The band positioned at 1018 cm^{-1} is attributed to the B–O stretch in BO_4 units from tri, tetra and penta-borate groups. The band observed around 684 cm^{-1} denotes the combined vibrations of B–O–B bending in BO_4 units and Te–O bond stretching in TeO_3 units. The band located around 490 cm^{-1} is due to the bending vibrations of Te–O–Te or O–Te–O linkages [3].

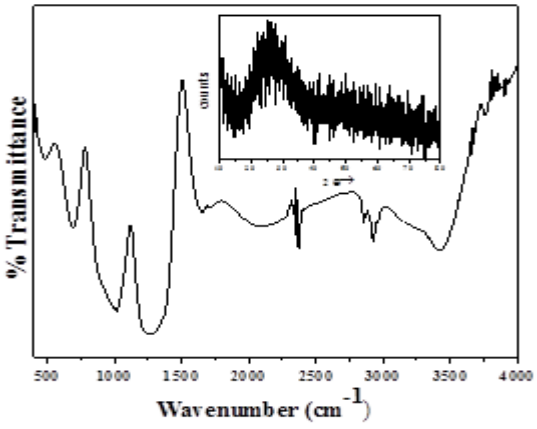

Figure 1. FTIR spectrum of the Sm^{3+} doped 1STFB glass. [Inset shows the XRD spectrum of the 1STFB glass]

4. Absorption spectral analysis and Judd–Ofelt parameters

The absorption spectrum of one of the Sm^{3+} ions doped 1STFB glass recorded in the UV-Vis-NIR region of wavelength range between 350–1700 nm is show in figure 2 as a representative case. The spectrum exhibit several absorption bands corresponds to the f-f transitions from the $^6H_{5/2}$ ground state to the different excited states of Sm^{3+} ions such as $^6F_{1/2}$, $^6H_{15/2}$, $^6F_{3/2}$, $^6F_{5/2}$, $^6F_{7/2}$, $^6F_{9/2}$, $^6F_{11/2}$, $^4I_{11/2}+^4M_{13/2}+^4I_{9/2}$, $^4I_{13/2}$, $^4G_{9/2}+^4M_{17/2}$, $^6P_{5/2}$, $^4M_{19/2}$, $^4L_{13/2}+^4F_{7/2}+^6P_{3/2}$, $^4L_{15/2}$, $^6P_{7/2}$ and $^4D_{3/2}$ positioned at around 6549, 6792, 7301, 8147, 9285, 10593, 17794, 21277, 21645, 22831, 23635, 23992, 24814, 25641, 26738 and 27777 cm^{-1} respectively [1,4]. Among all the absorption transitions, intensity of the $^6H_{5/2} \rightarrow ^6F_{7/2}$ and $^6H_{5/2} \rightarrow ^6P_{3/2}$ transitions are found to be sensitive to the nature of the ligand field environment around the RE ion site thus called as hypersensitive transitions. Further these transitions obey the selection rules, $|\Delta S| = 0$, $|\Delta S| \leq 2$ and $|\Delta J| \leq 2$. The bonding nature of the Sm^{3+}-ligand can be determined from the nephelauxetic ratios (β) and bonding parameter (δ) values since the RE^{3+} ions produce nephelauxetic effect when doped into the glass host matrix. From the average values of β (taken as $\bar{\beta}$) the bonding parameter can be evaluated from the formula $\delta = [(1-\bar{\beta})/\bar{\beta}] \times 100$, where β is the nephelauxetic ratio which calculated using the relation $\beta = \nu_c/\nu_a$, where ν_c is the wave number (in cm^{-1}) of a particular transition for an ion in the glass matrix and ν_a is the wave number (in cm^{-1}) of the same transition for the aqua-ion. The bonding nature (Sm^{3+}-ligand) will be covalent or ionic depending upon the positive or negative sign of δ [3,4]. The δ values of the studied glasses are presented in table 1 and the negative sign of δ values observed for all the glasses indicates the ionic nature of the Sm^{3+} ions with the surrounding ligands O^{2-}/F^{-} and the ionicity decreases gradually with the increase in Sm^{3+} concentration in the prepared glasses.

International Journal of
Scientific Research in Science and Technology (IJSRST)
Print ISSN : 2395-6011, Online ISSN : 2395-602X
International Conference on Advanced Materials
Held on 14, 15 December 2017, Organized by Department of Physics,
St. Joseph's College, Trichy, Tamilnadu, India

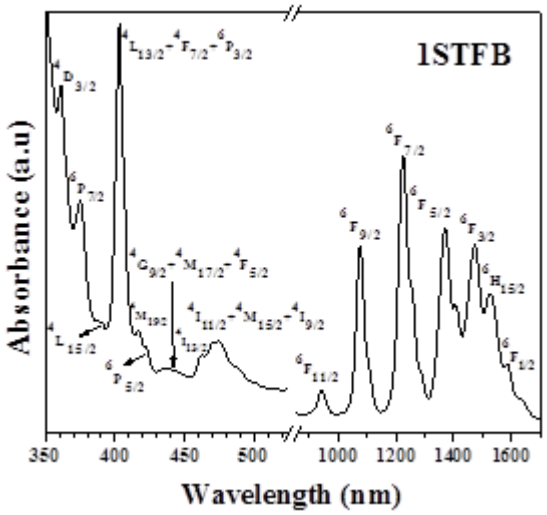

Figure 2. Absorption spectrum of the Sm^{3+} doped 1STFB glass

The Judd-Ofelt intensity parameters Ω_λ (λ= 2, 4 and 6) were calculated from the spectral intensities of the absorption spectra by using least square fitting method and the values of the same are presented in table 1. The Ω_2 parameter is sensitive to the chemical bonding between RE^{3+} ions and the ligand anions as well as asymmetry of local host environment around the RE^{3+} ions, whereas the Ω_4 and Ω_6 parameters are related to the rigidity and bulk properties of the host matrix [4,5]. In the present investigation, the trends of JO parameters are found to be in the order $\Omega_4>\Omega_6>\Omega_2$ for all the glasses and the lower Ω_2 values implies less covalent characteristic (more ionic) and higher symmetry around the Sm^{3+} ions with their surrounding ligands. The ratio between Ω_4 and Ω_6 is known as spectroscopic quality factor and the magnitude of the same is significant predictor to claim a good laser material. The higher Ω_4/Ω_6 value obtained for the prepared 1STFB glass can be suggesting the suitability for the development of lasers and various optical devices.

Table 1. Bonding parameters (δ) and Judd-Ofelt ($\times10^{-20}cm^2$) parameters of the Sm^{3+} doped xSTFB glasses

Glass codes		0.1S TFB	0.25S TFB	0.5S TFB	1S TFB	1.5S TFB
Parameters	δ	–0.253	–0.265	–0.269	–0.284	–0.313
	Ω_2	2.238	2.213	1.469	1.272	1.192
	Ω_4	5.724	5.427	3.309	5.072	5.931
	Ω_6	5.145	3.921	2.761	2.459	2.886
	Ω_4/Ω_6	1.113	1.384	1.198	2.063	2.055

5. Luminescence spectra and radiative parameters

The luminescence spectra of the xSTFB glasses recorded in the wavelength range of 550–750 nm with an excitation wavelength of 404 nm is depicted in figure 3. Each emission spectrum contains four emission bands centered at 563, 599, 646 and 708 nm corresponding to the transitions $^4G_{5/2}\rightarrow{}^6H_J$ (J = 5/2, 7/2, 9/2 and 11/2) respectively with considerable variation in their intensities. Among these, the transition $^4G_{5/2}\rightarrow{}^6H_{7/2}$ (at 599 nm) demonstrates maximum intensity in the unique reddish-orange region for all the glasses which appears to be suitable candidate for visible lasers emission [1,4,6].

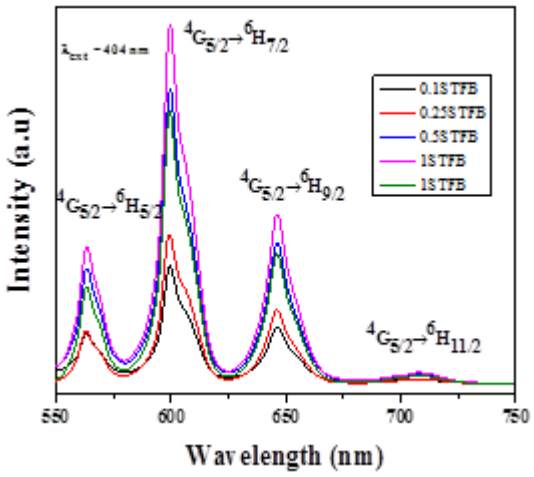

Figure 3. Luminescence spectra of the Sm^{3+} doped telluro-fluoroborate glasses

International Journal of
Scientific Research in Science and Technology (IJSRST)
Print ISSN : 2395-6011, Online ISSN : 2395-602X
International Conference on Advanced Materials
Held on 14, 15 December 2017, Organized by Department of Physics,
St. Joseph's College, Trichy, Tamilnadu, India

It is evident from figure 3 that, the luminescence quenching takes place at 0.5wt% of sm^{3+} ions in the studies glasses for all the emission bands. The same may occur either due to efficient energy transfer between nearby Sm^{3+} ions or cross-relaxation process which produced at higher Sm^{3+} ion concentrations.

From the luminescence spectral data along with JO parameters, the important laser properties such as effective bandwidth ($\Delta\lambda_{eff}$), stimulated emission cross-section (σ_e), radiative and experimental branching ratios (β_R) and radiative lifetime (τ_R) for the $^4G_{5/2}\rightarrow{}^6H_{5/2}$, $^6H_{7/2}$ and $^6H_{9/2}$ emission transitions of the title glasses were calculated and the results are presented in table 2. The β_R and σ_e are the significant lasing parameters which used to characterize the potential laser transition of the RE ions in the glass host matrices [4-7]. It is observed from the tabulated results that, of all the prepared glasses 1STFB glass exhibit higher β_R and σ_e values for the $^4G_{5/2}\rightarrow{}^6H_{7/2}$ (599 nm) transition and the same may be suggested for the fabrication of lasers and photonic devices operating in the visible region.

Table 2. The values of λ_p (nm), $\Delta\lambda_{eff}$ (nm), A (s^{-1}), β_R, σ_e (10^{-22} cm^2) and τ_R (ms) for the $^4G_{5/2}\rightarrow{}^6H_{5/2}$, $^6H_{7/2}$ and $^6H_{9/2}$ transitions of the prepared xSTFB glasses

Parameters		0.1STFB	0.25STFB	0.5STFB	1STFB	1.5STFB
$^4G_{5/2}\rightarrow{}^6H_{5/2}$	λ_p	563	563	563	563	563
	$\Delta\lambda_{eff}$	7.141	8.289	8.365	9.753	8.308
	σ_e	1.082	1.105	1.125	1.388	1.132
	β_R(cal)	0.048	0.051	0.057	0.059	0.053
	β_R(ex)	0.167	0.173	0.182	0.191	0.172
$^4G_{5/2}\rightarrow{}^6H_{7/2}$	λ_p	599	599	599	599	599
	$\Delta\lambda_{eff}$	8.471	8.562	8.893	9.329	8.775
	σ_e	7.351	7.819	8.214	9.652	8.712
	β_R(cal)	0.573	0.584	0.579	0.591	0.532
	β_R(ex)	0.652	0.667	0.672	0.694	0.661
$^4G_{5/2}\rightarrow{}^6H_{9/2}$	λ_p	646	646	646	646	646
	$\Delta\lambda_{eff}$	7.556	7.953	8.345	9.231	8.841
	σ_e	3.716	3.882	4.014	4.865	3.916
	β_R(cal)	0.303	0.316	0.332	0.341	0.317
	β_R(ex)	0.421	0.446	0.463	0.485	0.449
τ(cal)		2.831	3.016	3.281	2.912	2.721

6. CIE chromaticity co-ordinates

The chromaticity co-ordinates (x,y) of the Sm^{3+} telluro-fluoroborate glasses have been evaluated from the luminescence spectra using CIE 1931 system as per the procedure reported in the literature [3] in order to explore the prominent emission exhibited by the title glasses. The obtained values of chromaticity coordinates (x, y) are found to be (0.523, 0.465), (0.558, 0.441), (0.541, 0.452), (0.586, 0.403) and (0.511, 0.471) for the 0.1STFB, 0.25STFB, 0.5STFB, 1STFB and 1.5STFB glasses respectively.

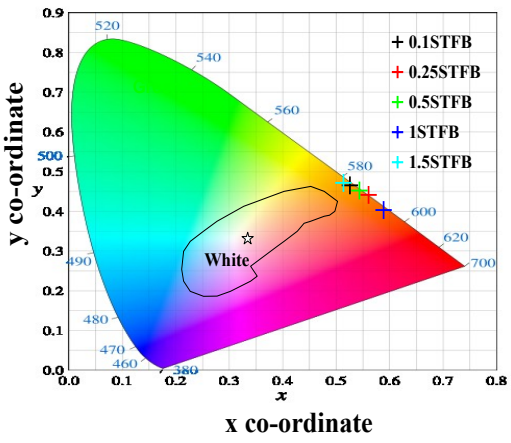

International Journal of
Scientific Research in Science and Technology (IJSRST)
Print ISSN : 2395-6011, Online ISSN : 2395-602X
International Conference on Advanced Materials
Held on 14, 15 December 2017, Organized by Department of Physics,
St. Joseph's College, Trichy, Tamilnadu, India

Figure 4. CIE coordinate diagram of the Sm^{3+} doped telluro-fluoroborate glasses

Figure 4 displays the CIE chromaticity diagram of the present glasses and it is observed from the figure that the x,y values of all the samples fall in the reddish-orange region. Hence, it is suggested that the prepared glasses are potential candidate for reddish-orange laser, light emitting diode and display device applications.

7. Conclusion

Concentration dependent Sm^{3+} ions doped telluro-fluoroborate glasses have been prepared and their structural, luminescence behaviors were explored through XRD, FTIR, absorption and luminescence measurements. The presence of fundamental functional groups such as OH stretching vibrations, B–O bond stretching vibrations in BO_3 and BO_4 units, O_3B–O–BO_3 bending vibrations and Te–O stretching vibrations in TeO_3 and TeO_4 units in the present glass network were analysed through FTIR spectral analysis. JO intensity parameters of the titled glasses follow the trend as $\Omega_4>\Omega_6>\Omega_2$ for all the glasses and the lower Ω_2 values implies less covalent characteristic and higher symmetry around the Sm^{3+} ions with their surrounding ligands. Emission spectra of the prepared glasses exhibit, unique strong reddish-orange emission for the transition $^4G_{5/2}\rightarrow{}^6H_{7/2}$ (at 599 nm) and the CIE coordinates of all the samples fall in the reddish-orange region suggest their potential for the reddish-orange laser, light emitting diode and display device applications. Among the prepared glasses 1STFB glass exhibit higher β_R and σ_e values for the $^4G_{5/2}\rightarrow{}^6H_{7/2}$ transition and the same may be suggested for the fabrication of lasers and photonic devices operating in the visible region.

8. References

[1] N. Deopa, A.S. Rao, Opt. Mater. 72, 2017, pp. 31–39.

[2] L. Yao, G. Chen, Tao Yang, Ying Luo, Y. Yang, J. Alloys Compd. 692, 2017, pp. 346–350.

[3] P. Suthanthirakumar, K. Marimuthu, J. Mol. Struct. 1125, 2015, pp. 443–452.

[4] M. Mariyappan, S. Arunkumar, K. Marimuthu, J. Mol. Struct. 1105, 2016, 214–224.

[5] S. Babu, A. Balakrishna, D. Rajesh, Y.C. Ratnakaram, Spectrochim. Acta Part A 122, 2014, pp. 639–648.

[6] T. Sasikala, L. Rama Moorthy, A. Mohan Babu, Spectrochim. Acta Part A 104, 2013, pp. 445–450.

[7] I.I. Kindrat, B.V. Padlyak, R. Lisiecki, Opt. Mater. 49, 2015, pp. 241–248.

International Journal of
Scientific Research in Science and Technology (IJSRST)
Print ISSN : 2395-6011, Online ISSN : 2395-602X
International Conference on Advanced Materials
Held on 14, 15 December 2017, Organized by Department of Physics,
St. Joseph's College, Trichy, Tamilnadu, India

Energy Transfer Studies in Dy^{3+} Ions Doped Aluminium Telluroborate Glasses

K. Annapoorani, P. Karthikeyan, K. Marimuthu*
Department of Physics, Gandhigram Rural Institute–Deemed University, Gandhigram – 624 302, India
*Corresponding author: mari_ram2000@yahoo.com

Abstract

Dy^{3+} ions doped aluminium telluroborate glasses were prepared following the melt-quenching technique by varying the Dy^{3+} ions concentration with respect to borate content. The optical behavior of the title glasses was explored by recording absorption and luminescence spectra. The ionic or covalent nature was determined from the energy positions observed in the absorption spectra using Nephelauxetic ratios. The Yellow/Blue ratio was calculated from the luminescence spectra to determine the degree of asymmetry in the prepared glasses. The luminescence intensity is found to quench beyond 1.0 wt% of Dy^{3+} ions doped aluminium telluroborate glass which may be due to the resonance energy transfer or cross-relaxation phenomena takes place and is analyzed with Inokuti-Hirayama model.

Keywords: Glasses, Absorption, Luminescence, Energy transfer, Decay Analysis

1. Introduction

Rare earth doped materials finds applications in various fields such as solid state lasers, upconvertors, optical memories, white light emitting diodes, optical amplifiers due to their sharp emission, high stability and long lifetime [1]. Among them, Dy^{3+} ions find applications in white LEDs due to its dominant emission from $^4F_{9/2} \rightarrow {}^6H_{15/2}$ (484 nm), $^4F_{9/2} \rightarrow {}^6H_{13/2}$ (576 nm) transitions whose integrated intensity ratio can be tuned with ligand field environment. Many researchers such as Venkata Krishnaiah et al. [2], Joanna Pisarska et al. [3] studied the optical properties of Dy^{3+} ions in various host matrices and discussed the energy transfer mechanism involved in it. In the present work, energy transfer mechanism involved in the Dy^{3+} ions doped aluminum telluroborate glasses were studied with luminescence, decay spectral analysis and their results were discussed and compared with the reported literature.

2. Experimental

Dy^{3+} ions doped aluminium telluroborate glasses were prepared with the chemical composition $(55–x)H_3BO_3+25TeO_2+20Al_2O_3+xDy_2O_3$ (where x =0.25, 0.5, 1.0, 2.0 in wt%) following the melt-quenching technique [4] and labeled as ATB0.25D, ATB0.5D, ATB1.0D, ATB2.0D respectively. High Purity (99.99%) chemicals (H_3BO_3, TeO_2, Al_2O_3, Dy_2O_3) from Sigma Aldrich were used as precursors for the preparation of these glass samples. The absorption spectral measurements were made using CARY 500 UV-Vis-NIR spectrophotometer in the wavelength region 300–2000 nm with a spectral resolution of ± 1 nm. The Luminescence spectra have been recorded employing JASCO spectrofluorimeter using xenon lamp (450 W) in the wavelength range 400–700 nm with a spectral resolution of ± 1 nm. The decay measurements were made employing the Edinburgh FLS–900 time resolved fluorescence spectrometer.

International Journal of
Scientific Research in Science and Technology (IJSRST)
Print ISSN : 2395-6011, Online ISSN : 2395-602X
International Conference on Advanced Materials
Held on 14, 15 December 2017, Organized by Department of Physics,
St. Joseph's College, Trichy, Tamilnadu, India

3. Absorption spectra

The absorption spectra of the Dy^{3+} ions doped aluminium telluroborate glasses were recorded in the wavelength region 300–2000 nm. Since there is no much variation in the spectral position with the increase in the concentration of Dy^{3+} ions in the prepared glasses, absorption spectrum of the ATB2.0D glass is shown in figure 1 as a representative case and the band assignments to the observed energy positions were made referring the literature reported by Carnal et al. [5] and is comparable to the reported literature [1,6]. The absorption edge was found to be red shifted with the increase in the concentration of the Dy^{3+} ions in the prepared glasses. Twelve inhomogeneously broadened peaks were observed due to the disorderliness present in the title glasses from the $^6H_{15/2}$ ground state to the various excited states such as $^6P_{7/2}$, $^6P_{5/2}$, $^4F_{7/2}$, $^4G_{11/2}$, $^4I_{15/2}$, $^4F_{9/2}$, $^6F_{3/2}$, $^6F_{5/2}$, $^6F_{7/2}$, $^6F_{9/2}$, $^6F_{11/2}$, $^6H_{11/2}$ positioning at 346, 365, 388, 425, 450, 470, 750, 800, 902, 1092 nm respectively. Among these transitions, $^6H_{15/2} \rightarrow {}^6F_{5/2}$ transition obeys the selection rule $\Delta J \leq 2$, $\Delta L \leq 2$, $\Delta S = 0$ and its intensity varies with the increase in the concentration of Dy^{3+} ions in the prepared glasses hence this transition is regarded as hypersensitive transition. From the energy positions of the absorption spectra, the covalancy nature was determined using Nephelauxetic ratios and bonding parameter values obtained by using the expressions reported in the literature [1] and the values are found to be – 0.0057, – 0.0056, – 0.0053, – 0.0051 corresponding to the prepared ATB0.25D, ATB0.5D, ATB1.0D, ATB2.0D glasses respectively.

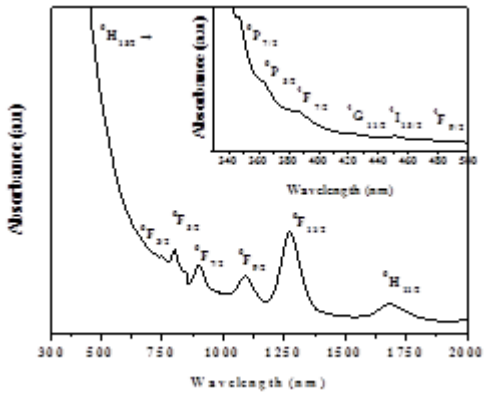

Figure 1. Absorption spectrum of 2.0 wt% of Dy^{3+} ion doped aluminium telluroborate glass

4. Excitation and emission spectra

Figure 2 shows the representative excitation spectrum of the ATB2.0D glass recorded in the wavelength region 250–500 nm by monitoring the emission at 484 nm and 575 nm. Eight excitation peaks were observed from the $^6H_{15/2}$ ground state to the various excited states $^6P_{3/2}$, $(^4F, {}^4D)_{5/2}$, $^6P_{7/2}$, $^6P_{5/2}$, $^4F_{7/2}$, $^4G_{11/2}$, $^4I_{15/2}$, $^4F_{9/2}$ positioning at 325, 338, 350, 365, 388, 426, 452, 473 nm respectively.

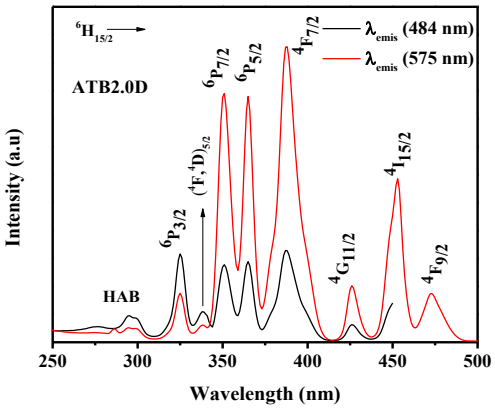

Figure 2. Excitation spectrum of ATB2.0D glass

Among them, peak corresponding to the $^6H_{15/2} \rightarrow {}^4F_{7/2}$ (388 nm) transition possess comparatively higher intensity for both the emission wavelengths thus suggest the fact that the prepared glasses can

International Journal of
Scientific Research in Science and Technology (IJSRST)
Print ISSN : 2395-6011, Online ISSN : 2395-602X
International Conference on Advanced Materials
Held on 14, 15 December 2017, Organized by Department of Physics,
St. Joseph's College, Trichy, Tamilnadu, India

effectively be excited at 388 nm. The same excitation wavelength is chosen to record the luminescence spectra for all the prepared glasses and is shown in figure 3. Three distinguishable emission peaks were observed at 483, 575, 662 nm corresponding to the $^4F_{9/2} \rightarrow {}^6H_{15/2}$, $^4F_{9/2} \rightarrow {}^6H_{13/2}$, $^4F_{9/2} \rightarrow {}^6H_{11/2}$ transitions respectively. Among them, $^4F_{9/2} \rightarrow {}^6H_{13/2}$ transition possesses higher intensity compared to the other transitions which occurs due to the interaction of electric dipole with photons whereas the $^4F_{9/2} \rightarrow {}^6H_{15/2}$ transition occurs due to the interaction of magnetic dipole with photons. The ratio between these two transitions ($^4F_{9/2} \rightarrow {}^6H_{13/2}$ and $^4F_{9/2} \rightarrow {}^6H_{15/2}$) act as a local field sensor because the intensity of the former transition depends upon crystal field while the later does not and the values were found to be 1.65, 1.91, 1.96, 1.76 for the present ATB0.25D, ATB0.5D, ATB1.0D, ATB2.0D glasses respectively. From these values it is confirmed that the aluminium telluroborate glass with 1.0 wt % Dy^{3+} ions concentration occupies higher asymmetry environment compared to the other prepared glasses.

Table 1. Observed band positions (cm^{-1}) and bonding parameters ($\bar{\beta}$ and δ) of the Dy^{3+} ions doped aluminium telluroborate glasses

Transition $^6H_{15/2} \rightarrow$	ATB 0.25D	ATB 0.5D	ATB 1.0D	ATB 2.0D	Aquo ion [2]
$^6H_{11/2}$	5945	5959	5906	5924	5850
$^6F_{11/2}$	7855	7825	7856	7823	7700
$^6F_{9/2}$	9124	9134	9141	9149	9100
$^6F_{7/2}$	11109	11060	11084	11106	11000
$^6F_{5/2}$	12505	12496	12463	12486	12400
$^6F_{3/2}$	13205	13336	13303	13298	13250
$^4F_{9/2}$	21110	21100	21101	21020	21100
$^4I_{15/2}$	22057	22047	22119	22126	22100
$^4G_{11/2}$	23514	23524	23534	23407	23400
$^4F_{7/2}$	25889	25839	25824	25807	25800
$^6P_{5/2}$	27293	27273	27367	27351	27450
$^6P_{7/2}$	28888	28838	28745	28858	28550
$\bar{\beta}$	1.0057	1.0056	1.0053	1.0051	-
δ	−0.0057	−0.0056	−0.0053	−0.0051	-

The luminescence intensity is found to quench beyond 1.0 wt% Dy^{3+} ion content glass and the same may be attributed to the resonance energy transfer or cross-relaxation mechanism which takes place as shown below [4].

$$^4F_{9/2} + {}^6H_{15/2} \rightarrow ({}^6H_{9/2} + {}^6F_{11/2}) + {}^6F_{5/2}$$

$$^4F_{9/2} + {}^6H_{15/2} \rightarrow ({}^6H_{7/2} + {}^6F_{9/2}) + {}^6F_{3/2}$$

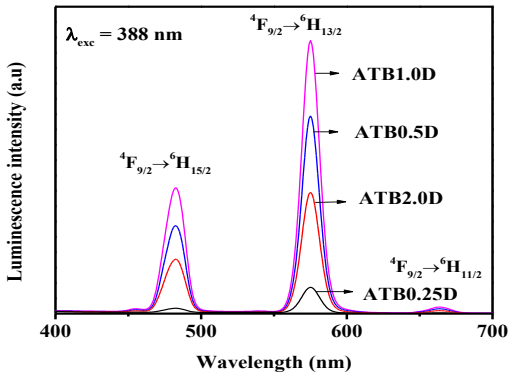

Figure 3. Emission spectra of Dy^{3+} ion doped aluminium telluroborate glasses

Resonance energy transfer takes place when the excitation and emission spectra overlaps and is shown in figure 4 for the $^4F_{9/2}$, $^6H_{15/2}$ state. The partial energy level diagram depicting these processes is shown in figure 5. When Dy^{3+} ion is excited to the $^4F_{7/2}$ energy level (388 nm), it non-radiatively decays to the $^4F_{9/2}$ energy level where from radiative transition takes place between ($^4F_{9/2}$, $^6H_{15/2}$), ($^4F_{9/2}$, $^6H_{13/2}$), ($^4F_{9/2}$, $^6H_{11/2}$) states. Due to the large energy gap between the $^4F_{9/2}$ level to the next lower energy level (~ 7000 cm^{-1}) multiphonon relaxation is less dominant where more number of phonons is required and the luminescence intensity quenches due to the above mentioned resonance energy transfer or cross-relaxation phenomenon.

International Journal of
Scientific Research in Science and Technology (IJSRST)
Print ISSN : 2395-6011, Online ISSN : 2395-602X
International Conference on Advanced Materials
Held on 14, 15 December 2017, Organized by Department of Physics,
St. Joseph's College, Trichy, Tamilnadu, India

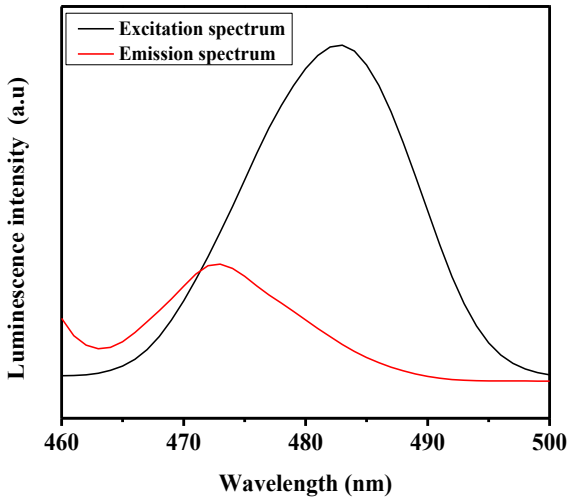

Figure 4. Resonance energy transfer for ($^4F_{9/2}$, $^6H_{15/2}$) state

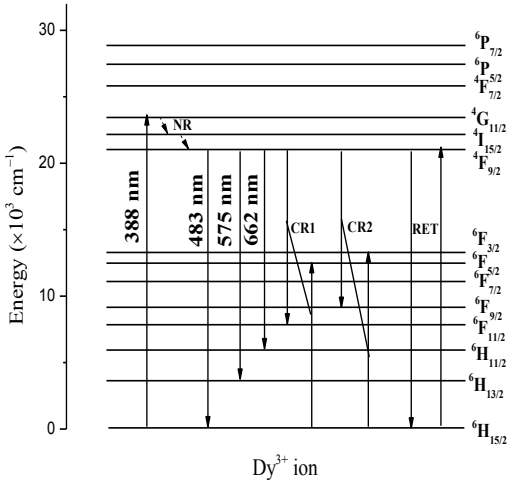

Figure 5. Partial energy diagram of Dy^{3+}ion doped aluminum doped glass

The strength of the luminescence intensity is measured through lifetime measurements recorded by monitoring an excitation at 388 nm and emission at 575 nm and is shown in figure 6. The decay curves were fitted following the below given bi-exponential function.

$$I = a_1 \exp(-x/t_1) + a_2 \exp(-x/t_2)$$

and the average lifetime (τ) values were calculated using the following expression

$$\tau = \frac{a_1 t_1^2 + a_2 t_2^2}{a_1 t_1 + a_2 t_2}$$

These values were found to decrease from 0.53 to 0.28 ms with the increase in the concentration of Dy^{3+} ions in the prepared glasses and the same is due to the increasing energy transfer process takes place between Dy^{3+}–Dy^{3+} ions.

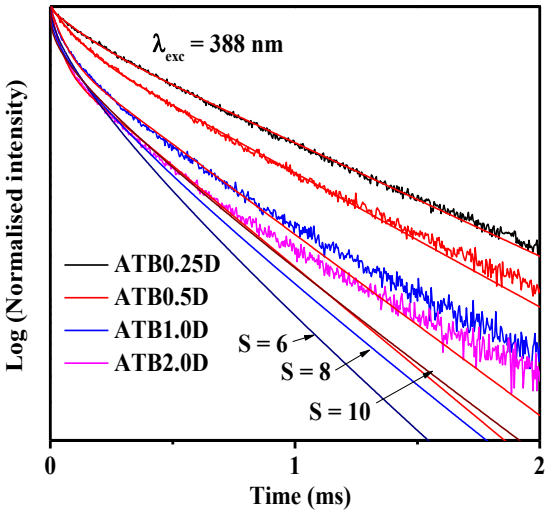

Figure 6. Decay curve of Dy^{3+} ions doped aluminium telluroborate glasses

These decay curves were fitted through Inokuti-Hirayama model [7] to determine type of interaction involved using the following expression

$$I(t) = I_0 \exp\left[\left(-\frac{t}{t_0}\right) - q\left(\frac{t}{t_0}\right).3/3\right]$$

where 't' is the time after pulsed excitation, t_0 is the intrinsic decay time of the donor in the absence of acceptors. The value of S (=6, 8, 10) determine the dominant interaction is of dipole-dipole, dipole-quadrupole, quadrupole-quadrupole type and the model is well fitted for S = 6 thus suggests the fact that the dipole-dipole interaction is dominant. Other parameters such as forster distance, donor-acceptor interaction were calculated using the expressions reported in the literature [8] and the

International Journal of
Scientific Research in Science and Technology (IJSRST)
Print ISSN : 2395-6011, Online ISSN : 2395-602X
International Conference on Advanced Materials
Held on 14, 15 December 2017, Organized by Department of Physics,
St. Joseph's College, Trichy, Tamilnadu, India

values were shown in table 2 along with the reported literature [1,6,8].

Table 2. Experimental lifetime (τ_{exp}, ms), donor-acceptor interaction parameter (C_{DA}, $\times 10^{-42}$ cm^6/s), critical distance (R_0, $\times 10^{-8}$ cm), energy transfer parameter (q) for Dy^{3+} ions doped aluminium telluroborate glasses under 388 nm excitation for the emission energy level $^4F_{9/2}$, $^6H_{13/2}$

Glass Code	τ_{exp}	q	C_{DA}	R_0
ATB0.25D	0.53	0.16	14.09	4.26
ATB0.5D	0.43	0.59	57.53	5.38
ATB1.0D	0.31	1.26	75.29	5.63
ATB2.0D	0.28	1.62	50.34	5.26
PKAZLFDy [1]	0.62	0.71	1.32	69.5
PKAND[6]	0.47	0.86	2.15	7.31
TBZnD [8]	0.41	0.65	2.42	6.9

5. Conclusion

Optical and energy transfer behavior of the Dy^{3+} ions doped title glasses have been studied and reported. The bonding parameter studies exhibits the ionic nature. Luminescence quenching has been experienced for glasses having Dy^{3+} ions concentration beyond 1 wt% and is due to RET and cross-relaxation process. The decay of the $^4F_{9/2}$ excited level is found to be single exponential for lower concentration and turns out to be non-exponential for higher concentration of Dy^{3+} ions in the prepared glasses. The non-exponential behaviour of the decay curve analysis through Inokuti-Hirayama model indicates that the energy transfer between Dy^{3+} ions is of dipole-dipole nature.

6. References

[1] K. Venkata Krishnaiah, K. Upendra Kumar, C.K. Jayasankar, Mater Express 3, 61–70 (2013)
[2] Joanna Pisarska, J. Phys. Condens. Matter 21, 285101 (1 – 6) (2009)
[3] G. Venkataiah, C. K. Jayasankar, J. Mol. Struct. 1084, 182 – 189 (2015)
[4] W. T. Carnall, P. R. Fields, K. Rajnak, J. Chem. Phys 49, 4424 – 4442 (1968)
[5] N. Vijaya, K. Upendra Kumar, C. K. Jayasankar, Spectrochim. Acta Part A 113, 145 – 153 (2013)
[6] Mitio Inokuti, Fumio Hirayama, J. Chem. Phys 43, 1978 – 1989 (1965)
[7] V. Uma, K. Mahesvaran, K Marimuthu, G. Muralidharan, J. Lumin. 176, 15 – 24 (2016)

International Journal of
Scientific Research in Science and Technology (IJSRST)
Print ISSN : 2395-6011, Online ISSN : 2395-602X
International Conference on Advanced Materials
Held on 14, 15 December 2017, Organized by Department of Physics,
St. Joseph's College, Trichy, Tamilnadu, India

1.5 µm Amplification and Upconversion Emission of Er^{3+} Doped Tellurite Glasses for Laser Applications

S. Arunkumar, K. Marimuthu*
Department of Physics, Gandhigram Rural Institute–Deemed University, Gandhigram – 624 302, India
*Corresponding author: mari_ram2000@yahoo.com

Abstract

In the present investigations, a series of Er^{3+} doped glasses with the composition $30TeO_2$ + (30–x) Bi_2O_3 + 20ZnO + 20CdO + xEr_2O_3 (x = 0.05, 0.1, 0.5, 1 and 3 wt%) were prepared by melt-quenching technique and characterized through FTIR, Raman, optical absorption, emission and decay curve measurements. Optical absorption spectra have been analyzed using Judd–Ofelt theory to interpret the local environment of the Er^{3+} ion site. In order to elucidate the potential application of Er^{3+} ions in the prepared glasses the radiative properties were calculated for the $^4S_{3/2} \rightarrow {}^4I_{15/2}$ and $^4I_{13/2} \rightarrow {}^4I_{15/2}$ emission transitions. The absorption and emission cross-section for the $^4I_{13/2} \rightarrow {}^4I_{15/2}$ transition at 1.5 µm were calculated using McCumbar theory and compared with the results obtained from JO theory. The decay curves of the $^4I_{13/2}$ level have been measured and the fall in lifetime value with the increase in Er^{3+} ion concentration can be attributed to the cross-relaxation between Er^{3+} ion to the free OH^- radical. The upconversion emission spectra were recorded at 980 nm excitation and their energy transfer mechanism through ground state absorption and various excited state absorption are discussed.

Keywords: Nephelauxetic effect, Judd-Ofelt theory, Gain Bandwidth, Upconversion emission, Lifetime.

1. Introduction

The spectroscopic and laser properties of RE ions are strongly affected by the local symmetry structure at the RE vicinity as well as the distribution of doping ions in the glass matrix [1]. The development of the new luminescent materials with appropriate composition doped with RE^{3+} ions is of interest for understanding the electronic excitation and relaxation phenomena RE ions in the chosen glass matrices. Heavy metal oxide (HMO) glasses are more suitable due to its high refractive index, low phonon energy and good chemical durability that help to improve the quantum efficiencies of the matrix [2,3]. Recent year, glasses containing HMO (Bi_2O_3, TeO_2, ZnO, CdO) have attracted attention for excellent infrared transmission due its higher refractive index since the stimulated emission cross-sections and gain bandwidths are proportional to refractive index [4]. The combination of favourable chemical and physical properties of heavy metal oxide glasses containing moderately high RE doping levels increases their applicability in laser active medium [5]. Among the trivalent RE ions, the erbium ion (Er^{3+}) has been extensively studied because of its ability to emit light within the near-ultraviolet to the near-infrared range upon excitation with infrared light in a number of hosts [6.7]. Er^{3+} ions doped glasses have been received much attention due to the 1.5µm emission from the $^4I_{13/2} \rightarrow {}^4I_{15/2}$ transition of Er^{3+} ions is eye safe and located in the optical third communication window where the losses are minimum [8.9].The present work presents a detailed investigation of the optical characteristics of Er^{3+} doped HMO:tellurite glasses.

2. Experimental

Er^{3+} ions doped glasses were a composition of $30TeO_2$+(30–x)Bi_2O_3+20ZnO+20CdO+xEr_2O_3 (x= 0.05,

International Journal of
Scientific Research in Science and Technology (IJSRST)
Print ISSN : 2395-6011, Online ISSN : 2395-602X
International Conference on Advanced Materials
Held on 14, 15 December 2017, Organized by Department of Physics,
St. Joseph's College, Trichy, Tamilnadu, India

0.1, 0.5, 1 and 3 wt%) prepared prepared by conventional melt quenching technique [10]. All the starting materials were purer than 99.9%. Batches of 15 g were weighed and taken into porcelain crucible melted at 900°C for 45 minutes in electric furnace. The homogenous melt were poured onto a well polished preheated brass mold followed by annealing at 300°C for 12 hours and then allowed to reach room temperature gradually to remove the thermal strain and air bubbles. Finally the glasses were polished on both sides with dimensions of 2.5×1.5×0.4cm^3 before further optical investigations. The absorption spectral measurements were made using CARY 500, UV-Vis-NIR spectrophotometer in the wavelength range 400–1900 nm with a spectral resolution of ±1.0 nm. NIR luminescence spectra were recorded using EG&G Princeton Applied Research model 5210 spectrophotometer with a spectral resolution of ±0.5 nm. The decay curves corresponding to the $^4I_{13/2} \rightarrow {}^4I_{15/2}$ transition were recorded by exciting the samples with a 10 ns pulsed optical parametric oscillator (OPO) pumped by a Nd-YAG laser (EKSPLA NT342/3/UVE) and the signal from the extended PMT was acquired by a digital oscilloscope (LeCroy wavesurfer 424). All these measurements were carried out at room temperature.

3. Nephelauxetic effect

Figure 1 shows the absorption spectra of the present Er^{3+} doped glasses. The absorption spectra exhibit various electronic transitions such as $^4I_{13/2}$ (6531), $^4I_{11/2}$ (10266), $^4I_{9/2}$ (12481), $^4F_{9/2}$ (15311), $^4S_{3/2}$ (18345), $^2H_{11/2}$ (19256), $^4F_{7/2}$ (20474), $^4F_{5/2}$ (22111), and $^4F_{3/2}$ (22567) (in cm^{-1}) from the $^4I_{15/2}$ ground state. Due to the nephelauxetic effect the absorption band position of the Er^{3+} ion shift towards the higher energy side which indicates that the Er–O bond is of ionic in nature in the prepared glasses. From the optical absorption spectra, Nephelauxetic ratios and bonding parameter values have been calculated to study the nature of the Dy^{3+}-ligand bond in the prepared glasses. The δ values are found to be 0.016, 0.052, 0.089, 0.057 and 0.036 for the prepared BiZnCdTe:xEr^{3+} glasses. The positive magnitude of the δ values indicate the covalency of the Er–O bond and the covalency of the Er–O bond is found to increase with increase in Er^{3+} ion content upto 0.5 wt% and after that, the covalency decreases due to the nephelaxetic effect.

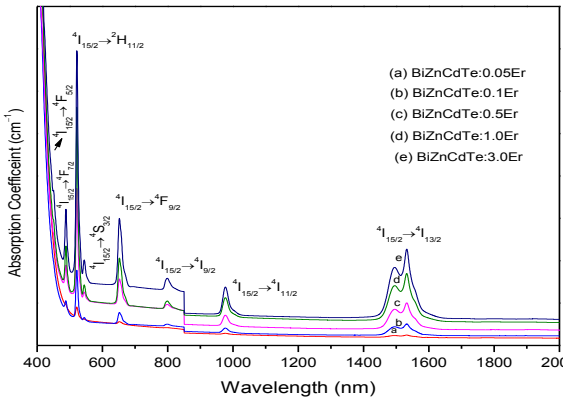

Figure 1. Absorption spectra of the Er^{3+} doped BiZnCdTe:xEr glasses

4. JO intensity parameter and covalancy

Judd-Ofelt theory have been used to analyses the absorption spectral intensities based on the assumption that the average energy difference between the 4f levels is much larger than the energy spread of the excited configuration. Oscillator strength of the transition expresses the probability of radiative transitions between a given pair of J multiplets. The f_{exp} and f_{cal} values of the $^2H_{11/2}$ hypersensitive transition are found to be higher than the reported Er^{3+} doped [4-7] glasses. The JO intensity parameters (Ω_2, Ω_4 and Ω_6) gives information about the local field symmetry around the RE ion site and the nature of the bond between RE ions with its surrounding ligands. The values of Ω_2 is very sensitive to the local environment of the RE ions and often gives information about the

International Journal of
Scientific Research in Science and Technology (IJSRST)
Print ISSN : 2395-6011, Online ISSN : 2395-602X
International Conference on Advanced Materials
Held on 14, 15 December 2017, Organized by Department of Physics,
St. Joseph's College, Trichy, Tamilnadu, India

symmetry of the coordination structure, polarizability of ligands and the nature of the RE–O bonding in the ligand field [1]. The Ω_4 parameters is related to the bulk properties and Ω_6 is inversely related to the rigidity of the medium and also affected by the vibronic transitions of the RE ions. The JO intensity parameters of the present Er^{3+} doped glasses are presented in table 1 along with the reported Er^{3+} doped glasses [3-4]. The observed $\Omega_2>\Omega_6>\Omega_4$ trend represents a change in the surrounding ligand field environment do not show any symmetry inversion symmetry around the cation. Among the prepared glasses, 0.5wt% glass exhibits higher spectroscopic quality factor (Ω_4/Ω_6 = 1.70) value and is found to be higher than the reported [1-6] glasses thus suggests its potential for various photonic applications.

Table 1. Judd-Ofelt ($\times10^{-20}$cm^2) parameters of Er^{3+} doped BiZnCdTe:xEr glasses

Glass codes	Ω_2	Ω_4	Ω_6	Ω_4/Ω_6
BiZnCdTe:0.05Er	9.32	3.12	2.35	1.33
BiZnCdTe:0.1Er	9.67	3.87	2.54	1.52
BiZnCdTe:0.5Er	10.45	4.30	2.51	1.70
BiZnCdTe:1.0Er	9.41	3.33	2.06	1.61
BiZnCdTe:02.0Er	8.93	3.45	2.35	1.47
Bismuthborate [1]	4.44	1.17	1.64	0.71
oxyfluoride [3]	8.57	2.05	2.60	0.79
Lead-telluroborate	5.69	0.31	1.74	0.18

5. Down conversion emission spectra

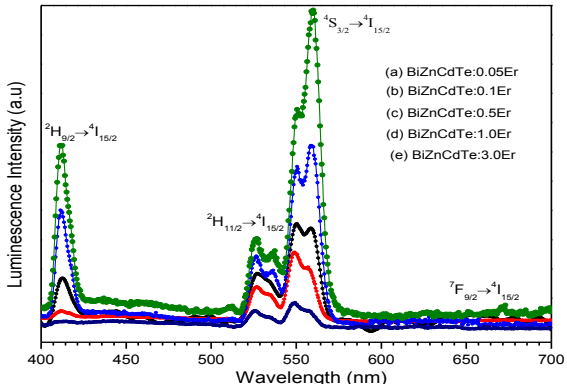

Figure 2. Downconversion emission spectra of Er^{3+} doped BiZnCdTe:xEr glass

Figure 2 shows the emission spectra of the prepared Er^{3+} doped glasses under 485 nm excitation. The emission spectra exhibit intense $^2H_{9/2}\rightarrow{}^4I_{15/2}$ and $^2H_{11/2}\rightarrow{}^4I_{15/2}$, $^4S_{3/2}\rightarrow{}^4I_{15/2}$ and weak $^7F_{9/2}\rightarrow{}^4I_{15/2}$ emission transitions corresponding to the band positions at 409, 528, 557 and 654 nm respectively. It is observed from figure 2 that the intensity of the emission bands increases up to 0.5 wt% Er_2O_3 content and after that quenching occurs and the role of energy transfer is studied with lifetime analysis. The quenching of emission intensities with increase of Er^{3+} ion concentration is due to the increase of non-radiative energy transfer [2]. Cross-relaxation is a important quenching center caused by migration of the excitation energy among the Er^{3+} ions through the resonant energy transfer between two Er^{3+}–Er^3 [5-9]. The possible cross-relaxation channels are ($^4F_{9/2}\rightarrow{}^4I_{11/2}$:$^4I_{15/2}\rightarrow{}^4I_{11/2}$), ($^4F_{9/2}\rightarrow{}^4I_{9/2}$: $^4I_{15/2}\rightarrow{}^4I_{11/2}$) which reason for the luminescence quenching. The radiative parameters of the prepared glasses have been calculated. The stimulated emission cross-section value is found to be maximum for $^4S_{3/2}$ level for all the prepared glasses. The stimulated emission cross-section and the radiative lifetime values for the $^4S_{3/2}\rightarrow{}^4I_{15/2}$ transition are found to be 22.54, 25.15, 31.73, 28.16, 26.67 ($\times10^{-21}$ cm^2) and 0.22, 0.15, 0.11. 0.17. 0.18 (μs) corresponding to 0.05, 0.1, 0.5, 1 and 3 wt% content of Er^{3+} ions, respectively. The higher value of the stimulated emission cross-section is favorable for achieving low threshold and high gain to obtain CW laser action. Among the prepared glasses, BiZnCdTe:0.5Er glass possesses higher stimulated emission cross-section and branching ratio values and is suggested for suitable green laser applications.

International Journal of
Scientific Research in Science and Technology (IJSRST)
Print ISSN : 2395-6011, Online ISSN : 2395-602X
International Conference on Advanced Materials
Held on 14, 15 December 2017, Organized by Department of Physics,
St. Joseph's College, Trichy, Tamilnadu, India

6. Optical Amplification at 1.5 µm

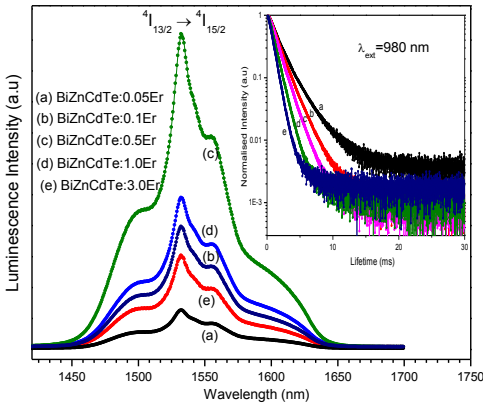

Figure 3. NIR Emission and decay curve of $^4I_{13/2} \rightarrow {}^4I_{15/2}$ level of Er^{3+} ions in prepared glasses

Figure 3 shows the NIR emission spectra exciting at 980 nm corresponding to the $^4I_{13/2} \rightarrow {}^4I_{15/2}$ transition of the Er^{3+} ions. The full width at half maximum (FWHM) is an important parameter for laser action and the FWHM values are found to be 85, 91, 96, 93 and 88 nm corresponding to 0.05, 0.1, 0.5, 1 and 3 wt% content of Er^{3+} ions, respectively. It clearly indicates that, higher FWHM values of the broad emission bands are suitable for tunable laser medium and it could be used as a potential candidate for compact and efficient eye safe NIR lasers. The decay curves of the $^4I_{13/2}$ excited level of the Er^{3+} ions were recorded and presented in inset of figure 3. The calculated and experimental lifetime of the $^4I_{13/2}$ level is found to be 2.57, 2.34, 2.11, 1.97, 1.81 and 2.29, 1.99, 1.63, 1.34 0.98ms corresponding to the prepared 00.05, 0.1, 0.5, 1 and 3 wt% content of Er^{3+} containing glasses, respectively. The quantum efficiency is an important parameter which is defined as ratio of the number of photons generated in radiative transition to the number of photons absorbed [3]. The quantum efficiency values are found to be 89, 85, 77, 68 and 54 for the prepared Er^{3+} doped BiZnCdTe:xEr glasses, respectively.

The absorption and emission cross-section values for the $^4I_{13/2} \rightarrow {}^4I_{15/2}$ transition of the Er^{3+} ions in the prepared glasses are calculated using McCumbar theory. The mesured σ_a and σ_e values of the BiZnCdTe:0.5Er glass is shown in figure 4 and values are 5.24, 5.33 ($\times 10^{-21}$ cm^2) which comparably higher than the reported Er^{3+} doped glasses [6,8,9]. The σ_a σ_e values are found to decrease with the increase in Er^{3+} ion content. The gain coefficient were derived from the σ_a σ_e values using expression $G=N[P\sigma_e(\lambda)-(1-p)\sigma_a(\lambda)$, where P is the population inversion (0 to 1) and N is the total concentration (in ions/cm^3) of the Er^{3+} ions. From the measured absorption and emission cross-section values as a function of wavelength the gain coefficient for the 0.5wt%Er content glass have been calculated for the various P (0.1, 0.2, 0.4, 0.6, 0.8 and 1.0) values and the results are presented in inset of figure 4. It is clearly observed that, the zero-shift in the peak values of the gain coefficient for various P values and the zero gain coefficient were observed for P=0.4 due to the fact that ground state and excited states are equally populated [4,5]. The gain coefficient of 0.5wt% Er^{3+} containing glass is found to be 0.52 cm^{-1} and is closer to the reported Er^{3+} glasses [6,7,8] which indicates the prepared BiZnCdTe:0.5Er glass is more suitable for designing the Er^{3+}doped broad-band optical amplifiers.

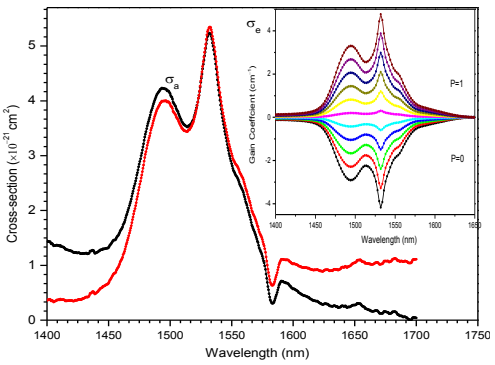

Figure 4. The σ_a, σ_e and Gain coefficient (inset) of $^4I_{13/2} \rightarrow {}^4I_{15/2}$ level of Er^{3+} in BiZnCdTe:0.5Er glass.

International Journal of
Scientific Research in Science and Technology (IJSRST)
Print ISSN : 2395-6011, Online ISSN : 2395-602X
International Conference on Advanced Materials
Held on 14, 15 December 2017, Organized by Department of Physics,
St. Joseph's College, Trichy, Tamilnadu, India

7. Upconversion Emission spectra

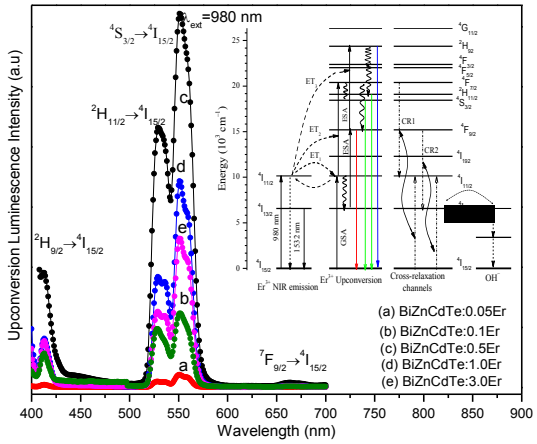

Figure 5. Upconverion emission through GSA, ESA and possible energy transfer of quenching mechanism of Er^{3+} ions in prepared glasses.

Figure 5 shows the upconversion emission spectra of prepared glasses at 980 nm excitation and their possible energy transfer mechanism through ground state absorption and various excited state absorption are shown in the inset of figure 5. The upconversion emission spectra exhibit $^2H_{9/2}\rightarrow{}^4I_{15/2}$, $^2H_{11/2}\rightarrow{}^4I_{15/2}$, $^4S_{3/2}\rightarrow{}^4I_{15/2}$ emission transitions. For the green emission, Er^{3+} ions are excited from the ground state to the $^4I_{11/2}$ state through GSA and further promoted to the $^4F_{7/2}$ state through ESA and then Er^{3+} ion relaxes to the various excited states ($^4S_{3/2}$, $^2H_{11/2}$ and $^2H_{9/2}$) through the energy transfer, multiphonon relaxation and cross relaxation process taking place between two Er^{3+} levels through the following energy transfer mechanism [9]. The $^4I_{11/2}$ level is directly excited at 980 nm and the excitation processes based on the long-lived $^4I_{11/2}$ excited level follows through the energy transfer (ET) $I_{11/2}+4I_{11/2}\rightarrow{}^4F_{7/2}+{}^4I_{15/2}$ and excited state absorption (ESA) $^4I_{11/2}+h\nu\rightarrow{}^4F_{7/2}$ mechanism. The populated $^4F_{7/2}$ level may relax non-radiatively to the next lower levels $^2H_{11/2}$ and $^4S_{3/2}$ separated by a small energy gap (721 cm^{-1}) responsible for green emission. The $^2H_{11/2}$ state can non-radiatively decay to the $^4S_{3/2}$ state due to the multiphonon relaxation process because of the fact that, the 535 nm emission band possess lower intensity than the 555 nm emission band due to the higher multiphonon relaxation rate [8]. Thus the $^2H_{11/2}\rightarrow{}^4I_{15/2}$ and $^4S_{3/2}\rightarrow{}^4I_{15/2}$ two radiative transitions correspond to the green emission. The energy transfer mechanism for the red emission which originates from the $^4F_{9/2}\rightarrow{}^4I_{15/2}$ transition and the population of $^4F_{9/2}$ state follows as: ESA: $^4I_{13/2}+h\nu\rightarrow{}^4I_{9/2}$ and ET between Er^{3+} ions: $^4I_{13/2}+{}^4I_{11/2}\rightarrow{}^4F_{9/2}+{}^4I_{15/2}$. The $^4I_{13/2}$ level is populated due to the non-radiative relaxation from the upper $^4I_{11/2}$ level. The raditive transition from the $^4F_{9/2}$ level to the $^4I_{15/2}$ level contributes to the red emission [6].

8. Conclusion

Concentration dependent optical absorption and emission properties of Er^{3+} doped HMO glasses have been studied and reported. The bonding parameter studies reveal the covalent nature of the metal-ligand bond in the title glasses and the covalency decrease beyond 0.5wt% content of Er^{3+} ions. The JO intensity parameters follows the trend as $\Omega_2>\Omega_4>\Omega_6$ uniformly for all the prepared glasses and the higher Ω_2 values indicate the presence of higher asymmetry around the Er^{3+} ion site. Among the prepared glasses, BiZnCdTe:0.5 glass possess higher A, β, σ_a, σ_e and η values for $^4S_{3/2}$ emission transition suggesting its suitability for green laser applications and the higher values of these parameters for $^4I_{13/2}$ transition is suitable for higher gain optical amplifiers.

9. Acknowledgement

One of the authors Dr. S. Arunkumar is grateful to the University Grants Commission (UGC), for the award of the Postdoctoral Research Fellowship (No. F./31-1/2017/PDFSS-2017-18-TAM-15016).

International Journal of
Scientific Research in Science and Technology (IJSRST)
Print ISSN : 2395-6011, Online ISSN : 2395-602X
International Conference on Advanced Materials
Held on 14, 15 December 2017, Organized by Department of Physics,
St. Joseph's College, Trichy, Tamilnadu, India

10. References

[1] Y.H. Liu, Y.J. Chen, Y.F. Lin, Z.D. Luo, Y.D. Huang, Opt. Mat.30 (2008) 1883–1888.

[2] C.R. Kesavulu, V.B. Sreedhar, C.K. Jayasankar, K Jang, D Shin, S Soo Yi, Mat. Res. Bull. 51 (2014) 336–344.

[3] K. Selvaraju, K. Marimuthu, J. Lumin. 132, 1171–1178 (2012).

[4] M.V. Vijaya Kumar, K. Rama Gopal, R.R. Reddy, G.V. Lokeswara Reddy, B.C. Jamalaiah, J. Lumin. 142 (2013) 128–134

[5] A.A Reddy, S. Surendra Babu, G. Vijaya Prakash, Opt. Comm. 285 (2012) 5364–5367

[6] B.C. Jamalaiah, T. Suhasini, L.R Moorthy, K.J. Reddy, I. Kim, D Yoo, K Jang, Opt. Mater. 34 (2012) 861–867.

[7] D. Ramachari, L. Rama Moorthy, C.K. Jayasankar, Opt. Mater. 36 (2014) 823–828.

[8] K. Selvaraju1, N. Vijaya, K. Marimuthu, and V. Lavin, Phys. Status Solidi A 210, No. 3, 607–615 (2013).

[9] J Coelho, J Azevedo, G Hungerford, N.S. Hussain, Opt. Mater. 33 (2011) 1167–1173.

International Journal of
Scientific Research in Science and Technology (IJSRST)
Print ISSN : 2395-6011, Online ISSN : 2395-602X
International Conference on Advanced Materials
Held on 14, 15 December 2017, Organized by Department of Physics,
St. Joseph's College, Trichy, Tamilnadu, India

Spectroscopic Investigation of Laser Treated Nano Material Cadmium Sulphide (CdS)

N. Ravi
Department of physics, St. Joseph's College, Tiruchirappalli620 002, Tamil Nadu, India
nr_sjc@yahoo.com

Abstract

The study of nano powder, particularly laser heat treatment of nano particles plays a major role in laser materials processing studies. The synthesis and charactersation techniques of nano particles attracted greater attention in material science due to their various applications. Cadmium sulphide is the important material used in solar cells as well as in electronics and photo optics. Now in this study we report the influence of laser heat treatment on nano powder CdS. The laser treated CdS samples are characterized and analysed by Xray diffraction, UVvisible absorption, FTIR spectra, Dielectric studies, DLS spectra and SEM. From the Xray analysis we observed that the laser treated CdS in with the structure of hexagonal and the crystalline size is in the range of 1127 nm. The UVvisible spectrum also confirms the presence of CdS nano particles with the average band gap energy of 5.1ev. The optical band gap values of CdS calculated are about 5.15.3ev. FTIR confirms the presence of CdS particles with various groups. Dielectric studies of laser treated CdS samples linear increase of values when the frequency increase (except for dipole laser heat treatment of samples for 30 minutes). Dynamic light scattering studies reveals that the particle size matches with Xray diffraction values that slightly differ with SEM studies.

1. Introduction

Cadmium sulphide nano particle belongs to the group of chalcogenides is a II–IV group semiconductor nano particles show size dependent, which finds number of applications particularly use in solar cells because of its high photo sensitivity. In recent years, greater attention has been given for synthesis and characterization of CdS because of its application in optical, electronic as well as thermo dynamic properties of particles.Several studies of CdS have been reported based on their size, shape and crystalline forms of particles. In general, the band gap energy is mainly based on particle size of the semiconducting particle[1]. With the use of laser heat treatment on semi conducting materials gives necessary enhancement either in conductivity or in band gap energy with the use of proper laser parameters [2]. This paper investigation the effect of laser irradiation on CdS nano particle with different time exposures. The structural analysis of the samples are analysed using Xray diffractometers. Similarly the spectroscopic investigations such as UV and FTIR are also investigated for with and without laser irradiated samples. Dielectric properties, DLS spectra and SEM studies show interesting information pertaining to band gap energy and particle size [3].

2. Experimental Procedure

Commercially available CdS powder (SigmaAldrich, 99.995% purity) is used for investigation (composition is given in Table1). Laser treatments are carried out by using 5.0mw low power HeNe gas laser with red light of (wavelength 633nm) and diode laser with green light of 5mw power (wave length 532nm). The structural analysis of with and without laser irradiated samples are analysed using PANalytical's Xray diffractometers (copper Kα radiation of wave length λ as 1.54060 A° and 1.54443A°). This system recorded the intensity as a function of Bragg's angle. While the average crystalline size of the particles can be estimated using full width at half maximum (FWHM) value of the xray diffraction peaks. The optical and spectroscopic investigation of the samples such as UV and FTIR

International Journal of
Scientific Research in Science and Technology (IJSRST)
Print ISSN : 2395-6011, Online ISSN : 2395-602X
International Conference on Advanced Materials
Held on 14, 15 December 2017, Organized by Department of Physics,
St. Joseph's College, Trichy, Tamilnadu, India

studies are performed using Perkin Elmer UV/VIS spectrophotometer (λ 365) and Perkin Elmer FTIR spectrometer. The Dielectric studies are performed using Digital LCRZ Meter TH2816A (50Hz 200KHz) with various frequencies. The DLS spectra (Measuring the Particle Size Distribution) recorded by Particulate system Nano plus Zeta/nano particle analyzer instrument. SnO_2 nano particles are analysed using SEM (ZEISS SEM instrument) micrographs. The laser processing parameters used for laser irradiation of samples are given in Table2 and the properties of sample used is given in Table3.

Table 1. Chemical composition of CdS

Element	Content (in %)
Cadmium	77.81
Sulphide	22.19

Table 2. Laser processing parameters of samples

Sample Number	HeNe laser irradiation	Diode green laser irradiation
1	Without laser	Without laser
2	15min	
3	30min	
4		15min
5		30min

Table 3. Properties of CdS

Property	Characteristics
Solubility	soluble in acid very slightly soluble in ammonium
Magnetic susceptibility	-50.0×10^{-6} cm^3/mol
Density	4.826 g/cm^3,solid
Molar mass	144.47 g/mol

3. Results and Discussion

3.1. UVVisible studies

The absorption of UV radiations on the nano powder CdS sample with and without laser irradiation shows appreciable results. From the data the band gap energy for the laser treated sample varies from 5.1eV to 5.2eV and the sample without laser irradiation is 5.3eV. The result proves that the laser influences the nano particle CdS towards band gap energy, particularly for large laser irradiation time for the both HeNe and Diode lasers.Table4 shows the band gap energy values for different laser irradiation with two different time exposures. Figure 1(a) Figure 5(b) shows the UVVisible absorption spectrum of with and without laser irradiated samples [1].

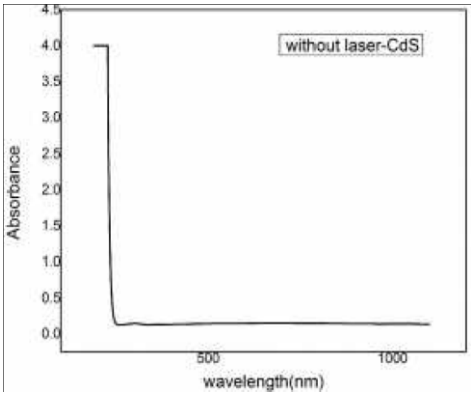

Figure 1(a). UVVis Absorption spectra cutoff wavelength (sample 1)

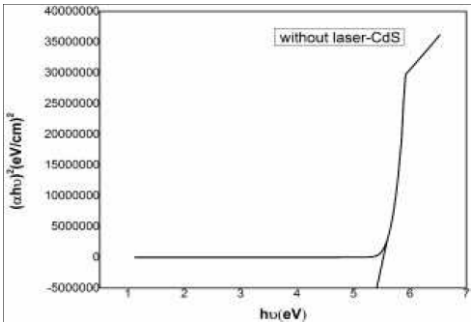

Figure 1(b). UVVis Absorption spectra band gap energy (sample 1)

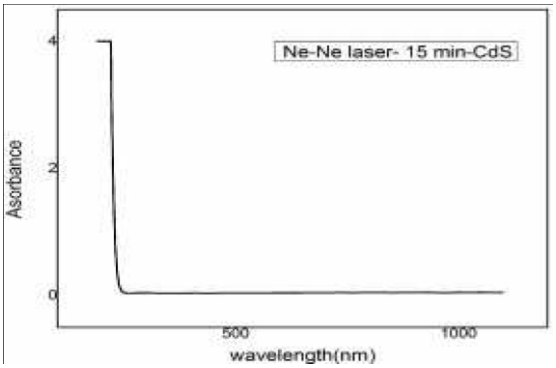

Figure 2(a). UVVis Absorption spectra cutoff wavelength (sample 2)

International Journal of
Scientific Research in Science and Technology (IJSRST)
Print ISSN : 2395-6011, Online ISSN : 2395-602X
International Conference on Advanced Materials
Held on 14, 15 December 2017, Organized by Department of Physics,
St. Joseph's College, Trichy, Tamilnadu, India

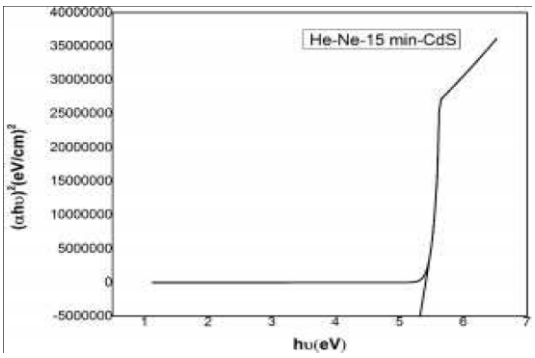

Figure 2(b): UVVis Absorption spectra band gap energy (sample 2)

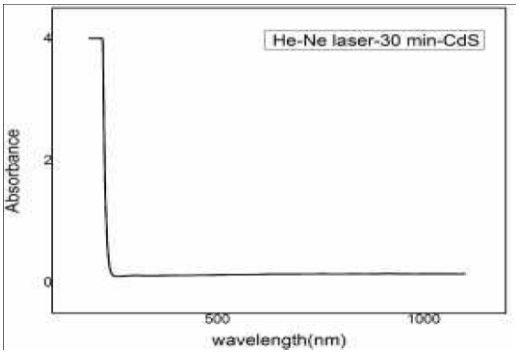

Figure 3(a). UVVis Absorption spectra cutoff wavelength (sample 3)

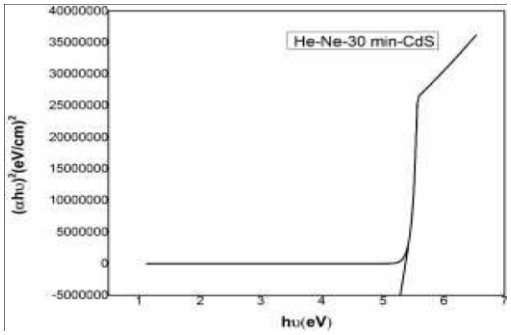

Figure 3(b). UVVis Absorption spectra band gap energy (sample 3)

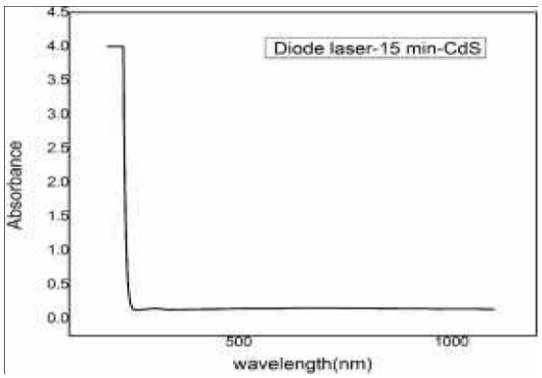

Figure 4(a). UVVis Absorption spectra cutoff wavelength (sample 4)

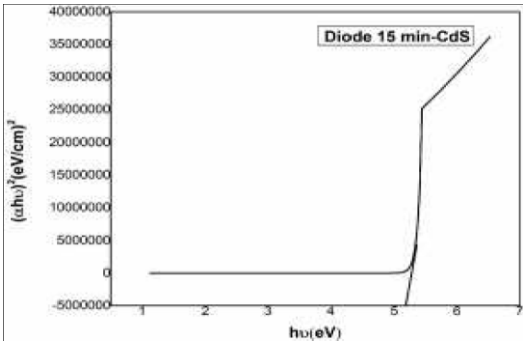

Figure 4(b). UVVis Absorption spectra band gap energy (sample 4)

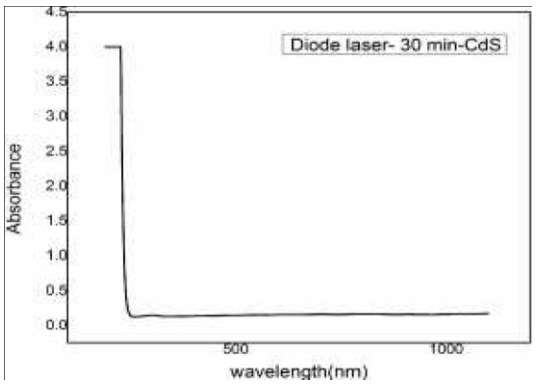

Figure 5(a). UVVis Absorption spectra cutoff wavelength (sample 5)

International Journal of
Scientific Research in Science and Technology (IJSRST)
Print ISSN : 2395-6011, Online ISSN : 2395-602X
International Conference on Advanced Materials
Held on 14, 15 December 2017, Organized by Department of Physics,
St. Joseph's College, Trichy, Tamilnadu, India

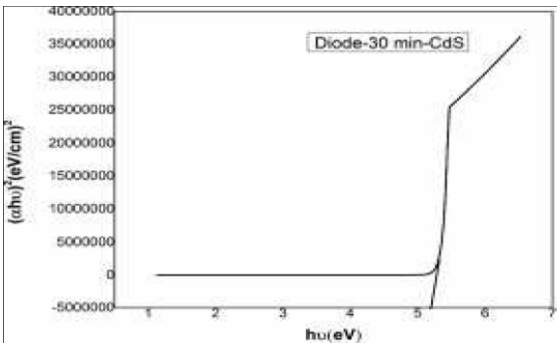

Figure 5(b). UVVis Absorption Spectra band gap energy (sample 5)

Table 4. Band Gap Energy Values For CdS Nanoparticles

Sample number	Time duration of laser irradiation (sec)	Band gap energy (eV)
1	Without laser irradiation	5.3
2	15 minutes (with HeNe laser irradiation)	5.2
3	30 minutes (with HeNe laser irradiation)	5.2
4	15 minutes (with Green Diode laser irradiation)	5.1
5	30 minutes (with Green Diode laser irradiation)	5.1

3.2. FTIR spectral studies

The FTIR spectrum of with and without laser treated CdS particles are given in Figure 6Figure 10. [2]

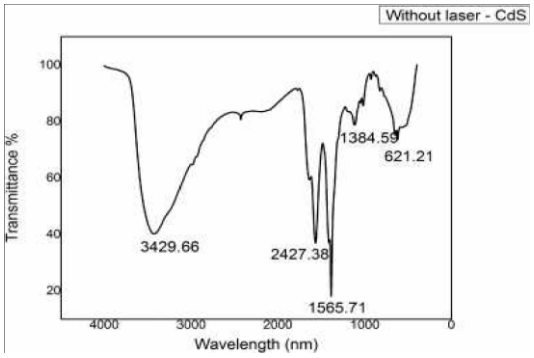

Figure 6: FTIR spectra (sample 1)

Table 5. FTIR functional analysis (Sample 1)

Group	Frequency	Vibrations	Intensity
OH (Hbonded)	3429.66	Broad Stretching	Strong
CH Alkanes	2427.38	Stretching	Strong
NH_2 Amines	1565.71	Scissoring bending	Mediumstrong
CH_2 Alkanes	1384.59	Deformation bending	Medium
SS Disulphide	621.21	Symmetry stretching	Weak

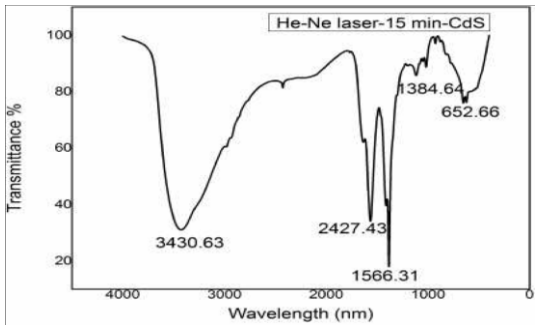

Figure 7: FTIR spectra (sample 2)

Table. 6. FTIR functional analysis (Sample 2)

Group	Frequency	Vibrations	Intensity
NH	3430.63	Stretching	Strong
NH Amines	2427.43	Stretching	Strong
CH	1566.31	Symmetry stretching	Strong
CX (iodoalkanes)	1384.64	Asymmetric stretching	Medium strong
CH_2 rocking	652.66	Bending	Weak

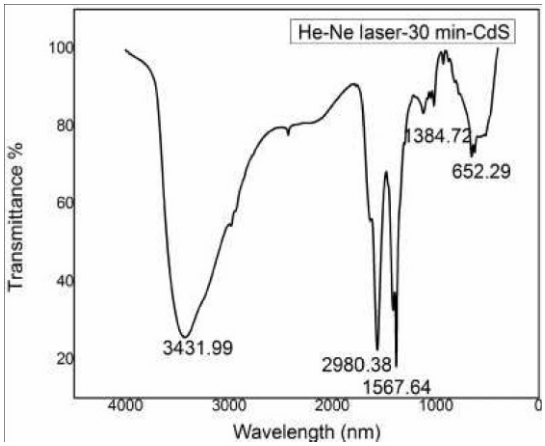

Figure 8: FTIR spectra (sample 3)

Table 7. FTIR functional analysis (Sample 3)

Group	Frequency	Vibrations	Intensity
NH	3431.99	Stretching	Strong
NH Amines	2980.38	Stretching	Strong
CH	1567.64	Symmetry	Strong

International Journal of
Scientific Research in Science and Technology (IJSRST)
Print ISSN : 2395-6011, Online ISSN : 2395-602X
International Conference on Advanced Materials
Held on 14, 15 December 2017, Organized by Department of Physics,
St. Joseph's College, Trichy, Tamilnadu, India

		stretching	
CX (iodo alkanes)	1384.72	Asymmetric stretching	Medium strong
CH_2 rocking	652.29	Bending	Weak

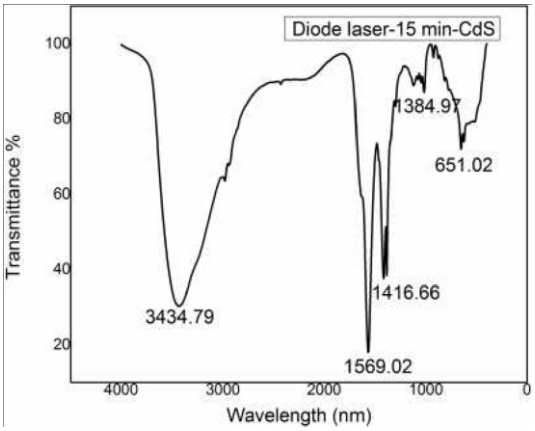

Figure 9. FTIR spectra (sample 4)

Table 8. FTIR functional analysis (Sample 4)

Group	Frequency	Vibrations	Intensity
NH (2 bonds)	3434.79	Stretching	Strong
NH_2 Amines	1569.02	Scissoring bending	Mediumstrong
α CH_2 (ketones)	1416.66	Bending	Strong
CX (bromo alkanes)	1384.97	Stretching	Mediumstrong
CH_2	651.02	Bending	Weak

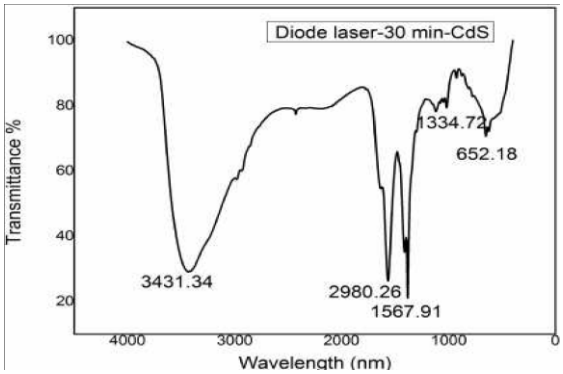

Figure 10. FTIR spectra (sample 5)

Table 9. FTIR functional analysis (Sample 5)

Group	Frequency	Vibrations	Intensity
NH (2 bonds)	3431.34	Stretching	Strong
NH_2 Amines	2980.26	Scissoring bending	Mediumstrong
S=0 (sulfoxide)	1567.91	Stretching	Strong
CX(bromo alkanes)	1334.72	Stretching	Mediumstrong
CH_2	652.18	Bending	Weak

3.3. XRay Diffraction Analysis

The Xray diffraction pattern of with and without laser treated samples are shown in Figure 11 – Figure 13.

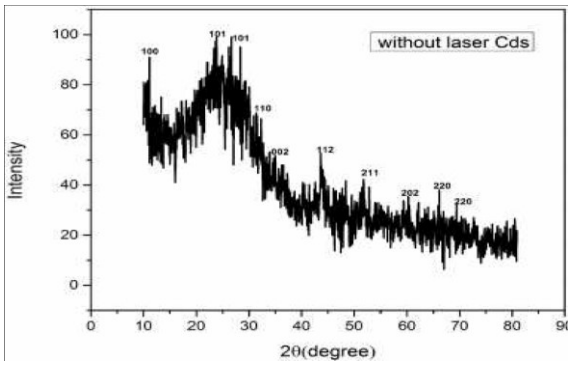

Figure 11. XRD spectrum (sample 1)

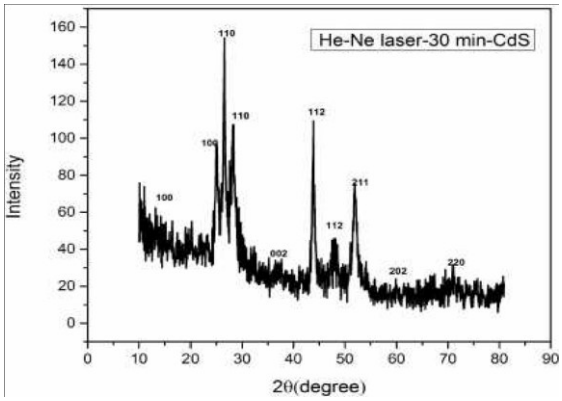

Figure 12. XRD spectrum (sample 3)

International Journal of
Scientific Research in Science and Technology (IJSRST)
Print ISSN : 2395-6011, Online ISSN : 2395-602X
International Conference on Advanced Materials
Held on 14, 15 December 2017, Organized by Department of Physics,
St. Joseph's College, Trichy, Tamilnadu, India

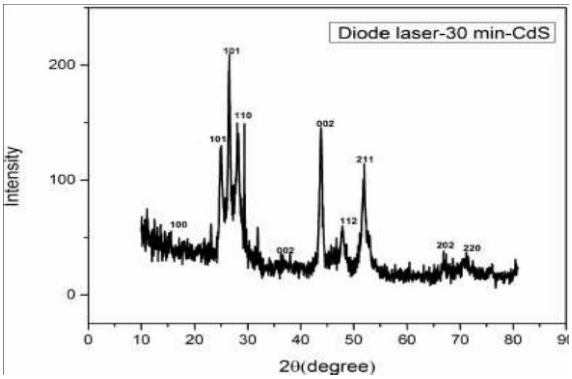

Figure 13. XRD spectrum (sample 5)

From the Xray diffraction studies, the structure of the CdS nano particle observed is hexagonal structure.The average particle size (D) was determined using the Scherer's equation [3]

$$D = K\lambda / \beta \cos\theta,$$

where, D is the crystallite size, K is the shape factor, being equal to 0.9, λ is the Xray wavelength, β is the full width at half maximum of the diffraction peak, and θ is the Bragg diffraction angle in degree. The average crystallite grain size calculated using Scherrer formula of CdS[3] of samples is given in Table 6.

Table 10. crystallite grain size of CdS samples

Sample No	Sample	Grain size (nm)
1	Without laser CdS	11.3
2	HeNe laser15minCdS	15.4
3	HeNe laser30minCdS	15.9
4	Diode laser15minCdS	26.8
5	Diode laser30minCdS	27.3

From Table10 we observed that calculated grain size is 27.3nm in sample5(Diode laser irteraction with time exposures of 30mins) which is slightly higher than the other samples.

3.4. Dielectric studies

The dielectric studies of laser treated nano particles CdS are measured using LCRZ instrument for various frequencies at room temperature (starting from 50Hz to 200 KHz).the corresponding effective capacitance (Cp) and effective resistance (Rp) are measured. Finally the dielectric constants, dielectric loss and ac electrical conductivity of the samples were calculated using the expression [4].

$$\sigma_{ac} = (f \varepsilon \tan(\delta)) / (1.8 \times 10^{10}), \quad (1)$$

where, f is the frequency applied field in Hz, (ε) is the dielectric constant or relative permittivity and tan(δ) is the dielectric loss tangent or loss factor.

$$\text{Dielectric constant } (\varepsilon) = (Cp\, L) / (\Sigma_o\, A), \quad (2)$$

where, Cp is the measured capacitance, L is the thickness of the sample, A is the electrode area and (Σ_o) is the permittivity of free space (8.854 X 10^{12} F/m).

The dielectric loss factor i.e. tan (δ) can be expressed by relation,

$$\tan(\delta) = \omega \cdot Cp.Rp, \quad (3)$$

where, Cp is the measured capacitance, Rp is the measured resistance and ω is the angular frequency. From the Fig.14(a)Fig.18(c) shows the graphical representation of dielectric constant, dielectric loss and a.c electrical conductivity.

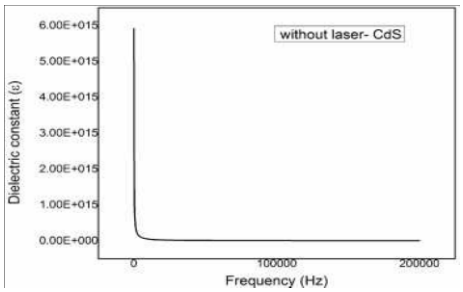

Figure 14(a). Dieletric curve of Dielectric constant (Sample 1)

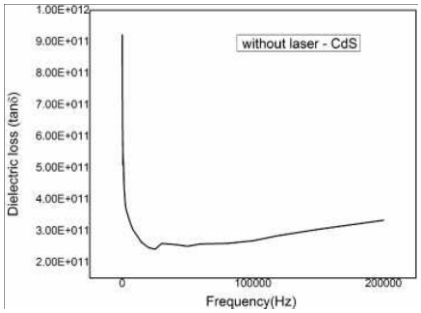

Figure 14(b): Dieletric curve of Dielectric loss (Sample 1)

International Journal of
Scientific Research in Science and Technology (IJSRST)
Print ISSN : 2395-6011, Online ISSN : 2395-602X
International Conference on Advanced Materials
Held on 14, 15 December 2017, Organized by Department of Physics,
St. Joseph's College, Trichy, Tamilnadu, India

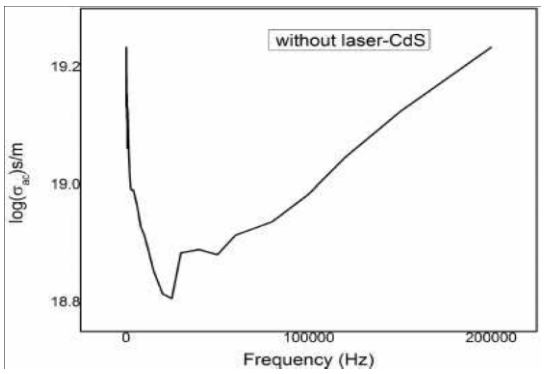

Figure 14(c). Dieletric curve of a.c electrical conductivity (Sample 1)

Table 11. Dielectric studies (Sample 1)

Frequency (KHz)	Dielectric constant (ε)	Dielectric loss (tanδ)	a.c conductivity (σ_{ac}) 10^5 s/m
10	5.0353 x10^{13}	2.9304x10^{11}	18.91368
50	1.0887x10^{13}	2.51429x10^{11}	18.88103
100	6.4643x10^{12}	2.68714x10^{11}	18.98454
150	5.2394x10^{12}	3.0492x10^{11}	19.12429
200	4.6270x10^{12}	3.33394x10^{11}	19.23402

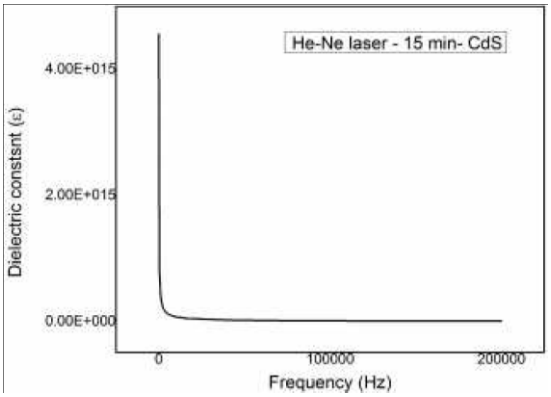

Figure 15(a). Dieletric curve of Dielectric constant (Sample 2)

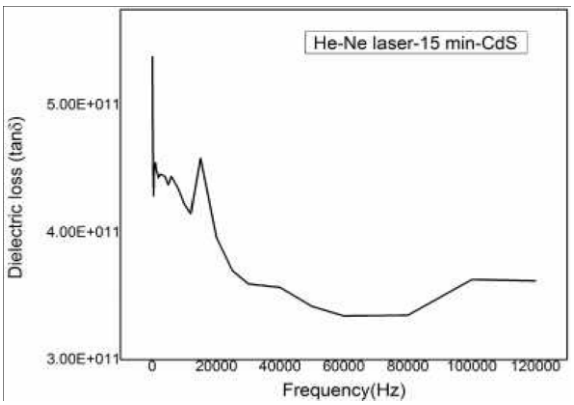

Figure 15(b). Dieletric curve of Dielectric loss (Sample 2)

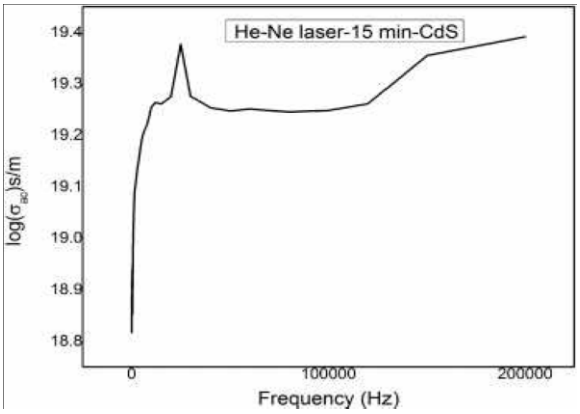

Figure 15(c). Dieletric curve of a.c electrical conductivity (Sample 2)

Table 12. Dielectric studies (Sample 2)

Frequency (KHz)	Dielectric constant (ε)	Dielectric loss (tanδ)	a. c conductivity (σ_{ac}) 10^5 s/m
10	7.2808x10^{13}	4.43897x10^{11}	19.25419
50	1.7691x10^{13}	4.22777x10^{11}	19.24722
100	9.5263x10^{12}	3.344x10^{11}	19.24792
150	7.4849x10^{12}	3.63x10^{11}	19.35492
200	6.1240x10^{12}	3.62057x10^{11}	19.39158

International Journal of
Scientific Research in Science and Technology (IJSRST)
Print ISSN : 2395-6011, Online ISSN : 2395-602X
International Conference on Advanced Materials
Held on 14, 15 December 2017, Organized by Department of Physics,
St. Joseph's College, Trichy, Tamilnadu, India

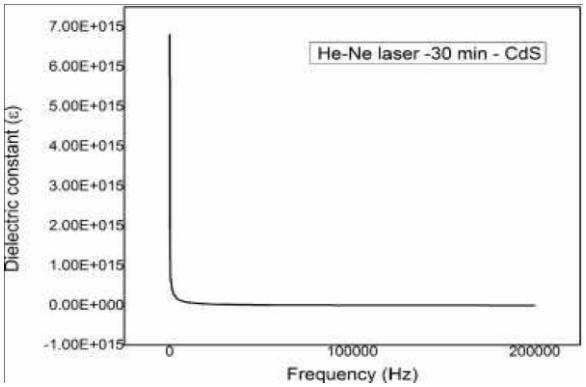

Figure 16(a). Dieletric curve of Dielectric constant (Sample 3)

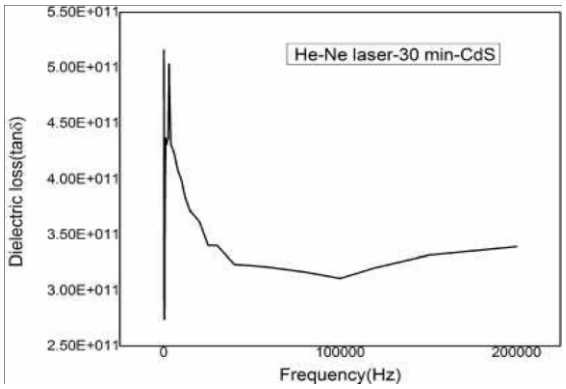

Figure 16(b). Dieletric curve of Dielectric loss (Sample 3)

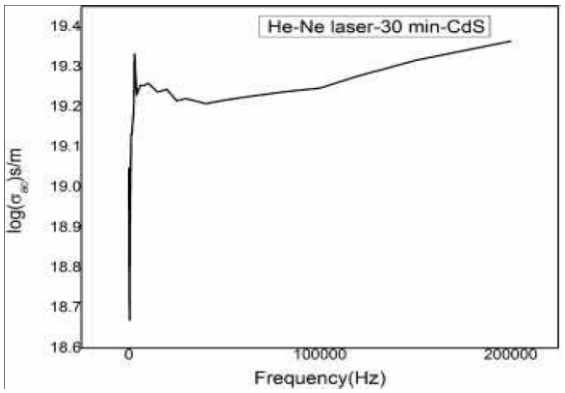

Figure 16(c). Dieletric curve of a.c electrical conductivity (Sample 3)

Table13: Dielectric studies (Sample 3)

Frequency (KHz)	Dielectric constant (ε)	Dielectric loss (tanδ)	a. c conductivity (σ_{ac})10^5 s/m
10	$8.1654x10^{13}$	$3.99771x10^{11}$	19.25852
50	$1.8372x10^{13}$	$3.22457x10^{11}$	19.21633
100	$1.0206x10^{13}$	$3.1143x10^{11}$	19.24658
150	$7.4849x10^{13}$	$3.31886x10^{11}$	19.316
200	$6.1240x10^{12}$	$3.39429x10^{11}$	19.36355

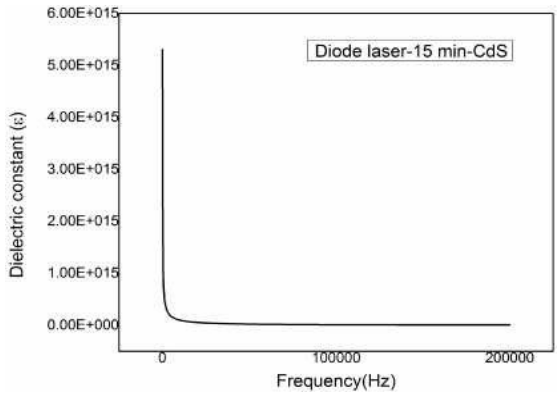

Figure 17(a). Dieletric curve of Dielectic constant (Sample 4)

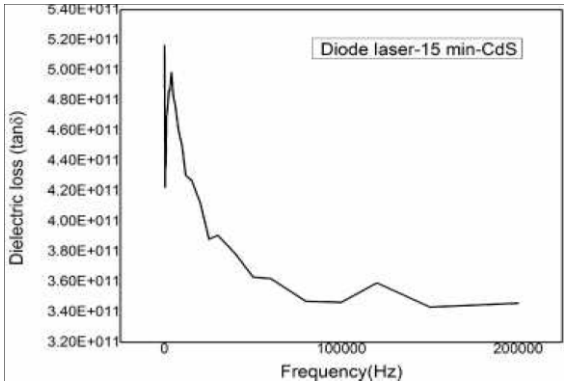

Figure 17(b). Dieletric curve of Dielectric loss (Sample 4)

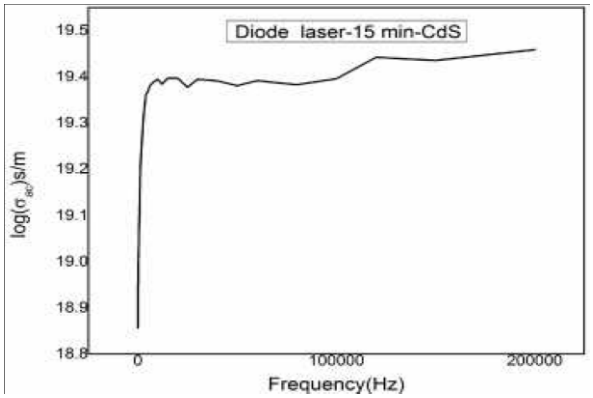

Figure 17(c). Dieletric curve of a.c electrical conductivity (Sample 4)

International Journal of
Scientific Research in Science and Technology (IJSRST)
Print ISSN : 2395-6011, Online ISSN : 2395-602X
International Conference on Advanced Materials
Held on 14, 15 December 2017, Organized by Department of Physics,
St. Joseph's College, Trichy, Tamilnadu, India

Table 14. Dielectric studies (Sample 4)

Frequency (KHz)	Dielectric constant (ε)	Dielectric loss (tanδ)	a.c conductivity (σ_{ac}) 10^5 s/m
10	$9.9346x10^{13}$	$4.4968x10^{11}$	19.39478
50	$2.3815x10^{13}$	$3.63x10^{11}$	19.38047
100	$1.3928x10^{13}$	$3.4633x10^{11}$	19.39579
150	$9.5263x10^{12}$	$3.432x10^{11}$	19.43529
200	$7.4849x10^{12}$	$3.4571x10^{11}$	19.45867

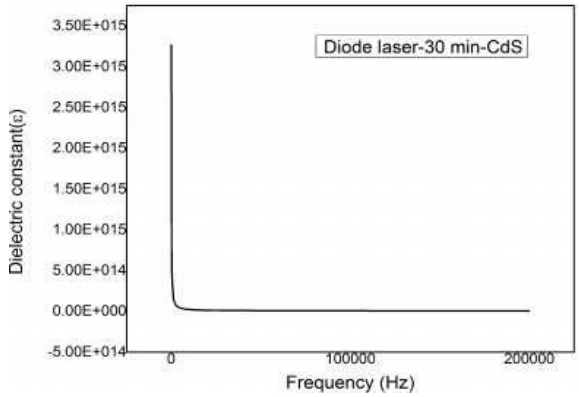

Figure 18(a). Dieletric curve of Dielectric constant (Sample 5)

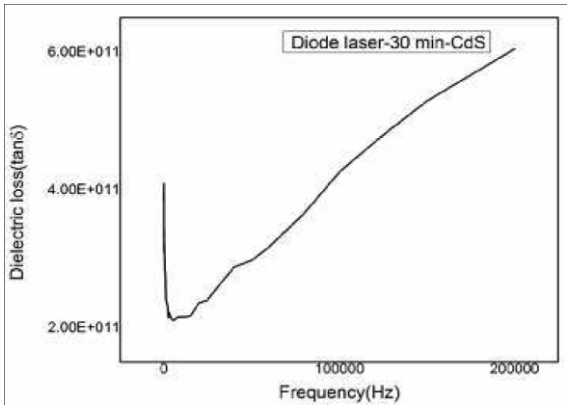

Fig 18(b): Dieletric curve of Dielectric loss (Sample 5)

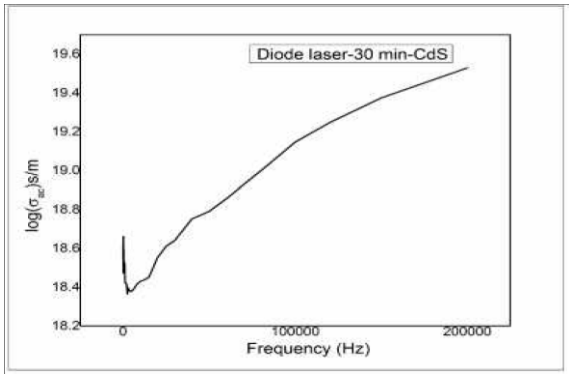

Figure 18(c). Dieletric curve of a.c electrical conductivity (Sample 5)

Table 15. Dielectric studies (Sample 5)

Frequency (KHz)	Dielectric constant (Σ)	Dielectric loss (tanδ)	a. c conductivity (σ_{ac}) 10^5 s/m
10	$2.2455x10^{13}$	$2.1572x10^{11}$	18.291934
50	$7.48498x10^{12}$	$2.9731x10^{11}$	18.7911
100	$5.91994x10^{12}$	$4.2654x10^{11}$	19.14701
150	$5.37558x10^{12}$	$5.2884x10^{11}$	19.37458
200	$5.03535x10^{12}$	$6.0468x10^{11}$	19.52932

The result shows liner decrease in dielectric constant values for increasing frequency and linear increase in dielectric loss for laser treated CdS nano particles(reverse action for without laser irradiated samples) and for a.c electrical conductivity linear increase for with and without laser irradiated samples when the frequency increases.

3.5. DLS Spectra (Measuring the Particle Size Distribution)

The DLS spectra of with and without laser treated samples are shown in Figure 19 – Figure 21.[5]

International Journal of
Scientific Research in Science and Technology (IJSRST)
Print ISSN : 2395-6011, Online ISSN : 2395-602X
International Conference on Advanced Materials
Held on 14, 15 December 2017, Organized by Department of Physics,
St. Joseph's College, Trichy, Tamilnadu, India

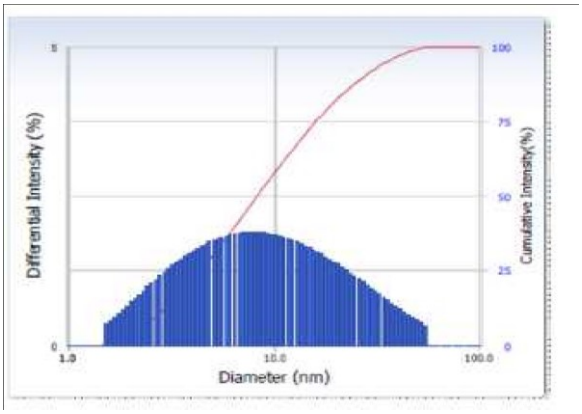

Figure 19. DLS spectra (sample 1)

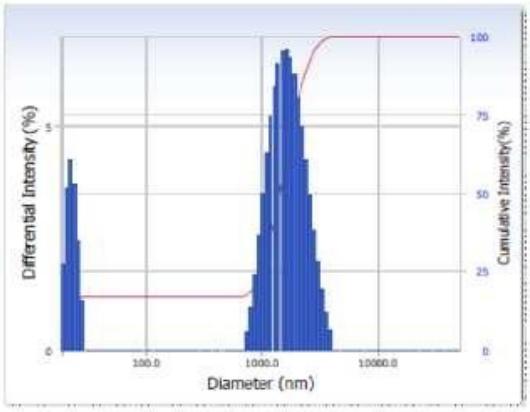

Figure 20. DLS spectra (sample 3)

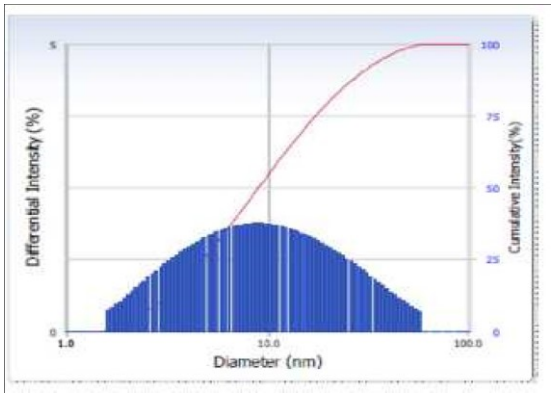

Figure 21. DLS spectra (sample 5)

Dynamic light scattering (DLS) studies revealed that the particle size distribution of Cadmium sulphide(CdS) nanoparticles are 2.1nm(sample1), 16.52nm(sample3), and 1.8 nm (sample 5).

3.6. SEM Analysis

The SEM Analysis of with and without laser treated samples are shown in Figure 22 – Figure 24. [6]

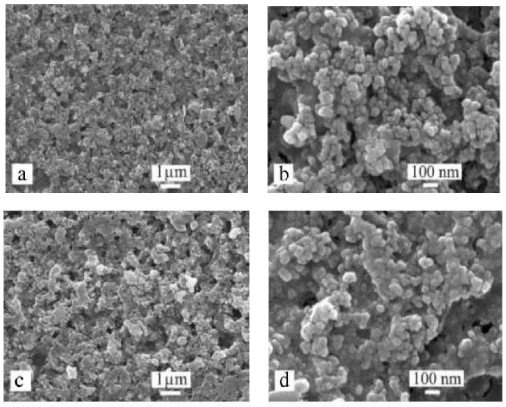

Fig 22: SEM image (sample1)

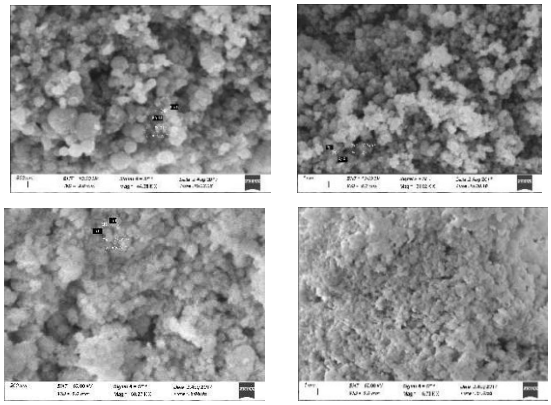

Figure 23. SEM image (sample3)

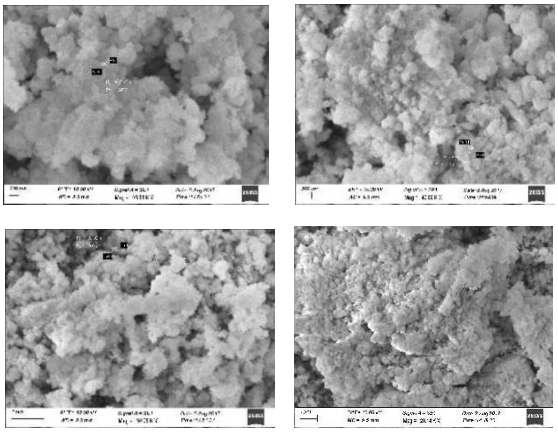

Figure 24. SEM image (sample5)

SEM analysis of Cadmium sulphide (CdS) Nano Particle, it is observed that the particles are in the

International Journal of
Scientific Research in Science and Technology (IJSRST)
Print ISSN : 2395-6011, Online ISSN : 2395-602X
International Conference on Advanced Materials
Held on 14, 15 December 2017, Organized by Department of Physics,
St. Joseph's College, Trichy, Tamilnadu, India

hexagonal shape within the particle size are in the range about 20 127nm (sample1), 34.9680.31nm (sample3), and 50.4867.02 nm (sample5). The average particle size observed in both SEM and XRD measurements are slightly different values.

Table 16. comparative study of particle size for Cadmium sulphide (CdS) Nanoparticle (sample 1, 3 and 5)

Sample	XRD Crystallite (nm)	DLS Particle (nm)	SEM Particle (nm)
1	11.3	2.1	20 – 127
3	15.88	16.52	34.96 –80.31
5	27.27	1.8	50.48 –67.02

4. Conclusion

In this, we investigated and reported the effect of laser heat treatment (HeNe laser and Diode laser) on nano particles CdS. The results observed are given below;

i. From the UVvisible spectrum studies, we observed thatthe band gap energy (for various laser exposures) from 5.1 eV – 5.2 eV (5.3 for sample1 without laser irradiation).
ii. The functional groups for different peaks in FTIR are analyzed and the type of vibration as well as intensity are studied.
iii. From the Xray diffraction studies, the structure of CdS nano particle (with and without laser irradiation) is hexagonal structure.
iv. The crystallite grain size of the samples calculated are 11.3 (sample1), 15.42 (sample2), 15.88 (sample3), 26.78 (sample4) and 27.27 nm (sample5) were observed from the XRD studies.
v. The dielectric properties of laser treated CdS nano particles and their relation with frequency, dielectric constant, dielectric loss and a.c electrical conductivity are investigated.
vi. Dynamic light scattering (DLS) studies revealed that the particle size distribution of Cadmium Sulphide CdS nanoparticles are 2.1nm (without laser), 16.52nm (HeNe laser treated with 30min), and 1.8 nm (Diode laser treated with 30min).
vii. From SEM analysis of Cadmium sulphide (CdS) Nano Particle, it is observed that the particles are in the hexagonal shape within the particle size are in the range about 20127nm (without laser),34.9680.31nm (HeNe laser treated with30min), and 50.4867.02 nm (Diode laser treated with30min)

References

[1] Saira Riaz, Anum Butt and Shahzad Naseem "Synthesis and Characterization of CdS and CdTe Inks for Solar Cells" Advances in Nano, Biomechanics, Robotics and Energy Research, August 2528, 2013.

[2] Anca Dumbrava, Daniela Berger, Gabriel Prodan, Florin Moscalu, Aurel Diacon "Facile synthesis, characterization and application of functionalized cadmium sulfide nano powders" Materials Chemistry and Physics xxx (2016) 1e8.

[3] Entidhar Alkuam, Muatez Mohammed, TarPin Chen "Fabrication of CdS nanorods and nanoparticles with PANI for (DSSCs) dyesensitized solar cells" Solar Energy 150 (2017) 317–324.

[4] Ziaul Raza Khan M. Zulfequar Mohd. Shahid Khan "Chemical synthesis of CdS nanoparticles and their optical and dielectric studies" J Mater Sci (2011) 46:5412–5416.

[5] Divya Vishambhar Kumbhakar, Animesh Kumar Datta, Aninda Mandal, Debadrito Das, Sudha Gupta, Bapi Ghosh, Sandip Halder & Suvendu Dey "Effectivity of copper and

cadmium sulphide nanoparticles in mitotic and meiotic cells of Nigella sativa L. (black cumin) – can nanoparticles act as mutagenic agents?" Journal of Experimental Nanoscience, 2016, PP 823_839.

[6] Bansal P, Jaggi N and Rohilla S.K "Green Synthesis of CdS nanoparticles and effect of capping agent concentration on crystallite size" Research Journal of Chemical Sciences 6971, August (2012).

[7] N. Nithya, Dr. G. Boopathi "Synthesis and Characterization of CdS and Ag Doped CdS Nanoparticle" International Journal of Science and Research (IJSR) 2013.

[8] S. Mathew, Boni Samuel, A. Mujeeb, M. Kailasnath, V.P.N. Nampoori, C.P. Girijavallabhan "Effect of Au coating on optical properties of CdS nanoparticles and their optical limiting studies" Optical Materials 72 (2017) 673e679

[9] Shaik Raziya, Bokka Durga, Santoshi G Rajamahanthe, Boddeti Govindh Nowduri Annapurna "Synthesis and Characterization of CdS Nanoparticles using Reishi Mushroom" International Journal of Advanced Technology in Engineering and Science.

[10] Sh. Jamali, E. SaievarIranizad and S. Farjami Shayesteh "Synthesis, optical and structural characterization of CdS nanoparticles" International Journal of Nanoscience and Nanotechnology December 2007.

[11] Olumide Oluwole Akinwunmi, Gabriel O. Egharevba, Ezekiel Oladele Bolarinwa Ajayi "Synthesis and Characterization of CdS, ZnS and CdZnS Nanoparticles Embedded in Polystyrene" Journal of Modern Physics, 2014, 5, 257266

[12] Pavan K. Narayanam, Purvesh Soni, P. Mohanta, R.S. Srinivasa, S.S. Talwar, S.S. Major "Effect of heat treatment on the photoluminescence of CdS nanocrystallites in cadmiumrich organic Langmuir Blodgett matrix" Materials Chemistry and Physics 139 (2013) 196e209.

[13] Rajendra Kumar Duchaniya "Optical Studies of Chemically Synthesis CdS Nanoparticles" International Journal of Mining, Metallurgy & Mechanical Engineering (2014).

[14] P. Kavitha, S. Suseela, R. Mary Mathelane "Synthesis and Characterization of Cadmium Sulfide Nanoparticles" The International Journal of Engineering and Science, pp. 108110 (2013).

[15] I. Yadroitsev, I. Smurov "Surface Morphology in Selective Laser Melting of Metal Powders" science direct 12 (2011) 264270.

[16] Joseph Lik Hang Chau, ChunYen Chen, ChihChao Yang "Facile synthesis of bimetallic nanoparticles by femtosecond laser irradiation method" Arabian Journal of Chemistry (2017) 10, S1395–S1401.

[17] Ricardo Almeida de Matos, Thiago da Silva Cordeiro, Ricardo Elgul Samad, Letícia Bonfante Sicchieri, Nilson Dias Vieira Júnior, Lilia Coronato Courrol "Synthesis of silver nanoparticles using agar–agar water solution and femto second pulse laser irradiation" Colloids and Surfaces A: Physicochem. Eng. Aspects 423 (2013) 58– 62.

[18] Thomas Paul Dumont "Laser Interaction with Materials From Transparent Materials to Thin Films" A dissertation submitted to the Swiss

Federal Institute of Technology Zurich for the degree of Doctor of Natural Sciences

[19] J.J. Ewing, Jeff Hecht "Introduction to Laser Technology'' Third Edition Breck Hitz

[20] Series Popular Science & Technology "Laser and ITS Applications"

[21] H.J. Eichler, B. Eppich, J. Fischer, R. Güther, G.G. Gurzadyan, A. Hermerschmidt, A. Laubereau, V.A. Lopota, O. Mehl, C.R. Vidal, H. Weber, B. Wende "Laser Physics and Applications" Sub volume A: Laser Fundamentals Part 1.

[22] Oleksiy Shulika Igor Sukhoivanov Editors "Advanced Lasers Laser Physics and Technology for Applied and Fundamental Science".

[23] I.Yadroitsev, I.Smurov "Selective Laser Melting Technology from the single Laser Melted track stability to 3D parts of complex shape" physics procedia 2010, pp.551560.

[24] A. Agostiano, M. Catalano, M.L. Curri, M. Della Monica, L. Manna, L. Vasanelli "Synthesis and structural characterisation of CdS nanoparticles prepared in a fourcomponents waterinoil microemulsion" Micron 31 (2000) 253–258

[25] Rajagopalan Thiruvengadathan, Yael LeviKalisman, Oren Regev, "Synergetic effect of ultrasound and sodium dodecyl sulphate in the formation of CdS nanostructures in aqueous solution" Ultrasonics Sonochemistry 14 (2007) 398–404.

[26] A.F.G. Monte, N.O. Dantas, P.C. Morais and D. Rabelo Synthesis and Characterisation of CdS Nanoparticles in Mesoporous Copolymer Template Brazilian Journal of Physics, June, 2006.

International Journal of
Scientific Research in Science and Technology (IJSRST)
Print ISSN : 2395-6011, Online ISSN : 2395-602X
International Conference on Advanced Materials
Held on 14, 15 December 2017, Organized by Department of Physics,
St. Joseph's College, Trichy, Tamilnadu, India

Thermal Analysis of Selective Absorber Coatings Based on Smoke for Application in Spiral Concentrating Type Solar Cookers

J. Packiam Julius, T.K. Jayaleka
Department of physics,Pioneer Kumaraswamy College, Nagercoil, Tamilnadu, India
Corresponding Author: dr.j.pjulius@gmail.com

Abstract

The thermal properties of selective absorber coating of a spiral concentrating type solar cooker has been analysed. Coating has been prepared using smoke. Even though the common type of solar cookers have been used for thermal analysis, the concentrating type solar cooker showed a better result to obtain very high temperatures. Investigations have been done with smoke which is readily available in Villages and cost effective. Various thermal parameters such as standard cooking power and overall efficiency have been calculated in this Study. Aluminium vessels with smoke coating has been used in this study which has been compared with the performance of Aluminium absorbers, coated with lamp black and black primer paint. The cost effective, readily available smoke was found to be a better solar selective coating which is suitable for villagers.

Keywords: Spiral concentrator, selective surface, thermal parameters.

1. Introduction

In rural areas solar cooker is a viable and a promising device that uses solar radiation to cook food, which preserves the nutrition value. The common type of solar cookers are box type cooker, parabolic concentrator, umbrella type cooker, hybrid cooker, conical concentrator, Fresnal concentrator, spiral concentrator etc. With spiral concentrators we can obtain very high temperatures. Considering the cost effectiveness, portability and simplicity, spiral concentrator is a suitable one for villagers.

Selective solar absorber coating is important in spiral concentrating type solar cooker, which converts solar radiation into heat energy. To get maximum photo thermal conversion, the selective absorber should have high absorptance and low emittance at operational temperature [1] Usually materials which are used for the fabrication of solar cooker are expensive. So for the people with low income, a low cost material for selective absorber must be identified. So a spiral cooker with stainless steel concentrator is fabricated with reduced constructing cost and locally available materials are used. [4,5,6]. The readily available material called smoke particles in rural areas has been used as a selective coating for absorber for spiral concentrating type solar cooker. The absorber with smoke coating is made to get exposed in direct sunlight under various weather changes for several hours.

2. Thermal Parameters

To compare different cookers thermal parameters are used [2]. The standard cooking power Ps and overall efficiency ηf are calculated using the formula.

$$Ps = Pc \ \frac{700w}{\frac{m^2}{I}}$$

Pc is cooking power and I is the insolation (w/m^2)

$$Pc = mc_p = \frac{dT}{dt}$$

m is the mass of water, Cp in the sp. heat capacity of water and T is the temperature of water at time t.
The overall efficiency [3] is calculated as

International Journal of
Scientific Research in Science and Technology (IJSRST)
Print ISSN : 2395-6011, Online ISSN : 2395-602X
International Conference on Advanced Materials
Held on 14, 15 December 2017, Organized by Department of Physics,
St. Joseph's College, Trichy, Tamilnadu, India

$$\int \frac{mCp(Twf - Twi)}{A(Idt}$$

where Twf and Twi is the final and initial temperature and A is the area of the concentrator.

3. Experimental

3.1. Preparation of the material coating

Smoke particles have been used as the coating for selective absorber and aluminium pot was selected. Smoke is applied uniformly over the outer surfaces of the pot by exposing them to the smoke from a candle or kerosene lamp. To compare the performance of smoke coating other pot painted with commercially available black primer paint and lamp black were used. The spiral concentrator with absorber is shown in Fig 1.

Figure 1. Concentrator with Absorber coated with smoke

3.2. Thermal parameter Measurement

3.2.1. Water heating test

In order to carryout the water heating tests, three Al vessels coated with smoke, lamp black and black primer paint were used. To start with, the stand is directed towards the sun to set azimuth. The absorbers were loaded with 0.964 kg of water. The concentrator is adjusted until the absorber is in the region of brightest illumination. Insolation temp of water and ambient temp. Were noted down at an interval of every 2 minutes. N.I precision, pyrheliometer was used for measuring solar insolation and temp of water was measured by digital thermometer. (portable)

Table 1. Water heating test for smoke, lamp black and black primer

Date : 30.05.17
Absorber material : Aluminum
Starting time : 12.41pm
Amount of water : 0.964kg
Ambient temp. : 29.5°C

Time Minutes	Insolation W.m^2	Temp of absorber coated with		
		Smoke °C	Lamp Black °C	Primer Paint °C
0	617	29	29	29
2	631	36	35.8	35.5
4	624	44.6	44.1	44
6	635	54.1	53.7	53.5
8	624	59.8	59.4	59
10	632	67	66.5	66.4
12	664	73.1	72.5	72.2
14	667	78.9	78.2	78.1
16	662	84.8	84.2	84.1
18	667	89.4	89.1	84.9
20	662.8	92.8	92.14	95.01
24	667	98	97.5	97.2
25	667	100	98	97.9

4. Result

By knowing the thermal parameters the coating performance was analyzed three absorbers were used to test the investigated coating. The overall efficiency was determined. The following table shows the effectiveness of the selective coating.

Table 2. Summary of thermal parameters

Coating Parameters	Smoke	Lamp black	Primer paint
Ps (Watts)	78	72	59
(%) η	82	76	20.5

5. Conclusion

The thermal efficiency and cooking power of smoke as a selective solar coating has been investigated. This coating depicts better results than other commercially available lamp black & primer paint coatings. The cheap material smoke could be

used as the selective solar coating for spiral concentrator

Acknowlegements

The authors are grateful to the management and teaching staff members of Pioneer Kumaraswamy College, Nagercoil for the support to carryout this work.

References

[1] Kennedy CE 2002 Review of Mid to High Temperature Solar Selective Absorber Materials. Technical Report NREL/TP-520-31267.

[2] Patera. R.P and Robertson H.S A Figure of Merit for solar Collectors - Alternative Energy Sources II. New York: Mc Craw hill – pp.73.

[3] Ari Rabi. Active solar collectors and their Applications: Oxford University press - 1985 pp110.

[4] Licciulli A, Diso D.Torsello G, Tundos, maffeszzoli, lomascola, and mazzer. "The Challenge of high performance selective emitters for thermophotovoltaic application S" Semiconoluctor Science and Technogy 18 (2003).

[5] M.Lanxner.Z Elgat "solar selective abosorber coating for high service temperature produced by plasma sputtering SPIE VOL 1272 Feb 15, 2005.

[6] Volnea M. Jeneif Bogamc, Duta A "solar selective coatings based on Nickel Oxlde obtained via spray pyrolisis, Journal of Nano science and nanotechnology Vol. 9, No. 7, July 2009, pp 4279.

International Journal of
Scientific Research in Science and Technology (IJSRST)
Print ISSN : 2395-6011, Online ISSN : 2395-602X
International Conference on Advanced Materials
Held on 14, 15 December 2017, Organized by Department of Physics,
St. Joseph's College, Trichy, Tamilnadu, India

Optical Efficiency and Selectivity Analysis of Lamp Black as Solar Selective Surface

T.K. Jayaleka[1], J. Packiam Julius[1], B. Usha[2], K. Jeyakumari[3], Bena Jothi[2]
[1]Department of Physics, Pioneer Kumaraswamy College, Nagercoil, Tamilnadu, India
[2]Women's Christian College, Nagercoil, Tamilnadu, India
[3]Sree Ayyappa College for Women, Nagercoil, Tamilnadu, India
Corresponding Author: gituniverse16@gmail.com

Abstract

This investigation has been directed towards the calculation of optical efficiency of spiral concentrating type solar cooker with lamp black as solar selective surface. Attempts were made to study the optical performance of the solar selective Coating. Spray painting technique has been adopted for coating the material. Aluminium and Stainless Steel Absorbers have been used and their optical efficiencies were compared with other black coatings. Water heating tests and indoor cooling efficiency. If has been concluded that the optical efficiency of the Spiral Concentrator has the maximum value with Aluminium absorber coated with lamp black.

Keywords: Selectivity, optical efficiency.

1. Introduction

Black solar absorbers are the chief component of concentrating type solar cookers. The Selectivity in defined an the ration of solar radiation (absorption) to thermal infrared radiation (emission) Typical value for a selective surface might be 0.90 solar absorptom and 0.10 thermal emissivity [1,3,4] The optical performance of an absorber depends on the optical constants and the thickness of the absorber coating. This selective surface was durable highly resistant to humidity, oxidizing atmosphere and less expensive [2].

2. Experimental

Ordinary lamp black is commercially available. It was spray painted over the Aluminium and stainless steel substrates. They were dried and used as absorbers. Water heating test was performed with the newly available absorber and it was compared with other commercially available black coatings.

Two pots one Aluminium and another stainless steel were used and the same lamp black was coated over the two absorbers. Water heating tests were performed individually to find the optical efficiency of the cooker with different absorbers..

To the tell whether the concentrator needs improvement it is important to evaluate the optical quality of the device. [5,7,8,9]

3. Result

The optical efficiency with the solar selective surface coating for Aluminium & S.S are fabulated

Table 1. Optical efficiency of Stainless Steel Absorber

Temp Region °C	Mean Temp °C	Energ lost q loss watts	Energy used q gain watts	Input AcId	Optical Efficiency %
30.5-38.2	5.35	10.331	269.07	618.73	45
38.2-45.2	12.7	25.9	344.18	627.7	43.03
45.2-52.8	20.05	40.96	368.5	633.5	48.88
52.9-60.2	27.55	56.29	254.85	635.5	48.92
60.2-67.1	34.85	70.80	240.69	637.6	48.8
71.8-77.9	45.85	83.85	212.79	635.6	48.2
84.3-87.9	57.1	116.87	125.58	619.9	39.07

International Journal of
Scientific Research in Science and Technology (IJSRST)
Print ISSN : 2395-6011, Online ISSN : 2395-602X
International Conference on Advanced Materials
Held on 14, 15 December 2017, Organized by Department of Physics,
St. Joseph's College, Trichy, Tamilnadu, India

Table 2. Optical efficiency of Aluminium absorber

Temp Region °C	Mean Temp °C	Energy lost q loss watts	Energy used q gain watts	Input Acid	Optical efficiency
35.8-44.1	10.5	16.83	287.2	812	49.64
44.1-53.7	18.4	29.49	332.2	619	38.38
59.4-66.5	32.46	50.70	359.2	620	49.3
66.5-72.3	40	64.79	207.6	618	44.08
72.5-78.2	45.85	72.59	197.2	623	43.2
78.2-84.3	31.75	76.54	211	612	46.9

From Table 1 & 2, it was found that solar selective coating of lamp black with Aluminum pot was more effective than S.S. Pot with lamp black coating. Because of the physical properties of stainless steel the optical efficiency is high, Moreover when lamp black in coated in different layers one over the other, the efficiency increases according to the thickness. The thickness of both Aluminium and Stainless steel pots with the thickness of the coatings decide the value of optical efficiency of the concentrator and overall efficiency of the cooker.

4. Conclusion

The water heating test and Indoor cooling tests were carried out in the calculation of optical efficiency of the solar selective surface [9]. The experimental results favour Aluminium with lamp black as solar selective surface because of durability, high tolerance to humid air and extreme temperature variation. It was able to retain the selective properties. [6]

5. Acknowlegements

The authors wish to acknowledge the management and professors of Pioneer Kumaraswamy College, Women's Christian College & Sree Ayyappa College for their help to complete this project.

6. References

[1] MF. Shaffei, N. Khattab, A.M. Award, H.S. Hussdia Characterization of black Ni & Sn as optically selective Abserber coatings Research Journal of Pharmaceutical, Biological & Chemical Science.

[2] Shib. HH. Huang Y.C J mater Process Technol. 2008, 12, 119.

[3] Gttass, J.B. Ramsey, J.B. Heancy and J.J., Trilo 'Reflactance, Solar Absorptivity and Thermal Emissivity of SiO_2 coated Aluminium. Applied optics. Vol. 8, Issue 2, 1969, pp. 275.

[4] D.M. Trottler Jr and AJ sievers. 'Spectral selectivity of high temperature solar Absorbers Applied optics, Vol. 19, No. 5, March 1980 pp. 711.

[5] M. Rubin, R. Powels and K. Von Rottkay Solar Energy, Vol. 66, No. pp. 267, 1999.

[6] John. F. Clare. "Comparison of four analutic methods for calculation of irradiance in integrating spheres". J. Opt. Soc. Am. A 15, 1998.

[7] Fuad Mammadov 'Study of selective surface of solar Heat receiver. 'International Journal of Energy Engineering 2012, 2(4), 138-144.

[8] Sasa R. Pavlovic, P. Stefanovic, Evangelos Bellos. "Design and Simulation of Solar Dish concentrator with spiral-coil smooth. Thermal Absorber". Thermal Science 2016. No. 4, pp. 1387-1397.

[9] T. Mouhib. A. Mouhsen M. Har Mouchi J.P. Vigneron P. Defrance. 'Stainless steel coating as selective material for passing raduative cooling applied Optical Materiah 31 (2009).

International Journal of
Scientific Research in Science and Technology (IJSRST)
Print ISSN : 2395-6011, Online ISSN : 2395-602X
International Conference on Advanced Materials
Held on 14, 15 December 2017, Organized by Department of Physics,
St. Joseph's College, Trichy, Tamilnadu, India

Study of Cost Effective Solar Selective Surface for Spiral Concentrator

T.K. Jayaleka, J. Packiam Julius
Department of Physics, Pioneer Kumaraswamy College, Nagercoil, Tamilnadu, India
Email: gituniversel16@gmail.com

Abstract

Solar selective surface has great importance in practical uses in solar energy thermal techniques. In this attempt, the use of lamp black + SiO_2 in different proportions as selective coating has been studied. Efforts have been taken to know whether the amount of SiO_2 in the mixture could be used to enhance the efficiency of the spiral concentrating type solar cooker. Spraying technique has been used for coating the material over the absorber. The absorber material used was Aluminium. Water heating tests were carried out during summer season. The Study revealed the fact that the amount of SiO_2 in SiO_2 lamp black mixture would decide the value of overall efficiency of the spiral concentrator and its performance. The studies were carried out in the natural weather conditions.

Key Words: Solar energy, selective surface, thermal conversion.

1. Introduction

For effective thermal conversion, the absorber should have high absorptance in the solar range but low thermal emittance. The selective surfaces maximize solar absorption and they suppress thermal re-radiation. At the operational temperature, the optical and thermal properties of the selective surface should be stable.

2. Analysis of selective coating

The solar selective coating with lamp black & SiO_2 was used in concentrating type solar cookers. The performance of an absorber coated with a solar selective surface is determined by the absorptance and thermal emittance.

For opaque materials,

spectral absorptance $\alpha(\lambda,\theta)$ in expressed using Kirchoff's law as,

$$\alpha(\lambda,\theta) = 1 - \rho(\lambda,\theta) \quad \ldots (1)$$

$$\& \ \varepsilon(\lambda,T) = \alpha(\lambda,T) \quad \ldots (2)$$

where $\rho(\lambda,\theta)$ is the sum of collimated and diffuse reflectance, λ is the wavelength, θ is the incidence angle of light and T is the given temperature.

The solar reflectance is studied using spectrophotometers in 0.3 – 2.5 μm wavelength range at near – normal $\theta = 0$ angle of incidence [1,5,6].

Emittance is measured at room temperature as

$$\varepsilon = \int_{\lambda\min}^{\lambda\max} \left(\left[1-"("("(",T)\right]B("(",T)d"(")/("T4)\right) \quad \ldots (3)$$

where (= 5.6696×10^{-8} $Wm^{-2}K^{-4}$ is the Stefan – Boltzmann constant

B(λ,T) is the spectral irradiance of a black body curve from,

$$B(\lambda,T) = c1/\left(C^5\left[e(c2/(T)-1\right]\right) \quad \ldots (4)$$

where c1 = 3.7405 × 108 W $\mu m^4 m^{-2}$

c2 =1.43879 × 104 μmK

which are Planck's first and second radiation constants.

The efficiency of a concentrator depends mainly on the absorber coating. selective coatings can degrade high temperature because of oxidation, humidity, atmospheric pollution, chemical reactions etc [2,3,7,8].

3. Experimental

SiO_2 mixed with lamp black has high degree of spectral selectivity. The coating is carried out by spraying technique. The use of this layer of lamp black on Aluminuim has been found to stabilize Aluminimum [4]

Lamp black and SiO_2 were mixed together in various proportions, a colloidal solution was got. It was coated on an Aluminimum absorber. Eight different vessels were used for eight proportions of lamp black & SiO_2. The concentrator along with the

International Journal of
Scientific Research in Science and Technology (IJSRST)
Print ISSN : 2395-6011, Online ISSN : 2395-602X
International Conference on Advanced Materials
Held on 14, 15 December 2017, Organized by Department of Physics,
St. Joseph's College, Trichy, Tamilnadu, India

stand was kept in position to receive maximum solar radialion. 1 kg of water in taken in the absorber. It is allowed to boil. It took nearly 20 minutes to boil. These tests were carried out during the month of May. The readings and calculations were tabulated as follows.

Table 1. Efficiency of the concentrator for different proportims of lampblack and S_iO_2

Lamp black (in gram) + S_iO_2 (in gram)	Efficiency %
1 +1	82
1.2 +0.8	81
1.4 +0.6	80.4
1.6+0.4	80.1
0.8 +1.2	82.2
0.6 +1.4	82.6
0.4+1.6	84.2

Date : 1-5-2017 Ambient temp:.30°C

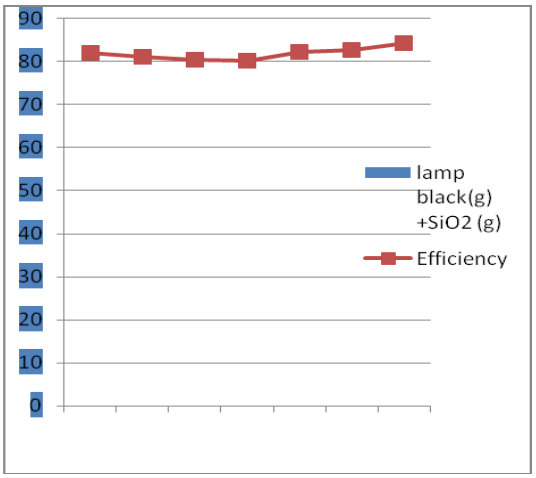

Figure 1. the graphical representation of the data.

It was found that the amount of S_iO_2 is directly proportional to the efficiency of the concentrator.

The average efficiency of the concentrator was calculated which is depicted in the following table

Table 2. Average Efficiency of Spiral Concentrator

Date	Direct Solar Radiation	Efficiency %
May 1	680	82
May 5	685	85
May 10	720	85
May 15	740	81
May 20	750	86
May 22	760	82
May 24	913	80
May 26	850	84

The experimental setup used is shown below.

Figure 2. Experimental setup

5. Conclusion

The technical parameter of the newly tried cost effective selective coating was found to be more effective than commercially available black coatings and pure lamp black. It was found that the mixture of lamp black and S_iO_2 is a promising one in the field of solar selective surfaces.

Acknowlegements

The authors are thankful to the Management and Professors of Department of Physics Pioneer Kumaraswamy College, Nagercoil for the help offered in doing experiments.

References

[1] Fuad Mammadove, 'Study of Selective Surface of Solar Heat Receiver' International Journal of Energy Engineering 2012.2 (4) 138-144.

[2] S. Brunold.U.Frei.B.Carisoon, K.Molier and M.Kohi.' Acceterated life testing of solar absorber coatings, testing procedure and results' Solar energy 68, 4,313(2000)

[3] W.D Duff and L. Hamasaki, 'Experimental Evaluation of Selective Surface Evacuated Solar Collectors. Proceedings of American solar energy conference.1978, P.345.

[4] Y.Noguchi, K.Naka, Isao, K.Naku Mara S.Sawada, T.Tani & S.Gords 'Fatrication of Zr Cx / Zr and Cr – Cr Ox films for practical solar selective absorption systems" SPIE,324,124(1982).

[5] G.Hass, J.B.Ramsey, J.B.heancy and J.J.Trilo. 'Reflectance, Solar Absorptivity and Thermal, emissivity of SiO_2-coated Aluminium Applied Optics Vol.8 Issue 2, 1969, pp. 275.

[6] D.M. Trotter Jr and A.J. Sievers. 'Spectral selectivity of high temperature solar Absorbers. "Applied optics Vol. 19, No.5, March 1980 PP 711.

[7] Zueco and Fr Alhama "Inverse estimation of temperature dependent emissivity of solid metals "Journal of quantitative spectroscopy & radiative transfer Vol.101.iss.1 pp 73.

[8] Ravindra N.M, Abedrabbo. S. Wei Chen Tong F.M. Nanda AK, Speranza A.C. 'Temperature dependent emissivity of silicon related materials and structures Semiconductor Manufacturing IEEE Transactions on Volume II. Issue 1, Feb.1998.pp 30.

International Journal of
Scientific Research in Science and Technology (IJSRST)
Print ISSN : 2395-6011, Online ISSN : 2395-602X
International Conference on Advanced Materials
Held on 14, 15 December 2017, Organized by Department of Physics,
St. Joseph's College, Trichy, Tamilnadu, India

n-type SnS:Cu Thin Films with High Surface Energy (111) Plane: Optimization of its Substrate Temperature

Gisa Grace Ninan, C. Sudha Kartha , K.P. Vijayakumar
Department of Physics, Cochin University of Science and Technology, Cochin-682022, Tamil Nadu, India
[1] email: gisagrace@gmail.com, [2] email: csk@cusat.ac.in, [3]email: kpv@cusat.ac.in.

Abstract

Using Chemical Spray Pyrolysis (CSP) Technique n- type Copper doped SnS (SnS:Cu) thin films were successfully deposited onto soda-lime glass substrate. According to earlier reports (111) orientation of SnS is suggested to be the preferred orientation for PV applications. This paper reports the preparation of SnS:Cu films with (111) orientation by varying the substrate temperature which is an important parameter of CSP technique. Using X-ray diffraction, Scanning electron microscopy, UV-Vis-NIR spectroscopy and Hall measurements the Structural, Morphological, Optical and Electrical properties of SnS:Cu films are studied. The substrate temperature of 375^{0}C is found to be the best for preparing good quality SnS:Cu thin films with preferred orientation in plane (111).

Keywords: Spray techniques, Optical properties, Electrical properties, Thin films.

1. Introduction

The binary semiconductor Tin sulfide (SnS) belonging to IV-VI group semiconductors, with earth abundant components, orthorhombic structure and having a band gap of around 1.4eV makes it a potential candidate for photovoltaic studies [1] [2]. SnS can be prepared as single crystals, thin films or nanostructures using various physical and chemical methods such as chemical bath deposition [3] spray pyrolysis [4], thermal evaporation [5] sputtering [6] etc according to required applications [7]. Properties of the thin film prepared by CSP technique is very much connected with the substrate temperature, as this parameter provides energy for pyrolytic reduction. With very high temperature, anionic species get re-evaporated where as with very low temperature proper pyrolytic reduction will not take place. Hence the substrate temperature is so critical to prepare an uniform thin films with required opto-electronic properties. The present study report the changes in Copper doped SnS thin films on varying the substrate temperature from 300^{0}C to 450^{0}C.

2. Experimental Details

SnS:Cu thin films were synthesized over glass substrates using CSP technique. Stannous chloride ($SnCl_2.2H_2O$), Thiourea ($CS(NH_2)_2$) and Cuprous Chloride ($CuCl_2.2H_2O$) is used as the precursors for the above study. The substrate temperature is varied as 300^{0}C, 350^{0}C, 375^{0}C, 400^{0}C and 450^{0}C. The samples are named as C300, C350, C375, C400 and C450 respectively. Compressed air is used as the carrier gas and the opto-electronic studies were carried out keeping all the spray parameters unchanged with Sn:S ratio at 1:2. Copper doping is fixed as 4% of tin concentration as reported elsewhere [8].

X-ray diffraction studies were carried out using Rigaku (D. Max.C) automated X-Ray diffractometer and diffraction pattern is recorded using filtered Cu Kα (λ = 1.5405 A^o) radiation and Ni filter operated at 30 kV and 20 mA.UV-VIS-NIR spectrophotometer (JASCO V 570 model) is used for optical studies. Surface morphology is studied using ZEISS Scanning electron microscopy.Ecopia model No HMS-53000, magnetic field = 0.57 T and capable of current

International Journal of
Scientific Research in Science and Technology (IJSRST)
Print ISSN : 2395-6011, Online ISSN : 2395-602X
International Conference on Advanced Materials
Held on 14, 15 December 2017, Organized by Department of Physics,
St. Joseph's College, Trichy, Tamilnadu, India

measurement in the range (1nA-20 mA) Hall system is used for electical studies.

3. Results and Discussions

Figure 1 depicts the XRD patterns of SnS:Cu films deposited at different substrate temperatures. All the samples except those prepared at very low and very high pyrolysis temperature had SnS phase crystallized in Orthorhombic structure (JCPDS 75-0925). At lower temperature 300^{0}C presence of Sn_2S_3 phase (JCPDS 14-0619) is observed along with SnS phase and at higher temperature 450^{0}C the SnS_2 phase (JCPDS 23-0677) become prominent.

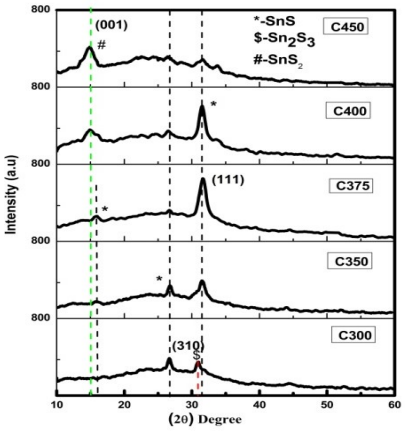

Figure 1. The X-ray diffractograms of SnS:Cu thin films by varying the substrate temperature

It is quite clear from our XRD data that, at substrate temperature 375^{0}C, the impurity phases are almost absent and has better crystallinity with prominent SnS (111) plane. It is already reported that for PV applications the (111) orientation of SnS is generally preferred because out of all the SnS based solar cells the maximum efficiency is for SnS with these orientation [9]. Even with the doping no peaks corresponding to Cu_xS phase is formed. According to reports the surface energies (σ) of orthorhombic structure increases as σ (100) < σ (001) < σ (010) < σ (111) and it is also mentioned that the (111) plane will grow only when an optimum number of Sulfur atoms is present around Sn atoms [7]. Hence at temperature 375^{0}C we could successfully synthesis SnS:Cu thin films with this high energy (111) plane.

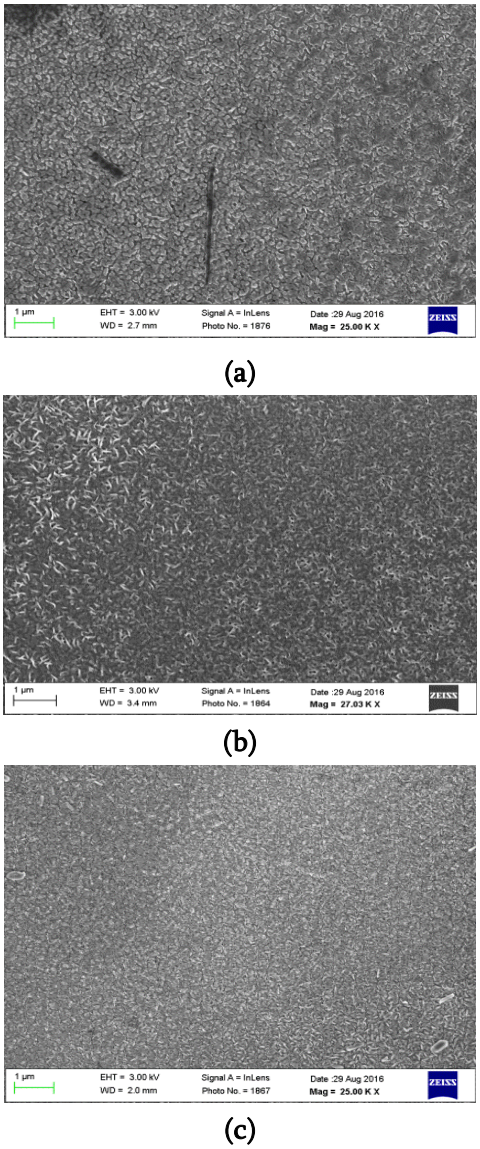

Figure 2. SEM images of SnS:Cu thin films prepared at (a) 300^{0}C, (b) 375^{0}C, (c) 450^{0}C

The Surface morphology of the temperature varied samples showed a noticeable difference as temperature changes. This change is clearly observed in Figure 2. The samples at low temperature (300^{0}C) showed spherical grains where as samples at 375^{0}C showed typical SnS:Cu needle like structure and as

International Journal of
Scientific Research in Science and Technology (IJSRST)
Print ISSN : 2395-6011, Online ISSN : 2395-602X
International Conference on Advanced Materials
Held on 14, 15 December 2017, Organized by Department of Physics,
St. Joseph's College, Trichy, Tamilnadu, India

the temperature is increased further to 450^{0}C the morphology changed partially as that of SnS_2 granules.

Optical band gap for films prepared at different substrate temperatures were determined using '$(\alpha h\nu)^2$ versus $h\nu$' plot (Figure 3). The absorption coefficient (> 10^5 cm^{-1}) is obtained for all the samples. The film synthesized at 375^{0}C has got optimum band gap around 1.4 eV. For lower and higher temperature the band gap is found to be greater than that of C375. The variation in band gap shows its tunability by merely changing the temperature alone.

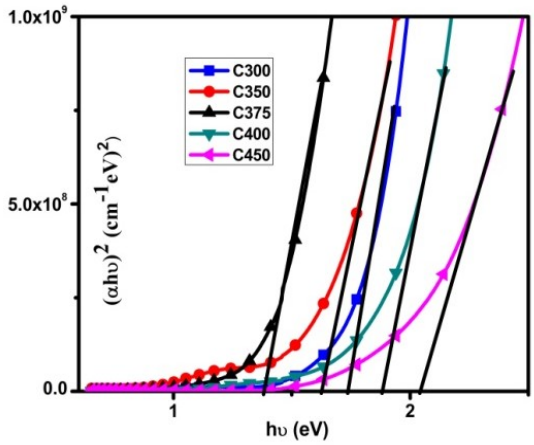

Figure 3. The band gap obtained for SnS:Cu thin films by varying the substrate temperature

The high band gap value obtained for lower and higher temperature is probably due to the presence of other phases like Sn_2S_3 and SnS_2 respectively [10].

The resistivity of all the samples were calculated using Hall measurement and found to be decreasing as temperature increases with minimum value for samples prepared at 375^{0}C; further increase in temperature resulted in increase of resistivity due to the formation of SnS_2. The minimum resistivity obtained for C375.

4. Conclusions

SnS:Cu thin films were deposited using CSP technique over glass substrate by varying the substrate temperature. The optimum temperature for fabricating phase pure SnS:Cu is determined to be 375^{0}C and its band gap is found to be around 1.4eV. These properties are quite promising for a good absorber layer in solar cell fabrication. This optimized film showed n-type conductivity with minimum resistivity. This work also shows the possibility of tuning the resistivity and band gap of SnS:Cu films by controlling the substrate temperature without any change in its conductivity type. All these superior properties are achieved without employing any post deposition treatments and hence it is quite useful for the development of low-cost thin film solar cells.

Acknowledgments

One of the authors [G.G.N.] would like to thank the UGC for providing fellowship in the form of 'Research Fellowships in Science for Meritorious Students' (UGC – RFSMS). The authors KPV and CSK would like to thank CSIR and KSCSTE respectively for financial assistance under "Emeritus Scientist" Scheme.

International Journal of
Scientific Research in Science and Technology (IJSRST)
Print ISSN : 2395-6011, Online ISSN : 2395-602X
International Conference on Advanced Materials
Held on 14, 15 December 2017, Organized by Department of Physics,
St. Joseph's College, Trichy, Tamilnadu, India

References

[1] Yu Kawano, Jakapan Chantana, Takashi Minemoto, "Impact of growth temperature on the properties of SnS film prepared by thermal evaporation and its photovoltaic performance", Current Applied Physics 15, 2015, pp. 897-901.

[2] Shuying Cheng, Gavin Conibeer, "Physical properties of very thin SnS films deposited by thermal evaporation", Thin Solid Films 520, 2011, pp. 837–841.

[3] E. Turan, M. Kul, A.S. Aybek, M. Zor, "Structural and optical properties of SnS semiconductor films produced by chemical bath deposition", J. Phys. Appl. Phys. 42, 2009, 245408. doi:10.1088/0022-3727/42/24/245408.

[4] G.G. Ninan, C.S. Kartha, K.P. Vijayakumar, "Spray pyrolysed SnS thin films in n and p type: Optimization of deposition process and characterization of samples", J. Anal. Appl. Pyrolysis. 120, 2016, pp. 121–125.

[5] P. Jain, P. Arun, "Influence of grain size on the band-gap of annealed SnS thin films", Thin Solid Films. 548, 2013, pp. 241–246.

[6] M. Leach, K.T.R. Reddy, M.V. Reddy, J.K. Tan, D.Y. Jang, R.W. Miles, "Tin Sulphide Thin Films Synthesised using a Two Step Process", Energy Procedia. 15, 2012, pp. 371–378.

[7] N. Koteeswara Reddy, "Studies of SnS thin films grown by SILAR method", ECS Journal of Solid State Science and Technology, 2 (6), 2013, pp. 259-263.

[8] Gisa Grace Ninan, V.G. Rajeshmon, C. Sudha Kartha, K.P. Vijayakumar, "Cu doping: An effective method for improving optoelectronic properties of sprayed SnS thin films", AIP Conference Proceedings, 1591, 2014, 1440.

[9] K.T.R. Reddy, N.K. Reddy, R.W. Miles, "Photovoltaic properties of SnS based solar cells", Sol. Energy Mater. Sol. Cells 90, 2006, 3041.

[10] Sajeesh, T.H., Optimization of deposition parameters of SnS thin films, Cochin University of Science and Technology, Kerala, India, Doctoral Thesis "Optimization of opto-electronic properties of SnS for possible photovoltaic application as an absorber layer", 2012, pp.134.

International Journal of
Scientific Research in Science and Technology (IJSRST)
Print ISSN : 2395-6011, Online ISSN : 2395-602X
International Conference on Advanced Materials
Held on 14, 15 December 2017, Organized by Department of Physics,
St. Joseph's College, Trichy, Tamilnadu, India

Spectral Properties of Ash for use as a Solar Selective Coating

J. Packiam Julius, T.K. Jayaleka
Department of Physics, Pioneer Kumaraswamy College, Nagercoil, Tamilnadu, India
Corresponding Author: dr.j.pjulius@gmail.com

Abstract

New attempts have been made to study the spectral properties of ash for use as a solar selective coating. Ash coating has been added as a better efficient coating to the other commercially available coatings. Investigations have been made to study the reflectance properties of ash coating. The reflectance of the ash coating was compared with that of other two coatings namely black chrome and black nickel. Ordinary painting method has been adopted as the coating technique. Aluminium absorber has been used which was coated with colloidal ash and was allowed to dry. Water heating test has been carried out to study the optical efficiency of ash on Aluminium vessel. For solar thermal applications, this coating has been proved to be one of the best solar selective coating with maximum optical efficiency.

Key Words: Reflectance, optical analysis, emissivity

1. Introduction

To get maximum efficiency and maximum temperature in spiral concentrator the absorber material should have a maximum absorbtance across the solar spectrum and minimum emissivity in the IR region. It should also be cheap and easy to prepare. The reflectance values got are shown and compared with other two coatings, namely black chrome and black nickel.

2. Experimental

The method of getting the solar selective coating to coat with metallic plate (Aluminium) with a colloid solution of ash and it was allowed to dry in shade for 2 or 3 days. After that, studies are done and compared with that of black chrome and black nickel.

3. Results

The reflectance properties got are shown in table 1.

Table 1. Comparison of reflectance of various coatings

	Ash	Black Chrome	Black Ni
Reflectance	0.130	0.132	0.133
Black body spectrum at 250°C	0.095	0.912	0.934

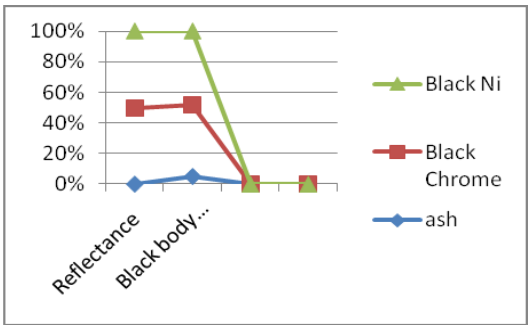

The optical analysis of the solar absorber could be done from these data in addition to transmittance and ellipsometry data by fither the data to other coatings [2,4,5] the optical constants of ash layer is some what lower than that of other coatings. The exinction coefficient is higher in the first layer of the coating Both effective refractive index and exinction coefficient of the ash layer increases with increasing wavelength as for metallic index [3,6,7,8]. The optical performance of the ash coating is 0.9/0.078 on Aluminium substrate.

International Journal of
Scientific Research in Science and Technology (IJSRST)
Print ISSN : 2395-6011, Online ISSN : 2395-602X
International Conference on Advanced Materials
Held on 14, 15 December 2017, Organized by Department of Physics,
St. Joseph's College, Trichy, Tamilnadu, India

Table 2 Optical efficiency of ash coating

Date : 06-05-17
Starting time : 12.14 pm
Amount of water : 0.964kg
Ambient temp : 29.5°C
Absorber : Aluminium

Temp Region °C	Mean temp above ambient °C	Energy lost Watts	Energy used Watts	Input Watts	Optical efficiency %
29-41.5	3.25	6.638	436.0	524.5	84.3
54.5-53.4	15.45	31.568	415.113	524.61	85
53.4-64.26	26.82	54.72	378.485	524.75	82.35
64.25-74.25	37.25	76.101	348.835	524.76	80.97
74.25-90.2	50.25	102.62	277.67	524.8	72.48

The optical efficiency hikes to a maximum value when ash is used as the solar selective coating for Aluminium absorber.

Optical efficiency depends on many factors such as insolation, optimum temperature, ambient temperature, wind velocity, percentage of humuidity in air etc, the absorber coating show a considerable increase in its value because of the nature of the material used namely ash. If a pressure cooker is used in the place of ordinary Aluminium pot, we expect the efficiency to increase more.

4. Conclusion

The spectral studies and optical analysis of Aluminium absorber coated with a solar selective ash coating has selective properties. This surface has been critical to high temperature solar thermal operations.

Acknowlegements

The authors wish to acknowledge the valuable assistance received from the Management & Professors of Department of Physics, Pioneer Kumaraswamy College, Nagercoil.

References

[1] H.C Barshilia, N. Selva Kumar & K.S Rajam Journal of Applied Physics 103, 023507 (2008). 15.

[2] Brown – Shaklec, W. Carty and D.D Edwards. Solar Energy Materials & Solar Cells 93 (2009) 1404 – 1410.

[3] Trotter Jr, Severs. J. "Spectral selectivity of high temperature solar absorbers.

[4] H.C. Barchilla, N. Selva Kumar & K.S. Rajam "structure and sptical properties of pulsed sputter deposited crs, Oy/Cr/Cr_2O_3 solar selective coating" journal of Applied Physics 103 (2008).

[5] Paeker D.S, J.E.R. Mcllvaine, Barkazi JF, Beal D.J & Anello M.T "Laboratory Testing of the Reflectance properties of Roofing Materials (2000) Florida solar Energy centre, Cocoa.

[6] B.V. Cockeram, D.P. Measures, A.J. Muiller "The development and tecsing of emissivity enhancement coatings for thermophotovoltaic radiator applications" Thin Solid films 1999, pp.17.

[7] S.R. Wenham M.A Green, S. Edminiton, P. Compbell L. Koschier, C.B. Honsberg et al., "Solar Energy Materials & Solar Cells. Vol. 41-42, June 1996, pp 3.

[8] Slamen M and Griessen, "Solar Collector Overheating protection", Solar Energy Volume 83, Issue 7, pp 982.

International Journal of
Scientific Research in Science and Technology (IJSRST)
Print ISSN : 2395-6011, Online ISSN : 2395-602X
International Conference on Advanced Materials
Held on 14, 15 December 2017, Organized by Department of Physics,
St. Joseph's College, Trichy, Tamilnadu, India

Investigating the Holographic Performance of a Developed Photopolymer Material by Hologram Recording

C.S. Rajesh[1], P. Safala[1], K. Anjana[1], G. Aswathy[1], C. Sudha Kartha[1]
[1]Department of Physics, CUSAT, Cochin-682 022, Kerala, india
Corresponding Author Email: csk@cusat.ac.in

Abstract

The present work explores the holographic performance of developed eosin sensitized Poly (vinyl alcohol)/Acrylamide based photopolymer material (EPVA) by hologram recording. The developed material can be used to record gratings with diffraction efficiency (DE) of 85% using 488 nm and 77% using 532 nm at exposure of 50 mJ/cm^2. Recorded Fourier Transform (FT) holograms and Projection type holograms showed the potential of this material for different holographic applications.

Keywords: Holography, Photopolymers, Gratings, Holograms.

1. Introduction

Holography is a versatile technology which can satisfy next generation needs since the industry demands cost effective and compact optical systems for data storage, data transfer, artificial intelligence, optical interconnects, display applications etc [i-vi]. In this regard, photopolymer systems have attracted much attention in recent years since they proved to be promising material system for holographic data storage and display applications [i-ii, vi]. Low cost, with excellent performing parameters like high diffraction efficiency, good photosensitivity, large refractive index modulation, high resolution, large dynamic range, made acrylamide based photopolymers to occupy an elevated position in the field of holography [ii,iv-vi]. The potential applications and markets of photopolymers in holography are based on the function of the hologram or diffractive feature (e.g. an image or Holographic Optical Elements) recorded in that material. One of the important properties of photopolymer is the self-processing, which makes them non-amenable to wet processing; a good criteria for holographic data storage, holographic optical elements (HOEs) and display applications [vi].

The present work is an investigation on the suitability of recording different holograms in an already developed Eosin sensitized Poly (vinyl alcohol)/Acrylamide photopolymer (EPVA) films [vii]. Existence of a close experimental relation between holographic data storage and fourier hologram recording methods, decided the priority of this hologram among others. Initially fourier holograms were recorded on the developed EPVA material. Another important class of holograms is 'projection holograms' which are actually hologram of a hologram and can be viewed in white also.

2. Materials and Methods

The photopolymer system used in this work consists of poly (vinyl) alcohol (PVA) - binder), triethanolamine (TEA) - initiator and Yellowish Eosin (EY) - photosensitizer dye and photopolymerizable monomer Acrylamide (AA)[vii]. The photopolymer films prepared using gravity settling method was allowed to dry at room temperature. Using double beam interferometry gratings were recorded on the dried photopolymer films with interbeam angle 40^0 and beam intensity ratio as 1:1. The recorded gratings were reconstructed using a He-Ne laser (Melles Griot - 632.8 nm) and the diffraction efficiency (DE) was determined using the relation,

$$DE\ (\%) = (I_d/I_i)\ x100$$

I_i-Incident beam intensity, I_d-First order diffracted beam intensity.

3. Results and discussion

3.1. Recording of holographic gratings

Spectral sensitivity of the developed photopolymer films was determined from absorption spectra (taken using JASCO V-570 UV-Visible-NIR spectrophotometer) of the samples. Absorption spectra of unexposed and

International Journal of
Scientific Research in Science and Technology (IJSRST)
Print ISSN : 2395-6011, Online ISSN : 2395-602X
International Conference on Advanced Materials
Held on 14, 15 December 2017, Organized by Department of Physics,
St. Joseph's College, Trichy, Tamilnadu, India

exposed samples show that this material can respond well to 532 nm and 488 nm wavelengths as shown in Figure 1.

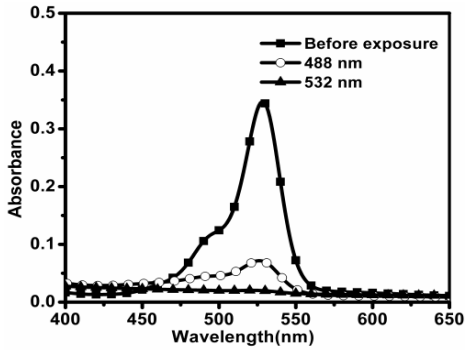

Figure 1. Absorption spectra of exposed and unexposed samples

In the previous work [vii], a DE of 85% at exposure of 50 mJ/cm^2 was reported using this material. The same material can be used to record gratings using 532 nm laser with DE of 77% at exposure 50 mJ/cm^2 as shown in Figure 2.

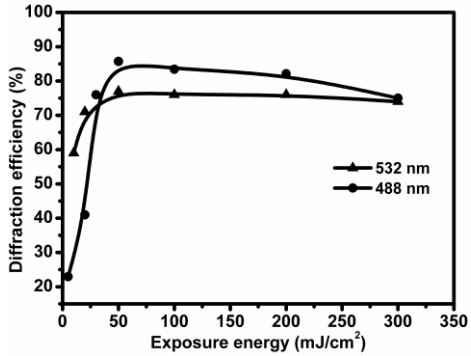

Figure 2. Variation in DE with Exposure energy

The variation in DE with exposure energy was similar to that of 488 nm wavelength laser. The studies revealed that the material shows good holographic performance for two wavelengths 488 nm and 532 nm.

Holographic device working with low power laser can reduce the cost of the system. Hence it is essential to assess the holographic performance of the material at lower laser power also. Figure 3 shows that even with 1 mW power laser, it is possible to record more than 80% DE gratings in this material.

In an interference pattern maximum fringe visibility is possible when the intensity ratio between the interfering beams are at 1:1. In the case of hologram recording, it is difficult to maintain a 1:1 beam ratio between the object and reference beams. So the effect of variation of beam intensity ratio was checked by varying the intensity ratio of interfering beams. From Figure 4 it was seen that even at a beam ratio of 1:0.2 it was possible to record gratings with more than 60% DE.

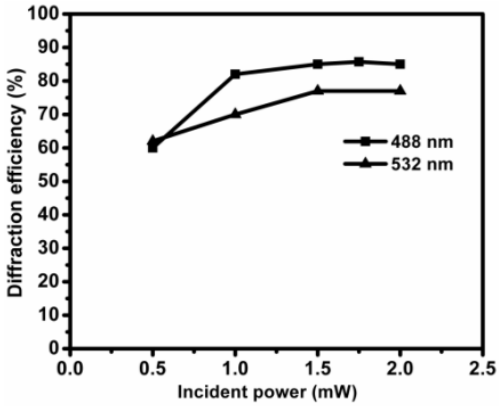

Figure 3. Recording of gratings with different laser

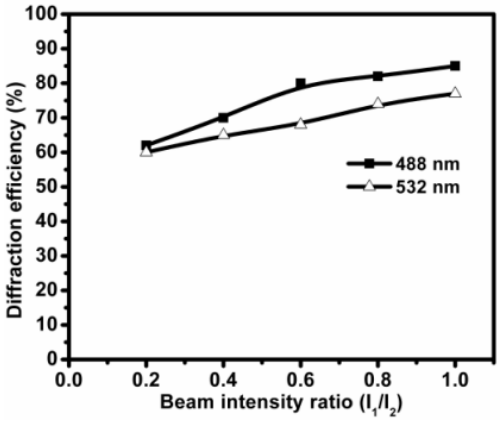

Figure 4. Variation in DE with beam ratio

3.2. Recording of Fourier Transform holograms

Apart from imaging, 'fourier holograms' are also suitable for data storage applications, because in holographic storage devices data pages are recorded using fourier transform (FT) method. Two dimensional holograms can be recorded on the material by consuming minimumsample area and the noise in the image could be reduced by incorporating suitable filters in the fourier plane. Usually, in storage devices the object beam is allowed to pass through a spatial

International Journal of
Scientific Research in Science and Technology (IJSRST)
Print ISSN : 2395-6011, Online ISSN : 2395-602X
International Conference on Advanced Materials
Held on 14, 15 December 2017, Organized by Department of Physics,
St. Joseph's College, Trichy, Tamilnadu, India

light modulator (SLM), but in the present study the object beam was passed through a transparency containing few letters. FT holograms were recorded using the experimental setup illustrated in Figure 5.

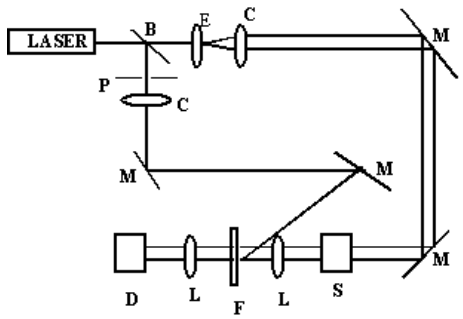

Figure 5. B-beam splitter, E-beam expander with spatial filter, P-Pinhole, C-Collimating lens, M-Mirror, S-Object, L-Lens, F- film, D-Detector

Figure 6. FT holograms and its reconstructed images

3.3. Recording of projection hologram

Projection holograms also known as standout hologram or as an image-plane hologram provide a dramatic visual with the entire image floating in front of the plate [viii]. For recording projection holograms the object beam used was not coming from a real object, but rather it is light that comes from a 'master hologram' and forms a real image of the object [viii-x].

When the copy hologram is processed, it is illuminated in the usual way for transmission holograms, and as always there will be a virtual image and a real image. With an ordinary hologram the images are well separated and they are not seen simultaneously. With the projection hologram they are both seen, since they are very close together and in fact join at the plate. The observer sees the virtual image behind the plate and the real image in front of the plate. Projection holograms can be used for display purposes as well as for making holographic lenses that can be used as compound lenses along with a real lens [viii].

For recording projection holograms, a master hologram was initially created using transmission geometry as shown in Figure 7 which is also known as Denisyuk method. Figure 8 is the photograph of a hologram recorded and reconstructed using 488 nm laser. This hologram was used as master hologram for producing a real image.

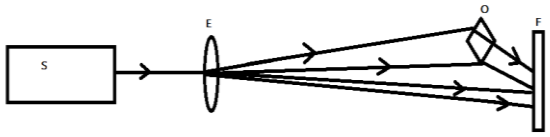

Figure 7. The experimental set up to record Denisyuk hologram; S-laser, E-beam expander with spatial filter, O-object, F-film

Figure 8. Photograph of Denisyuk hologram reconstructed using 488 nm laser

Figure 9 is the experimental setup for recording projection holograms. The master hologram was illuminated in such a way that the hologram is exposed to its conjugate beam giving a real image. This real image is caught on another plate and reference beam will be allowed to fall on the same plate to form a hologram.

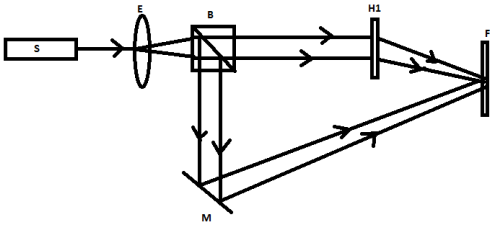

Figure 9. Recording set up for projection hologram;

International Journal of
Scientific Research in Science and Technology (IJSRST)
Print ISSN : 2395-6011, Online ISSN : 2395-602X
International Conference on Advanced Materials
Held on 14, 15 December 2017, Organized by Department of Physics,
St. Joseph's College, Trichy, Tamilnadu, India

S-laser, E-beam expander with spatial filter, B-beam splitter, H1-master hologram, M-mirror, F-polymer film

The photograph of a recorded projection hologram, reconstructed with white light is shown in Figure 10.

Figure 10. Photograph of a projection hologram viewed in white light

3.5. Conclusion

Feasibility study was conducted to assess the holographic performance of the developed eosin doped poly (vinyl alcohol)/acrylamide photopolymer films by recording different holograms. It was possible to record and reconstruct FT holograms successfully in this material. Fourier holograms recorded, ensured the suitability of this material for data storage applications as these type of holograms miniaturize the original size of the object (data) increasing the storage capacity. It was also possible to record 'Projection holograms' in this material, which are actually 'hologram of a hologram', can be viewed with white light in transmission mode also. Thus the developed material can be used for different applications such as data storage applications, HOEs, Display applications etc.

Acknowledgment

One of the authors (CSR) would like to thank UGC for fellowship and the author (CSK) would like to thank KSCSTE for supporting this work through the Emeritus Scientist Scheme.

References

[1] H. J. Coufal, D. Psaltis, and G.T. Sincerbox, Holographic Data Storage, Springer, New York (2000).

[2] Toal, V.; Introduction to Holography, CRC Press, Taylor & Francis, New York (2012).

[3] A. Pu, K. Curtis, D. Psaltis, "Exposure Schedule for multiplexing holograms in photopolymer films" Opt. Eng. 35, 2824(1996).

[4] J. Guo, M.R. Gleeson, and J.T. Sheridan, "A Review of the Optimisation of Photopolymer Materials for Holographic Data Storage," Physics Research International, 2012, 803439, (2012).

[5] H. Akbari, I. Naydenova and Suzanne Martin, "Using acrylamide-based photopolymers for fabrication of holographic optical elements in solar energy applications," Appl. Opt. 53, 1343-1353 (2014).

[6] D. Jurbergs, F.K. Bruder, F. Deuber, T. Fäcke, R. Hagen, D.Hönel, Thomas Rölle, M.S. Weiser, A. Volkov, "New recording materials for the holographic industry" Proc. of SPIE Vol. 7233, (2009).

[7] C.S. Rajesh, S.S. Sree Roop, V. Pramitha, Rani Joseph, K. Sreekumar, C. Sudha Kartha, "Study on the performance of eosin-doped poly(vinyl alcohol)/acrylamide photopolymer films for holographic recording using 488-nm wavelength," Opt. Eng.50 (2011).

[8] Joseph E Kasper, The Hologram Book, Prentice-Hall International Inc., New Jersey (1985)

[9] P. Hariharan, Optical Holography - Principles, techniques and applications, Cambridge University press, Cambridge (1984).

[10] Howard M. Smith, Principles of Holography, Wiley-Interscience, U.S.A (1969).

International Journal of
Scientific Research in Science and Technology (IJSRST)
Print ISSN : 2395-6011, Online ISSN : 2395-602X
International Conference on Advanced Materials
Held on 14, 15 December 2017, Organized by Department of Physics,
St. Joseph's College, Trichy, Tamilnadu, India

Synthesis and Characterisation of Nickel Ferrite Nanoparticles Prepared by Spray Pyrolysis Method

Anila I[1], Subin P. John[1], Jacob Mathew M[1*]
[1]Department of Physics, Mossbauer Research Group, St. Berchmans College, Changanassery, India
*Corresponding Author email: jacob.chrisdale@gmail.com

Abstract

Nickel ferrite nanoparticles of ultrafine size were successfully prepared by spray pyrolysis method. The structural characterization of the samples is done using XRD and FTIR. XRD pattern of all samples show the formation of single phase cubic spinel structure.The distribution of cations among the two interstitial sites has been estimated by the Rietveld refinement of XRD pattern. The FTIR spectra show two strong absorption bands, confirm the presence of metal - oxygen complexes within the spinel lattice. The HRTEM micrographs demonstrates ultrafine particles having cubic morphology and the average particle size obtained is in good agreement with that estimated from XRD. The elemental analysis has been carried out using EDS, confirmed the purity of the synthesized sample. The room temperature magnetic properties of the sample were measured by using a VSM and revealed the soft magnetic nature of the sample and the same has been confirmed by room temperature Mossbauer studies. The cation distribution estimated from Mossbauer spectroscopy and Rietveld refinement confirm the mixed spinel structure of the spray pyrolysis synthesized Nickel ferrite nanoparticles.

Keywords: Nickel ferrite, spray pyrolysis method, nano ferrite, Rietveld refinement, Mossbauer studies.

1. Introduction

Studies on magnetic nanoparticles (MNPs) belonging to spinel ferrites is an active area of research due to their potential use in recording media, information storage and magneto-optical devices [1]. Most of these studies are focussed on the influence of various synthesis conditions, starting materials and size and shape etc on the magnetic nature of such nano systems using state of art analytical tools [2]. Recently many studies are being carried on the usefulness of spinel magnetic nano systems in biomedical applications [3]. Nickel ferrite nano systems is one of the important groups of particles that has potential applications in biomedical field, especially in hyperthermia applications [3]. They are less toxic and chemically stable, compared to pure nickel, and appears to be a viable alternative for pure nickel in biomedical applications. In the present work, we have tried to synthesis nickel ferrite nanoparticles by spray pyrolysis of eco-friendly polymer precursor -polyvinyl alcohol (PVA). We have synthesized nickel ferrite nanosystems using a low-cost spray pyrolysis unit in which polymer precursor-mixture of metal nitrates and PVA dissolved in de-ionised water-sprayed over a hot glass plate kept at fixed temperature.

2. Material and methods

Nickel ferrites nanoparticles were synthesized by spray pyrolysis method. All the reagents used for the synthesis of nickel ferrite nanoparticles were analytical grade. The stoichiometric amounts of nickel nitrate ($Ni(NO_3)_2.6H_2O$) and ferric nitrate ($Fe(NO_3)_3.9H_2O$) were dissolved in deionized water

International Journal of
Scientific Research in Science and Technology (IJSRST)
Print ISSN : 2395-6011, Online ISSN : 2395-602X
International Conference on Advanced Materials
Held on 14, 15 December 2017, Organized by Department of Physics,
St. Joseph's College, Trichy, Tamilnadu, India

under magnetic stirring. The raw materials were mixed with aqueous solution of PVA. The resulting viscous solution of PVA metal nitrates is sprayed on a glass plate in the spray pyrolysis unit. The glass substrate slowly cooled and peal out sample from the substrate. The sample is annealed at 450,500,550,600^{0}C to obtain the single-phase spinel nickel ferrite nanoparticles and is named as NP1-NP4.

The crystallinity, phase structure and nano-behavior of the samples were characterized by X-ray diffraction (XRD). One of the samples is selected for further characterisation studies like High ResolutionTransmission electron microscopy (HRTEM), Fourier transform infrared spectroscopy (FT-IR), Energy dispersive electron spectroscopy (EDS), vibrating sample magnetometer (VSM) and Mossbauer techniques.

3. Results and Discussion

3.1. X-ray diffraction (XRD) analysis

X-ray patterns of samples are shown in Figure 1. The dominant peaks observed at 2θ = 30.298^0, 35.69^0, 37.48^0, 43.38^0, 53.99^0, 57.38^0, 63.02^0 and 75.45^0 corresponds to (220), (311), (222), (400), (422), (511), (440) and (533) planes of $NiFe_2O_4$ agrees well with a cubic spinel structure (JCPDS PDF card No: # 86-2267, $Fd\bar{3}m$ space group). The patterns confirm the formation of single phase cubic spinel ultrafine nickel ferrite nanoparticles. The broadening of diffraction peaks indicates samples are in nano regime. As the annealing temperature increases the intensity of diffraction peaks increases, especially for (311) peak, demonstrating the improvement of crystallinity of the sample. The average crystallite size of the nano crystallite sample is determined from the full width at half maximum (FWHM) of the XRD patterns using Scherrer's equation.

$$\text{Dhkl} = \frac{0.9\lambda}{\beta\cos\theta} \qquad (1)$$

where, 'D_{hkl}' is thecrystallite size, 'λ' is the wave length of the used X-ray (λ = 0.15406nm), 'β' is the full width at half maximum (FWHM) in radian and 'θ' is the half diffraction angle in degree. The average crystallite sizes have been estimated and found to increase with the increasing annealing temperature. This may be due to the coalescence of the particles by solid-state diffusion where the system reduces its free energy by reducing the surface area of the nanoparticles [4]. The lattice parameter 'a' of the samples were calculated by using the Bragg's equation,

$$\text{a} = d\sqrt{h^2+k^2+l^2} \qquad (2)$$

where 'h', 'k', 'l' are the Miller indices of the crystal planes and 'd' is the inter planer spacing.

The X-ray density of the samples are calculated using the formula,

$$\rho_x = \frac{8M}{Na^3} \qquad (3)$$

where 8 is the number of molecules per unit cell of spinel lattice, 'M' is the molecular weight, 'N' is Avogadro's number and 'a' is the lattice parameter. The average crystallite size, lattice parameter, and X-ray density of all the samples are calculated and the value obtained for NP3 is in good agreement with the reported value of 8.33 Å (Table1) [2]. The increases of lattice constant values from 8.32 to 8.34 Å with the temperature is because of the expansion of the particle volume with temperature. Thelattice parameter and crystallite size growth as functions of temperature are plotted in Figure 2.

International Journal of
Scientific Research in Science and Technology (IJSRST)
Print ISSN : 2395-6011, Online ISSN : 2395-602X
International Conference on Advanced Materials
Held on 14, 15 December 2017, Organized by Department of Physics,
St. Joseph's College, Trichy, Tamilnadu, India

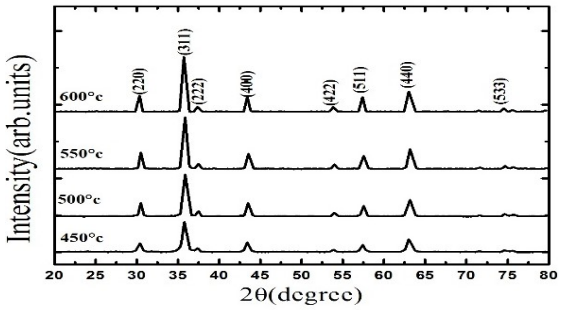

Figure 1. XRD patterns of $NiFe_2O_4$ nanoparticle annealed at different temperatures

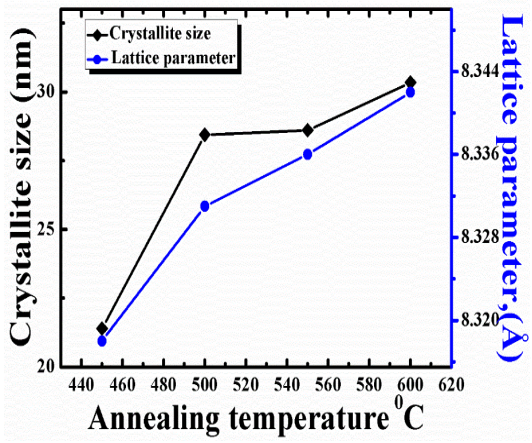

Figure 2. The lattice parameter and crystallite size growth as functions of annealing temperature

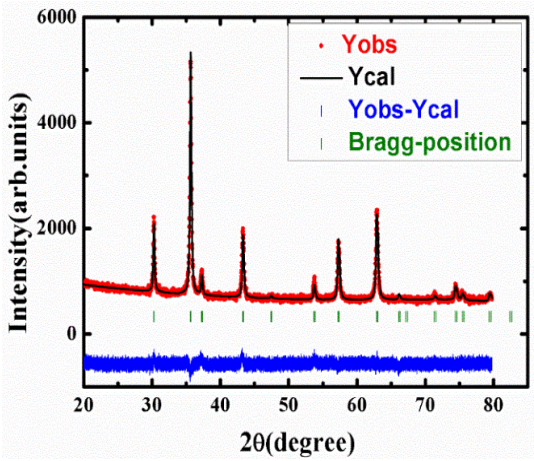

Figure 3. Rietveld refined x-ray diffraction pattern of the sample NP3

The lattice constant calculated for sample NP3 matches well with values reported in literature [2] and therefore selected for further characterisation studies using advanced techniques. The accurate knowledge of cation distribution over the crystallographic sites is significant in the determination of the physical properties of the synthesized sample. It can be estimated from the Rietveld refinement of X-ray diffraction pattern by using Full-Prof programme and the refined pattern of the sample NP3 is shown in Figure 3. Here, the red dots represent the experimental data, and calculated intensities are shown as black solid line. The bottom blue line represents the difference between the measured and the calculated intensities. The allowed Braggs positions for $Fd\bar{3}m$ space group are marked as verticallines. The pattern confirms the formation of single phase cubic spinel structure without any signature of secondary phase. The refined parameters of sample NP3 are summarized in Table 1. The lattice parameter obtained from the Rietveld refinement is perfectly matches with the experimental results obtained from XRD pattern (table 1). The R_p factor is found to be large [5]. It could be due to the low signal to noise ratio of XRD patterns for nanocrystalline materials. However, the low value of χ^2 justifies the goodness of refinement. The estimated cation distribution from the Rietveld analysis for sample NP3 is given in Table 1, which reveals that the sample have mixed spinel structure.

Table 1. Parameters estimated from XRD of $NiFe_2O_4$ nanoparticle annealed at different temperatures andRietveld refinement parameters & Cation distribution of the sample NP3

International Journal of
Scientific Research in Science and Technology (IJSRST)
Print ISSN : 2395-6011, Online ISSN : 2395-602X
International Conference on Advanced Materials
Held on 14, 15 December 2017, Organized by Department of Physics,
St. Joseph's College, Trichy, Tamilnadu, India

Sample code	Crystallite size from XRD, D_{XRD} (nm)	Lattice parameter, a (Å)	X-ray density (gm/cm^3)	Crystal system	Space group	R_p	χ^2	a = b = c (Å)	Cation distribution
NP1	21.40	8.318	5.39	-	-	-	-	-	-
NP2	28.44	8.331	5.42	-	-	-	-	-	-
NP3	28.61	8.336	5.43	Cubic	$Fd\bar{3}m$	33.8	1.36	8.335	$(Ni_{0.11}Fe_{0.89})A$ $[Ni_{0.89}Fe_{1.11}]^B O_4$
NP4	30.34	8.342	5.38	-	-	-	-	-	-

3.2. HRTEM studies

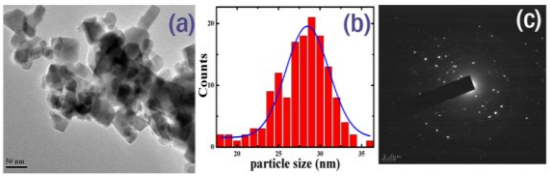

Figure 4. (a) HRTEM image, (b) particle size distribution and (c) SAED pattern of the sample NP3

The morphology and particle size distribution of the sample NP3 is investigated by using HRTEM. HRTEM micrographs demonstrates ultrafine particles having cubic morphology and average particle size obtained from HRTEM is 28.49 nm which is in good agreement with particle sizes estimated from XRD. The broken rings in the SAED pattern reveal polycrystalline nature of the sample. The particle sizedistribution can be well fitted to lognormal distribution and is given in figure 4.

3.3. FTIR Analysis

FTIR spectra of the sample NP3 is shown in the figure 5. The spectra show two main absorption bands v_1 and v_2 in the range of 400 cm^{-1} to 1000 cm^{-1} as a common feature of all spinel structures. The higher band, v_1 observed around in the frequency range 550-600 cm^{-1} is attributed to the intrinsic metal oxygen stretching vibrations at the tetrahedral site whereas, the v_2 lowest band is usually observed around in the frequency range 450-500 cm^{-1}, is assigned to octahedral metal oxygen stretching vibrations [6], which confirms the formation of spinel cubic ferrites nanoparticles. There are two bands at 551 and 594 cm^{-1} (v_1). These are the sub-bands of tetrahedral A-site. The splitting of tetrahedral band shows that some of the Ni^{+2}ions are shifted from octahedral site to tetrahedral site [7]. The cation distribution deduced from the Rietveld refinement of the sample NP3 confirm some fraction Ni^{+2} ions present in the tetrahedral sites (A-sites). Accordingly, the weak band at v_1 = 594 cm^{-1} could be attributed to the vibration of Ni^{2+} - O^{2-} in tetrahedral sites. FTIR spectra confirm the inverse spinel structure of the synthesized sample.

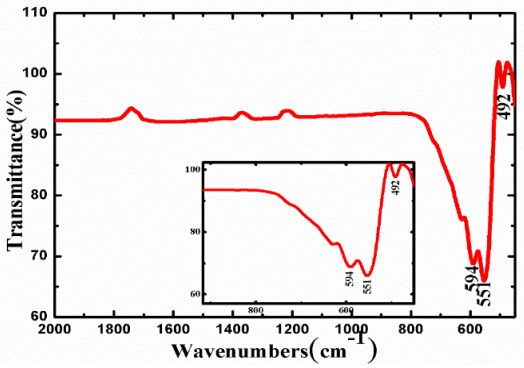

Figure 5. FT-IR spectrum of the sample NP3

3.4. EDS Analysis

The Energy Dispersive X-ray Spectroscopy analysis (EDS) was done to determine the chemical composition of the sample and confirmed stoichiometry of the investigated sample. EDS patterns of the sample is shown in figure 6 and the

International Journal of
Scientific Research in Science and Technology (IJSRST)
Print ISSN : 2395-6011, Online ISSN : 2395-602X
International Conference on Advanced Materials
Held on 14, 15 December 2017, Organized by Department of Physics,
St. Joseph's College, Trichy, Tamilnadu, India

atomic weight percentage of various cations in the investigated sample is given in table 2. There is no trace of any impurity was found which indicates purity of the sample.

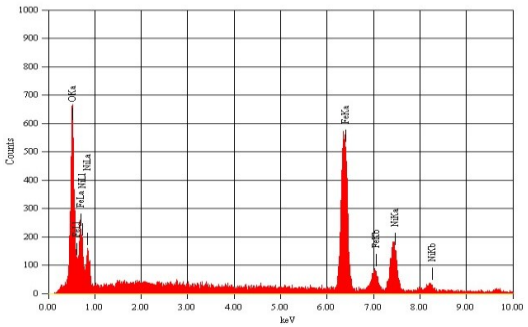

Figure 6. EDS spectrum of sample NP3

Table 2. Parameters obtained from of EDS spectrum of sample NP3

Element	(keV)	Mass%	Atom%	K
O K	0.525	36.79	67.35	46.31
Fe K	6.398	43.55	22.84	32.71
Ni K	7.471	19.67	9.81	13.58
Total		100	100	

3.5. Magnetic Studies

The room-temperature magnetization measurement of the sample up to maximum applied field of ± 15kOe is performed using a vibrating sample magnetometer (VSM). Hysteresis curve (M-H) curve of the sample is shown in the figure 7. The various magnetic properties like saturation magnetization (M_s), remanent magnetization (M_R), squareness ratio (S) and coercivity (H_c) are estimated from the M-H curve. The M-H curve with small value of coercivity reflects soft ferrimagnetic nature of the sample. The parameters obtained from hysteresis curve are listed in the Table 3.

The saturation maximum magnetization of the sample was found to be 42.35 emu/g, which is about 15% smaller than the saturation magnetization of 50 emu/g of bulk $NiFe_2O_4$ samples [8]. This reduced value of saturation magnetization with grain size reduction is explained in terms of the core shell structure of magnetic nanoparticles having spin glass like magnetically dead surface layer, where a ferrimagnetic core is surrounded by a surface layer of canted spins (existence of random canting of particle surface spins). According to Chen et al. [9], the thickness of dead layer is deduced from the equation

$$t = \frac{D}{6}\left(1 - \frac{M_s(nano)}{M_s(bulk)}\right) \qquad (4)$$

Here 'D' is the particle size obtained from lognormal distribution of HRTEM, M_s(nano) saturation of magnetization values of the samples, and the values of the M_s(bulk) were taken from Maensiri et al. [8]. The estimated value of the dead layer thickness 't' is listed in the table 3. The existence of the nonmagnetic dead layer might be caused by the canting of the surface spins or loss of the long-range order in the surface layer.

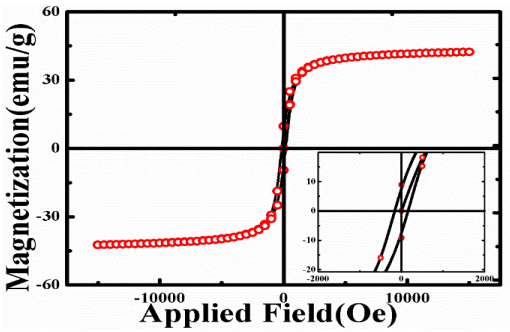

Figure 7. Room temperature magnetic hysteresis of the sample NP3 and portion near the origin is given in insight

Table 3. Magnetic parameters obtained from M-H curve, dead layer thickness (t), Yafet-Kittel angle (θ_{YK}), magnetic moment (μ_B) of the sample NP3

Sample code	Crystallite size (nm)	Hc (Oe)	Ms (emu/g)	Mr (emu/g)	Mr/Ms	t (nm)	θ_{YK}	μ_B
NP3	28.6	162.05	42.35	6.74	0.159	0.73	24.71	1.77

The observed reduction in Ms in the NP3 may be explained on the basis of Neel's theory of ferrimagnetism. According to Neel's theory, three

International Journal of
Scientific Research in Science and Technology (IJSRST)
Print ISSN : 2395-6011, Online ISSN : 2395-602X
International Conference on Advanced Materials
Held on 14, 15 December 2017, Organized by Department of Physics,
St. Joseph's College, Trichy, Tamilnadu, India

kinds of exchange interaction exist in ferrites: interaction between magnetic ions in tetrahedral (A) and octahedral (B) sites (A-B interaction), interaction between the magnetic ions in octahedral (B) sites (B-B interaction) and interaction between the magnetic ions in tetrahedral (A) site (A-A interaction). But A-B interaction is very strong compared with A-A and B-B. According to Neel's theory magnetic moment per formula unit is given by,

$$\mu_{TH} = M_B - M_A \qquad (5)$$

where M_B and M_A represent the magnetic moment of ions in the octahedral and tetrahedral sites respectively. The net moments are determined according to the cations distribution estimated from the Rietveld refinement by assuming the magnetic moment of Fe^{3+} ion is 5 μ_B and that of Ni^{2+} ion is 1.7 μ_B. The total magnetic moments of ions present in the A site is much less than that of B site. This strengthens B-B interaction compared with A-B interaction and the collinear spin arrangement of B sub lattice gets disturbed. This suggests that canting angle is established and it can be explained by Yafet-Kittel sub lattice model [10][11]. According to Yafet-Kittel (Y-K) model, the canting angle (θ_{YK}) was calculated from the following equation,

$$\theta_{YK} = \frac{\cos^{-1}(M_A + \mu_B)}{M_B} \qquad (6)$$

where μ_B is the experimental magnetic moment per formula unit in Bohr magnetron (μ_B) of the sample and it is calculated from the equation,

$$\mu_B = \frac{Molecular\ weight \times M_s}{5585} \qquad (7)$$

The Y-K angles (θ_{YK}) are determined from the experimental magnetic moment (in Bohr magneton) estimated from the proposed cation distribution based on the Rietveld refinement. The estimated values of experimental magnetic moment (μ_B) and Yafet-Kittel (θ_{YK}) angle is given in the table 3. Y-K angles support the non-collinear spin structure in the B sub lattice and hence reduction in saturation magnetization value observed in the sample NP3.

3.6. Mossbauer Studies

Mossbauer spectra of the sample NP3 is shown in the figure 8. Mossbauer measurements were done at room temperature for exploring the magnetic nature prevailing at the cation sites. The Mossbauer spectrum was fit with NORMOS–SITE program and results obtained for the hyperfine parameters, which are the full width at half maxima (FWHM), isomer shift (IS), quadrupole splitting (QS) and the magnetic hyperfine field (BHF) are listed in the table 4. We could fit double sextet pattern in the room temperature spectrum, corresponding to Fe^{3+} ions at the A sites and B sites of the spinel structure, respectively. The hyperfine field calculated for the A and B sites are 48.9 T and 51.13T [12]. This is in good agreement with values reported for nano nickel ferrites in literature. Further, area under sextets pattern indicating Fe^{3+} ions in both sites equally contributing to the ferrimagnetic nature of the sample. Using fractional area of each sub spectrum, the Fe^{3+} ion ratio in both octahedral (B) and tetrahedral (A) site was calculated.The degree of inversion can be obtained from the equation

$$\frac{Area(A-site)}{Area(B-site)} = \frac{f_A}{f_B}\frac{x}{(2-x)} \qquad (8)$$

here $\frac{f_A}{f_B}$ is the ratio of the recoilless fractions equivalent to 0.94 at room temperature, x is the amount of Fe^{3+} ions present in the A-site and (2 – x) is the amount present in B-site. The estimated cations distribution for the samples is listed in table 4. It should be noted that the estimated cations distribution is well matches with that obtained from the Rietveld refined x-ray diffraction pattern (Table1).

International Journal of
Scientific Research in Science and Technology (IJSRST)
Print ISSN : 2395-6011, Online ISSN : 2395-602X
International Conference on Advanced Materials
Held on 14, 15 December 2017, Organized by Department of Physics,
St. Joseph's College, Trichy, Tamilnadu, India

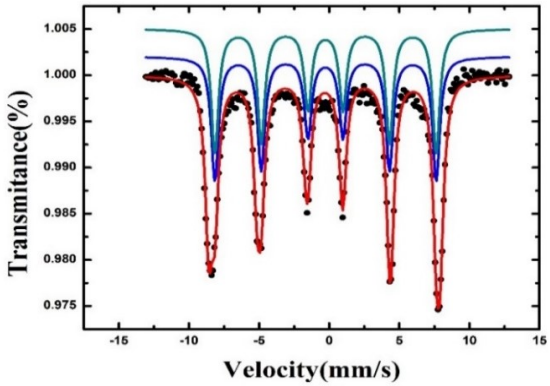

Figure 8. Mossbauer spectrum of the sample NP3

Table 4. Hyperfine parameters and cation distribution from Mossbauer spectra analysis of the sample NP3

	Site	FWHM Γ (mm/s)	Isomer Shift δ (mm/s)	quadrupole shift (mm/s)	Hyperfine field (Tesla)	% Area	Cation distribution
NP3	B-site	0.62	0.26	0.012	48.91	51.05	$[Ni_{0.89}Fe_{1.11}]^{B}O_4$
	A-site	0.62	0.35	0.023	51.13	48.95	$(Ni_{0.11}Fe_{0.89})^{A}$

4. Conclusion

Nickel ferrite nano-powders were successfully synthesized by a simple spray pyrolysis method – a low cost, low temperature high yield process. The effects of annealing on the structural properties of the samples are studied by XRD. The crystallite size of the samples increases with annealing. HRTEM micrograph confirmed ultrafine particles with cubic shape. Two strong absorption bands at v_1 and v_2 in the FTIR spectrum confirm spinel structure of the sample. The weak band at the tetrahedral site in the FTIR spectrum shows the mixed spinel structure of nickel ferrite nanoparticles. The magnetic parameters, determined from room temperature VSM, are in conformity with that of soft ferrimagnetic nature of the prepared sample. The same has been confirmed from room temperature Mossbauer studies of the sample. Further, the cation distribution obtained from the Mossbauer studies matches well with that obtained from theRietveld refinement of XDR pattern, thereby confirming the mixed spinel structure in the nickel ferrite nanoparticles.

References

[1] Y. Yang et al., "Synthesis of nonstoichiometric zinc ferrite nanoparticles with extraordinary room temperature magnetism and their diverse applications," J. Mater. Chem. C, vol. 1, no. 16, p. 2875, 2013.

[2] Z. Karcıoğlu Karakaş, R. Boncukcuoğlu, İ.H. Karakaş, and M. Ertuğrul, "The effects of heat treatment on the synthesis of nickel ferrite ($NiFe_2O_4$) nanoparticles using the microwave assisted combustion method," J. Magn. Magn. Mater., vol. 374, pp. 298–306, 2015.

[3] X. Lasheras et al., Chemical Synthesis and

Magnetic Properties of Monodisperse Nickel Ferrite Nanoparticles for Biomedical Applications, vol. 120, no. 6. 2016.

[4] A. Jafari, S. Farjami Shayesteh, M. Salouti, and K. Boustani, "Effect of annealing temperature on magnetic phase transition in Fe_3O_4 nanoparticles," J. Magn. Magn. Mater., vol. 379, no. December, pp. 305–312, 2015.

[5] L. Kumar, P. Kumar, and M. Kar, "Cation distribution by Rietveld technique and magnetocrystalline anisotropy of Zn substituted nanocrystalline cobalt ferrite," J. Alloys Compd., vol. 551, no. February, pp. 72–81, 2013.

[6] R.D. WALDRON, "Infrared spectra of Ferrites," Phys. Rev., vol. 99, no. 6, pp. 1727–1734, 1955.

[7] S.A. Mazen, "Tetravalent ions substitution in Cu-ferrite; structure formation and electrical properties," Mater. Chem. Phys., vol. 62, no. 2, pp. 131–138, 2000.

[8] S. Maensiri, C. Masingboon, B. Boonchom, and S. Seraphin, "A simple route to synthesize nickel ferrite (NiFe2O4) nanoparticles using egg white," Scr. Mater., vol. 56, no. 9, pp. 797–800, 2007.

[9] J. Chen, C. Sorensen, K. Klabunde, G. Hadjipanayis, E. Devlin, and A. Kostikas, "Size-dependent magnetic properties of $MnFe_2O_4$ fine particles synthesized by coprecipitation," Phys. Rev. B, vol. 54, no. 13, pp. 9288–9296, 1996.

[10] H.M. El-Sayed, I.A. Ali, A. Azzam, and A.A. Sattar, "Influence of the magnetic dead layer thickness of Mg-Zn ferrites nanoparticle on their magnetic properties," J. Magn. Magn. Mater., vol. 424, pp. 226–232, 2017.

[11] Y. Yafet and C. Kittel, "Antiferromagnetic Arrangements in Ferrites," Phys. Rev., vol. 87, no. 2, pp. 290–294, 1952.

[12] V. Šepelák et al., "Nanocrystalline nickel ferrite, $NiFe_2O_4$: Mechanosynthesis, nonequilibrium cation distribution, canted spin arrangement, and magnetic behavior," J. Phys. Chem. C, vol. 111, no. 13, pp. 5026–5033, 2007.

International Journal of
Scientific Research in Science and Technology (IJSRST)
Print ISSN : 2395-6011, Online ISSN : 2395-602X
International Conference on Advanced Materials
Held on 14, 15 December 2017, Organized by Department of Physics,
St. Joseph's College, Trichy, Tamilnadu, India

Effect of Mg Substitution on the Structural, Magnetic and Hyperfine Properties of $ZnFe_2O_4$ Nanopowders Synthesized by Spray Pyrolysis Method

Subin P. John, Jacob Mathew*
Mossbauer Research group, St. Berchmans Autonomous College, Kerala, India.
*Corresponding author: e-mail- jacob.chrisdale@gmail.com

Abstract

$Mg_xZn_{1-x}Fe_2O_4$ nanoparticles were synthesized by spray pyrolysis method using polymer precursor and characterized their structural, magnetic and hyperfine properties as a function of magnesium concentration. X-ray diffraction revealed cubic spinel structure of the prepared samples and structural refinement was done by Rietveld method. Cation distribution obtained from the Rietveld method reflected migration of cations among the interstitial sites. Fourier transform infrared spectroscopy confirmed the formation of spinel structure of the nanoparticles and shift of band center with magnesium doping due to cation migration was observed. Saturation magnetization increased with magnesium concentration due to enhancement in A-B superexchange interaction and coercivity varied in accordance with Brown's relation. The curve fitting of the magnetization data revealed coexistence of superparamgnetic, paramagnetic and ferromagnetic phases in the prepared nanoparticles. Mossbauer spectroscopy, a technique with different operating time scale than that of vibration sample magnetometer, indicated incomplete magnetic ordering and strongly confirmed the enhancement of A-B interaction with magnesium concentration. The Mossbauer studies further confirmed the coexistence of different magnetic phases in the sample.

Keywords: Mg-Zn nanoferrites, Cation migration, A-B super exchange interaction, Superparamagnetism, Coexistence of magnetic phases, Mossbauer spectroscopy

1. Introduction

Ferrites have wide range of technological applications owing to their unique electric and magnetic properties in the fields of high-frequency devices, magnetic fluids, microwaves, magnetic data storage, biomedical applications, magnetic resonance imaging and gas sensors. Ferrites in nanoscale exhibit improved physical, chemical and magnetic properties and are recently used for developing nanosized devices in biomedical field [1,2]. The cubic spinel ferrite with general formula $MeFe_2O_4$ (Me = Fe, Co, Ni, Mn, Mg, Zn...) belongs to space group $Fd\bar{3}m$. Unit cell of spinel ferrites has eight molecules of $MeFe_2O_4$ and oxygen ions forms a face centered cubic (f c c) lattice. In this structure two kinds of interstitial sites occur, the tetrahedral (A) and octahedral (B) sites which are surrounded by four and six oxygen ions respectively [3].

Superparamagnetic (SPM) nanoparticles–a new genre of magnetic particles-have recently shown rapid advance in the field of magnetic hyperthermia because of high level of heat generation, non-retainment of magnetization after the removal of applied magnetic field, easy targeting, suitability for human body magnetic fields and easy circulation through capillaries without agglomeration. Among many nanospinel ferrites that exhibit SPM properties and having potential for application in magnetic hyperthermia, Mg-Zn ferrite turns out to be a promising candidate due to their inhibitory nature on cancer cell growth. Moreover the Mg-Zn ferrites have the capability of fine tuning its magnetic properties to desirable values by controlling the doping concentrations of cations [4]. Doping of Mg^{2+} in zinc ferrite, can

International Journal of
Scientific Research in Science and Technology (IJSRST)
Print ISSN : 2395-6011, Online ISSN : 2395-602X
International Conference on Advanced Materials
Held on 14, 15 December 2017, Organized by Department of Physics,
St. Joseph's College, Trichy, Tamilnadu, India

induce hopping of ions between the tetrahedral and octahedral sites. As the ions at the A and B sites greatly control the properties of ferrites, the gradual substitution of Mg^{2+} can vary the structural and magnetic properties to desired values. In this paper, we report the cost effective synthesis of Mg-Zn ferrite nanoparticles by polymer assisted spray pyrolysis method and the effect of magnesium substitution on structural and magnetic properties of zinc ferrite. We investigated the magnetic and hyperfine properties using vibration sample magnetometer and Mossbauer spectroscopy having different operating time scales and the analysis observed a coexistence of superparamagnetic, ferrimagnetic and paramagnetic phases in the prepared Mg-Zn ferrite nanoparticles.

2. Experimental

Magnesium doped zinc ferrite nanoparticles with formula $Mg_xZn_{1-x}Fe_2O_4$ (where x = 0.1, 0.2, 0.3, 0.4 and 0.5) were synthesized by spray pyrolysis method. The starting materials: magnesium nitrate ($Mg(NO_3)_2 6H_2O$, Merck GR), zinc nitrate ($Zn(NO_3)_2.6H_2O$, Merck LR) and ferric nitrate ($Fe(NO_3)_3.6H_2O$, Himedia AR) were dissolved in double distilled water in accordance with doping concentrations. These nitrate solutions were added to 2 wt% polyvinyl alcohol (PVA, Loba Chemie, LR) and stirred continuously until the solution became homogenous. The solution was transferred to a spray gun and sprayed to a glass plate in spray pyrolysis unit kept at 130˚C. When sprayed solution became a geliish layer, the glass plate was taken out and cooled. Sample layer on the glass plate was peeled off and calcinated at 450˚C to obtain magnesium zinc ferrite nanoparticles.

The x-ray diffraction (XRD) analysis of the samples was done with PANlytical X'Pert-PRO X-ray diffractometer using Cu-Kα radiations (λ = 1.54060 Å). The morphological analysis was done by transmission electron microscopy (TEM) (Jeol/JEM 2100) operated at 200 kV. Fourier transform infrared spectroscopy (FTIR) of the samples was recorded using Thermo Nicolet, Avatar 370 spectrometer in the range 400-4000 cm^{-1} at a resolution of 4 cm^{-1}. The variation of magnetization with applied magnetic field in the range 0 - 15,000 Oe at room temperature was studied using a Lakeshore 7410 vibration sample magnetometer (VSM). Fe^{57} Mossbauer measurements were carried out at room temperature in transmission mode with a $^{57}Co/Rh$ radioactive source in constant acceleration mode using a standard personal computer based Mossbauer spectrometer.

3. Results and Discussion

3.1. X-ray diffraction studies

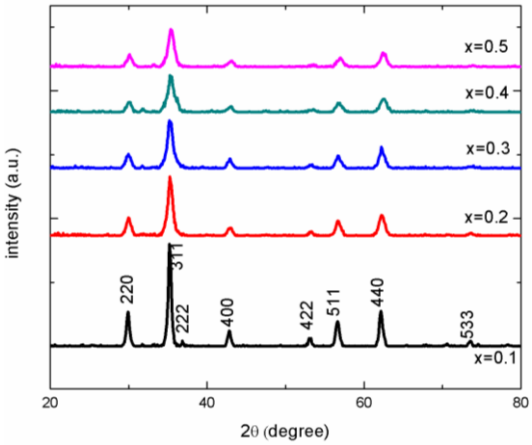

Figure 1. XRD patterns of $Mg_xZn_{1-x}Fe_2O_4$ nanoparticles

The structural analysis of $Mg_xZn_{1-x}Fe_2O_4$ (x = 0.1, 0.2, 0. 3, 0.4 and 0.5) nanoparticles was performed using x-ray diffraction technique. The XRD patterns are shown in Figure 1 were indexed by Bragg law. The presence of (220), (311), (222), (400), (422), (511) and (440) planes with most intense (311) reflection in the XRD pattern revealed the face centered cubic spinel structure of the samples. It is also evident from the Figure 1 that all the peaks are intense and broadening of the peaks are attributed to nonideal Bragg reflection occurring in nanoparticles. Structural refinement of the nanoferrites was done by Rietveld method using FULLPROFF program and refinement pattern is shown in Figure 2. The refinement was started using the space group $Fd\bar{3}m$ in which the oxygen anions occupy wyckoff

International Journal of
Scientific Research in Science and Technology (IJSRST)
Print ISSN : 2395-6011, Online ISSN : 2395-602X
International Conference on Advanced Materials
Held on 14, 15 December 2017, Organized by Department of Physics,
St. Joseph's College, Trichy, Tamilnadu, India

position 32e with coordinates (0.25, 0.25, 0.25), tetrahedral sites at 8f with coordinates (0.125, 0.125, 0.125) and octahedral sites occupy 16c positions with coordinates (0.5, 0.5, 0.5). The Rietveld method was performed refining scale coefficient, background, instrumental parameters, cell parameters, full width half maximum (FWHM) parameters, isothermal parameters, atomic positions, occupancy and shape parameters in sequence mode. The background was modeled with six coefficient polynomial function and the experimental profile with Thompson-Cox-Hastings pseudo-Voight function [5]. The cation distribution of the samples by the Rietveld refinement is shown in Table 1, where the ions on the tetrahedral sites are given in front of the square brackets and the octahedral ions between the brackets. Also the lattice constant and the oxygen position parameter obtained from the Rietveld method is listed in Table 2. The crystallite size was determined using Scherrer equation. The x-ray density defined as the weight of atoms in unit cell per volume of unit cell were calculated by the formula

$$D_x = \frac{8M}{Na^3} \qquad \ldots (1)$$

where N is Avagadro's number (= 6.0225 x 10^{23} atom/mole), M is the molecular weight of the sample, 'a' is the lattice constant and the factor '8' represents number of molecules in the unit cell. We have, further, calculated lattice strain using the modified Williamson and Hall equation

$$\eta = \frac{2d|K-1|}{D} \qquad \ldots (2)$$

where d is the lattice spacing for (311) planes, K(0.89) is the shape factor and D is the average crystallite size [6]. The variation of lattice constant and x-ray density is shown in Figure 2.

The crystallite size obtained from Scherrer formula lies in the range 10.28-16.83 nm, indicating that the prepared samples are in the nano reigm and Mg doping in zinc ferrite has not considerable size effect. Zinc ferrite has a normal spinel structure in which Zn^{2+} and Fe^{3+} ions occupying tetrahedral (A) and octahedral (B) sites respectively [7]. When Mg^{2+} ions, a B site specific diamagnetic cation was doped in zinc ferrite, it might initiate migration of Fe^{3+} ions to A sites. This is possible since number of A site vacancies are enhanced due to reduction in A site specific zinc cations [8]. From the Table 1, although Mg^{2+} and Zn^{2+} have strong preferences to octahedral and tetrahedral sites respectively, they occupy the other sites in small amount. The Fe^{3+} ions migrate from octahedral to tetrahedral site with the increase of magnesium concentration. The lattice constant decreased with magnesium concentration owing to replacement of cations with larger ionic radius (Zn = 0.82 Å) by cation with smaller ionic radius in accordance with Vegard's law [9]. Even though lattice constant decreased with magnesium concentration, the x-ray density also followed same trend and this is due to the fact that reduction in molecular weight is greater than the decrease of volume of unit cell (Figure 3) [10].

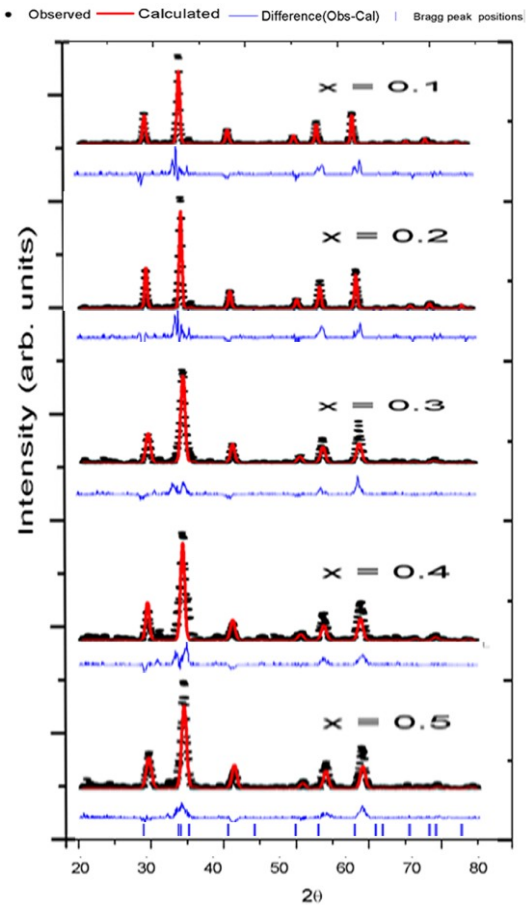

International Journal of
Scientific Research in Science and Technology (IJSRST)
Print ISSN : 2395-6011, Online ISSN : 2395-602X
International Conference on Advanced Materials
Held on 14, 15 December 2017, Organized by Department of Physics,
St. Joseph's College, Trichy, Tamilnadu, India

Figure 2. Rietveld refined XRD patterns of $Mg_xZn_{1-x}Fe_2O_4$ nanoferrites

Table 1. Cation distribution of the nanoferrites

Chemical Formula	Cation Distribution
$Mg_{0.1}Zn_{0.9}Fe_2O_4$	$Mg_{0.02}Zn_{0.77}Fe_{0.01}[Mg_{0.08}Zn_{0.13}Fe_{1.99}]O_4$
$Mg_{0.2}Zn_{0.8}Fe_2O_4$	$Mg_{0.06}Zn_{0.67}Fe_{0.06}[Mg_{0.14}Zn_{0.13}Fe_{1.94}]O_4$
$Mg_{0.3}Zn_{0.7}Fe_2O_4$	$Mg_{0.09}Zn_{0.65}Fe_{0.04}[Mg_{0.21}Zn_{0.05}Fe_{1.96}]O_4$
$Mg_{0.4}Zn_{0.6}Fe_2O_4$	$Mg_{0.12}Zn_{0.48}Fe_{0.12}[Mg_{0.28}Zn_{0.12}Fe_{1.88}]O_4$
$Mg_{0.5}Zn_{0.5}Fe_2O_4$	$Mg_{0.17}Zn_{0.45}Fe_{0.19}[Mg_{0.33}Zn_{0.05}Fe_{1.81}]O_4$

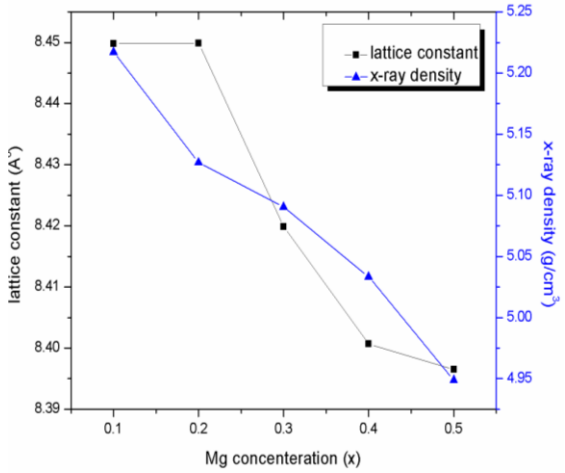

Figure 3. Lattice parameter and x-ray density as a function of Mg content in $Mg_xZn_{1-x}Fe_2O_4$ system

Table 2. Structural parameters of $Mg_xZn_{1-x}Fe_2O_4$ system

Magnesium Concentration (x)	Crystallite Size (nm)	Strain (η)	Lattice Constant (Å)	Oxygen Parmeter (u)	x-ray density (g/cm^3)
0.1	16.8384	0.0024	8.4498	0.2539	5.2173
0.2	12.803	0.0044	8.4499	0.2545	5.1269
0.3	13.7566	0.0044	8.4199	0.25635	5.0905
0.4	10.2860	0.0070	8.4007	0.2600	5.0334
0.5	11.2249	0.0052	8.3965	0.2622	4.9489

3.2. Transmission Electron Microscopy Studies

The TEM image of $Mg_{0.5}Zn_{0.5}Fe_2O_4$ is shown in Figure 4 and the majority of particles have spherical morphology. The average particle size obtained was about 15 nm and particle size ranges from 9-19 nm as shown in the histogram. The TEM image of $Mg_{0.5}Zn_{0.5}Fe_2O_4$ is shown in Figure 4 and the majority of particles have spherical morphology. The average particle size obtained was about 15 nm and particle size ranges from 9-19 nm as shown in the histogram.The particle size distribution suggest a possibility of coexistence of small superparamagnetic particles and some bigger particles [11]. The particle size obtained from TEM is nearly equal to the cryatallite determined from Scherrer formula indictes that the entire particle is a single crystallite. The selected area electron diffraction (SAED) pattern emphasis on the polycrystalline nature of the sample[12]. Inter planar distance of (311) plane from TEM image (2.50 Å) is in good agreement with XRD data (2.53 Å). The slight agglomoration of the particles is due to magnetic nature of samples. [13, 14].

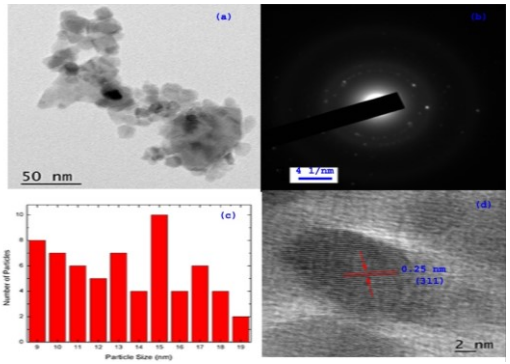

Figure 4. (a) TEM micrograph, (b) SAED pattern, (c) histogram of particle size and (d) interplanar spacing of $Mg_{0.5}Zn_{0.5}Fe_2O_4$ nanoparticles

3.3. Fourier transform infrared spectroscopy studies

FTIR spectra of the $Mg_xZn_{1-x}Fe_2O_4$ nanoparticles are presented in Figure 5. There exist two metal–oxygen bands in the FTIR spectra of spinel ferrites by the band vibration of metals at the tetrahedral and octahedral sites with the oxygen. The ν_1 band formed by the intrinsic stretching vibration of metal at tetrahedral sites with oxygen is observed in the range 500 - 600 $cm^{-1}$and the ν_2 band formed by the intrinsic stretching vibration of metal at

International Journal of
Scientific Research in Science and Technology (IJSRST)
Print ISSN : 2395-6011, Online ISSN : 2395-602X
International Conference on Advanced Materials
Held on 14, 15 December 2017, Organized by Department of Physics,
St. Joseph's College, Trichy, Tamilnadu, India

octahedral site is observed in the range 385- 430 cm^{-1}[15]. The centre of the ν_1 band shifted to higher wavenumber with magnesium concentration and the shift is because of the migration of Fe^{3+} ions from octahedral to tetrahedral sites replacing Zn^{2+} as in the Table 1. Since stretching wavenumber is inversely proportional to atomic weight, the increasing content of comparatively lighter Fe^{3+} at tetrahedral sites replacing Zn^{2+} may be attributed to shift in ν_1 band to higher values. As there is no splitting or shoulders in the ν_1 band, presence of Fe^{2+} at the A site can be ruled out[16]. Since the detection limit of FTIR instrument was above 400 cm^{-1}, the ν_2 band was not detected[17]. The bands at 1400-1700 and 2925-2810 cm^{-1} were assigned to carboxyl group (COO^-) and stretching of C-H bonds respectively. The broad band centered at 3430 cm^{-1} is attributed to hydrogen bonded O-H groups arising from surface hydroxyl groups on nanoparticles and adsorbed water [18].

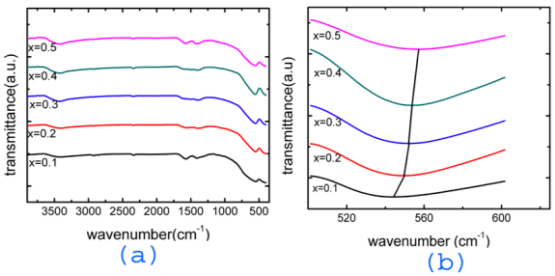

Figure 5. (a) FTIR spectra of $Mg_xZn_{1-x}Fe_2O_4$ nanoparticles and (b) enlarged ν_1 band

3.4. Magnetic Studies

Variation of magnetization of $Mg_xZn_{1-x}Fe_2O_4$ nanoparticles with applied field at room temperature measured by VSM is shown in Figure 6. Magnetic parameters: saturation magnetization (M_s), magnetic moment per formula unit (η_B), coercivity (H_c), retentivity (Mr) and squareness ratio (M_r / M_s) of the nanoparticles are tabulated in Table 3 and plotted in Fig 7. The magnetic moment per formula unit in Bohr magnetons is obtained from the equation,

$$\eta_B = \frac{MW \times M_s}{5585} \quad \ldots (4)$$

where MW is the molecular weight and M_s is the saturation magnetization in emu/g. The magnetocrystalline anisotropy constant (K_1) was estimated using Brown's relation

$$H_c = \frac{2K_1}{M_s} \quad \ldots (5)$$

where M_s is the saturation magnetization and H_c is the coercivity.

The saturation magnetization and moment per formula unit increased with magnesium concentration from 14.34 emu/g and 0.61 μ_B for x = 0.1 to 42.28 emu/g and 1.66 μ_B for x=0.5 respectively even though the particle size remained the same. This kind of magnetic behaviour may be attributed to controlled doping of site specific cations in the sample. The variation of magnetic parameters in different samples can be understood through either by size effect or by cation distribution. The kind of magnetization observed in our samples with almost uniform particle size as shown in Table 2, supports dominant role of cationic distributions in magnetization over size/surface effects [19]. It is reported that the magnetic behaviour in spinel ferrites depends on the distribution of cations at A and B sites, superexchange interaction and the non-collinear nature of moments at B site. There are three kind of superexchange interactions: intra A-A, B-B and inter sublattice A-B interactions, among which A-B superexchange interaction is the strongest [13]. According to Neel's two sublattice model of ferrimagnetism, the resultant magnetic moment per formula unit is given by

International Journal of
Scientific Research in Science and Technology (IJSRST)
Print ISSN : 2395-6011, Online ISSN : 2395-602X
International Conference on Advanced Materials
Held on 14, 15 December 2017, Organized by Department of Physics,
St. Joseph's College, Trichy, Tamilnadu, India

$$M(x) = M_B(x) - M_A(x) \quad \text{... (6)}$$

where M_B and M_A are the magnetic moments at B and A sites respectively in Bohr magnetons. The Neel's model is modified by Yaffet-Kittel (Y-K) model incorporating the subdivision of B-sublattice into two sublattices having magnetic moments equal in magnitude and each making angle α_{YK} with direction of net magnetization at 0 K. According to Y-K model, the resultant magnetization is expressed as

$$M(x) = M_B \cos\alpha_{YK} - M_A \quad \text{... (7)}$$

where angle α_{YK} can vary from 0° to 180°. The subdivision occurs when the B-B interaction becomes less stronger than the A-B interaction. In zinc ferrite, which is a normal spinel, the Zn^{2+} and Fe^{3+} ions occupy A and B sites respectively. In this system, Zn^{2+} in A site is diamagnetic, no magnetic moment is expected because the only interaction happening here is B-B superexchange interaction and the B site magnetic moments are antiparallel to each other. The enhancement of magnetization with doping of magnesium which is a B site specific cation is attributed to enhancement of A-B sub lattice interactions by the migration of Fe^{3+} ions from B to A site [20]. It seems that a threshold percentage of Mg is required for initiating the cation distribution in the lattice. All the magnetic parameters remain steady till x = 0.3 beyond which M_s and magnetic moment per formula unit values shoots up supporting Fe^{3+} ions migration from B site to A site and hence enhancing inter sub-lattice A-B superexchange interaction. The coercivity values decreased with magnesium concentration because of its inverse relation with saturation magnetization in accordance with Brown's relation.

In order to determine the magnetic components present in the prepared nanoparticles, M-H curves were fitted with different combinations of magnetic phases. For all the samples, the best fit was obtained for the combination of paramagnetic, superparamagnetic and ferromagnetic phases Fig 8 using the equation (8).

The first, second and third terms in the equation represents ferromagnetism, superparamagnetism and paramagnetism respectively, where M is the magnetization, M^S_F is the saturation magnetization of ferromagnetic component, H_c is the coercivity, S is the squareness ratio, M^s_{sp} is the saturation magnetization of the superparamagnetic component, μ is the magnetic moment per particle, H is the applied field, k is the Boltzmann constant, T is the temperature in Kelvin and χ is the paramagnetic susceptibility. The ferromagnetism in the nanoparticles is evolved from A-B superexchange interaction. The magnetic particles smaller than critical diameter exibit superparamagnetism and paramagnetism arise from the surface spin disorder of the nanoparticles. Thus, the fitting of the M-H data revealed coexistence of ferromagnetic, superparamagnetic and paramagnetic phases in the nanoparticles

$$M = \frac{2M_F^s}{\Pi}\tan^{-1}\left[\left(\frac{H \pm H_c}{H_c}\right)\tan\left(\frac{\Pi S}{2}\right)\right] + M_{sp}^s\left[\coth\left(\frac{\mu H}{kT}\right) - \left(\frac{\mu H}{kT}\right)^{-1}\right] + \chi H \quad \text{... (8)}$$

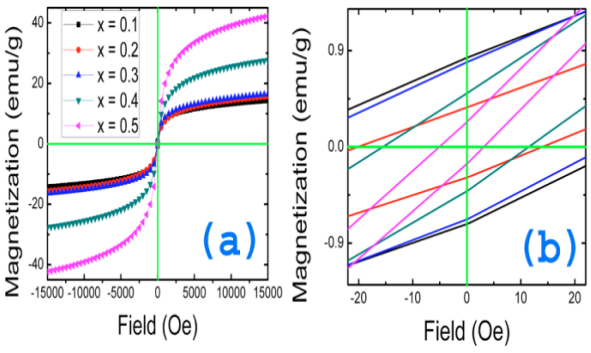

Figure 6. M versus H curves $Mg_xZn_{1-x}Fe_2O_4$ nanoparticles at room temperature. Inset shows magnificent of magnetic hysteresis at low fields

International Journal of
Scientific Research in Science and Technology (IJSRST)
Print ISSN : 2395-6011, Online ISSN : 2395-602X
International Conference on Advanced Materials
Held on 14, 15 December 2017, Organized by Department of Physics,
St. Joseph's College, Trichy, Tamilnadu, India

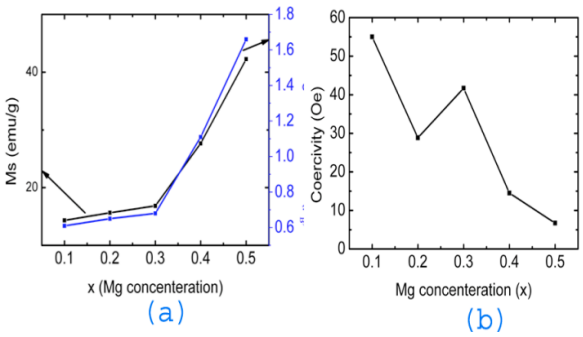

Figure7. Dependence of (a) saturation magnetization, magnetic moment and (b) coercivity

Table 3. Magnetic parameters of $Mg_xZn_{1-x}Fe_2O_4$ nanoparticles

Mg content (x)	Saturation Magnetization Ms (emu/g)	Coercivity H_c (Oe)	Retentivity Mr (emu/g)	magnetic moment (μ_B)	Squareness ratio (Mr/Ms)	Anisotropy Constant K1 (erg/cm^3)
0.1	14.34	55.010	0.7688	0.61	0.0536	2057.810
0.2	15.65	28.838	0.325	0.65	0.0208	1156.913
0.3	16.84	41.705	0.7300	0.68	0.0433	1787.558
0.4	27.66	14.497	0.4536	1.11	0.0164	1009.170
0.5	42.27	6.721	0.1865	1.66	0.0044	702.977

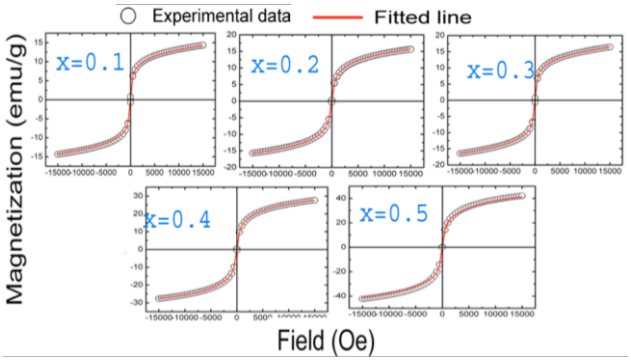

Figure 8. Fitting of M-H data of $Mg_xZn_{1-x}Fe_2O_4$ nanoparticles using eq.(8)

3.5. Mossbauer Spectra Analysis

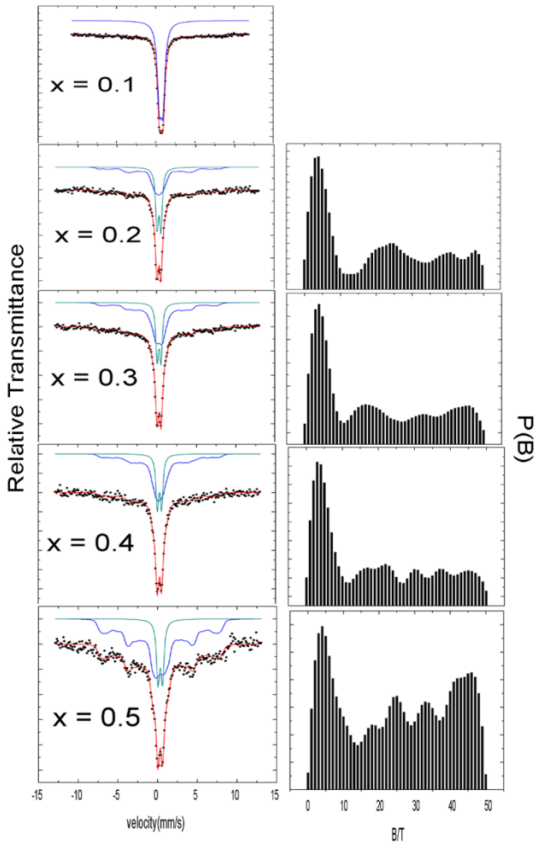

Figure 9. Room temperature Mossbauer spectra of $Mg_xZn_{1-x}Fe_2O_4$ samples with different Mg content. Black dots (•) are the experimental data, red lines represent the best fit, blue and green lines are the subspectra used for fitting. Corresponding distribution of hyperfine field P(Bhf) of respective fractions is given on the right side.

The Mossbauer spectra of the nanoparticles were recorded at room temperature and fitted with Normos/Site and Normos/Dist for discrete sites and distributions respectively. The sample with x = 0.1 is fitted with Normos/Site and others by Normos/Dist as shown in Figure9 along with their distribution of hyperfine fields. In the case of discrete fitting Lorentzian line shape is assumed in all cases. Various hyperfine parameters deduced from Mossbauer spectra, namely isomer shifts (IS),

International Journal of
Scientific Research in Science and Technology (IJSRST)
Print ISSN : 2395-6011, Online ISSN : 2395-602X
International Conference on Advanced Materials
Held on 14, 15 December 2017, Organized by Department of Physics,
St. Joseph's College, Trichy, Tamilnadu, India

quadrupole splitting (QS), line widths (Γ), average hyperfine fields <H(T)> and relative areas the fitted doublets and distribution are listed in Table 4.

For a magnetic nanoparticle, magnetization direction fluctuates spontaneously with a relaxation time (Ƭ). Above blocking temperature, the relaxation time Ƭ<<Ƭs (where Ƭs is the Mossbauer measurement time) and the internal magnetic field at the nucleus is averaged out giving rise to a quadrupolar doublet in the Mossbauer pattern. Below the blocking temperature, Ƭ>>Ƭs, a sextet Mossbauer pattern is observed and near the blocking temperature when Ƭ~Ƭs, a partially collapsed sextet with broad lines are seen [21]. Mossbauer spectra of all fractions exhibited simultaneous presence of a central superpararamagnetic / paramagnetic doublet superposed on a weak single magnetic sextet except in one sample(x = 0.1). The Mossbauer spectrum of the low Mg fraction(x = 0.1) closely resembled $ZnFe_2O_4$ with single superparamagnetic / paramagnetic doublet. Unlike other reported results [22], IS value of the doublet is greater than 0.5(Table 4) indicating that most of the Fe^{3+} ions occupy octahedral sites in their high spin state since the presence of Fe^{2+} is not a possibility of the sample prepared using a polymer precursor annealed at and around 450°C[23]. For fractions x = 0.2, 0.3, 0.4 and 0.5 we could fit spectra only by considering hyperfine magnetic field distributions. The results revealed their superparamagnetic / paramagnetic (strong single doublet) and weak magnetic ordering (a less intense sextet). The broad sextet and broad magnetic hyperfine field distribution P(Bhf) in Fig 9 is due to the variation of A-B interaction from region to region [24]. In these fractions, intensity of sextet increases with the concentration of Mg^{2+} ions and this trend is reported by many researchers [21], [24]–[29]. As in the Table 4 the relative area of distribution increased with Mg content and the average magnetic hyperfine field changed from 17.6 T for x = 0.2 to 24.77 T for x = 0.5. These findings can be explained by the enhancement of A-B superexchange interaction strength due to the redistribution of Fe^{3+} ions among tetrahedral and octahedral sites (Table 1)[26]. In general, hyperfine field at the B site decreases with Zn concentration in A sites according to the relation

$$H_n = H_o(1 - n\Delta H) \qquad \text{... (10)}$$

where H_o is the field at B site with no Zn ion in A site, n is the number of Zn ions in A sites and ΔH is the fractional decrease in hyperfine field[30]. The Mossbauer spectra for x > 0.1 are consistent with the formation of a fairly good solid solution as local inhomogeneous clusters with a central doublet characteristic of particles undergoing SPM relaxation or having paramagnetic character and an emerging sextet attributable to bigger ferrite particles with their relaxation time approximately is of the order of the characteristic Mossbauer measurement time. Probability distribution of hyperfine fields of all the samples have most probable field around 4 T(low field), representing doublets indicated majority of particles are undergoing superparamagnetic relaxation. The samples with x = 0.2, 0.4 and 0.4 have only low intense peaks at higher fields (Table 4 , Fig 10) and x = 0.5 has comparatively more intense peaks confirmed the presence of particles that contribute to a relaxation time comparable to measurement time. Thus Mossbauer spectra analysis corroborated the presence of ferromagnetic, superparamagnetic and paramagnetic phases determined by M-H curve fitting. No trace of impurity was detected in the samples.

International Journal of
Scientific Research in Science and Technology (IJSRST)
Print ISSN : 2395-6011, Online ISSN : 2395-602X
International Conference on Advanced Materials
Held on 14, 15 December 2017, Organized by Department of Physics,
St. Joseph's College, Trichy, Tamilnadu, India

Table 4. Variation of isomer shift and quadrupole splitting of $Mg_xZn_{1-x}Fe_2O_4$ samples

Mg Content(x)	Sub-spectrum	IS (mm/s)	QS (mm/s)	Γ (mm/s)	Area (%)	<H(T)>	Peak Values of P(Bhf)
0.1	Doublet	0.70	0.45	0.615	100	-	-
0.2	Doublet distribution	0.33 0.32	0.49 -	0.41 0.40	41.97 58.03	- 17.6	- 4.03, 24.52, 40.58, 48.01
0.3	Doublet distribution	0.32 0.34	0.48 -	0.4 0.4	29.82 70.18	- 17.4	4.02, 17.0, 33.57, 46.23
0.4	Doublet distribution	0.32 0.30	0.54 -	0.41 0.39	26.56 73.44	- 17.7	3.17, 22.31, 30.67, 37.51, 45.53
0.5	Doublet distribution	0.34 0.27	0.56 -	0.46 0.4	17.94 82.06	- 24.77	4.02, 18.03, 25.04, 33.42, 46.23

4. Conclusions

$Mg_xZn_{1-x}Fe_2O_4$ nanoparticles were synthesized using spray pyrolysis method and the effect of Mg doping on the structural, magnetic and hyperfine properties were investigated using XRD, FTIR, VSM and Mossbauer spectroscopy. The XRD patterns revealed the cubic spinel structure and structural refinement was done by Rietveld method using FULLPROF program. The cation distribution, lattice parameter and oxygen position parameter were extracted from the Rietveld refinement. The migration of Fe^{3+} ions from octahedral to tetrahedral site with magnesium doping was observed from the cation distribution. The lattice parameter decreased with magnesium concentration obeying Vegard's law owing to comparatively smaller ionic radii of Mg^{2+} than Zn^{2+} and by change in the cations in interstitial sites. The average particle size obtained from TEM image of $Mg_{0.5}Zn_{0.5}Fe_2O_4$ was about 15 nm and majority of particles were spherical. The particle size lies in the range of 9-19 nm with possibility of coexistence of superparamagnetic particles with some bigger particles. The FTIR analysis confirmed spinel structure and center of the υ_1 band in the FTIR spectra shifted to longer wavenumber with Mg doping because of the replacement of Zn^{2+} by Fe^{3+} with comparatively lower atomic weight at the tetrahedral sites. The curve fitting of M-H data revealed the coexistence of superparamagnetic, ferromagnetic and paramagnetic particles. Saturation magnetization and magnetic moment per formula unit were found to increase with Mg doping due to enhancement of A-B superexchange interaction by the redistribution of Fe^{3+} ions among the interstitial sites. The Mossbauer spectrum of the samples except with x = 0.1 is a centerall superparamagnetic doublet superposed on weak single magnetic sextet. The Mossbauer spectra and hyperfine field distribution with most probable field at low field suggest majority of particles are undergoing superparamagnetic relaxation and few are ferromagnetic whose relaxation time equals Mossbauer measurement time. The area of the sextet and mean hyperfine field increased with magnesium concentration owing to increase in the A-B superexchange interaction as in the magnetization data analysis. The Mossbauer analysis strongly confirmed the coexistence of superparamagnetic, ferromagnetic and paramagnetic phases observed in magnetization data fitting by the superposition of a doublet and a collapsed sextet.

Acknowledgements

The authors wish to thank Dr. V R Reddy (UGC-DAE Consortium for Scientific Research, Indore) for the Mossbauer measurements and STIC, Cochin for the TEM and FTIR analysis.

References

[1] H.M. Zaki, A. Umar, T. A. Elmosalami, and H.A. Dawoud, "Magnesium-Zinc Ferrite

Nanoparticles : Effect of Copper Doping on the Structural, Electrical and Magnetic Properties," J. Nanosci. Nanotechnol., vol. 13, pp. 4056–4065, 2013.

[2] H.-C. Wu et al., "Magnetic and transport properties of epitaxial thin film MgFe2O4 grown on MgO (100) by molecular beam epitaxy," Sci. Rep., vol. 4, no. 1, pp. 1–6, 2015.

[3] J. Smit and H. P. J. Wijn, Ferrites. London: Philips' Technical Library, 1959.

[4] V.D. Kassabova-zhetcheva, L.P. Pavlova, B.I. Samuneva, Z. P. Cherkezova-zheleva, I. G. Mitov, and M.T. Mikhov, "Characterization of superparamagnetic $Mg_xZn_{1-x}Fe_2O_4$ powders," Centeral Eur. J. Chem., vol. 5, no. 1, pp. 107–117, 2007.

[5] L.M. Salah, A.M. Moustafa, and I.S.A. Farag, "Structural characteristics and electrical properties of copper doped manganese ferrite," Ceram. Int., vol. 38, no. 7, pp. 5605–5611, 2012.

[6] C. Srinivas et al., "Structural and magnetic characterization of co-precipitated $Ni_xZn_{1-x}Fe_2O_4$ ferrite nanoparticles," J. Magn. Magn. Mater., vol. 407, pp. 135–141, 2016.

[7] F. Luo and C. Yan, "Anti-phase boundaries pinned abnormal positive magnetoresistance in Mg doped nanocrystalline zinc spinel ferrite," Chem. Phys. Lett., vol. 452, pp. 296–300, 2008.

[8] L. J. Berchmans, R. K. Selvan, P. N. S. Kumar, and C.O. Augustin, "Structural and electrical properties of $Ni_{1A_x}Mg_xFe_2O_4$ synthesized by citrate gel process," J. Magn. Magn. Mater., vol. 279, pp. 103–110, 2004.

[9] S. D. Chhaya, M. P. Pandya, M. C. Chhantbar, K. B. Modi, G. J. Baldha, and H. H. Joshi, "Study of substitution limit, structural, bulk magnetic and electrical properties of Ca^{2+} substituted magnesium ferrite," J. Alloys Compd., vol. 377, pp. 155–161, 2004.

[10] V. B. Kawade, G. K. Bichile, and K. M. Jadhav, "X-ray and infrared studies of chromium substituted magnesium ferrite," Mater. Lett., vol. 42, no. 1, pp. 33–37, 2000.

[11] M. V Limaye et al., "High Coercivity of Oleic Acid Capped $CoFe_2O_4$ Nanoparticles at Room Temperature," J. Phys. Chem. B, vol. 113, pp. 9070–9076, 2009.

[12] A. Gholizadeh and E. Jafari, "Effects of sintering atmosphere and temperature on structural and magnetic properties of Ni-Cu-Zn ferrite nano-particles: Magnetic enhancement by a reducing atmosphere," J. Magn. Magn. Mater., vol. 422, pp. 328–336, 2017.

[13] H. Sozeri, Z. Durmus, and A. Baykal, "Structural and magnetic properties of triethylene glycol stabilized $Zn_xCo_{1A_x}Fe_2O_4$ nanoparticles," Mater. Res. Bull., vol. 47, no. 9, pp. 2442–2448, 2012.

[14] H. Wu, T. Li, L. Xia, and X. Zhang, "Microwave-polyol controlled synthesis and magnetic properties of monodisperse Co x Ni 1 A x Fe 2 O 4 / MWCNT nanocomposites," Mater. Res. Bull., vol. 48, no. 11, pp. 4785–4790, 2013.

[15] A. Baykal, F. Gözüak, H. Kavas, and Y. Köseog, "Structural and magnetic properties of $Co_xZn_{1A_x}Fe_2O_4$ nanocrystals synthesized by microwave method," Polyhedron, vol. 28, pp. 2887–2892, 2009.

[16] V. Jagadeesha Angadi, A. V. Anupama, R. Kumar, S. Matteppanavar, B. Rudraswamy, and B. Sahoo, "Observation of enhanced magnetic pinning in Sm3+ substituted nanocrystalline Mn-Zn ferrites prepared by propellant chemistry route," J. Alloys Compd., vol. 682, pp. 263–274, 2016.

[17] F. Gozuak, Y. Koseoglu, A. Baykal, and H. Kavas, "Synthesis and characterization of

$Co_xZn_{1}A_xFe_2O_4$ magnetic nanoparticles via a PEG-assisted route," J. Magn. Magn. Mater., vol. 321, pp. 2170–2177, 2009.

[18] A.A. Ati, Z. Othaman, and A. Samavati, "Influence of cobalt on structural and magnetic properties of nickel ferrite nanoparticles," J. Mol. Struct., vol. 1052, pp. 177–182, 2013.

[19] T. Zaki, K. I. Kabel, and H. Hassan, "Using modified Pechini method to synthesize α-Al2O3 nanoparticles of high surface area," Ceram. Int., vol. 38, no. 6, pp. 4861–4866, 2012.

[20] H. Wu, N. Zhang, L. Mao, T. Li, and L. Xia, "Controlled synthesis and magnetic properties of monodisperse Ni 1 A x Zn x Fe 2 O 4 / MWCNT nanocomposites via microwave-assisted polyol process," J. Alloys Compd., vol. 554, pp. 132–137, 2013.

[21] B. K. Nath, P. K. Chakrabarti, S. Das, U. Kumar, P. K. Mukhopadhyay, and D. Das, "P HYSICAL J OURNAL B M ¨ ossbauer , X-ray diffraction and AC susceptibility studies on nanoparticles of zinc substituted magnesium ferrite," EUOROPEAN Phys. J. B, vol. 425, pp. 417–425, 2004.

[22] M. A. Ã. Gabal, "Effect of Mg substitution on the magnetic properties of NiCuZn ferrite nanoparticles prepared through a novel method using egg white," J. Magn. Magn. Mater., vol. 321, no. 19, pp. 3144–3148, 2009.

[23] V. Sepelak, M. Menzel, K. D. Becker, and F. Krumeich, "Mechanochemical reduction of magnesium ferrite," J. Phys. Chem. B, vol. 106, no. 26, pp. 6672–6678, 2002.

[24] V. Jagadeesha Angadi et al., "Dose dependent modifications in structural and magnetic properties of γ-irradiated nanocrystalline Mn0.5Zn0.5Fe2O4 ceramics," Ceram. Int., vol. 43, no. 1, pp. 523–526, 2017.

[25] H. Spiers et al., "Self propagating high temperature synthesis of magnesium zinc ferrites ($Mg_xZn_{12x}Fe_2O_3$): thermal imaging and time resolved X-ray diffraction experiments {," J. Mater. Chem., vol. 14, pp. 1104–1111, 2004.

[26] F. Nakagomi, M. S. Silva, A. F. Jr, V. K. Garg, A. C. Oliveira, and P. C. Morais, "Raman study of cations' distribution in $Zn_xMg_{12x}Fe_2O_4$ nanoparticles," J. Nanoparticle Res., vol. 14, no. 798, pp. 1–10, 2012.

[27] M.E. Abbasher M Gismelseed, K.A.Mohammed, HM Widatallah, A D Al-Rawas and E. and A. A. Yousif, "Structure and magnetic properties of the $Zn_xMg_{1-x}Fe_2O_4$ ferrites," in International Conference on the Applications of the Mössbauer Effect (ICAME 2009), 2009, vol. 217, pp. 1–4.

[28] M.A. Gabal and Y.M. Al Angari, "Effect of diamagnetic substitution on the structural, magnetic and electrical properties of $NiFe_2O_4$," Mater. Chem. Phys., vol. 115, no. 2–3, pp. 578–584, 2009.

[29] S.M. Attia, "Study of Cation Distribution of Mn-Zn Ferrites," Egypt. J. Solids, vol. 4, no. 29, pp. 329–340, 2006.

[30] C.S. Kim, W.C. Kim, S.Y. An and S.W. Lee, "Structure and Mössbauer studies of Cu-doped Ni–Zn ferrite," J. Magn. Magn. Mater., vol. 215, pp. 213–216, 2000.

International Journal of
Scientific Research in Science and Technology (IJSRST)
Print ISSN : 2395-6011, Online ISSN : 2395-602X
International Conference on Advanced Materials
Held on 14, 15 December 2017, Organized by Department of Physics,
St. Joseph's College, Trichy, Tamilnadu, India

Effect of Thickness on Catalytic Performance of Cu Doped TiO_2 Thin Films

Vidhya.R[1], Gandhimathi.R[2], Sankareswari.M[1], Neyvasagam.K[3]*
[1]Department of Physics, V.V. Vanniaperumal College for Women, Virudhunagar, India.
[2]Department of Physics, AMET University, Kanathur, Chennai, India.
[*3]PG and Research Department of Physics, The Madura College, Madurai, India.
Email id: srineyvas@yahoo.co.in

Abstract

Thickness plays a vital role in determining properties of thin films and its variation influences performance of the thin films remarkably. In this work, the impact of thickness on the structural, morphological and optical properties of Cu-TiO_2 thin films have been investigated in detail. Copper doped Titanium dioxide thin films with different thickness (~1.89 to 2.44μm) were deposited on glass substrates by sol gel dip coating technique and were annealed at 500°C for 3 h. The annealed films were subjected to different characterization studies. The surface morphology and stoichiometry of the prepared films were characterized by Scanning Electron Microscopy (SEM) and Energy Dispersive X-ray spectroscopy (EDX) respectively. The microstructural parameters such as crystallite size, dislocation density and micro strain of deposited films demonstrate notable variations with increased film thickness. The optical absorption of Cu-TiO_2 thin films show shift towards long wavelength region depending upon thickness. The photocatalytic activity of the different layered thin films was also tested via the degradation of Methylene Blue (MB) and Methylene Orange (MO) dye solutions under visible irradiation. The threshold thickness for best catalytic efficiency was acquainted and reported.

Keywords: Cu-TiO_2 thin films, XRD, SEM, UV-Visible, Photocatalytic activity

1. Introduction

Due to the increase in the demand of thin films in diverse fields such as semiconductor device fabrication, optical coating, magnetic recording, photovoltaics and photocatalytic turn out thin film techniques as one of primary materials processing methods. The fundamental properties of thin films rely on deposition parameters such as film thickness, grain size and substrate quality. The transition metal oxide TiO_2 semiconductor possesses a range of applications in various fields due to its exceptional properties such as nontoxicity, high catalytic activity, low cost, and long-term stability [1, 2]. TiO_2 has been synthesized using numerous methods such as chemical vapor deposition (CVD), plasma, hydrothermal and sol-gel [3]. Among these methods, sol-gel is the simplest technique in which the different material parameters such as morphology, surface area, average crystallite size and phase structure can be controlled and extended in determining photocatalytic activity of TiO_2 compound [4]. Pristine TiO_2 has band gap energy of about 3.2eV. TiO_2 photocatalyst stimulates production of highly oxidative hydroxyl radicals (OH) and Super-oxide radicals (O_2-), resulting in the decomposition of any organic pollutants present in the environment through a natural occurring oxidation process. Thus, TiO_2 have gained considerable attention as a self-cleaning material for environmental purification and clean energy. The key factors governing the photocatalytic activity of TiO_2 are lowering of band gap energy in visible region and prevention of electron hole recombination rate. One of the methods to improve photocatalytic activity of TiO_2 in the long wave length region is doping metal impurities in the TiO_2 matrix or coupling low band gap semiconductor with TiO_2 [5-7]. The integration of metal ions in TiO_2 lattice bids a way to trap the charge carrier thus improving the efficiency of TiO_2 catalyst [8].

International Journal of
Scientific Research in Science and Technology (IJSRST)
Print ISSN : 2395-6011, Online ISSN : 2395-602X
International Conference on Advanced Materials
Held on 14, 15 December 2017, Organized by Department of Physics,
St. Joseph's College, Trichy, Tamilnadu, India

In this work, efforts have been taken to prepare Cu doped TiO_2 thin films of different thickness by sol-gel dip coating method and the influence of thickness on optical and catalytic properties of Cu-TiO_2 thin films was investigated effectively.

Materials and methods

2.1. Raw materials

Titanium (IV) isoproxide (TTIP, 99.95 %, Fluka Sigma-Aldrich), and copper (II) nitrate trihydrate ($Cu(NO_3)_2.3H_2O$) were used as raw materials to prepare Cu-TiO_2 thin films. Ethanol (C_2H_5OH, 99.9%, Merck Germany) was used as solvent in the preparation of samples.

2.2. Thin films preparation

Cu doped TiO_2 thin films of various thicknesses (5, 7 & 9 dipping cycles) were prepared via sol-gel dip coating method. In the beginning 2.8 ml of Titanium (IV) isoproxide (TTIP) was mixed with 20 ml of ethanol and the mixture was vigorously stirred at room temperature for 10 min. And then 0.6 ml of acetic acid was added drop by drop to this solution and the blend was stirred for another 10 min. A suitable amount of copper (II) nitrate trihydrate was added into this solution slowly. Eventually, it was stirred at room temperature for 90 min., until clear sol was formed. To fabricate 5 dip Cu-TiO_2 thin films, the sol was deposited on glass substrates by five dipping with the drawing speed of about 1.5 mm/s at room temperature and the process was repeated to obtain 7 & 9 dip thin film samples of different thickness. The coated specimens were calcined at the temperatures of 500°C for 3 h with a heating rate of 10°C/min. The thickness was measured by surface profile meter. The thickness of films of 5, 7 & 9 dip is about 1.89, 2.17 & 2.44 μm respectively.

2.3. Characterization

The crystallite size of the Cu-TiO_2 thin films prepared with different Cu concentrations were estimated by X–Ray Diffraction method (XRD) using X'PERT PRO X–ray diffractometer which was operated at 40 KV and 30 mA with CuKα1 radiation of wavelength 1.5407Å. UV–visible spectra were recorded in the range of 300 – 800 nm using the Schimadzu 1800 UV–VIS–NIR spectrophotometer. The surface morphology observation and elemental were done by Carl Zeiss and Supra 55 respectively.

The surface topology was studied using Atomic Force microscope (AFM) Nano surf Easy scan 2. The thickness of the film was measured using Mitutoyo Surfest SJ-301stylus profilometer. Photocatalytic activity of the prepared Cu-TiO_2 thin films was studied by examining the degradation of aqueous solution of methylene blue (MB) under visible light irradiation using 500-W halogen lamp.

3. Results and Discussion

3.1. XRD Analysis

The XRD patterns of Cu doped TiO_2 thin films are shown in Figure1. It confirmed the presence of anatase phase of tetragonal structure with high intensity peak in (101) orientation. The other orientations observed at (210), (200) and (105) for all samples with low intensities, agree with JCPDS file no. 89-4203. Cu compound phase cannot be found in the XRD peaks due to small amount of Cu doping. The calculated micro structural parameters such as crystallite size, micro strain and dislocation density are tabulated in Table 1. The variation in dislocation density and micro strain with the thickness of films is shown in Figure 2. The reduction in FWHM reveals that the crystallization becomes more perfect when the thickness of film was increased by depositing more layers of Cu-TiO_2 on the substrate [9]. It was also noted that dislocation density 'δ' and micro strain (μ) decrease with increasing number of coatings as stress is liberated by minimized stacking fault [10].

International Journal of
Scientific Research in Science and Technology (IJSRST)
Print ISSN : 2395-6011, Online ISSN : 2395-602X
International Conference on Advanced Materials
Held on 14, 15 December 2017, Organized by Department of Physics,
St. Joseph's College, Trichy, Tamilnadu, India

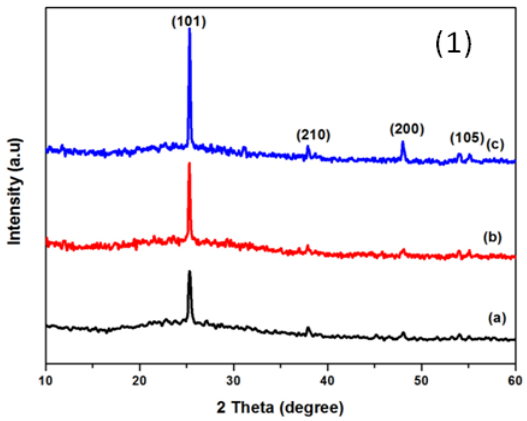

Figure 1. XRD patterns of Cu-TiO_2 thin films for different number of coatings

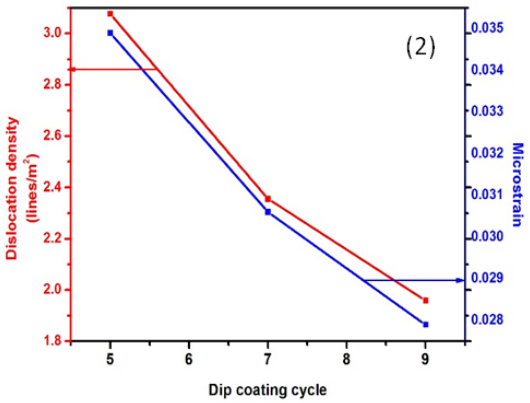

Figure 2. Variation of Dislocation density and Microstrain with different dipping cycles

Table 1. Micro structural parameters of Cu-TiO_2 films deposited at different dipping cycles

Dip coating cycles	Thickness (μm)	Crystallite size D (nm)	FWHM β	Dislocation Density δ x 10^{14} (lines/m^2)	Micro Strain ε	Bandgap (eV)
5	1.89	57.01	0.1432	3.0767	0.0349	3.14
7	2.17	65.15	0.1253	2.3558	0.0306	2.92
9	2.44	71.46	0.1094	1.9583	0.0279	2.79

3.2. Surface morphology and Quantitative Analysis

The surface morphology of deposited films was investigated by scanning electron microscope. Figure 3a & 3b show the SEM images of Cu doped TiO_2 thin films coated with 5 & 7 dip cycles. The images illustrate irregular flake like cracked morphology. During deposition, films undergo significant tensile stress which is relieved as cracks by annealing [11]. The surface cracks gradually rise with the increase in coating cycles. The EDAX picture shown in Figure 3c depicts only characteristic peaks of Ti, O and Cu elements.

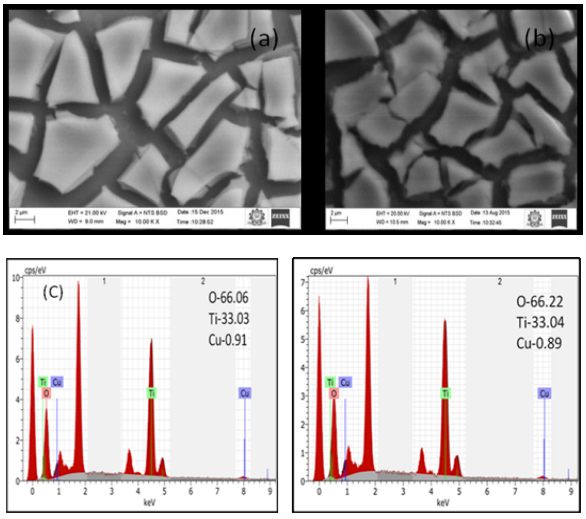

Figure 3. SEM images of the film deposited for 5 coatings (a) and 7 coatings (b) of Cu-TiO_2 thin films with EDAX spectrum (c)

3.3. Surface topography

Atomic force microscope was used to characterize the surface morphology and roughness of the deposited samples. The AFM image of Cu doped TiO_2 (9 dip) is shown in Figure 4. We can see dispersal of aggregated spherical grains of different sizes on the surface. The surface roughness parameters values such as the root mean square roughness (R_q) and average roughness (R_{ave}) are calculated as 11.26 nm and 8.567nm respectively.

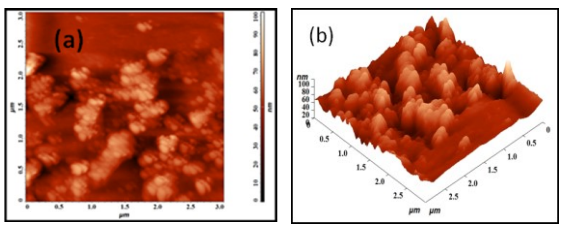

Figure 4. AFM (a) 2D and 5 (b) 3D image of Cu-TiO_2 thin films

International Journal of
Scientific Research in Science and Technology (IJSRST)
Print ISSN : 2395-6011, Online ISSN : 2395-602X
International Conference on Advanced Materials
Held on 14, 15 December 2017, Organized by Department of Physics,
St. Joseph's College, Trichy, Tamilnadu, India

3.4. Optical analysis

The UV-Visible optical absorption spectra of the copper doped TiO_2 thin films are shown in Figure 5. Depositing more layers of Cu-TiO_2 films (5 to 9 dipping) resulted in shifting the absorption edge towards the visible region up to 440nm. The shift in the absorption edge is attributed to change in the crystallite size and thin film density with various thickness [12]. Also, the absorption edge movement towards longer wavelengths represents a decrease in the bandgap of about ~0.35eV [13]. Thus, the addition of Cu-TiO_2 layers on the substrate alter the optical responses of samples, causing a decrease in the bandgap energy and resulting in wide range absorbance of visible light, which can be used in photocatalytic application.

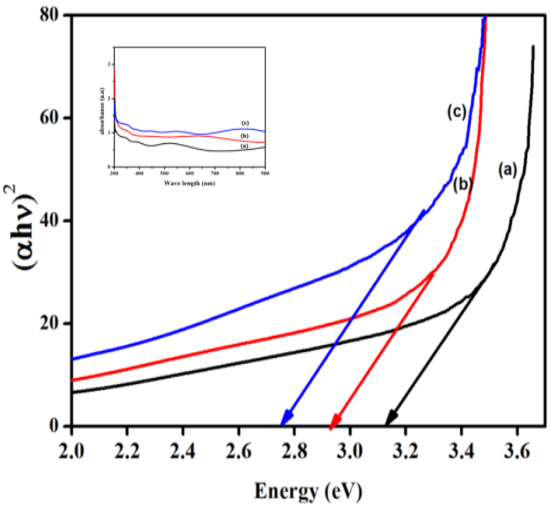

Figure 5. Direct bandgap of Cu-TiO_2 thin films (a) 5dip (b) 7dip & (c) 9dip

3.5. Photocatalytic activity

3.5.1. Thickness effect on photocatalysis

Photocatalytic activity of Cu doped TiO_2 thin films was analysed by examining the degradation of methylene blue (MB) and methylene orange (MO) dye solutions. The thin films were soaked into dye solutions and kept under visible light for irradiation. After that the 5ml of the degradation solution was taken and subjected to Schimadzu-1800 UV-Vis spectrometer to measure the absorbance.

To analyze the effect of thickness on catalytic performance, the thin films with different thicknesses were dipped into MB solution and kept under irradiation for 3hour.The absorbance spectra of degraded MB with Cu-TiO_2 thin films of different thickness are shown in Figure 6a. The reduced band gap energy and increased surface roughness (act as reaction sites) play important role in determining catalytic efficiency [14, 15]. It was observed that the photocatalytic activity of Cu-TiO_2 film was depending on the thickness. All the three films show degradation effect but the film with 5 coatings depicts the more enhanced catalytic activity than other films. The amount of photo generated electron hole pairs reaching the surface is abridged when thickness of the film increases above 1.89 μm. It was found that the thickness of Cu-TiO_2 (5-dip) film is optimum for better photo catalytic efficiency. The percentage of degradation of MB with the catalyst is shown in Figure 6b. The degradation effectiveness of samples decreases with the increase in thickness. The film with minimum thickness~1.89 μm shows the highest percentage of degradation about 80% than that of film prepared with the thickness of 2.44 μm.

International Journal of
Scientific Research in Science and Technology (IJSRST)
Print ISSN : 2395-6011, Online ISSN : 2395-602X
International Conference on Advanced Materials
Held on 14, 15 December 2017, Organized by Department of Physics,
St. Joseph's College, Trichy, Tamilnadu, India

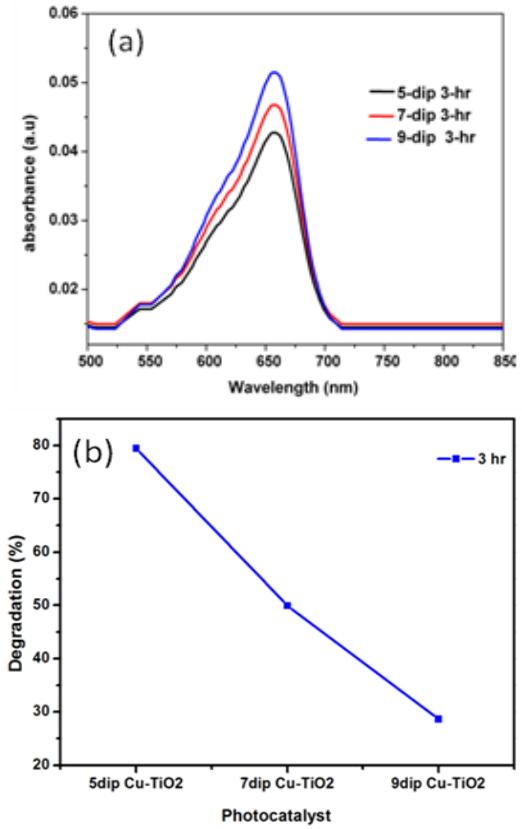

Figure 6 (a). Optical absorption spectra of degradation of MB dye thin films (b) Percentage of degradation of MB for different thickness of the films

3.5.2. Time Effect on photocatalysis

The degradation time effect on MB and MO dyes was examined by soaking Cu-TiO_2 thin films in MB and MO solutions respectively for 1, 2,3 and 4hour under visible light. The changes in the concentration of dye solutions MB and MO as a function of time with Cu-TiO_2 catalyst are shown in Figure 7(a & b). In photocatalytic activity, the degradation efficiency is more reliant on the illumination time. If the illumination time is longer, the degradation will be higher. The degradation efficiency increases with increase time with Cu-TiO_2 thin films. Figure 7c shows degradation percentage of MB & MO dye with the catalyst Cu-TiO_2 (5dip). It was seen that complete decomposition took place in MB solution after 240 minutes. Hence, the optimum illumination time for degradation of MB is 240 minutes. However, in MO solution, we could see still the presence of little dye after 240 minutes degradation. Thus, it is resolved is that Cu-TiO_2 catalyst was more efficient for the degradation of MB.

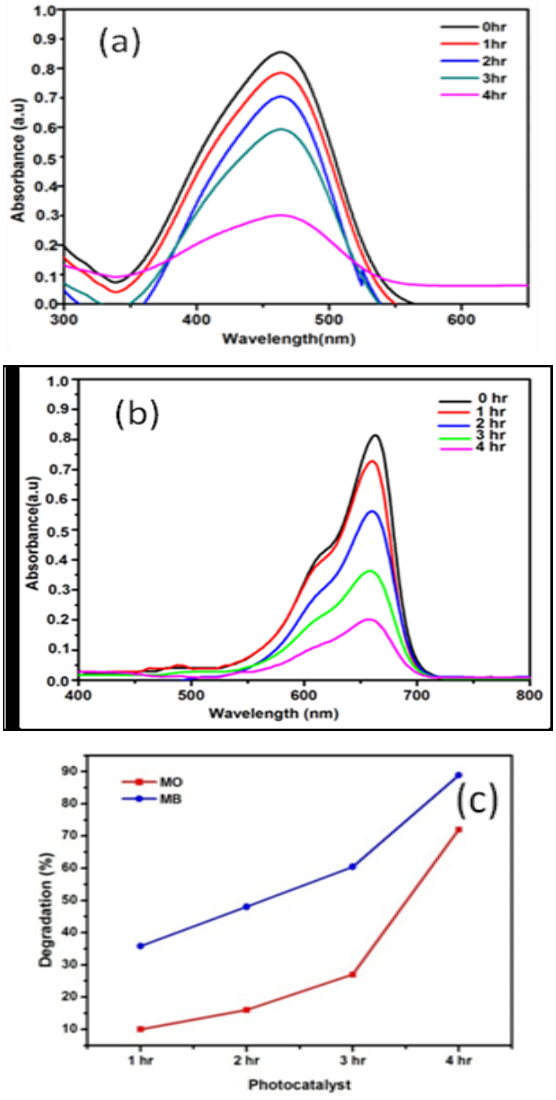

Figure 7 (a & b) . Optical absorption spectra of degradation of MO & MB dye thin films
(b) Percentage of degradation of MO & MB for Cu-TiO_2 films

4. Conclusion

International Journal of
Scientific Research in Science and Technology (IJSRST)
Print ISSN : 2395-6011, Online ISSN : 2395-602X
International Conference on Advanced Materials
Held on 14, 15 December 2017, Organized by Department of Physics,
St. Joseph's College, Trichy, Tamilnadu, India

This work reveals dependences of structural, optical and degradation properties on the thickness of Cu-TiO_2 films deposited onto glass substrates by dip coating technique. The thin films exhibited homogeneous surface grain aggregation, improvement in the optical activity and reduced bandgap energy. Degradation of MB dye solution under visible light rationalizes the dependence of thickness of Cu-TiO_2 thin films on the photocatalytic activity property. The film with ~1.8μm thickness (5-dip) show better degradation efficiency since only the excitons present in the surface region of few nm involves vigorously in photo catalytic reactions. Degradation time effect analysis shows that the film removes more MB molecules in short time. Hence it is proposed that Cu-TiO_2 thin film (~1.89μm) can act as an excellent photocatalyst under visible-light excitations.

References

[1] M.E.Yang Juan, Sen and J.M.F. Ferreira Hydrothd, Synthesis of nano sized Titania powders: Influence of tetra alkyl ammonium hydroxides on particle characteristics, J. Am. Ceram. Soc. 84(8), 2001, pp.1696-1706.

[2] Hang Ru-bin and Gao Lian, Effect of peptization on phase transformation of TiO_2 nanoparticles, J. Mater Res Bull., 36, 2001, pp.1957- 1965.

[3] M.R. Hoffman, S.T. Martin, W. Choi, D.W. Bahnemann, Environmental applications of semiconductor photocatalysis, Chemical Reviews, 95, 1995, pp69.

[4] D. Byun, Y. Jin, J. Kim, K. Lee, P. Hofmann, Photocatalytic TiO_2 deposition by chemical vapour deposition, J. Haz. Mater., 73, 2006, pp.199.

[5] X. Chen. S.S. Mao, Titanium dioxide nanomaterials synthesis, properties, modifications and applications, Chemical Reviews, 107, 2007, pp.2891.

[6] T.C. Dang, D.L. Pham, H.C. Le, V.H. Pham, TiO_2/CdS nanocomposite film: Fabrication, characterization, electronic and optical properties, Advances in Natural Sciences: Nanoscience and Nanotechnology 01, 2010, pp.5002.

[7] B. Tryba, M Piszcz, A.W. Morawski, Photocatalytic activity of TiO_2-WO_3 composites, Hindawi Publishing Corporation, International Journal of Photoenergy Volume 2009, Article ID 297319, pp.7.

[8] P. Dharmarajan, A. Sabastiyan, M. Yosuvasuvaikin, S. Titus and C. Muthukumar, Photocatalytic Degradation of Reactive Dyes in Effluents Employing Copper Doped Titanium Dioxide Nanocrystals and Direct Sunlight, Chem Sci. Trans, 2(4), 2013, pp.1450-1458.

[9] P. Malliga, J. Pandiarajan, N. Prithivikumaran, K. Neyvasagam, Influence of Film Thickness on Structural and Optical Properties of Sol – Gel Spin Coated TiO_2 Thin Film, IOSR Journal of Applied physics, 6, 2014, 22-28.

[10] Effect of Film Thickness on Structural and Electrical Properties of Sputter-Deposited Nickel Oxide Films Hao-Long Chen, Yang-Ming Lu and Weng-Sing Hwang, Materials Transactions, Vol. 46, No. 4, 2005, pp. 872 - 879.

[11] Senjiang Yu, Xiaofei Zhang, Xiaofei Xiao, Hong Zhou and Miaogen Chen, Wrinkled stripes localized by cracks in metal films deposited on soft substrates, Soft Matter, 11, 2015, pp.2203-2212

[12] D.L. Domtau, J. Simiyu, E.O. Ayieta, B. Muthoka, J.M. Mwabora, Optical and Electrical

Properties Dependence on Thickness of Screen-Printed TiO_2 Thin Films, Journal of Materials Physics and Chemistry, 4, 2016, pp.1-3.

[13] Gurpreet Kaur, AnirbanMitra, K.L.Yadav, Pulsed laser deposited Al-doped ZnO thin films for optical applications, Progress in Natural Science: Materials International, 25, 2015, pp.12-21.

[14] Yen-Hua Chen and Kuo-Jui Tu, Thickness Dependent on Photocatalytic Activity of Hematite Thin Films, International Journal of Photoenergy, 2012, Article ID 980595, pp.6.

[15] Masoud Rismanchian, Farideh Golbabaei, Yadollah Mortazavi, Gholamhossein Pourtaghi, Abbas Rahimi Foroushani, and Parvin Nassiri, A Comparative Evaluation of TiO_2 Suspension Coating Techniques: A Novel Technique to Achieve Optimal Thickness and Uniformity of Photocatalytic Film, International Journal of Photoenergy, 2012, pp.6.

International Journal of
Scientific Research in Science and Technology (IJSRST)
Print ISSN : 2395-6011, Online ISSN : 2395-602X
International Conference on Advanced Materials
Held on 14, 15 December 2017, Organized by Department of Physics,
St. Joseph's College, Trichy, Tamilnadu, India

Synthesis and Characterization of CSA protonated Poly(2,5-dimethoxyaniline)/TiO_2 Hybrid Thin Film

Maggie Dayana[1], Victor Williams[2]
[1]Department of Physics, St. Joseph's College (Autonomous), Trichy, Tamilnadu, India
[2]Department of Physics, St. Joseph's College (Autonomous), Trichy, Tamilnadu, India
Mail id: maggie.dyna@gmail.com

Abstract

In this work, Poly (2,5-dimethoxyaniline) has been synthesized by oxidative polymerization using ammonium per sulfate as oxidant and protonated by camphor sulfonic acid. Protonated Poly (2,5-dimethoxyaniline) was doped with TiO_2 for different weight ratio and spin coat as thin film using m-cresol as solvent. Tio_2 doped Poly(2,5-dimethoxyaniline) thin films were characterized using X-ray diffraction, UV-Vis spectrophotometer, Photoluminescence and Fourier transform infrared spectroscopy for the analysis of structural confirmation, band gap, electronic transition and chemical composition. SEM micrograph images of the film confirmed the rod like structure. The band gap value and DC conductivity of the hybrid films found to be influenced by the ratio of TiO_2 nanoparticles.

Keywords: Camphor sulfonic acid, poly (2,5-dimethoxyaniline), Tio_2, hybrid thin film, photoluminence

1. Introduction

Tailoring organic and inorganic materials have potential applications as gas sensors [1], PV cells [2], DSSC [3], photo catalyst [4], electro chromic devices [5] etc. Organic conducting polymers are semiconductors and have conjugate molecular structure and possess delocalized π-electrons over the whole polymer chain. One of the well investigated conjugate polymer with environmental stability, low cost, controllable electrical property is Polyaniline[6]. Polyaniline (PANI) exist in three forms known as Leucoemeraldine base (fully reduced state), emeraldine base (50% oxidized state) and pernigraniline base (fully oxidized state). Emeraldine base (EB) with protic acid gets protonated by H^+ ions forming the Emeraldine salt (ES) which is the conducting form of PANI [7]. Poly (2,5-dimethoxyaniline) (PDMA) which is a derivative of PANI with methoxy group ($-OCH_3$) at ortho and meta position where it is acting as an electron donor substituents[8]. Though CdS, CuS, MnO_2, ZnO are most studied inorganic semiconductors, among the list, selected is TiO_2 due to nontoxic, high chemical and thermal stability, large band gap, and rapid recombination of photo generated electron hole pairs.

Many studies on PANI/ TiO_2 nano- composite have been reported so far but for the first time, studies on CSA protonated poly(2,5-dimethoxyaniline)/ TiO_2 nano composite hybrid thin films have been reported in this work.

2. Experimental

2.1. Chemicals

The chemicals monomer Dimethoxyaniline (DMA), (1s)-(+)-10 Camphorsulfonic acid were purchased from Sigma Aldrich. Ammonium persulfate, HCl (37%), m-cresol and diethyl ether were purchased from Merck. All chemicals were used without any further purification.

2.2. Synthesis of Poly (2, 5-dimethoxyaniline)

PDMA have been synthesized by oxidative polymerization by taking 1:1 molar ratio of DMA

International Journal of
Scientific Research in Science and Technology (IJSRST)
Print ISSN : 2395-6011, Online ISSN : 2395-602X
International Conference on Advanced Materials
Held on 14, 15 December 2017, Organized by Department of Physics,
St. Joseph's College, Trichy, Tamilnadu, India

monomer and Ammonium peroxodisulfate (APS) as an oxidant. DMA dissolved in 1M HCl and stirred at a temperature of 0-5°C for half an hour. To this precooled solution an aqueous solution of APS in 1 M HCl is added drop by drop until brown color monomer turns into green color solution of HCl doped Emeraldine Salt (ES) indicating the formation of polymer, PDMA. The solution was stirred for another 5 hours, then filtered using Whatman paper and washed with deionized water to remove the unreacted monomers. The filtered ES - PDMA was dried in open hot air condition for 2 hours. Emeraldine Base (EB) has been prepared by suspending a part of ES-PDMA in 1M NH_4 OH solution. The solution was stirred for 3 hours., filtered and washed with diethyl ether to obtain EB form of PDMA. It was dried in open hot air condition for an hour to get deep blue color powder form of EB- PDMA.

The protonated ES-PDMA obtained by treating EB–PDMA with CSA of same weight to maintain 1:1 ratio.

2.3. Synthesis of Poly (2,5-dimethoxyaniline) / TiO_2 hybrid thin film:

ES –PDMA with different weight ratio of TiO_2 was dissolved in 2ml of m-cresol solvent with constant stirring for 30 mins. The viscous solution was spin coated under 1500 rpm for 60 sec to get thin film over precleaned fluorine doped tin oxide coated glass substrate and as well as on glass substrate. The thin films were dried under open air condition over a hot plate maintained at 60°C for 5hrs.The films were designated as CPT1, CPT2, CPT3 corresponding to weight ratio 1:0.5, 1:1, 1:2 respectively.

2.4. Material characterization

X-ray diffraction of the thin films were performed using XPERT-PRO Diffractometer with Cu Kα2 radiation. Scanning electron microscopic (SEM) of PDMA thin films were observed using ZEISS EVO 18. Fourier transform infrared (FTIR) spectra of the thin films were obtained by Perkin Elmer spectrum Rx1 spectrometer. UV-Vis spectra of the thin films were obtained using Lambda 365 Perkin Elmer spectrophotometer. Photoluminence spectra of the thin films spectro-flurometer (Jobin Yvon_Flurolog- FL3-11). DC conductivity by two probe method for thin films were carried out by Kiethley sourcemeter model 2450.The thickness of the films were measured using Gravimetric method.

3. Results and Discussion

3.1. X-ray diffraction

The X-ray diffraction pattern of EB, ES, CPT1, CPT2, CPT3 are shown in Fig1. The small peaks around 2θ = 25°, 37°, 48° are assigned to (101), (004), (200), (105) planes of anatase phase of TiO_2 [9]. Peaks observed at 2θ = 18° and 19° are due to CSA dopant in the hybrid films and it is well observed in the ES form of PDMA[10]. The peak at 2θ = 26° found to increase in intensity with increasing TiO_2 ratio. High crystallinity observed for PDMA/ TiO_2 hybrid films when compared with CSA doped PDMA which may be due to symmetric effect of polymer chain. The peak at 27° shows the characteristic distance between the ring planes of Benzene ring in adjacent chain and also the close contact interchain distance [11]. The peak at 2θ = 33° due to periodicity which is perpendicular to the polymer chain. The peaks showed minimum shift for different weight ratio of TiO_2 that shows the impact of TiO_2 in PDMA matrix [12]. Using Scherer equation the average crystallite size found to be ~29nm.

International Journal of
Scientific Research in Science and Technology (IJSRST)
Print ISSN : 2395-6011, Online ISSN : 2395-602X
International Conference on Advanced Materials
Held on 14, 15 December 2017, Organized by Department of Physics,
St. Joseph's College, Trichy, Tamilnadu, India

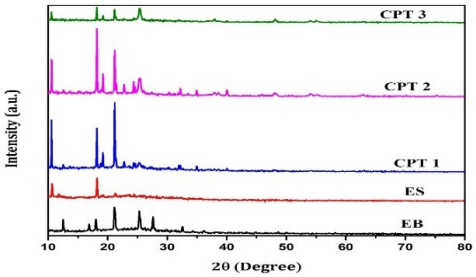

Figure 1. XRD pattern of Emeraldine base, Salt and CSA-PDMA/TiO_2 (1:0.5,1:1,1:2)

3.2. Surface morphology

The SEM images of CSA protonated PDMA/ TiO_2 for the weight ratio 1:1, 1:2 are shown in figure 2(a) and 2 (b) respectively. The SEM images illustrates the morphological changes from plate structure for ratio1:0.5 to rod with the increase of the dopant concentration. The plate like structure may be due to agglomeration of polymer particles representing the amorphous nature of the material. On doping with CSA the main chain of the polymer stretches due CSA - PDMA as well as CSA- m-cresol-PDMA bond. The CSA- PDMA bond is due to association of H^+ with Nitrogen of PDMA and the second bond is formed due to π- π stacking interaction of m-cresol with PDMA and TiO_2[13]. Owing to the linearization of main chain the rod like structure is observed representing the crystalline nature of the material figure 2(b) and (c). Beyond the limiting concentration of the dopant material become less crystalline may due to the predominant CSA-PDMA bonding disturbing the linear structure figure 2(d).

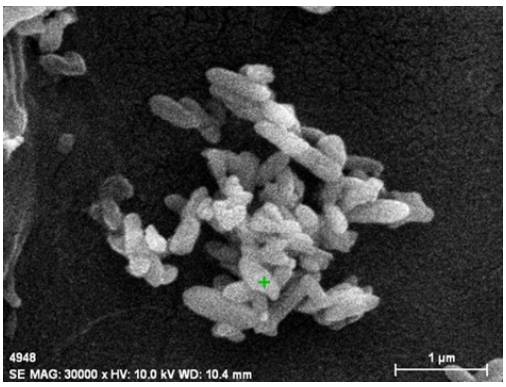

Figure 2 (a). CSA-PDMA /TiO_2 (1:1)

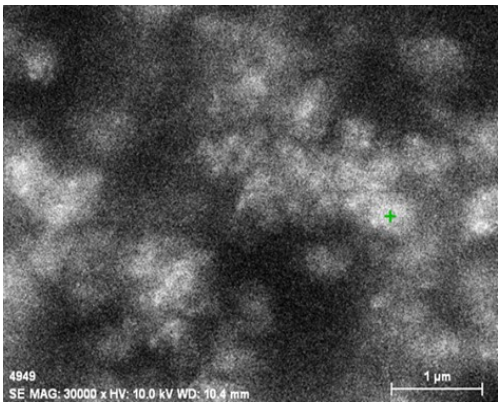

Figure 2(b). CSA-PDMA /TiO_2 (1:2)

3.3. Optical characterization

3.3.1. UV-Vis spectroscopy

UV-Vis absorption spectra shown in Fig 2. A broad hump observed around 620nm shows the formation or existences of EB of PDMA[7]. A shoulder at 480nm and 900nm represents the CSA protonated ES form of PDMA [14]. For different weight ratio of TiO_2 the absorbance of the films were found to be varied thereby indicating the influence of TiO_2in PDMA matrix. The absorption edge at 406nm shows slight blue shift for the ratio 1:2 due to redistribution of polar density in the Band gap of PDMA emeraldine due to the presence of TiO_2 [1] A broad hump around 480nm for all the hybrid film confirms the emeraldine phase of PDMA and due to π –π transition.[15]

International Journal of
Scientific Research in Science and Technology (IJSRST)
Print ISSN : 2395-6011, Online ISSN : 2395-602X
International Conference on Advanced Materials
Held on 14, 15 December 2017, Organized by Department of Physics,
St. Joseph's College, Trichy, Tamilnadu, India

To determine the optical band gap, the fundamental law,

$$\alpha = A (Eg - h\nu)^n$$

was followed, where α is the absorption coefficient, hν is the photon energy in eV, A is a proportionality constant and n = ½ for direct transition and n = 2 for indirect transition. By plotting $(\alpha h\nu)^n$ versus hν for different values of n to get a linear graph from which the optical band gap of the material was noted from the extrapolation of the linear portion of the graph shown in fig 4. The optical band gap of EB, ES of PDMA and for different dopant level of TiO_2 were determined as 4.03eV, 2.92eV, 2.34 eV and 3.06 eV respectively. ES and 1:0.5 ratio film found to be of same band gap which may be due to weak interaction of TiO_2 with PDMA. Band gap found to be decreased for the weight ratio 1:1 whencompared to CSA protonated PDMA thin film.

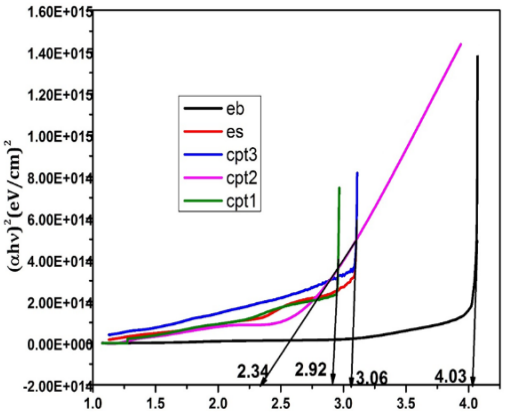

Figure 3. Band gap of Emeraldine base, Salt and CSA-PDMA/TiO_2(1:0.5,1:1,1:2)

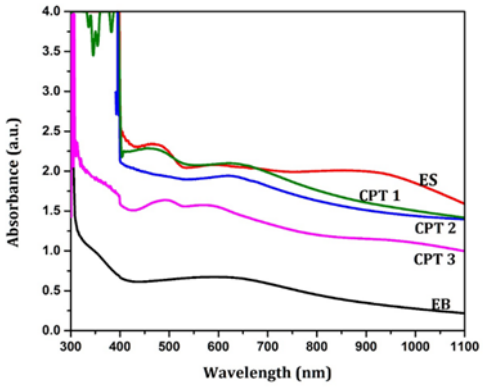

Figure 3(b). UV-Vis absorption spectra of Emeraldine base, Salt and CSA-PDMA/TiO2 (1:0.5, 1:1, 1:2)

3.3.2. Photoluminescence

The Photoluminescence spectra for the samples CPT1, CPT2, CPT3 and CPT4 are shown in the figure 5. In the present work, all the samples were excited with the excitation wavelength of 300nm. CSA PDMA/ TiO_2 films shows sharp and defined peak both in UV and visible region particularly at 360nm and 496nm which are attributed to $\pi \rightarrow \pi^*$ and polaron $\rightarrow \pi$ transition respectively [16]. A small peak observed around 410nm for all the samples with less intensity for EB and higher for higher dopant concentration may be due to protonation and TiO_2 in the polymer matrix. The occurrence of these peaks marked an impression of semiconducting nature by Shimano et al. PDMA thin films with different concentration of TiO_2 showed enhanced PL spectra which may be due to regular alignment of Benzenoid and Quinoid units which prefers the exciton generation and the extension of delocalization length of an exciton [17].

International Journal of
Scientific Research in Science and Technology (IJSRST)
Print ISSN : 2395-6011, Online ISSN : 2395-602X
International Conference on Advanced Materials
Held on 14, 15 December 2017, Organized by Department of Physics,
St. Joseph's College, Trichy, Tamilnadu, India

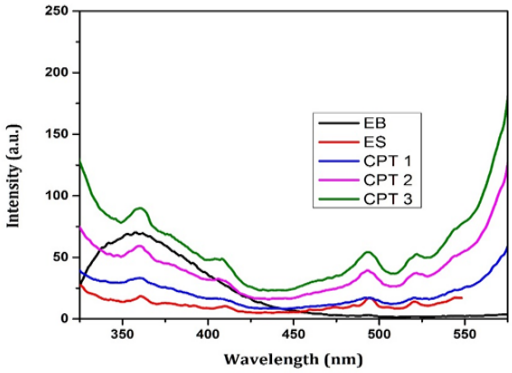

Figure 4. Photoluminescence spectra of Emeraldine base, Salt and CSA-PDMA /TiO_2 (1:0.5, 1:1, 1:2)

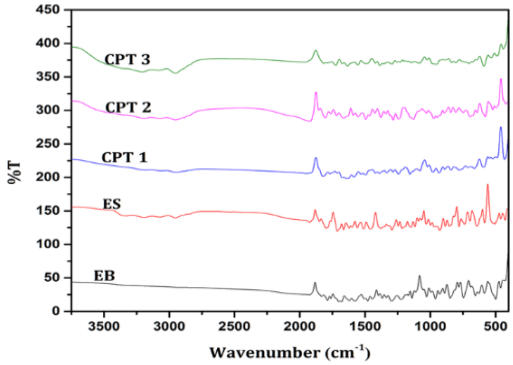

Figure 5. FTIR spectra of Emeraldine base, Salt and CSA-PDMA /TiO2 (1:0.5, 1:1, 1:2)

3.4. Functional group confirmation

Figure 6 shows the FTIR spectrum of EB, ES and CSA–PDMA/TiO_2 thin films for the wavelength range of 4000cm^{-1} to 400 cm^{-1}. The absorption peaks at 1586 cm^{-1}, 1590 cm^{-1}, 1555 cm^{-1} and 1531 cm^{-1}, 1553 cm^{-1}, 1494 cm^{-1} are attributed to stretching modes of C=N, C=C for Quinoid and Benzoid rings [18]. The bands at 1230 cm^{-1}, 1202 cm^{-1}, 1243 cm^{-1} and 951 cm^{-1}, 974 cm^{-1}, 979 cm^{-1} are due to presence of –OCH_3 group of DMA[19]. The peaks observed at 1293 cm^{-1}, 1285 cm^{-1} are due to C-N stretching [20]. All hybrid films showed peaks at 1079 cm^{-1} and 1769 cm^{-1} due to stretching vibration of sulfonic and carbonyl groups of CSA [21]. Presence of band around 600 cm^{-1} and strong vibration around lower wavenumber region confirms TiO_2 anatase phase [16].

3.5. DC conductivity

Electrical conductivity of the pristine and doped PDMA thin film coated on a FTO substrate was measured at room temperature. The voltage, current and resistance of the thin films have been measured. The specific resistivity of the samples were calculated using the following equation,

$$\rho = RA/L$$

where R is the resistance of the thin film measured, A is the cross sectional area of the film and L is the thickness of the film. For all the films the thickness was maintained around 1µm. the DC electrical conductivity of the EB and CSA- PDMA/TiO_2 are shown in the table 1. DC conductivity of CSA-PDMA/TiO_2 hybrid thin film for the ratio 1:1 is found to be low when compared to other ratio.

Table 1

PDMA thin film	DC conductivity S/cm
EB	4.5×10^{-7}
1:0.5(TiO_2)	1.4×10^{-7}
1:1(TiO_2)	7.7×10^{-5}
1:2(TiO_2)	3×10^{-7}

International Journal of
Scientific Research in Science and Technology (IJSRST)
Print ISSN : 2395-6011, Online ISSN : 2395-602X
International Conference on Advanced Materials
Held on 14, 15 December 2017, Organized by Department of Physics,
St. Joseph's College, Trichy, Tamilnadu, India

Conclusion

For the first time, Camphor sulfonic acid protonated Poly (2,5-dimethoxyaniline)/TiO_2 thin films were fabricated by spin coating technique. Poly (2, 5-dimethoxyaniline) has been synthesized by oxidative polymerization and doped with different weight ratio of TiO_2 and principle investigation were carried out. From UV-Vis absorption spectra the optical band gap was calculated as 2.92eV, 2.34 eV and 3.06 eV for hybrid thin films. The crystalline nature of the CSA-PDMA / TiO_2 thin films were identified from their XRD pattern. The functional groups have been identified by FTIR spectrum. Semiconducting nature of the thin films were confirmed by the PL spectrum. The optimization of dopant level has been done by DC electrical conductivity. This material can be used as solar absorber in organic solar cells, thin film capacitor, electrodes in DSSC, gas sensors and exploring the right application may be the future work.

References

[1] S. Nasirian and H. Milani Moghaddam, "Hydrogen gas sensing based on polyaniline/anatase titania nanocomposite," Int. J. Hydrogen Energy, vol. 39, no. 1, pp. 630–642, 2014.

[2] S.M. Ebrahim, I. Morsi, M.M. Soliman, M. Alshrkawy, and a.a. Elzaem, "A novel CuInS <inf>2</inf>/ polyaniline base heterojunction solar cell," Control Autom. Syst. (ICCAS), 2010 Int. Conf., pp. 366–369, 2010.

[3] E. Alkuam, M. Mohammed and T.P. Chen, "Fabrication of CdS nanorods and nanoparticles with PANI for (DSSCs) dye-sensitized solar cells," Sol. Energy, vol. 150, pp. 317–324, 2017.

[4] M.Q. He, L.L. Bao, K.Y. Sun, D.X. Zhao, W.B. Li, J.X. Xia and H.M. Li, "Synthesis of molecularly imprinted polypyrrole/titanium dioxide nanocomposites and its selective photocatalytic degradation of rhodamine B under visible light irradiation," Express Polym. Lett., vol. 8, no. 11, pp. 850–861, 2014.

[5] D. Ragupathy, S.C. Lee, S.S. Al-Deyab and A. Rajendren, "Electrochemical synthesis of a novel poly(2,5-dimethoxy aniline) nanorod for ultrasensitive glucose biosensor application," J. Ind. Eng. Chem., vol. 20, no. 3, pp. 930–936, 2014.

[6] Y. Li, "Conducting Polymers," in Organic Optoelectronic Materials, Y. Li, Ed. Cham: Springer International Publishing, 2015, pp. 23–50.

[7] V. Patil, S. R. Sainkar, and P. P. Patil, "Growth of poly(2,5-dimethoxyaniline) coatings on low carbon steel," Synth. Met., vol. 140, no. 1, pp. 57–63, 2004.

[8] P. Mungkalodom, N. Paradee, A. Sirivat and P. Hormnirun, "Synthesis of Poly (2,5-dimethoxyaniline) and Electrochromic Properties," Mater. Res., vol. 18, pp. 669–676, 2015.

[9] G.K. Bhullar, R. Kaur and K.K. Raina, "Hybrid polyaniline-TiO_2 nanocomposite Langmuir-Blodgett thin films: Self-assembly and their characterization," J. Appl. Polym. Sci., vol. 132, no. 5, pp. 1–7, 2015.

[10] L.M. Huang, T.C. Wen and A. Gopalan, "Synthesis and characterization of soluble conducting poly(aniline-co-2, 5-dimethoxyaniline)," Mater. Lett., vol. 57, no. 12, pp. 1765–1774, 2003.

[11] C. Yuan, L. Zhang, L. Hou, J. Lin, and G. Pang, "Green interfacial synthesis of two-dimensional poly(2{,}5-dimethoxyaniline) nanosheets as a promising electrode for high performance electrochemical capacitors," RSC Adv., vol. 4, no. 47, pp. 24773–24776, 2014.

[12] D. Patil, Y. K. Seo, Y. K. Hwang, J. S. Chang and P. Patil, "Humidity sensitive poly(2,5-dimethoxyaniline)/WO_3 composites," Sensors Actuators, B Chem., vol. 132, no. 1, pp. 116–124, 2008.

[13] K.H. Lee, B.J. Park, D.H. Song, I.J. Chin and H.J. Choi, "The role of acidic m-cresol in polyaniline doped by camphorsulfonic acid," Polymer (Guildf)., vol. 50, no. 18, pp. 4372–4377, 2009.

[14] A. Kato and Y. Fukushima, "Colorimetric chemosensor for ATP based on phthalimide-appended poly(2,5-dimethoxyaniline)," Polym. Bull., vol. 70, no. 12, pp. 3519–3527, 2013.

[15] B. Palys, A. Kudelski, A. Stankiewicz, and K. Jackowska, "Influence of anions on formation and electroactivity of poly-2,5-dimethoxyaniline," Synth. Met., vol. 108, no. 2, pp. 111–119, 2000.

[16] D. Geethalakshmi, N. Muthukumarasamy and R. Balasundaraprabhu, "Structural and optical study of spin-coated camphorsulfonic acid-doped polyaniline / titanium-di-oxide nanoparticles hybrid thin films," Superlattices Microstruct., vol. 82, pp. 447–460, Jun. 2015.

[17] D. Geethalakshmi, N. Muthukumarasamy and R. Balasundaraprabhu, "CSA-doped PANI semiconductor nanofilms: synthesis and characterization," J. Mater. Sci. Mater. Electron., vol. 26, no. 10, pp. 7797–7803, Oct. 2015.

[18] S. Xiong, Z. Kong, J. Lan, S. Yi, Y. Wang, R. Zhang, M. Gong, B. Wu, J. Chu, and X. Wang, "Fabrication of high yield and highly crystalline poly(2,5-dimethoxyanline) nanoplates using various organic sulfonic acids as the dopant agents and soft-templates," J. Mater. Sci. Mater. Electron., vol. 27, no. 11, pp. 11142–11150, 2016.

[19] A. Khosravi, M. Vossoughi, S. Shahrokhian and I. Alemzadeh, "HRP-dendron nanoparticles: The efficient biocatalyst for enzymatic polymerization of poly(2,5-dimethoxyaniline)," J. Mol. Catal. B Enzym., vol. 90, pp. 139–143, 2013.

[20] R.K. Singh, A. Kumar, K. Agarwal, D. Dwivedi, K.N. Sood and R. Singh, "Influence of Binary Oxidant (FeCl3:APS) Ratio on the Spectroscopic and Microscopic Properties of Poly(2,5-Dimethoxyaniline)," Open J. Polym. Chem., vol. 2, no. 3, pp. 105–112, 2012.

[21] B.T. Raut, M.A. Chougule, S.R. Nalage, D.S. Dalavi, S. Mali, P.S. Patil and V.B. Patil, "CSA doped polyaniline/CdS organic–inorganic nanohybrid: Physical and gas sensing properties," Ceram. Int., vol. 38, no. 7, pp. 5501–5506, 2012.

International Journal of
Scientific Research in Science and Technology (IJSRST)
Print ISSN : 2395-6011, Online ISSN : 2395-602X
International Conference on Advanced Materials
Held on 14, 15 December 2017, Organized by Department of Physics,
St. Joseph's College, Trichy, Tamilnadu, India

Construction of Solar Cells Using Organic Dyes

A. Clara Dhanemozhi[1], R. Deepika devi[2], Anitta[2], Murugalaksmi[2], N. Bagavathi[3]

[1]Associate Professor, Department of Physics, Jayaraj Annapackiam College for Women (Autonomous) Periyakulam-625601, Theni, Tamil Nadu, India.

[2]II M.Sc., Scholar Department of Physics, Jayaraj Annapackiam College for Women (Autonomous) Periyakulam-625601, Theni, Tamil Nadu, India.

[3]M.Phil. Scholar Department of Physics, Jayaraj Annapackiam College for Women (Autonomous) Periyakulam-625601, Theni, Tamil Nadu, India.

e-mail: jdhanemozhi@gmail.com

Abstract

This work is mainly based on the fabrication and characterization of Dye Sensitized Solar Cell (DSSC) using organic dyes and to compare its efficiencies. DSSCs were made with glass plates coated with Titanium dioxide, Tartaric acid, dish washing liquid which is non -toxic and more efficient. Glass plates were coated with TiO_2, dishwashing liquid and Tartaric acid mixture as different blocks or cells and were dried for 24 hrs. Organic dye was prepared from beet root, henna, opuntia stincta, lawsone inermics extract. The as prepared dyes were coated on the TiO_2 coating and it is dried. Aluminium foil and copperwire were used as working electrodes and were mounted on each cell. The cells were connected in series. This is completely covered with another glass plate and it was clipped. The cell was kept on the terrace to have the optimum sunlight and its output voltages were measured and efficiencies were calculated and compared.

Keywords: DSSC; glass plates; dyes, voltage

Introduction

The energy and fuel crisis is the major concern in the world today. The demand for energy is growing day by day and many countries around the world have no alternative to increase the energy sources. So there is an urgent need of sustainable energy resources, such as the solar energy, which is considered as an environmentally friend, novel alternative and promising candidate to address this problem. However, solar energy has a limited application that directly related to its high cost. In present time, technology of solar cells based on crystalline silicon is facing a problem of silicon-based raw materials. So, low cost alternatives and hence new types of low cost solar cells are the need of the hour today.

In photoelectrochemical (PEC) solar cells, light energy may be converted into electrical and/or chemical energy. The efficiency of a solar cell device mainly depends upon its design and the properties of the photovoltaic materials included mainly on the light absorbers and their connections to the external circuit.

In 1972, Honda and Fujishima managed to split water into hydrogen and oxygen by illuminating titanium dioxide semiconductor electrodes [i]. Since titanium dioxide absorbs light mainly in the ultraviolet (UV) wavelength region, the efficiency in converting light energy to chemical and electrical energy is low. In order to form an efficient solar energy converter the semiconductor should have an energy band gap optimized for the spectral distribution of solar radiation and also

International Journal of
Scientific Research in Science and Technology (IJSRST)
Print ISSN : 2395-6011, Online ISSN : 2395-602X
International Conference on Advanced Materials
Held on 14, 15 December 2017, Organized by Department of Physics,
St. Joseph's College, Trichy, Tamilnadu, India

exhibit chemical resistance against corrosion and dissolution. One way to increase the spectral response is to sensitize the semiconductor material with dye molecules.

In 1991, Grätzel and O'Regan presented an efficient dye-sensitized PEC cell containing a highly porous nanocrystalline titanium dioxide electrode sensitized with a monolayer of a ruthenium complex [ii-iii]. By this invention, high light absorption was achieved in the visible part of the solar spectrum. Dye-sensitized solar cells (DSSCs), a new type of solar cells, have attracted considerable attention due to their environmental friendliness and low cost of production. A DSSC is composed of a nanocrystalline porous semiconductor electrode-absorbed dye, a counter electrode, and an electrolyte containing iodide and triiodide ions. In DSCs, the dye as a sensitizer plays a key role in absorbing sunlight and transforming solar energy into electric energy. Numerous metal complexes and organic dyes have been synthesized and utilized as sensitizer.

Natural dyes can replace synthetic dyes since they can be easily extracted from fruits, vegetable and flowers with simple and direct chemical procedures, whereas the earlier normally requires many steps procedures, organic solvents and, purification procedures [iv-v]. The pigments are present in the different part of the plant including flowers petals, fruits, leaves, stems and roots.

Here we have constructed the DSSC with TiO2, ZnS and with dyes from the fruit of Opuntia Stricta and the leaves from Lawsonia inermis (Henna). Tartaric acid and the dishwashing liquid are used as fixers. The output voltages were measured and compared.

Opuntia Stricta

Prickly pear is an edible cactus plant that grows in the arid and semi-arid regions of the world. Broad, leaves and sharp spines characterize the prickly pear cactus, and the colorful into edible bulb-shaped fruits. It is grown mostly as a fruit crop, the plant is valued for its large, sweet fruits called fugs or tunas. The fruits are rich in dyes.

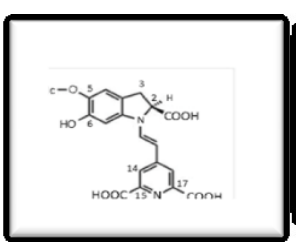

Figure 1. Opuntia stricta **Figure 2**. Chemical formula

Lawsonia inermis

Figure 3 shows a schematic chemical structure of lawsone pigment in henna leaves. Henna's coloring properties are due to lawsone, (2-hydroxy-1,4-naphthoquinone) [32], also known as hennotannic acid, $C_{10}H_6O_3$, a burgundy organic compound that has an affinity for bonding with protein. Lawsone is primarily concentrated in the leaves. Fresh henna leaves will not stain color until the lawsone molecules are made available (released) from the leaves and they are smashed with a mildly acidic liquid. The lawsone will gradually migrate from the henna paste/solution into the outer layer of the skin and bind to the proteins in it known as keratin, creating a fast stain. Lawsone is a skin protective since it strongly absorbs UV light.

International Journal of
Scientific Research in Science and Technology (IJSRST)
Print ISSN : 2395-6011, Online ISSN : 2395-602X
International Conference on Advanced Materials
Held on 14, 15 December 2017, Organized by Department of Physics,
St. Joseph's College, Trichy, Tamilnadu, India

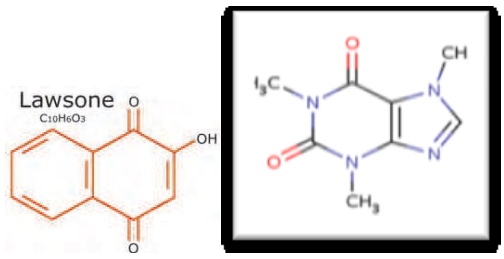

Figure 4. Chemical formula for Lawsonia inermis (Henna leaves)

PREPARATION OF DYE

The extract of the fruit Opuntia Stricta was taken in a beaker and it is stirred for one hour in the magnetic stirrer, and it is set for few minutes. The unwanted particles deposit at the bottom. It is filtered with filter paper. Then again it is stirred at a temperature of 70º C for one hour. After one hour, it is reduced to the room temperature and is washed with ethanol several times and was further used in the preparation of solar cells. The same procedure was followed to prepare the dye from Lawsonia inermis (Henna leaves).

U-V-Characterization

Ultra violet-visible characterization study was done for the as prepared dyes. It was observed that the absorption peaks occurred at 517nm, 381nm, 269nm and 246nm for opuntia stricta and the absorption peaks at 335nm, 288nm for lawsonia inermis. It matches with the wavelength absorption of the red oxide dye. Hence, it confirms that it is best suitable for the solar cell application.

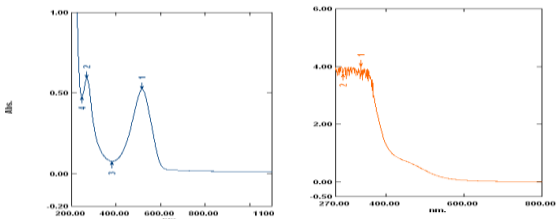

Figure 4(i) **Figure 4(ii)**

Figure 4. U-V Absorption spectra for (i) lawsonia inermis (ii) opuntia Stricta

PREPARATION OF PASTE

The paste to be coated was prepared as follows:

20 gms of TiO_2 was taken and it was mixed with 20ml of distilled water and 20ml of Ethanol. 1.5 gm of Tartaric acid was added to it. 5 drops of dishwashing liquid is added to mixture slowly and mixed well. This paste was used as a coating material for the solar cell.

CONSTRUCTION OF SOLAR PANEL

STEP: 1

A Glass plate was taken and is rinsed with water to remove unnecessary greases. Then the glass plate was cleaned with ethyl alcohol. 30cm x 22cm, 28cm x 20cm sizes of glass plates with 0.5mm thickness were purchased and were used for the construction of solar cells.

STEP: 2

The glass plates were equally divided into separate cells using cellotapes as shown in Fig 5(i)

STEP: 3

Titanium dioxide mixtures were then spread on the surface of each block and was dried for few hours as shown in Fig 5(ii).

STEP: 4

Then the as prepared dyes were coated over the TiO_2 mixtures and were dried for few hours. Several coatings of mixture were applied on the plates. Figure 5 (iii) shows the plate coated with dye from Opuntia Stricta and Lawsonia inermis

STEP: 5

After completely drying, the tapes were then removed carefully and are again dried for few hours.

International Journal of
Scientific Research in Science and Technology (IJSRST)
Print ISSN : 2395-6011, Online ISSN : 2395-602X
International Conference on Advanced Materials
Held on 14, 15 December 2017, Organized by Department of Physics,
St. Joseph's College, Trichy, Tamilnadu, India

STEP: 6

To prepare the working electrodes, aluminium foil and copper wire were cut about half of the size of the block. The aluminium foil and copper wire were mounted on each block layered with titanium dioxide mixture which will serve as the terminal point, where aluminium foil as the negative terminal and copper wire as the positive terminal as in Figure 5(iv)

STEP: 7

The connection of each block cell will be in series circuit which means the total voltage output is the sum of all the voltage on each block cell.

STEP: 8

Cover the prepared glass plate with another glass plate on same size and seal it with binding clips as in Figure 5(v) and now the cell is ready for use.

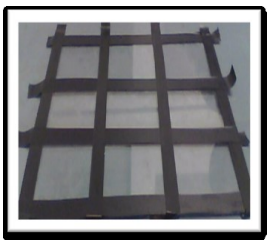

Figure 5(i)

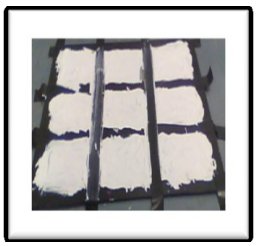

Figure 5(ii)

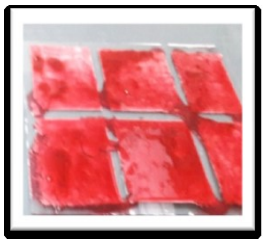

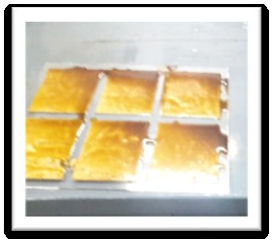

Figure 5(iii)

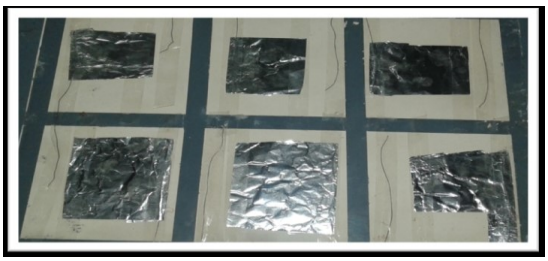

Figure 5(iv)

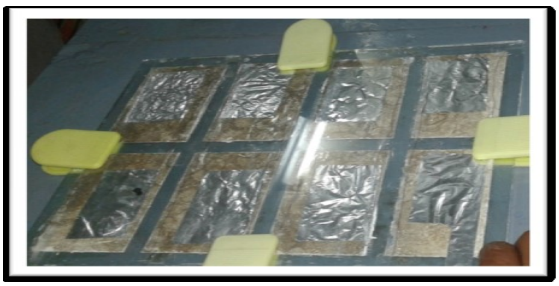

Figure 5(v)

EXPERIMENTAL OBSERVATIONS

The prepared cells were kept on the terrace at 9'0 clock everyday and the observations were made every one hour. The cells were placed inclined at an angle of 20º, facing east direction to receive optimum sunlight and were slowly moved to the direction of the sun. Output voltage was measured every one hour from 10.00 a.m. to 4.00 p.m. and the intensity of the sun was also recorded with sun meter. It was observed that, the output voltage increases gradually with time, and then decreases. The maximum output voltage was recorded between 11.00 a.m. to 12.00 noon.

Since the coated area of the cell is small, the output voltage measured was in millivolts, when the area of the cell is increased, the output voltage may increase. The observations were done from 16th February, 2017 to 10th March, 2017 as we received high intensity of sun light during these periods.

Observations

International Journal of
Scientific Research in Science and Technology (IJSRST)
Print ISSN : 2395-6011, Online ISSN : 2395-602X
International Conference on Advanced Materials
Held on 14, 15 December 2017, Organized by Department of Physics,
St. Joseph's College, Trichy, Tamilnadu, India

The cells were constructed with TiO_2, ZnS, as coating materials and its output voltages were measured and compared. TiO_2 was mixed with Tartaric acid, Dish washing liquid and was coated on the plate. Then the dye was coated on it and the output was measured

Table 1 Output voltages for two different cells for the dye Lawsonia inermis

Maximum intensity: 592w/m²

Time (hour)	Voltage (mV)	
	TiO_2	ZnS
10.00a.m	419	372
11.00a.m	507	419
12.00a.m	514	440
13.00p.m	521	475
14.00p.m	478	463
15.00p.m	462	353

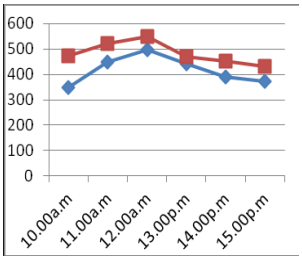

Table 2. Output voltages for two different cells for the dye Opuntia stricta

Maximum intensity: 602w/m²

Time (hour)	Voltage (mV)	
	TiO_2	ZnS
10.00a.m	419	372
11.00a.m	507	419
12.00a.m	514	440
13.00p.m	521	475
14.00p.m	478	463
15.00p.m	462	353

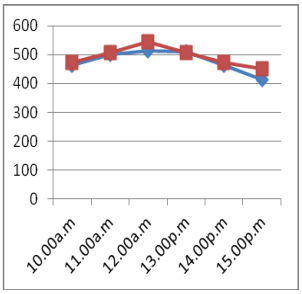

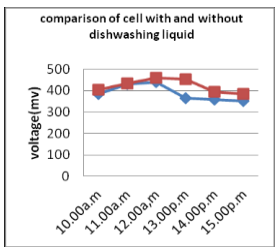

Figure 6 (i) Opuntia Stricta Max.intensity: 592W/m²

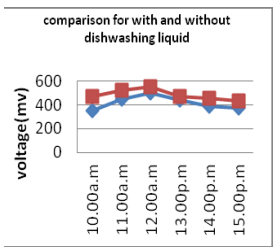

Figure 6(ii) Lawsone inermis Max.intensity: 602W/m²

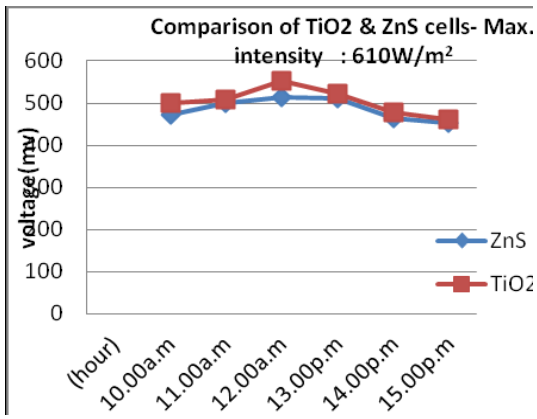

Figure 7 comparison of the cells for the dyes

From the observations, it was found that the cells coated with TiO_2 have more output voltages than the ZnS coated cells. The cells coated with the dye Lawsonia inermis give better output than opuntia stricta.

Conclusion

A simple solar cell was constructed with ordinary glass plates, easily available dyes and TiO_2 and ZnS materials. A good voltage output was got for the Lawsonia inermis dye with TiO2 as the coating material. The main disadvantage is that the dyes easily evaporate. This must be reduced with further improvements.

References

[1] K. Honda, A. Fujishima, Nature **1972**, 238, 37.

[2] B. O'Regan, M. Grätzel, Nature **1991**, 353, 737.

[3] K. Nazeeruddin, A. Kay, I. Rodicio, B.R. Humphry, E. Mueller, P. Liska, N. Vlachpoulos, M. Grätzel, J. Am. Chem. Soc. **1993**, 115, 6382

[4] A. Sarto Polo, Murakami Iha, N.Y.; Itokazu, M.K. "Metal complex sensitizers in dye-sensitized solar cells". Coord. Chem. Rev. 248, 1343-1361, (2004),

[5] J.M.R.C. Fernando,; Sendeera, G.K.R. "Natural anthocyanins as photosensitizers for dye-sensitized solar devices". Res. Comm. Current. Sci., 95, 663-666, (2008).

[6] H.W. Lai,; Su, Y.H.; Teoh, L, "Commercial and natural dyes as photosensitizers for a water-based dye sensitized solar cell loaded with gold nanoparticle". J. Photochem. Photobiol. A: Chemistry, 195, 307-313, (2008).

[7] Synthesis of titanium dioxide nanoparticles by sol-gel technique, International journal of innovative research in science, engineering and technology

[8] Synthesis and characterization of titanium dioxide nanopowders in hydrothermal and sol-gel methods, International journal of advancement in research and technology volume2, issue 4,april 2013 ISSN 2278-7763

[9] Synthesis and characterization of titanium dioxide nanoparticles ant their applications to textiles for microbe resistance, TATM journal of textile and apparel, technology and management volume 6, issue 2, fall 2009.

International Journal of
Scientific Research in Science and Technology (IJSRST)
Print ISSN : 2395-6011, Online ISSN : 2395-602X
International Conference on Advanced Materials
Held on 14, 15 December 2017, Organized by Department of Physics,
St. Joseph's College, Trichy, Tamilnadu, India

Characterisation of Spray Deposited MnO_2 Thin Films

T. Vandhana, and Dr. A.J. Clement Lourduraj*
Department of Physics, St. Joseph's College (Autonomous), Tiruchirrapalli – 620002, Tamil Nadu, India
Corresponding Author Email – ajeevaclement@gmail.com

Abstract

Manganese dioxide is a low band gap, high optical constant semiconductor that exhibits ferroelectric properties. This material has in recent years had a variety of applications, particularly as an electrode, in electrochemical and electrochromic batteries, in fuel cells as well as in energy efficient device applications. Like most of the pure oxide crystals, undoped MnO_2 is normally an electrical, insulator. Manganese dioxide is prepared by spray pyrolysis technique due to simple, inexpensive and reproducible property. Complementary investigation such as X-Ray Diffraction, SEM are used to study structural and morphology of MnO_2 thin film Microstructural studies indicate that powders were crystalline in nature. It was found that grain size for the preferential orientation is in the order of nanometer.

Keywords: Electrochemical, Morphology, XRD, Thin Film.

1. Introduction

Thin films have received intensive applications after Second World War due to various technological applications. The beginning of "Thin Film Science" can possibly be traced to the observations of Grove [1] who noted that metal film formed by sputtering of cathodes with high-energy positive ions. Rapid developments in thin film technology have been spurred by the growing importance of microelectronics. "A thin film may be scientifically defined as a solid material having one of its dimension in the order of few Å to micron formed by the process of condensation of atomic, molecular or ionic species either by physical or chemical and or electro chemical process on a solid support (substrate)"

1.1. Aim of the work

The aim of the present work is to prepare MnO_2 thin film on glass substrate by spray pyrolysis method and to study its structural, optical and morphological properties.

1.2. Need of Thin Films

Different materials in the forms of thick or thin films, powder or pellet and gels are being prepared by many methods for various needs. Devices or components made in thin film form have advantages over the bulk materials because of

1. Extreme compactness and corresponding reduction in size and weight.
2. Superior performance and high reliability coupled with the low cost of production
3. Low power consumption etc.

Hence material in thin film forms are preferred much in the field of space science, solar energy utilization, high memory computer elements, sensors, micro batteries and hybrid circuits. Also transition from bulk to the thin film state may even cause a drastic change in its properties, arises because of their thickness, large surface to volume ratio, and preparative factors such as rate of deposition, substrate temperature, environmental conditions, residual gas pressure in the system, purity of the material to the deposited, inclusion of foreign matter, in homogeneity of the film, structural and compositional variations of films.

1.3. Application of Thin Films

Thin films are deposited onto bulk materials (called as substrate) to achieve properties unattainable or not easily attainable in the substrate alone. The following table divides the properties required into six basic categories and gives examples of typical application with each category.

International Journal of
Scientific Research in Science and Technology (IJSRST)
Print ISSN : 2395-6011, Online ISSN : 2395-602X
International Conference on Advanced Materials
Held on 14, 15 December 2017, Organized by Department of Physics,
St. Joseph's College, Trichy, Tamilnadu, India

Examination of below table shows that the range of thin film applications is very broad in deed. Often, multiple properties are obtainable simultaneously.

S. No.	Thin Film property	Typical application
1.	Optical	Reflective /antireflective coating Interference filters Decoration (colour, luster) Memory disc (CDs) Wave guide
2.	Electrical	Insulation Conduction Semiconductor devices Piezo electric devices
3.	Magnetic	Memory disc
4.	Chemical	Barriers to diffusion against oxidation or corrosion Gas / Liquid sensor
5.	Mechanical	Tribological (wear resistant coatings) Hardness Adhesion Micro mechanics
6.	Thermal	Barrier layers Heat sinks

For, example Cr coating used on plastic parts for automobiles impart hardness, metallic cluster, and protection against ultraviolet light. The Cr coating on a plastic part achieves the functionality of the same part made from bulk metal, but at significant savings in cost and weight.

2. Preparation Techniques

Variety of thin film materials such as metals, semiconductors, insulators or dielectric etc, are prepared and for this purpose various preparative techniques have been developed [11-12]. Newer methods are also being evolved to improve the quality of the deposits with maximum reproducible properties. Any thin film deposition process involves three main steps.

1. Production of the appropriate atomic, molecular, or ionic species
2. Their transport to the substrate and
3. Condensation on the substrate either directly or chemical and or electro chemical reaction to form a solid deposit.

The techniques of thin film deposition can be classified as below.

I. Vapour phase deposition
II. Liquid phase / solution deposition

2.1. Spray Pyrolysis Technique

A large number of metallic salt solutions when sprayed onto a hot substrate decompose to yield oxide films. It was used as early as 1910 to obtain transparent oxide films. In 1960s Chamberlin et al.,extended the technique to produce sulphide and selenide films. The technique involves a thermally stimulated reaction between clusters of liquid / vapour atoms of different chemical species. Spray pyrolysis method lies some where in the regime between a thin film and a thick film technique, depending on the atom cluster size. The following are the physical, chemical aspects and growth kinetics of spray pyrolysis technique.

2.1.1. Physical Aspects

The spray pyrolysis technique involves different stages like spraying a solution, usually aqueous, containing soluble salts of the constituent atoms of the desired compound onto a substrate maintained at elevated temperatures. The sprayed droplet reaching the hot substrate surface undergoes pyrolytic (endothermic) decomposition and forms a single crystalline or a cluster of crystallites of the product. The other volatile by-products and the excess solvent escape in the vapor phase. The substrate provides the thermal energy for the thermal decomposition and subsequent recombination of the constituent species followed

International Journal of
Scientific Research in Science and Technology (IJSRST)
Print ISSN : 2395-6011, Online ISSN : 2395-602X
International Conference on Advanced Materials
Held on 14, 15 December 2017, Organized by Department of Physics,
St. Joseph's College, Trichy, Tamilnadu, India

by sintering and recrystallization of the clusters of crystallites giving rise to a coherent film.

2.1.2. Chemical Aspects

The chemicals used for spray pyrolysis have to satisfy the following condition i) on thermal decomposition the chemicals in solution form must provide the species/complexes that will undergo a thermally activated chemical reaction to yield the desired thin film material and ii) the remainder of the constituents of the chemicals, including the carrier liquid should be volatile at the spray temperature. For a given thin film materials, the above conditions can be met by a number of combinations of chemicals. However, different deposition parameters are required to obtain comparable quality films.

2.2. Features of the Spray Pyrolysis Process

2.2.1. Growth Rate

The chemical nature, temperature of the substrate, and concentration of the spray solution, its additives, and the spray parameters largely determine the growth rate. The growth rates can be as large as 100 Å min^{-1} for oxide films and 50 Å min^{-1} for sulphide films.

2.2.2. Substrate Effects

In general the spray pyrolysis process affects the substrate surface. When it is not desirable for the substrate to take part in the pyrolytic reactions, neutral substrates such as glass, quartz, ceramics or appropriate oxide/carbide coated substrates are employed. In the case of certain oxide films on Si some desirable etching takes place during deposition. Metallic substrate have not been found suitable for this process.

Generally, at lower substrate temperature foggy and diffusely scattering films are obtained. High substrate temperature yields thinner, continuous, hard and spectrally scattering films. Moreover, at higher temperatures, re-evaporation of anionic species may occur, leading to metal-rich deposits.

2.2.3. Properties of Spray deposited films

In general, spray deposited films are strongly adherent, mechanically hard, pinhole-free and stable with time and temperature. The surface topography of the films is rough and the roughness depends on the spray conditions and the substrate temperature. The microstructure ranges from amorphous to microcrystalline depending on the droplet mobility and chemical reactivity of various constituents.

2.2.4. Preparation of Manganese Dioxide Thin Films

Manganese dioxide thin films have been deposited on glass substrate by spray pyrolysis technique using Analar grade salts. The salt used to prepare MnO_2 films were: manganese acetate [$Mn(CH_3COO)_2.4H_2O$], of 0.1M dissolved in 50ml of deionized water. A home made spraying system shown in figure (a) has been developed to obtain high quality thin films. It consists of i) spray gun ii) plate heater with thermostat and iii) glass chamber with exhaust system. Spray gun is made up of two co-axial glass nozzles of length 15cm.

The solution was sprayed at an angle of 45˚ onto preheated glass substrate kept at a distance of 50cm from the spray gun. Prior to deposition, the substrate were chemically cleaned. Compressed dry air at a pressure of 2 kg/cm^2 from an air compressor via an air filter-cum regulator was used as the carrier gas and spray rate of the solution was maintained at 3 ml/min. To avoid excessive cooling of substrates, successive spraying process was used

International Journal of
Scientific Research in Science and Technology (IJSRST)
Print ISSN : 2395-6011, Online ISSN : 2395-602X
International Conference on Advanced Materials
Held on 14, 15 December 2017, Organized by Department of Physics,
St. Joseph's College, Trichy, Tamilnadu, India

with time period of 15 seconds between successive bursts. Substrate temperature was controlled by a chrome-nickel thermocouple fed to a temperature controller with an accuracy of ±2˚C. The temperature on top side of the substrate is measured by placing thermocouple on a reference glass substrate kept nearer to the coating substrate so as to measure the exact temperature.

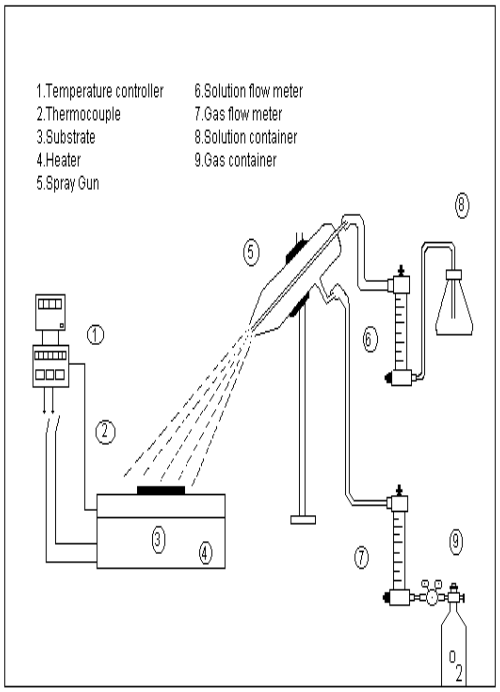

Figure 1(a). Experimental setup of Spray Pyrolysis Unit

3. Analysis Technique

3.1. X-ray Diffraction Characterization

English physicists Sir W.H. Bragg and his son Sir W.L. Bragg developed a relationship in 1913 to explain why the cleavage faces of crystals appear to reflect X-ray beams at certain angles of incidence. This observation is an example of X-ray wave interference commonly known as X-ray diffraction (XRD), and was direct evidence for the periodic atomic structure of crystals postulated for several centuries. The Braggs were awarded the Nobel Prize in physics in 1915 for their work in determining crystal structures beginning with NaCl, ZnS and diamond. Although Bragg's law was used to explain the interference pattern of X-rays scattered by crystals, diffraction has been developed to study the structure of all states of matter with any beam, e.g., ions, electrons, neutrons, and protons, with a wavelength similar to the distance between the atomic or molecular structures of interest.

3.2. Optical absorption measurements

The optical study of a solid concerns not only with the physical phenomena such as refraction, reflection, transmission, absorption, polarization and interference of light but also the interaction of photon energy with matter and the consequent changes in the electronic states. Absorption of light by different materials can induce various types of transitions such as band to band, between sub-bands, between impurity levels and bands, transitions of free carriers within a band and also resonance due to vibrational state of lattice and impurities. Absorption of light by an semiconductor or insulator takes place broadly by two process, namely, i) by raising the electrons from the valence band to conduction band ii) by exciting the lattice vibrations of the material. The later process provides information regarding the bond length of the lattice, the effective charge of the lattice atoms and the characteristic lattice vibration frequency.

The optical method provides a very simple way of finding the band gap as compared to the method using thermal excitation, which is less reliable.

3.3. Scanning Electron Microscope (SEM) studies

This is one of the most useful and versatile instruments for the investigation of surface topography, grain size, microstructural feature, etc.

International Journal of
Scientific Research in Science and Technology (IJSRST)
Print ISSN : 2395-6011, Online ISSN : 2395-602X
International Conference on Advanced Materials
Held on 14, 15 December 2017, Organized by Department of Physics,
St. Joseph's College, Trichy, Tamilnadu, India

It provides a pictorial display of the surface layer with a high depth of focus greater than that possible in an electron microscope. The principle involved in imaging is to make use of the scattered secondary electrons when a finely focused electron beam impinges on the surface of the film. The secondary electron are formed by the interaction of the primary electron beam with the loosely bound electrons of the surface atoms and their emission is very much sensitive to the incident beam direction and the topography of the surface atoms. The more oblique is the surface, the greater will be the surface area from which secondary electron can emit.

The surface morphology of the films is studied using HITACHI S-3000H model shown in fig (d). It consists of an electron source, a series of lens system to produce a finely focused electron beam on the film surface and two pairs of deflection coils at right angles to each other. The emitted secondary electrons are collected in a collector, which is amplified and then fed to a CRT. As the electron beam scans the film surface there will be a change in the secondary electron emission according to the surface texture. The scanning picture observed on the CRT represents the image of the surface.

4. Results and Discussion

Large numbers of MnO_2 thin films were prepared to optimize preparation conditions. The as grown films were subjected to study further characterization. Film thickness was estimated by weighing method and verified with cross sectional view of SEM image. To investigate the microstructural detail of the film, PANalytical X-ray diffractometer (Model D/MAX ULTIMA III) using Ni-filtered CuKα X-radiation (λ = 1.54056Å), was employed with generator setting of 30mA and 40kV. Continuous scanning was applied with a speed of 10˚/min. A range of 2θ from 10˚ to 100˚ was scanned from a fixed slit type, so that all possible diffraction peaks could be detected. X-ray line broadening technique is adopted to determine microstructural details. Optical studies were carried out using Elico SL 159 spectrophotometer in the wavelength range 300 -1100nm.

4.1. Structural Analysis

Pos. [°2Th.]	FWHM [°2Th.]	h k l
22.61	0.99	1 1 0
37.12	0.84	2 0 1
52.85	0.76	5 1 0
63.17	0.72	5 1 1

Figure 1(b) shows the XRD pattern of MnO_2 films prepared at 250°C on glass substrate. The precursor salt concentration is fixed to 0.05M. The film is of polycrystalline nature and peaks match with standard JCPDS card no. 2-2169. The planes are indexed to (110), (201), (510) and (511) with cubic crystal structure. XRD lines shows broadened in their shape when compared with standard JCPDS line. The prepared MnO_2 film shows polycrystalline in nature, and hence large number of grains with various relative positions and orientations cause variations in the phase difference between the wave scattered by one grain and the others. On the other hand, lattice strain broadening is caused by varying displacement of the atoms with respect to their reference-lattice positions. A uniform compressive or tensile strain (macrostrain) results in peak shift [3] of X-ray diffraction lines, whereas a non-uniform of both tensile and compressive strain results in broadening of diffraction lines (microstrain). Thus grain size and microstrain effects are interconnected in the line broadening of peaks, which makes it difficult to separate.

International Journal of
Scientific Research in Science and Technology (IJSRST)
Print ISSN : 2395-6011, Online ISSN : 2395-602X
International Conference on Advanced Materials
Held on 14, 15 December 2017, Organized by Department of Physics,
St. Joseph's College, Trichy, Tamilnadu, India

θ rad	β rad	Interplanar spacing (10^{-10}m) d=nλ/2sinθ	Microstrain (arb. Unit) S=d/(D*sqrt(12))
0.197209	0.008635	3.92	0.007
0.323769	0.007327	2.42	0.003
0.460969	0.006629	1.73	0.002
0.550983	0.00628	1.47	0.001

θ rad	β rad	Grain Size (nm) D=κλ/βCOSθ	Dislocation density (10^{15} lines/m) ρ=1/D²
0.197209	0.008635	16.1	3.81
0.323769	0.007327	19.7	2.56
0.460969	0.006629	23.0	1.87
0.550983	0.00628	25.6	1.52

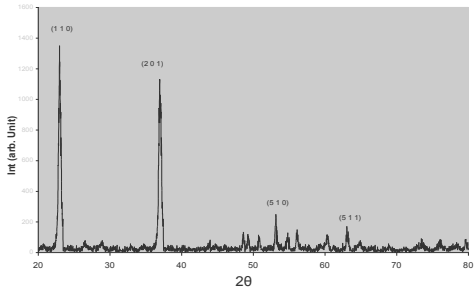

Figure 1(b). XRD pattern of spray deposited MnO_2 thin film

It is observed that as deposition temperature increases grain size of preferential orientation peaks increases from 30 to 60nm due to coalescence of grains Also microstrain found to decreases from 0.00034 to 0.00021 as deposition temperature increases. This is attributed due to decreases in defect and perfect crystalline nature.

4.2. Optical and Morphology studies

Figure 1(c) and (d) show the optical transmittance and surface morphology of the film. The smooth increase in optical transmittance indicates the good crystalline nature of the film. Also the morphology show well connected spherical shape grains.

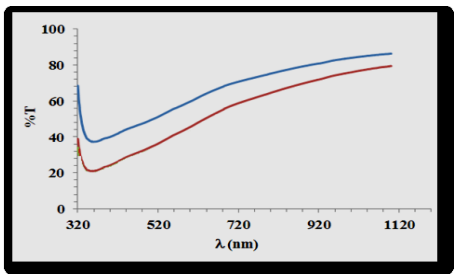

Figure 1(c). Optical transmittance of MnO_2 films annealed at two different temperature (Blue line – 350°C and Red line – 250°C)

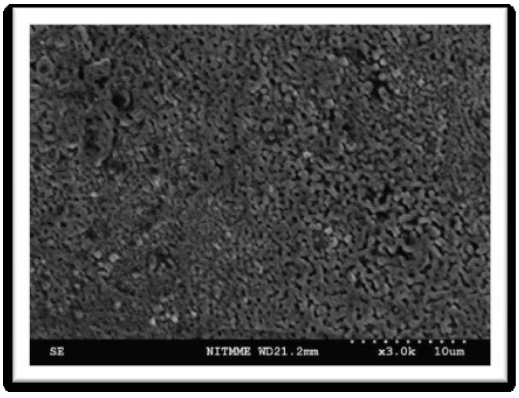

Figure 1(d). Surface morphology of spray deposited MnO_2 thin film

Conclusion

MnO_2 thin films were prepared by home built spray pyrolysis unit on glass substrate. Microstructural studies indicate that films were polycrystalline in nature. The preferential orientation is along (110) plane. X-ray line broadening technique is adopted to correct instrumental broadening effect. It was found that grain size for the preferential orientation is in the order of nanometer. Also X-ray pattern indicate a small shift in 2theta value as compared with standard value. This result is due to strain created between tin oxide nanoparticles during growth stages. Optical transparency found to be nearly 75% in the entire visible region. Scanning electron micrograph confirms the presence of grains on the

surface with size of nanometer range. Further work has to done to still minimize the grain size either by chemical or physical route.

References

[1] T. Prasada Rao, M.C. Santhosh Kumar, A. Safarulla, V. Ganesan, S.R. Barman and C. Sanjeeviraj, Physica B: Condensed Matter, 405, 9, (2010) 2226.

[2] B.J. Lokhande, P.S. Patil, M.D. Uplane, Materials Letters 57 (2002) 573.

[3] Williamson G K, Hall W H 1953 Acta Metall. 1 22.

[4] Sciti D, Celotti G, Pezzotti G, Guicciardi S 2007 Appl. Phys. A. 86 243.

[5] A. L. Patterson, Phy. Rev. 56, 978 (1939).

[6] D. Chen, L. Gao, J. Colloid Interface Sci., 279 (2004) 137.

[7] R.R. Chamberlin WPAFB contract No AF 331657-7919 (1962).

[8] J.E. Hill and R.R. Chamberlin, U.S. Patent 3148084 (1964).

[9] R.R. Chamberlin and J.S. Skarman, J. Electrochem. Soc., 113 (1966) 86.

International Journal of
Scientific Research in Science and Technology (IJSRST)
Print ISSN : 2395-6011, Online ISSN : 2395-602X
International Conference on Advanced Materials
Held on 14, 15 December 2017, Organized by Department of Physics,
St. Joseph's College, Trichy, Tamilnadu, India

Synthesis of Few Layer Graphene Using Mechanical Exfoliation of Kitchen Blender Method for Super Capacitor Applications

S. A. Thaneswari, A. J. Clement Lourduraj
PG and Research Department of physics, St. Joseph's College, Trichy- 620002, Tamil Nadu, India
*Corresponding author's Email: ajeevaclement@gmail.com

Abstract

Facile and single step preparation of few layer graphene (FLG) by mechanical exploitation kitchen blender method. The obtained few layered graphene was characterized by FTIR, XRD, SEM, HR-TEM. The morphology images of SEM and HR-TEM was high-quality and defects free. The electrochemical measurements of cyclic voltammetry (CV) revealed that Electric double-layer capacitor (EDLC). The charge discharge measurements from specific capacitance was calculated (Csp) – 33 F/g at current density 1 A/g. The Electrochemical impedance spectroscopy (EIS) performed was charge transfer resistance (Rct) value for 8.57 ohm. Few layer graphene was obtained from simple kitchen method. This method active material for supercapacitors applications were observed in first time reported. The kitchen blender mechanical exfoliation techniques shows to great promising future industrial-scale synthesis of high-quality defect free graphene for energy storage device applications.

Keywords: Graphene, kitchen blender method, Mechanical exfoliation, energy storage, Supercapacitors.

1. Introduction

The recent development of two-dimensional (2D) nature materials in interest of research society on this material is continuously growing materialistic world and recent innovation by micro mechanical exfoliation led to the synthesis of single layer graphene [1,2]. The advancing 2D carbon nano structured of graphene research field is majorly focused by the interest of society towards unique and amazing properties possesses by graphene. Due to the strong mechanical, electronics, electrochemical, physical properties of graphene, it has high potential for application as energy storage and conversion applications, electronic devices, and biological applications [2-6]. In the next decade, graphene will find commercial applications in many areas but researchers focus electrical energy storage applications as important, such as graphene based supercapacitor applications. Hence, large scale energy storage electrode active materials will require industrial scale production of defect free graphene in desired form bulk graphite to few layered graphene sheets. Widely, used as a synthesis of graphene as different methods Chemical oxidation [7], physical methods [8]. Among, these methods were producing shown to produce some defects, long time process, purification, low yield graphene. However, no scalable method exists to give large quantities of graphene that is also defect-free. At present, the mechanical exploitation or cleavage method has emerged to be a scalable route to cost wise graphene-based few sheets in considerable quantities for industrializes production [9-11]. The large scale industrial production by kitchen mechanical exfoliation for Energy storage electrodes will almost certainly be require large quantities of graphene in the form of liquid suspensions. While, large scale exfoliated graphene were proved very useful in applications for energy storage device applications.

International Journal of
Scientific Research in Science and Technology (IJSRST)
Print ISSN : 2395-6011, Online ISSN : 2395-602X
International Conference on Advanced Materials
Held on 14, 15 December 2017, Organized by Department of Physics,
St. Joseph's College, Trichy, Tamilnadu, India

In this paper, preparation of defects free graphene single step methods by kitchen mixer mechanical exfoliating tool can be used as for bulk graphite. The few layer graphene for economically commercial industrial scale production. In this method large-scale production graphene used as supercapacitor application, first time reported. The FLG materials were characterized and electrochemical analysis supercapacitor applications in three electrode system.

2. Experimental

The few layered graphene (FLG) was synthesized by mechanical kitchen blender method. In detailed mechanically kitchen blender as new process of exfoliation of graphene by mixing in 5 litter large vessel 5 blade blender above mixed a co-mixing of 5 gram graphite powder (purchased from three different suppliers, Aldrich) (7 – 20 μm) and home used soap liquid few drops in a mixing volume of 800 ml with ultrapure water (Millipore). The5 liters mixture head vessel with speed increased gradually until the desired speed was reached 5000 rpm. The process will start switched on the mixer blender initial speed blade rotating 1000 rpm. The main controls of mixing/exfoliated parameters speed 1000 rpm to maximum speed 5000rpm and whole exfoliation process time for 40 mints. The vessel inside solution volume has increased so original volume after every paused interval (3 mints). The resulting FLG liquid samples are through multiple filtrations with followed by centrifugation steps to obtain FLG dispersions with high pure water (Millipore). The resulting exfoliated large scale few layer graphene sheets powder of dried at 100 °C for 12 h. The collected fine black colored powder few layer graphene by the kitchen blender will be further materials characterizations and electrochemical applications.

2.1. Characterization

The materials were characterized graphite and Few Layer Graphene (FLG), crystal structures and planes were determined by high angle X–ray diffraction (XRD) system using X'PERT-PRO model. Laser Raman spectroscopy was performed using Princeton instruments Acton (SP–2500) with 514.5 nm laser. The surface morphology of graphite and FLG of the samples were characterized by using scanning electron microscope (SEM) with VEGA–3 TESCAN instrument and high resolution transmission electron microscope (HR–TEM) with TECNAI, T–30, operated at 250 KV. The Fourier transformation infrared spectroscopy (FT–IR) spectra were performed by using Model JEOL–234.

3. Result and Discussion

3.1. X-Ray Diffraction (XRD)

The X–ray diffraction pattern of purified (MWCNTs) is shown in the Figure 2. The pattern shows the broad diffracted peaks appears at $2\theta=25.9^{\circ}$ was assigned correspond to (002) plane. The diffraction peak corresponds to (002) plane and d-spacing value 3.39 Å. From XRD pattern shows for MWCNTs the results reveals that the carbon nanotubes with hexagonal structure with carbon phase and diffraction patterns typically well graphitized.

2.2. Electrochemical Measurements

The working electrode was prepared by adding the FLG active materials, the total weight ratio of the Material (mass ratio 80:15:5) well mixed and the solid paste like mixture was casted by placing stainless steel (S.S) mesh as working electrode. Working, Reference & Counter electrodes were used corresponding to the (S.S) mesh, Ag/ AgCl & Pt wire, respectively with1 M H_2SO_4 aqueous solution was

International Journal of
Scientific Research in Science and Technology (IJSRST)
Print ISSN : 2395-6011, Online ISSN : 2395-602X
International Conference on Advanced Materials
Held on 14, 15 December 2017, Organized by Department of Physics,
St. Joseph's College, Trichy, Tamilnadu, India

used as the electrolyte. The capacitive performance was tested on a High Performance electrochemical workstation Autolab (PGSTAT-302N). Cyclic voltammetry (CV) and impedance and galvanostatic charge-discharge was carried out a by three-electrode system electrochemical setup.

3. Results and discussion

3.1. XRD and RAMAN

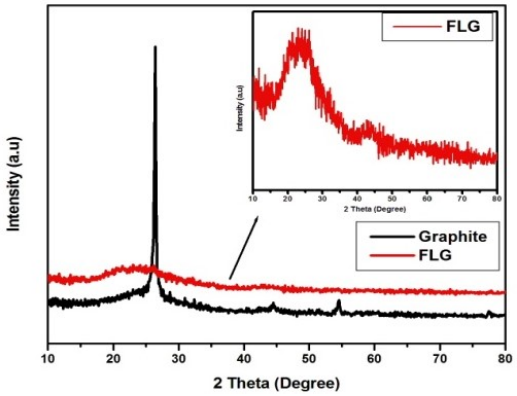

Figure 1. the XRD patterns of FLG

The X-ray diffraction (XRD) pattern Figure 1 shows a single-phased graphite and Few Layer Graphene (FLG). From the X–ray diffraction pattern with different plane values graphite and few layer graphene diffracted peaks at 26º (d-spacing value 3.42 Å) and 26.36º (d-spacing value 3.37Å) are assigned to the (002) planes, respectively. Compare to the graphite peak value, the FLG broad diffraction peak at 25.6º could be related to the (002) plane of the hexagonal structure.

3.2. XRD and RAMAN

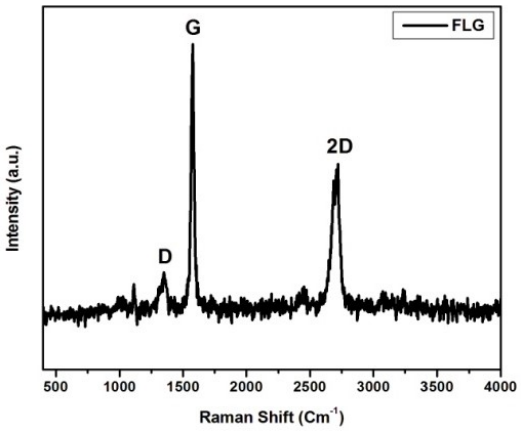

Figure 2. Raman spectra of FLG

As shown the Raman spectra in Figure 2, the Graphite and FLG were significant order and disorders can be characterized the intensity of the D band (1346 cm^{-1}) relative to the G band (1578 cm^{-1}). Compare to G band and D band slightly due to small disorder. Intensity of order/ disorder I_D/I_G = 0.17, its low disorder ratio less than 1, From Raman spectra 2D (2723 cm^{-1}) band indicating that clearly visible few layer graphene indicated and basal plane defects free are introduced during the kitchen blender-assisted exfoliation.

3.2. SEM and TEM

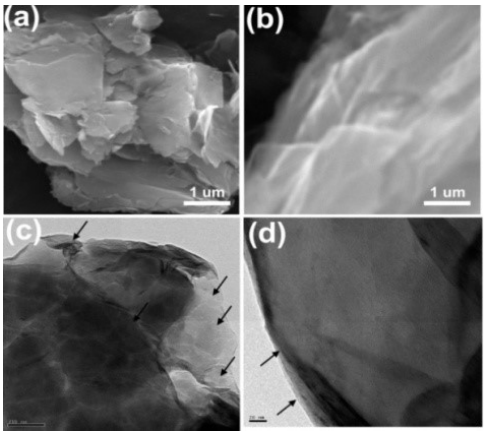

Figure 3.(a) Graphite and (b) SEM images of FLG. (c and d) HR-TEM of FLG

International Journal of
Scientific Research in Science and Technology (IJSRST)
Print ISSN : 2395-6011, Online ISSN : 2395-602X
International Conference on Advanced Materials
Held on 14, 15 December 2017, Organized by Department of Physics,
St. Joseph's College, Trichy, Tamilnadu, India

The surface morphological images are analyzed by SEM and HR-TEM analysis and the images are presented in Figure 3. Figure 3(a) shows the SEM image of graphite bulk particles. Fig 3(b) clearly shows after exfoliations very fine few layer sheets. The HR-TEM images of Figure 3(c) and 3(d) shows demonstrated the free stacked few layer Graphene sheet and the thicknesses of the Graphene nano sheets are around 20 nm. These results revels that Few layers indicates (aero mark) that a particular in edges of the sheets with some layers are overlapped for the mechanical shear exfoliation of Graphene in graphite. Fig 3 (d) defect free surface area morphology and edges of the sheets few layer kitchen blender method from graphite source.

3.3. FT-IR

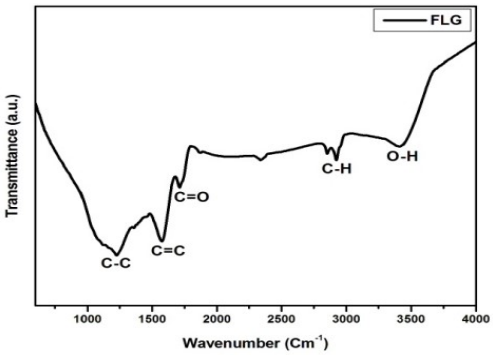

Figure 4. FT-IR spectra of FLG

FTIR spectrum of FLG materials for Figure 4. From the FT-IR spectra was observed the presence of functional groups in which the main absorption band at different carbon functionalities. The important characteristic peaks at 1229 cm^{-1} and 1580 cm^{-1} can be assigned to C–C stretching and C=C (aromatics) of carbon majority functional groups. The FT-IR peaks at 2921 cm^{-1} are assigned to the C–H stretching vibrations. The broad and wide peak at 3412 cm^{-1} is assigned to the O-H group stretching vibrations is significantly low band width due to directly exfoliation from graphite.

4. Electrochemical Measurements

The electrochemical performance of the Few Layer Graphene (FLG) was investigated by Cyclic Volta Metry (CV) measurements using three electrode system in 1Mole H_2SO_4 aqueous electrolyte. Figure 5 (a) shows the Cyclic Volta Metry (CV) curves at different scan rates (100 mV/s and 50 – 30 mV/s) in the potential range of -0.55 to 0.64 V vs. Ag/AgCl electrode.CV curves are observe that all represent similar shape with a pair rectangular shape, which can be attributed to the electrochemical double layer capacitor (EDLC) defect free surface FLG and in the interlayer structure pure carbon.

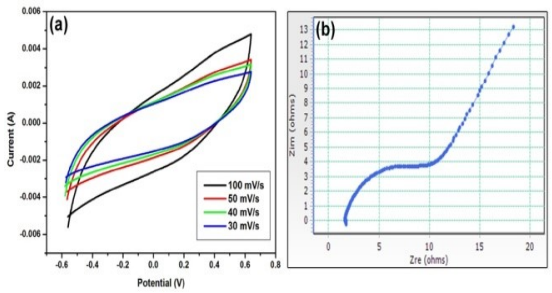

Figure 5. (a) Electrochemical analysis of CV for FLG and
(b) Impedance spectra of FLG

To electrochemical impedance spectroscopy (EIS) measurements were employed FLG material was obtained Nyquist plots shown in Figure 5 (b). The semicircle in the high frequency region reflects the charge transfer resistance (Rct). It indicates that Rct at the electrode/electrolyte interface the charge transfer resistance decreases in FLG material. From Nyquist plots Rct – 8.57 ohm was determined from the intercept of the semicircle on the real part axis at high frequency region. From EIS analysis FLG materials is low Rct value, electrode is obviously

International Journal of
Scientific Research in Science and Technology (IJSRST)
Print ISSN : 2395-6011, Online ISSN : 2395-602X
International Conference on Advanced Materials
Held on 14, 15 December 2017, Organized by Department of Physics,
St. Joseph's College, Trichy, Tamilnadu, India

good conducting few layer materials that the energy storage applications.

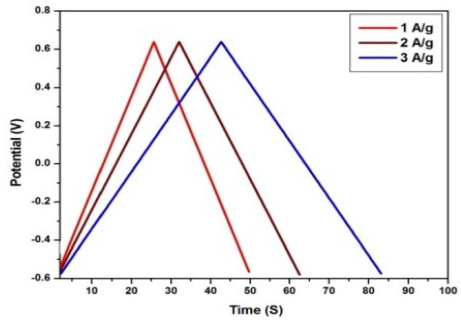

Figure 6. Charge–discharge curves atdifferent current densities 1-3 A/g.

The electrochemical analysis of galvanostatic charge–discharge was measured for Few Layer Graphene (FLG) material. The Specific capacitance (Csp) was calculated using following the equation (Eq - (1).

$$Csp = \frac{I \times \Delta t}{m \times \Delta V} \quad - \quad \text{Eq-(1)}$$

where Eq. (1) Csp (F/g) is the specific capacitance single electrode, I (A) is discharge current, (s) Δt (s) is the discharge time, ΔV represents the potential window during charge - discharge, and m (g) is the mass of the active material. Figure 6 From charge-discharge using Eq-(1) calculated the supercapacitors specific capacitances value 33.61 F/g, and 25.6 F/g and 20.28 F/g different current density values 1 A/g, 2 A/g, 3 A/g respectively. The FLG materials with promise that the excellent achievements for future energy storage device applications.

5. Conclusion

A facile, economic and practical method we have successfully demonstrated a facile scalable technique for producing relatively high-quality few layer graphene by kitchen blender method. The large scale produced FLG nanosheets with little nanometer thickness production of few layer graphene in average from SEM and HR-TEM. The XRD and Raman analysis were observed good crystalline and defects free graphene. The FLG materials were good conductive and free of surface plane defects and any other further oxidation. This was achieved using high Shear cleavage-exfoliations in bulk graphite to graphene mechanical-exfoliation through kitchen blender method. As prepared few layer graphene was done first time used as a electrode materials for supercapacitors applications. From electrochemical studies measurements CV is Electric Double Layer Capacitor (EDLC) nature. The galvanostatic charge-discharge was exhibited maximum specific capacitance Specific Capacitance of few layer graphene Amphere / gram(SCP) of FLG value of 33 F/g was calculations for current density at 1 A/g. The kitchen blender can strongly reveals that industrial scale exfoliation production or future energy applications.

Acknowledgments

The authors wish to thank the PG and research department of Physics, St. Joseph's College, Trichy, for providing lab facilities and instrumentation center facilities to carry out characterization.

References

[1] K.S. Novoselov, A.K. Geim, S.V. Morozov, D. Jiang, Y. Zhang, S.V. Dubonos, et al. Electric field effect in atomically thin carbon films. Science 306 (2004) 666-669.

[2] Geim, A.K., Novoselov, K.S.: The rise of graphene. Nat. Mater. 6 (3) (2007) 183–191.

[3] Allen, M.J., Tung, V.C. & Kaner, R.B. Honeycomb carbon: A review of graphene. Chem. Rev. 110 (2010) 132-145.

[4] Zhu, Y.W. et al. Graphene and graphene oxide: Synthesis, properties and applications. Adv. Mater. 22, (2010) 3906-3924.

[5] Y.W. Zhu et al. Graphene and graphene oxide: synthesis, properties, and applications. Adv. Mater. (2010) 22, 3906–3924.

[6] Lee, C., Wei, X., Kysar, J.W., Hone, J.: Measurement of the elastic properties and intrinsic strength of monolayer graphene. Science 321 (2008)385–388.

[7] Hummers, W.S. and Offeman, R.E. (1958) Preparation of Graphitic Oxide. Journal of The American Chemical Society, 80, 1339.

[8] V. Thirumal, A. Pandurangan, R. Jayavel, R. Ilangovan, Synthesis and characterization of boron doped graphene nanosheets for supercapacitor applications, Synthetic Metals 220 (2016) PP. 524–532.

[9] S. Castarlenas, C. Rubio, A. Mayoral, C. Tellez, J. Coronas, Few-layer graphene by assisted-exfoliation of graphite with layered silicate, Carbon, July 2014, Vol.73, pp. 99-105.

[10] Keith R. Paton et al, Scalable production of large quantities of defect-free few-layer graphene by shear exfoliation in liquids, Nature Materials, 13 (2014) 624–630.

[11] Hernandez, Y. et al. High-yield production of graphene by liquid-phase exfoliation of graphite. Nature Nanotech. 3 (2008) 563-568.

[12] Coleman, J.N. et al. Two-dimensional nanosheets produced by liquid exfoliation of layered materials. Science 331 (2011) 568-571.

International Journal of
Scientific Research in Science and Technology (IJSRST)
Print ISSN : 2395-6011, Online ISSN : 2395-602X
International Conference on Advanced Materials
Held on 14, 15 December 2017, Organized by Department of Physics,
St. Joseph's College, Trichy, Tamilnadu, India

Non-Vacuum Based Preparation of Heterojunction Thin Film Layers for Photovoltaic Application

G. Genifer Silvena, Bincy John, A. Leo Rajesh
Department of Physics, St. Joseph's College (Autonomous), Tiruchirappalli - 620002, Tamilnadu, India
*Corresponding author's Email: aleorajesh@gmail.com
Tel.: +91-9444122070

Abstract

Earth abundant and non-toxic materials were chosen for the fabrication of thin film solar cell using simple and widely applicable deposition techniques. Cu_2ZnSnS_4 (CZTS) thin films was used as a p-type absorber layer in the device and TiO_2 was used as the n-type layer. A p-n junction was formed with TiO_2 and CZTS layers prepared by sol-gel spin coating and spray pyrolysis technique respectively. The device was constructed on a FTO substrate and Al was used as the back electrode with the device structure Glass/FTO/TiO_2/CZTS/Al. The structural, optical and optoelectronic response of the device was studied using Glancing Incidence angle X-ray Diffraction (GIXRD), UV-Visible spectrum and I-V measurements. The GIXRD analysis revealed the polycrystalline nature of the material and the structural formation of each layer. The fabricated device was analyzed to study with photocurrent response. The device showed an open circuit voltage (Voc) of 647 mV and a short circuit current density (Jsc) of 4.5 nA/cm^2 upon illumination. The UV-Visible measurement after depositing each layer shows the variation in transmittance after each layer deposition.

Keywords: Thin films, Cu_2ZnSnS_4, p-n junction, Photocurrent response.

1. Introduction

Cu_2ZnSnS_4 based thin film photovoltaic devices are widely studied in the recent years because of its abundant elemental availability, non-toxic nature and less processing cost [1]. The material possesses an optimum bandgap of 1.45 eV with a high absorption coefficient of 10^4 cm^{-1} which is suitable for p-type absorber layer in thin film solar cells [2]. In the same way TiO_2 is an optimum material to act as an n-type layer which has a wide bandgap of 3.3 eV [3].

The studies of the p-n junction formation with these two materials are of wide interest in photovoltaic research due to its simple and easy preparation using chemical deposition techniques such as spray pyrolysis [4, 5], sol-gel [6], chemical bath deposition [7] and dip coating technique [8]. The photovoltaic device fabricated with this material has a high throughput and is an upcoming development in this field of research [9-12].

In this present work, the fabrication of cost efficient and eco-friendly thin film photovoltaic device is fabricated using versatile chemical deposition techniques with the superstrate device structure FTO/TiO_2/CZTS/Al.

2. Experimental Procedure

The device was fabricated in a layer by layer manner with a superstrate structure. The first Glass/FTO was purchased from Sigma Aldrich with 13Ω/cm^2 resistance. The n-type TiO_2 layer was deposited on top of FTO substrates using sol-gel spin coating technique. The sol-gel solution was prepared by taking Titanium tetra isopropoxide as precursor material for titanium in 10 ml of iso-propyl alcohol solvent. The gelation time took about 2 h. The sol-gel

International Journal of
Scientific Research in Science and Technology (IJSRST)
Print ISSN : 2395-6011, Online ISSN : 2395-602X
International Conference on Advanced Materials
Held on 14, 15 December 2017, Organized by Department of Physics,
St. Joseph's College, Trichy, Tamilnadu, India

solution was deposited at 4000 rpm for 30 s using spin coating technique and the coating was repeated again to improve the film thickness. The next p-type CZTS layer was deposited over the n-layer using chemical spray pyrolysis technique. The precursor solution was prepared with copper (II) chloride dihydrate ($CuCl_2.2H_2O$), Zinc (II) chloride dihydrate ($ZnCl_2.2H_2O$), Tin (II) chloride dihydrate ($SnCl_2.2H_2O$) and thiourea (CH_4N_2S) in 2-methoxyethanl solvent. The solution was sprayed at a substrate temperature of 350˚C with a constant pressure of 1.2 kg/cm^2 and a continuous solution flow rate of 4 ml/min was maintained. The back electrode Aluminum was deposited using thermal evaporation.

The fabricated device with the structure FTO/TiO_2/CZTS/Al was characterized by Glancing Incidence X-ray diffraction (GIXRD, XPERT-PRO diffractometer) equipped with Cu-K_α (λ = 1.54060 Å, 45 kV, 40 mA with a step size of 0.02 degree and scan range from 10˚ to 90˚). The optical properties were studied using UV-Visible spectroscopy (Perkin Elmer Lambda 576) for a wavelength region of 300-1100 nm. The photocurrent measurement was carried out for the device using Keithley (source meter 2450) with a Xenon lamp illumination of 100 mW/cm^2 with a voltage range from -1 V to 1 V.

3. Results and Discussion

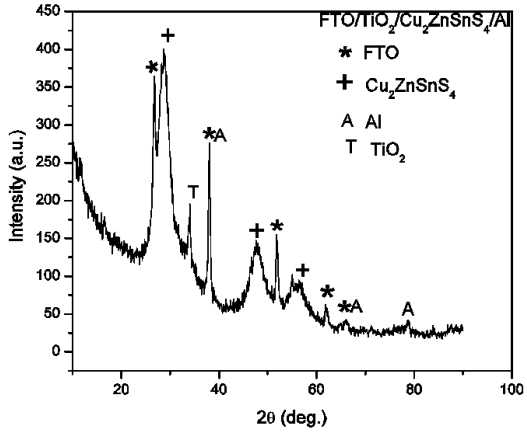

Figure 1. GIXRD pattern of the multilayered device

The GIXRD pattern of Figure 1 shows the structural formation of the multi-layered device. The major peaks at 2θ = 28.5˚ (112), 47.5˚ (220) and 56.3˚ (312) corresponds to the Cu_2ZnSnS_4 product formation with the kesterite phase and tetragonal crystal structure (JCPDS no. 26-0575) [13]. The 2θ peaks at 25.3˚, 25.7˚ and 36.2˚ corresponding to the planes (210), (111) and (102) respectively shows the Brookite phase formation of the TiO_2 layer with orthorhombic crystal structure (JCPDS no.65-2448) [14]. The Al and FTO peaks are also present in the figure at 2θ = 38.2˚, 52.6˚, 62.8˚, 65.4˚, 78.4˚ [15].

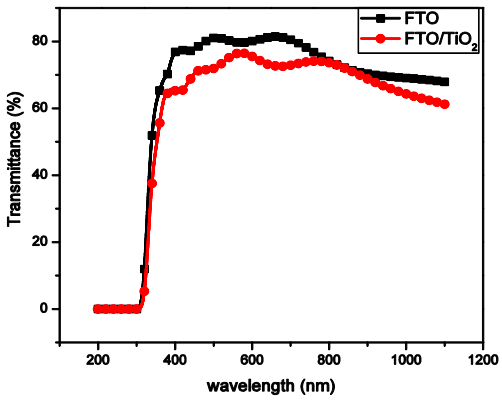

Figure 2. Transmittance spectrum of FTO and FTO/TiO_2 layers

Figure 2 shows the transmittance spectrum of FTO substrate and TiO_2 deposited FTO substrate. The decrease in transmittance value from 80% to 75% for FTO to FTO/TiO_2 is clearly observed from the graph. In the device the transmittance varies from the transparent conducting layer (FTO) to n-type window layer (TiO_2) in this manner. The transmittance has to be more for the TCO and window layer in order for the photons to reach the absorber layer.

International Journal of
Scientific Research in Science and Technology (IJSRST)
Print ISSN : 2395-6011, Online ISSN : 2395-602X
International Conference on Advanced Materials
Held on 14, 15 December 2017, Organized by Department of Physics,
St. Joseph's College, Trichy, Tamilnadu, India

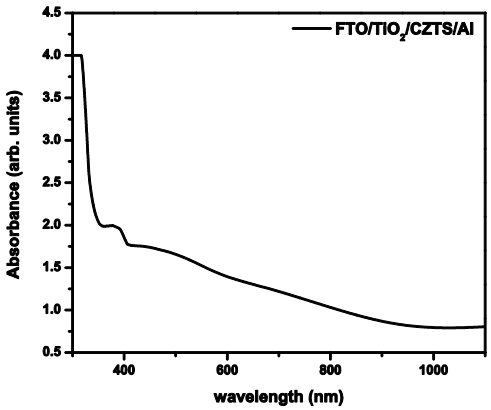

Figure 3. Absorbance spectrum of the device

The absorbance spectrum of the device is shown in Figure 3. From the figure the multiple cut-off wavelengths of different layers can be observed. The cut-off wavelength around 360 nm, 409 nm and 860 nm corresponds to FTO, TiO_2 and CZTS layers respectively. The band gap values are calculated to be 3.44 eV, 3.03 eV and 1.44 eV for FTO, TiO2 and CZTS layers respectively. The TCO and n-type layer has a wide bandgap while the absorber layer has a narrow bandgap. The bandgap values obtained are optimum values of the corresponding material.

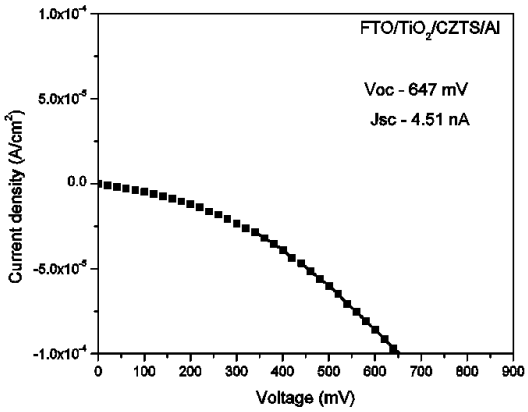

Figure 4. Photocurrent (I-V) response of the device

The fabricated device photocurrent (I-V) response is shown in Figure 4. It shows a very less development of current. The short circuit current density (Jsc) is observed as 4.51 nA and the open circuit voltage (Voc) is measured to be 647 mV. The light current response alone is shown in the figure. The dark current response is not shown here which is of negligible order.

4. Conclusions

Superstrate structured heterojunction device was fabricated using non-vacuum based techniques such as spray pyrolysis and so-gel spin coating techniques. The deposited layers of TiO_2 and CZTS materials are earth abundant and environment friendly. The structural formation of the device was confirmed from the GIXRD pattern. The optical response of each layer and the optical and opto-electric response of the device were studied. It showed a photovoltaic response in the fabricated device.

References

[1] Norio Nakayama, Kentaro Ito, "Sprayed films of stannite Cu_2ZnSnS_4", Appl. Surf. Sci. **92**, 1996, pp. 171-175.

[2] Kentaro Ito, Tatsuo Nakazawa, "Electrical and Optical Properties of Stannite-Type Quaternary Semiconductor Thin Films", Jpn. J. Appl. Phys., **27**, 1988, pp.2094-2097.

[3] Ramamoorthy Raja, Maheswari Govindaraj, Maggie Dayana Antony, Karthika Krishnan, Eswaramoorthi Velusamy, Anandan Sambandam, Manoharan Subbaiah, Victor Williams Rayar, "Effect of TiO_2/reduced graphene oxide composite thin film as a blocking layer on the efficiency of dye-sensitized solar cells", J. Solid State Electrochem., **21**, 2017, pp. 891–903.

[4] Srinivasan Thiruvenkadam, Jovina, D., Leo Rajesh, A., "The influence of deposition temperature in the photovoltaic properties of spray deposited CZTS thin films", Sol. Energy, **106**, 2014, pp.166–170.

[5] Genifer Silvena, G., Bincy John, Anne Sarah Christinal, R., Santhosh Kumar, M.C., Sujay Chakravarty, Leo Rajesh, A., "Solution Processed p-Type Cu_2ZnSnS_4 Thin Films for Absorber Layer", J. Inorg. Organomet. Polym., **27**, 2017, pp. 1556–1562.

[6] Sanjay Kumar Swami, Anuj Kumar, Viresh Dutta, "Deposition of Kesterite Cu_2ZnSnS_4 (CZTS) Thin Films by Spin Coating Technique for Solar Cell Application", Energy Procedia, **33,** 2013, pp. 198-202.

[7] Wangperawong, A., King, J.S., Herron, S.M., Tran, B.P., Pangan-Okimoto, K., Bent, S.F., "Aqueous bath process for deposition of Cu_2ZnSnS_4 photovoltaic absorbers", Thin Solid Films, **519**, 2011, pp. 2488–2492.

[8] Rajesh,G., Muthukumarasamy, N., Subramaniam, E.P., Agilan Dhayalan Velauthapillai, S., "Synthesis of Cu_2ZnSnS_4 thin films by dip-coating method without sulphurization", J. Sol-Gel Sci. Technol., **66**, 2013, pp. 288-292.

[9] Houshmand, M., Hamid Esmaili, Hossein Zandi, M., Nima Gorji, E., "Degradation and device physics modeling of TiO_2/Czts ultrathin film photovoltaics", Mat. Lett., **157**, 2015, pp. 123-126.

[10] Georgi Xosrovashvili, Nima Gorji, E., "Numerical analysis of TiO_2/Cu_2ZnSnS_4 nanostructured PV using SCAPS-1D", J. Mod. Opt, **60**, 2013 pp. 936-940.

[11] Yu Wang, Chunxiang Li, Xijiang Yin, Hai Wang, Hao Gong, "Cu_2ZnSnS_4 (CZTS) Application in TiO_2 Solar Cell as Dye", ECS J. Solid State Sci. Technol., **2**, 2013, pp. 95-98.

[12] Masato Kurokawa, Kunihiko Tanaka, Katsuhiko Moriya, Hisao Uchiki, "Fabrication of Three-Dimensional-Structure Solar Cell with Cu_2ZnSnS_4", Jpn. J. Appl. Phys. **51**, 2012, pp. 10NC33-1-4.

[13] Hong Tak Kim, Donghwan Kim, Chinho Park, "Temperature Effects on Cu_2ZnSnS_4 (CZTS) Films Deposited by Spraying Method", Mol. Cryst. Liq. Cryst., **564**, 2012, pp. 155–161.

[14] Kan Li, Jinlei Xu, Wenye Shi, Yanbin Wang, Tianyou Peng, "Synthesis of size controllable and thermally stable rice-like brookite titania and its application as a scattering layer for nano-sized titania film-based dye-sensitized solar cells", J. Mater. Chem. A, **2**, 2014, pp. 1886–1896.

[15] Haridas Dhaygude, D., Surendra Shinde, K., Ninad Velhal, B., Lohar, G.M., Vijay Fulari, J., "Synthesis and characterization of ZnO thin film by low cost modified SILAR technique", AIMS Materials Science, **3**, 2016, pp. 349-356.

International Journal of
Scientific Research in Science and Technology (IJSRST)
Print ISSN : 2395-6011, Online ISSN : 2395-602X
International Conference on Advanced Materials
Held on 14, 15 December 2017, Organized by Department of Physics,
St. Joseph's College, Trichy, Tamilnadu, India

Sphere-like $CuSbS_2$ Nanoparticles Synthesized by Solvothermal Method for Photovoltaic Applications

Bincy John, G. Genifer Silvena, A. Leo Rajesh*
Department of Physics, St. Joseph's College (Autonomous), Tiruchirappalli - 620002, Tamilnadu, India
*Corresponding author's Email: aleorajesh@gmail.com
Tel.: +91-9444122070

Abstract

$CuSbS_2$ nanoparticles with orthorhombic crystal phase and sphere like morphology were synthesized using solvothermal method. The obtained $CuSbS_2$ nanoparticles were characterized by means of suitable analytical technique such as X-ray powder diffraction (XRD), Dynamic light scattering (DLS), Field Emission Scanning Electron Microscope (FESEM), Photoluminescence spectroscopy (PL), Cyclic Voltammetry and Impedance spectroscopy respectively. The XRD results showed that the obtained sample as orthorhombic crystallinity with (310), (111), (410), (301), (620) and (521) planes of the $CuSbS_2$ nanoparticles. The dynamic light scattering results provided a hydrodynamic average diameter of 7 nm and the morphological investigation given by the FESEM showed the uniform sphere like particles. PL shows that the emission is near IR region and the impedance analysis depicts a semicircular pattern with a diagonal line of 45˚ angle. These results indicate that $CuSbS_2$ nanomaterials are a promising absorber material for photovoltaic application.

Keywords: $CuSbS_2$, Solvothermal, Nanomaterials, Photovoltaic.

1. Introduction

Ternary $CuSbS_2$ is considered as one of the most suitable absorber material for solar cell applications owing to its abundance, less toxicity, large absorption coefficient of 10^4- 10^5 cm^{-1} in the visible region of the solar spectra, charge carrier concentration that can be tuned in wide range from 10^{16} to 10^{20} cm^{-1} and acting as a platinum-free potential counter electrode material for dye-sensitized solar cells [1–5]. High optical absorption and optimum band gap energy in the range of 1.4-1.6 eV are the most important parameters that are strongly influencing on the cell efficiency [6,7]. Besides, the maximum conversion efficiency achieved so far based on $CuSbS_2$ phase is 3.1% [8]. Various deposition techniques such as, chemical vapor deposition [9], sputtering [10], thermal evaporation [3], spray pyrolysis [11], precursor-based routes [12], solvothermal [13] and hot injection [6] methods have been carried out for fabrication of thin film photovoltaic cell.

Recently, the development of simple and low cost methods such as solvothermal and drop casting are carried out for the synthesis and deposition of $CuSbS_2$ nanomaterials. In this approach, ethylenediamine together with 0.5 g of PVP as surfactant for different reaction temperatures is analyzed. Herein, the work is carried out to synthesize $CuSbS_2$ nanoparticles with the addition of 0.5 g of PVP along with other precursor and investigated the structural, morphological, optical and electrical properties.

2. Experimental Procedure

Synthesis of $CuSbS_2$ nanoparticles were synthesized utilizing solvothermal method. In a typical reaction, 2.5 mM copper (II) acetate monohydrate, 2.5 mM antimony (III) chloride and 7.5 mM thiourea were

International Journal of
Scientific Research in Science and Technology (IJSRST)
Print ISSN : 2395-6011, Online ISSN : 2395-602X
International Conference on Advanced Materials
Held on 14, 15 December 2017, Organized by Department of Physics,
St. Joseph's College, Trichy, Tamilnadu, India

dissolved in ethylenediamine under constant stirring for 30 min. Later 0.5 g Polyvinylpyrrolidone (PVP) was added to the above mixture, inorder to stabilize the growth and allow the formation of well defined structure. When the chemicals were completely dissolved, the precursor solution was transferred into a Teflon lined stainless steel autoclave, placed it in a hot air oven and maintained at 180˚C for 24 h. Once the reaction was over the oven was cooled down to reach the ambient temperature. The nanoparticles were collected using centrifuge at 3000 rpm for 10 min. Centrifugation process was carried out several times using deionized water and ethanol inorder to obtain final product. The obtained product was gray in color and kept for drying overnight.

The synthesized $CuSbS_2$ nanoparticles were characterized by powder X-ray diffraction (XRD, Rigaku) equipped with Cu-K β (λ=1.39220 Å, 40 kV, 30 mA and step width 0.02 degree). The hydrodynamic size of the $CuSbS_2$ nanoparticles was characterized using a Nano Plus Zeta / Nanoparticle analyzer instrument. The particle size and morphology of the sample were determined by field emission scanning electron microscope (FE-SEM, ZEISS at accelerating voltage 5 KV). To study the optical properties, the room temperature photoluminescence spectroscopy was taken with a Perkin Elmer (Model Lambda 45). The electrical characterizations such as Cyclic Voltammetry and Impedance of the $CuSbS_2$ nanoparticles were recorded using Princeton Applied Research.

3. Results and Discussion

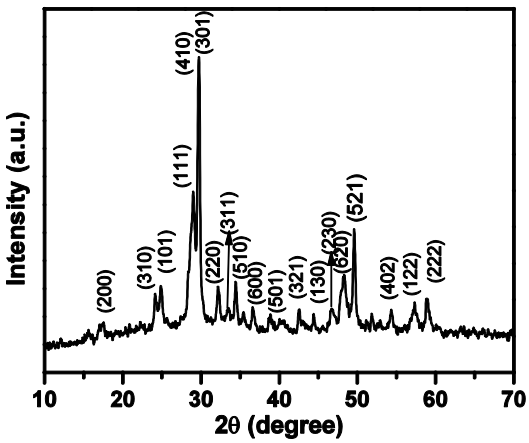

Figure 1. XRD pattern of the synthesized $CuSbS_2$ Nanoparticle

The XRD pattern of $CuSbS_2$ nanoparticles that are shown in Fig. 1 shows the major peaks at 2θ = 23.58º, 28.44º, 28.72˚, 29.91˚, 48.23˚ and 49.78º that are attributed to the planes of (310), (111), (410), (301), (620) and (521). These planes are perfectly indexed as $CuSbS_2$ nanoparticles with orthorhombic crystal structure which is matching well with that of the standard JCPDS, card no. 44-1417 [14]. The average crystallite size of $CuSbS_2$ nanoparticles is determined using Debye-Scherrer formula and is found to be 7.2 nm.

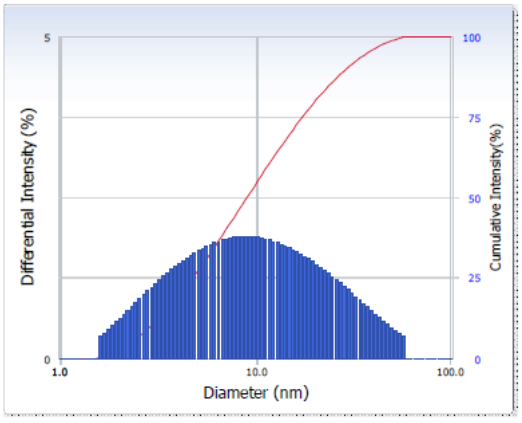

International Journal of
Scientific Research in Science and Technology (IJSRST)
Print ISSN : 2395-6011, Online ISSN : 2395-602X
International Conference on Advanced Materials
Held on 14, 15 December 2017, Organized by Department of Physics,
St. Joseph's College, Trichy, Tamilnadu, India

Figure 2. The size distribution of $CuSbS_2$ nanoparticles using dynamic light scattering measurement

Fig. 2 shows the size distribution of the synthesized $CuSbS_2$ nanoparticles using dynamic light scattering measurement. Here the size distribution profile of small $CuSbS_2$ nanoparticles in dispersion are carried out and the obtained result gives a hydrodynamic average diameter of 7 nm and a Polydispersity Index of 0.006.

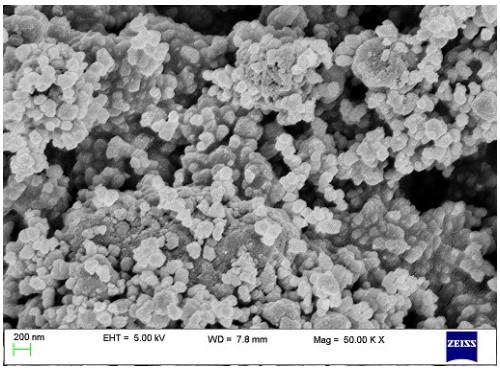

Figure 3. FESEM images of the synthesized $CuSbS_2$ Nanoparticles

The surface morphology of the synthesized $CuSbS_2$ nanoparticles analyzed using the field emission scanning electron microscope and the images are shown in Fig. 3. From the images it is clear that the ethylenediamine together with PVP influences the final morphology of the particles and the obtained $CuSbS_2$ nanoparticles are composed of a large number of homogenous and uniform spheres like particles.

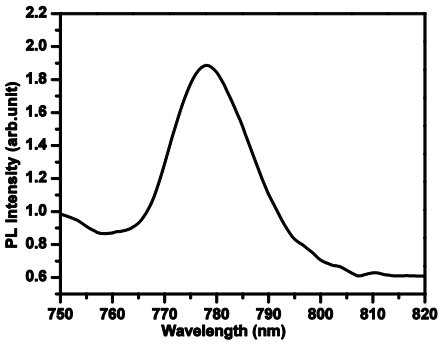

Figure 4. Photoluminescence spectra of the synthesized $CuSbS_2$ nanoparticles

The Photoluminescence spectra that are recorded with an excitation wavelength of 520 nm are as shown in Fig.4. The pattern in the PL spectra illustrates that the emission is near IR region with a band edge emission of 778 nm.

The electrochemical behavior of the material is studied using the impedance analysis and Cyclic Voltammetry is shown in Fig.5. Here a small amount of tetrabutylammonium perchlorate is added as an electrolyte. The three electrodes used for the impedance analysis such as $CuSbS_2$ as working electrode, Calomel the reference electrode and platinum as the counter electrode. The aim of impedance measurement is to understand the materials performance based on the transport resistance.

The obtained Nyquist plot is shown in Fig. 5 (a) which depicts a semicircular pattern with a diagonal line of 45° angle. This semi circle arc is small suggesting the small value of charge transfer resistance of $CuSbS_2$ nanoparticles based photo electrode and is found to be 5 KΩ. The diagonal line of 45° angle shows the diffusion process of the material. Hence it can be concluded that the materials small charge transfer resistance and the long electron life time leads to have an excellent performance in solar cell applications [15]. To

International Journal of
Scientific Research in Science and Technology (IJSRST)
Print ISSN : 2395-6011, Online ISSN : 2395-602X
International Conference on Advanced Materials
Held on 14, 15 December 2017, Organized by Department of Physics,
St. Joseph's College, Trichy, Tamilnadu, India

understand the electrochemical reaction of the $CuSbS_2$ nanoparticles cyclic Voltammetry analysis is carried out and the obtained pattern is shown in Fig. 5(b). The peaks suggest that the ternary $CuSbS_2$ nanoparticles involve two electrochemical reactions that are having two electron transfer system. These peaks are at 1.25 V and -0.68 V.

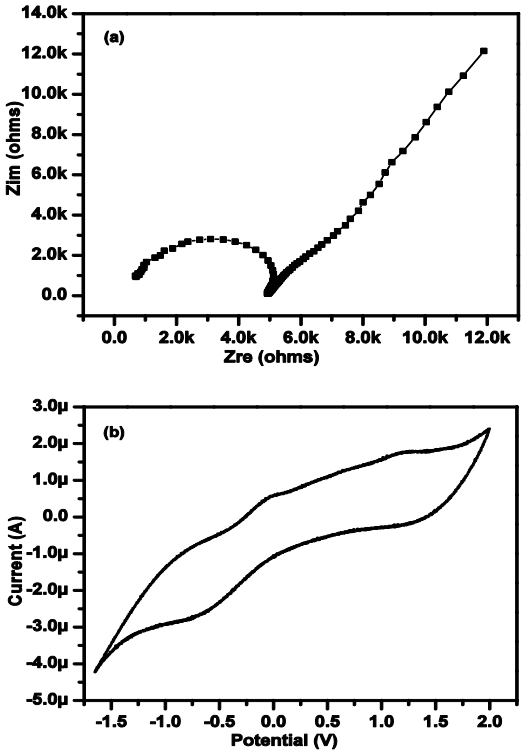

Figure 5. (a) Nyquist plot measured from Electrochemical Impedance Spectroscopy and (b) Cyclic Voltammetry profile of the obtained $CuSbS_2$ nanoparticles

4. Conclusions

$CuSbS_2$ nanoparticles were synthesized by facile solvothermal method. Here ethylenediamine and PVP played major role for the production of well defined sphere like $CuSbS_2$ nanoparticle without agglomeration. The average crystallite size of the obtained $CuSbS_2$ nanoparticle was found to be 7.2 nm. The orthorhombic crystal structure of the synthesized nano powder was confirmed by XRD. From FESEM analysis it was clear that obtained $CuSbS_2$ nanoparticles are homogenous sphere like particles and the DLS analysis gave the hydrodynamic average size of 7 nm. PL emission spectrum shows that the emission was near IR region. Electrical studies based on CV analysis revealed that the material was having two electron transfers. The above mentioned results highlight $CuSbS_2$ nanoparticle are promising p-type absorber material for photovoltaic applications.

Acknowledgement

One of the authors Ms. Bincy John thanks the University Grants Commission of India, for providing research fellowship (Maulana Azad National Fellowship, Grant No: F1-17.1/2016-17/MANF-2015-17-KER-53161). This research was performed using facilities at CeNSE, Indian Institute of Science, Bangalore, funded by the Department of Electronics and Information Technology (Deity), Govt. of India.

References

[1] Rabhi, A., Kanzari, M. and Rezig, B., "Growth and vacuum post-annealing effect on the properties of the new absorber $CuSbS_2$ thin films", Mater. Lett., **62,** 2008, pp.3576–3578.

[2] Garza, C., Shaji, S., Arato, A.,erez Tijerina, E., Alan Castillo, G., Das Roy and T.K., Krishnan B., "P-Type $CuSbS_2$ thin films by thermal diffusion of copper into Sb_2S_3", Sol. Energy Mater. Sol. Cells, **95,** 2011, pp. 2001-2005.

[3] Suriakarthick, R., Nirmal Kumar, V., Shyju, T.S. and Gopalakrishnan, R., "Effect of substrate temperature on copper antimony sulphide thin films from thermal evaporation", J. Alloys Compd., **651,** 2015, pp. 423–433.

[4] Ramasamy, K., Tien, B., Archana, P. S. and

Gupta, A., "Copper antimony sulfide ($CuSbS_2$) mesocrystals: A potential counter electrode material for dye-sensitized solar cells", Mater. Lett., **124,** 2014, pp. 227–230.

[5] Ramasamy, K., Sims, H., Butler, W. H. and Gupta, A., " Selective Nanocrystal Synthesis and Calculated Electronic Structure of All Four Phases of Copper Antimony–Sulfide", Chem. Mater., **26,** 2014, pp. 2891–2899.

[6] Yan, C., Su, Z., Gu, E., Cao,T., Yang, J., Liu, J., Liu, F., Lai, Y., Li, J. and Liu, Y.," Solution-based synthesis of chalcostibite ($CuSbS_2$) nanobricks for solar energy conversion": Supplement., RSC Adv., **2,** 2012, pp. 10481.

[7] McCarthy, C. L., Cottingham, P., Abuyen, K., Schueller, E.C., Culver, S.P. and Brutchey, R.L.,"Earth Abundant $CuSbS_2$ Thin Films Solution Processed from Thiol-Amine Mixtures", J. Mater. Chem. C, **4,** 2016, pp. 6230-6233.

[8] Septina, W., Ikeda, S., Iga, Y., Harada, T. and Matsumura, M., " Thin film solar cell based on $CuSbS_2$ absorber fabricated from an electrochemically deposited metal stack", Thin Solid Films, **550,** 2014, pp. 700–704.

[9] Colombara, D., Peter, L. M., Rogers, K. D., Painter, J. D. and Roncallo, S., "Formation of $CuSbS_2$ and $CuSbSe_2$ thin films via chalcogenisation of Sb-Cu metal precursors", Thin Solid Films, **519,** 2011, pp. 7438–7443.

[10] Colombara, D., Peter, L. M., Rogers, K. D. and Hutchings, K., " Thermochemical and kinetic aspects of the sulfurization of Cu–Sb and Cu–Bi thin films", J. Solid State Chem., **186,** 2012, pp. 36–46.

[11] Manolache, S., Duta, A., Isac, L., Nanu, M., Goossens, A. and Schoonman, J.," The influence of the precursor concentration on $CuSbS_2$ thin films deposited from aqueous solutions", Thin Solid Films, **515,** 2007, pp. 5957-5960.

[12] Choi, Y.C., Yeom, E.J., Ahn, T.K. and Seok, S. Il., "$CuSbS_2$-sensitized inorganic-organic heterojunction solar cells fabricated using a Metal thiourea complex solution", Angew. Chemie - Int. Ed., **54,** 2015, pp.4005-4009.

[13] Bincy, J., Genifer, S. G. and Leo, A. R., "Investigating the effect of solvents for the preparation of $CuSbS_2$ nanoparticles by solvothermal method", **50007,** (2017).

[14] Bincy, J., Genifer, S.G. and Leo, A. R., "Temperature dependent solvothermal synthesis of Cu-Sb-S nanoparticles with tunable structural and optical properties, Mater. Res. Bull., 95, 2017, pp. 267–276.

[15] Han, M., Jia, J. and Wang, W.," A novel $CuSbS_2$ hexagonal nanobricks @ TiO_2 nanorods heterostructure for enhanced photo electrochemical characteristics, J. Alloys Compd., 2017, DOI: 10.1016/j.jallcom.2017.02.185.

International Journal of
Scientific Research in Science and Technology (IJSRST)
Print ISSN : 2395-6011, Online ISSN : 2395-602X
International Conference on Advanced Materials
Held on 14, 15 December 2017, Organized by Department of Physics,
St. Joseph's College, Trichy, Tamilnadu, India

Role of ZnO as a Transparent Layer in Thin Film Solar Cells Using Spray Pyrolysis Technique

R. Anne Sarah Christinal[1], G. Genifer Silvena[1], Bincy John[1], Sujay Chakravarty.[2], A. Leo Rajesh[1*]

[1]Department of Physics, St. Joseph's College (Autonomous), Tiruchirappalli - 620002, Tamilnadu, India

[2]UGC-DAE Consortium for Scientific Research, Kalpakkam, Tamilnadu 603104, India

*Corresponding author's Email: aleorajesh@gmail.com

Tel.: +91-9444122070

Abstract

A versatile and cost effective spray pyrolysis technique was used to prepare the Zinc Oxide (ZnO) thin film on a glass substrate. The feature of the obtained film was characterized using Glancing incidence angle X-ray diffraction (GIXRD), Scanning Electron Microscope (SEM), UV-Visible Spectroscopy and Photoluminescence (PL). GIXRD confirmed that the structure of the ZnO film was polycrystalline having wurtzite structure. SEM image revealed root-like morphology on the surface of ZnO thin film and the shortest root diameter was about 91.2 nm. From UV-Visible spectrum an optical transmittance of about 85% in the visible region and direct optical band gap energy of 3.2 eV was calculated. The PL analysis showed that the film exhibited a strong emission peaks at violet and green region. From the characterized results, spray pyrolysis is the viable technique to deposit ZnO thin film on a glass substrate, which can be used as a transparent layer in thin film solar cells.

Keywords: ZnO Thin Film, Spray Pyrolysis, Transparent layer, Solar Cell.

1. Introduction

Recently, Zinc oxide film has gained more attention due to its potential use in many applications such as transparent conductive electrode, solar cell, gas sensor, light emitting diodes, lasers and varistors which attributed to its wide and direct band gap (3.37 eV) and a larger exciton binding energy (60 meV) [1]. In particular, ZnO is nontoxic and also provides good transparency, high electron mobility, chemical and thermal stability which perfectly matches the requirement of transparent contacts in photovoltaic cells [2]. ZnO thin films have been deposited by different deposition techniques like chemical vapour deposition (CVD) [3], magnetron sputtering [4], pulsed laser deposition (PLD) [5], electron beam evaporation (EBM) [6]. Most of these methods need high vacuum and high operating temperatures to work, which make them high cost techniques. Chemical based solution routes such as sol–gel [7], co-precipitation [8] and spray pyrolysis [9] can be considered as simple and economic methods involving low cost equipment and raw materials.

Among these chemical based techniques, spray pyrolysis is a useful alternative to the traditional methods for obtaining pure ZnO thin films. It is of particular interest because of simplicity, low cost of the source materials, producing high quality films and minimal waste production. The spray pyrolysis process allows the coating of large surface area and uniform deposition with very thin layers with specific composition, morphology, good adhesion between the deposited films [10].

International Journal of
Scientific Research in Science and Technology (IJSRST)
Print ISSN : 2395-6011, Online ISSN : 2395-602X
International Conference on Advanced Materials
Held on 14, 15 December 2017, Organized by Department of Physics,
St. Joseph's College, Trichy, Tamilnadu, India

In the present work, ZnO thin film is prepared using the spray pyrolysis technique and show high optical transmittance in UV, VIS and IR regions which is suitable material for transparent layer on solar cell. The structural, morphological, optical properties of the deposited ZnO thin film is studied using Glancing incidence angle X-ray diffraction (GIXRD), scanning electron microscope (SEM), UV-visible spectroscopy and fluorescence spectroscopy.

2. Experimental Procedure

Thin film of ZnO was deposited on a glass substrate by simple and economical spray pyrolysis technique. A solution of 0.1 M using zinc acetate dihydrate [Zn (CHCOO).2H_2O] was used as a precursor prepared by dissolving in mixture of deionized water and isopropyl alcohol (2: 3) volume ratio. The film has been deposited on ultrasonically cleaned glass substrates kept at 450˚C. The nozzle was at a distance of 20 cm from the substrate during deposition. The solution flow rate was held 4ml/min. Compressed air was used as a carrier gas. The pressure was maintained at 1.2 kg/cm^2. This results in the formation of well adherent and uniform ZnO film. The as deposited film of ZnO was transparent with light whitish color.

The crystal structure and phase identification of the prepared ZnO thin film was characterized using Glancing incidence X-ray diffractometer (XPERT PRO) at a scanning range of 20˚ to 80˚ with CuKα1 source radiation (= 1.54051 Å). The surface morphology of the thin film was examined using scanning electron microscope (SEM). The optical properties of the ZnO thin film were determined by UV-Visible spectrometer (Model-lambda) in the wavelength range of 300-1100 nm. The room temperature photoluminescence characteristic of ZnO film was investigated using Perkin Elmer (Model- Lambda 45).

3. Results and Discussion

The crystallinity, crystallographic orientation and phase evaluation of the ZnO thin film prepared at 450˚C is studied by Glancing incidence x-ray diffraction (GIXRD) is shown in Fig. 1. The diffraction peaks obtained between the 2θ ranges are from 20˚ – 80˚. Seven diffraction peaks were observed at 2θ = 31.9˚, 34.6˚, 36.5˚, 47.7˚, 56.9˚, 63.0˚, 69.5˚ which can be attributed to (100), (002), (101), (102), (110), (103) and (112) planes of ZnO thin film obtained by IPA solution. The sharp and narrow diffraction of the peaks demonstrated that all ZnO thin film is of good crystalline in quality and also found that, the films are polycrystalline with hexagonal wurtzite structure. Here the film exhibits highest peak at (101) plane with preferential orientation which is located at 2θ = 36.5˚. This can be due to the highest density of Zn atoms in this plane. The other small peaks which are shown in figure are due to the non-decomposed organic compounds or impurities in the solution used for deposition of the film.

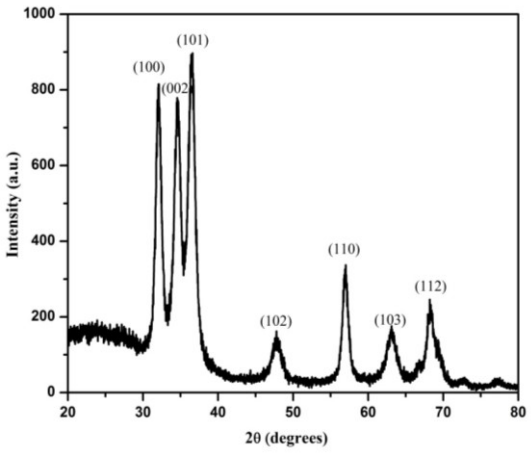

Figure 1. GIXRD pattern of ZnO thin film

International Journal of
Scientific Research in Science and Technology (IJSRST)
Print ISSN : 2395-6011, Online ISSN : 2395-602X
International Conference on Advanced Materials
Held on 14, 15 December 2017, Organized by Department of Physics,
St. Joseph's College, Trichy, Tamilnadu, India

The crystallite size of the deposited film is calculated using the Scherer's equation [11]

$$D = \frac{0.9\lambda}{\beta \cos\theta}$$

where D is the crystallite size, λ is the wavelength of the target CuKα1 (= 1.54051 Å), β is the full-width half maximum value and θ is the position of respective Bragg peaks. The crystallite size of ZnO is calculated along this plane, which gives the value of 10 nm.

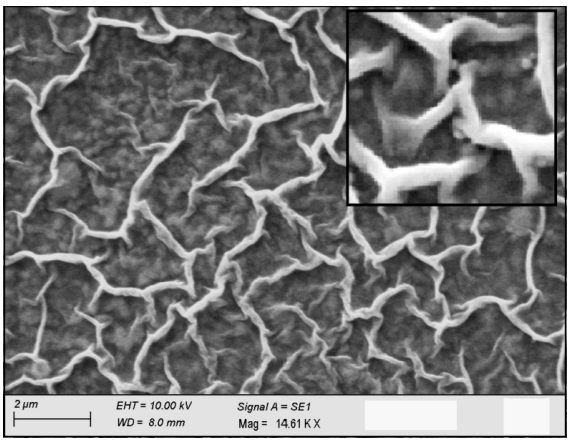

Figure 2. SEM image of ZnO thin film

The surface morphology and size of the zinc oxide thin film using scanning electron microscope technique is shown in Fig 2. SEM micrograph reveals that the ZnO film exhibit root-like structure. The texture of the film is found to be crack free and having uniform morphology over the entire film. In ZnO image, the particles are linked to each other to make long structure of ZnO which is called root-like morphology [12]. The average diameter of the shorter root-like is about 91.2 nm.

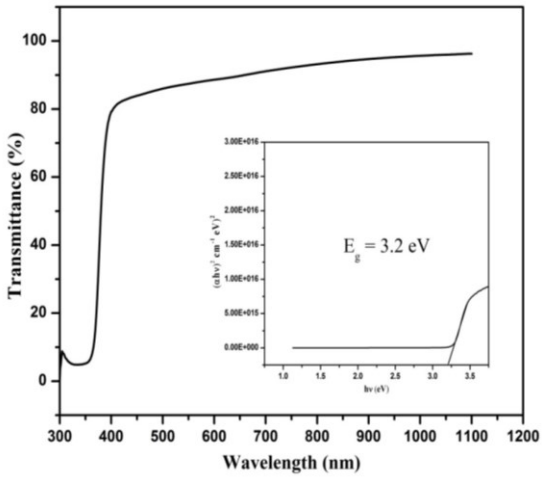

Figure 3.1. UV transmittance spectrum with tauc plot of ZnO thin film (inset shows the band gap energy of the material)

The optical transmission spectrum obtained in the wavelength range of 300 to 1200 for the deposited ZnO film is shown in the Fig 3.1. From UV–Visible spectrum it is clear that the film shows high transparency in the visible region with an average transmittance reaching up to 85%, which indicates the better crystal structure with less defects. A sharp ultraviolet cut-off at approximately 333 nm is observed for the prepared film. The high transparency obtained for the ZnO film in the visible region shows its potential application in the solar device applications.

The optical band gap energy is calculated using Tauc plot is shown as the inset in Fig 3.1. The direct band gap energy obtained from the extrapolation of the linear part of the curve in the plot of hν in eV versus $(\alpha h\nu)^2$ in $(cm^{-1}\ eV)^2$. The absorption coefficient (α) of the deposited film is determined from the equation related to the photon energy is given by

$$\alpha h\nu = A\,(h\nu - Eg)^n$$

where Eg is the energy band gap of the semiconductor, A is a constant, and n = ½ for direct

International Journal of
Scientific Research in Science and Technology (IJSRST)
Print ISSN : 2395-6011, Online ISSN : 2395-602X
International Conference on Advanced Materials
Held on 14, 15 December 2017, Organized by Department of Physics,
St. Joseph's College, Trichy, Tamilnadu, India

allowed transitions. The Tauc plot gives the direct band gap of the samples and calculated band gap is found to be 3.21 eV which is matching well with of the reported values.

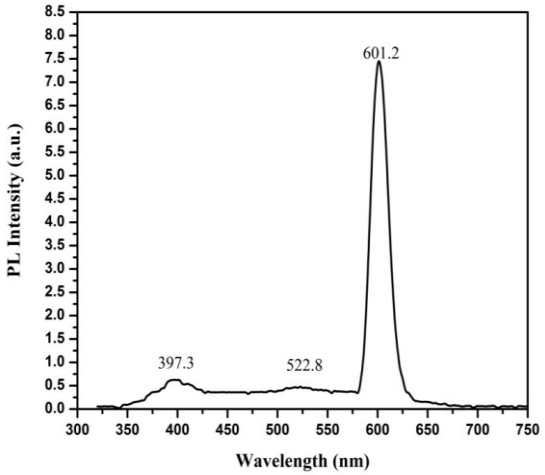

Figure 3.2. Photoluminescence spectrum of ZnO thin film

The luminescence property of deposited thin films is studied using photoluminescence spectroscopy. The photoluminescence (PL) spectrum of prepared ZnO thin film is depicted in fig 3.2. The spectrum of ZnO film showed that the near band edge (NBE) emission is in the UV region and the deep-level emission (DLE) in the visible spectrum composed of green and red bands [13]. A low intensity with broad emission peaks centered at 397.3 nm in the UV region is attributed to the recombination of free excitons in the surfaces of ZnO particles. And also another low intensity with broad peak located at 522.8 nm in the green emission region which is due to impurities and structural defects. A strong peak located at 601.2 nm, which is in red band emission that can be attributed to the presence of excess oxygen.

4. Conclusions

In this present work, the highly transparent ZnO thin film was prepared by spray pyrolysis technique. The GIXRD pattern showed that the deposited film had a polycrystalline hexagonal wurtzite structure with strong orientation along (101) plane with an average crystalline size was about 10 nm. The SEM image revealed that the ZnO film exhibited root-like morphology with uniform distribution. The investigation from UV-Visible spectrum showed that the obtained film was highly transparent in the visible region with an average transmittance reaching upto 85% with the better crystalline nature with less defects. PL spectrum of the film showed emission in both UV and visible region. The simple and low-cost spray pyrolysis technique offers an attractive alternative to the PVD or CVD fabricated ZnO films. The above mentioned results showed that the deposited ZnO film with good crystallinity and high transparency is a promising n-type material for thin film solar cell.

References

[1] Godbole, B., Badera, N., Shrivastava, S., Jain, D. and Ganesan, V., "Growth Mechanism of Zno Films Deposited by Spray Pyrolysis Technique", Mater. Sci. Appl., 2, 2011, pp. 643–648.

[2] Vimalkumar, T.V.," Highly conductive and transparent ZnO thin film using Chemical Spray Pyrolysis technique : Effect of doping and deposition parameters", Cochin University of Science and Technology, Cochin, Kerala, Doctoral Thesis, 2011.

[3] Purica, M., Budianu, E., Rusu, E., Danila, M., and Gavrila, R., "Optical and structural investigation of ZnO thin films prepared by

chemical vapor deposition (CVD)", Thin Solid Films, 402-403, 2015, pp. 485-488.

[4] Dave, P.Y., Patel, K.H., Chauhan, K.V., Chawla, A.K. & Rawal, S.K., "Examination of Zinc Oxide Films Prepared by Magnetron Sputtering", Procedia Technol., 23, 2016, pp.328–335.

[5] Ramamoorthy, K.," Development of a novel high optical quality ZnO thin films by PLD for III-V opto electronic devices", Curr. Appl. Phys., 6, 2006, pp. 103-108.

[6] Giri, P. K.," Studies on zinc oxide nanorods grown by electron beam evaporation technique", Synth. React. Inorganic, Met. Nano-Metal Chem., 37, 2007, pp. 437–441.

[7] Anand, V.K., Sood, S.C. and Sharma, A., "Characterization of ZnO thin film deposited by sol-gel process", AIP Conf. Proc., 1324, 2010, pp. 399–401.

[8] Kolodziejczak-Radzimska, A. and Jesionowski, T.," Zinc oxide-from synthesis to application: A review", Materials (Basel), 7, 2014, pp. 2833–2881.

[9] C. Nehru, L., Umadevi, M., and Sanjeeviraja, C.," Studies on Structural, Optical and Electrical Properties of ZnO Thin Films Prepared by the Spray Pyrolysis Method", Int. J. Mater. Eng., 2, 2012, pp. 12–17.

[10] Tarwal, N. L.," Growth of multifunctional ZnO thin films by spray pyrolysis technique", Sensors Actuators, A Physl., 199, 2013, pp. 67–73.

[11] Mahmoud, F.A., and Kiriakidis, G.," Nanocrystalline ZnO Thin Film for Gas Sensor Application", Bull. Mater. Sci., 5, 2009, pp. 15–20.

[12] Komaraiah, D., "Optical, Structural and Morphological Properties of Photocatalytic ZnO Thin Films Deposited by Pray Pyrolysis Technique"., Mod. Res. Catal., 5, 2016, pp. 130–146.

[13] Inguva, S., Vijayaraghavan, R.K., McGlynn, E., and Mosnier, J.P.," Highly transparent and reproducible nanocrystalline ZnO and AZO thin films grown by room temperature pulsed-laser deposition on flexible Zeonor plastic substrates", Mater. Res. Express, 2, 2015, pp.96401.

International Journal of
Scientific Research in Science and Technology (IJSRST)
Print ISSN : 2395-6011, Online ISSN : 2395-602X
International Conference on Advanced Materials
Held on 14, 15 December 2017, Organized by Department of Physics,
St. Joseph's College, Trichy, Tamilnadu, India

The Electrical Studies on Sol-Gel Routed Molybdenum Oxide Thin Film

P. Adal Arasu [1], R. Victor Williams [2]

[1]Department of Physics, St. Joseph's College, Trichy, Tamil Nady, India

Corresponding Author: mr.adalphysics@gmail.com

Abstract

This paper investigates electrical properties of sol-gel routed spin coated Molybdenum trioxide (MoO_3) thin films. Prepared films were annealed at 400 °C. The phase transformation from amorphous to α-orthorhombic phase with preferential orientation (0 2 2) has been found by XRD for the film annealed at 400 °C. The vibration modes of α-orthorhombic MoO_3 have been examined by Raman spectrum. The predominant Raman's band of α-orthorhombic MoO_3 thin film has been found at the frequency range 1000–600 cm^{-1}. Using UV-Vis spectrum the band gap of the film is found to be 3.3-3.8eV. The surface morphology of the MoO_3 films has been examined by scanning electron microscope. The resistivity of the film found to be 1.4 x 10^7 Ωm. The AC conductivity measurement of MoO_3 film has been carried out in the frequency range 10-10^6 Hz. The frequency dependence of the impedance has been plotted in the complex plane. The Variation of the capacitance and dielectric constant of MoO_3 film with respect to temperature and frequency has been analyzed. Tunability of capacitance and figure of merit of the film are also determined.

Keywords: Sol-gel, electrical conductivity, Dielectric constant, capacitance, tunability, Curie-temperature, Figure of merit.

Introduction

In modern technological era, the need for new materials with good dielectric behavior has increased. The wide band gap transition metal oxides with notable dielectric behavior have attracted the researchers to fabricate the device with low leakage current level for their operations. The metal oxides exhibit different Optoelectronic properties such as electrochromic, photochromic, gas sensing and some of them exhibit high dielectric constant and low dielectric loss that make them a best alternative for conventional SiO_2 in the fabrication of DRAM and super capacitors. The molybdenum trioxide is one of the transition metal oxides which exhibit good dielectric behavior. Different deposition techniques such as chemical vapor deposition [1], electrode deposition [2], electron beam deposition [3], sputtering [4] and spray pyrolysis [5] have been employed to produce MoO_3 films. The sol-gel technique has been receiving considerable attention to prepare the high quality films at low cost with simpler deposition procedure [6]. In this present work, the sol-gel routed spin coating technique has been used for obtaining thin film with required thickness. Prepared films were annealed at 400° C. This work investigates the structural, optical and electrical properties of the molybdenum trioxide thin film. The novelty of the present work is to study the effect of temperature and concentration on the electrical properties of MoO_3 thin film respectively.

1. Materials and Method

The precursor solution was prepared by mixing MoO_3 powder (99.999%, SigmaAldrich) into excess H_2O_2 (30%, Sigma-Aldrich) and the solution was refluxed for 30 minutes at 60°C in air. The resulting yellow coloured solution was cooled to room temperature and left for gellation and during the gellation time the viscosity and concentration of the solution were adjusted by adding polyethylene glycol (average Mn 200, Sigma-Aldrich) and 2-ethoxyethanol (Sigma-Aldrich). The solution with sufficient viscosity was spin-coated on clean FTO substrates with a sheet resistance of 10Ω/square. The Film was coated as

International Journal of
Scientific Research in Science and Technology (IJSRST)
Print ISSN : 2395-6011, Online ISSN : 2395-602X
International Conference on Advanced Materials
Held on 14, 15 December 2017, Organized by Department of Physics,
St. Joseph's College, Trichy, Tamilnadu, India

multiple layers to obtain the required thickness. After each layer of coating the film was dried at 100° C for about 5 minutes. The solution-processed films were annealed at 400° C for 2 hours by keeping the rate of temperature at 4°C per minute. The thickness of the film was measured by stylus profilometer (Mitutoyo, SJ-301). The X-ray diffraction for phase identification was performed using XPERT-PRO X-ray diffractometer with Cu-Kα (λ = 0.154nm) radiation source. The surface morphology of MoO_3 film was examined by VEGA3 TESCAN scanning electron microscope. The optical characterization was done by Perkin Elmer Lambda - 35 UV-Visible spectrometer. The measurements of dielectric properties were carried out using a MIM structure. Capacitance vs Voltage, dielectric constant and dielectric loss measurements were carried out using Impedance analyzer (Princeton Applied Research, VersaSTAT MC) and LCRZ meter. Using the impedance data the Nyquist plot was plotted and the possible equivalent circuit has been identified. Using the temperature variable capacitance measurement set-up the phase transition temperature of the MoO_3 has been determined.

2. Structural parameters

The XRD pattern of MoO_3 thin film of thickness of 2.5 μm (Figure 1) exhibits amorphous nature for the film annealed below 250°C and crystalline nature for the film annealed at higher temperatures. The films annealed at 400°C exhibit α-orthorhombic phase with preferential orientation along (0 2 0) plane. The peak intensity increases with increase of concentration, due to the increase in grain size of the crystal lattice [7]. The various structural parameters like crystallite size (D), dislocation density (δ), strain (ε), and number of crystallites per unit area (N) of MoO_3 film are calculated (Table 1). The crystallite size D is evaluated from Scherrer formula:

$$D = \frac{0.94\lambda}{\beta \cos\theta} \qquad \ldots (1)$$

where β is full width at half maximum of XRD peak. The crystallite size increases with increase of concentration. According to the theory of kinematical scattering the narrow peak is due to larger crystallite size and fewer defects present in the crystals. In the present work, the sharp and higher peak of XRD confirm larger crystallite size and improvement in crystalline nature [8]. The dislocation density is evaluated from the relation [9]:

$$\delta = \frac{1}{D^2} \qquad \ldots (2)$$

The decrease of dislocation density with increase of concentration indicates the reduction of defects. The strain (ε) and number of crystallites per unit area (N) of the film is calculated from the relations [9]:

$$\varepsilon = \frac{\beta \cos\theta}{4} \qquad \ldots (3)$$

$$N = \frac{t}{D^3} \qquad \ldots (4)$$

where, t is thickness of the thin film. The reduction of strain with increase of concentration reveals the enhancement of crystalline nature. The number of crystal lattice per unit area decreases with increases of concentration due to increase of crystallite size. The surface morphology of the film has been investigated by SEM (Figure 2). It shows that the film is homogeneous and the grain boundaries are evenly distributed though out the sample.

Table 1. Structural properties

Concentration (mol)	grain size (nm)	Dislocation density(δ)(x 10^{-18})	strain (ε)	Number of crystal lattice (N) x 10^{21})
0.5	29	3.18	0.007	7.08
1	34	2.49	0.005	4.36
1.5	61	2.34	0.005	1.07
2	74	1.9	0.003	1.91

Crystallite size (D), Strain (ε), Dislocation Density (δ), Number of Crystallites per unit area(N).

International Journal of
Scientific Research in Science and Technology (IJSRST)
Print ISSN : 2395-6011, Online ISSN : 2395-602X
International Conference on Advanced Materials
Held on 14, 15 December 2017, Organized by Department of Physics,
St. Joseph's College, Trichy, Tamilnadu, India

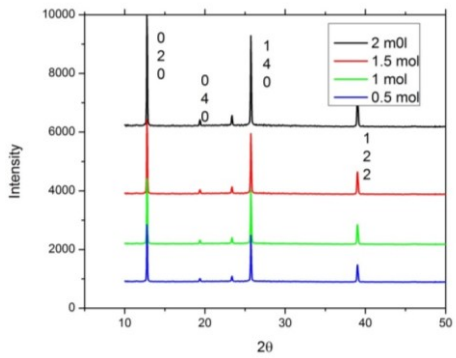

Figure 1. XRD spectrum of MoO_3 Thin film

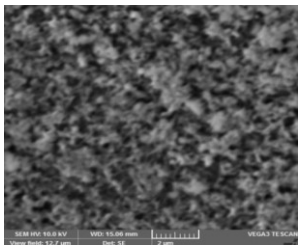

2A

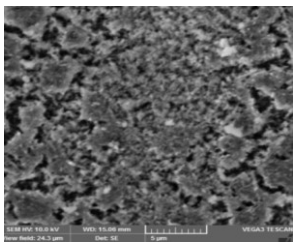

2B

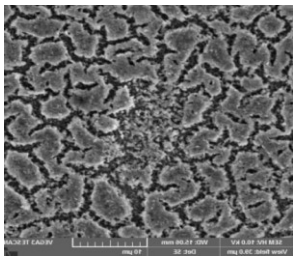

2C

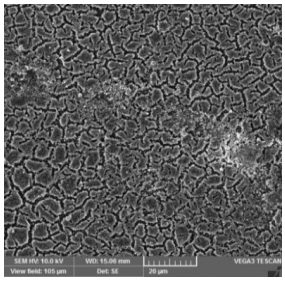

2D

Figure 2: SEM images of MoO_3 Thin film

2.1. Micro Raman Studies

A typical Raman spectrum of the MoO_3 thin film is shown in (Figure 3). The vibration modes appearing in the frequency ranges of 1000–600 cm^{-1} and 600–200 cm^{-1} correspond to the stretching and deformation modes respectively. The narrow band at 994 cm^{-1} is assignable to the anti symmetric $\nu_{as}(Mo{=}O)A_g$ stretching, in which the strong band at 830 cm^{-1} represents the symmetric $\nu_s(Mo{-}O_3{-}Mo)A_g$ stretching. The weak and broad bands at 666 and 470 cm^{-1} are ascribable to the anti symmetric $\nu_{as}(Mo{-}O_2{-}Mo)B_{2g}$ stretching and bending respectively. The bands at 377 and 364 cm^{-1} correspond to the $\delta\ (O_2{=}Mo{=}O_2)B_{1g}$ scissor. The Raman band at 830 cm^{-1} reveals the formation of α orthorhombic phase in MoO_3 film at higher annealing temperature [10].

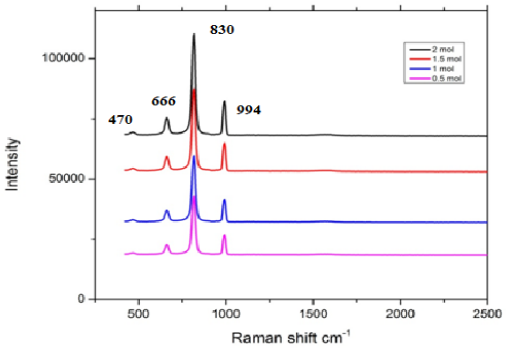

Figure 3. Raman Spectrum of MoO_3 Thin film

3. Optical Properties

The optical transmission spectra of MoO_3 films prepared at 400°C with various concentration exhibit good transparency at 570 nm (Figure 4). The film prepared at 0.5 mol exhibits maximum transparency of 80%. The transparency of the film decreases with increase of the concentration. The films prepared at 2 mol exhibits only 40% of transparency at 570 nm that might be due to the free carrier absorption and formation of micro crystallites leading to the scattering of light[11]. The higher transmittance in the higher wave length region indicates the reduction in optical band gap (E_g) with increase of the concentration.

International Journal of
Scientific Research in Science and Technology (IJSRST)
Print ISSN : 2395-6011, Online ISSN : 2395-602X
International Conference on Advanced Materials
Held on 14, 15 December 2017, Organized by Department of Physics,
St. Joseph's College, Trichy, Tamilnadu, India

From the transmission spectrum the absorption coefficient (α) is determined by the relation[12].

$$\alpha = \frac{1}{t}\ln T \qquad \ldots (5)$$

where t is thickness of the film and T is transmittance. The band gap of the film is determined from the relation [13].

$$(\alpha h\nu)^{\frac{1}{n}} = A\left(h\upsilon - E_g\right) \qquad \ldots (6)$$

A is the energy dependent constant, E_g optical band gap energy of the material and n = ½, 2, 3/2 and 3 corresponding to the allowed direct, allowed indirect, forbidden direct and forbidden indirect transitions respectively. The optical band gap depends upon the absorption coefficient (α). The MoO_3 is found to be direct band gap material (n= 1/2). The extrapolation of linear portion (α=0) gives the optical band gap energy of the film. Figure 5 shows the plot of $(\alpha h\upsilon)^2$ vs hυ for MoO_3 at different concentration. It reveals that the optical band gap of the MoO_3 film decreases with increase of the concentration that may be due to the formation of oxygen ion vacancies and the improvement of crystallinity in the film [11]. This inference is consistent with our XRD finding. The optical band gap value of MoO_3 film prepared at 0.5 mol, 1.5 mol and 2 mol are 3.8, 3.5and 3.3eV respectively.

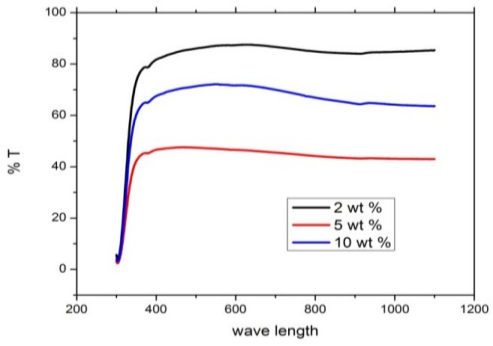

Figure 4. UV Transmittance spectrum of MoO_3 Thin film

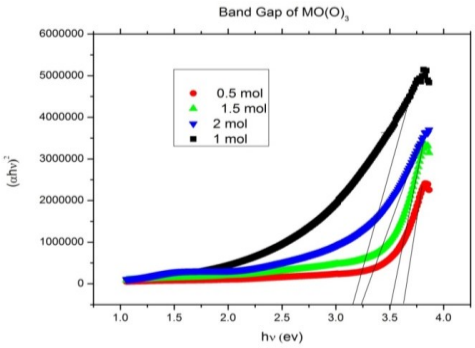

Figure 5. The Band gap of MoO_3 Thin film

4. Electrical Properties

The resistivity measurement of MoO_3 film carried out by two-probe method, V-I plot of MoO_3 (Figure 6A) film with different concentration shows the increment in the conductivity with increase of concentration. The resistivity of the film found to be 1.4 x 10^7 Ωm for higher concentration. The measurements of dielectric properties were carried out using a MIM structure .The value of dielectric constant decreases with increase of frequency (Figure 6B). It might be due to alignment of permanent dipoles along with the direction of electric field at lower frequency and it contributes to the total polarization of the dielectric material. On the other hand, at higher frequency as the field rapidly vary the dipole can no longer follow the field [14]. Hence their contribution to the polarization becomes negligible and it leads to increment in the dielectric loss and decrement in dielectric constant (Figure 8). The increment in the dielectric constant with increase of temperature is attributed to bulk effect of the system and also due to increase of energy absorption by the dielectric material [14] (Figure 7).

Table 2. Electrical Properties

Concentration (mol)	(ρ) Ωm	(σ) x 10^{-8} Ω^{-1} m^{-1}
0.5	3.7 x 10^8	2.6
1	5.5 x 10^7	1.8

International Journal of
Scientific Research in Science and Technology (IJSRST)
Print ISSN : 2395-6011, Online ISSN : 2395-602X
International Conference on Advanced Materials
Held on 14, 15 December 2017, Organized by Department of Physics,
St. Joseph's College, Trichy, Tamilnadu, India

1.5	$3.5x10^{7}$	1.5
2	1.4×10^{7}	1.3

Resistivity (ρ) Ωm, conductivity (σ) x 10^{-8} Ω^{-1} m^{-1}

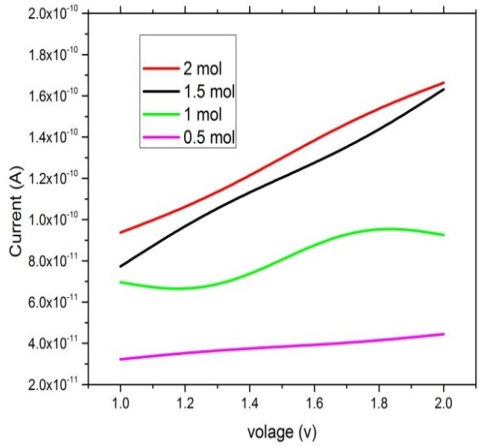

Figure 6A. Resistivity measurement of MoO_3 Thin film

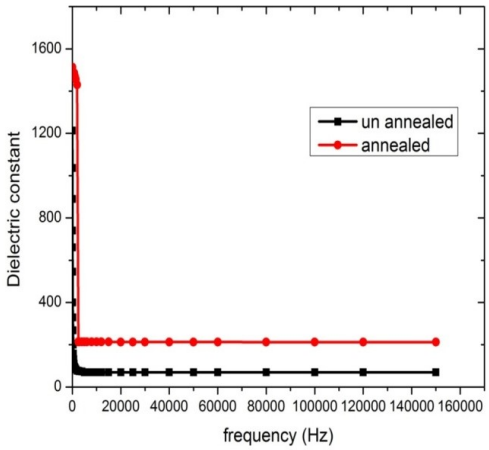

Figure 6B. Frequency dependent Dielectric constant of MoO_3 Thin film

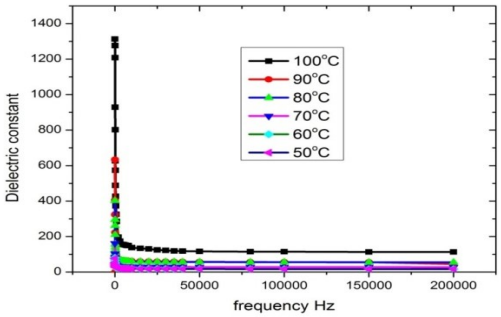

Figure 7. Temperature dependent Dielectric constant of MoO_3 Thin film

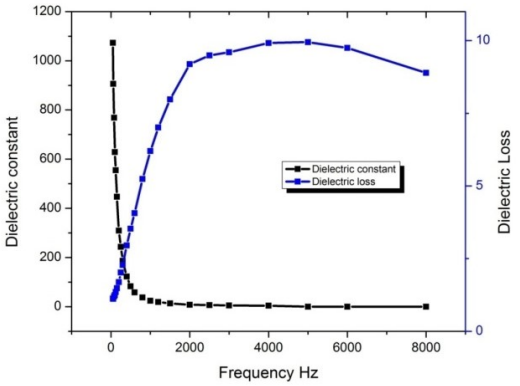

Figure 8. Dielectric constant Vs Dielectric Loss

Figure 9A & 9B shows that the variation of the capacitance and dielectric constant of the MoO_3 thin film with respect to temperature, it fits very well with curie–wiess law. At 260°C the capacitance and dielectric constant reach a maximum value which indicates the phase transition in the material [15]. This temperature is the transition temperature or Curie temperature (T_c), beyond which the material behaves as paraelectric. The above fact is supported by the XRD data. The XRD spectrum of the sample annealed above 250°C reveals the crystalline nature of MoO_3 thin film.

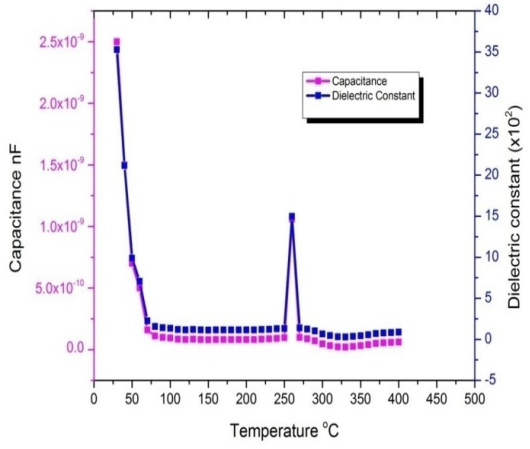

Figure 9A. Curie temperature

International Journal of
Scientific Research in Science and Technology (IJSRST)
Print ISSN : 2395-6011, Online ISSN : 2395-602X
International Conference on Advanced Materials
Held on 14, 15 December 2017, Organized by Department of Physics,
St. Joseph's College, Trichy, Tamilnadu, India

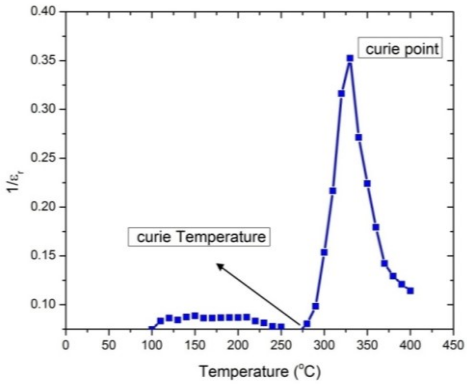

Figure 9B. Curie temperature

The measurement of capacitance with respect to dc electric field was carried out at room temperature for 1 KHz and 100 KHz (Figure 10). The tunability and figure of merit were determined from the following relations [16]:

$$Tunability = \frac{C_{max} - C_{min}}{C_{min}} \times 100 \quad \ldots \quad (7)$$

$$\text{Figure of merit} \frac{\%\ \text{Tunability}}{\%\ \text{dielectric loss}} \quad \ldots (8)$$

where, C_{max} is the capacitance value for zero bias fields. C_{min} denotes the capacitance of applied field. The applied field is in the order of 10^6 V/m. The Tunability and FOM of the MoO_3 film increase with increase of applied potential (Figure 11). The tunability of the dielectric properties of the material might be attributed to internal stress among the grains [17].

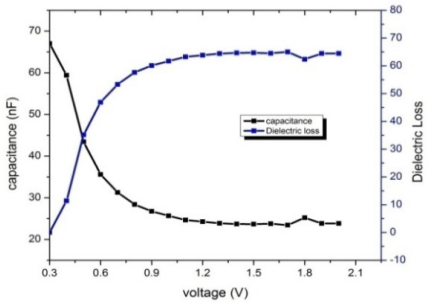

Figure 10. variation of capacitance and dielectric Loss with respect to Voltage

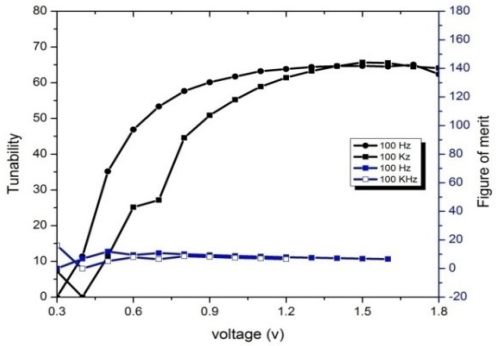

Figure 11. Variation of tenability and figure of merit with respect to Voltage

4.1. The impedance studies

The impedance spectroscopy studies on MoO_3 thin film were carried out by using the complex impedance spectra. It can be fitted with a simple electrical model R_b ($R_{gb}C_{gb}$).where R_b and R_{gb} are bulk and grain boundary resistance respectively and C_{gb} is the capacitance across the grain boundary. The impedance of the film with resistance R_{gb} in parallel with a capacitance C_{gb} is given by the expression [18]

$$z_{gb} = \frac{1}{R_{gb}^{-1} + j\omega C_{gb}} \quad \ldots (9)$$

where $\omega = 2\pi f$.

The above equation can be expressed as

$$\left(\frac{\left(Z'_{gb} - R_{gb}\right)}{2}\right)^2 + Z''_{gb} = \left(\frac{R_{gb}}{2}\right)^2 \quad \ldots (10)$$

where Z'_{gb} and Z''_{gb} are the real and imaginary components of the Z_{gb} respectively. The corresponding plot of the real Z_{gb} against the imaginary component of Z_{gb} (Figure 12 Nyquist plot) is a semi circle of radius $R_{gb}/2$. The R_{gb} and R_b values derived from the intercept at low and high frequency impedance values respectively. The capacitance C_{gb} can be obtained from the maximum value of the reactance. A semicircle at high frequency indicates that the relaxation time of the bulk and the grain boundaries are closer to

International Journal of
Scientific Research in Science and Technology (IJSRST)
Print ISSN : 2395-6011, Online ISSN : 2395-602X
International Conference on Advanced Materials
Held on 14, 15 December 2017, Organized by Department of Physics,
St. Joseph's College, Trichy, Tamilnadu, India

each other [19]. In the mid frequency region linear progress of the diffusion characteristic of MoO_3 is observed. At low frequency region, the capacitive behavior is observed which reveals the characteristic response of blocked diffusion. The impedance response of the grain dominates at high frequency and resistance of the grain R_g is deduced from the left intercept to real axis. The right intercept of the semicircular to real axis z' at low frequency indicates the sum of resistance of grain R_g and grain boundaries R_{gb}. The intercept at the high frequency depicts the resistance of the grain only. The Figure 12(B) shows that the increment in the resistance of the bulk and grain boundaries have been observed, it might be due to increase of grain size by heat treatment.

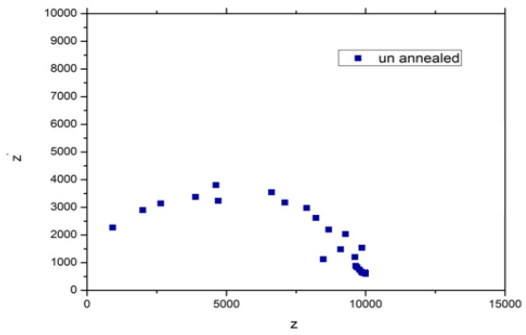

Figure 12 A. Nyquist plot of unannealed MoO_3 Thin film

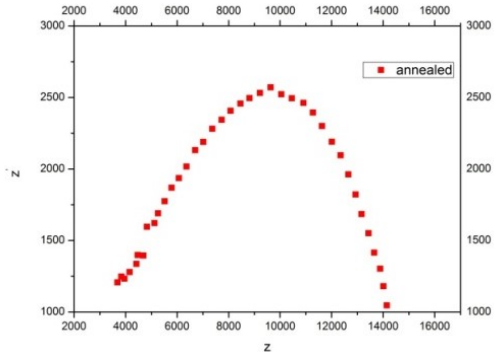

Figure12 B. Nyquist plot of annealed MoO_3 Thin film

Conclusion

The effect of concentration and temperature on the Electrical properties of sol-gel routed spin coated Molybdenum trioxide (MoO_3) thin film has been investigated. The phase transformation from amorphous to α-orthorhombic phase has been found by XRD for the film annealed at higher temperature. The Raman spectrum reveals that, the predominant Raman's band of α-orthorhombic MoO_3 thin film has been found at the frequency ranges of 1000–600 cm^{-1}. The band gap of the film is found to be 3.3-3.8eV. SEM image shows that the film is homogeneous and the grain boundaries are evenly distributed though out the sample. The impedance plot in the complex plane reveals semicircular arc. The system could be represented by an equivalent circuit of parallel resistance–capacitance combination. The Variation of the capacitance and dielectric constant of MoO_3 film with respect to temperature and frequency has been analyzed. Tunability and figure of merit of the film are also determined. The obtained data can be utilized for fabrication of dielectric devices.

References

[1] H.R. An, H.J. Ahn, J.W. Park, High-quality, conductive, and transparent Ga-doped ZnO films grown by atmospheric-pressure chemical-vapor deposition, Ceram. Int. 41 (2015) 2253–2259. doi:10.1016/j.ceramint.2014.10.028.

[2] R.S. Patil, M.D. Uplane, P.S. Patil, Structural and optical properties of electrodeposited molybdenum oxide thin films, Appl. Surf. Sci. 252 (2006) 8050–8056. doi:10.1016/j.apsusc. 2005.10.016.

[3] J. Tamaki, C. Naruo, Y. Yamamoto, M. Matsuoka, Sensing properties to dilute chlorine gas of indium oxide based thin film sensors prepared by electron beam evaporation, Sensors Actuators, B Chem. 83 (2002) 190–194. doi:10.1016/S0925-4005(01)01039-5.

[4] S.-W. Fu, H.-J. Chen, H.-T. Wu, K.-T. Hung, C.-F. Shih, Electrical and optical properties of Al:ZnO films prepared by ion-beam assisted sputtering, Ceram. Int. 42 (2016) 2626–2633. doi:10.1016/j.ceramint.2015.10.067.

[5] K.S. Hwang, Y.S. Jeon, S. Hwangbo, J.T. Kim, Praseodymium-doped calcium stannates phosphor coatings prepared by electrostatic spray deposition, Ceram. Int. 39(2013)8555–8558. doi:10.1016/j. ceramint.2013.04.002.

[6] Q.G. Chi, Y. Cui, Y. Chen, J.Q. Lin, X. Wang, Q.Q. Lei, Low temperature preparation and electric properties of highly (100)-oriented $(Na_{0.85}K_{0.15})_{0.5}Bi_{0.5}TiO_3$ thin films prepared by a sol–gel route, Ceram. Int. 42 (2016) 2497–2501. doi:10.1016/j.ceramint.2015.10.050.

[7] S.A. Vanalakar, S.W. Shin, G.L. Agawane, M.P. Suryawanshi, K. V. Gurav, P.S. Patil, et al., Effect of post-annealing atmosphere on the grain-size and surface morphological properties of pulsed laser deposited CZTS thin films, Ceram. Int. 40 (2014) 15097–15103. doi:10.1016/j. ceramint.2014.06.121.

[8] D. Fang, P. Yao, H. Li, Influence of annealing temperature on the structural and optical properties of Mg-Al co-doped ZnO thin films prepared via sol-gel method, Ceram. Int. 40 (2014) 5873–5880. doi:10.1016/j.ceramint. 2013.11.030.

[9] P.A. Arasu, R.V. Williams, Effect of Annealing Temperature on Structural and Optical Parameters of Sol–Gel Routed Molybdenum Oxide Thin Film, Surf. Rev. Lett. 22 (2015) 1550054. doi:10.1142/S0218625X15500547.

[10] R. Boughalmi, A. Boukhachem, M. Kahlaoui, H. Maghraoui, M. Amlouk, Physical investigations on Sb_2S_3 sprayed thin film for optoelectronic applications, Mater. Sci. Semicond. Process. 26 (2014) 593–602. doi:10.1016/j.mssp.2014.05.059.

[11] K.S. Usha, R. Sivakumar, C. Sanjeeviraja, Optical constants and dispersion energy parameters of NiO thin films prepared by radio frequency magnetron sputtering technique, J. Appl. Phys. 114 (2013). doi:10.1063/1.4821966.

[12] S.P. Anthony, J.I. Lee, J.K. Kim, Tuning optical band gap of vertically aligned ZnO nanowire arrays grown by homoepitaxial electrodeposition, Appl. Phys. Lett. 90 (2007) 19–22. doi:10.1063/ 1.2711419.

[13] B.P. Kafle, S. Acharya, S. Thapa, S. Poudel, Structural and optical properties of Fe-doped Zno transparent thin films, Ceram. Int.42 (2016) 1133–1139. doi:10.1016/j.ceramint. 2015.09.042

[14] P. Kumar, Dielectric Relaxation in Complex Perovskite Oxide $Sr(Gd_{0.5}Nb_{0.5})O_3$, Mater. Sci. Appl. 03 (2012) 369–376. doi:10.4236/ msa. 2012.36053.

[15] L. Shi, B. Zhang, Q. Liao, L. Zhu, L. Zhao, D. Zhang, et al., Piezoelectric properties of Fe_2O_3 doped $BiYbO_3$-$Pb(Zr,Ti)O_3$ high Curie temperature ceramics, Ceram. Int. 40 (2014)

11485–11491.
doi:10.1016/j.ceramint.2013.10.043.

[16] V. Eswaramoorthi, R.V. Williams, Effect of thickness on microstructure, dielectric and opticl properties of single layer $Ba_{0.6}Sr_{0.4}TiO_3$ THIN FILM, Surf. Rev. Lett. 21 (2014) 1450020. doi:10.1142/S0218625X14500206.

[17] V. Eswaramoorthi, R. Victor Williams, Structural, optical and electrical properties of sol–gel derived $(Ba_{0.6}Sr_{0.4})$ $(Ni_xTi_{1-x})O_3$ thin films, Ceram. Int.41 (2015) 2434–2438. doi:10.1016/j.ceramint.2014.10.057

[18] M.A. Ponce, R. Parra, R. Savu, E. Joanni, P.R. Bueno, M. Cilense, et al., Impedance spectroscopy analysis of TiO2 thin film gas sensors obtained from water-based anatase colloids, Sensors Actuators, B Chem. 139 (2009) 447–452. doi:10.1016/j.snb.2009.03.066.

[19] R. Mariappan, V. Ponnuswamy, P. Suresh, N. Ashok, P. Jayamurugan, A. Chandra Bose, Influence of film thickness on the properties of sprayed ZnO thin films for gas sensor applications, Superlattices Microstruct. 71 (2014) 238–249. doi:10.1016/j.spmi.2014.03.029.

International Journal of
Scientific Research in Science and Technology (IJSRST)
Print ISSN : 2395-6011, Online ISSN : 2395-602X
International Conference on Advanced Materials
Held on 14, 15 December 2017, Organized by Department of Physics,
St. Joseph's College, Trichy, Tamilnadu, India

Preparation and Characterization of Spray-Coated Pure and Copper Doped Tin Oxide Thin Films

Ranjith Rajasekar J[1], Sathyaseelan G[1], Senthil kumar M[2*]
[1]Department of physics, St. Joseph's college Trichy, Tamil Nadu, India
[2]Department of physics Govt Arts college Kumbakonam, Tamil Nadu, India
*corresponding author mail id: msenthilprof@gmail.com.

Abstract

Pure and Copper (Cu) doped tin oxide thin films have been deposited from tin chloride ($SnCl_2$) as a precursor and Copper chloride ($CuCl_2$)for doping onto glass substrates by spray pyrolysis technique at the substrate temperature of 400°C. The doping concentration of Cu was varied from 2 to 5 wt.% while all other deposition parameters such as spray rate, carrier air gas pressure and distance between spray nozzle to substrate were kept constant. The structural properties and optical properties of the as-deposited thin films have been studied by X-ray diffraction (XRD) and UV visible spectroscopy. Also the chemical composition were analyzed by Fourier transform Infra-red Spectroscopy (FT-IR). The structural and optical studies were carried out on these films reveal their columnar and compact structure.

Keywords: Spray pyrolysis, Tin oxide, SEM, EDX, Optical band gap

1. Introduction

TCOs belong to a unique class of semiconducting materials that exhibit high optical transparency in the visible range and good electrical conductivity, simultaneously. These materials are widely used in several devices such as thin film solar cells, touch screens, flat panel displays, sensors, low emissive windows and flexible transparent electronic components. The most common TCOs include tin oxide, zinc oxide, indium oxide, cadmium oxide, titanium di-oxide and the like. TCOs find potential applications in electro chromic windows and oxide based thin film transistors (TFTs). To enhance the transparent conducting properties of TCOs, they are generally doped with suitable anionic or cationic impurities. The Cu doped SnO_2 thin films have been prepared by spray pyrolysis method and it was observed that the transmittance of the films was found to increase from 42% to 55 % on initial addition of Cu and then decreased for higher level of Cu doping [7]. To improve the quality of the films as well as the physical and chemical properties.

Various methods such as sol gel spin coating, spray pyrolysis, electron beam evaporation; vapour deposition, pulsed laser deposition, chemical vapour deposition, molecular beam epitaxy, magnetron sputtering, reactive evaporation and thermal evaporation etc. have been used for the preparation of pure or doped thin films. Among them spray pyrolysis deposition (SPD) technique provides a simple route of synthesizing thin films because of its simplicity, low cost experimental set up from an economical point of view. In addition, this technique could be used for the production of large-area thin film deposition without any high vacuum system. The main objective of this work is to prepare pure and Cu doped SnO_2 thin films from $SnCl_2.2H_2O$ precursor and to explore its structural and optical properties. In this paper we are reporting the effect of Cu doping on the structural

International Journal of
Scientific Research in Science and Technology (IJSRST)
Print ISSN : 2395-6011, Online ISSN : 2395-602X
International Conference on Advanced Materials
Held on 14, 15 December 2017, Organized by Department of Physics,
St. Joseph's College, Trichy, Tamilnadu, India

and optical properties of SnO_2 films prepared by chemical spray pyrolysis technique (SPT).

2. Experimental details

2.2.1. Sample preparation

By using absolute ethanol solvent, 0.1M tin chloride solution was prepared. And to dope copper chloride with prepared tin chloride solution, different atomic weight percentage was selected. The solution was stirred in magnetic stirrer for 20 minutes before deposition.

2.2.2 Spray pyrolysis technique

The precursor solution was deposited by simple and modified chemical spray pyrolysis technique. Before deposition, the hot plate and the spray gun were cleaned by hydrochloric acid (conc.HCL) and distilled water. The substrate was placed at the middle of the furnace and spray gun was focused to the substrate in order to get a uniform, coating. The distance between the nozzle and the substrate is 30 cm. The spray rate of 5ml/min was maintained constant by using compressed air as a carrier gas. The substrate temperature was kept constant at 400˚C and it was maintained by using temperature controller.

The substrate temperature was measured by using IR sensor. Now, the prepared precursor solution was deposited on the glass substrate for three minute continuously. Due to high temperature, the chloride and ethanol present in the precursor gets evaporated and oxidation takes place to gets a fine tin oxide thin film. The deposited tin oxide and copper doped tin oxide thin film where annealed at 400°c for one hour in open air atmosphere. Due to annealing, the atoms present in the molecule are properly arranged to get a fine and uniformed thin film.

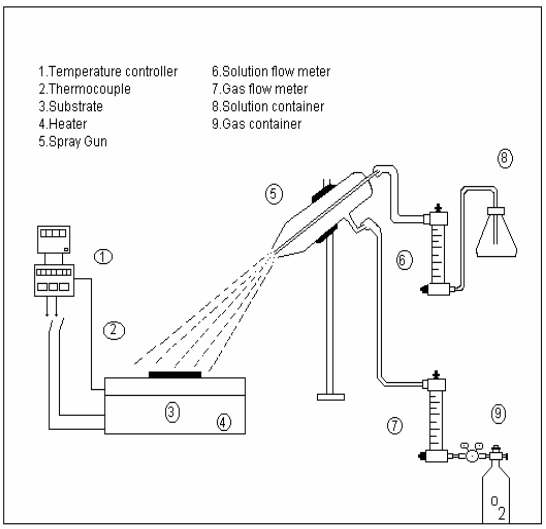

2.2.3. Films deposition

Figure 1 shows the schematic diagram of the spray pyrolysis set up. Tin chloride ($SnCl_2.2H_2O$) and Copper chloride [$CuCl_2$] were used as source of Sn and Cu. In order to prepare precursor solution tin chloride ($SnCl_2.2H_2O$) was added with 50 ml of ethanol (CH_3CH_2OH). The amount of $CuCl_2$ was added from 2–5 wt%. The precursor solution was deposited by simple and modified chemical spray pyrolysis technique. Before deposition, the hot plate and the spray gun were cleaned by hydrochloric acid (conc.HCL) and distilled water. The substrate was placed at the middle of the furnace and spray gun was focused to the substrate in order to get a uniform coating. The distance between the nozzle and the substrate is 30-35 cm. The spray rate of 5ml/min was maintained constant by using compressed air as a carrier gas. The substrate temperature was kept constant at 400˚C and it was maintained by using temperature controller.

The substrate temperature was measured by using IR sensor. Now, the prepared precursor solution was deposited on the glass substrate for three minute continuously. Due to high temperature, the chloride and ethanol present in the precursor gets evaporated and oxidation takes place to gets a

International Journal of
Scientific Research in Science and Technology (IJSRST)
Print ISSN : 2395-6011, Online ISSN : 2395-602X
International Conference on Advanced Materials
Held on 14, 15 December 2017, Organized by Department of Physics,
St. Joseph's College, Trichy, Tamilnadu, India

fine tin oxide thin film. The deposited tin oxide and copper doped tin oxide thin film where annealed at 400°C for one hour in open air atmosphere. Due to annealing, the atoms present in the molecule are properly arranged to get a fine and uniformed thin films.

3. Result and Discussion

3.1. Structural Analysis

3.1.1. X-Ray Diffraction

The XRD patterns of Pure and Cu doped SnO_2 films were shown in Figure 3.1. The films deposited showed five peak namely (110), (101), (200), (211) and (220). Since all the peaks are sharp it is evident that the films deposited are polycrystalline in nature and the positions of X-ray diffraction peaks fit well the tetragonal structure of SnO_2.**(JCPDS card:tin oxide, 41-1445)** [30]. As seen from Figure 3.1, the prepared orientations is (110) plane for Pure SnO_2 film. The addition of Cu atoms do not affect the prepared orientation along (110) plane and crystal structure. The dopant does not form extra peaks in the XRD pattern of doped SnO_2 films because dopant atoms incorporate homogeneously into the tin oxide matrix. In the present study, the most conspicuous feature observed in the XRD analysis of the films is orientation along the (110) plane. In literature published on SnO_2 films doped with different atoms such as Al, Zn and Co exhibited similar behaviors [28-30]. This result is consistent with the analysis of microstructure of Pure SnO_2 films prepared by spray pyrolysis from various solutions by Smith et al. [32].

From the diffraction pattern, the (h k l) values for each diffraction peak are indexed and the lattice parameters were calculated using 'check cell' software. Table 3.1 shows the calculated lattice constants of SnO_2 films. It was seen that they match well with the standard **JCPDS data card 41-1445**. It was also observed that the Cu doping atoms did not change the lattice parameters.

Table. 3.1. Lattice parameters and crystallite size values of SnO_2 films prepared for various dopant atoms

Doping Atoms	a (Å)	b (Å)	c (Å)
Pure	4.90	3.31	0.68
Cu	4.92	3.32	0.68

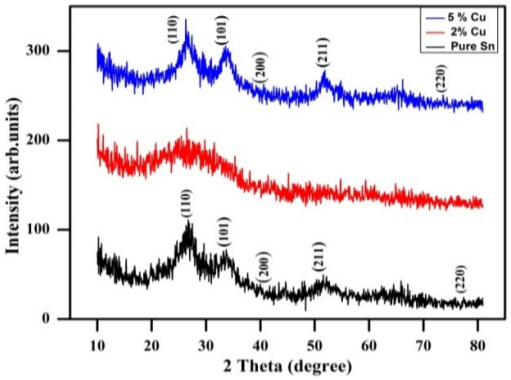

Figure 3.1. XRD spectrum of 0% (pure), 2% and 5% copper doped tin oxide thin films

3.2. Evaluation of Optical Constants

3.2.1. Fourier Transform Infrared Spectroscopy

Fourier Transform Infrared Spectroscopy has been used to analyze the functional groups present in the compound and to confirm the molecular structure of the compound. Functional groups with strong dipole interaction give rise to strong absorption in the IR region. In order to analyze qualitatively the presence of the functional in pure and copper doped SnO_2 was recorded using spectrum RXI FTIR spectrometer in the range 400-4000 cm^{-1}. The resultant spectra were shown in Figure 3.2.

International Journal of
Scientific Research in Science and Technology (IJSRST)
Print ISSN : 2395-6011, Online ISSN : 2395-602X
International Conference on Advanced Materials
Held on 14, 15 December 2017, Organized by Department of Physics,
St. Joseph's College, Trichy, Tamilnadu, India

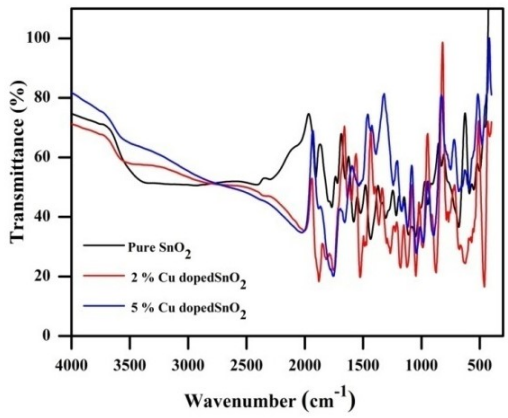

Figure 3.2. FTIR spectrum for pure and copper doped SnO_2 thin films

3.3. Optical Properties

The optical measurements of tin oxide thin films are studied using LAMBDA 35 UV-Visible Spectrophotometer wavelengths range from 300 nm to 1100 nm are shown Figure 3.3.

From this figure 3.3 the optical transmittance spectra of the SnO_2 films for pure and copper doped atoms. The transmittances of pure and copper doped films were increased in an apparent way with wavelength of entire visible and near the IR region. The absorption coefficients (a) were determined by means of the optical transmittance spectra using the relation. The transmittance threshold shift towards the higher wave length region indicates the reduction in optical band gap (E_g). From the transmission spectrum the absorption coefficient (α) is determined by the relation

$$\alpha = \frac{1}{t}\ln T$$

where t is the thickness and T is the transmittance of the film at a particular wavelength. The optical band gap E_g of the film was calculated using the Tauc relation, which is given as

$$\alpha h\upsilon = A(h\upsilon - E_g)^n$$

A is the energy dependent constant, E_g optical band gap energy of the material and n = 1/2, 2, 3/2, 3 corresponding to the allowed direct, allowed indirect and forbidden direct and forbidden indirect transitions respectively. The optical band gap depends upon the absorption coefficient (α). The plot of $(\alpha h\upsilon)^2$ versus $h\upsilon$ is shown in Figure 3.4. The optical band gap was obtained from extrapolating the linear portion of $(\alpha h\upsilon)^2$ versus $h\upsilon$ plot to $(\alpha h\upsilon)^2 = 0$ as 3.4 eV for Pure and 2.9 eV for Cu doped SnO_2 thin films.

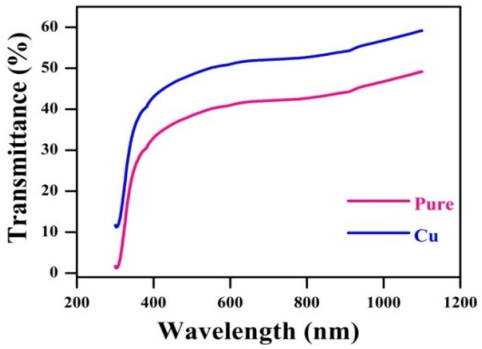

Figure 3.3. Transmittance spectra of SnO_2 films for pure and Cu doped thin films

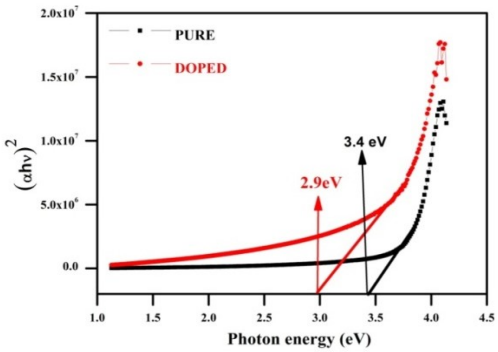

Figure 3.4 .The variation of $(\alpha h\nu)^2$ vs. $h\nu$ for SnO_2 films for pure and Cu doped thin films

4. Conclusion

In the present work, an attempt is made to prepare pure and copper doped tin oxide thin films by Spray pyrolysis techniques utilizing an ethonalic solution containing $SnCl_2.2H_2O$ and $CuCl_2$. The low cost spray pyrolysis deposition (SPD) technique has

International Journal of
Scientific Research in Science and Technology (IJSRST)
Print ISSN : 2395-6011, Online ISSN : 2395-602X
International Conference on Advanced Materials
Held on 14, 15 December 2017, Organized by Department of Physics,
St. Joseph's College, Trichy, Tamilnadu, India

been used to obtain uniform conductive layers of pure and copper doped tin oxide thin films with good repeatability. The thickness of the synthesized films was found to be about 300 nm for 3 minutes deposition time. The average transmittance of copper doped tin oxide films in the visible region is higher than the tin oxide films and the higher transmittance is found at 2% copper doping and the lowest average transmittance at 5% of copper doping. The direct band gap of pure film is found to be 3.4eV and reduces to 2.9eV Cu doped SnO_2 films. In X-ray diffraction analysis, SnO_2:Cu films prepared at 400°c with various copper doped concentrations are polycrystalline in nature. Since the tin oxide thin films are highly transparent, it can be widely used to make optoelectronic displays and photocell devices.

References

[1] Bagheri Mohagheghi, M.; Shahtahmasebi, N.; Alinejad, M.R.; Youssefi, A.; Shokooh Saremi, M. Physica B. 2008,403, 2431–2437.

[2] Preparation and characterization of undoped and optically pure copper doped tin oxide thin films deposited by spray pyrolysis technique. S.S. Roy, and J. Podder. Transport conducting Sn-doped copper oxide. E. Elangovan, K. Rammurthi, Cryt. Res. Technol., (2003).

[3] Optical and electrical properties of tin doped copper oxide R.W. Siegal, E.H.Hu, M.C. Roco, WTEC panel report.

[4] Structural optical and electrical properties of molybdenum doped cadmium oxide thin films prepared by spray pyrolysis method R. Kumaravel et al., Applied physics A 109, 579 (2012).

[5] Characterization of copper doped tin oxide thin films deposited by spray pyrolysis technique. J.B. Yoo, A.L. Fahrenbruch, R.H. Bube, J. Appl. Phys. (1990).

[6] Thin film ultrasonic spray of CVD process in copper doped tin oxide thin film deposited by spray pyrolysis technique. M.G. Krishna and A.K. Bhatnagar, Bull. Mater. Sci. (2006).

[7] Khan, A.F. Mehmood, M.; Aslam, M.; Ashraf, M. Applied Surface Science. 2010, 256, 2252–2258.

[8] Moharrami, F. Bagheri Mohagheghi, M.M.; Azimi Juybari, H. Thin Solid Films. 2012, 520, 6503–6509.

[9] Rani, S. Roy, S.C. Bhatnagar, M.C. Sensors and Actuators B. 2007,122, 204–210.

[10] Maekava, T. Suzuki, K. Takada, T. Kobayashi, T. Egashira, M. Sensors and Actuators B. 2001, 80, 51-58.

[11] Agashe, C. Hüpkes, J. Schöpe, G. Berginski, M. Solar Energy Materials & Solar Cells. 2009, 93, 1256–1262.

[12] Introduction to thin films, K.ravichandran, K.Swaminathan, B.Sakthivel., Research India Publications, India.

[13] Thin films fundamentals, A. Goswami, New Age international Ltd. Publishers, (1996).

[14] An introduction to physics and Techonology of Thin Films, Alfred Wagendristel and Yumin Wang, World Scientific Publishing Co. Ltd., Singapore (1928).

[15] Yin, L.T. Chou, J.C. Chung, W.Y.; Sun, T.P.; Hsiung, S.-K. Sensors and Actuators B. 2000, 71, 106-111.

[16] Ouerfelli, J. Djobo, S. Ouro.; Bernède, J.C. Cattin, L. Morsli, M.; Berredjem, Y. Materials Chemistry and Physics. 2008, 112, 198–201.

[17] Kikuchi, N. Kusano, E. Kishio, E. Kinbara, A. Vacuum. 2002, 66, 365–371.

[18] Kim, W.J. Koo, W.H.; Jo, S.J.; Kim, C.S. Baik, H.K.; Lee, J. Im, S. Applied Surface Science. 2005,252, 1332–1338.

[19] Fang, T.H. Chang, W.J. Applied Surface Science. 2003, 220, 175–180.

[20] Dippel, A.C.; Schneller, T.; Gerber, P.; Waser, R. Thin Solid Films. 2007, 515, 3797–3801.

[21] Ma, J.; Hao, X.; Huang, S. Huang, J. Yang, Y. Ma, H. Applied Surface Science. 2003, 214, 208–213. Elangovan, E. Ramesh, K.; Ramamurthi, K. Solid State Communications. 2004, 130, 523–527.

[22] Serin, T. Serin, N. Karadeniz, S. Sari, H.; Tugluoglu, N.; Pakma O. Journal of Non-Crystalline Solids. 2006, 352, 209–215.

[23] Alsac, A.A. Yildiz, A.; Serin, T. Serin, N.J. Appl. Phys. 2013, 113, 063701.

[24] Miao, D. Zhao, Q. Wu, S. Wang, Z.; Zhang, X. Zhao, X. Journal of Non-Crystalline Solids. 2010, 356, 2557–2561.

[25] Ahmed, SK.F. Khan, S. Ghosh, P. K. Mitra, M. K. Chattopadhyay, Patil, S.B. Patil, P. P. More, M. A. Sensors and Actuators B. 2007, 125, 126–130.

[26] Safonova, O.V. Rumyantseva, M.N. Ryabova, L.I.; Labeau, M. Delabouglise, G. Gaskov, A.M. Materials Science and Engineering Joseph, D.P.; Renugambal, P. Saravanan, M.; Raja, S.P. Venkateswaran, C. Thin Solid Films.2009,517, 6129–6136..

[27] Huang, Y. Li, G; Feng, J.; Zhang, Q. Thin Solid Films. 2010, 518, 1892–1896.

[28] Gao, K.H. Lin, T. Liu, X.D.; Zhang, X.H. Li, X.N. Wu, J. Liu, Y. F. Wang, X. F. Chen, Y. W.; Ni, B.; Dai, N.; Chu, J.H. Solid State Communications. 2013, 157, 49–53.

[29] Ma, Y.J. Zhou, F. Lu, L. Zhang, Z. Solid State Communications. 2004,130, 313–316.

[30] Bansal, S. Pandya, D.K. Kashyap, S.C. Thin Solid Films. 2012, 524, 30–34.

[31] Ramaiah, K.S. Raja, V.S. Applied Surface Science. 2006, 253, 1451–1458.

[32] JCPDS Powder Diffraction File card 41–1445.

[33] Vijayalakshmi, S. Venkataraj, S. Subramanian, M. Jayavel, R. J. Phys. D: Appl. Phys. 2008, 41, 035505 (7pp).

[34] Smith, A.; Laurent, J.M.; Smith, D.S.; Bonnet, J.P.; Clemente, R.R. Thin Solid Films.1995, 266, 20-30.

International Journal of
Scientific Research in Science and Technology (IJSRST)
Print ISSN : 2395-6011, Online ISSN : 2395-602X
International Conference on Advanced Materials
Held on 14, 15 December 2017, Organized by Department of Physics,
St. Joseph's College, Trichy, Tamilnadu, India

Molecular Docking and Spectroscopic Analysis of (Z)-3-(3-chloro-2,6-difluorophenyl)-1-(1H-imidazol-1-yl)prop-2-en-1-one

K. Kumanan[1], R. Raj Muhamed[1*], M. Raja[2], V. Sathyanarayanamoorthi[3], M. Yaseen Mowlana[4], S. Arulappan[1]

[1]Department of Physics, Jamal Mohamed College, Tiruchirappalli 620020, Tamil Nadu, India.
[2]Department of Physics, Govt Thirumagal Mills College, Gudiyattam 632602, Vellore, India.
[3]Department of Physics, PSG College of Arts and Science, Coimbatore 641014, Tamil Nadu, India.
[4]Department of Chemistry, Jamal Mohamed College, Tiruchirappalli 620020, Tamil Nadu, India.
Corresponding Author: ponnu_68@yahoo.com

Abstract

Theoretical and experimental FT-IR and FT-Raman spectra characterization of 2(Z)-3-(3-chloro-2,6-difluorophenyl)-1-(1H-imidazol-1-yl)prop-2-en-1-one were recorded and calculated. The vibrational wavenumbers were computed using DFT quantum chemical calculations. The molecular geometry (bond length, bond angle) and vibrational frequencies of the title compounds have been calculated by using DFT/B3LYP method with 6-311++G(d,p) basis set. The title compounds were screened in vitro for antimicrobial activity against three bacterial and three fungal strains. Molecular docking studies reveal that title compound play a vital role in bonding and results draw us to the concluded that title compound inhibit different antimicrobial proteins and that have good biological activities.

Keywords: DFT; FTIR; FT-Raman; Antimicrobial; Molecular docking.

1. Introduction

The imidazole nucleus is well known to play an important role in living organisms since it is incorporated into the histidine molecule and many other important biological systems. Imidazole derivatives are the most used class of antifungal drugs [1], being active against pathogenic and nonpathogenic fungi [2]. Particularly, imidazole and its derivative of (Z)-3-(3-chloro-2,6-difluorophenyl)-1-(1H-imidazol-1-yl)prop-2-en-1-one have broadened scope in clinical medicines. Its molecular formula is $C_{12}H_7ClF_2N_2O$. Medicinal properties of imidazoles include anti-inflammatory, anticancer, anticoagulants, antifungal, antibacterial, antitubercular, antiviral, antimalarial and antidiabetic [3,4]. In the present work has been undertaken to give a complete description of the molecular geometry and molecular vibration of the 3CDIPO.

In the present work has been undertaken to give a complete description of the molecular geometry and molecular vibration of the 3CDIPO. FTIR and Raman spectra of (Z)-3-(3-chloro-2,6-difluorophenyl)-1-(1H-imidazol-1-yl)prop-2-en-1-one (3CDIPO) have been reported together with the assignments of the vibrational modes supported by PED. The agar diffusion methods were used to study the antimicrobial activity of the title compound against three bacteria (Moraxella, Enterobacter and Pseudomonas aeruginosa), and three fungi organisms (Candida albicans, A.niger and Trichophyton) and the title showed a broad spectrum of activities against the microbes. Due to the different potential biological

International Journal of
Scientific Research in Science and Technology (IJSRST)
Print ISSN : 2395-6011, Online ISSN : 2395-602X
International Conference on Advanced Materials
Held on 14, 15 December 2017, Organized by Department of Physics,
St. Joseph's College, Trichy, Tamilnadu, India

activity of the title compound, molecular docking of the title compound is also reported.

2. Material and Methods

2.1. Synthesis

For the synthesis of ((Z)-3-(3-chloro-2,6-difluorophenyl)-1-(1H-imidazol-1-yl)prop-2-en-1-one (3CDIPO) compound, Equimolar quantity of 1-acetyl imidazole (0.01 mol) and 3-chloro-2,6-diflurobenzaldehyde (0.01 mol) were dissolved in 20 ml of ethanol in a 150 mL round bottomed flask. The reaction mixture was magnetically stirred for 3h in ice-cold condition, during stirring 10 ml of 10% sodium hydroxide solution was added drop wise. A flocculants precipitate was formed. The precipitate was filtered and washed with cold water. The solid obtained was purified by column chromatography using silica gel 60-120 mesh and n-hexane: acetone (7:3 v/v) as elevate. The reaction scheme is shown in Figure 1.

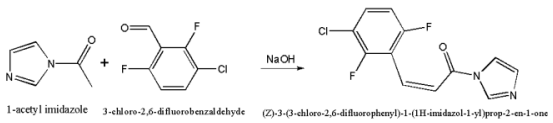

Figure 1. The scheme of the synthesis of 3CDIPO

2.2. Experimental details

The FT-IR spectrum of the synthesis compound (Z)-3-(3-chloro-2,6-difluorophenyl)-1-(1H-imidazol-1-yl)prop-2-en-1-one (3CDIPO) was recorded in the region 4000-450 cm^{-1} in evacuation mode using a KBr pellet technique with 1.0 cm^{-1} resolution on a PERKIN ELMER FT-IR spectrophotometer. The FT-Raman spectrum of the 3CDIPO compound was recorded in the region 4000-100 cm^{-1} in a pure mode using Nd: YAG Laser excitation wavelength of Raman 100 mW with 2 cm^{-1} resolution on a BRUCKER RFS 27 at SAIF, IIT, Chennai, India.

2.3. Computational details

In this work, all the calculations were performed by using Gauss-View molecular visualization program [5] and Gaussian 09 W program package [6]. Molecular docking (ligand-protein) simulations have been performed by using autoDock 4.2.6 software package.

3. Results and discussion

3.1. Geometrical structure analysis

The optimized geometry is performed at B3LYP/6-311++G(d,p) basis set of 3CDIPO molecule with atom numbering scheme is shown in Figure 2. The theoretical results are compared with related molecule such as (Z)-3-(9-Anthryl)-1-(4-chlorophenyl)-2-(4-nitro-1H-imidazol-1-yl)prop-2-en-1-one [7]. The comparative optimized structural parameters such as bond length, bond angle along with its experimental data's are presented in Table 1. This title molecule has ten C – C bond lengths, seven C – H bond lengths, five C – N bond lengths, two C – F bond lengths, one (C – O) bond length presented in title molecule and these values are listed in Table 1. From table 1 shows the calculated and experimental results are very good agreement. So the title molecule optimized successfully.

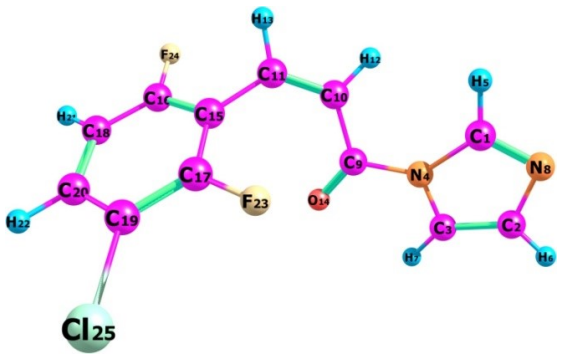

Figure 2. The theoretical optimized geometric structure with atoms numbering of 3CDIPO

International Journal of
Scientific Research in Science and Technology (IJSRST)
Print ISSN : 2395-6011, Online ISSN : 2395-602X
International Conference on Advanced Materials
Held on 14, 15 December 2017, Organized by Department of Physics,
St. Joseph's College, Trichy, Tamilnadu, India

3.2. FT-IR and FT-Raman spectra

The maximum number of potentially active observable fundamentals of a nonlinear molecule which contains N atoms is equal to (3N-6), apart from three translational and three rotational degrees of freedom. Hence, 3CDIPO molecule, that was planar, has 25 atoms with 69 normal modes of vibrations. The observed and simulated infrared and Raman spectra of 3CDIPO are shown in Figs. 3 and 4, respectively. The observed and scaled theoretical frequencies using DFT (B3LYP) method with PEDs are listed in Table 2.

The C-C stretching vibrations are expected in the range from 1650 to 1100 cm^{-1} which are not significantly influenced by the nature of the substituents [8]. The C-C stretching vibrations of the 3CDIPO compound were observed from1670 to 890 cm^{-1}. In this present study, the C-C stretching vibrations are found at 1568(vs), 1597(vs), 1444(vs), 1235(vs), 1162(vs), 1067(s), 938(m) cm^{-1} in FT-IR and 1647(s), 1595(vs), 1415(s), 1177(w), 1104(m), 973(w), 947(m), 905(m) cm^{-1} in FT-Raman respectively. The theoretical wavenumbers at 1697, 1583, 1443, 1411, 1239, 1190, 1146, 1100, 1080, 989, 944 and 891 cm^{-1} are assigned as C-C stretching vibrations with PED contribution of 68, 46, 24, 63, 34, 24, 30, 25, 22, 21, 25 and 36% respectively.

Table 1. Optimized geometrical parameters of 3CDIPO obtain by B3LYP/6-311++G(d,p) basis set

Parameters	Exp[a]	B3LYP/	Parameters	Exp[a]	B3LYP
Bond length(Å)			Bond angle(°)		
C1-N4	1.364	1.391	N4-C1-H5	123.9	122.6
C1-H5	0.930	1.078	N4-C1-N8	112.2	111.9
C1-N8	1.305	1.301	C1-N4-C3	106.9	106.0
C2-C3	1.357	1.361	C1-N4-C9	128.0	129.7
C2-H6	0.930	1.078	H5-C1-N8	127.9	125.5
C2-N8	1.369	1.389	C1-N8-C2	106.9	105.6
C3-N4	1.369	1.393	C3-C2-H6	127.9	128.0
C3-H7	0.930	1.075	C3-C2-N8	112.8	110.9
N4-C9	1.431	1.418	C2-C3-N4	104.2	105.6
C9-C10	1.488	1.483	C2-C3-H7	127.9	133.4
C9-O14	1.216	1.210	H6-C2-N8	123.9	121.1
C10-C11	1.341	1.342	N4-C3-H7	123.9	120.9
C10-H12	0.930	1.083	C3-N4-C9	125.0	124.3
C11-H13	0.930	1.086	N4-C9-C10	116.1	115.6
C11-C15	1.477	1.470	N4-C9-O14	118.1	119.9
C15-C16	1.402	1.399	O14-C9-O14		124.4
C15-C17	1.402	1.400	C9-O14-C11		125.4
C16-C18	1.384	1.382	C9-C10-H12	115.3	116.9
C16-F24		1.352	C11-C10-H12	119.7	117.5
C17-C19	1.402	1.391	C10-C11-H13	115.3	116.6
C17-F23		1.339	C10-C11-C15	129.4	129.4
C18-C20	1.402	1.391	H13-C11-C15	115.3	114.1
C18-H21	0.930	1.082	C11-C15-C16	119.6	119.6
C19-C20	1.402	1.392	C11-C15-C17	123.4	124.4
C19-Cl25		1.744	C16-C15-C17	117.3	115.9
C20-H22	0.930	1.082	C15-C16-C18	123.5	123.6
			C15-C16-F24		117.7
			C15-C17-C19	122.4	122.1
			C15-C17-F23		118.9
			C18-C16-C24	118.8	118.7
			C16-C18-C20	118.6	118.6
			C16-C18-H21	119.8	119.8
			C19-C17-F23		118.9
			C17-C19-C20	119.6	119.6
			C17-C19-CL25		119.8
			C20-C18-H21	120.7	121.6
			C18-C20-C19	120.4	120.2
			C18-C20-H22	120.5	120.5
			C20-C19-CL25		120.6
			C19-C20-H22	119.3	119.3

[a] Taken from Ref [13]

In the heterocyclic compounds, the C-H stretching wavenumbers appear in the range 3000-3100 cm^{-1} [9]. In this present study, the C-H stretching vibrations are observed at 3166, 3122, 3090 and 3031 cm^{-1} by B3LYP/6-311++G(d,P) method show good agreements with experimental vibrations. The bands observed in the recorded

International Journal of
Scientific Research in Science and Technology (IJSRST)
Print ISSN : 2395-6011, Online ISSN : 2395-602X
International Conference on Advanced Materials
Held on 14, 15 December 2017, Organized by Department of Physics,
St. Joseph's College, Trichy, Tamilnadu, India

FT-Raman spectrum 3163(w), 3106(m), 3082(m) and 3034(w) cm^{-1}. The PED corresponding to this pure mode of title molecule contributed 95, 94, 97 and 92% is shown in Table 2.

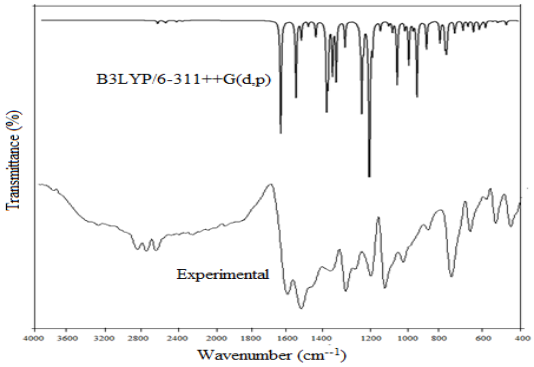

Figure 3. Experimental and theoretical FT-IR spectra of 3CDIPO

Table 2. Calculated vibrational frequencies (cm^{-1}) assignments of 3CDIPO based on B3LYP/6-311++G(d,p) basis set

Mode no	Experimental wave number (cm^{-1})		Theoretical wave number (cm^{-1})		I_{IR} [c]	I_{RAMAN} [d]	Assignments (PED)[a,b]
	FTIR	FT-Raman	**Unscaled**	Scaled			
69			3295	3166	1	7	γCH(95)
68			3259	3132	0	5	γ CH (96)
67		3106(m)	3248	3122	1	13	γ CH (94)
66		3082(m)	3215	3090	0	22	γ CH (97)
65			3203	3078	0	6	γ CH (97)
64			3186	3062	1	11	γ CH (91)
63			3154	3031	0	7	γ CH (92)
62	1668(vs)	1647(s)	1765	1697	49	9	γ CC (68)
61			1678	1612	34	100	γ CC(40)+ β HCN (14)
60	1597(vs)	1595(vs)	1647	1583	8	19	γ CC (46)
59		1513(m)	1607	1544	2	3	β HCC (31)
58			1564	1503	7	3	γ CC (60)
57	1444(vs)		1502	1443	35	4	β HCN(14) +γ NC(31) + γ CC (24)
56			1493	1435	23	1	β HCC(26)
55		1415(s)	1468	1411	23	8	γ CC (63)
54	1365(vs)	1376(w)	1447	1390	26	3	β HCC(19)+ β HCN(10)
53	1317(s)		1396	1342	11	1	β HCN(42) + γ NC (12)
52			1324	1272	1	3	γ CC (61)
51			1309	1258	5	6	γ NC (45) + β CNC(20)
50			1300	1249	38	4	γ CC (36)
49	1235(vs)		1289	1239	8	8	β HCN (12) + γ CC (34)
48		1218(w)	1267	1217	1	3	
47			1256	1207	100	1	β HCN (15) + γ (13)
46		1177(w)	1238	1190	11	0	γ CC(24) + β HCC (24)
45	1162(vs)		1193	1146	4	2	β HCC (11) + γ CC (14)
44		1104(m)	1145	1100	2	1	β HCC (20) + γ CC (10)

International Journal of
Scientific Research in Science and Technology (IJSRST)
Print ISSN : 2395-6011, Online ISSN : 2395-602X
International Conference on Advanced Materials
Held on 14, 15 December 2017, Organized by Department of Physics,
St. Joseph's College, Trichy, Tamilnadu, India

Mode no	Experimental wave number (cm^{-1})		Theoretical wave number (cm^{-1})		I_{IR} [c]	I_{RAMAN} [d]	Assignments (PED)[a,b]
	FTIR	FT-Raman	**Unscaled**	Scaled			
43	1067(s)		1124	1080	4	1	γ NC (37) + γ CC (12) + βHCN (12)
42			1096	1054	28	6	β HCN (36)+ γ CC (27)
41		1021(w)	1052	1011	4	0	γ NC (30)
40			1030	989	19	1	γ CC (21)
39			1005	966	3	7	τ HCCN (38)
38	938(m)	947(w)	983	944	33	1	γ CC (25)+ β HCN (12)
37			948	911	0	0	τ HCCCI (68) +τ HCCF (15)
36			927	891	12	1	γ CC (36)
35			908	872	1	1	β HCN (63)
34		855(w)	893	858	0	0	τ HCCH (90)
33	816(vs)		851	817	9	1	γ CC (10) +β HCC (10)
32			820	788	10	0	τ HCCC (70)
31			813	782	10	0	τ HCNC (76)
30			809	777	6	4	
29		745(w)	766	736	5	0	τ HCNC (53)
28	718(m)		760	730	1	1	τ HCNC (21)
27			718	690	4	1	γ CC (14)
26		669(w)	690	663	2	0	τ HCCO (24)
25	633(w)	633(w)	658	632	5	0	τ HCNC (49)
24			624	600	4	1	
23			618	594	1	0	τ HCCC (28)
22	586(w)		611	588	1	3	τ HCNC (11)
21			588	565	3	0	γ CC (10) + τ HCCC (11)+ β HCC (10)
20	508(w)		547	525	0	0	β HCC (25)
19			518	498	1	1	
18			502	483	0	0	τ HCCC (10) +τ HCCO (18)
17		437(w)	470	451	2	0	β HCC (39)
16			400	384	0	3	τ HCCC (18)
15		377(w)	381	366	1	1	β HCC (35) +τ HCCC (12) +γ CC (13)
14		346(w)	349	335	0	0	β CNC (10)
13			331	318	0	0	τ HCCF (51)
12			304	292	4	0	β HCC (12)
11			271	260	0	1	τ HCCC (19)
10		205(w)	245	235	0	0	β CCC (35)
9			201	193	0	0	τ HCNC (11)
8			157	151	0	0	β HCC (10)+ τ HCNC (14)
7			149	143	1	0	τ HCNC (54)
6			124	119	0	0	τ HCCCI (64)
5		107(w)	115	110	1	1	τ HCCN (11)+ τ HCCC (24)
4		72(w)	82	79	0	0	τ HCCC (14)
3			49	47	0	0	τ HCCN (11) +τ HCCC (22)
2			38	37	0	1	β HCC (11) +τ HCCC (11)
1			17	16	0	0	τ HCCN (30)

[a]γ-stretching, β- bending , τ-torsion, vs-very strong, s- strong, m-medium, w-weak, vw-very weak.

International Journal of
Scientific Research in Science and Technology (IJSRST)
Print ISSN : 2395-6011, Online ISSN : 2395-602X
International Conference on Advanced Materials
Held on 14, 15 December 2017, Organized by Department of Physics,
St. Joseph's College, Trichy, Tamilnadu, India

[b]scaling factor : 0.961 for B3LYP/6-311+G(d,p)
[c]Relative absorption intensities normalized with highest peak absorption equal to 100.
[d]Relative Raman intensities normalized to 100.

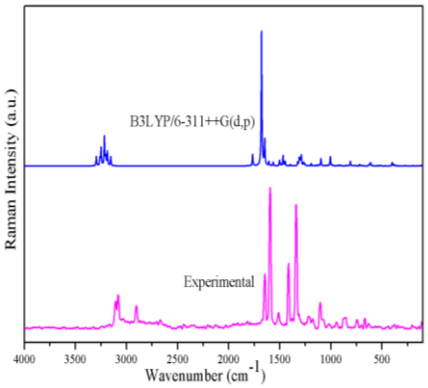

Figure 4. Experimental and theoretical FT-Raman spectra of 3CDIPO

3.3. Antimicrobial studies

The title compound have been examined for in-vitro antibacterial activity against three bacterial strains such as, Moraxella, Enterobacter, Pseudomonas aeruginosa and three fungal strains such as, Candida albicans, A.niger and Trichophyton, which were selected for the present investigation by agar-disk diffusion method. Antimicrobial (antibacterial and antifungal) activity of DMSO extracts with different concentration (25, 50, 75 and 100 µl) inhibition Zone (mm) in agar well diffusion method is tabulated in Table 3.

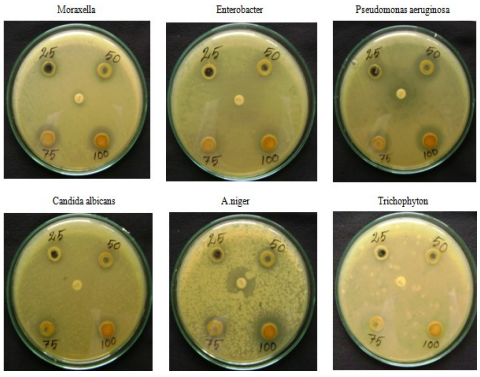

Figure 5. Antibacterial activity and antifungal activity of title molecule

Title compound is more active Moraxella, Enterobacter, Pseudomonas aeruginosa, Candida albicans, A.niger and Trichophyton compared than standard drug. Together, these results indicate that 3CDIPO shows broad-spectrum antimicrobial activity against. The activities of 3CDIPO against bacterial and fungal pathogens are shown in Figure5.

Table 3. Antimicrobial activity of 3CDIPO

Organism	DMSO Extract added and Zone of inhibition (mm/ml)				
	Control	25 µl	50 µl	75 µl	100 µl
Moraxella	11	12	15	17	19
Enterobacter	25	15	19	22	26
Pseudomonas aeruginosa	25	12	15	16	20
Candida albicans	13	13	15	18	20
A.niger	20	12	15	18	25
Trichophyton	10	12	15	20	24

3.4. Molecular docking

The molecular docking is used to predict the preferred binding orientation, binding energy and activity of molecules and their protein targets. The aim to investigate the binding mode, a molecular modeling study was performed and 3CDIPO was selected to be docked into the active site of three receptors 3F03, 4UM7 and 4HOE of antimicrobial proteins.

The AutoDockTools graphical user interface [10] was used to remove the ligand and water molecules present in the target proteins. The first rank docking parameters such as binding energy, inhibition constant and intermolecular energy of the molecule with respect to the targeted proteins are listed in Table 4. The preferred binding orientation of the 3CDIPO ligand with respect to the target proteins are represented in Figs. 6-8. In Figure 6-8, the yellow line indicates the formation of intermolecular hydrogen bond between 3CDIPO

International Journal of
Scientific Research in Science and Technology (IJSRST)
Print ISSN : 2395-6011, Online ISSN : 2395-602X
International Conference on Advanced Materials
Held on 14, 15 December 2017, Organized by Department of Physics,
St. Joseph's College, Trichy, Tamilnadu, India

ligand and the proteins. These results indicate that the 3CDIPO ligand exhibits the lower binding energy and inhibition constant for the targeted protein associated with the 3F03 compared with the other targeted proteins associated with the 4UM7, 4HOE. Among them, 3F03 exhibited the lowest free energy at -6.50 kcal/mol and most docked inhibitors interacted with the ligand within the 3F03 binding site. They exhibited up to two hydrogen bonds involving ARG 324 and ARG 324 with RMSD being 8.79 Å. The docking simulation shows the best binding mode of the 3CDIPO into 3F03. These findings confirm that the 3CDIPO molecule can act as a good inhibitor against 3F03.

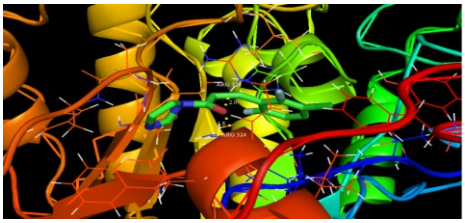

Figure 6. Docking and Hydrogen bond interactions 3CDIPO with 3F03 protein structure

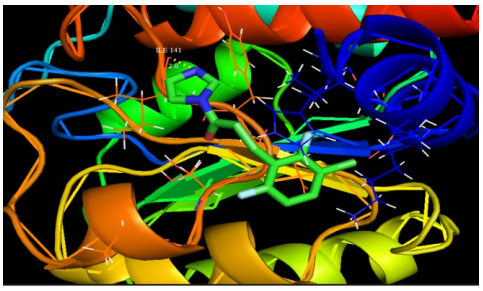

Figure 7. Docking and Hydrogen bond interactions 3CDIPO with 4UM7 protein structure

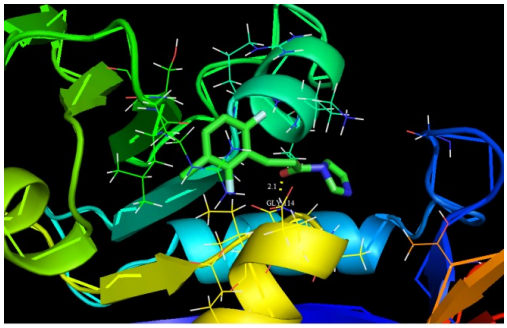

Figure 8. Docking and Hydrogen bond interactions 3CDIPO with 4HOE protein structure

Table 4. Hydrogen bonding and molecular docking with antimicrobial protein targets

Protein (PDB ID)	Bonded residues	No. of hydrogen bond	Bond distance (Å)	Estimated Inhibition Constant (μm)	Binding energy (kcal/mol)	Reference RMSD (Å)
3F03	ARG 324	2	2.0	17.15	-6.50	8.79
	ARG 324		1.8			
4UM7	ILE 141	1	2.0	245.72	-4.92	21.75
4HOE	GLY 114	1	2.1	17.20	-6.48	33.45

4. Conclusion

The investigation of the present work is illuminate the spectroscopic properties such as molecular parameters, frequency assignments and electronic transition and of title compound by using FTIR, FT-Raman and tools derived from the density functional theory. Due to the lack of experimental information on the structural parameters available in the literature, the optimized geometric parameters (bond lengths and bond angles) was theoretically determined at B3LYP/6-311++G(d,p) level of theory and compared with the structurally similar compound. The vibrational FT-IR and FT-Raman spectra of the 3CDIPO were recorded and computed vibrational wavenumbers and their PED were calculated.

References

[1] Bell, A.S., Triazole antifungals: Itraconazole (Sporanox), fluconazole (Diflucan), Voriconazole (Vfend) and fosfluconazole (Prodif), In The Art of Drug Synthesis, 5 (2007)72–73.2

[2] Narasimhan, B., Sharma, D., Kumar, P., Biological importance of the imidazole nucleus in the new millennium. Med. Chem. Res. 20 (2011) 1119-1140.

[3] Congiu, C., Cocco, M.T., Onnis, V., Design, synthesis and in vitro antitumor activity of new 1, 4-diarylimidazole-2-ones and their 2-thione analogues. Bioorg Med Chem Lett 18 (2008) 989–993.

[4] Siddiqui, I.R., Singh, P.K., Srivastava, V., Singh, J., Facile synthesis of acyclic analogues of carbocyclic nucleoside as potential anti-HIV pro-drug. Indian Journal of Chemistry 49B (2010) 512-520.

[5] GaussView, Version 5, Roy Dennington, Todd Keith, and John Millam, Semichem Inc., Shawnee Mission, KS, 2009.

[6] Frisch, M.J., Trucks, G.W., Schlegel, H.B., Scuseria, G.E., Robb, M.A. Gaussian 09, Revision E.01, Gaussian, Inc., Wallingford CT, 2009

[7] Wang, G.Z., Lu, Y.H., Zhou, C.H., Zhang, Y.Y., (Z)-3-(9-Anthryl)-1-(4-chlorophenyl)-2-(4-nitro-1H-imidazol-1-yl)prop-2-en-1-one, Acta Cryst. E65 (2009) o1113.

[8] Sundaraganesan, N., Illakiamani, S. Meganathan, C., Joshua, B.D., Vibrational spectroscopy investigation using ab initio and density functional theory analysis on the structure of 3-aminobenzotrifluoride, Spectrochim. Acta A 67 (2007) 214-224.

[9] Swarnalatha, N., Gunasekaran, S., Muthu, S., Nagarajan, M. Molecular structure analysis and spectroscopic characterization of 9-methoxy-2H-furo[3,2-g]chromen-2-one with experimental (FT-IR and FT-Raman) techniques and quantum chemical calculations, spectrochim. Acta part A 137 (2015) 721-729.

[10] Morris, G.M., Goodsell, D.S., Halliday, R.S., Huey, R., Hart, W.E., Belew, R.K., Olson, A.J., J. Comput. Chem. 19 (1998) 1639–1662.

International Journal of
Scientific Research in Science and Technology (IJSRST)
Print ISSN : 2395-6011, Online ISSN : 2395-602X
International Conference on Advanced Materials
Held on 14, 15 December 2017, Organized by Department of Physics,
St. Joseph's College, Trichy, Tamilnadu, India

A Study on Electrolyte Interactions With Polymer and Nanofiller for Dye Sensitized Solar Cells

G. Maheswari[1*], R. Victor Williams[2]

[1] Associate Professor & Head, PG Department of Physics, Cauvery College for Women, Annamalai Nagar, Tiruchirappalli – 620 018, Tamilnadu, India.

[2]Associate Professor & Head (Retired), PG & Research Department of Physics, St. Joseph's College (Autonomous), Tiruchirappalli – 620 001, Tamilnadu, India.

Corresponding author email id: *reemaarasu@gmail.com

Abstract

In the current scenario, electrolyte plays a crucial role in the fabrication of Dye-Sensitized Solar Cells (DSSCs). To advance the performance of DSSCs, it is essential to explore electrolyte with polymers. Polyvinyl alcohol (PVA) is non toxic, bio compatible, bio degradable, thermally and chemically stable water-soluble polymer with excellent mechanical strength and transparency, which is anticipated to be an excellent candidate in DSSCs. An attempt was made on Polymer based electrolyte with nano filler thin films which are prepared using dip coating technique. The properties of the prepared films are characterized by various experimental techniques such as FTIR, UV-Vis and Electro Chemical Impedance spectroscopy. The Fourier Transform Infrared (FTIR) analysis reveals the complexation of the polymer nanocomposite network and the UV–visible spectral study shows the optical band gap. Besides, the impedance analysis indicates high ionic conductivity which is due to ionic mobility and segment motion of polymer network. The outcome of the studies reveals the interaction of electrolyte with polymer and nano filler for Dye -Sensitized Solar Cells.

Keywords: FTIR, UV-Visible, Impedance, conductivity, band gap.

1. Introduction

There is a sustained interest for clean/alternative energy strategies and for environmental remediation. Growing environmental concerns related to the extensive use of non-sustainable fossil fuels and a constantly increasing energy demand will force mankind, sooner or later to tap into clean and sustainable source of energy. Solar cell is expected to make a great contribution to both environmental treatment and renewable energy. Solar energy is widely considered to be future clean energy carriers in many applications such as environmentally friendly vehicles, domestic heating and stationary power generation [1-2].

Dye – Sensitized Solar Cells (DSSCs) have been under investigation for the past decade due to their attractive features such as high energy conversion efficiency and low production cost [3-4]. Polymers have played an integral role in the advancement of DSSCs. Regenerable redox couples (eg I^-/I_3^-) are usually dissolved in an organic solvent, which results in high energy conversion efficiency but it has got some drawbacks such as leakage and evaporation of the solvent [5-6]. Therefore, several attempts have been made to substitute liquid electrolyte with solid or quasi-solid state electrolyte such as solid polymer electrolyte (SPEs) [7], Polymer gel electrolyte (PGEs) [8] and organic hole-transport materials [9].

Among them nanocomposite solid polymer electrolyte have achieved considerable attention because of their excellent properties such as easy fabrication, low cost and good stability. So they have obtained growing interest in solid state batteries, electrochromic devices and fundamental research of ion transport in disordered phases [10].

Polyvinyl alcohol (PVA) based polymer electrolytes also attracted much interest due to their good film forming capability, hydrogen bonding enhanced

International Journal of
Scientific Research in Science and Technology (IJSRST)
Print ISSN : 2395-6011, Online ISSN : 2395-602X
International Conference on Advanced Materials
Held on 14, 15 December 2017, Organized by Department of Physics,
St. Joseph's College, Trichy, Tamilnadu, India

mechanical strength, wide temperature window in which they are stable in gel phase and biodegradability.

Recently, a new class of materials in which an inorganic/ceramic nanosized filler or high molecular weight organic filler was dispersed into the polymer electrolyte matrix as the third component, seems to be an attractive approach for the formation of nanocomposite polymer electrolyte.

In the present study, the polymeric material used to prepare the nanocomposite thin film is Polyvinyl Alcohol (PVA), and the electrolyte material is Potasssium Iodide (KI) and Iodine (I_2) and also the nanofiller is Zinc Oxide.

In this study, we report on the preparation and characterization of PVA based electrolyte with nanofiller. Polymer nano composite electrolyte system composed of PVA as a host polymer, Potassium iodide and iodine as salt and nano sized ZnO as filler. The FTIR, UV and ionic conduction study for the polymer nanocomposite are investigated.

2. Experimental

2.1. Materials

Poly (Vinyl Alcohol) PVA having molecular weight 1,20,000 and Potassium Iodide (KI), Iodine (I2) and Zinc Oxide (-30 nm) from sigma Aldrich were used. Dimethyl Sulfoxide (DMSO) of Purity> 99% obtained from Merck is used as solvent.

2.2. Preparation of Polymer Electrolyte films

Polymer electrolyte solution containing of 0.5g of PVA was dissolved in Dimethyl Sulfoxide (DMSO). Different amount of KI (0.04, 0.06, 0.08. 0.1g) were then added to the solution. The solution was then heated to 393K and maintained for 30 minute until a viscous like solution was formed. The solution was allowed to cool down to 323K and some iodine (10% of weight) crystals were added with continuous stirring until a homogeneous polymer electrolyte was produced. It was then casted on FTO glass slides as thin films by using dip coating unit (Model: SPEKTRODIP Dip coater. The prepared thin films are stored safely in desiccators for further study.

UV visible spectra (UV-Vis recording spectrophotometer Lambda 35) is taken. The transmission (T%) is measured in the spectral range 250 to 1100 nm at room temperature. The thickness of the thin films are measured by a digital micrometer screw gauge. Electrochemical impedance spectroscopy (EIS) is done to determine the impedance of the electrolytes.

3. Results and Discussion

3.1. FTIR study of PVA, PVA /KI, PVA/KI/I2 and PVA/KI/I2/ZnO

FTIR transmission spectra of Pure PVA (a) PVA/KI/I2 (b) PVA/KI/I2/ZnO (c) are shown in figure 1.

Pure PVA

The spectra of 0.5 g of PVA shows the broad band observed between 3500 and 3200 cm^{-1} refers to the intermolecular hydrogen bonding and O-H stretching vibration. The vibrational band between 3000 cm^{-1} and 2888 cm^{-1} is associated with the C-H asymmetric stretching from alkyl groups and absorption peaks between 1700 cm^{-1} and 1690cm^{-1} which is due to stretching of C-O from acetate group remaining in PVA [11-12].

Coates has mentioned in his paper that stretching hydroxyl (O-H) group occurs between the regions of 3570-3200 cm^{-1}. Coates [13] and Awadia and Agarwal [14] have also mentioned that O-H stretching occurs at 3615-3050 cm^{-1}.

The Peak at 3402 cm^{-1} in pure PVA is ascribed to hydroxyl group (O-H) stretching and it is not due to absorbed solvent. The band corresponding to methylene (CH_2) group asymmetric stretching and aliphatic C-H stretching vibration of pure PVA occurs at about 2997, 2913 cm^{-1} [15-18].

2.3. Characterization

The FTIR (FTIR Spectrophotomer -Jasco 6300) is done for wavenumber range between 400 to

International Journal of
Scientific Research in Science and Technology (IJSRST)
Print ISSN : 2395-6011, Online ISSN : 2395-602X
International Conference on Advanced Materials
Held on 14, 15 December 2017, Organized by Department of Physics,
St. Joseph's College, Trichy, Tamilnadu, India

4000cm^{-1}, to study the functional groups and the interaction between the polymer and electrolyte.

PVA with KI & I2

From the table 1 it is inferred that the O-H stretching vibration at 3402 cm^{-1} (28%) is shifted to 3533 cm^{-1} (24%). For a change in amount of I_2 from 0.002g, 0.004g, 0.006g and 0.008g, the shift in vibrations are 3407, 3560, 3241 and 3509 cm^{-1} are shown in fig 1 b. These changes indicate that I_2 can act as a secondary dopant on PVA, the maximum influence of I_2 is observed at 0.006g of I_2, the O-H peak intensity and position both being affected tremendously at this concentration. This effect begins at 0.004g of I_2, as evident from large number of bands in the region 2596 cm^{-1} to 1911 cm^{-1} at this concentration.

The C-C stretching vibration in PVA located at 1577 cm^{-1} and 1578 cm^{-1} in PVA-KI mixtures are shifted to 1663, 1655, 1660 cm^{-1} on adding I_2 (0.002, 0.004, 0.006 & 0.008g). These changes are attributed to strong interaction of the secondary dopant I_2 on PVA-KI doped polymer matrix. The changes in the C-C stretching & O-H in plane bending mode at 1430 cm^{-1} is shifted from 1436 cm^{-1} to 1418, 1436, 1433 cm^{-1} as I_2 concentration changes. The maximum effect of I_2 on changing polymer configuration is evident at 0.004g of I_2 & 0.006g of I_2 as evident from the initial blue shift (18 cm^{-1} with decreased intensity 27%) then red shift (18 cm^{-1} with increased intensity 7%) then a blue shift 93 cm^{-1} with increased intensity of 16%) as concentration of I2 changes from 0.002, 0.004, 0.006, 0.008g.

The C-O stretching vibration is affected by about 8 cm^{-1} with random changes in the intensity from 26% to 40%, 42% to 21% as I2 concentration increases uniformly by 0.002g. The bending vibrations in the region 950 cm^{-1} - 600 cm^{-1} appear to become broad with increased intensity. The C-I vibration expected at 550 cm^{-1} due to doping by I_2 is not separately found as a band. Hence I_2 should be present in between the polymer chain converting the polymer to the expanded coil arrangement. KI & I_2 may interact to produce I_3^- ions that may bind to O-H groups of polymer, favouring expanded coil networking of PVA-KI_3 skeleton.

PVA-KI-I2-ZnO

FTIR spectra of PVA-KI-I_2 -ZnO is shown in figure 1c. The Spectra of Polymer electrolyte/ Zinc Oxide nanocomposite films clearly exhibit characteristics absorption peaks corresponding to only polymeric groups of Pure PVA with PVA-KI-I_2. That is, the FTIR spectra of the nanocomposite films show no apparent change or shift in the characteristic peaks of PVA with the addition of ZnO nanoparticles. The pure PVA, PVA-KI-I_2 and PVA- KI-I_2-ZnO nano composite films yielded the same FTIR spectra which means a poor chemical interaction between the polymer electrolyte and Zinc oxide occurred or the ZnO characteristics peaks is overlapped by the polymer electrolyte characteristic peaks (Table 1).

ZnO nanoparticles are generally polar and thus strong self – interaction is induced between the nanoparticles. Such a scenario results in hard agglomerates [22]. The high polarity of ZnO nanoparticles impedes the chemical interaction between ZnO and the polymer matrix. This in turn causes no change or shift in the characteristic peak found in the FTIR analysis. The changes in the position, shape, intensity, formation of new peaks and disappearance of peak infers the interaction between PVA, KI, I_2 and ZnO. Therefore it can be concluded that electrolyte is associated in the polymer matrix. IR spectra results prove that the complexation of PVA with KI &I_2 are summarized in Table 1.

International Journal of
Scientific Research in Science and Technology (IJSRST)
Print ISSN : 2395-6011, Online ISSN : 2395-602X
International Conference on Advanced Materials
Held on 14, 15 December 2017, Organized by Department of Physics,
St. Joseph's College, Trichy, Tamilnadu, India

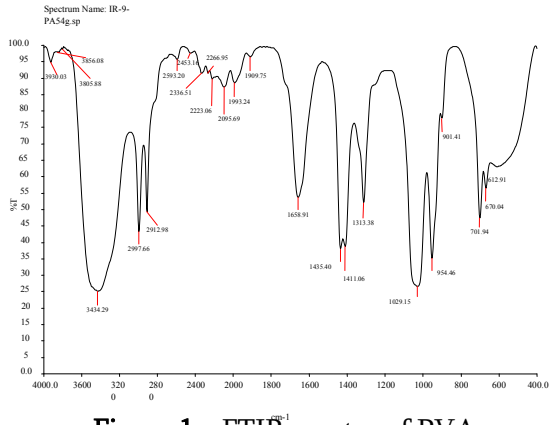

Figure 1a. FTIR spectra of PVA

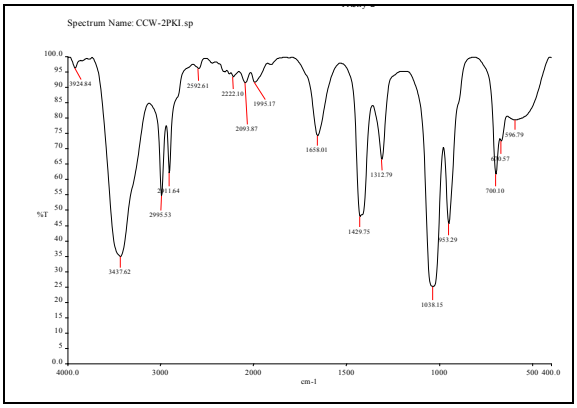

Figure-1b. FTIR spectra of PVA/KI/I2

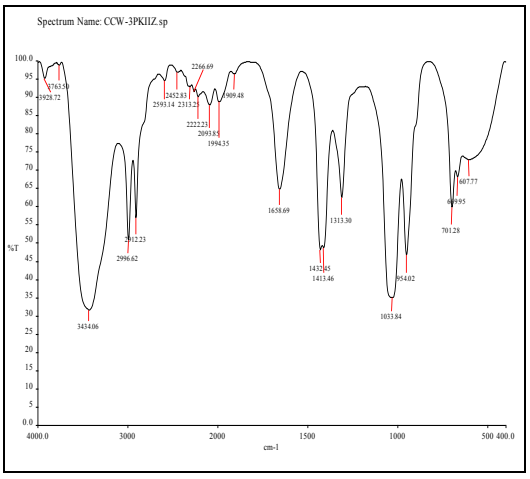

Figure1.c. FTIR spectra of PVA/KI/I2/ZnO

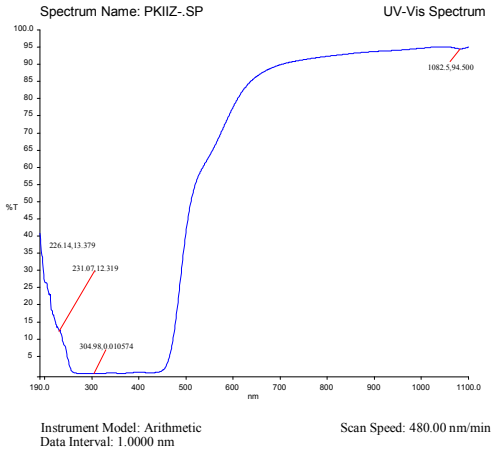

Figure 2. UV-Visible spectra of PVA composite film

3.2. Optical Properties

The Optical Properties of Polymers can be suitably modified by the addition of dopants depending on their reactivity with the host matrix [23]. The optical absorption spectrum is an important tool to obtain optical band gap energy of crystalline and amorphous materials. The fundamental absorption which corresponds to the electron excitation from the valence band to the conduction band can be used to determine the nature and value of the optical band gap. The optical transmittance spectra of composite films of PVA-KI-I2-ZnO is shown in figure 2.

It is inferred that the film possess transmittance of above 80% in the wavelength region $\lambda > 400$ nm and absorption edges lies in the ultraviolet region of the spectrum. The relation between the absorption coefficient (α) and incident photon energy ($h\nu$) can be written as [24, 25].

$$\alpha h\nu = c\,(h\nu - E_0)^m \text{ --------(1)}$$

where c is a constant, E_0 is the optical band gap of the material and the exponent m depends on the type of transition, m is an index which ban be assumed to have values of 1/2, 3/2, 2 and 3 depending on the nature of the electronic transition responsible for absorption, m is equal to 1/2 for allowed direct transitions, 3/2 for direct forbidden transitions, 2 for allowed indirect

International Journal of
Scientific Research in Science and Technology (IJSRST)
Print ISSN : 2395-6011, Online ISSN : 2395-602X
International Conference on Advanced Materials
Held on 14, 15 December 2017, Organized by Department of Physics,
St. Joseph's College, Trichy, Tamilnadu, India

transitions and 3 for forbidden indirect transitions. The indirect band gaps of films E_0 can be obtained from equation (1) by extrapolating linear portion of $(\alpha h\nu)^{1/2}$ to zero absorption in the $(\alpha h\nu)^{1/2}$ Vs hν plot as shown in the figure 3.

The addition of (KI & I_2) & ZnO causes a decrease in E_0 which may be explained on the basis of incorporation of amount of dopant forms charge transfer complexes (CTCS) in the host lattice, which enhance the lower energy transitions leading to the observed change in optical band gap. These CTCs increase the electrical conductivity by providing additional charges in the lattice and hence a decrease of band gap [26, 27]. The values of direct band gaps of the composite films of PVA, KI, I2 and ZnO are around 3.33eV.

Vibrational Peaks and assignments of $(PVA)_{0.5g}$, $(PVA)_{0.5g}$:$(KI)_{0.06g}$, $(PVA)_{0.5g}$:$(KI)_{0.08g}$, $(PVA)_{0.5g}$:$(KI)_{0.08g}$: $(I2)_{0.002g}$, $(PVA)_{0.5g}$: $(KI)_{0.08g}$: $(I2)_{0.004g}$, $(PVA)_{0.5g}$: $(KI)_{0.08g}$: $(I2)_{0.006g}$, $(PVA)_{0.5g}$: $(KI)_{0.08g}$: $(I2)_{0.008g}$, $(PVA)_{0.5g}$: $(KI)_{0.08g}$: $(I2)_{0.006g}$: $(ZnO)_{0.004g}$

		Vibrational Peaks of PVA + KI + I_2 (cm^{-1})						Assignments
Pure $(PVA)_{0.5g}$	**$(PVA)_{0.5g}$ + $(KI)_{0.06g}$**	**$(PVA)_{0.5g}$:$(KI)_{0.08g}$**	**$(PVA)_{0.5g}$: $(KI)_{0.08g}$:$(I2)_{0.002g}$**	**$(PVA)_{0.5g}$: $(KI)_{0.08g}$: $(I2)_{0.004g}$**	**$(PVA)_{0.5g}$: $(KI)_{0.08g}$: $(I2)_{0.006g}$**	**$(PVA)_{0.5g}$: $(KI)_{0.08g}$: $(I2)_{0.008g}$**	**$(PVA)_{0.5g}$: $(KI)_{0.08g}$: $(I2)_{0.006g}$:$(ZnO)_{0.004g}$**	
3927 3402	3928, 3396	3927 3402	3754 3930 3533	3846 3928 3407	3927 3560 3241	3928 3755 3509	3434 3763 3928	O-H stretching
2997 2913	2999, 2915	2997 2913	2997 2914	2998 2916	2997 2913	2997 2913	2912 2996	C-H asymmetric stretching of CH_2
2593	2594	2594	2594	2596	-----	2594		C-H stretching
2452	2332	2452 2321	----	2452 2315	-----	-----	2593	
2222	2222	2222	----	2218	-----	-----	2313 2452	
2097	2096	2096	2091	2096	-----	2093	2093 2222 2266	
1994, 1910	1992	1993, 1909	1989, 1908	1991, 1911	1985	1990 1909	1909 1994	
---	---	1727	1727	1725	---	-----	1658	C-O stretching
1577	1577	1578	1663	1665	1665	1660		C=O stretching and C=C stretching
1405	1403	1403	1436	1418	1436	1433	1432 1413	O-H bending and C-H bending of CH_2
1315	1331	1323	1313	1315	1312	1313		CH-OH bending and CH_3 in plane deformation
1258	1258	1256, 1117	1251	-----	-----	-----	3434 3763 3928	C-H wagging and C-O stretching
---	1119	1034	1033	1029	1037	1031		C-C, C-O stretch and O-H bending
1037	---	955	953	952	953	952		O-H out of plane bending and CH_2 rocking vibrations
954	955	831	-----	-----	----	----		C-C stretching and CH_2 rocking
830	830	758	786,702	-----	791	----		O-H twisting
757	760	699	-----	701	704	701		
700	699	655	-----	----	---	----		

International Journal of
Scientific Research in Science and Technology (IJSRST)
Print ISSN : 2395-6011, Online ISSN : 2395-602X
International Conference on Advanced Materials
Held on 14, 15 December 2017, Organized by Department of Physics,
St. Joseph's College, Trichy, Tamilnadu, India

		Vibrational Peaks of PVA + KI + I_2 (cm^{-1})						Assignments
Pure $(PVA)_{0.5g}$	**$(PVA)_{0.5g}$ + $(KI)_{0.06g}$**	**$(PVA)_{0.5g}$:$(KI)_{0.08g}$**	**$(PVA)_{0.5g}$:$(KI)_{0.08g}$:$(I2)_{0.002g}$**	**$(PVA)_{0.5g}$: $(KI)_{0.08g}$: $(I2)_{0.004g}$**	**$(PVA)_{0.5g}$: $(KI)_{0.08g}$: $(I2)_{0.006g}$**	**$(PVA)_{0.5g}$: $(KI)_{0.08g}$: $(I2)_{0.008g}$**	**$(PVA)_{0.5g}$: $(KI)_{0.08g}$: $(I2)_{0.006g}$:$(ZnO)_{0.004g}$**	
-----	426	596	-----	-----	-----	-----	607	C-I stretching

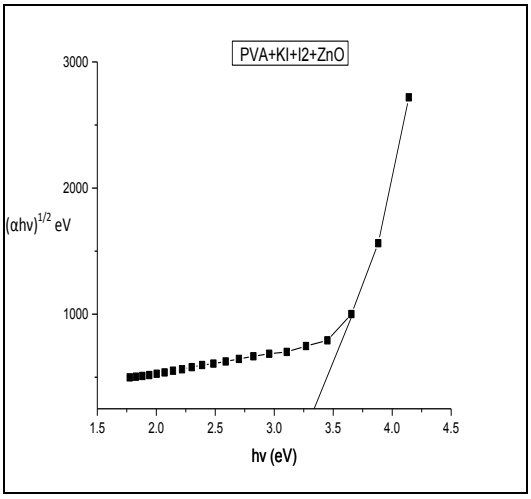

Figure 3 . (hν) vs $(\alpha h\nu)^{1/2}$ plots of PVA composite film

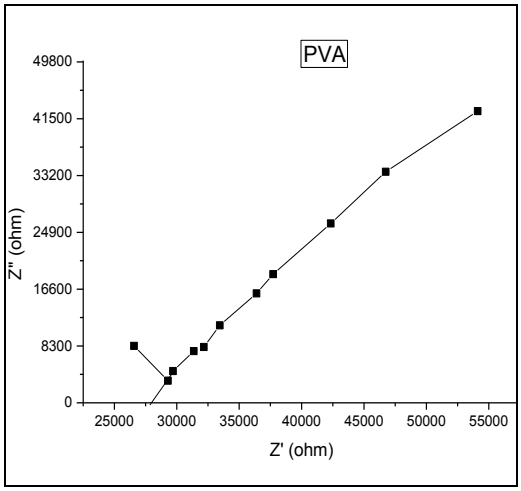

Figure 4 a. Real and imaginary part impedance of pure PVA

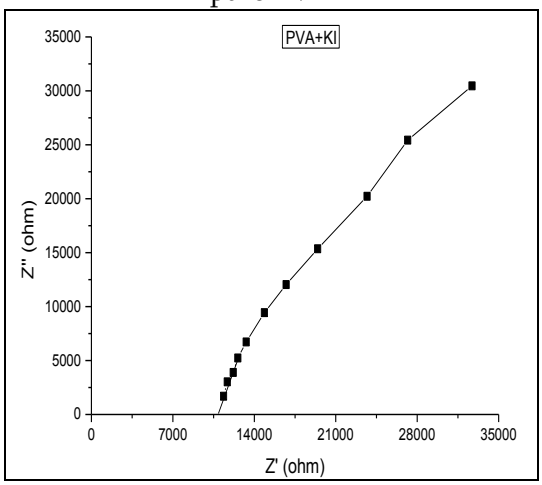

Figure 4 b. Real and imaginary part impedance of PVA+KI

3.3. Conductivity studies

The conductivities of the polymer complexes are calculated from the bulk resistance obtained by the intercepts of the typical impedance curves of (Nyquist Plot) for various films of PVA, PVA+KI+I2 and PVA+KI+I2+ZnO.

The real and imaginary parts are taken along the x axes and y axes which is shown in figure 4 a, b, c respectively. Intercept of the curve on the real axis gives the bulk resistance (R_b) of the sample. The bulk conducties σ are calculated using the relation.

$$\sigma = l / R_b A \text{-----(1)}$$

where l is the thickness, R_b is bulk resistance and A is contact area of the electrolyte film during the experiment.

International Journal of
Scientific Research in Science and Technology (IJSRST)
Print ISSN : 2395-6011, Online ISSN : 2395-602X
International Conference on Advanced Materials
Held on 14, 15 December 2017, Organized by Department of Physics,
St. Joseph's College, Trichy, Tamilnadu, India

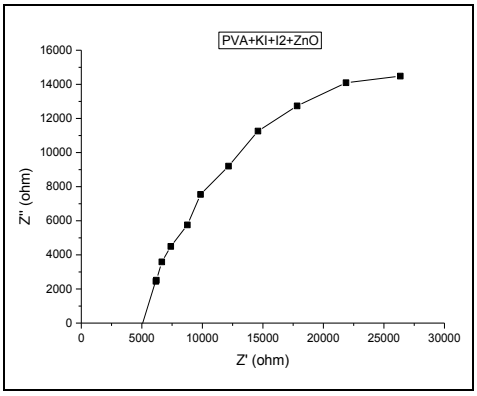

Figure 4 c. Real and imaginary part impedance of PVA+KI+I_2 thin film

The increase in ionic conductivity of polymer electrolyte is due to the reduction in the energy barrier, thereby facilitating the ionic transport. The ionic conductivity of about 0.4115 x10^{-3} S cm^{-1} for pure polymer and 2.307x10^{-3} s cm^{-1} is observed for the composition of PVA + KI + I_2 + ZnO at 25°C which is shown in the table 2.

Table 2.Bulk resistance (Rb), Conductivity (σ), dielectric constant (ε) in the Polymer and Polymer nano composite thin films at 100 Hz

Sample	R_b	σ x 10^{-3} (S cm^{-1})	ε
PVA	27845.23	0.4115	3.7204
PVA+KI	10682.94	1.0727	49.366
PVA+KI+I2	5345.24	2.1439	116.4285
PVA+KI+I2+ZnO	4966.659	2.3074	153.8322

3.4. Dielectric Properties

The study of dielectric relaxation in solid polymer electrolytes is a powerful approach for obtaining information about the characteristics of ionic and molecular interactions. The dielectric parameters associated with relaxation processes are of particular significance in ion conducting polymers where the dielectric constant plays a fundamental role which shows the ability of polymer material to dissolve salts. The dielectric constant is used as an indicator to show the increase in conductivity which is mainly due to an increase in the number density of mobile ions. The frequency-dependent conductivity and dielectric relaxation are both sensitive to the motion of charged species and dipoles of the polymer electrolytes.

The complex dielectric constant of a system ε^* is defined by

$$\varepsilon^* = \varepsilon' - i\,\varepsilon'' \qquad \text{------(2)}$$

Real part of dielectric constant ε' of the material is expressed as $\varepsilon' = cd/\varepsilon_o A$

where c is the parallel capacitance, d is the thickness of the film, ε_o is the permittivity of the free space and A is the area of the contact area of the film. The variation of the real part of the dielectric constant ε' as a function of frequency for the Polymer nanocomposte thin film is shown in figure 5.The observed variation in ε' with frequency could be attributed to the formation of a space charge region at the electrode and electrolyte interface, which is known as the non – Debye type of behaviour where the space charge region with respect to the frequency is explained the interaction of ion diffusion. The material electrode interface polarization of the composites masks the other relaxation processes at low frequencies. On the other hand, with increasing frequency there is no time for charge build-up at the interface because of the increasing rate of reversal of the electric field. Therefore, the polarization due to charge accumulation decreases which leads to the decreases in the value of ε'.

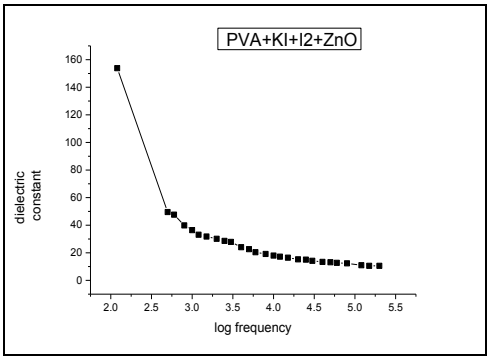

Figure 5. Log frequency Vs dielectric constant of PVA composite film

International Journal of
Scientific Research in Science and Technology (IJSRST)
Print ISSN : 2395-6011, Online ISSN : 2395-602X
International Conference on Advanced Materials
Held on 14, 15 December 2017, Organized by Department of Physics,
St. Joseph's College, Trichy, Tamilnadu, India

Conclusion

The polymer electrolyte based on PVA, KI, I_2 and ZnO thin film is obtained using dip coating technique. FTIR spectra prove that the complexation of PVA with KI, I_2 and Zno. The addition of I_2 and ZnO to the PVA-KI polymer electrolytes has proved to be a convenient method to increase the ionic conductivites of the membranes at $2.307X10^{-3}$ S/cm at ambient temperature. The increase of degree of amorphousity in the polymeric material increases ε' values. The decrease in the optical band gap can be correlated to the formation of the charge transfer complexes within the polymer network on dispersing I_2 in it. From a practical point of view, the polymer based electrolyte is a potential candidate for Dye sensitized solar cells.

Acknowledgement

This work was financially supported by UGC, NO.F MRP-6166/15 (SERO/UGC).

References

[1] Rowe, R.D., Lang, C.M., Chestnut, L.G., Latimer, D., Rae, D., Bernow, S.M., ESEERCO, New York state environmental externalities cost study, New York, Oceana Publications, 1995.

[2] Sastrawan, R., Beier, J. Belledin, U., Hemming, S. Hinsch, A. Kern, R. Vetter, C. Pterat, F.M., Prodi-Schwab, A., Lechner, P., Hoffmann, W., Sol. Energy. Mater. Sol. cells, Vol. 90, 2006, pp. 1680-1691.

[3] Regan, B.O., and Gratzel, M., Nature, Vol. 353, 2006, PP 1680-1691.

[4] Gratzel, M., Nature, Vol. 414, 2001, pp. 338-344.

[5] Gratzel, M., Prog. Photovolt. Res. Appl. Vol. 8, 2000, pp. 171-185.

[6] Nogueira, A.F., Durrant, J.R. and De Paoli, M.A. Adv.Mater.Vol 13, 2001, pp. 826-830.

[7] Stergiopoulos, T., Aravatzis, I.M., Katsaros, G. and Falaras, P., Nano.Lett.,Vol 2, 2002, PP. 1259-1261.

[8] Kubo, W., Kitamura, T., Hanabusa, K., Wada, Y. and Yanagida, S., Chem. Commun. Vol 4, 2002, pp 374-375.

[9] Gebeyehu, D., Brabec, C.J., Sariciftci, N.S., Vaegenugden, D., Kiebooms, R., Vanderzande, D., Kienberger, F., and Schindler, H. Synth. Met. Vol. 125, 2002, pp 279-287.

[10] Abdelkader, K.A., Anwar, Z., and J. Anwar, J.Appl.Polym.Sci, Vol.2, 2006, pp 1146-1151.

[11] El–Hefian, E.A., Nasef, M.M., Yahaya, A.H., E-J Chem 7(4), 2010, 1212–1219

[12] Leones, R., Sentanin, F., Rodrigues, L.C., Marrucho, I.M., Esperança, JMSS, Pawlicka, A., Silva, M.M., PolymLett 6(12), 2012, pp. 1007–1016.

[13] Coates, J., In Meyers RA (ed) Encyclopedia of analyticalchemistry, Wiley, Chichester, 2000, pp 10815–10837.

[14] Awadhia, A., Agrawal, S.L., Solid State Ionics, 2007.

[15] Rajendran, S., Sivakumar, M., Subadevi, R., J. Appl. Polym. Sci, 2003, pp.2790- 2794

[16] Rajendran, S., Sivakumar, M., Subadevi, R., Wu, N.L, Lee, J.Y., J. Appl. Polym. Sci, 2007.

[17] Rajendran, S., Sivakumar, M., Subadevi, R., Mater. Lett, 2004.

[18] Rajendran. S, Sivakumar. M, Subadevi. R (2004) Solid State Ionics 167:335

[19] Reddy, C.V.S., Sharma, A.K., Rao, V.V.R.N., Polymer, Volume 47, 2006, pp 1717-1723.

[20] Jana, S., Thapa, R., Maity, R., Chattopadhyay, K.K., Phys .E. Low. Dimens Syst. Nanostruct. Volume 40, 2008, pp 3121-3126.

[21] El-Khodary, A., Physica, B., Volume 405, 2010, pp 3401-3408.

[22] Chaurasia, V., Chand,N., Bajpai, S.K., Macromoi, F., Pure Appl. Chem. 2010.

[23] Reddy, C.H.V.S., Sharma,A.K., Rao, V.V.R.N., Polymer, 2006, 47(4), pp.1318-1323.

[24] Jana, S., Thapa, R., Maity, R., Chattopadhyay, K.K., Phys. E. Low. Dimens. Syst. Nanostruct 2008, pp.3121-3127.

[25] Khodary. E.L.A., Physica –B, 2010, pp. 3401-3408.

[26] Raja, V., Sharm, A.K., Rao, V.V.R.N., Mater. Lett. 2003, pp.4678- 83.

[27] Mahendia, S., Tomar, A.K., Kumar, S.H., Mater. Sci. Eng. B. 2011, pp. 530-534.

International Journal of
Scientific Research in Science and Technology (IJSRST)
Print ISSN : 2395-6011, Online ISSN : 2395-602X
International Conference on Advanced Materials
Held on 14, 15 December 2017, Organized by Department of Physics,
St. Joseph's College, Trichy, Tamilnadu, India

Lattice Dynamical Investigation on the Diffusion of Hydrogen Isotopes in $HfTi_2$

[a]Lakshmi Balasubramanian, [b]Arasavel Thangavel, [c]Antony Muthaiyan,
[b]Lawrence Nallathambi*

[a]Department of Physics, Vivekanandha College of Arts & Sciences for Women,
Namakkal- Tamilnadu - 637 205, India.

[b]Department of Physics, St. Joseph's College (Autonomous), Tiruchirappalli, 620 002, India

[c]Department of Physics, Arul Anandar College, Karumathur, Madurai, 625514, India

Corresponding Author: nlawdines@yahoo.co.in

Abstract

The Laves phases structure AB_2 type intermetallic compound $HfTi_2$ is accomplished of storing hydrogen and its isotopes. The eigen values and eigen vectors of the host system are computed using a Born-von Karman formalism. The mean square displacements of hydrogen isotope and its surrounding host crystal atoms are computed using scattering matrix formalism and green function method. Diffusion parameters of hydrogen isotopes are estimated using reaction coordinate approach incorporating the scattering matrix formalism and green function technique. The theoretically calculated results are comparable with the existing experimental results.

Keywords: $HfTi_2$, eigen values, eigen vectors, mean square displacement, diffusion parameters, hydrogen isotopes, green function technique, scattering matrix formalism and reaction coordinates

1. INTRODUCTION

$HfTi_2$ belongs to AB_2 type intermetallic compound, which is capable of storing hydrogen and its isotopes in its interstitial positions. $HfTi_2$ has Laves phase structure having AB_2 type lattice in which A sub-lattice is cubic whereas B sub-lattice is tetrahedral sharing one [1]. The quadruple defect formation as well as the vapour pressure as function of temperature have been described in terms of Ising model using the Bragg Williams approximation in Laves phases [2]. The location of hydrogen atoms in the compound $HfTi_2H_x$ is determined [3] and the hydrogen occupancies are two types with tetrahedral positions of 32e sites (AB_2) and 96g sites (A_2B_2) in $HfTi_2$. In this compound at x=4.0, the e site positions are 82.5% and g site positions are only 5.83% occupied and at x=4.5, the e site position are 67.5% and g site positions are only 15% are filled. Moreover, the hydrogen stabilized cubic Laves phases (λ phase) is observed at x=4.0. The hydrogen diffusion parameters in the hydrogen stabilized Laves phase compound C15 – $HfTi_2H_x$ have been estimated using a pulsed field gradient Nuclear Magnetic Resonance method [4]. Using pulsed field gradient NMR technique, two types of jump mechanism were observed in C15 – $HfTi_2H_x$ on different time scales: long range diffusion from e site to e site through intermediate g-site and a fast localized motion [5]. Using the effective pair potentials for Ti, Zr, Hf, V, Nb, Ta and their hydrides from the first principle by inverting the ab initio inverted pair potentials, the elastic constants, bulk modulus and thermal properties of these hydrides are estimated [6]. Through X-ray diffraction study, it is observed that there is formation of a single hydrogen stabilized λ-phase in $HfTi_2H_x$ at x=4.0 and 4.5 [7]. Though there are

International Journal of
Scientific Research in Science and Technology (IJSRST)
Print ISSN : 2395-6011, Online ISSN : 2395-602X
International Conference on Advanced Materials
Held on 14, 15 December 2017, Organized by Department of Physics,
St. Joseph's College, Trichy, Tamilnadu, India

few experimental studies dealing with the diffusion of hydrogen in this intermetallic compound, there are no theoretical studies except hydrogen diffusion in nanostructured $HfTi_2$ using green's function approach in this direction [8]. Hence, in this study, theoretically calculated values of defect modes, Debye Waller factor of host atoms surrounding hydrogen and the diffusion parameter of hydrogen isotopes are reported.

2. METHOD OF CALCULATION

The diffusion parameters of ${}_1^1H$, ${}_1^2H$ and ${}_1^3H$ in this system are estimated using a green's function approach considering scattering matrix formalism and reaction coordinate method. To calculate the green's function values of the host material $HfTi_2$, its complete phonon spectrum is needed. The phonon spectrum of $HfTi_2$ is estimated using Born Von Karman formalism considering interaction up to six neighbors.

The force constant parameters used for the estimation of phonon spectrum of $HfTi_2$ are calculated using a Long-Range Empirical potential with parameters [9 & 10] and are arranged in table-1.

Table 1. Force constant values in 10^4 dynes cm^{-2}

A_{11}=-0.1868	A_{21}, A_{31}=4.5629	A_{23}=-0.0672	A_{31} = 4.5629	A_{41}, A_{61} 4.535	A_{51} =4.535
B_{11} = -0.1868	B_{21}=-1.4109	B_{23}=-0.093	B_{31} = -1.4109	B_{41},B_{61}=4.535	B_{51} =4.535
C_{11} = 0.1526	C_{21}=0.5041	C_{23}=-0.033	C_{31} = 0.5041	C_{41},C_{61}=-0.991	C_{51} = -0.9918
A_{12}=-0 .1239	D_{21}=0.5041	D_{23} =0.0085	D_{31} = 0.5041	A_{42},A_{62}=-0.088	A_{52} = -0.2193
B_{12} = 0.1795	A_{22} = -0.6177	E_{23} = -0.0046	A_{32} = -6.177	B_{42},B_{62}= -0.088	B_{52} =-0.01582
A_{13} =-0.0026	B_{22}= -0.1574	E_{33} = -0.0046	B_{32} = -0.1574	C_{42},C_{62}=0.0343	C_{52} = 0.097
B_{13} = -0.0026	C_{22}= 0.1363	F_{23} = -0.0041	C_{32} = 0.1363	A_{43},A_{63}=-0.099	D_{52} = 0.176
C_{13} = 0.0005	D_{22}=0.1363	B_{33} = -0.093	D_{32} = 0.1363	B_{43},B_{63}=0.0381	A_{53} = -0.0992
A_{33} = -0.0672	D_{43},D_{63} =0.0275	C_{33} = 0.033	D_{33} = 0.0085	C_{43},c_{63}= 0.0153	B_{53} =0.0381
	F_{33} = -0.0041		D_{53} = 0.0152		C_{53} = 0.0275

In order to calculate the defect modes and amplitudes of vibration of host crystal atoms and the defects, which involved in the estimation of reaction coordinates, one has to calculate the green's function values using the equation [11].

$$G_{\alpha\beta}\begin{pmatrix} l & l' \\ k & k' \end{pmatrix}:\omega^2\Big) = \frac{1}{N\sqrt{m_k m_{k'}}}\sum_{qj}\frac{e_\alpha(k\,|\,\vec{q}j)\,e_\beta(\kappa\,|\,\vec{q}j)}{\omega^2_{\max}}\exp\left[i\vec{q}.(\kappa(l)-\vec{\kappa}(l'))\right] \quad \ldots (1)$$

where $\omega_{max}$is the maximum frequency among all normal modes of the crystal.

The defect modes are estimated using the green's function values by solving the secular equation,

$$\Delta(\omega^2) = |I - g(\delta l + a\gamma a^T)| = 0 \quad \ldots (2)$$

where I, g, a, δl and γ respectively are the unit, green's function, change in dynamical, interaction of hydrogen with neighbors and interstitial green's function matrices. The displacement of neighboring atoms to the hydrogen isotope is computed using the equation

$$u_1 = \{I + g(\delta l + a\gamma a^T)\,[I - g(\delta l + a\gamma a^T)]^{-1} \quad \ldots (3)$$

where $u_\alpha\begin{pmatrix} l \\ k \end{pmatrix}:\vec{q}j\Big) = \left\{\frac{\hbar}{2Nm_k\omega_{qj}}\right\}^{\frac{1}{2}} e_\alpha(\kappa,qj)\exp\left[i\vec{q}.\vec{r}\begin{pmatrix} l \\ k \end{pmatrix}\right]$

with ω_{qj} and e_α(k, qj) as phonon frequencies and eigen vectors respectively.

The displacement of hydrogen isotope is computed using the equation

$$\xi = -\gamma a^T u_1 \quad \ldots (4)$$

In the jump process of hydrogen isotope, the jump is initiated as a result of fluctuation in the energy and momentum of the hydrogen isotope assisted by the phonon created by lattice vibrations. The reaction coordinate is estimated using the equation

$$\chi = \left(\xi_d - \frac{1}{m'}\sum_j \vec{u}_j.\vec{x}\right) \quad \ldots (5)$$

where $\vec{\xi}_d$ and $\vec{u}_j$ are displacements of diffusing atom and host atoms respectively.

Using the reaction coordinate, the jump frequency is computed using the equation [12 & 13]

$$\Gamma = \frac{\left(\sum_{\vec{q}\kappa}\left[\omega^2(\vec{q}\kappa)\,|\,\chi(\vec{q},\kappa)\,|\right]\right)}{\left(\sum_{\vec{q}\kappa}|\,\chi(\vec{q},\kappa)\,|\right)^{\frac{1}{2}}}\exp\left[-\chi_2^c/\sum_{\vec{q}}|\chi(\vec{q},\kappa)|\right] \quad \ldots (6)$$

From this equation, Γ_0 is identified as

International Journal of
Scientific Research in Science and Technology (IJSRST)
Print ISSN : 2395-6011, Online ISSN : 2395-602X
International Conference on Advanced Materials
Held on 14, 15 December 2017, Organized by Department of Physics,
St. Joseph's College, Trichy, Tamilnadu, India

$$\Gamma_0 = \frac{\left(\sum_{(\vec{q},\lambda)} \left[\omega^2(\vec{q},\lambda)\,|\,\chi(\vec{q},\lambda)\,|\right]^2\right)^{\frac{1}{2}}}{\left(\sum_{(\vec{q},\lambda)} |\,\chi(\vec{q},\lambda)\,|\right)}$$

Using the Golden rule

$$\Gamma = \Gamma_0 \exp\left[-\frac{E_a}{k_B T}\right] \qquad \ldots (7)$$

the activation energy E_a is calculated.

The pre-exponential factor of diffusion constant D_0 is calculated using the formula

$$D_0 = \frac{\Gamma_0 l^2}{6} m^2 s^{-1} \qquad \ldots (8)$$

3. RESULTS AND DISCUSSION

a) Eigen values and eigen vectors

The computed force constant values have been substituted in the dynamical matrix to calculate eigen values and eigen vectors by diagonalising the dynamical matrix for 84 wave vector points obtained by uniformly dividing the Brillouin zone [14].

b) Mean Square Displacement

The presence of interstitial hydrogen alters the displacement of nearby host atoms. The mean square displacement values for different temperatures are calculated and are compared with defect free situation as shown in fig. 1. It increases with temperature as expected. More over the MSD values of atoms surrounding ${}_1^1H$, ${}_1^2H$ and ${}_1^3H$ defects are decreased drastically. This may be due to the creation of resonance modes. During the resonance nodes of vibration, the vibrational amplitude of hydrogen isotope is expected to be high with the expense of that of the surrounding atoms.

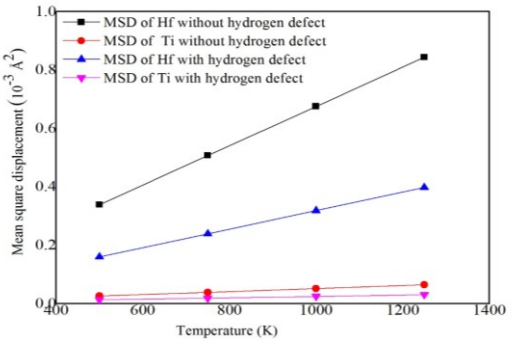

Figure 1(a). Mean square displacement of atoms surrounding the H-defect

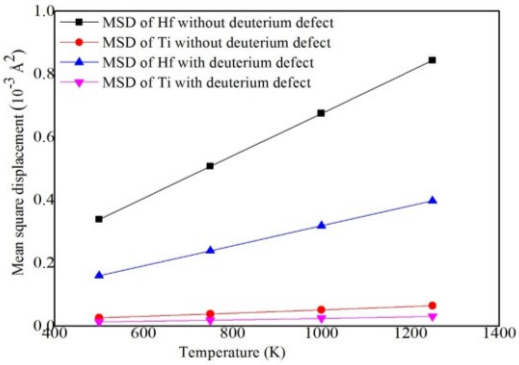

Figure 1 (b). Mean square displacement of atoms surrounding the ${}_1H^{2-}$ defect

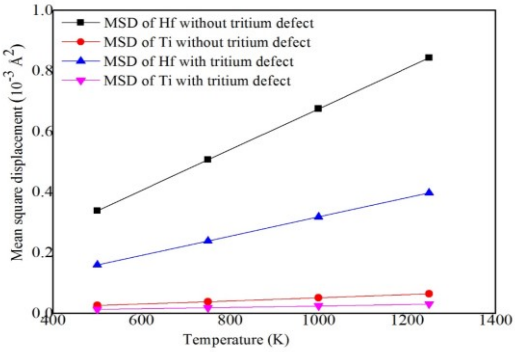

Figure 1(c). Mean square displacement of atoms surrounding the ${}_1H^{3}$ -defect

c) Jump frequency values

Using green's function values and the change in dynamical matrix due to the presence of hydrogen and their isotopes (H, D and T) the jump frequency values were calculated using reaction coordinate

International Journal of
Scientific Research in Science and Technology (IJSRST)
Print ISSN : 2395-6011, Online ISSN : 2395-602X
International Conference on Advanced Materials
Held on 14, 15 December 2017, Organized by Department of Physics,
St. Joseph's College, Trichy, Tamilnadu, India

technique for different temperatures and these values are given in table 2. From this table, it is clear that jump frequency values increase with increase in temperature as expected.

Table 2. Jump frequency values at different temperature

Isotopes	Temperature (K)	Jump frequency Γ sec^{-1}
$_1H^1$	500	3.05E+11
	750	1.37E+12
	1000	2.93E+12
	1250	4.62E+12
$_1H^2$	500	2.83E+11
	750	1.31E+12
	1000	2.82E+12
	1250	4.48E+12
$_1H^3$	500	2.76E+11
	750	1.29E+12
	1000	2.79E+12
	1250	4.44E+12

d) Diffusion parameters

The lnΓ versus reciprocal of temperature curve is as shown in fig. 2, which was found to be a straight line. From the intercept and slope, the pre exponential value of jump frequency Γ_0 and activation energy Ea values are determined. The D_0 value was calculated using the Eqn.

$$D_0 = \frac{\Gamma_0 l^2}{6} \quad \ldots (4.1)$$

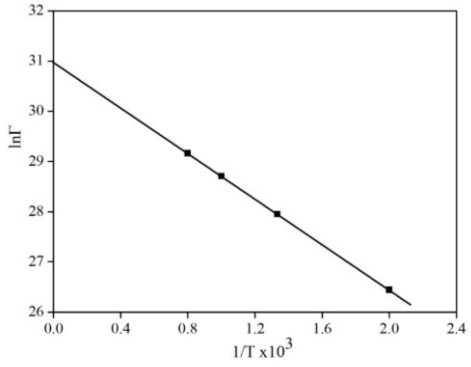

Figure 2 (a). Logarithmic of Jump frequency vs. 1/T for $_1H^1$ in $HfTi_2$

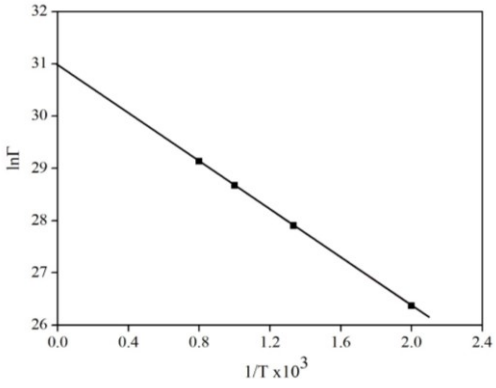

Figure 2 (b). Logarithmic of Jump frequency vs. 1/T for $_1H^2$ in $HfTi_2$

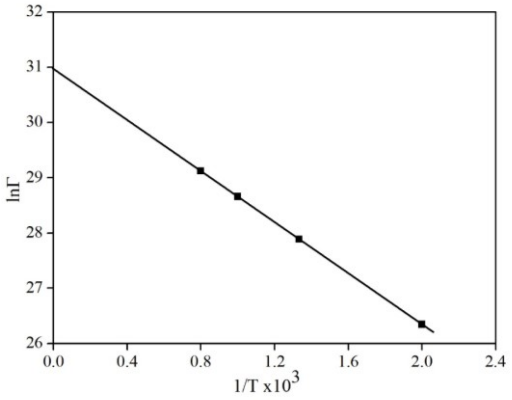

Figure 2 (c). Logarithmic of Jump frequency vs. 1/T for $_1H^3$ in $HfTi_2$

Our results are compared with that computed employing Quasielastic neutron scattering [3] and NMR studies [4] [5] in table 3. Our result is found to be comparable with the experimental results. Since the activation energy is very low of the order of 226 meV, there is no formation of permanent hydrides. As a consequence, it is easy to retrieve the hydrogen isotope back. Hence this system is a good candidate to store hydrogen and its isotopes.

International Journal of
Scientific Research in Science and Technology (IJSRST)
Print ISSN : 2395-6011, Online ISSN : 2395-602X
International Conference on Advanced Materials
Held on 14, 15 December 2017, Organized by Department of Physics,
St. Joseph's College, Trichy, Tamilnadu, India

Table 3. Experimental values of diffusion parameters of H in $HfTi_2$

Diffusing atom	Pre-exponential factor D_0 (10^{-8} m^2 sec^{-1})	Activation energy E_a (meV)	Reference
$_1H^1$	6.7081	226.4	This study
$_1H^2$		230.1	
$_1H^3$		231.3	
$_1H^1$	6.291	195	[8]
$_1H^1$	4.6 ± 1.6	230 ± 10	[3]
$_1H^1$	1.2 ± 0.3	210 ± 10	[4]
$_1H^1$	0.8	210	[5]

A comparative study is made as shown in table 4. Last two columns show that, D_1H^2/D_1H^1 and $D_1H^3/D_{1H}{}^1$ values are found to be less than one as expected. This result is in support for the application towards isotope separation.

Table 4. Comparative study

Temp. (K)	D_1H^1	D_1H^2	D_1H^3	Ratio D_1H^2/D_1H^1	Ratio $D_1H^3/D_{1H}{}^1$
500	9.96022E-31	4.21882E-31	3.42328E-31	0.42356704	0.343695221
750	4.0524E-23	2.28557E-23	1.98836E-23	0.564003032	0.490661892
1000	2.58484E-19	1.68227E-19	1.51538E-19	0.650820282	0.586255252
1250	4.95755E-17	3.5159E-17	3.23398E-17	0.709200222	0.652333073

4. CONCLUSION

A Born-von Karman formalism has been used to work out the eigen values and eigen vectors of the cubic Laves phased compound $HfTi_2$. The localized vibrational modes have been worked out with hydrogen atoms as an interstitial defect in this system. A green's function technique and scattering matrix formalism are used to work out the MSD values of hydrogen isotopes ($_1H^1$, $_1H^2$ and $_1H^3$) and its neighbors at 500, 750, 1000 and 1250 K temperatures. A reaction coordinate technique has been used to work out the diffusion parameters of hydrogen isotopes ($_1H^1$, $_1H^2$ and $_1H^3$) in $HfTi_2$. Estimated values are found to be in good agreement with the existing experimental results.

References

[1] Johnston, R.L. and R. Hoffmann, 1992. Structure bonding relationships in laves phases. Zeitschrift Anorganische Allgemeine Chemie, **616**: 105-120.

[2] Modder, I.W. and H. Bakker, 1997. On quadruple defect formation in C15 laves phases. Phys. Status Solidi B, **199**: 369-378.

[3] Kozhanov, V.N., A.V. Skripov and E.P. Romanov, 1998. Hydrogen in $HfTi_2$ alloy: A formation of the hydrogen stabilized $HfTi_2H_x$ phase with the C15 types host lattice. J.s Alloys Compd., **269**, 141-143.

[4] Eberle, U., G. Majer, A.V. Skripov and V.N. Kozhanov 2002. NMR studies of hydrogen diffusion in the hydrogen–stabilized laves phases compound C_{15}-$HfTi_2H_x$ J. Phys.: Condens. Matter, **14**:153-164.

[5] Majer, G., U. Eberle, F. Kimmerle, E.Stanik and S. Orimo, 2003. Hydrogen diffusion in metallic and nanostructured materials. Phys. B.: Condens. Matter, **328**: 81-89.

[6] Liu, S.J., S.Q. Shi, H. Huang and C.H. Woo, 2002. Interatomic potentials and atomistic calculations of some metal hydride systems. J. Alloys Compd., **330-332**: 64-69.

[7] Skripov, A.V., J. Combet, H. Grimm, R. Hempelmann and V.N. Kozhanov, 2000. Quasielastic neutron scattering study of H motion in the hydrogen – stabilized C15 type phases $HfTi_2H_x$ and $ZrTi_2H_x$, J. Phys.: Condens. Matter, **12**:3313-3324.

[8] Antony, M., N. Lawrence and R.J.B. Balaguru, 2014. Hydrogen diffusion in nanostructured $HfTi_2$: A green's function approach. Asian J. Applied Sci., **7(8)**: 705-712.

[9] Liang, S.H., Y. Dai, J.H. Li and B.X. Liu, 2010. Glass forming region of Cu-TI-HF ternary metal system derived from the n-body potential through molecular dynamics simulation. J. Phys. Chem. B, **114**: 9540-9545.

[10] Cui, Y., J. Dai and B. Liu, 2010. Proposed truncated CU-HF tight-binding potential to

study the crystal-to-amorphous phase transition. J. Applied Phys., Vol. **108**. 10.1063/1.3477191.

[11] Maradudin, A.A., E.W. Montroll, C.H. Weiss and I.P. Ipatova, 1971. Theory of Lattice Dynamics in the Harmonic Approximation. Academic Press, New York, Page: 708.

[12] Kac, M. (1943). On the distribution of values of trigonometric sums with linearly independent frequencies. Am. J. Math. **65**, 609.

[13] Slater, N.B., 1959. Theory of Unimolecular Reactions. Cornell University Press, New York, Pages: 230.

[14] Balaguru, R.J.B., N. Lawrence and S.A.C Raj, 2002. Lattice Instability of 2H-$TaSe_2$. Int. J. Mod. Phys. B, **16**: 4111-4125.

Organised By

Department of Physics
School of Physical Sciences
St. Joseph's College (Autonomous),
Tiruchirappalli-620 002
Tamilnadu, India

Publisher

Technoscience Academy

Website : www.technoscienceacademy.com
Email: info@technoscienceacademy.com